29th Aerospace Mechanisms Symposium

Dr. W. C. Schneider, Editor
Lyndon B. Johnson Space Center
Houston, Texas

*Proceedings of a symposium held at the South Shore
Harbour Resort and Conference Center, League City,
Texas, and co-sponsored by NASA Johnson Space Center
and Lockheed Missiles and Space Company, Inc.
May 17-19, 1995.*

1995

PREFACE

The Aerospace Mechanisms Symposium (AMS) provides a unique forum for those activities in the design, production and use of aerospace mechanisms. A major focus is the reporting of problems and solutions associated with the development and flight certification of new mechanisms. The National Aeronautics and Space Administration and Lockheed Missiles & Space Company, Inc. share responsibility for organizing the AMS. Now in its 29th year, the AMS continues to be well attended, attracting participants from both the U.S. and abroad.

The 29th AMS, hosted by the NASA Johnson Space Center, was held in Houston on May 17, 1995. During these three days, 24 papers and 8 posters were presented. Topics included robotics, deployment mechanisms, bearings, actuators, scanners, boom and antenna release, and test equipment. Hardware displays during the poster session gave attendees an opportunity to meet with developers of current and future mechanisms components.

The high quality of this symposium is due the efforts of many people and their efforts are gratefully acknowledged. This extends to the voluntary members of the symposium organizing committee representing the 8 NASA field centers, LMSC, and members from the European Space Agency. Also to be thanked are the session chairs, the authors, and particularly the personnel at NASA JSC responsible for the symposium arrangements and the publication of these proceedings. Thank you goes to the symposium executive committee at LMSC who are responsible for the year-to-year management of the AMS, including paper processing and preparation of the program.

The use of trade names of manufacturers in this publication does not constitute an official endorsement of such products or manufacturers, either expressed or implied, by the National Aeronautics and Space Administration.

CONTENTS

SESSION 4:   ACTUATORS
Session Chair: Frank Cepollina

SESSION 5:   BOOMS/SOLAR ARRAYS
Session Chair: Kornel Nagy

SESSION 6:   BEARINGS/SCANNERS
Session Chair: Rick Abramowitz

SESSION 7: MECHANISMS
Session Chair: Rob Cohen

Session 1: Robotics

Session Chair: Andre Borrien

Design, Testing and Evaluation of Latching End Effector

B. Walker* and R. Vandersluis*

Abstract

The Latching End Effector (LEE) forms part of the Space Station Remote Manipulator System (SSRMS) for which Spar Aerospace Ltd, Space Systems Division is the prime contractor. The design, testing and performance evaluation of the Latching End Effector mechanisms is the subject of this paper focusing on a) ambient, thermal and vibration testing b) snare/rigidize performance testing and interaction during payload acquisition and c) latch/umbilical test results and performance.

Introduction

The Latching End Effector is a descendant of Shuttle Remote Manipulator System End Effector. The Space Station Arm required substantial increases in the life, load carrying capabilities, maintainability and reliability. The end effector design will a) provide compatibility with existing grapple fixture interfaces, b) provide a high-tolerance-to-misalignment payload interface and c) provide a stiff, backlash free interface with high load carrying capability.

Lee Design Overview

The complete Latching End Effector assembly (Figure 1) is an orbit replaceable unit. The Latching End Effector consists of the snare and rigidize subassembly inside the shell (Figure 2), and four latch/umbilical subassemblies outside the shell (Figure 3). The snare and rigidize mechanisms provides the capability to reduce large interface misalignments of free flying objects to the very accurate positioning required for latching. The latch mechanism was added to withstand large moment loads required by the larger payloads anticipated by Space Station use. An umbilical mechanism was built into the latch to provide an electrical connection for power and data across the end effector/payload interface.

Latching End Effector Mechanism Design & Development

The Latching End Effector design requirements for the space station were as follows:
    a) compatibility with existing grapple fixtures as well as new Power Data
        Grapple Fixtures for the Space Station.
    b) 30 second free flyer capture time (snare/rigidize and latch).
    c) increased on-orbit life (without maintenance).
    d) increased redundancy.
    e) stiff, backlash free interface.
    f) improved maintainability by on orbit replaceability of the entire end effector.

---

* Spar Aerospace Ltd, Space Systems Division, Brampton, Ontario, Canada

Snare/ Rigidize Mechanism

The snare mechanism motor module is mounted on the inner carriage. The motor drives through a three stage planetary gearbox to a segment gear mounted on a rotating ring (Figures 2 and 4) to which one end of each of the three snare cables are mounted. As the motor/gearbox drives the rotating ring with respect to the fixed ring the snare cables contact with the grapple shaft and wrap around the probe centering it (Figure 3). Once a successful snare has been completed, the snare brake is engaged and the rigidize mechanism can now be actuated.

The rigidize mechanism motor module, mounted on the rear outer shell and drives a two stage planetary gearbox (Figure 2). A ballscrew drives directly from the gearbox output mounted centrally in the rear outer shell. As the ballscrew rotates, the ballnut mounted on the inner carriage translates, moving the carriage along three sets of linear bushings mounted to the inside of the shell. A load cell located under the ballscrew measures the rigidize load.

After completion of the snare operation, the rigidize mechanism is commanded to retract the carriage. Initial carriage retraction (Figure 4) cause the snare cables to slide along the grapple shaft until the underside of the shaft end grapple cam contacted. The carriage continues to retract drawing the end effector and grapple fixture together until the three large grapple fixture cams align, first removing pitch and yaw misalignments (Figure 4), followed by the grapple cam/end effector pocket engagement to remove roll misalignments. Finally the two curvic couplings at the interface engage to remove backlash and provide precise alignment with the rigidize mechanism being preloaded to 4893 N (1100 lb).

Latch/Umbilical Mechanism

Each of the four latches consists of the parts shown in Figure 5. The tension bracket support and the ball nut pinion housing are stationary parts fixed to the shell. Four ball nut pinions driven by a ring gear on the outside of the shell (Figure 2), allows a single motor gearbox package to simultaneously drive the latches, maintaining the synchronization established at assembly.

The motor drives the ball screws moving the electrical connector carriers toward the grapple fixture in the sequence shown by Figures 6 through 9. The connector carrier rides on linear bearings (Figure 9) moving along tracks fixed to the shell.

Initially the sequencing rollers roll up the straight portion of the sequencing cams, holding the latch levers in their angled position. In this position, the latch deployment rollers are held captive by the levers causing the tension bracket to be pulled along with the connector carriers.

At the deployed position of the latch, the sequencing cam no longer restricts the movement of the levers. The disc spring stack's outer preload bushing has contacted the underside of the tension bracket support, preventing the tension bracket from moving any further unless the disc spring stack is compressed.

Continued movement causes the latch levers to spread, achieving the initial contact position (Figure 8). As the grapple fixture rollers continue to move up, the grapple fixture ramp, the pivot points on the latch lever (and thus the tension bracket) move up by about 3 mm. This movement compresses the belleville springs to result in a load between 16013 to 17125 N (3600 to 3850 lb) at each of the four latches. This 64054 N (14,400 lb) total load is a significant improvement over the 4894 N (1100 lb) rigidize load. This load applied at the curvic coupling teeth (Figure 1) at end effector/grapple fixture allows the capture and movement of large payloads without backlash or separation.

In the latched/connector mated position deployment rollers are on a "flat" portion of the latch lever (Figure 2). As the connector carrier moves between the connector mated position and the latched position (Figure 9) the compression of the disc spring stack remains constant. As the spring stack is not being compressed, the ball screw force required to move between the connector mated position and the latched position involves only overcoming bearing friction and the force to mate or demate the connector(about 222-445 N (50 to 100 lb) total)

The reverse delatch sequence is such that the disc spring stack is relaxing rather than being compressed. Since the disc springs are relaxing the retraction forces are substantially lower than the engagement forces.

Engineering Model Testing

In 1993, testing of the latching end effector and power data grapple fixture was carried out at ambient (room temperature) conditions and at hot and cold temperature extremes (representative of operating extremes in space). These tests were conducted after vibration testing (which simulated launch conditions), and after subjecting the end effector latched to the grapple fixture to structural loading (representative of the worst case loading conditions expected during operation and launch) and including representative simulation of capture envelope.

Test Rig Operation/Description

The Performance Test Rig design and geometry (Figure 10) articulates to enable the rig to simulate a pitch/yaw/roll misaligned end effector/grapple fixture interface. The test rig contains a data acquisition capability for real time monitoring of all mechanism parameters, the applied and reacted loads, and test rig position (in 6 Degrees of Freedom) during various misalignment simulations. The test rig also provides representative worst external joint load during capture.

Data Acquisition

Raw data was recorded at 50 millisecond intervals, in ASCII format. The forces in the mechanism; the motor current; the open or closed status of microswitches, a count of motor revolutions (from the motor resolver) multiplied by appropriate gear ratios so as to represent travel of the mechanism were measured as a function of time. The software also calculated the speed of the mechanism over the 50 millisecond intervals.

Data Reduction

Initial tests were run at a slow speed requiring up to 80 seconds for a latch/delatch resulting in 28,800 numbers for a single test. A dozen tests run at this speed resulted in 345,600 numbers. This amount of data becomes overwhelming if not summarized.

For the latch/umbilical results, computer spreadsheet macro analysis was used to determine the average value, and maximum and minimum value for each of the recorded parameters over each one tenth inch travel increment for each individual test. These values were then attributed to the average travel over the increment. As long as the extremes (max and min) and the average values compared favorably to the expected theoretical results the individual test run was considered to be successful.

The range of values of the seven latch ambient tests at slow speed was small and showed no significant variations. These test runs were considered as a consistent stable homogeneous group of results. Because of this, further summarization of all the ambient test at the slow speed was done. The overall average, overall maximum and overall minimum values of the variables in these seven test runs (Figure 15) became the criteria representative of "normal and expected" results; to be used to judge further test results against.

In the case of snare/rigidize mechanisms, performance is more directly influenced by the overall effect of misalignment loads during capture and hence the same detailed analysis is not required.

Normal and Expected Results

Having established a criteria for "normal and expected" results, it was found that changing the speed of latching from 40 seconds, to the normal operating speed requiring 6 seconds to latch had no significant effect. Similarly the comparison of slow speed for snare and rigidize to fast speed had no significant effect. Ambient test runs after the vibration tests, structural load tests also showed normal results.

Theoretical Results Compared to Test Results

Motor current is one of the more important test variables because from it the mechanism output force can be calculated. This is done by multiplying the current by the drive train gear ratio, by the drive train efficiencies assumed during analysis, by other appropriate constants which include the mechanism motor torque constant. The theoretical ball screw force was calculated based on the analysis of the equilibrium between (a) the ball screw force, (b) the sliding and rolling friction forces in the bearings, rollers and mechanism components, and (c) the forces in the belleville springs and structure as they were compressed.

For the snare mechanism, the determination of snare drive train torque must be translated from the gearbox to the cables mounted on the rotating ring as they are

wrapped around the probe thereby compress belleville springs mounted on the cable ends.

Snare/Rigidize Results

Snare
The snare mechanism ambient performance testing consisted of a series of runs from maximum grapple probe misalignment to fully aligned. The worst case capture scenario was with a radial offset was 4 inches, a pitch/yaw 15 degree misalignment and with a side load of 156 N (35 lb) (derived from the theoretical force to back drive the closest arm joint). A significant number of runs were performed under each misalignment case in order to verify performance of the mechanism. This data demonstrated mechanism repeatability under the various conditions.

Snare ambient performance is summarized in Figure 11. The highest current peaks occur at 0 and 75 degrees of rotation of the rotating ring. These high currrents at the start and finish of the snare represent the acceleration and deceleration of the high rotating inertia of the rotating ring. This motor load must then be accelerated (under closed loop control) to the maximum speed (300 $^{rad}/_s$), drive the snare cables to near end of travel (75 degrees) and decelerate the drive train within the maximum time of 3 seconds. The deceleration peak at 75 degrees is 0.5 amps lower than the acceleration peak, because of the cables tensioning and the 156 N (35 lb) external load, both act tend to slow the motor down, there by reducing the servo braking the motor must deliver.

The next load peak (Figure 11) is at 30 degrees and occurs at the maximum misalignment of the grapple fixture. Comparing this peak with subsequent peaks (as alignment is improved), shows the magnitude of the load is decreasing. This is a result of improved alignment geometry. Separating out dynamic inertia load effects from the constant 156 N (35 lb) radial load was accomplished by comparing the slow and fast snare runs. Fast snare operation runs were 5 times faster than the slow snare operation runs, resulting in the inertia load effect of 25 times greater. The much more benign slow speed runs (60 $^{rad}/_s$ motor speed) therefore allowed a relative comparison of the inertia effects versus the steady state 156 N (35 lb) radial load. The external loading from the rig (proportional to motor current[1]) correlated well to analytical predictions and control simulations. Overall mechanism performance with and without external loads was assessed by comparing snare (loaded and unloaded) as well as desnare performance to assess the mechanism performance in both directions.

Mechanism thermal and post vibration baseline tests were performed using the same test rig misalignment case (Figure 12). Thermal extreme runs were carried out and results were as anticipated. The cold case runs (-36° C) exhibited lower overall

---

[1] Separate motor module performance tests under similar ambient and thermal conditions enabled most of the uncertainties in assuming the current is proportional to the load (e.g., running friction, motor parameter variations) to be accounted for and hence removed from the absolute current for analysis purposes.

efficiency (i.e., higher torque to complete an operation). Hot (+71° C) snare operation resulted in the lowest torque. The ambient run was consistent with previous runs.

Rigidize
Rigidize testing simulated both worst case payload misalignment (15 degrees pitch/yaw and 10 degrees roll offset and an axial offset) and the best case with only the axial misalignment. The test rig imposed a 448 N (100 lb) axial load to simulate an average arm back driving while rigidizing. Friction in the rigidize mechanism was higher than expected, therefore current could not be relied on as an indicator of applied load. This was overcome by using the rigidize load cell (Figure 3) which provided axial load measurement as well as the strain gauged grapple shaft.

As with the snare ambient performance, dynamic loading was found to have a significant effect particularly under high speed, and at maximum misalignment conditions. Again it was found that dynamic loads could be accounted by comparison of the fast and slow runs. This in turn leads to a better understand and analysis the effects of the alignment load effects. Rigidization of loaded grapple shafts was compared to unloaded rigidizations in the absence of a grapple shaft. Loaded rigidize data was compared to unloaded derigidize operation provided bidirectional test results.

Rigidize mechanism thermal and post vibration baseline tests were performed using only the axial/longitudinal misalignment (Figure 14). Unlike the other mechanisms, there was no appreciable difference between temperature extremes. In addition the current "ripple" seen consistently throughout the ambient runs is not present in the cold (-36° C) case.

The relationship between current and external force (including dynamic effects) were validated using the multiple degree of freedom test rig. The relative sliding and alignment forces were determined to be within acceptable limits. However testing still needs to be carried in thermal vacuum to complete interface validation.

Abnormal and Unexpected Results

Rigidize mechanism friction losses were higher than expected resulting in lower than expected efficiency. Disassembly showed a multiple source interference problem within the rigidize gearbox. The resultant design changes will be implemented on the Qualification Model LEE with the gearbox to be tested prior to integration to ensure the problem has been solved.

Latch/Umbilical Results

Normal Results
The average ball screw force during ambient testing has a peak value of 1081 N (243 lb) and the maximum 1214 N (273 lb)and minimum 1005 N (226 lb) peak for a +133/-75 N (+30/-17 lb) tolerance around the average value. These values correspond very well to the 1112 N (250 lb)maximum ball screw force per screw predicted in the

theoretical analysis. This fact leads to the conclusion that the analysis and the efficiencies assumed are correct.

Abnormal and Unexpected Results

During the thermal testing, test runs while the latch mechanism was at hot temperature extremes of 60 and 75°C showed no adverse results. However, each run at cold temperature extremes (at -25 and -36°C) showed that more motor current was required to achieve a the latched condition (Figure 16). For the cold cycles, the average ball screw force (based on the motor current) has a peak value of 1601 N (360 lb) and the maximum 1904 N (428 lb) and minimum 1468 N (330 lb) peak such that a tolerance of +302/-133 N (+68/-30 lb) applies around the average value. These values exceed the 1557 N (350 lb) worst case ball screw force per screw predicted in the analysis.

The theoretical worst case 1557 N (350 lb) ball screw force was expected to arise due to deterioration in the coefficients of friction late in the life of the mechanism. Maximum forces as large as the 1904 N (428 lb) were not anticipated this early in the life of the mechanism.

Causes of Abnormal Results

The bearings and ball screws used in the mechanism were standard catalogue items modified only in that they used dry lubricants suitable for space. Analysis of bearings and ball screws and their housing and shaft fits under cold temperature conditions showed that additional clearances over and above that offered by the standard catalogue items is required.

Bearings suitable for cold temperatures will be available for the next set of qualification tests. It is anticipated that a significant improvement in operation will result.

Problems Caused By Deceptive Spreadsheet Graphs

Figure 17 attempts to illustrate the average latch load as a function of travel at the various temperatures, using the graph generated by spreadsheet commands. The problem with this graph is in the region of 95 mm (3.74 in) of travel. At this travel there is an 3781 N (850 lb) variation in load due to the temperature variation. The graph also indicates that the 8896 N (2000 lb) load occurs over a 3.8 mm (0.15 in) travel range depending on the temperature. A rough calculation of the possible thermal expansion and contraction of a 304.8 mm (12 in) long latch made of aluminum and steel accounts for less than 0.127 mm (0.005 in) of this 3.8 mm (0.15 in)variation. These graphs seem to indicate an unexplained load variation not behaving according to our analysis.

After investigation of potential explanations, it was discovered that the problem was in the limitations of the spreadsheet graphs themselves. The spreadsheet can plot the five load curves (due to the various temperatures) on the same graph, if and only if the five curves have a common ordinate relating the five curves. Table 1 illustrates the problem considering only the temperature extremes and the ambient case. In order to

plot multiple curves on one grid the spreadsheet requires that column B, F, and J be plotted against the travel in column A.

In spite of the best efforts in generating this graph (by lining up the data to start when the current was first applied), by the time the travel in column A reaches 5.84 mm (0.23 in) the travel in column F is up to 6.35 mm (0.25 in) and column I is down to 4.57 mm (0.18 in) for a +0.51/-1.27 mm (+.02/-.05 in) travel plotting error. By the time column A gets to 5.00 inches of travel, this error has increased to +0.25/-5.84 mm (+.01/-0.23 in). Plotting errors like this are sufficient to explain our 12.7 mm (0.15 in) variation.

Table 2 (below Table 1) illustrates the result of a Macro written to overcome this problem. What the macro does is to take the travel data of column E (in Table 1) and place it below the data of column A. The force data from column F was then moved so that the appropriate latch force was opposite the appropriate travel which used to be in column E. Similarly column I was relocated into column A below the rest of the data and column K relocated appropriately. The whole spreadsheet is then sorted so that column A is in ascending order. The columns B, F, and J remain associated with the appropriate travel of column A during this sort. This results in column A having a number in every space and columns B, F, and J having some values and some blank spaces between them.

Looking at table 2 illustrates this. Each of the values enclosed by a rectangle represents the number that exist after the above sorting process for which a corresponding set of values can be found in Table 1. The values that are not enclosed by a rectangle are blank at this point. The macro then goes down rows B, F, and J and linearly interpolates loads values between the values in the rectangles to correspond to the travel values in column A. The result is as illustrated in Table 2. The plot of this data gives a true picture of the relationships between the load data at various temperatures as shown in Figure 18. The reason for the now true representation is that each and every load ordinate has a corresponding travel abscissa, and each and every abscissa has a corresponding ordinate in each column.

It was felt that additional analysis was required to demonstrate that the original spreadsheet graphs were deceptive. The load/travel curves (Figure 17) all consist of 4 approximately straight lines 0 to 76.2 mm(0 to 3 in) travel, 88.9-94 mm (3.5 to 3.7 in), 101.6-114.3 mm (4 to 4.5 in), and 121.9-129.5 mm (4.8 to 5.1 in). These 4 lines are joined to each other by relatively sudden curves. Somewhere in these curved regions are the points at which the four straight lines would intersect if they were truly straight lines. This point at which the lines intersect will be referred to as the "point of inflection".

For each temperature, a spreadsheet linear regression analysis of the "straight lines" was carried out. Using the equations of the linear regression lines allowed the determination of the points of inflection. The various points of inflection occurred essentially at the same place within a +/- tolerance of about 0.762 mm (0.030 in). The 578 N (130 lb) load variation around the average 16605 N (3733 lb) load at 127 mm (5 in) of travel of Figure 18 is about a 3.5 % variation. This variation due to different temperatures is half of the 7 % predicted load variation. This prediction was based on

the fact that at high temperatures the modulus of elasticity of the disc springs is expected to change and the spring rate is expected to soften. This variation in itself is sufficient to explain the ±0.762 mm (+/- 0.030 in) tolerance on the point of inflection and convince skeptics that the problems of Figure 17 are due to the limitations of the spreadsheet graphing capability.

Discussion and Conclusions

These tests demonstrated a sophisticated (real time data acquisition) test rig simulation of the snare/rigidize process. The performance was verified in both thermal and ambient performance environments.

The tests show that having a multitude lot of test data is easier to handle as long as computers are available to analyze and summarize the data into a comprehensible summary.

However, the use of computers to reduce data to something that can be comprehended occasionally points to false conclusions (as with the deceptive graphs). Care must be taken to avoid the blind acceptance of computer generated data and the possible false conclusions that result.

In process testing (at subassembly level) would have highlighted the rigidize gearbox problems earlier in the design.

Cold temperature operation is the latch mechanism's most significant concern. Further qualification testing with bearings having suitable clearances calculated by our analysis should alleviate this concern.

A successful design and development program is dependent not only on theoretical analysis, but just as importantly on hardware testing that provides direct design validation and confidence in the analysis.

Figure 1 SSRMS Latching End Effector
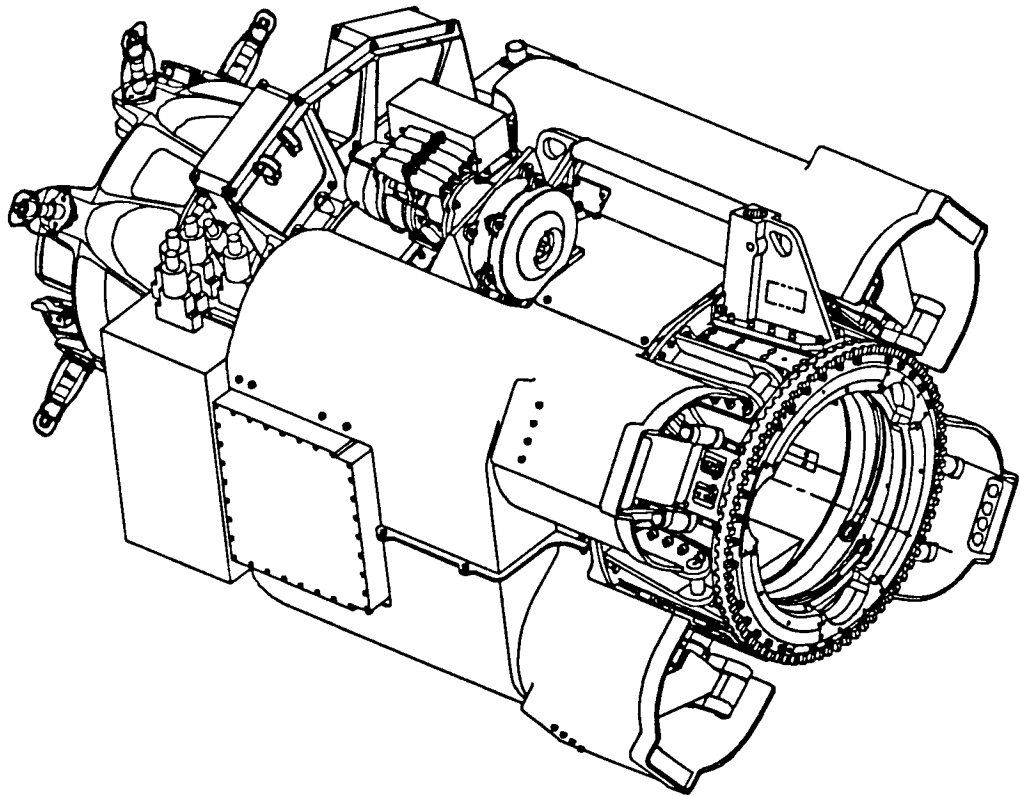

Rigidize Ballscrew Gearbox

Backplate

Ballscrew   Snare Motor Modules

Ballnut and Bellville Washers
Modules   Snare Drive Gearbox

Segment Gear

Rigidize Motor Modules

Carriage Spider
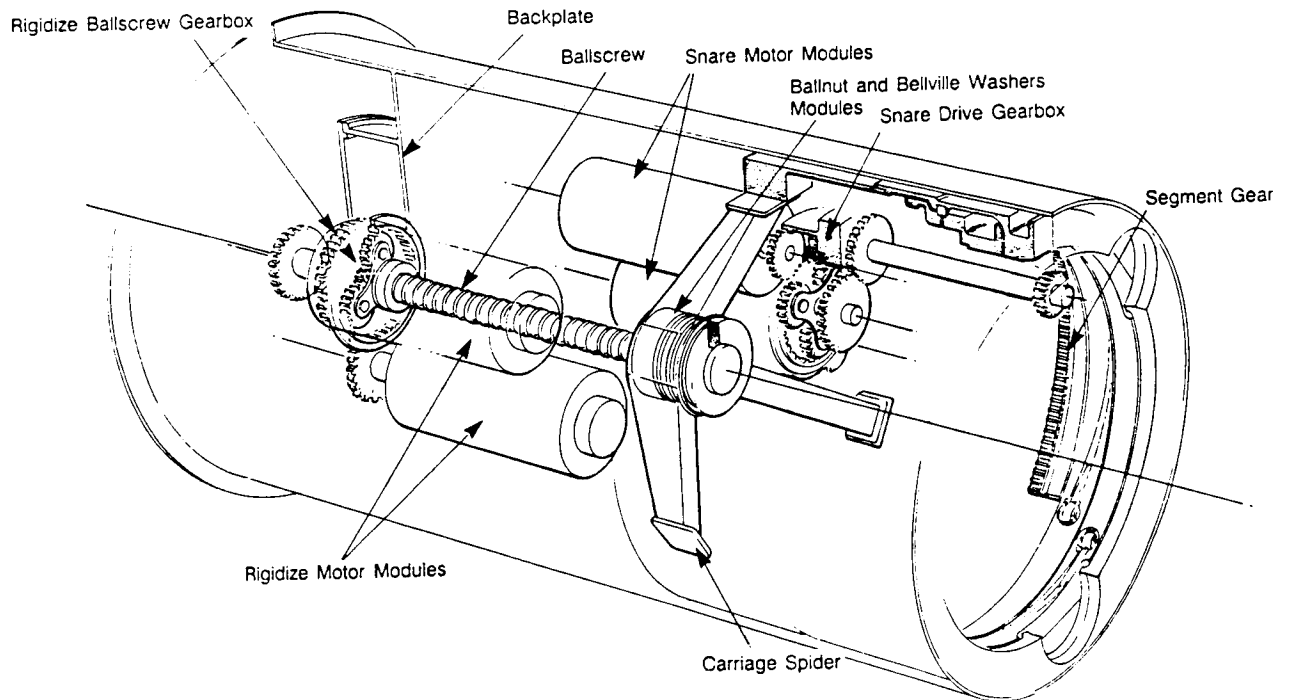
Figure 2 Snare/Rigidize Configuration

Umbilical
Connector

Fixed Ring

Rotating
Ring

Snare
Cables

X

Latch Spring
Stack

Latch Drive
Pinion

Snare
Gearbox

Spider

Carriage Retracts

Latch
Ballscrew

Rigidize
Ballscrew

Latch Drive
Rotating Ring

Snare
Motor

Rigidize
Load Cell

Rigidize
Gearbox

Figure 3 Snare/Rigidize Mechanisms

11

PAYLOAD GRAPPLE

2
PAYLOAD GRAPPLE INSIDE OPEN END OF END EFFECTOR WIRE STORED.

WIRES STORED

END EFFECTOR

3
END EFFECTOR RING BEGINS TO ROTATE. WIRES BEGIN TO CLOSE ONTO PAYLOAD GRAPPLE.

4
END EFFECTOR RING FULLY ROTATED. WIRES CLOSED ON PAYLOAD GRAPPLE, CENTERING IT & CAPTURING PAYLOAD.

1
WITH RING IN FORWARD POSITION, WIRES STORED. PAYLOAD GRAPPLE ENTERS OPEN END OF EFFECTOR.

SNARED POSITION

INNER ROTATING RING

OUTER RING

PAYLOAD GRAPPLE

PAYLOAD

5
OPERATION OF BALL SCREW & NUT WITHDRAWS WIRES PULLING PAYLOAD INTO FULL CONTACT & KEYED ORIENTATION. FURTHER OPERATION TENSIONS WIRES RIGIDIZING THE CONTACT.

LEE/PAYLOAD INTERFACE

Figure 4 LEE Capture/Rigidize Sequence

12

Figure 5 Latch Parts

Connector Backshell
Electrical Connector
Grapple Fixture Roller
Connector Cover Plate
Latch Lever
Equalizing Bracket
Latch Deployment Rollers
Electrical Connector Carrier
Sequencing Cams
Ball Screw
Latch Lever Pivot
Latch Lever Deployment Spring
Split Adjusting Ring
Tension Bracket Support
Outer Preload Bushing
Disc Spring Shack
Inner Preload Bushing
Tension Bracket
Guide Bushing
Ball Nut
Ball Nut Pinnion
Ball Nut Pinnion Housing

Figure 6 Fully Retracted Position

Grapple Fixture
Flat Portion of Latch Lever
End Effector
2.976 REF
Ramp Portion of Latch Lever
Sequencing Rollers

Figure 7 Deployed

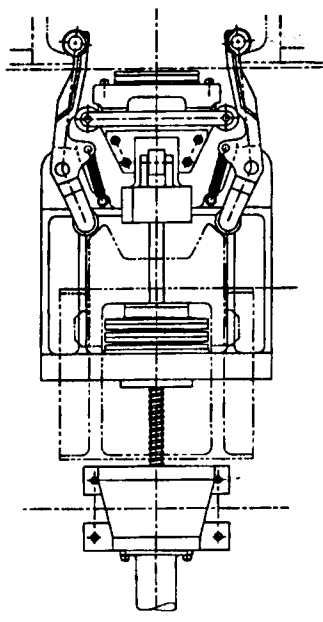Grapple Fixture Ramp
Straight Portion of Sequencing Cams
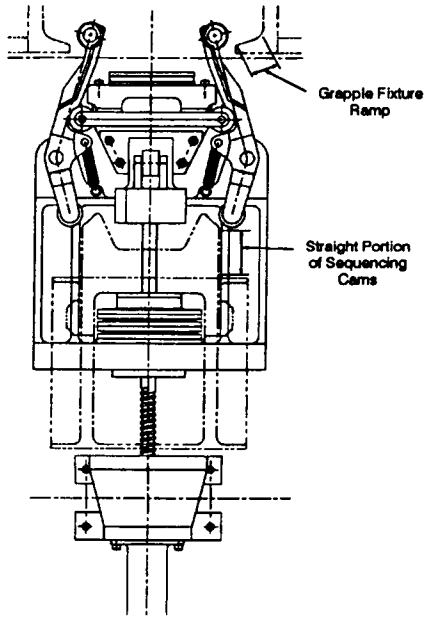
Figure 8 Initial Contact
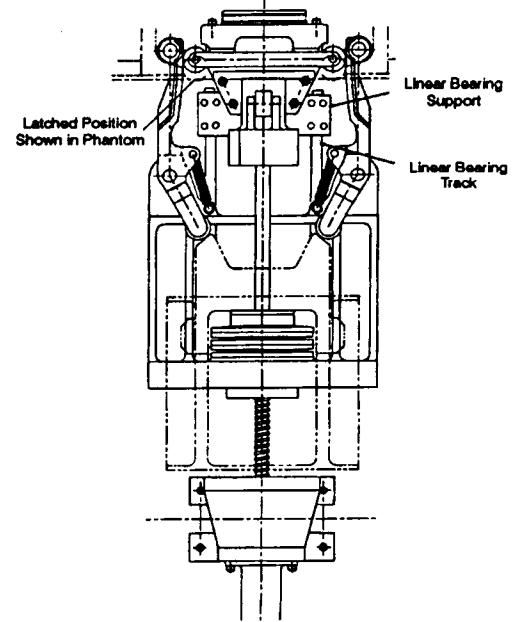
**Figure 9
Latched and Mated
Position**

Latched Position Shown in Phantom
Linear Bearing Support
Linear Bearing Track

13

PDGF Yaw Tension
Springs &
Screw Jacks

PDGF Roll Tension
Springs &
Screw Jacks

(Torque Sensor)

LEE Yaw Tension
Springs &
Screw Jacks

PDGF Axial Motion

- PLAN VIEW

PDGF Yaw
Pivot

PDGF

LEE

LEE Yaw Pivot

PDGF Pitch
Adjustment

PDGF/LEE Roll Axis

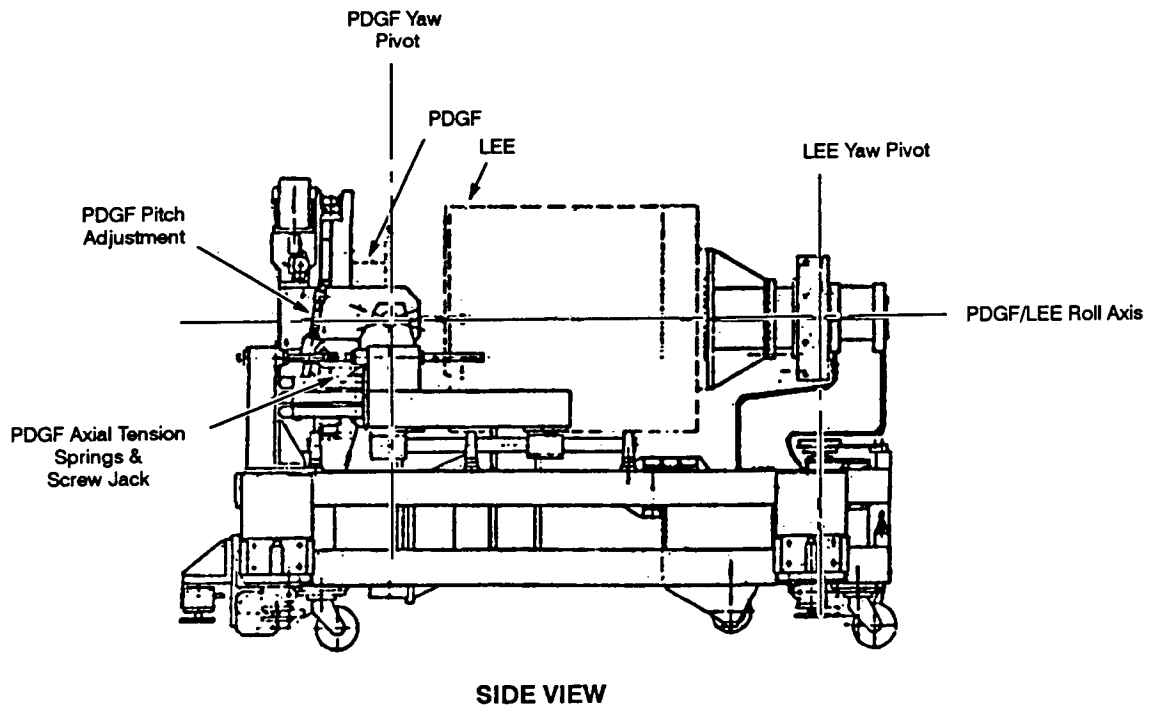PDGF Axial Tension
Springs &
Screw Jack

SIDE VIEW

Figure 10 LEEPTR General View

14

Snare Mechanism Ambient Performance

Mechanism Inertia
Acceleration

Maximum Grapple
Probe Misalignment

Probe
Fully Aligned

Mechanism Deceleration

Current (Amps)

Mechanism (Degrees)

FIGURE 11

Snare Thermal Baseline Performance

COLD (-36c)

HOT (+71c)
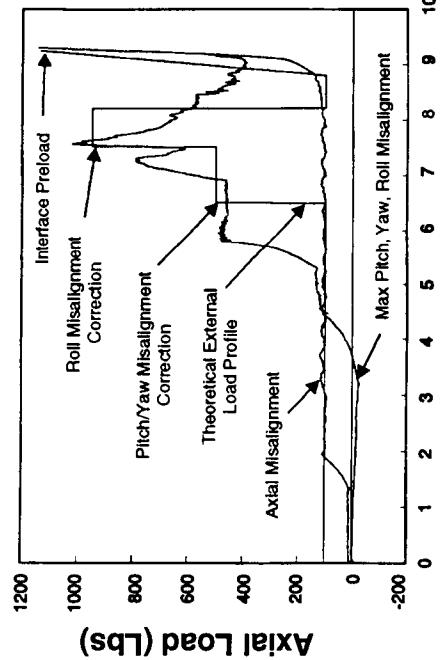
Ambient

Current (Amps)

Snare Position (Degrees)

FIGURE 12

Rigidize Mechanism Ambient Performance

Interface Preload

Roll Misalignment
Correction

Pitch/Yaw Misalignment
Correction

Theoretical External
Load Profile

Axial Misalignment

Max Pitch, Yaw, Roll Misalignment

Axial Load (Lbs)

Travel (Inches)

FIGURE 13

Rigidize Thermal Baseline Performance

100 LBF
Axial Load

No Load

HOT (+71c)

Ambient

COLD (-36c)

Current (Amps)
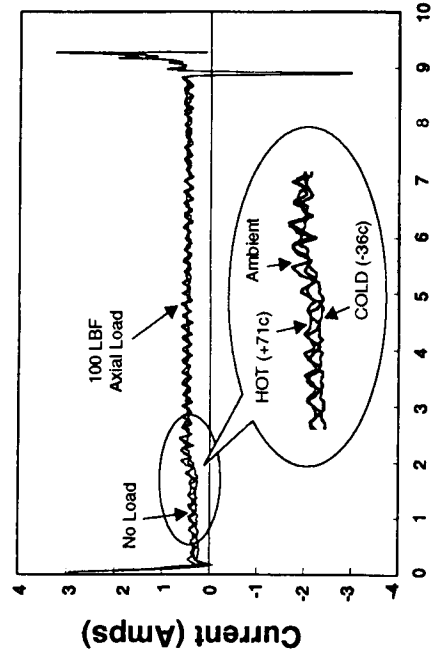
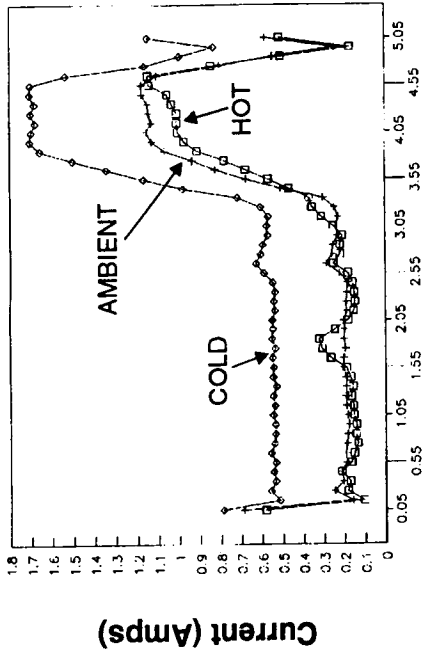Travel (Inches)

FIGURE 14

Ballscrew Force vs Travel
Seven Ambient Test Runs
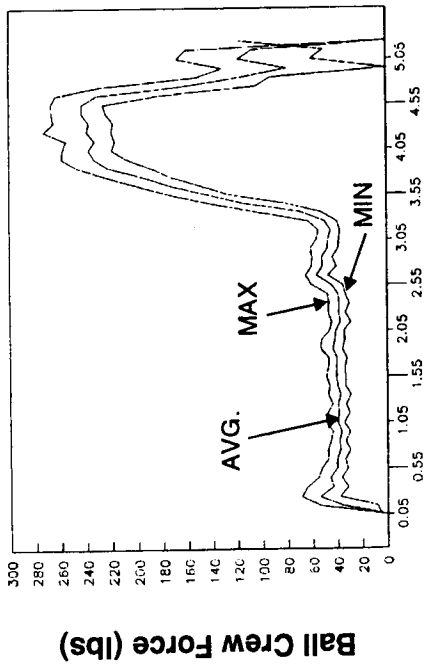
FIGURE 15
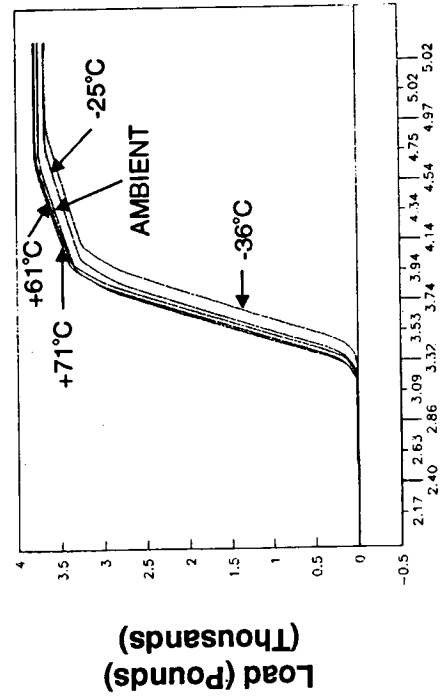
Current & Travel
Various Temperatures

FIGURE 16

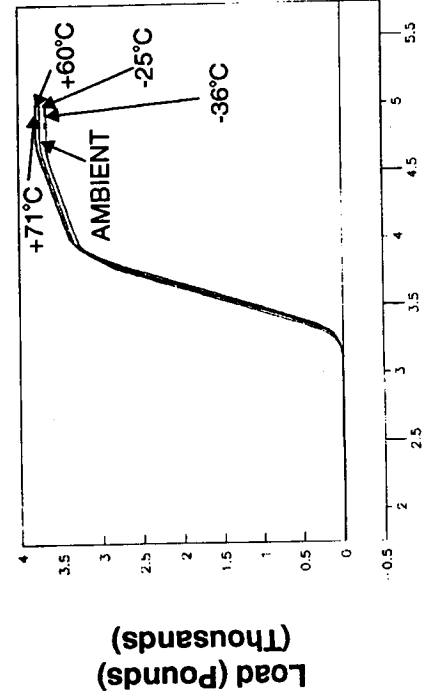**Latch Loads/Travel**
Figure 8 - Temperatures as Noted

FIGURE 17

Load vs Travel After Corrections
Temperatures as Noted

FIGURE 18

16

Some mechanical design aspects of the European Robotic Arm

Peter J. Lambooy*, Wart M. Mandersloot* and Richard H. Bentall**

Abstract

The European Robotic Arm (ERA) is a contribution to the Russian Segment of the International Space Station Alpha. It will start operating on the Russian Segment during the assembly phase. ERA is designed and produced by a large industrial consortium spread over Europe with Fokker Space & Systems as prime contractor.

In this paper, we will describe some of the overall design aspects and focus on the development of several mechanisms within ERA. The operation of ERA during the approach of its end effector towards the grapple interface and the grapple operation is discussed, with a focus on mechanisms. This includes the geometry of the end effector leading edge, which is carefully designed to provide the correct and complete tactile information to a torque-force sensor (TFS). The data from this TFS are used to steer the arm such that forces and moments are kept below 20 N and 20 N·m respectively during the grappling operation. Two hardware models of the end effector are built. The problems encountered are described as well as their solutions.

The joints in the wrists and the elbow initially used a harmonic drive lubricated by MoS_2. During development testing, this combination showed an insufficient lifetime in air to survive the acceptance test program. The switch-over to a system comprising planetary gearboxes with grease lubrication is described. From these development efforts, conclusions are drawn and recommendations are given for the design of complex space mechanisms.

Introduction

On the International Space Station Alpha, the assembly of the Russian elements will be supported by a robotic arm, the European Robotic Arm, as a result of the joint ESA-Russia cooperation. After completion of its assembly tasks, the arm will be used for inspection, External Vehicle Activity (EVA) support, and exchange of Orbit Replaceable Units (service units and experiment units). By having two end effectors, the arm can "walk" over the Russian Segment of the Space Station. Its many tasks, its long life in orbit, and its mobility over the Space Station impose severe environmental conditions on the ERA.

---

* Fokker Space & Systems BV, Leiden, The Netherlands
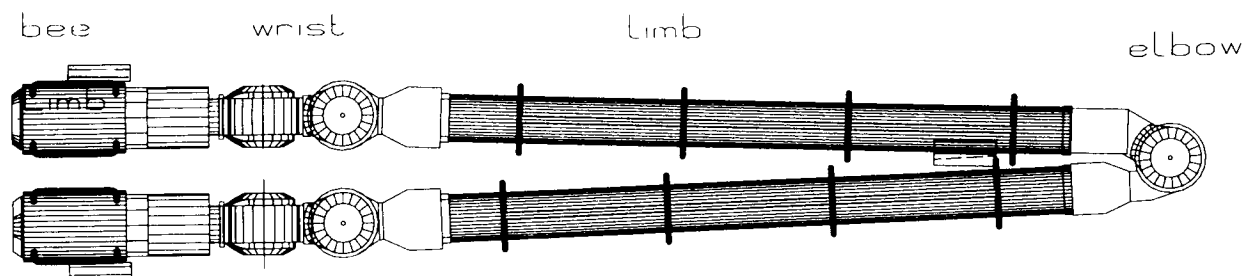** ESA, Noordwijk, The Netherlands

bee   wrist   Limb   elbow

Figure 1. ERA arm configuration

ERA tasks and operations

Tasks

ERA will be used as the robotic arm on the Russian Segment. The tasks that it will perform can be divided into four main categories:

- moving payloads
- mechanical and electrical servicing of payloads
- inspection with video cameras
- support to extra vehicular activities

The category "moving payloads" firstly requires ERA to grapple a payload. To this purpose, a grapple fixture (GF) will be attached to every payload that will be moved by ERA. The GF is a standard interface bracket, containing the interfaces necessary to transfer data, video signals and electrical power to the payload. Also built-in is the capability to transfer mechanical power to the payload. This mechanical power will be delivered by a servicing tool, an "electrical screwdriver," integrated in the end effector. Not all payloads will use all servicing capabilities. However, the possibilities are provided in the standard interface to allow more flexibility to the payload designer.

Inspection of the station or a payload will be performed by video cameras mounted on ERA. To assure that video images can be supplied in all light conditions, each camera is equipped with its own lighting unit. The camera near the elbow can be used for an overview of the working site, whereas the camera in the end effector delivers a close-up view for detailed inspection. The video images can be inspected on monitors inside the Space Station, but it is also possible to perform an off-line inspection after telemetry to a ground station.

Support to EVA can be performed in two ways. The ERA can hold and manipulate a payload to enable the cosmonaut to perform the necessary tasks. Alternatively, the cosmonaut uses ERA as a support platform. ERA will grapple the EVA support tool on which the cosmonaut can stand and moves the cosmonaut to the location where he has to work. An EVA man-machine interface, operated by a second cosmonaut, controls the ERA during the process.

To be able to perform these tasks, ERA must be able to reach all potential work sites. There are two ways for ERA to move on the Russian Segment. The first is to move along the main truss structure of the Russian Segment, mounted on a trolley. The trolley is a Russian development. It runs on two rails over the truss structure. The four basepoints (BP) on this trolley enable it to form a moveable working site for ERA operations. To reach other parts of the RS that cannot be reached from one of the BPs on the trolley, ERA needs to relocate itself. The symmetrical design with two identical end effectors enables ERA to step over from one BP to another. These BPs are located on all parts of the Russian Segment where ERA has to perform tasks.

Example of operation

An example of a typical ERA task is the installation of the solar arrays of the Russian Segment. This task consists of the following sequence. At first, ERA moves to the docking port where a transport vehicle is located. Then the GF of the solar array module is grappled by ERA. The structural interface between the solar array and the transport vehicle is decoupled by EVA. After decoupling, ERA moves the solar array to the trolley and fixes it temporarily onto the trolley, relocating itself back onto the trolley. When the trolley moves from the docking port to the end of the truss structure, ERA is in stand-by mode. Then ERA moves the solar array from the trolley to its installation site where the solar array is connected to its interface by EVA. For the deployment of the solar array, the mechanical servicing capability of ERA may be used, the servicing tool driving the deployment mechanism of the solar array. After full deployment and latch-up, ERA ungrapples (disconnects) and moves with the trolley to its home-position on the truss structure.

Design and characteristics of ERA

The design of ERA is driven largely by the requirement to be self-relocating and the necessity to have autonomous computing capabilities. Among the features resulting from this are:
- (almost) symmetrical layout
- 7 joints (only 6 degrees of freedom needed for operations)
- control computer built in, part of load bearing structure
- stiffness and torque requirements for the hand and wrist side are equivalent (=stringent) to those for the shoulder side

Configuration

Because the layout of ERA is symmetric, the two end effectors are identical, as well as the two wrists. Each wrist has three degrees of freedom. Together with the elbow joint (1 degree of freedom), ERA has 7 rotating joints. ERA will be operated as an anthropomorphic arm with only six degrees of freedom. Thus, only six joints will be used simultaneously while one joint, the yaw joint at the shoulder side, will be fixed in neutral position during operations.

The total length of ERA is 10.4 m. The total mass is about 400 kg. The speed at the end effector level can be controlled within a range of 0.001 $^m/_s$ to 0.2 $^m/_s$. At a low speed or at standstill, ERA can exert external forces up to 30 N and moments up to 100 N•m.

Electrical

The on-board computer gives ERA a high level of autonomy. All kinematic translations and all subsystem control functions are performed by the control computer. Its RISC processor, the THOR, also performs the image processing to locate the visual target on the GF, this closed-loop position control allowing an accurate positioning of the end effector. Communication between the control computer and the Russian Segment is performed by a Manchester databus, the 1553 protocol.

The design of ERA includes many sensors to monitor internal parameters. Some of these sensors are used for control purposes. Examples of these are the sensors to measure the motor speed in the joints and the encoder to measure the angular position of the output shaft. Other sensors are primarily used for safety functions, like the electrical current monitors, mechanical microswitches, and thermal sensors. A very sophisticated sensor is the Torque-Force Sensor in the end effector. It includes 32 strain gauges to measure the torques and forces transferred through it during grappling operations.

EVA compatibility

The tasks to be performed require ERA to be compatible with manned operations. This imposes not only stringent requirements on safety, but also on the strength and the overall stiffness. The latter is necessary when the EVA uses ERA as a working platform. A firm support is required in this case. Regarding the safety, the requirements for ERA are to be single failure operational and double failure safe. These requirements have largely driven the electrical and software design of ERA.

All mechanisms within ERA have the capability to be manually driven by EVA. For this purpose, a $^9/_{16}$" hexagonal input shaft is included at the motor axis of the joints and at an intermediate stage in the gear train of the end effector.

Mechanical

The mechanical configuration can be characterized by the fact that almost all subsystems are part of the primary load path. Even the box for the control computer is integrated in the limbs of the arm. Only the cameras are attached to the outside of the arm. The limbs themselves are carbon-fiber reinforced plastic tubes, with the cable harness and thermal hardware attached to the outside. The joints are driven by a brushless motor, electrically redundant. A disc brake is connected directly to the motor output axis. The brake is automatically engaged when the electrical power is switched off. A four stage planetary gearbox performs the reduction between the motor and the output axis of the joint. The total reduction ratio is 1:450. The design of the end effector will be described later in more detail.

Approach and grapple strategy

Approach in four phases
The approach of the end effector to an object to be grappled is performed in four phases:

A - open loop positioning
B - positioning with optical proximity target
C - contact phase with tactile feedback
D - rigidization with three grapple hooks

The final accuracy that will be reached in each of these phases is:

A - 40 mm, 1°
B - 5 mm, 1°
C - <1 mm, <1°
D - 0.1 mm, 0.1°

Open loop positioning (phase A)
The open loop positioning is performed without any optical or tactile feedback. The overall positioning accuracy in this phase depends entirely on the accuracy of the systems within ERA. Sources of errors are production tolerances, resolution and accuracy of angular position sensors and thermal distortion of all structural parts of ERA. The achievable accuracy in this phase is 40 mm linear and with an angular error of less then 1°. Since this mode does not need feedback from external references (e.g. targets), the accuracies are relative to the ERA BP.

Positioning with optical proximity target (phase B)
Each grapple fixture and each basepoint includes an optical target. This target is brought into field of view of the camera of the end effector with open loop positioning. The location of the end effector relative to this target is determined by the control computer. The optical pattern of the target is recognized and analyzed. The positioning accuracy achieved in this phase is 5 mm linear and 1° angular. When the end effector is within the acceptance cone of the grapple mechanism, ERA switches over to the contact phase.

Contact phase with tactile feedback (phase C)
The TFS in the end effector consists of two parts, one connected to the arm side of the end effector and one connected to the hand side. The two parts are connected to each other by flexible elements. The deformations of these elements are measured by strain gauges. This provides the information about the torques around three axes and the forces in three directions transferred through the TFS.

During operations where it is not necessary to measure the torques and forces and where the additional flexibility of the TFS is a disadvantage, the TFS will be rigidized. When the end effector acts at the shoulder side, the TFS will always be rigidized.

During the contact phase, the torques and forces measured by the TFS are used by the control algorithms of ERA to keep the contact forces below 20 N and moments below 20 Nm. The grappling mechanism can grapple and rigidize with these disturbing forces.
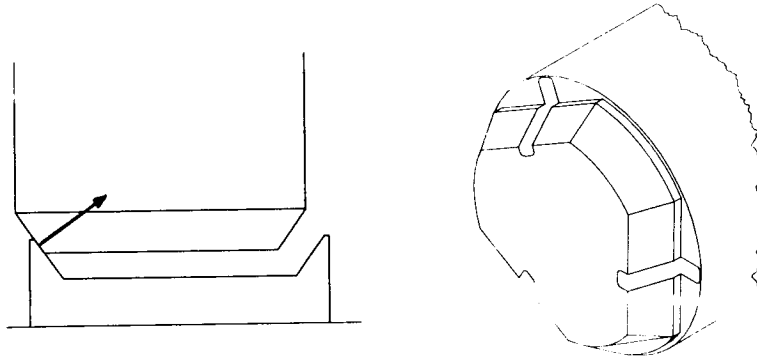

Figure 2. Geometry of the end effector leading edge

The geometry of the end effector front end and of the part to be grappled are carefully designed to provide correct and complete information. The information provided can be used to identify the correct movements of the end effector to arrive at the correct final position.

Geometry of contact areas
The following example illustrates the necessity of designing the contact geometry in order to get a correct tactile feedback. The end effector shown on the left in Figure 3 has a box-shaped front, which is to be inserted in a complementary box-shaped hole in the surface. A linear +Y misalignment results in a force +X and a moment -Z. However, a rotational misalignment +Z results in the same force +X and moment -Z. Thus the signals from the TFS do not lead to unique and correct information about the corrections needed to achieve a proper alignment. The end effector shown on the right side in Figure 3 is designed to provide unambiguous tactile feedback to the TFS. The correct information about the axial rotational position requires a triangular or rectangular baseform. The signals from the TFS can successfully be used to make the correct alignment corrections. The achievement of a correct final position during the contact phase is essential for a good start of the next phase, the rigidization.

Rigidization phase with three grapple hooks (phase D)
The rigidization of the connection between the end effector and its counterpart is performed by the grapple mechanism in the end effector. This grapple mechanism consists of three grapple hooks that capture three corresponding contact plates.
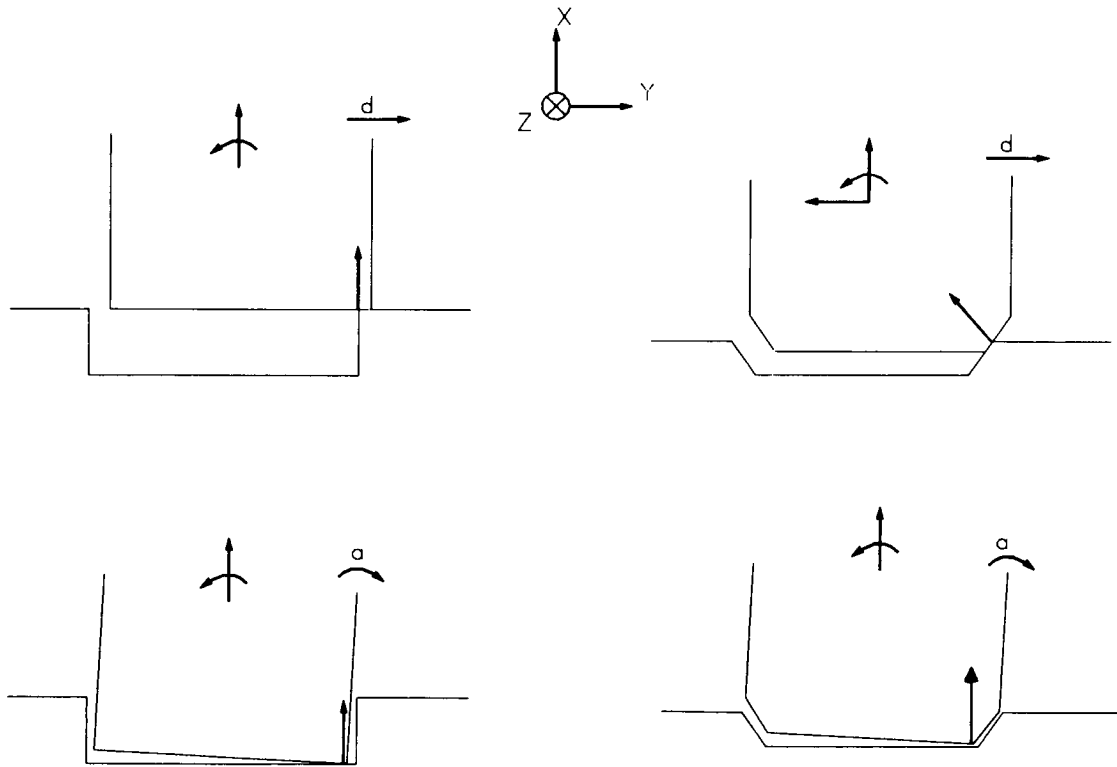
Figure 3. Tactical feedback from contact point

The movement of the hooks is indicated in Figure 4. In the final phase, the hooks are preloaded by over-centering the driving shaft. These provide a rigid connection between the end effector and the GF or BP. Especially for the end effector acting as the shoulder this rigid interface is extremely important.
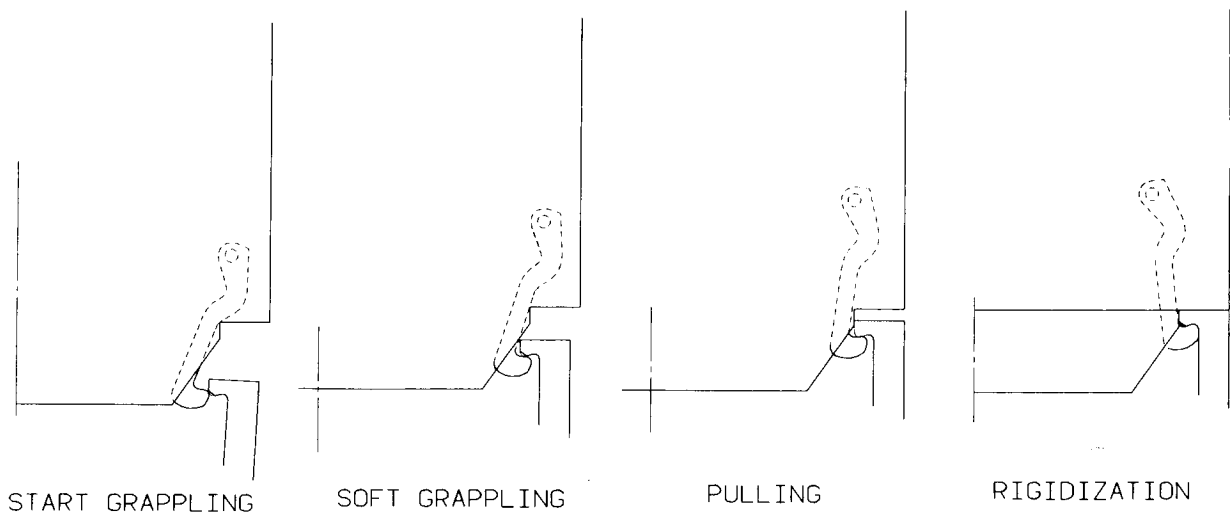

START GRAPPLING   SOFT GRAPPLING   PULLING   RIGIDIZATION

Figure 4. Rigidization of the grapple mechanism

Requirements for the end effector

The strategy for approach, grappling and rigidization as described above requires that the end effector is designed to be compatible with this approach. The main requirements that guarantee this compatibility are described below, focusing on the requirements associated with the grappling mechanism.

- The end effector must be able to perform the grappling operation for starting misalignments of up to 25 mm in any direction, including the axial direction and a rotational error of up to 3° around any axis.

- During the grappling operation, the grappling mechanism must also be able to cope with external disturbance forces of up to 20 N in any direction and moments of up to 20 N•m around any axis.

- Each of the grapple hooks must be rigidized with a preload of 7000 N. This high preload is necessary to provide the high stiffness and high strength required to function as a shoulder.

- The TFS in the end effector must have the ability to measure torques up to 100 N•m and forces up to 100 N in any direction. The accuracy of these measurements must be better then 2 N•m and 2 N. The TFS must be able to transfer loads above the measuring range without damage, up to 500 N and 500 N•m. To achieve this, the flexible element is protected by mechanical end stops. When the end effector acts as a shoulder, the TFS must be rigidized. In this rigidized configuration, measuring capability is not required.

- The cable harness is routed via the end effector. During grappling, the end effector must mate three large connectors to connect the total system harness, consisting of 42 pairs or triplets of cables.

- The mechanical servicing tool must be integrated in the end effector. The pop-in device for insertion of the tool head into the payload is located at the center of the end effector.

End effector design
Overall layout
In Figure 5, the overall layout of the end effector is given. The motor is a brushless DC motor. It drives a reducing gear train including a worm gear to prevent the mechanism from being backdriven. The worm gear actuates a large central spur gear, which rotates the three spindles. The bearings at the top of the spindles, which are mainly axially loaded, need a hard preload to avoid axial play. The three roller screws on the spindles are mounted with a limited floating capability onto the central platform. The central platform is moved upwards and downwards by the rotating roller screws.
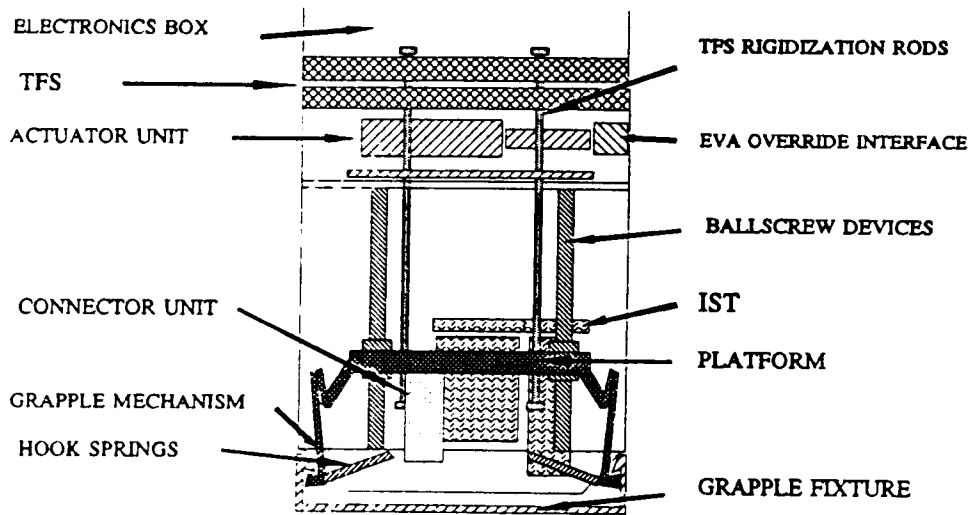
Figure 5. Layout of the end effector

The moving platform performs four functions. In order of actuation, these are driving the grappling mechanism, inserting the three connectors, inserting the mechanical tool head, and rigidizing the TFS. The torque-force sensor itself is mounted between the mechanisms described above and the electronics unit.

Grapple mechanism

The grapple mechanism comprises three hook / lever systems, which are coupled to the moving platform. The set of two levers and one hook is needed to perform the complicated movement of catching, soft grappling and rigidizing. The relative motion of the levers and hook is illustrated in Figure 6. The hook is constantly pressed outwards by coil springs. When the hook touches an obstacle during grappling, the coil spring exerts a force of about 30 N to the obstacle. During the soft grappling phase, the three grapple mechanisms start pulling at the grapple fixture until the gap between the grapple fixture and the end effector is closed and the grapple mechanisms are rigidized. In the final rigidized phase, the mechanism is slightly over-centered. No electrical power is needed to maintain this rigidized state.
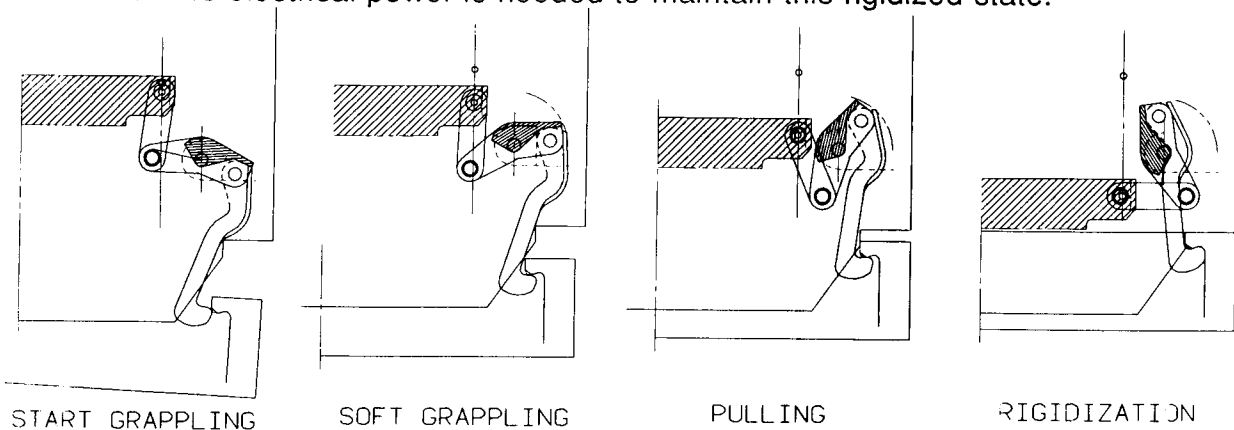

START GRAPPLING   SOFT GRAPPLING   PULLING   RIGIDIZATION

Figure 6. Motion of the grapple mechanism

25

Development model

A breadboard model of the end effector was built of hard polystyrene foam to assess the action of the mechanical parts. The movement of the platform was hand-driven and care was needed to avoid applying too much force after reaching the end position. Still, this breadboard model fully satisfied its objectives in that the concept of the lever system driven by a central platform was proven and the self-alignment capability of the mechanism was demonstrated. The model also enabled refinement of the geometry of the grapple hooks.

The current model is a full-scale model, constructed of flight-representative materials. During integration and the subsequent testing, several problems were encountered. They are summarized below as "lessons learned."

The grapple mechanism comprises complicated three dimensional movements (see Figure 7). During integration, several small interferences were found between the levers and the hooks of the grapple mechanism and the moving platform. These interferences had not been detected on the two dimensional design drawings. They could have been prevented by early application of 3-D CAD, which enables checking the position of the mechanism in every intermediate position. On the other hand, a 3-D CAD system is not a substitute for hardware and having an early hardware model gave valuable experience with the design.
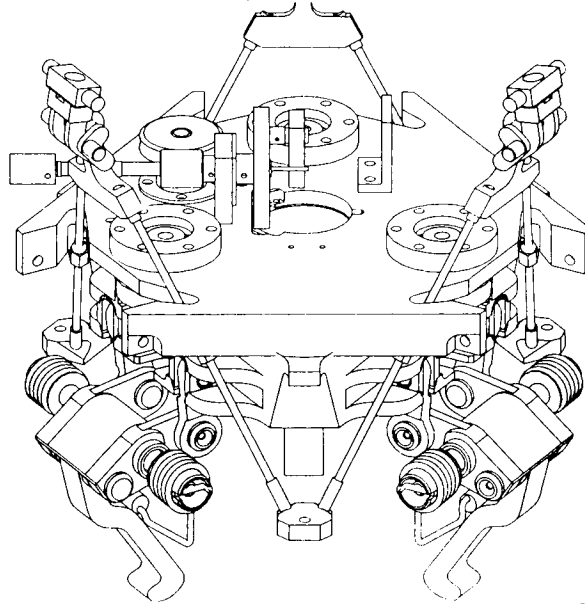
Figure 7. Complicated 3-D mechanism

It has been difficult to achieve a constant preload in the grapple hooks. This preload proved to be sensitive to small variations in dimensions and adjustments. The solution was found in maintaining tight tolerances and introducing shims in a few locations. A better solution would be to incorporate flexible elements. Small, well-designed flexibilities in the system will provide more predictable and more stable behavior.

Wear areas were found on the front face of the end effector after several tests (see Figure 8). These were caused by scuffling by the relatively sharp edges on the contact plates of the grapple fixture. The problem was solved by introducing a radius of 2 mm on the edges and the corners. A consequence of this was that the surface hardening of these contact areas was lost, at least on this development model.
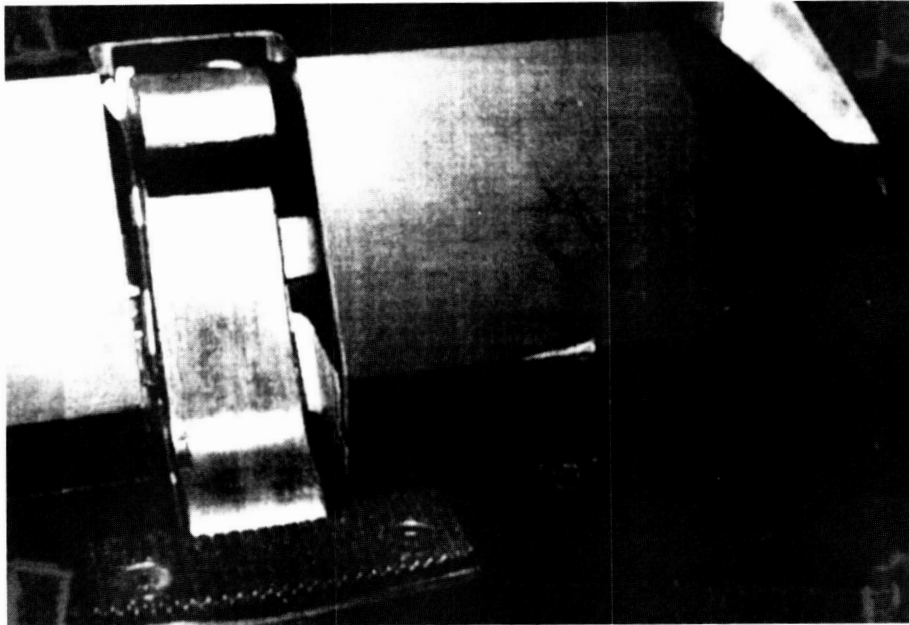

Figure 8.   Scratches on the grapple fixture

Tribology
Duty cycle and lifetime

The lifetime of ERA on the Russian segment of the ISSA will be 10 years. In addition, a lifetime of 5 years for ground testing and storage is required. The duty cycle for ERA is heavy. It can be characterized by the following key parameters:

joints:
- 1000 hours running time
- 450 N·m maximum motor driving torque
- 750 N·m maximum braking torque
- 300 brake operations with maximum inertia

end effector:
- 2000 grappling operations
- 7000 N preload on each grapple hook

In addition, an extensive acceptance test program on subsystem as well as system level is foreseen. The design of the elements of ERA must take this test program into account. It is impossible to perform the complete test program in vacuum and almost impossible to provide flushing with dry nitrogen for all mechanisms. Therefore, the lubricants must be compatible with use in air as well as in vacuum. For the mechanisms within the joints and the end effector, the operational temperatures will span from -50°C to +80°C.

Gear tribology

The gearbox of the joint is heavily loaded and a long lifetime is required. Because of the precision required for the robotic functions of ERA, the gearbox is required to deliver a high stiffness and a very low backlash.

In the drive mode, i.e. the motor drives the movement of the joints, the torque losses in the gearbox must be minimized. The brake is connected directly to the motor, i.e. to the input axis of the reduction gearbox. In the braking mode, the variations in the backdrive behavior of the gearbox must be minimized to provide a predictable braking behavior. In practice, this means that the backdrive efficiency of the gearbox should be high.

The initial design consisted of a harmonic drive gearbox lubricated with sputtered MoS_2. The advantages of this design were the compactness, the virtual absence of backlash and the low weight. The forward drive efficiency was acceptable, but backward drive efficiency was marginal. The advantages of sputtered MoS_2 are the low friction in vacuum and the friction being almost independent of the temperature. Disadvantages include restrictions on in-air use and the release of wear particles inside the gears.

Two test models were produced. Both models were subjected to tests. This test program consisted of a duty cycle comparable to the acceptance test program. The tests were performed in air, because this is the most critical environment for MoS_2.

After the tests, the harmonic drives were disassembled and inspected. Scratches were found on the flexspline and on the outer gear surfaces. The MoS_2 had been removed locally (Figure 9). Although the gearboxes performed well until the end of the test program, the damage was considered unacceptable, and a change in lubricant considered necessary.

One option was to lubricate the harmonic drive with a grease. However, the efficiency of this combination will be lower; especially the backdrive efficiency at low temperature would be unacceptably low. Therefore, the design of the joints had to be changed more drastically. The new design of the joint includes a four-stage planetary gearbox. Braycote 601 is chosen as the lubricant. The advantages of the new design are the good forward and backdrive efficiency, the long lifetime, the reliability and the improved air-run capabilities. The disadvantages are the higher mass and the increased backlash.

To decrease the backlash of the planetary gearbox to the low level required for a robotic application, it was necessary to use extremely small clearances on the last stage. This makes the gearbox more sensitive to external moments and thermal loads. To overcome this problem, the last stage is supported with a radial flexible suspension. This reduces mechanical loads on the gearbox itself and prevents high thermal gradients within the gearbox. The design is currently in development stage.
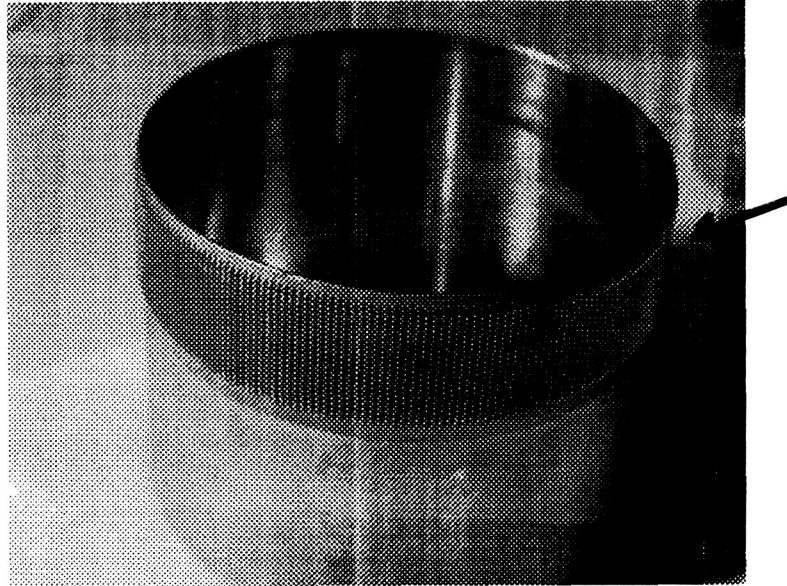
Figure 9. MoS$_2$ is locally removed from flexspline (scratch on right side)

Conclusions and recommendations

From the development efforts described in this paper, conclusions can be drawn that are applicable to the design of many space mechanisms.
- Start with a simple hardware model of the mechanism as soon as possible.
- If the mechanism includes complex movements, a 3-D CAD system can be useful to check the geometry in all positions.
- For high preloads, try to use flexible elements. This decreases the dependency upon tight tolerances, i.e. it improves repeatability of the preloads and reduces thermal sensitivity.
- When designing mechanisms, consider from the start:
  - The complete operating and survival environments. Ground testing or launch may very well drive the design.
  - Materials and lubrication must be selected as a combination. These two can not be chosen independently. A non-optimal combination may affect the performance of the mechanism more than expected.

Advanced Development for Space Robotics with Emphasis on Fault Tolerance

D. Tesar, J. Chladek*, R. Hooper, D. Sreevijayan, C. Kapoor, J. Geisinger, M. Meaney, G. Browning, K. Rackers

ABSTRACT

This paper describes the ongoing work in fault tolerance at the University of Texas at Austin. The paper describes the technical goals the group is striving to achieve and includes a brief description of the individual projects focusing on fault tolerance. The ultimate goal is to develop and test technology applicable to all future missions of NASA (lunar base, Mars exploration, planetary surveillance, space station, etc.).

INTRODUCTION

The University of Texas at Austin, in concert with the Robotics Division at JSC and funding support by the telerobotics program at NASA headquarters, has undertaken a long term effort to establish advanced component and system technology for space robotics with emphasis on fault tolerance [Butler et al.][Tesar '89][Tesar et al.]. The goal is to develop and test technology applicable to all future missions of NASA (lunar base, Mars exploration, planetary surveillance, space station, etc.). This technology would be in balance with the astronaut sharing tasks based on performance, cost, and availability issues. In order to reduce costs, the system would be made up of a finite number of modules (both hardware and software) proven by extensive testing in space. This set of modules would be constantly under technical development so that "tech mods" would be feasible at any time. Also, the repair and logistics functions (warehousing of spares in space) would be based on these modules to further reduce costs. This architecture would allow the specification of a robot configuration "on demand" reducing the threat of obsolescence and freeing the mission planner to aggressively use advanced (yet proven) technology.

The following is an overview of the structure of the program at The University of Texas at Austin.

1. **Actuator Technology** — Present actuator technology is largely unchanged since 1965 except for the utilization of rare earth motors and improved electronic controllers. The goal is to aggressively develop component technology which can be integrated in a carefully designed class of actuator modules made up of dual motors, brakes, gear drives, clutches, sensors, electronic controllers, etc., which would provide fault tolerance for dramatically improved performance and reliability of space mechanisms including robotics.

J. Chladek is of NASA/JSC, the others are of the Robotics Research Group at the University of Texas at Austin

2. Modular Architecture — A true modular architecture (in the same form as has proven useful for computer systems) can not only reduce life cycle costs (repair, tech mods, logistics spares planning, etc.) but can dramatically increase performance while unfettering the designer to more freely and quickly develop actual operating systems to satisfy future space missions. It is proposed to assemble and reconfigure a broad population of systems from a very small collection of proven and optimized modules produced at lower costs.

3. Task Planning — The complex motion of a body in space to trace out precision trajectories requires the sophisticated theory of algebraic curves to smoothly coordinate all 6 DOF of the end-effectors. The need for dependable task planning derives from a spectrum of demanding physical tasks such as debris damage inspection, precision wiring disassembly and assembly, force fit assembly, dual arm operations, etc. while avoiding obstacles. The goal would be to make task planning more automated requiring primarily supervisory involvement by the astronaut - reducing their time burden and potential fatigue.

4. Dual Arm Operations — Due to the lack of frictional stability generated by gravity forces, all parts must be under control at all times to prevent "dropping". This means that either special fixtures (the bane of data base control in manufacturing) must be employed or dual arms must perform the relative motion tasks (force fit assembly, control of ungainly objects that may be easily damaged, removal of insulation wrappings, bending to fit, etc.) that are sure to occur on long duration missions. No real time operation of a dual arm system capable of these tasks exists today. For two manipulators of 7 DOF each, this requires a level of control (precision force and position of 14 inputs to control 6 relative outputs) far beyond any standard approaches (PID, fuzzy logic, sliding mode control, adaptive control, etc.).

5. Task Performance — Long duration space missions suggest an enormous range of physical tasks of great complexity (handling of large modules, precision welding and forming, unstructured tasks associated with joining and fastening, precision machining, etc.). This complexity can be met only by a criteria based decision control structure based on accurate system parameters (using careful metrology) and hundreds of performance criteria. A prioritized selection of these criteria will be used to create performance indexes to compare the model based performance with the actual performance derived from a very broad collection of sensor signals. Differences between actual and modeled performance will be the basis for adjusting the control inputs to the system.

6. Condition Based Maintenance — Having established a model reference control structure comparing actual with predicted performance, it becomes feasible to monitor the system over time to determine when basic maintenance (replacement of actuator components, sensors, controllers, etc.) should be performed and to provide an archival record of that performance. This should improve the system's reliability, reduce the cost of operation, prevent unexpected failures, and provide lesson's learned for the operator and the designer of future

components as well as to the mission planner for module selection to make up systems for other tasks.

7. Fault Tolerance — Fault tolerance is virtually non-existent in present robotics development for space. A full architecture for fault tolerance involves four levels (alternate physical pathways) of mechanical structure to avoid faults. The UT program strongly recommends a 10 DOF manipulator system (level III) made up of dual actuators (level I).. This level of choice (20 actuator inputs to control 6 outputs) can only be achieved by a criteria based decision making structure based on performance indexes composed of hundreds of physical criteria (which demands an extremely high computational capacity). Such superior system controller technology (several gigaflops) is emerging as a commodity (at reasonable cost) in the near term. Hence, fault tolerance is not only feasible but it can only be achieved through a comparative analysis between an accurate and complete analytical model reference and a sensor based actual model of the system. This makes Fault Detection and Isolation (FDI) possible. No other method of control does.

8. Man-Machine Interface — Because of the extraordinary value associated with the time of the astronaut, the interface between man and machine is being recognized as a key resource to maximize overall performance and to train (skill) the system's operator. Very complex operations (dual arms, disturbance rejection, unstructured tasks, precision assembly at small scales, multiple slaves, obstacle avoidance, etc.) require an exceptional level of dexterity and task performance. This is best achieved by setting operational priorities (selection of criteria, performance indexes, threshold levels for fault identification, etc.) by human intervention. Specially designed actuators, human augmentation software, fault tolerance, etc., must be built into future manual controllers to maximize the task performance of an increasingly complex slave manipulator technology.

9. Ground Based Control — As space missions develop (by analog, with the aircraft pilot), the astronaut will be less available to perform mundane, repetitive, and low valued tasks. In order to reduce costs, the demand on the astronaut's time, and to reduce risks, the robot will either have to be operated remotely from a protected module or it will have to be operated from a stand-off position (say the moon or from a control center on earth). This set of conditions leads to the inevitable conclusion that an enhanced man-machine interface to remotely control an array of deployed slave manipulators (robots) in space is essential.

10. Augment RRC Technology — The Robotics Research Corporation has produced a sophisticated modular manipulator of high smoothness and resolution which is widely used in NASA laboratories as a demonstrator. The AARMS facility at JSC is made up of two 7 DOF RRC arms on two separate precision 2 DOF pedestals to make up a valuable demonstrator of the technology for space station operations. A 17 DOF system (two 7 DOF arms and a 3 DOF torso by RRC) has been made available by Grumman Corporation to The University of Texas at Austin. Both of these systems will be used to integrate and evaluate much of the technology described in this paper. The goal is to test the most advanced control

software for performance, condition based maintenance, and fault tolerance in real time (say 10 milli-sec.) and to do so with improved operator intervention.

Overall, the program at The University of Texas is concentrating on two levels: the actuator as the driver of the system (equivalent to the computer chip as the driver of computers) and at the system performance level (equivalent to the operating system in personal computers). The objective is to make these two technologies standards for the field of intelligent machines and robotics. This universality is what has created the value in personal computers: increased performance at lower costs. In addition, the program is laying the foundation of a revolutionary approach to control the complex, coupled, and highly nonlinear structures involved, to show the continuum from task performance, condition based maintenance, to fault tolerance all of which depend on a computationally based model reference compared to a sensor identified model. This continuum now becomes unified because of the availability as a commodity of a low cost system controller of several gigaflops.

The central part of this paper will outline on-going development activity at The University of Texas at Austin to meet these 10 technical objectives. The final section of the paper will provide a projection of further development where not only will space requirements be addressed, but also aggressive implementation for industrial technology (manufacturing) will benefit from this investment by NASA.

ARCHITECTURES

The level of performance and versatility expected from space robots makes it imperative that particular emphasis be placed on the question of architecture across multiple domains. While such design issues have to be addressed for each of those domains (mechanical, electronic, and software), certain essential principles may be allowed to pervade the system's architectural considerations. These principles are 1) modularity and 2) redundancy.

Traditionally, mechanical systems have had monolithic architectures that do not permit easy repair and replacement, nor the fluent incorporation of advances in component technologies. Ease of repair and replacement are directly linked to the *availability* of the system and is, therefore, a matter of immediate concern to space systems. The deficiencies of such a philosophy, or lack of one, are best offset by aiming for an architecture that is highly structured and modular. A true modular architecture helps reduce life cycle costs and frees the designer to quickly prototype and develop actual operational systems for future space missions. The UT program has been concerned with the development of modular structures for space robotics, across the domains of mechanisms, electronics and software.

Redundancy is demanded by twin operational considerations for space operations: safe and enhanced performance provided by redundant systems--to be explained in a later section--and the ability to tolerate faults. *Fault tolerance* in a robotics context may be defined * as the capability of the system to sustain a failure and still continue operation

---

* due to C. Price [Tesar et al.]

without significant impact on the manipulator payload or its immediate environment. Graceful degradation is often inadequate as a requirement and uncontrolled motion must at all costs be minimized. Fault tolerance is assured by the incorporation of protective redundancies and their organization into an effective and responsive architecture. While the causes of unreliability do not disappear, their effects are counteracted by the capability of the system to be intelligent, and to mask the failure or reconfigure itself in the event of component failure. It must be emphasized that these redundancies are *active redundancies* that are operational at all times and which enhance the performance of the robot through the optimization of secondary criteria. We now consider general modular manipulator architectures for fault tolerance.

The Four-level Architecture

The conceptual outline of a total architecture based on modularity principles has been presented in [Butler et al.]. While the issue of architecture depends ultimately on the context and specific tasks envisaged of the robot, it is possible to devise a broad architectural scheme that is based on the requirement [Chladek] that the system be two-fault tolerant. The resulting architecture, in its most general form, is capable of providing a masking redundancy at the first level and a dynamic or reconfiguring redundancy to tolerate the second fault. The organization of these redundancies may be conceived in four levels and they constitute a subsumptive architecture [Sreevijayan]. The four levels are:

1) extra actuators per joint (e.g., prime mover duality)
2) extra joints per DOF (redundantly actuated parallel structures, e.g., 4-legged spherical shoulder)
3) extra DOF per arm (redundant manipulators)
4) extra arms per manipulator system (e.g., dual arm robots, four-fingered hands, etc.)

We now discuss specific prototypes being developed at the University of Texas at Austin that will provide component technologies for realizing modular and redundant space manipulators.

2-DOF Redundant Knuckle Mechanism

The knuckle, shown in Figure 1., can operate either as a force feedback joystick or as a 2 Degree-Of-Freedom (DOF) manipulator. The knuckle demonstrates modularity and Level I fault tolerance at the servo level. It uses two independent servo systems per single DOF to obtain Level I mechanical redundancy. Modularity is demonstrated in the servo control hierarchy (see description of DISCs). The system is designed to handle a minimum of 1 fault before failing. The system controller acts as a supervisor in analyzing the sensory feedback with a Fault A servo system can either remove itself from the system or be removed from the control hierarchy by its parallel controller. Each servo system consists of a clutch, a brushless resolver, a brake, a Hall-effect sensor and a three-phase Brushless DC motor The system controller consists of a 486 PC operating under the Lynx O/S® real-time operating system. The system controller communicates to the servo controllers via a HDLC medium at a rate of 1 MBit/s. HDLC is a communications protocol based on IEEE RS-532 standard.
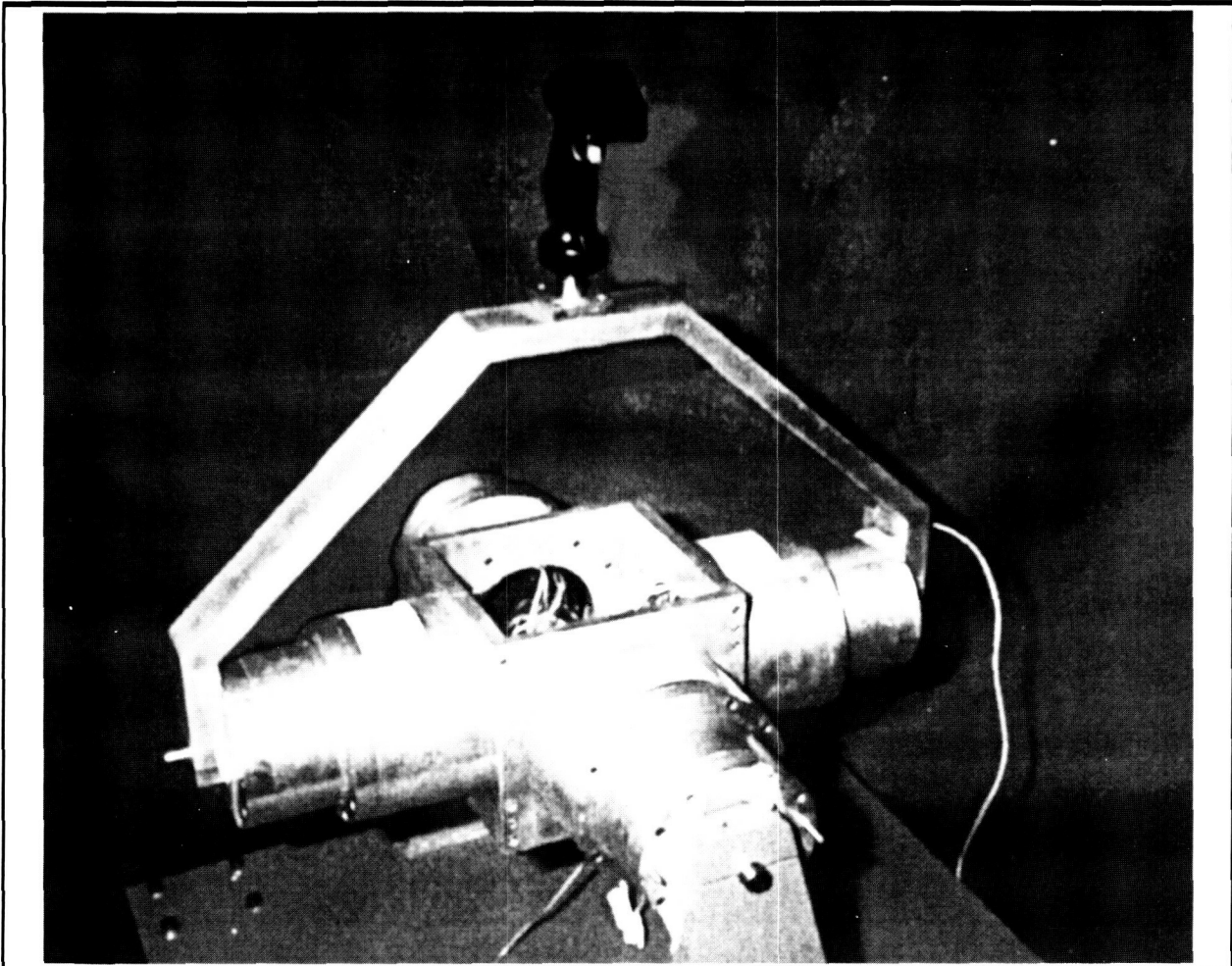
Figure 1.　　The fault tolerant knuckle.

Modular Brakes for the Fault-Tolerant Actuator

A new brake was developed for use in the next generation of robot actuator technology. The caliper disk brake has an annular geometry that capitalizes on the structural integrity of the robot actuator shell. One to four independent brake calipers can be positioned around the rim of the disk to give a redundant capability. The torque path goes directly from the calipers to the actuator shell to produce a truly, lightweight, integrated design. An ultra-low power consumption is achieved since only a very small current is required to hold the brake pads in the released position. The brake design is very compact, lightweight and has a high torque/weight ratio. Performance parameters were determined from prototype testing and compared to a set of average performance parameters derived from a database of commercially available high performance brake modules. The new brake design has achieved a number of improvements when compared to standard practice.

Criteria	Benefit
Torque/weight Ratio	3X Better
Compactness	2X Better
Response Time	2X Faster
Operating Power Consumption	700X Better

Table 1. Benefits Of The Improved Modular Robot Brake

The Digital Intelligent Servo Controller (DISC)

The Robotics Research Group has developed a Digital Intelligent Servo Controller (DISC), shown in Figure 2., that expands the actuator controller technology. The DISC is a very compact brushless DC servo controller that offers numerous features not contained in any single commercial system available today. Some of the features include: multiple sensor interfacing, compact 'smart' power electronics, fault tolerance, and high speed digital communications designed in a modular package.
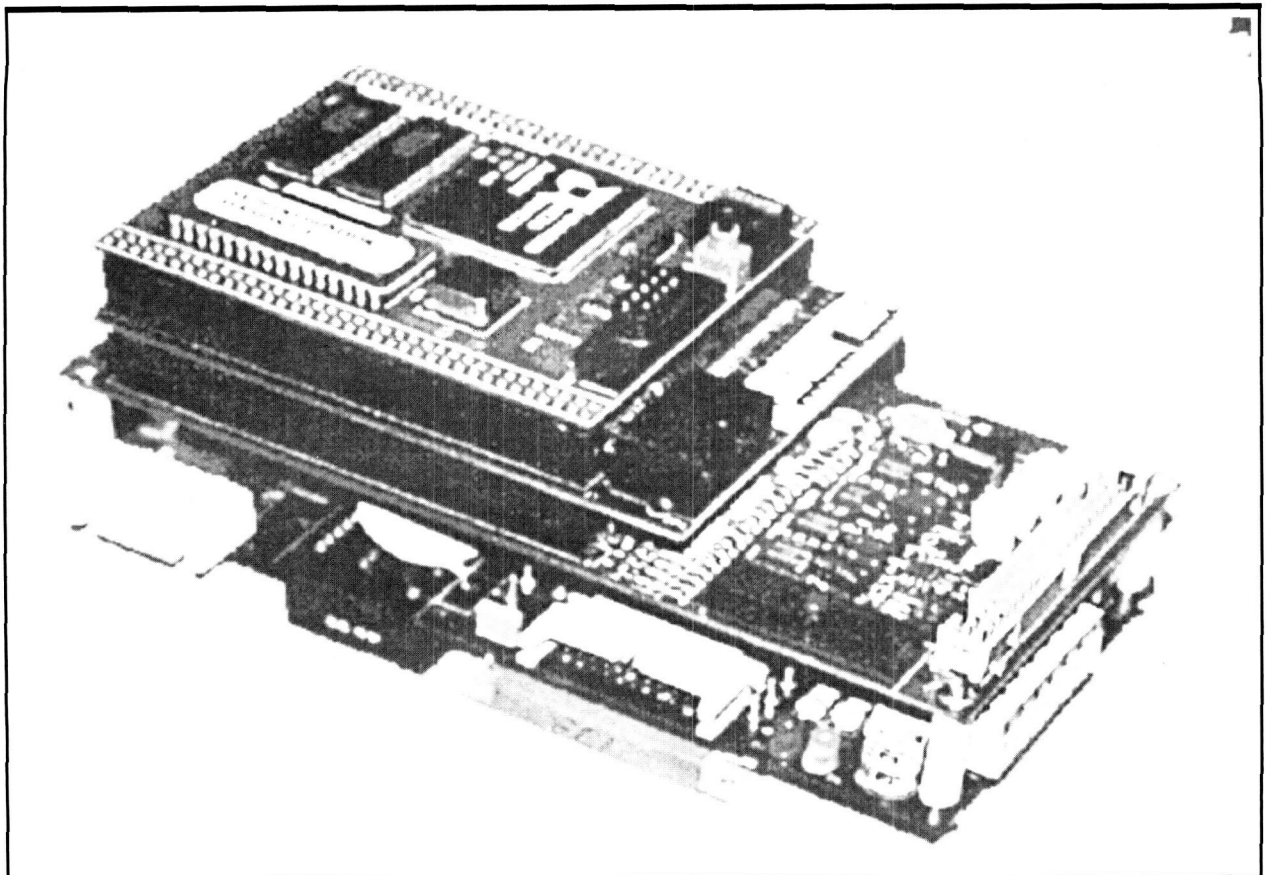

Figure 2.   This DISC fault-tolerant electronic controller.

Object-Oriented Software Architectures

The Robotics Research Group at U.T. is in the final phase of designing and developing a unique object-oriented software for advanced robots. This software provides abstractions for various robotic concepts like kinematics, dynamics, decision making, and fault-tolerance. The abstractions are implemented as a part of an inheritance hierarchy. This software is developed in a modular and extensible fashion, with the user having the capability of connecting various modules as desired. This promotes rapid-prototyping. Also, the framework provides for reuse and extensibility. For example, if a generalized inverse kinematics module would not satisfy user needs, the user could easily substitute that module with a custom inverse kinematics module. Such a change does not affect the structure of the rest of the software. This software provides an ideal environment for robotics research and allows for interaction at all levels of abstraction. Moreover, the rapid-prototyping capability of the software allows for easy experimentation. In addition, due to the general nature of this software, it is applicable to a wide variety of robotic structures.

DECISION-MAKING AND CONTROL

A redundant robot is an extremely complex system with essentially limitless options for performing most tasks. The extra resources demand active utilization during normal operation. This refers to the *redundancy management* mode of operation where the control inputs are selected based on the optimization of selected performance criteria. Our position is that no single criteria is sufficient for decision-making and control, but rather that a suite of weighted and ranked criteria must form the basis for any intelligent decision making process. Towards this goal we have conceptualized over 100 different performance criteria and mathematically formulated 30 of these. The section on criteria development describes some of them.

After formulating and prioritizing the performance criteria for a given system, there still remains the problem of incorporating them into a decision making system that will maximize performance while simultaneously satisfying operational constraints. Fault-tolerance places additional demands on the decision maker because the robot may suddenly lose one or more resources, thus requiring a change in control emphasis from one of redundancy management to that of *failure management.* The failure management further breaks into chronological stages. First is fault detection and isolation (FDI). The fault detection routines must continuously monitor the system and upon detection of a fault, must isolate and identify the source of the fault. At this point, the reconfigurable control system responds to the change in the robot's resources and automatically restructures the control algorithm so that the control inputs are reconfigured while at the same time maintaining task performance. Finally, condition-based maintenance on the robot will restore it to full-capability.

Serial Robot with 21 Degrees of Freedom

As an example of redundancy resolution in a fault-tolerant system, consider the inverse kinematics problem for the massively-redundant serial robot with 21 degrees of freedom shown in Figure 3. Though this is clearly a conceptual robot, it represents a system with

a tremendous degree of redundancy. We have developed a unique redundancy resolution technique based on the method of sequential filters developed by Eschenbach and Tesar [Eschenbach].
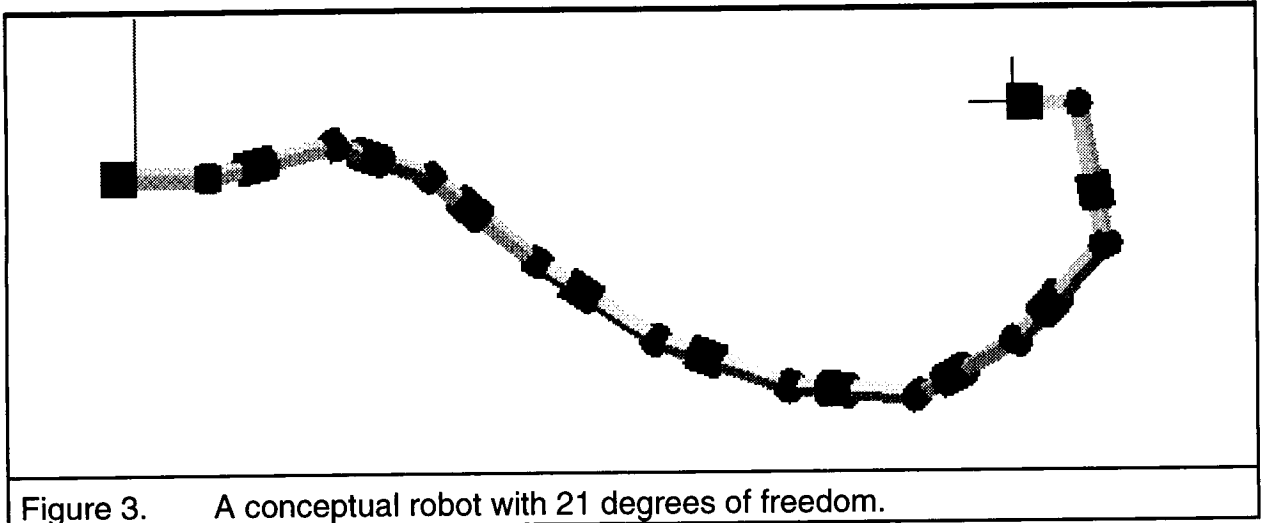

Figure 3.   A conceptual robot with 21 degrees of freedom.

This method of redundancy resolution explicitly identifies a set a feasible options for the robot's motion in the next instance using a series of joint-level perturbations. Perturbing the joint displacements a small amount, $\Delta\theta$, from their current values, $\underline{\theta}$, generates a set of local configuration options, $\hat{\underline{\theta}}$: $\hat{\underline{\theta}} = \underline{\theta} + \underline{\varepsilon}\Delta\theta$, where $\underline{\varepsilon}$ is an arbitrary sweep vector with all elements equal to ± 1 or 0. The vector of current displacement values, $\underline{\theta}$, is the base point for the perturbations. At the base point, $\underline{\varepsilon} = \underline{0}$. All other $\underline{\varepsilon}$ with elements equal to combinations of ± 1 and 0 generate points on the faces, edges, and vertices of an n-dimensional hypercube with n equal to the number of degrees of freedom. The sequential filters then evaluate and rank the options based on the performance criteria and operational constraints. The logical sequence first applies the least computationally demanding constraints, and then evaluates the remaining options based on the higher-level performance criteria. The application of equality constraints on the end-effector's placement, followed by travel, speed, and acceleration limits at the joint-level will typically eliminate the vast majority of the options. A fault in one of the joints simply removes the options associated with perturbations of the faulty joint from the feasible set. Using this technique, we can resolve the redundancy of this extremely complex system at hundreds of cycles per second on common personal computers.

Performance Criteria

The ability of a decision making system to control a redundant robot system depends on the quality of the information it is provided to make those decisions. *Performance criteria* are mathematically rigorous metrics which are derived from the kinematic and dynamic robot models Each performance criterion quantifies a characteristic inherent to the operation of the robot and thereby provides vital information concerning its current state.

The decision making system may make use of these criteria to determine the *quality* of various self-motion configurations and select a solution that best achieves the specified goals.

Performance criteria may divided into two categories based on the information they require. *Task dependent* criteria rely on information concerning the current state of the robot's task; such as velocity or force specifications. Conversely, *task independent* measures are defined only from the physical parameters inherent to the robot; geometry, inertia, and compliance for example. While both categories provide useful information, the robotics program has focused on a criteria formulation free of the predetermination of the robot task. This task abstraction will extend the application base to which the criteria may be applied. Performance criteria developed at The University of Texas at Austin's Robotics Group consists of 29 measures, defined in these categories:

- **Geometric**..........based on first and second order kinematic properties of the manipulator,
- **Inertial**...............based on the inertial terms in the manipulator's dynamic equations,
- **Kinetic Energy**.. based on system level kinetic energy content and individual link contributions
- **Compliance**.......based on the link and joint compliances (stiffnesses) of the manipulator.

A simple, yet very powerful example of a geometric criterion is derived from the First-Order velocity equation which is given as

$$\underline{\dot{u}} = \left[G_\phi^u \right] \underline{\dot{\phi}},$$

where,

- $\underline{\dot{u}}$ is the end-effector velocity,
- $\underline{\dot{\phi}}$ is the joint velocity, and
- $\left[G_\phi^u \right]$ is the manipulator Jacobian.

The *singularity detection criterion* is derived from this mapping of joint to end-effector space as

$$\eta_\sigma = \sigma_{\min}.$$

where, $\sigma_{\min}$ is the minimum singular value of the manipulator Jacobian, and is determined from the *singular value decomposition*..

Level III Fault Tolerance

Figure 4. shows a serial robot with 10 degrees of freedom and fault-tolerance at Levels II and III. This kinematic arrangement affords the robot complete dexterity even if any one of the joints failed and is locked. The manipulator has a regional structure with 6 degrees of freedom (that is built on a regional sub-structure with 3 degrees of freedom) and an orientation structure with 4 degrees of freedom. The use of two-roll joints in the regional structure provides positional fault-tolerance and the 4 DOF orientation structure retains all joint axes intersecting at right angles even if any one of the wrist joints fails.
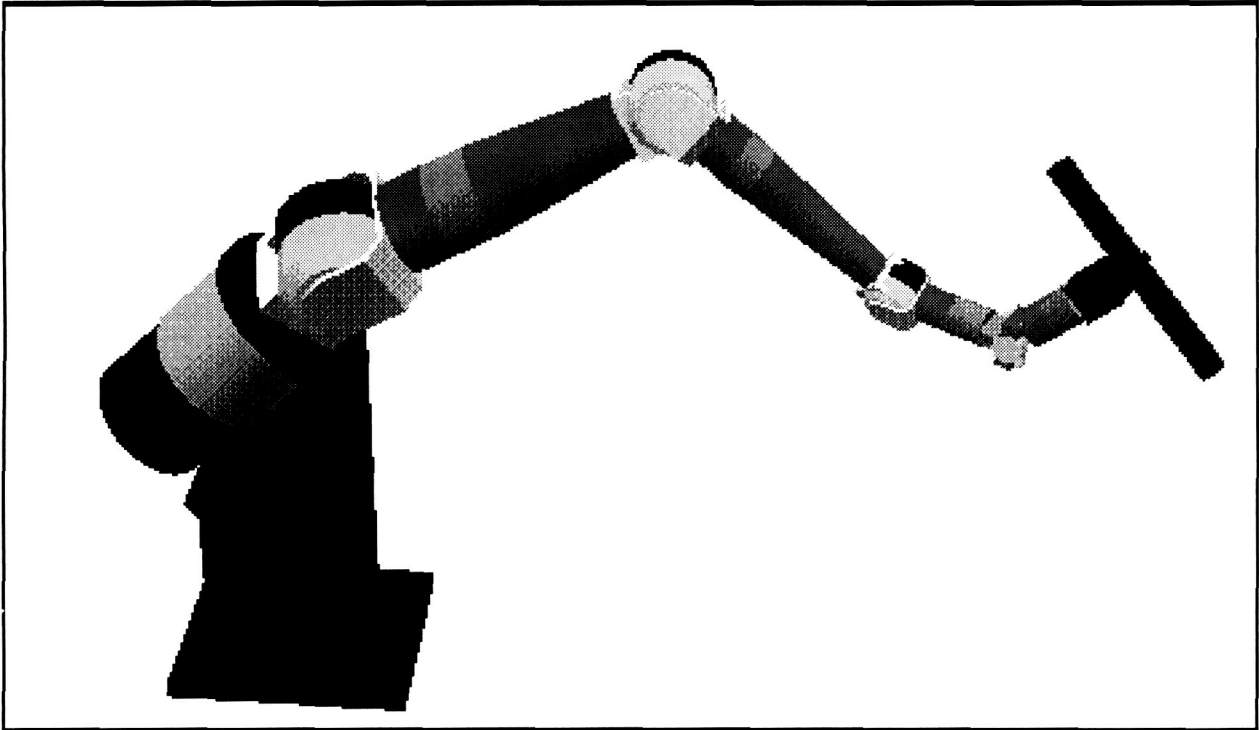
39

Figure 4.   A conceptual fault-tolerant robot with 10 degrees of freedom.

In the decision-making and control algorithm for this system, the fault-detection and identification sub-system identifies the faulty joint and informs the decision making sub-system. The decision making sub-system selects any six joints of the robot for application of the inverse kinematics subsystem. The inverse kinematics sub-system then returns the joint displacements to the decision-making sub-system or an error flag if the calculations were unsuccessful due to mathematical singularity or workspace violations. The entire decision-making and control system executes at approximately 300 Hz. on an Indigo R4400.

DUAL ARM OPERATIONS

An advanced 17 degree-of-freedom dual arm robotic system, shown in Figure 5., is being integrated into a technology demonstration testbed in the UT Robotics Laboratory. The robot is capable of demonstrating Level III fault tolerance with each of its redundant DOF arms and Level IV fault tolerance with its dual arm configuration.

The robot utilized in the UT testbed is a K/B-2017 Dexterous Manipulator manufactured by Robotic Research Corporation [Karlen et al.] It incorporates two seven-axis manipulators on a three-axis torso assembly providing a total of 17 DOF. Grippers attached to the end of the manipulators each provide an additional DOF, making the entire system 19 DOF. Each joint drive module is comprised of an electric servomotor, harmonic drive gear reducer, and joint position and torque transducers.

Control of the system will be based on a task oriented architecture. A robot task such as application of a large force or precise motion of the end-effectors would be identified by the operator for a given operation. The operator may then concentrate on task completion while the robot's command and control architecture manages the robot's redundant resources and makes compensations for any system faults. The control system determines the best robot motion or arm poise to meet the physical task requirements by optimizing one or more of a set of dual arm performance criteria.
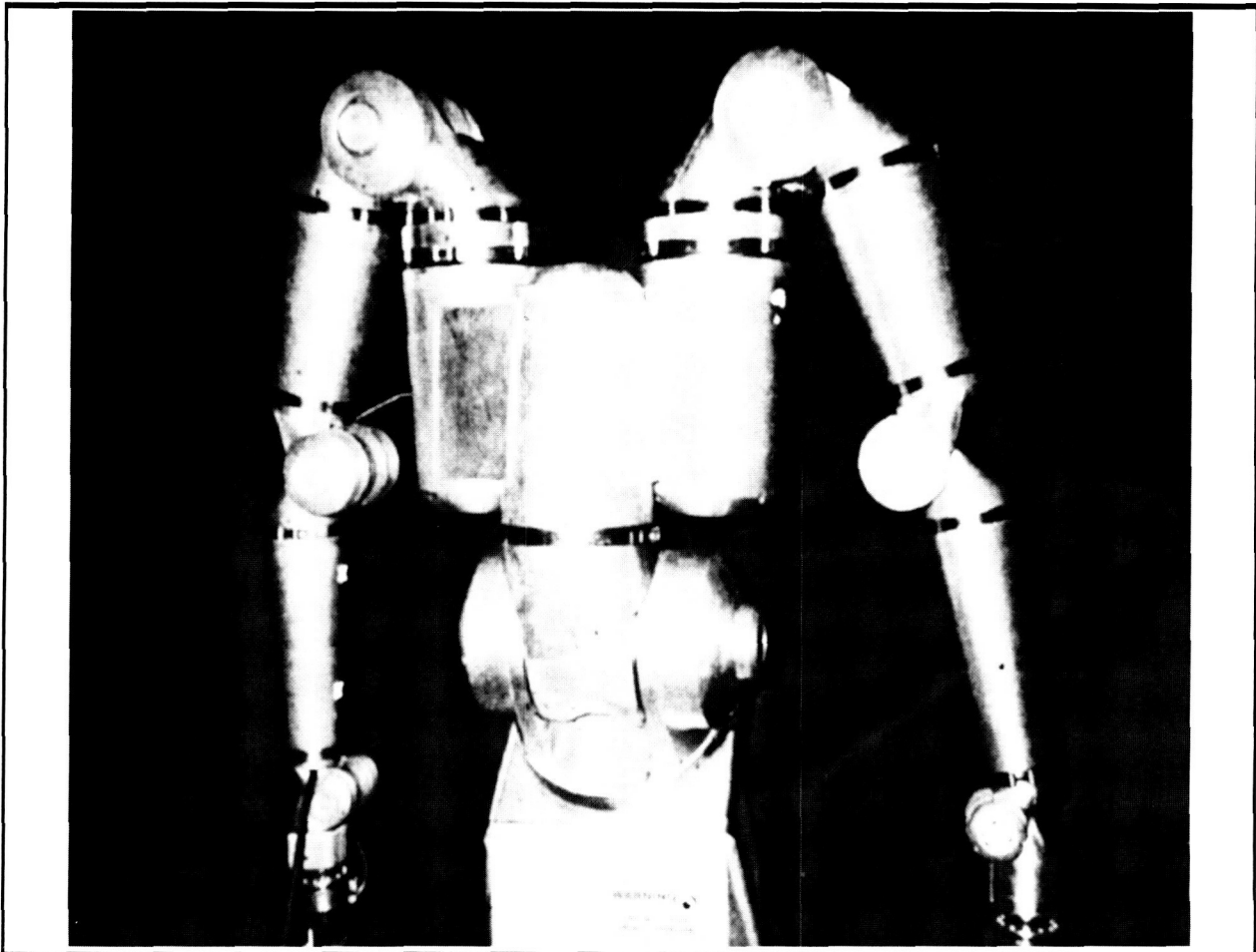

Figure 5.   The Robotics Research Co. KB-2017 dual-arm robot.

The UT program has identified and mathematically formulated 25 dual arm criteria. The criteria are addressed at three separate levels of control: Operation level, End-Effector level, and Manipulator level. At each level, criteria are used to characterize different distinct kinematic and dynamic attributes. Multiple criteria have been successfully demonstrated in computer simulated dual arm task [Cox]. The task include heavy payload lifting, fixtureless assembly on-the-fly, and work piece deformation.

Failure Detection and Isolation

The subject of machine self-diagnostics and failure detection and identification (FDI) in dynamic systems is not new [Willsky][Isermann], but the integration of such schemes into a real-time failure responsive control system is yet to be realized. A key element of such an FDI scheme is its capability to detect *incipient* failure, which gives the reconfiguration and recovery stages ample time to respond to the failure in such a manner as to minimize error excursions and reconfiguration shock.

Two basic types of FDI schemes exist: model-free and model-based methods. The latter methods are more suited for real-time autonomous systems as the former invariably tend to be off-line and require operator assistance. Model-based methods rely on the use of mathematical descriptions of the monitored system, called *analytical redundancies*. The methods involve the generation of a *residual*, whose on-line statistics are compared against nominal ones in a decision unit where fault detection, isolation and identification take place. The decision unit then generates a control impairment status (CIS) report, that provides quantitative and qualitative information about the status of the monitored system, based on which the failure responsive control system takes subsequent actions.

The University of Texas has been investigating FDI techniques for robotic manipulators. A sensor fault detection scheme that employs parity relations among temporal redundancies has been derived [Sreevijayan] and implemented [Rubin] for the knuckle module of Figure 1. The failure of any one sensor (position or velocity) is masked, thus making FDI and sensor reconfiguration transparent to the control system . The scheme, as designed, can be configured in a triple or n-modular redundancy (NMR) setup so that faulty sensors can be isolated and dynamically configured out of the system. Actuator FDI for the knuckle is realized using parameter identification techniques based on the work in [Isermann]. In this technique, failure is detected and identified depending on the statistical variations of the on-line estimated values of the physical parameters of the actuator from their fault-free ones. The changes, in orientation and magnitude, of on-line estimated vectors in parameter space provide the necessary diagnostic information.

Reconfigurable Control

The problem of control of fault-tolerant systems, in particular those with redundant control inputs is of sufficient general interest across a variety of disciplines (robotics, flight control systems, etc.) that it warrants the investigation and development of a general theoretical framework. While preliminary efforts at deriving fault tolerance schemes that take into account the full dynamics of a manipulator have met with success [Menon][Ting], the absence of a formal mathematical framework restricts our ability to answer qualitative questions like existence and optimality of solutions to such problems. With this in mind, the University of Texas program has embarked on an in-depth study of the theoretical issues underlying the utilization (under normal and failure modes) of redundant control elements in general nonlinear control systems. We are currently pursuing an operator-theoretic approach which treats the control problem in an input-output framework. The problem is then to solve appropriate operator equations that yield infinite solutions by optimizing a prescribed functional. The functional so

prescribed will reflect useful criteria during normal operation and will reflect the failure status of control actuators when the FDI system signals a fault. The mathematical framework may be thought of as generalizing the familiar generalized inverse problem in robot kinematics to the more complex realm of operators that map, say, one Hilbert space into another. We expect to be able to fully and formally characterize the nature of redundancies in any control system, in a manner analogous to the concept and formulation of *available redundancy* in the kinematics of Level III manipulators [Sreevijayan].

CONCLUSIONS

The University of Texas at Austin's Robotics program has developed a broad technical base for the development of component and system level technologies for space robotics. This paper gave an overview of our ongoing work in several key areas that are geared to address the needs of NASA's future missions. Our emphasis, driven by the needs of such missions, continues to be on enhanced accuracy and performance, condition monitoring and condition-based repair, modularity, criteria-based decision making and, above all, fault tolerance with reconfigurable control. To support the stated goals of our mission, and to fully integrate the component technologies described in this paper, we are also doing an in-depth study of micro-sensor technologies, sensor fusion and software architectures for failure-responsive control. This will allow us to realize the kind of machine intelligence that will animate the robots of the future.

REFERENCES

Chladek, J.T., "Fault Tolerance for Space Based Manipulator Mechanisms and Control System," *First International Symposium on Measurement and Control in Robotics,* Houston, Texas, June 1990.

Cleary, K., Tesar, D., "Decision Making Criteria for Redundant Manipulators", Presented at the *NATO Advanced Research Workshop,* Salo, Italy, June 1988.

Cox, D., Tesar, D., "Multi-level Criteria for Dual-Arm Robotic Operations", *Proc. of the 1994 IEEE International Conf. on Robotics and Automation,* San Diego, CA, pp. 1243-1249, May 1994.

Eschenbach, P.W., Tesar, D., "Optimization of Four-Bar Linkages Satisfying Four Generalized Coplanar Positions", *Journal of Engineering for Industry,* pp. 75-82, February, 1969.

Isermann, R., "Model Based Fault Diagnosis and Supervision of Machines and Drives", *Proc. of the 11th IFAC World Congress,* Vol. 4, pp. 1-12, Tallinn, Estonia, August 1990.

Karlen, J.P., et al., "Design and Control of Modular, Kinematically-Redundant Manipulators", Second AIAA/NASA/USAF Symposium on Automation, Robotics, and Advanced Computing for the National Space Program, March 9-11, Arlington, VA, 1987.

Menon, V.K., Sreevijayan, D., and Tesar, D., "A Preliminary Torque Redistribution Scheme for the Operation of Fault Tolerant Serial Manipulators", *Proc. of the International Symposium on Measurement and Control in Robotics*, Turin, Italy, Sept. 1993.

M.D. Rubin, " Development of Real-Time Operational Software for a Fault Tolerant Testbed", Masters Thesis, University of Texas at Austin, Austin, Texas, June 1993.

Sreevijayan, D., "On The Design of Fault-Tolerant Robotic Manipulator Systems," Masters Thesis, University of Texas at Austin, Austin, Texas, May 1992.

Tesar, D., "Thirty-Year Forecast: The Concept of a Fifth Generation of Robotics--The Super Robot", *ASME Transactions on Manufacturing Review*, Vol. 2, No. , pp. 16-25, March 1989.

Butler, M. S. and Tesar, D., "A Generalized Modular Architecture for Robot Structures," *Manufacturing Review,* Vol. 2, pp. 91--118, June 1989.

Tesar, D., Price, C., Sreevijayan, D., "Four-Level Fault Tolerance in Manipulator Design for Space Operations", Presented at the *First International Symposium on Measurement and Control in Robotics,* NASA Johnson Space Center, June 20-22, 1990.

Ting, Y., Tosunoglu, S., and Tesar D., "A Control Structure for Fault-Tolerant Operation of Robotic Manipulators," *Proceedings of the 1993 IEEE International Conference on Robotics and Automation*, Vol. 3, pp. 684--690, Atlanta, Georgia, May 2--7, 1993.

Van Doren, M.J., Tesar, D., "Criteria Development to Support Decision Making Software for Modular, Reconfigurable Robotic Manipulators, The University of Texas at Austin, Report to U.S. Dept. of Energy under Grant No. DE-FG02-86NE37966, March 1992.

Willsky, A.S., "A Survey of Design Methods for Failure Detection in Dynamic Systems", *Automatica,* Vol. 12, pp. 601-611, 1976.

Performance of the Satellite Test Assistant Robot in JPL's Space Simulation Facility

Douglas McAffee, Mark Long, Ken Johnson, and Georg Siebes*

Abstract

An innovative new telerobotic inspection system called STAR (the Satellite Test Assistant Robot) has been developed to assist engineers as they test new spacecraft designs in simulated space environments. STAR operates inside the ultra-cold, high-vacuum, test chambers and provides engineers seated at a remote Operator Control Station (OCS) with high resolution video and infrared (IR) images of the flight articles under test. STAR was successfully proof tested in JPL's 25-ft (7.6-m) Space Simulation Chamber where temperatures ranged from +85 °C to -190 °C and vacuum levels reached $5.1 \cdot 10^{-6}$ torr. STAR's IR Camera was used to thermally map the entire interior of the chamber for the first time. STAR also made several unexpected and important discoveries about the thermal processes occurring within the chamber. Using a calibrated test fixture arrayed with ten sample spacecraft materials, the IR camera was shown to produce highly accurate surface temperature data. This paper outlines STAR's design and reports on significant results from the thermal vacuum chamber test.

Introduction

Before a new spacecraft design is flown in space, it must first undergo severe testing in a simulated space environment where it is exposed to high vacuum, cold temperatures or varying intensities of artificial solar light. These environmental tests are used to establish the spacecraft's flight worthiness.

Conducting these tests can be relatively expensive. Hundreds of thousands of dollars can be invested in a typical two or three day test. Often the test articles are instrumented with several hundred thermocouples, but it is difficult (or impossible) to cover the test article sufficiently to obtain all the data one would like. If anomalies occur during the test or if the article performs in an unexpected manner, the engineers and chamber operators typically have no way of adjusting sensors and have only limited visual access inside the chamber once the test is begun. It can be very costly to stop a test, open the chamber, make adjustments and then restart. Because of the expense involved, it is important that the test data be reliable and complete the first time. In addition, a significant amount of man-hours are needed each year to perform routine chamber calibration and maintenance.

---

* Jet Propulsion Laboratory, California Institute of Technology, Pasadena, CA

In 1992, under the sponsorship of NASA Code C (now Code X), engineers in JPL's Robotics and Automation Section and the Environmental Test Chamber Operations Group began a new project to use existing technology and expertise to develop a remotely controlled telerobotic inspection system. The new device would augment and improve existing data collection capabilities and help reduce the costs of performing tests within the environmental test chambers. Significant savings could be obtained if the mobile inspection capabilities of the new device could help prevent even one premature test shutdown. The new device could also help reduce costs by helping chamber operators locate and identify faulty or malfunctioning equipment. This new project is called STAR (the Satellite Test Assistant Robot).

This paper presents an overview of the STAR system design and reports on the successful proof tests conducted in JPL's 25-ft (7.6-m) Space Simulation Chamber.
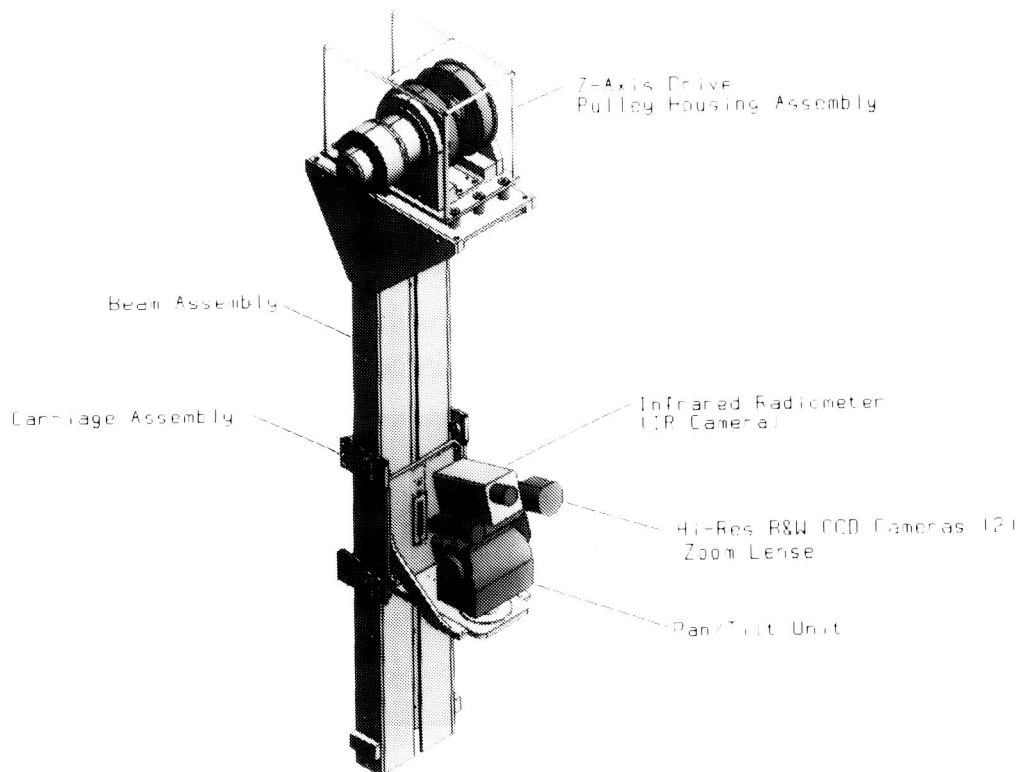

Figure 1.   Satellite Test Assistant Robot (STAR) In-Chamber Equipment

The STAR Design

Building anything that can operate in space, or in our case a simulated space environment, is an exceptionally challenging undertaking. And it's not inexpensive. The original design concept, which proved to be quite overly ambitious, called for building of a 25-ft (7.6-m) tall by 25-ft (7.6-m) diameter, heavy lift, clean-room quality robotic gantry system inside JPL's Space Simulation Chamber where temperatures can drop to -190°C. The robotic gantry system was to carry a 3.6-m (12-ft) long, multi-DOF robotic arm and a pan/tilt system with stereo camera capability [1]. Budgetary constraints, as they often do, forced a much needed reality check and the design was subsequently scaled back to satisfy only the most essential needs of the end-user, i.e., the chamber operators and spacecraft test engineers.

The current implementation of STAR consists of a vertical positioning system (the Z-Axis) and a pan/tilt unit that articulate a set of video and IR cameras. The length of the Z-Axis beam can be easily changed, anywhere from 0.6 to 7.6 m (2 to 25 feet) or more, for mounting in a variety of thermal vacuum test chambers. A 2.4-m (8-ft) Z-Axis is shown in Figure 1 and was used during STAR testing in JPL's smaller 10-ft (3-m) Chamber in 1993 [2]. The in-chamber equipment, shown in Figure 1, is remotely controlled from an Operator Control Station (OCS) shown later in Figure 6.

STAR Z-Axis

One of the most significant design challenges in the STAR project was the design of the vertical Z-Axis. How can you get anything to move over large distances, reliably, smoothly, accurately and cleanly at -190°C, and design it economically? As shown in Table 1, we evaluated several design alternatives. The characteristics and design parameters of interest are listed in the column on the left in Table 1. The various candidate drive mechanisms considered are listed across the top . On a scale from 1 to 5, with 1 being the best, an engineering judgment was made as to how well each of the candidate drives met the design criteria. The comparison clearly revealed the best design solution was to use a metal belt design.

After a significant amount of research and consultations with JPL materials experts a choice was made to use a 0.2-mm (0.008 in) thick x 50.8-mm (2 in) wide half-hard 304 stainless steel belt which wraps over a 25.4-cm (10 in) diameter pulley. Of primary concern was brittleness and fatigue strength of the material at LN$_2$ temperatures. During this time in the design process, we were still expecting the belt drive design would need to lift 136 to 180 kg (300 to 400 lb) of robot arm (this requirement was later changed and greatly reduce during a project de-scope). Because of the catastrophic consequences of a broken drive belt, a redundant two-belt system was designed. Laboratory tensile tests on sample belts and mounting brackets at room temperature revealed that each belt can withstand a 907 kg (2000 lb) load before breaking.

Table I

Comparison of Candidate Drive Mechanisms

MECHANIZATION / CHARACTERISTIC	RACK AND PINION	LEAD/BALL SCREW	CHAIN DRIVE	CABLE DRIVE	METAL BELT DRIVE
A. MATERIALS					
Properties at Cryo Temps	3	3	4	2	1
Properties over Wide Temp Range	4	4	4	2	1
Vacuum Rated	2	2	4	4	1
Non-Outgassing	2	2	3	4	1
Availability (Stock or Custom Comp)	2	4	3	3	3
Overall Mass	4	5	2	1	1
Comparitive Reliability	3	2	4	4	3
Est. Development Time	2	3	3	3	3
Simplicity of Assembly/Install.	3	4	3	2	1
Maintainability	3	4	4	3	2
Overall Cost	2	5	3	1	2
B. CLEANLINESS					
Lubrication Required	4	4	4	1	1
Rubbing vs. Rolling Contact	3	4	4	3	1
Ease of Cleaning	3	4	4	5	1
Debris Generation	3	3	4	3	1

1= BEST SELECTION   5= WORST SELECTION

The resulting Z-Axis belt drive design is a relatively inexpensive, easily scaleable, highly reliable, fail-safe, clean-room quality drive mechanism.

The Z-Axis is driven by a 7 N•m (62.5 in•lb) brushless DC motor that is rated to operate in the space-like environment. Connected at the back of the motor shaft is a 24 VDC fail-safe brake that engages whenever power is removed from the system. There is also a 1000 line optical encoder. The Z-Axis motor drives dual 25.4-cm (10 in) diameter pulleys through a 50:1 harmonic drive resulting in a 240 kg (530 lb) lifting capacity.

The carriage assembly was designed with 12 spring-loaded Vespel guide wheels (Figures 2 and 3). The wheels are spring loaded to accommodate the significant dimensional changes caused by the large thermal variations in a typical chamber test.

Even though it is by far the largest individual component in the entire STAR assembly, the Z-Axis beam, by design, is one of the most inexpensive. It's basically just a standard 10 x 30.5 cm (4 x 12 in) aluminum 6061-T6 C-channel beam that has been black anodized (See cross section in Figure 2). As mentioned before, the beam can be cut to any length for mounting in various sizes of chambers.

Another challenging design problem was the electrical cable design for the Z-Axis Carriage. At -190 °C, most materials, including copper wires, tend to become quite stiff and do not like to bend. In typical space flight applications, this problem is overcome by pre-warming mechanisms having electrical wires attached to at least -50°C before being actuated. In our design situation, that was not practical since we wished to have the STAR structure blend in with surrounding chamber cold shrouds. Another design consideration was that we wished to have the electrical cable contained within the vertical beam for two reasons: first to avoid snagging the cable on flight hardware as STAR was moved within the chamber, and secondly, the metal structure of the beam would act as a faraday shield to help reduce any electro-magnetic interference (EMI) caused by STAR. EMI pollution in the chamber during a test was to be minimized since it may affect sensitive spacecraft instruments.

These problems were overcome by designing the Z-Axis Carriage cable to be contained within the Z-Axis beam at all times. A special cable was constructed with a unique flat braided weave. The cable attaches inside the beam at the half height point. A length of cable equal to at least half the travel of the carriage is then looped down within the beam, forming a traveling loop. The flat cable weave allows an 28 cm (11 in) diameter, 180° bend in the cable to travel up and down inside the C-channel behind the metal drive belts as the carriage is lifted and lowered.

STAR Pan/Tilt Unit

The pan/tilt unit in STAR is an off-the-shelf product that has been adapted for use in the thermal vacuum test chamber environment. This particular design actually violates most of the design goals we were trying to achieve in the STAR design, i.e. avoiding rubbing contacts points and chain drives that produce contaminates, avoiding the use of AC motors to reduce EMI output, etc. However, it has two major benefits going in its favor. First of all, it has a usage heritage. A pan/tilt unit very similar to the one we selected had been used several times before within the chamber during thermal vacuum operation. The chamber operators were confident and comfortable in using the design. And secondly, it was inexpensive. Our limited design and fabrication budget at the time was the real determining factor that drove us to go with this particular off-the-shelf design (see Figures 4 and 5). The pan/tilt unit cost about $1500. It could of easily cost 10 times that amount to design, build and qualify a better design. In the age of faster-better-cheaper, sometime cost is the determining factor.

The off-the-shelf pan/tilt was modified for use in the thermal vacuum environment by 1) completely disassembling the entire unit, motors and all, 2) removing paint from parts
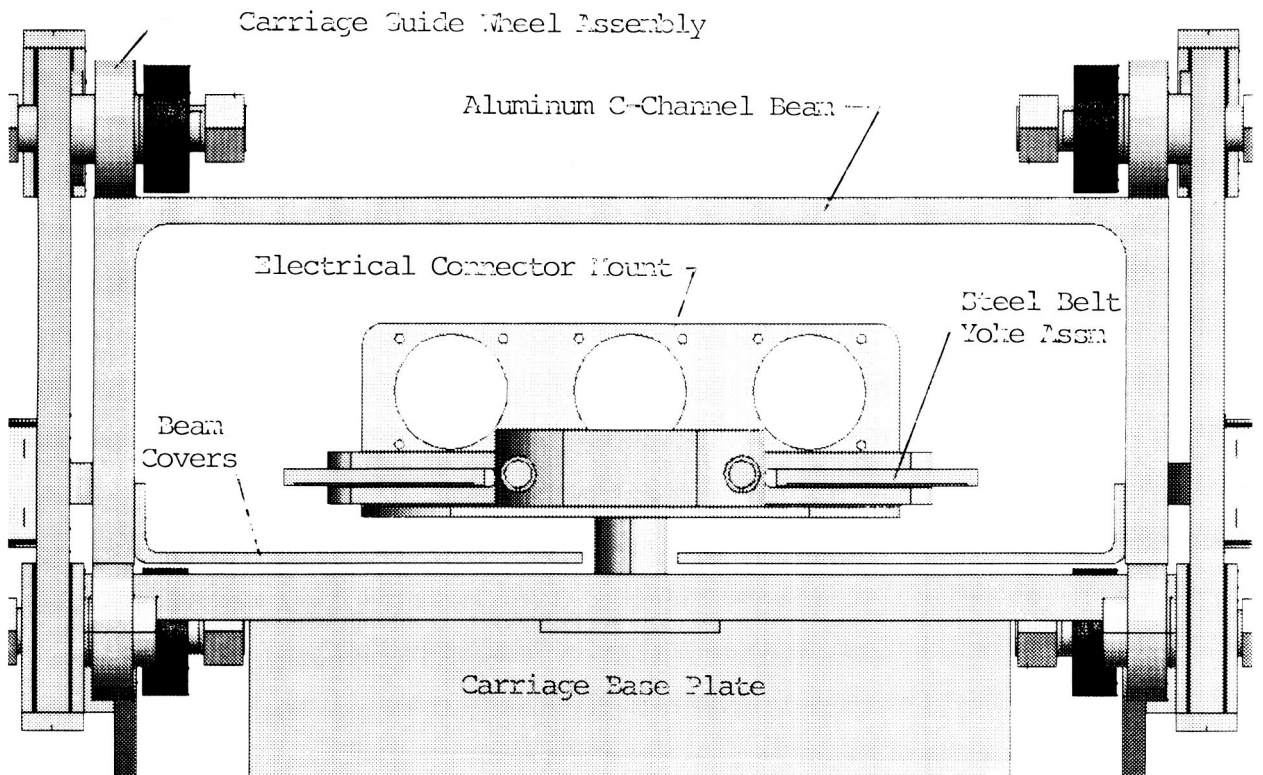
Carriage Guide Wheel Assembly

Aluminum C-Channel Beam

Electrical Connector Mount

Steel Belt
Yoke Assm

Beam
Covers

Carriage Base Plate

Figure 2.   STAR Carriage and Z-Axis Beam Assembly, Top View Cross Section

Metal Belt Drive
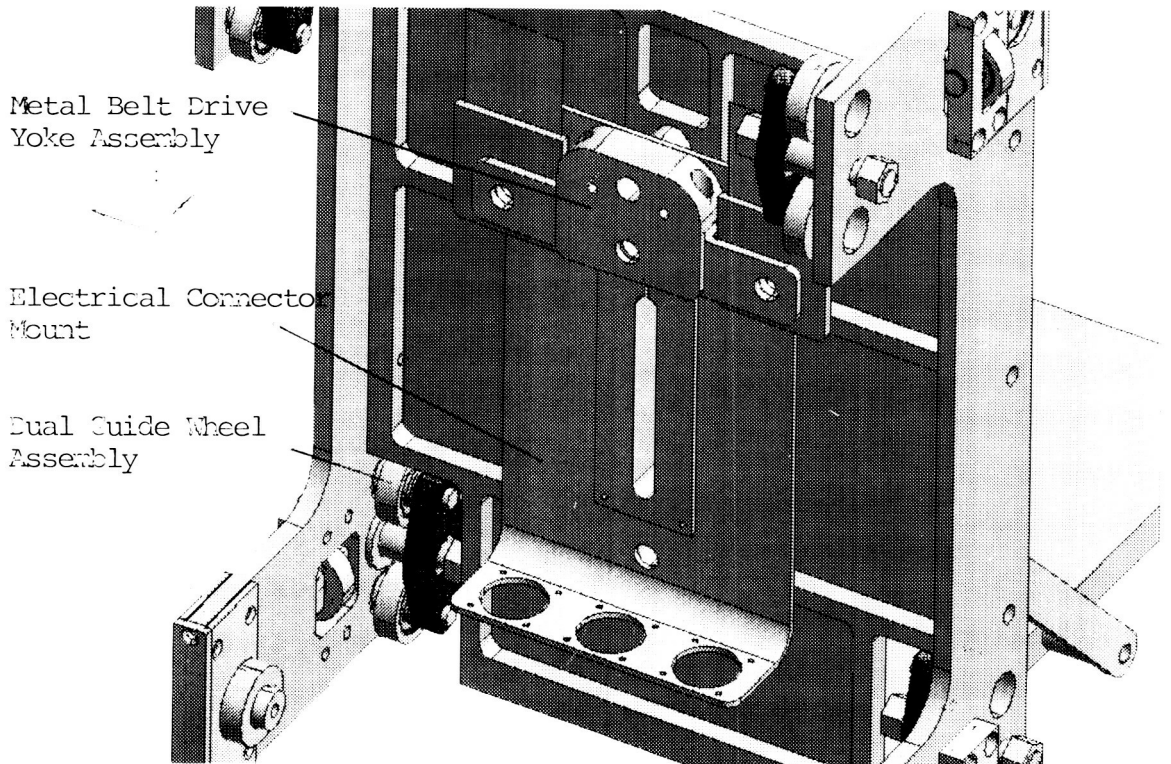Yoke Assembly

Electrical Connector
Mount

Dual Guide Wheel
Assembly

Figure 3.   STAR Carriage Assembly, Back Isometric View
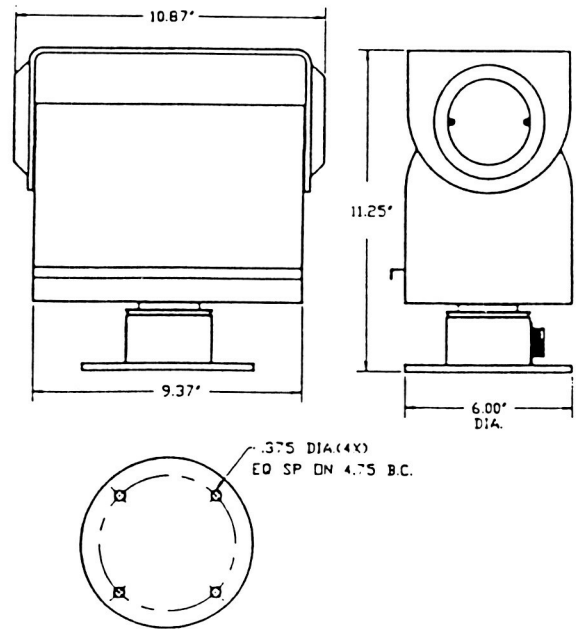
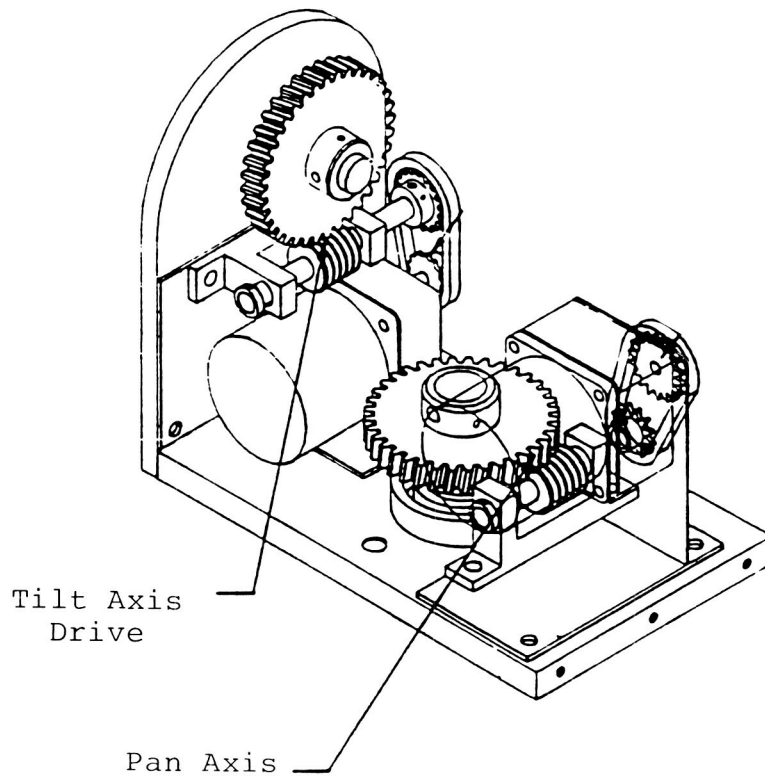**Figure 4   STAR Pan/Tilt Unit, Front, Side and Bottom Views**

Tilt Axis
Drive

Pan Axis

Figure 5   STAR Pan/Tilt Unit, Internal Drive Mechanisms

and anodizing, 3) removing all grease and oils in bearings and gears throughout and recoating the worm drives with a 10% Braycote 600 vapor deposition, 4) removing all electrical wiring and replacing it with flight quality Teflon insulated wire, 5) fabricating a new pan/tilt cover that could be sealed to prevent escape of any particulate contaminates, and 6) baking out (out-gassing) the entire unit in a high temperature, high vacuum, bell jar chamber.

It is pointed out here that the selection of this pan/tilt design, as opposed to designing one from scratch, was a somewhat risky proposition. However, later test results showed that it worked well in a thermal vacuum environment, but it also, surprisingly, was a very clean piece of hardware. The ability to achieve extremely high vacuum levels during bake out indicated that the pan/tilt hardware produced an exceptionally small amount of out-gassing.
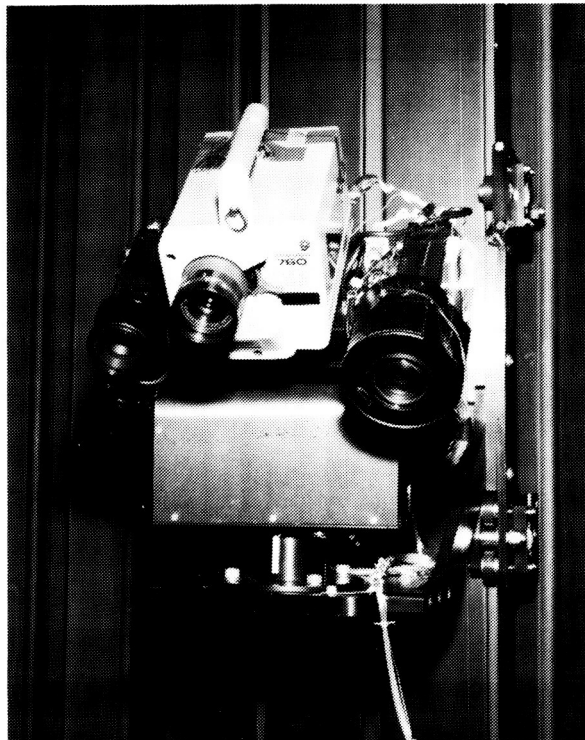
Figure 6   STAR Video & IR Camera Instrument Package & Pan/Tilt Unit

STAR Instruments

Of the technological contributions made by STAR, one of the most important is the introduction of IR imaging technology into the thermal vacuum test chamber environment. Engineers can now perform non-contact temperature measurements on all exterior spacecraft surfaces.

As mentioned previously, the STAR instrument platform, shown in Figure 6, consists of two high-resolution vacuum-rated Pulnix CCD video cameras fitted with fixed and zoom lenses. In addition, it has an Inframetrics Model 760 Infrared Radiometer (IR Camera) and computer-controlled lighting. A series of heating elements and thermostats were mounted to these instruments to maintain vendor-specified operating temperature ranges. The front half of the camera assembly was covered by a thermal blanket to protect from direct solar light irradiation.

STAR Operator Control Station (OCS)

An operator seated at STAR's OCS outside the chamber can remotely control the instrument platform inside the chamber by using a computer touch screen display and graphical user interface (GUI). Operators can control the elevation and orientation of STAR's instrument platform and make adjustments to camera settings, capture and manipulate images, adjust lighting conditions and perform system diagnostics, etc.

STAR's OCS is the double rack console shown in the left forefront of Figure 7. It was a new development for FY'94 and serves as the primary user interface for system operation. The main OCS control computer is a standard NEC 486-PC running Windows. It incorporates a touch screen display from Micro-Touch and a new LabView-based GUI that provides easy and simple access to all of STAR's functions via the touch screen. The OCS control computer is equipped with Precision MicroControls' DCX PC100 servo control modules and analog and digital I/O. A three-channel video board from Win/TV provides on-screen video image capture and processing. The OCS also has two high-quality video monitors and a built-in VCR. The OCS rack also houses a system I/O Interface Box with manual control switches, a Power Distribution Box, and the motor amplifier that powers STAR's vertical Z-Axis.

Putting STAR to the Test

On December 20, 1994, STAR successfully completed a critical thermal/vacuum qualification test in JPL's 25-ft (7.6-m) Space Simulation Facility where chamber temperatures ranged from +85 °C to -190 °C and vacuum levels reached 5.1×10^{-6} torr. During the test, STAR performed extremely well and provided much new information about the dynamic processes within the thermal vacuum test chamber.

The overall objectives of this test were two-fold: 1) functionally test the STAR hardware in the space simulator and 2) determine the accuracy of the IR Camera. The primary motivation for conducting this test was to further validate STAR's functionality and performance in harsh thermal/vacuum environments. Last year, much of the STAR's in-chamber hardware underwent two previous thermal/vacuum tests conducted in JPL's smaller 10-ft (3-m) Chamber [2]. Testing in the 25-ft (7.6-m) Chamber qualified the STAR hardware operations in that chamber and it also provides additional levels of confidence and experience operating the equipment in harsh environments.
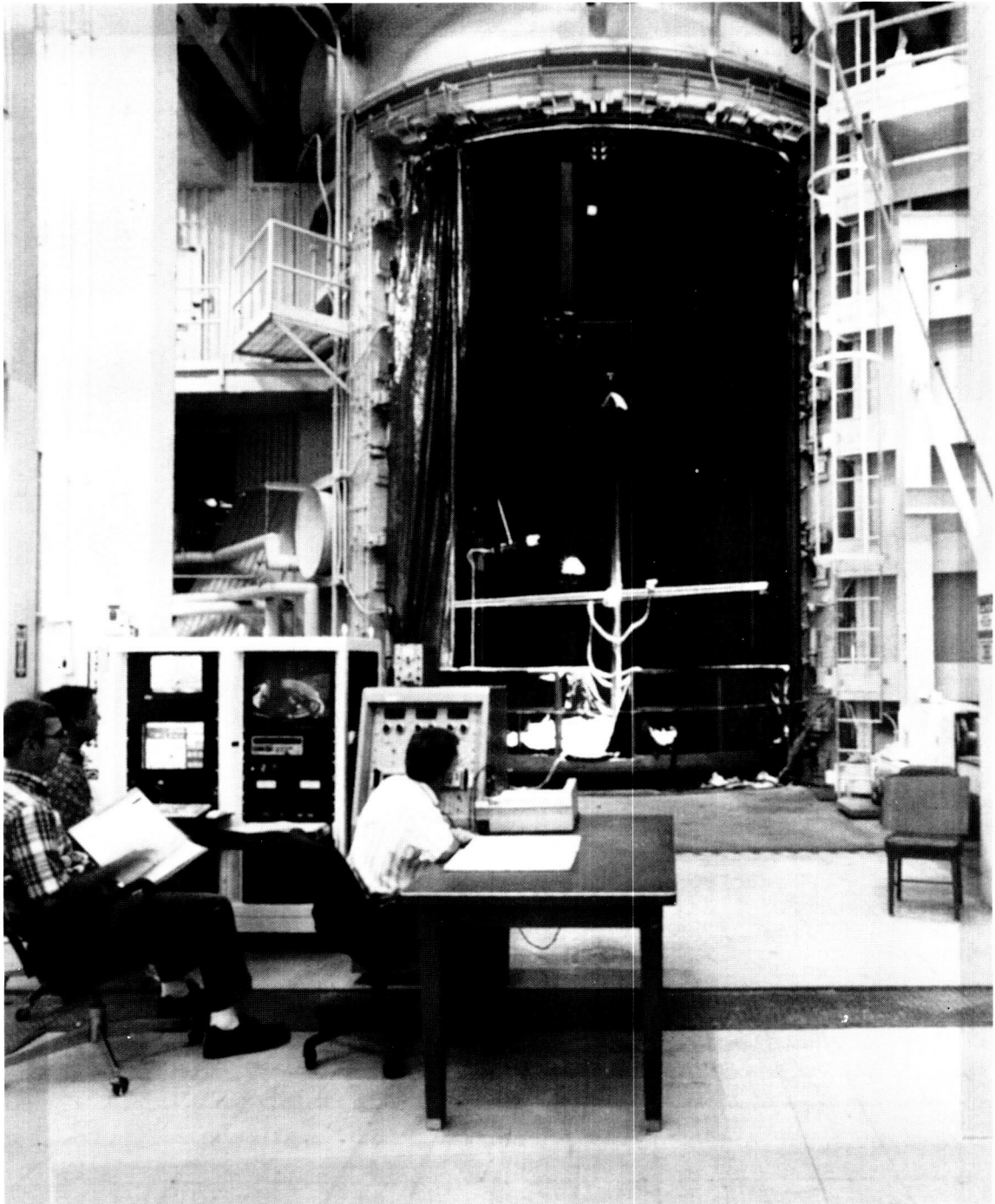
Figure 7   STAR during installation in JPL's 25-ft (7.6 m) Space
Simulation Facility

Of primary interest in this test was the performance of several off-the-shelf, non-flight, non-vacuum rated components contained in STAR's mechanical and electrical subsystems, of particular note are the Inframetrics IR Camera, Cosmicar fixed and zoom lenses, and the Pelco pan/tilt unit. These items were modified or adapted for use in the harsh thermal/vacuum environment [3]. Inclusion of these items within the STAR system represented a significant known risk taken in order to meet cost and schedule requirements. Their inclusion also marked a significant variation from traditional hardware design and development practice resulting in a far more inexpensive end product. During the test, we focused much of our attention on these critical items.

The STAR IR Camera was shown to be highly accurate at measuring surface temperatures across a wide variety of sample spacecraft materials. Even on difficult, low emissivity materials the IR Camera's thermal measurements differed from those measured by conventional thermocouple networks by only 0.5 °C. Part of the test was to investigate what is the coldest temperature range the IR Camera can resolve. Surprisingly we were able to image temperatures to about -70 °C with only 4 to 5 °C discrepancy from traditional thermocouple measurements.

During this test STAR was instrumental in making several significant new discoveries about thermal dynamic processes within the 25-ft (7.6-m) Space Simulation Facility. These discoveries include:

1. For the first time chamber operators were able to find distinct blockages in several individual chamber shroud radiator tubes. Figure 8 is a captured video image showing the lower portion of the 25-ft (7.6-m) Chamber's door cooling shroud. Figure 9 is an image from the IR Camera showing 4 blocked shroud cooling tubes. The original IR image is in vivid color but in this black and white image the blocked tubes show up as dark gray.

2. STAR was also able to pin-point and quantify several chamber hot spots.

3. STAR's vivid thermal images clearly showed a more than 70°C lag between the chamber's door shroud and the rest of the chamber.

4. STAR's IR Camera also found that a surprisingly large thermal gradients existed across a commonly used heat exchanger plate.

Results and Conclusions

The STAR hardware and software performed extremely well throughout the test with only a few minor glitches, for example, during the access of an IR Camera GUI sub-menu item the main control computer hung which required a system reboot. The sub-menu software interface will be modified in the future. The functionality of all systems and subsystems were randomly checked about every 20 minutes and 18 hours of

Figure 8   Captured Video Image of Chamber Door Shroud
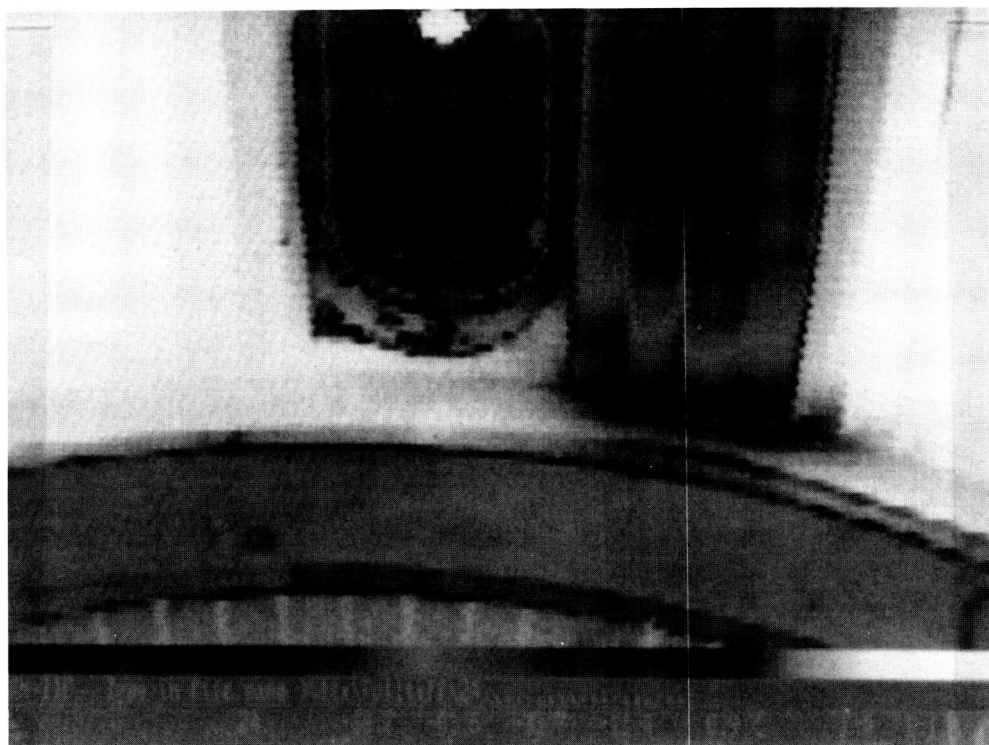

Figure 9   IR Camera Image of Chamber Door Shroud Revealing Blocked Tubes

video tape were recorded of all images displayed to STAR's main OCS monitor. There were also 24 IR Camera images were captured and saved to diskette.

Thermal engineers and chamber operators at JPL participated in the test and seem to be very enthusiastic about using STAR in future spacecraft thermal/vacuum environmental tests. STAR allows, for the first time, non-contact measurements to be made in the harsh high vacuum, ultra-cold temperature test chamber environment. This opens up a whole new way of testing spacecraft at JPL and will be extremely valuable when performing tests on difficult surfaces to instrument with traditional thermocouple techniques such as on antennas, solar panels, radiators, optical surfaces, and moving targets such as rovers and mechanism deployments.

Using STAR's IR Camera, engineers can now thermally map the external surfaces of a spacecraft. The high-resolution video cameras allow detail inspection and documentation of the spacecraft as it is being tested.

STAR's most significant contribution may be that it provides engineers with a means of addressing unforeseen anomalies that often occur during the complicated spacecraft testing process. Once a test is underway, it is very expensive to stop, open the chamber, and make adjustments to sensors or equipment.

STAR was also designed to aid in the calibration and maintenance of the test chambers and the results from this initial test in the 25-ft (7.6-m) Space Simulation Chamber produced an astonishing amount of new information as to how the thermal components within the chamber perform.

Acknowledgments

References

[1] McAffee, D., Kerrisk, D. and K.R. Johnson, "Satellite Test Assistant Robot (STAR)", SOAR Conference, AUG 92

[2] McAffee, D. "Significant Accomplishment Report: STAR Thermal/Vacuum Test Completion, JPL Interoffice Memorandum, Oct. 8, 1993.

[3] McAffee, D. and M. Long. Satellite Test Assistant Robot (STAR) Thermal Vacuum Test Report, JPL D-12384, December 21, 1994,

The Alpha-Proton-X-Ray Spectrometer Deployment Mechanism -- An Anthropomorphic Approach to Sensor Placement on Martian Rocks and Soil

Richard S. Blomquist*

ABSTRACT

On July 4,1997, the Mars Pathfinder spacecraft lands on Mars and starts conducting technology and science experiments. One experiment, the Alpha-Proton-X-ray Spectrometer, uses a sensor head placed against rocks and soil to determine their composition. To guarantee proper placement, a deployment mechanism mounted on the Mars Rover aligns the sensor head to within 20° of the rock and soil surfaces.

In carrying out its task, the mechanism mimics the action of a human hand and arm. Consisting of a flexible wrist, a parallel link arm, a brush dc motor actuator, and a revolutionary non-pyrotechnic fail-safe release device, the mechanism correctly positions the sensor head on rocks as high as 0.29 m and on targets whose surfaces are tilted as much as 45° from the nominal orientation of the sensor head face. The mechanism weighs less than 0.5 kg, can withstand 100 g's, and requires less than 2.8 N·m of actuation torque.

The fail-safe coupler utilizes Cerrobend, a metal alloy that melts at 60° C, to fuse the actuator and the rest of the mechanism together. A film heater wrapped around the coupler melts the metal, and Negator springs drive the mechanism into its stowed position. The fail-safe actuates using 6.75 Watts for 5 minutes in the event of an actuator failure.

INTRODUCTION

The Mars Pathfinder mission, launched in December 1996, promises to reap a harvest of geological information about Mars. One of the nearly half dozen instruments making this science data possible is the Alpha Proton X-ray Spectrometer (APXS). Using a curium source and backscattering techniques, the APXS will determine the elemental composition of rocks and soil around the landing site.

To ensure information of high fidelity, the APXS sensor face must be aligned within 20° to the surface of each rock and soil sampling location, maintain a distance of 0.040 to 0.050 m from the sampling target, and be held in place for up to 10 hours. The most straightforward way to accomplish this task is to have a stowaway take the sensor in hand and place it on a rock or soil. The next best answer is the anthropomorphic APXS Deployment Mechanism (ADM).

---

* Jet Propulsion Laboratory, California Institute of Technology, Pasadena, CA

Consisting mainly of a flexible wrist capable of +/-25 degrees bending compliance in two axes, a parallel link arm, and a brush dc motor actuator with a gear ratio of 2000 to 1, the ADM operates in a 1.30 kPa CO_2 atmosphere at temperatures as low as -100° C. Using the Mars Rover as a transport (see Figure 1), the ADM both actively and passively positions the APXS sensor head on rocks as high as 0.29 m and on soil as low as 0.05 m below the bottom of the Rover rear wheels, while at the same time minimizing impact on Rover turn radius, ground clearance, and power. In the event of an actuator failure, a fail-safe mechanism composed of a Negator spring pack and a low-temperature-melting metal coupler decouples the mechanism from the actuator and retracts it into its stowed position. The entire mechanism fits in a 0.24 m long by 0.21 m wide by 0.14 m high envelope and weighs less than 0.5 kg.
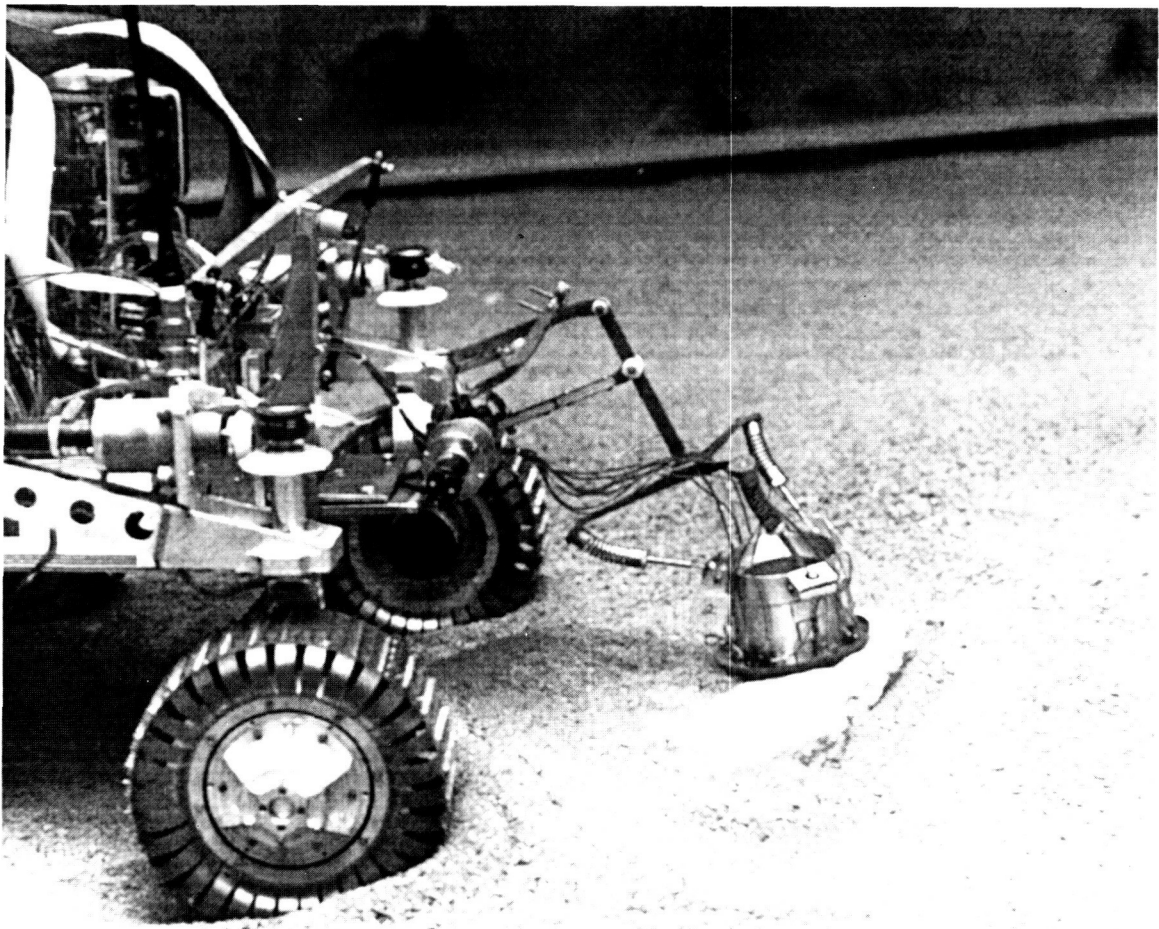

Figure 1. ADM mounted on the Mars Rover.

The ADM design underwent dozens of iterations to accommodate the performance goals of the instrument and to meet all the conflicting requirements levied by the APXS principle investigators, Rover developers, and Mars Pathfinder lander engineers. This paper explains the details of the final design, including the reasoning behind the choices made. At the end of the paper, test results show the performance of the ADM, providing empirical evidence of its capabilities.

DESIGN EVOLUTION

Flexible Wrist

Many technical challenges drove the ADM design evolution. The foremost obstacle was providing adequate sensor head compliance within the allowed volume. The problem is best illustrated by the following example. Imagine a person holding the sensor head with a 0.040 m long cylindrical spacer (see Figure 2) attached to the front. As the person contacts a rock with the front of the cylinder, the area of contact acts as a fulcrum. To align the sensor head completely with the surface of the rock, the person rotates the cylinder about the initial contact point until the cylinder is touching the rock in two other places. In completing the positioning, the person translates and rotates the sensor head, meaning that 5 degrees of compliance are required for the maneuver.
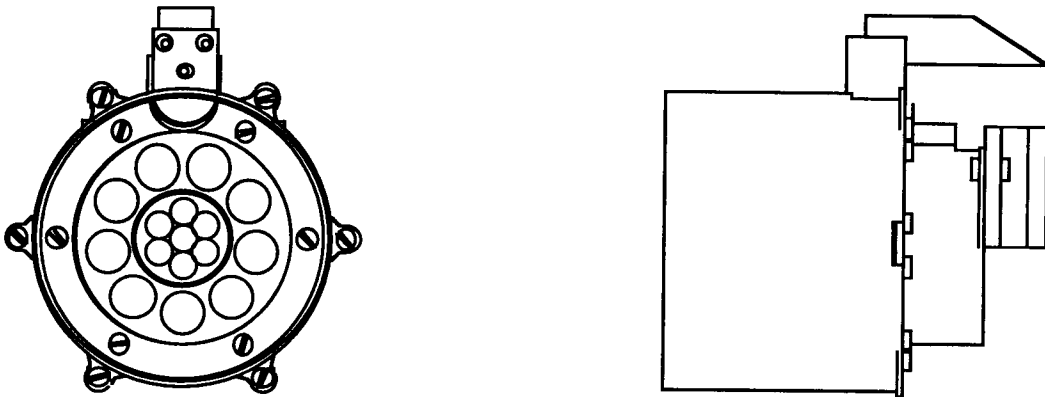

Figure 2. APXS sensor head with spacer attached.

This positioning operation is similar to the two-dimensional task that James Nevins and Daniel Whitney of Draper Laboratories studied[1]. They considered the robotic placement of a peg in a hole and what type of compliance is necessary in the peg gripper to compensate for robot positioning errors. As seen in Figures 3a and 3b, Nevins and Whitney noted that a gripper with parallel link supports is capable of compensating for translational errors, whereas a gripper with links angled inward is capable of allowing for rotational errors. The intersection of the lines down the longitudinal axes of the links is the initial center of rotation. Combining the two types of link supports as shown in Figure 3c, they produced a platform that accommodates both translational and rotational errors. If restoring force is required, they suggested that deformable wires be substituted for links, as depicted in Figure 3d.

---

[1] Nevins, James L. & Whitney, Daniel E., "Computer-controlled Assembly", Scientific American, February, 1978, pgs 62-74.
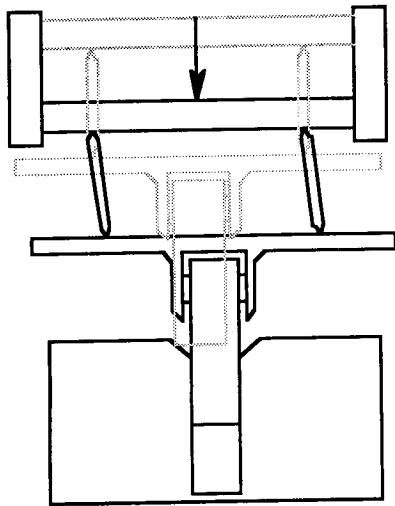
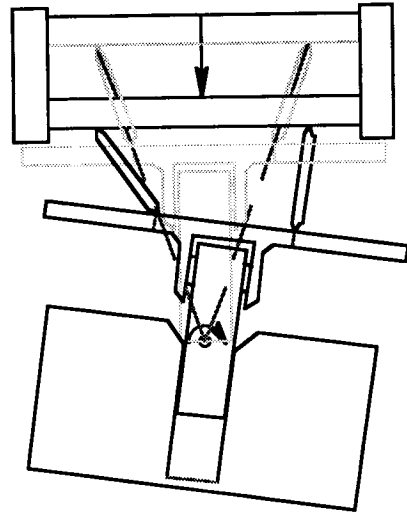**Figure 3a. Translational compliance.**

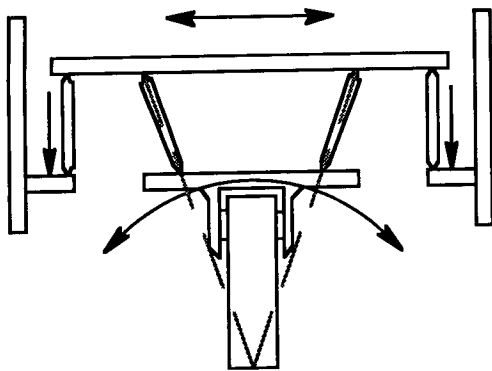**Figure 3b. Rotational compliance.**

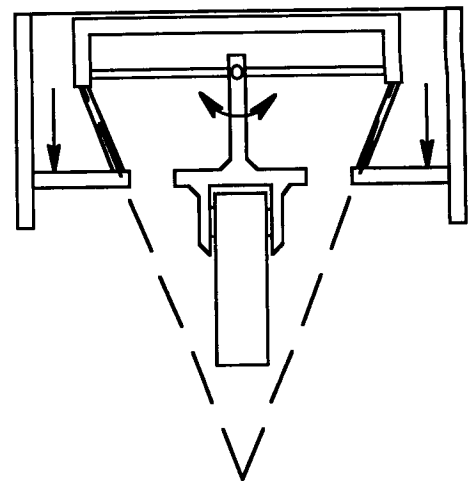**Figure 3c. Translational and Rotational compliance.**

Figure 3d. Deformable wires used instead of links.

Applied to the APXS sensor head, Nevins and Whitney's link supports look like Figure 4a. Springs act as the restoring force in the figure. The size and weight of the support shown is prohibitive. But, by intelligent choice of the slanted link geometry, the translational compliance requirement can be reduced to below the amount of slop and flex in the mechanism, and the translational stage can be eliminated. Furthermore, by mounting the links on springs, the supporting geometry can shrink to the size and shape shown in Figure 4b.
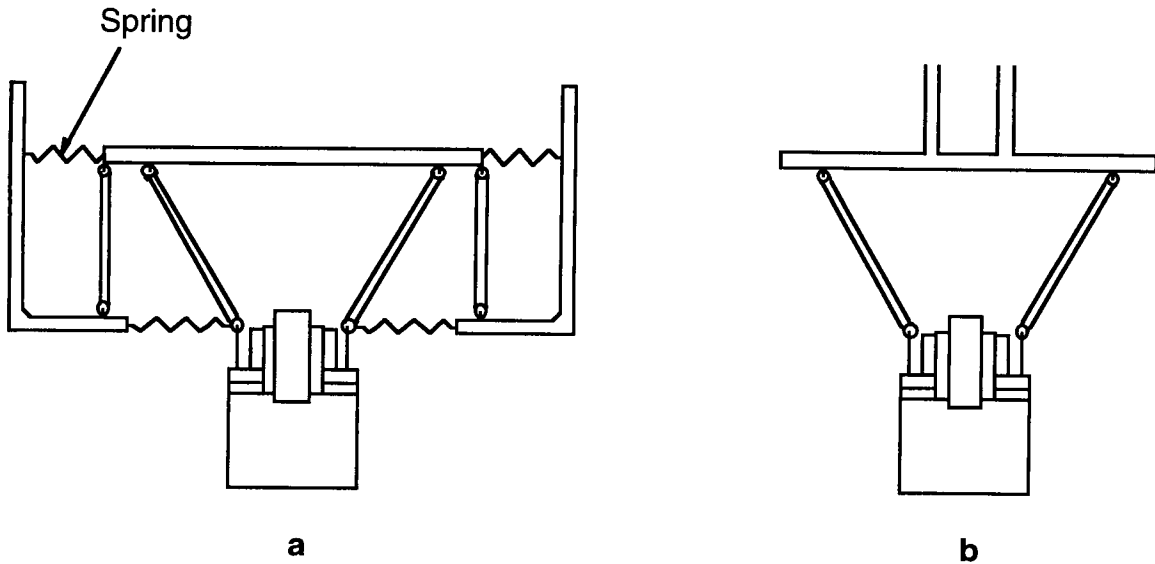
Figure 4. Nevins and Whitney's compound compliant support, APXS version. a) both translational and rotational compliant stages present; b) translational stage removed, links mounted on springs.

To determine the proper slanted link geometry, the kinematic equations of motion are solved until both the lateral translation target and the rotational capability target are met. Figure 5 illustrates the problem to be solved. For this design, translation less than 0.006 m and rotation of +/-25° are the targets. A geometry with A equal to 0.066 m, B equal to 0.125 m, and L equal to 0.053 m gives adequate results while still fitting into the design envelope.
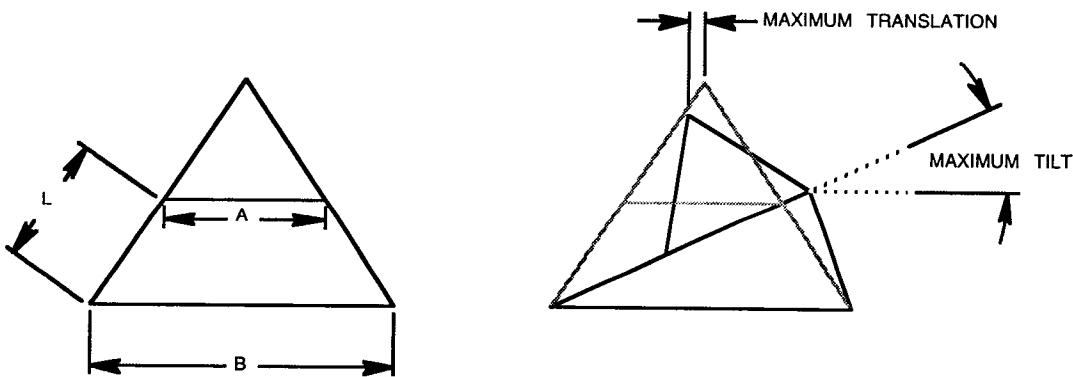

Figure 5. Wrist link geometry.

Converting the above kinematic study into three-dimensional hardware is straightforward, as links spaced 120° apart on a base support plate is the three-dimensional equivalent to the problem. Helical-cut springs mounted at the base of the links provide restoring force, as shown in Figure 6. Notice that the attachment points of the links to the sensor head are located so that the initial instantaneous center of rotation is in front of the sensor head, creating a stable compliance no matter where the sensor head contacts a rock.
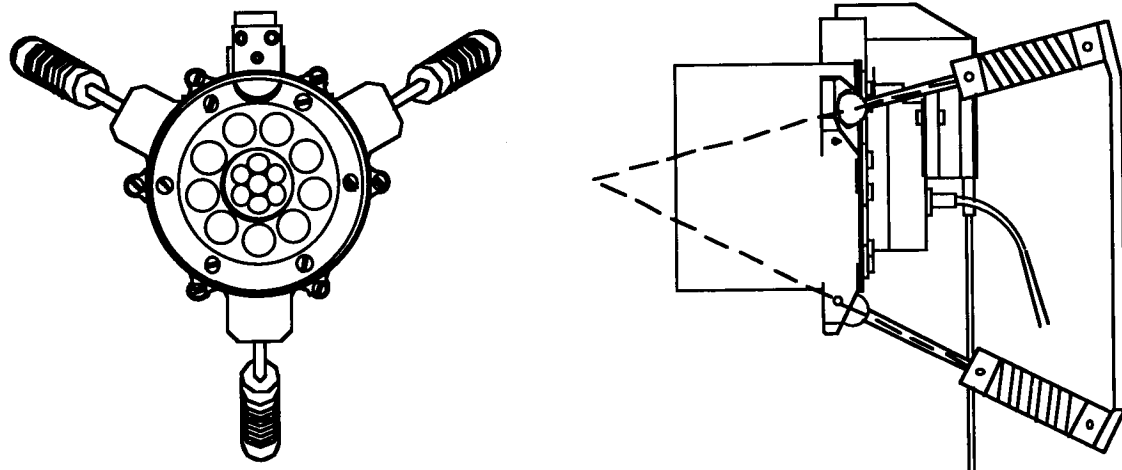
Figure 6. APXS flex wrist support. Intersection of dashed lines is the initial instantaneous center of rotation.

Alignment Indication System

Another design dilemma, whose solution goes hand in hand with the flexible wrist design, is alignment indication. A 0.04 m long cylindrical spacer mounted on the front of the sensor head easily insures that the low end of the 0.04 to 0.05 m sensor-to-target requirement is met. However, proper angular alignment requires a feedback system.

One design considered for this purpose consists of a 0.076 m diameter bumper mounted on three soft-spring-loaded plungers equally spaced around the cylinder (see Figure 7). As the bumper contacts its target, the plungers compress the springs and the bumper lines up flush to the target; then, the flexible wrist aligns the sensor head. When the plungers deflect, the body of each plunger immediately blocks the light path between an LED/phototransistor pair mounted at the base of the plunger. This sends a contact indication to the Rover control system. When all three LED/transistor pairs give a signal, then the sensor head positioning stops.
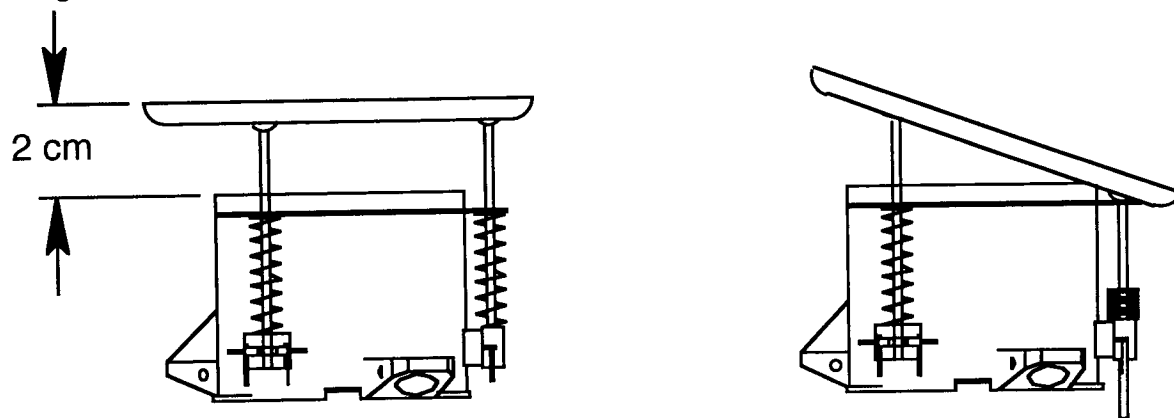

Figure 7. Bumper on soft springs. Alignment indication based on position.

To satisfy its requirements, this system must work successfully in the two extreme situations: an approach at an angle 45° off the normal to the surface, forty five degrees coming from the 25° of wrist compliance plus the 20° alignment requirement, and an approach straight-on. For the proposed system to work, the bumper must stick out 0.02 m past the front of the cylinder to allow for greater than 20° compliance. Also, the plungers must cause a contact indication after only a small amount of deflection, to take full advantage of the bumper compliance.

During the 45° off-angle approach, the bumper first complies to the target to within 25°. Then, the sensor head starts to rotate into alignment. At this point, one or two plungers are compressed as shown in Figure 7, but the third is not. As the sensor nears the 20° alignment requirement, the bumper becomes flush with the target surface, the third plunger starts to compress, the third LED/transistor pair gives a contact signal, and positioning stops.

For the straight-on approach, as the bumper contacts a rock, the three plungers deflect simultaneously, causing all three LED-transistor pairs to give a contact indication. Because the bumper is still protruding approximately 0.02 m past the cylinder at this point, the 0.04 to 0.05 m spacing requirement is violated. The cylinder must therefore move at least 0.01 m closer to the rock before the sensor head reaches proper alignment.

This design concept is faulty, for three reasons. First, the mechanism most likely is capable of aligning the sensor head more closely than 20°, as long as the original off-angle approach is less than 45°. Second, the protruding bumper increases the rover turn radius and increases the chance of the bumper snagging on a rock. Third, no feedback control exists for the last 0.01 m of travel during a straight-on approach.

A better design idea uses basically the same hardware, but has LED/transistor signal attainment based on force and not position; In other words, the LED/transistor pairs give alignment indication only after the flexible wrist support has positioned the sensor head the best it can and has either reached its end of travel or aligned the sensor head perfectly. Then, as the rover or actuator continues to push the sensor into its target, the force in the bumper builds up until stiff springs preloading the plungers compress. In this way, the plungers travel only 0.002 to 0.003 m, just enough for the plungers to block the contact switch light path, and the bumper protrudes a maximum of 0.005 m past the front of the cylinder. This scenario works as long as the sensor head approaches the target within 45°.

An important aspect of the alignment indication design is the shape of the bumper. One school of thought is that the bumper should be as smooth as possible to prevent it from catching on something. However, the bumper often needs to catch on a rock feature before the wrist can start aligning the sensor head; otherwise, the sensor head frequently ends up sliding over the rock surface. Another viewpoint is that the bumper should be pointy, like a set of pencil-shaped pokers. This works well on rocks, though the cross-sectional area necessary for the sensor head to align to the fine sand surface of Mars is nonexistent. Combining the two ideas results in a bumper shaped as shown in Figure 8. The sharp edge on the front surface is excellent for rock positioning, the

frontal area of the bumper is sufficient for soil samples, and the smooth backside helps prevent the bumper from snagging during retraction.
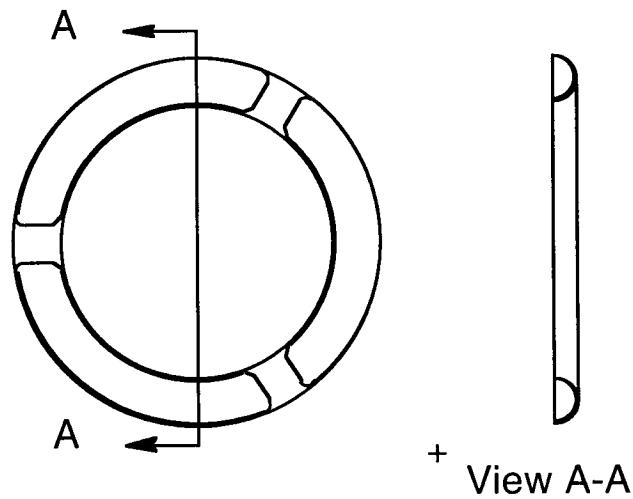

Figure 8. Bumper shape.

Vertical adjustment

In actively positioning the sensor head, the mechanism must be able to do four things: first, the mechanism must be capable of pulling the sensor head in close to the rover to minimize rover turn radius; second, the mechanism must be capable of extending the sensor head sufficiently past the edge of the rover solar panel so that the solar panel does not hit as the rover moves the sensor head into a rock; third, the mechanism must be capable of raising and lowering the sensor head to varying rock levels; and fourth, the mechanism must move vertically in its final motion down to the soil surface, not in a sweeping fashion, to eliminate the possibility of wedging the sensor head into the ground like a door stop, and to impede the bumper from scooping up dirt. Throughout its motion, the mechanism should keep the sensor from pointing upward, as the sensor is hypersensitive to direct sunlight and falling dust.

Ideally, the active positioning part of the ADM should move the sensor horizontally away from its stowed position, rotate it 90°, and then move it vertically down to the surface (see Figure 9). Mimicking this motion in a simple mechanism is tricky. Chain drives, clutches, pulleys, and parallel links can all do the job to one extent or another. The best answer however, due to its simplicity, is a parallel link system.
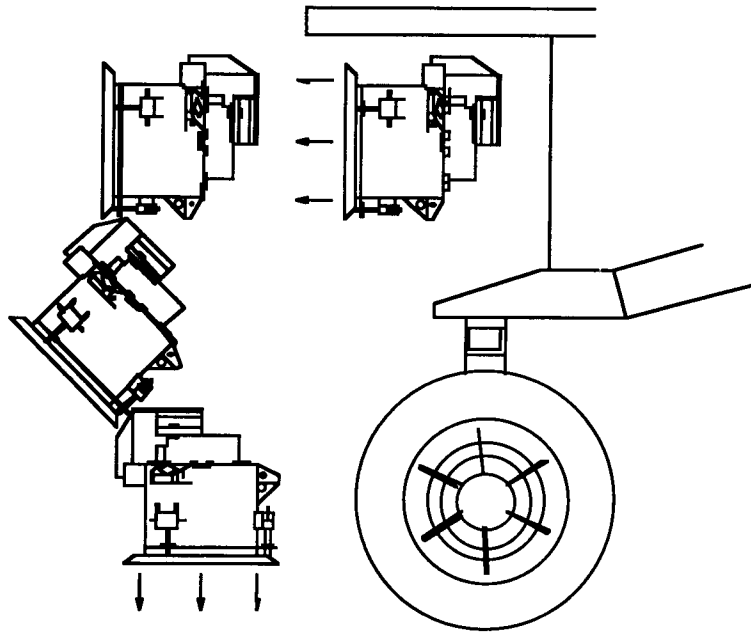
Figure 9. Ideal travel of the sensor head.

Parallel links of equal length most closely achieve horizontal or vertical motion at the apex of travel. Therefore, parallel links positioned as shown in Figures 10d and 10a accomplish the critical vertical motion of the sensor down to the surface and the less critical horizontal motion away from the rover. To create the sweeping transition between the two linear motions, one of the parallel links hits a stop, allowing the entire assembly to rotate about the drive axis, as shown by comparing Figures 10b and 10c.
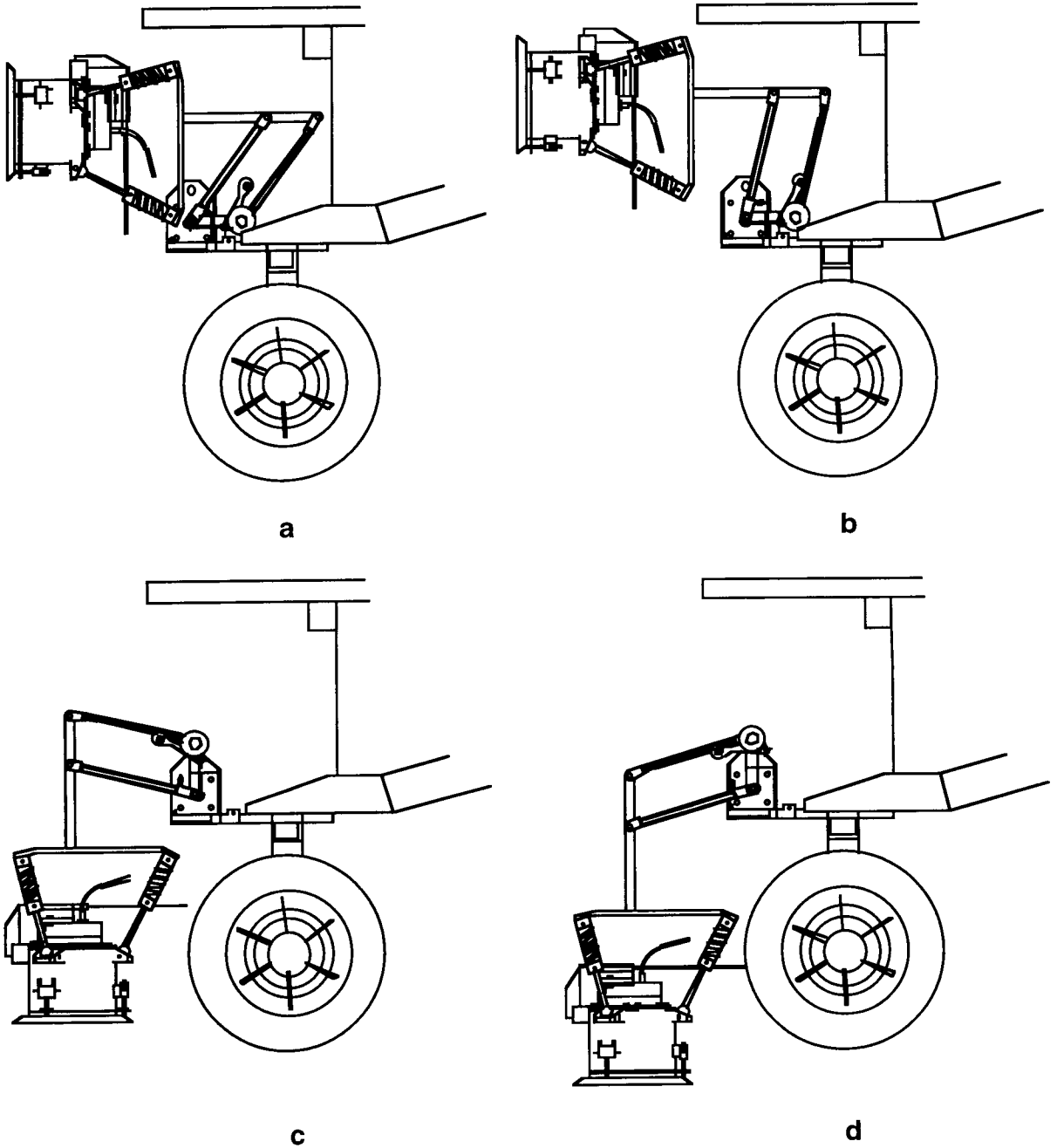
Figure 10. Travel and orientation of the parallel link system: a, stowed position; b, back parallel link contacting stop, horizontal extension stopped; c, links rotated 90°; d, links extended vertically downward.

The details of the parallel link hardware and its workings follow (see parts nomenclature in Figures 11a and 11b). An actuator consisting of a Maxon brush DC motor and a Globe gearbox with a 2000:1 gear ratio drives the front parallel link at its base. A transverse link connects the base of the front link to the base of the back link, and a horizontal link connects the tops of the front and back links. A tab on the transverse link rests on the mechanism shelf. To keep the tab resting on the shelf during the initial horizontal movement of the mechanism, a torsion spring acting between the back link and the transverse link drives the back link toward the front link, resulting in a contact load between the tab and the shelf. As long as the contact load exists, the back parallel link acts as if it were anchored to the shelf.

After the mechanism moves the sensor horizontally, the back link comes in contact with a spring-loaded stop, loaded against the transverse link with another torsion spring. The spring load on the stop is greater than the spring load on the back link, so the mechanism stops extending and the parallel links effectively lock up. As the actuator continues to drive the front link forward, the entire mechanism rotates. After 90° of rotation, the transverse link comes in contact with a hard stop, and rotation ceases. Torque from the actuator then overpowers the spring-loaded stop and the mechanism moves the sensor head vertically down to the soil.

Because the mechanism has only one active degree of freedom, a potentiometer connected to the front link gives all the information needed for the Rover control system to determine the basic configuration of the mechanism. Using the potentiometer, the control system can position the mechanism anywhere along its travel path, while at the same time being aware of the position and nominal angular orientation of the sensor head.
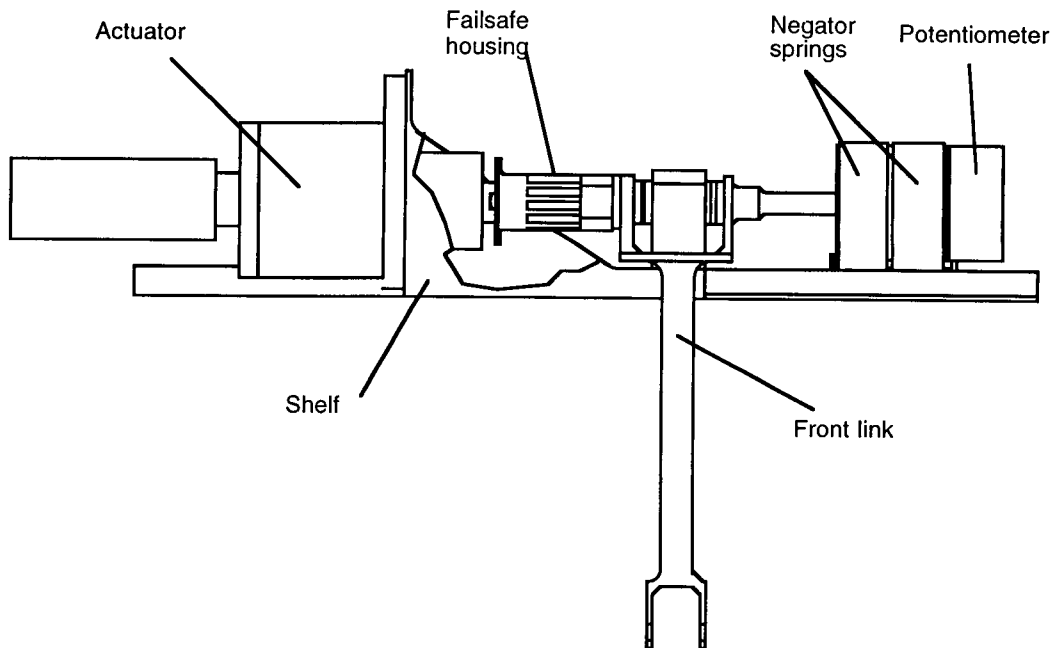

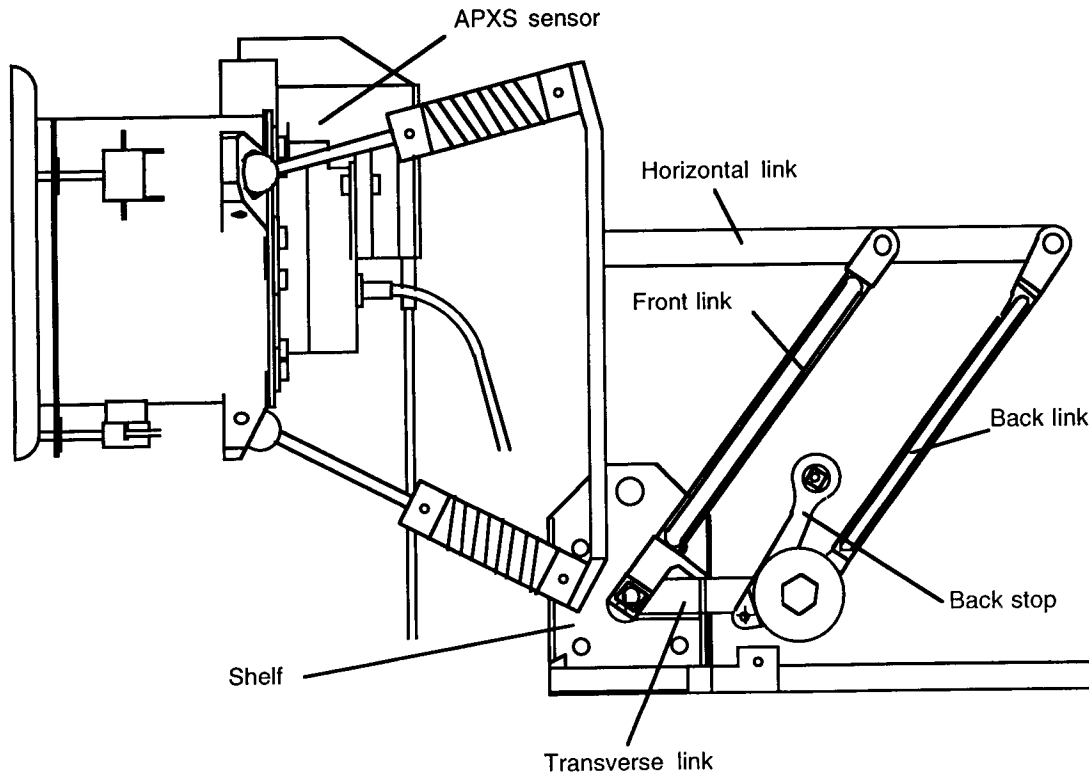**Figure 11a. ADM parts nomenclature: front link base axis.**

Figure 11b. ADM parts nomenclature: ADM side view, with Negator springs, potentiometer, fail-safe housing, and actuator removed.

Fail-safe Mechanism

If the actuator fails when the mechanism is in its deployed position, rover clearance is reduced to zero and the rover is crippled. To ensure recovery from a failed actuator , a rotary fail-safe mechanism must be included in the mechanism design. This fail-safe, when actuated, must retract the mechanism fully into its stowed position. It must also provide at least 1.1 N·m of retraction torque, withstand 100 g's and 17 N·m of torque, and survive temperatures from -110° C to +70° C and atmospheric pressures ranging from high vacuum to 101.3 kPa. Furthermore, rover constraints require it to have no pyro firing and use less than 10 Watts for a maximum of 10 minutes when operating in Mars ambient conditions (-100° C and 1.3 kPa CO_2). Finally, the fail-safe mechanism should weigh 0.020 to 0.030 kg, fit into a 0.025 m x 0.050 m x 0.050 m volume, and be inexpensive.

Since pyrotechnics are out of the question, alternative release devices become prime candidates. Among several possibilities are wax pellet actuators, but their size, cost, and power consumption make them prohibitive. Another idea is a nitinol pin puller, with multiple strands pulling on the pin. However, due to friction imposed on the pin, the energy necessary to activate the nitinol wire and maintain adequate pulling margin exceeds the design limit. The final idea consideration is a low-melting-point metal pellet coupler in parallel with a Negator spring pack (see Figure 11a and Figure 12). In

its solid state, the metal rigidly connects the driver (the actuator) and the driven part (the mechanism). When commanded, a strip heater wrapped around the coupler housing melts the metal pellet, allowing the driven part to turn independently of the driver. With the pellet melted and the mechanism decoupled, the Negator spring retracts the mechanism to its fully stowed position. This concept meets all the design criteria and provides an added benefit. When the metal rehardens, the coupler once again rigidly connects the actuator and the mechanism as it did before actuation.
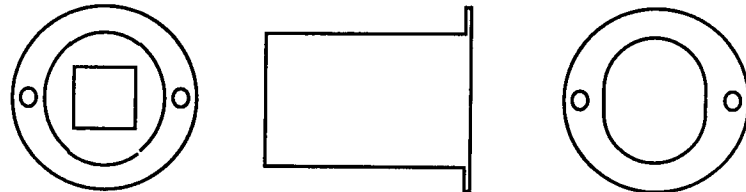
Cerrobend housing, side and end views

Front link   Felt washer   Housing   Paddle on shaft
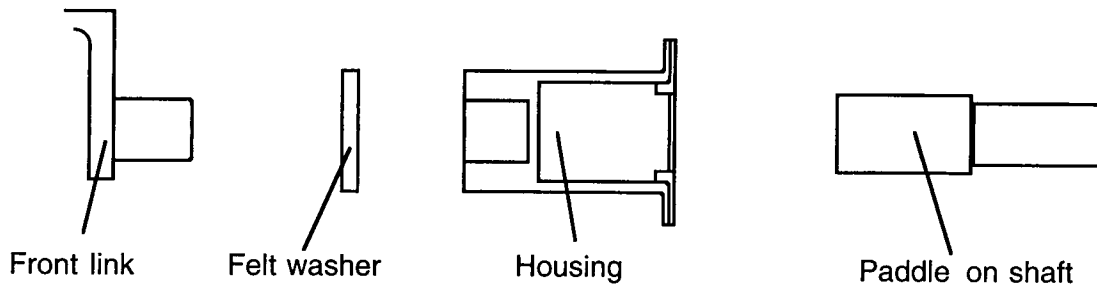
Exploded, cut-away view of housing mounting

Figure 12. Fail-safe housing.

The concept of a metal alloy coupler originated with a metal in mind, namely Cerrobend. This material typically is used in fusible links such as fire suppression sprinklers and as structural support during machining of thin-walled parts. Cerrobend consists of bizmuth, lead, tin, and cadmium, and melts at 60° C. In its liquid state, it has the consistency and cohesiveness of mercury. In its solid state, it looks like lead and has a shear strength of around 25 MPa.

Because a strip heater wraps around the outside of the coupler, the Cerrobend pellet housing has to be thermally conductive. Yet, it must be able to withstand 17 N·m of torque when filled with Cerrobend. Its shape should also keep the Cerrobend pellet from turning inside and from deforming under load. A cylindrical shape is inadequate, as the shear strength between the pellet and the housing wall is insufficient to keep the pellet from rotating . An aluminum housing with an elliptical shape and 0.0004 m thick wall, however, is thermally conductive, prevents the Cerrobend pellet from turning even under high loads and is strong enough to survive 17 N·m of torque.

The elliptical shape also makes it easier to effectively mount a strip heater around the coupler housing using RTV66, a silicone adhesive rated for cold temperature use. Although RTV66 is not an excellent conductor, it is used because only a very thin layer is required for adequate bonding. As an added safety feature, shrink wrap placed over the strip heater redundantly keeps the heater in place.

The end of the drive shaft is shaped like a paddle to increase shear area between the driver and the Cerrobend. This configuration provides enough area to meet the design criteria, even though the shear strength of Cerrobend is only around 25 MPa.

To more fully thermally isolate the coupler, the drive shaft, the drive paddle, and the front link are all made of titanium, because of its low thermal conductance. A felt spacer between the coupler and the front link provides added thermal conduction isolation and a felt booty wrapped around the coupler housing virtually eliminates convective and radiative losses in the coupler.

The concept presented here can easily be applied to other applications where release devices are needed. For example, spring-loaded pin puller/pusher devices can use Cerrobend pellets to hold the pins in place before actuation. Also, electrical disconnect mechanisms can disconnect wires via a spring-loaded Cerrobend spreader. The issues to be concerned with are thermal isolation, proper setting of the parts before actuation, and possible outgassing concerns. However, when these issues are overcome, the resulting release mechanism can promise to be the most light, simple, power-conserving alternative available.

Launch Configuration

Tying the mechanism down during launch, descent and landing is the last great technical obstacle. The optimal approach is to hold the sensor down to the rover and eliminate any direct tie to the lander. However, such a stowage device is too heavy for the rover to carry. Taking advantage of the compliance of the mechanism, the sensor is instead pulled down to the lander mounting surface and held in a launch support saddle with a cable, as shown in Figure 13. The helical springs in the wrist attenuate rover/lander load transfer through the mechanism.
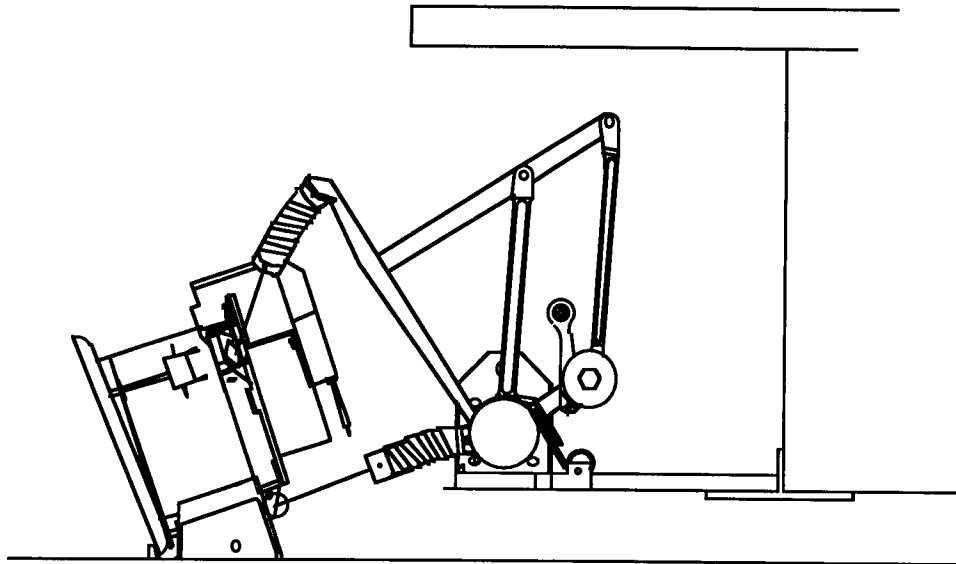
Figure 13. ADM launch stow configuration.

TESTING

A barrage of tests performed on the ADM prototype validate the design. These tests include the following:

> Flexible wrist compliance force and stability
> Bumper assembly functional tests
> Parallel link functional tests
> Actuator characterization tests from room temperature down to -100° C
> Full-up functional and torque margin tests at Earth and Mars ambient conditions
> Fail-safe actuation tests at Earth and Mars ambient conditions

Other tests scheduled for the flight and spare units in February and March of 1995 include all the above plus:

> Vibration and static load tests
> Thermal vacuum tests
> Thermal cycling tests
> Contamination tests
> Post-environmental functional and margin tests

The parts underwent a stress analysis using ADAMS, a dynamic simulation program, and COSMOS, an FEA package. Although the predicted flight loads are less than 70 g's, the hardware is designed to withstand greater than 100 g's.

Some of the detailed results of the prototype testing are listed below and provide an idea of the capability of this hardware.

Wrist Compliance Force

The force required to tip the sensor head 25° varies from 1.38 N to 2.45 N. This variance is due to the location of the applied force. If the force acts in the location of a spring-mounted support rod, less force is necessary, as one spring contributes most of the alignment resistance. If the force acts in the area between support rods, then two springs together provide the majority of alignment resistance.

When 4.9 N of force is applied, the three support rods of the flexible wrist may rapidly twist around the sensor head. This instability phenomenon occurs only when the approach is straight-on. Although it typically does not affect sensor head alignment, 4.9 N does act as an upper limit for flight operation, in that the hardware alignment indication system is designed to give alignment indication before the force on the sensor reaches 4.9 N

Alignment Indication

The bumper requires less than 4.9N to compress all three plungers and 1.35 to 2.2 N of force to compress just one. This is almost the same as the force required for maximum wrist compliance, so the bumper will indeed compress only after the flexible wrist aligns the sensor head to the best of its capability.

Torque Required

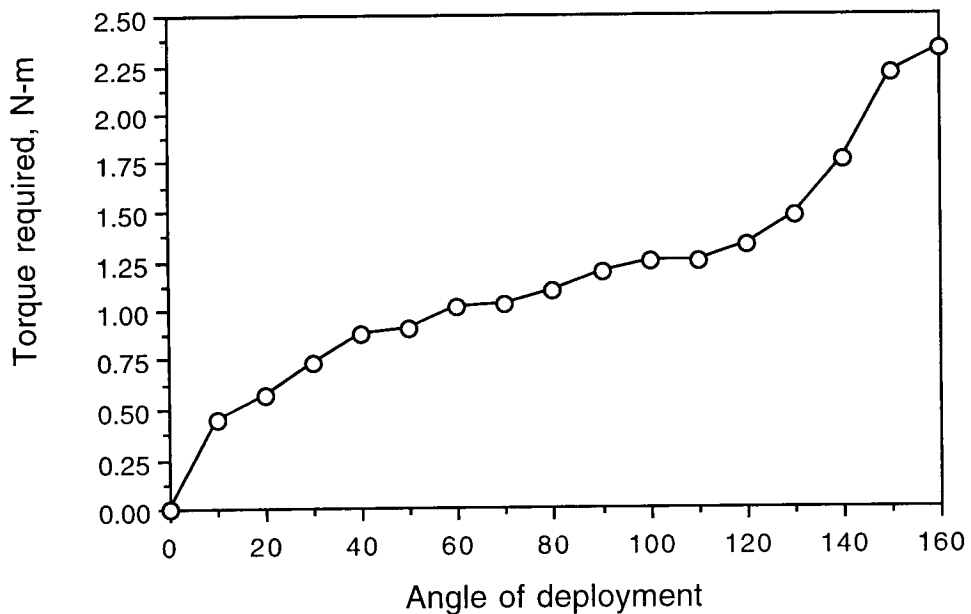Measurements of the torque required for deployment and retraction are shown in Figure 14 below.

Figure 14. ADM torque required to deploy.

Actuator Tests

From results of the actuator characterization tests, the actuator has the following operating characteristics:

Free-running speed	1.2 rpm
Working load speed (1.0 N·m)	0.6 rpm
Back-driveability	4.0 N·m
Stall torque	4.5 N·m at 23° C, up to 11 N·m at -100° C

This translates into a minimum torque margin of 0.88 at 23° C and 3.58 at -100° C. The rise in actuator capability at cold temperatures is due to lower electrical resistance and only a very small increase in drag in the actuator.

The prototype actuator design did survive preliminary vibration tests and operating temperatures as low as -116° C without any noticeable side effects.

Fail-safe Operation

Testing results show that in a Martian environment of -95° C and 1.3 kPa CO_2 atmosphere, the 0.01 m x 0.0125 m x 0.02 m fail-safe coupling takes approximately five minutes to actuate when 6.75 Watts of power are provided. A graph of typical temperature vs heating time is shown in Figure 15. In these cold conditions, the fail-safe coupler melts gradually, resulting in a slow, benign retraction of the mechanism.

The operating equilibrium temperature, represented by the asymptote of the graph, appears to be 70° C, only 10° higher than the melting temperature. The low margin is a result of the lack of felt insulation around the coupler housing. Addition of a felt washer and a felt booty as previously described in the mechanism description will increase the margin.

Torque tests at Earth ambient conditions indicate that the fail-safe coupler can withstand more than 17 N·m of torque with no slipping. However, multiple actuations of the fail-safe mechanism cause the withholding torque and actuation time to both decrease, due to incomplete melting of the Cerrobend around the drive shaft. This is attributed to the shape of the paddle. In the prototype, the cross-section of the paddle had the shape of a plus sign (+). The Cerrobend did not melt sufficiently in the corners of the paddle before the fail-safe retracted. During resolidification, discontinuities appeared, causing the torque holding capability and actuation time to decrease.

To ameliorate the problem, the paddle was changed to a flat, oar-like shape, as shown in Figure 12.
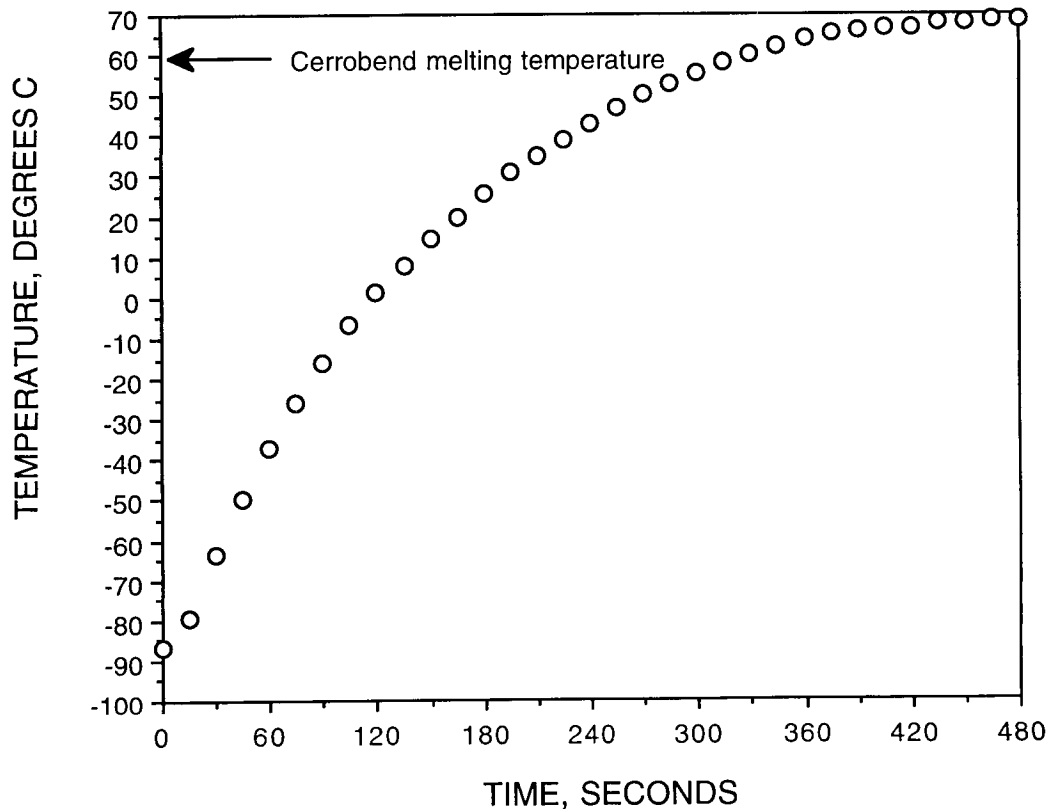
Figure 15. Typical Temperature vs time graph for Cerrobend fail-safe coupler.

CONCLUSIONS

Functional tests of the prototype unit indicate that the hardware meets its requirements. Environmental tests for the flight and spare units are not yet done, so full validation of the design will have to wait until March of 1995. However, analyses verify that the hardware will pass these tests, too.

The ADM is an amalgamation of unique solutions to challenging design problems. The resulting design is light, flexible, and nearly autonomous. Its straightforward operation rivals that of a human arm in simplicity and elegance. Its successful operation will greatly contribute to the cornucopia of useful information gleaned from the Mars Pathfinder mission.

REFERENCES

1. Nevins, James L. & Whitney, Daniel E., "Computer-controlled Assembly", Scientific American, February, 1978, pgs 62-74.

Solar Array Deployment Mechanism

Mark C. Calassa* and Russell Kackley*

Abstract

This paper describes a Solar Array Deployment Mechanism (SADM) used to deploy a rigid solar array panel on a commercial spacecraft. The application required a deployment mechanism design that was not only lightweight, but also could be produced and installed at the lowest possible cost. This paper covers design, test, and analysis of a mechanism that meets these requirements.

Introduction

Figure 1 shows a sketch of the solar array in its on-orbit, fully deployed configuration. The SADM is used to deploy the solar array panel shown in the figure. The panel is of typical construction, using aluminum face-sheets bonded to an aluminum honeycomb core. During launch, the solar array is stowed against the main structure. Once on orbit, commands are sent to release devices to release the solar array. The SADM provides the torque to rotate the solar array to a prescribed angle and the stop device to hold it in position at the end of deployment.

Design Description

Figure 2 shows the SADM components and their physical interfaces to the adjacent spacecraft structure. The SADM consists of two hinge assemblies, one fixed and one floating, and a foldable semi-lenticular ("C-section") strut. These mechanisms provide torque to rotate each solar array panel from the stowed (launch) configuration to the deployed (functional) position. The solar array deployment is a one-time, passive event that can not be stopped once initiated.

Each hinge assembly has a torsion spring that drives the solar array panel into its deployed position. Figure 3 shows an exploded view of the fixed hinge assembly. Self-lubricated, Teflon-lined journal bearings provide a low-friction rotational joint. Each hinge is rotationally redundant since the hinge pin is free to rotate in both the tang part and the clevis part. A sealed Rotary Viscous Damper (RVD) mounts on the fixed hinge assembly. The RVD was designed to control deployment speed to reduce the solar array panel lock-up loads (at the strut attach point) from 1112 N (250 lb) (undamped) to 600 N (135 lb) (damped) to protect solar array components. A resistive element heater is bonded to the exterior of the RVD to limit cold temperatures to greater than -36 °C. Figure 4 shows an exploded view of the floating hinge assembly. The clevis gap dimension on the floating hinge assembly was sized to accommodate differential thermal expansion between the graphite-epoxy spacecraft structure and the aluminum substrate of the solar array panel. The tang part of the floating hinge

---

* Lockheed Missiles and Space Company, Inc., Sunnyvale, CA

also incorporates a spherical bearing (monoball) to help prevent hinge binding during deployment.

The stop and alignment strut (shown in Figure 2) is made of 0.305 mm (0.012 in) titanium sheet formed into a C-section with a 38.1 mm (1.5 in) radius of curvature. It is 58.4 mm (2.3 in) wide and 1.3 m (51 in) long. The strut is folded between the spacecraft and the solar array panel when stowed, and provides deployment torque, an end-of-motion stop, and alignment when the solar array panel is fully deployed.

The solar array transfers power to the satellite by means of wire harnesses crossing the hinge axis. The harnesses are located between the fixed and floating hinge. The harnesses include power, grounding, and data cables. Except for the RVD and wire harnesses, all components in the SADM were designed to be insensitive to large temperature variations. All relative rotating surfaces (radial and sliding) have positive clearances even at worst case temperature extremes. The wire harnesses crossing the joint were included in the design and testing because they present the major resistance torque against which the SADM must work.

Requirements

The table below shows the requirements and capabilities matrix for the SADM.

SADM Requirements and Capabilities Matrix

SUBJECT	REQUIREMENT	CAPABILITY	VERIFICATION METHOD
Deployment Time	Less than 7 minutes	5 seconds to 5 minutes	Analysis and test
Deployed Frequency	Greater than 0.5 Hz	Greater than 0.5 Hz	Analysis and test
Mechanical Alignment •Azimuth •Elevation	Less than 0.25° Less than 0.30°	0.245° max 0.204° max	Analysis Analysis
Mass (each)	< 1.50 kg (3.3 lbm)	1.23 kg (2.72 lbm)	Analysis
Torque Margin	Greater than 0	1.0 (100%) Minimum	Analysis and test
Thermal	81 °C Max/-64 °C Min 55 °C Max/-36 °C Min for Rotary Viscous Damper	Comply by design	Analysis and test
Reliability	Greater than 0.999	Greater than 0.999999	Analysis
Shelf Life	7 years	Comply	Analysis
Ground Test Life	20 deployments	Comply, more than 50 deployments done	Test

Design Features

The SADM has several interesting design features. These features were required to support the low cost of production and installation goals. The first is the semi-lenticular strut, which provides moderate deployment force, an end-of-travel stop, deployed alignment repeatability, and increased deployed frequency. The strut was selected over other stop and alignment devices because it is compact, lightweight, has high axial stiffness, and does not require complex adjustments to correctly align the solar array. It also acts as a kick-off spring because of energy stored in the flattened section when it is folded. The strut cross-section was selected as a semi-lenticular shape over a closed lenticular shape to minimize manufacturing costs. A fully lenticular strut would have required extensive tooling and inspection for shaping, welding, and heat treating, while the C-section is simply bump formed and then stress relieved. The cost was further reduced by requiring that the C-section radius only be inspected for a 15.2 cm (6 in) zone surrounding the mid-span of the strut radius instead of for the entire 1.3 m (51 in) length. The inspection zone corresponds to the area of the strut where the curved C-section becomes flat when stowed, and the stresses in the titanium reach a maximum. Material thickness, curvature radius, and stowage bend radius, are all critical design parameters influencing the performance of the strut. An extensive development test program was conducted to perform design trades of conflicting parameters such as buckling stability, stowage envelope, deployment torque, and material stress levels. The final design was derived from a careful compromise of these parameters.

A second such design feature is the RVD. The basic RVD design has an extensive flight history with NASA and commercial programs. However, several design improvements were made for the SADM application, as shown in Figure 5. The most significant of these are the change from two fasteners to one (to reduce fastener part count), the unique-sided shaft to prevent improper installation, the fluid fill inspection port, the precision bonded bearings, and the precision pilot boss to provide precise alignment between the hinge axis and the damper shaft. The "indexed" shaft design requires that the damper shaft be in the 0° (stowed) position before installation. This prevents the damper from being installed with the shaft in a deployed position, which would prevent the solar array panels from deploying, thus causing a mission failure. In addition, there is 8° of deadband between the shaft and the hinge shaft boss. The deadband allows easy assembly of the damper into the hinge without worrying about tolerance build-up or the use of an expensive, heavy, coupling design. The fluid fill inspection port enabled the assembly to be inspected for the presence of air bubbles without the costly, time consuming, and sometimes inaccurate, x-ray method. The use of a mandrel type tool to locate and bond bearings into place reduced the major source of variability in damping rate by precisely aligning the vane shaft in the damper case thus reducing leakage past the vanes of the vane shaft.

Finally, most parts of the SADM are aluminum to reduce manufacturing costs.

Testing

An extensive development test program was conducted to verify that all components would function properly before beginning the qualification program. Component tests were performed on the RVD (to determine strength and damping rate), wire harnesses (to determine bending torque), torsion springs (to determine torque output), hinges (to determine friction torque), and the strut (to determine torque output, axial stiffness, and buckling stability). The RVD and wire harnesses were tested at ambient and qualification temperatures (hot and cold).

Figure 6 shows a sketch of the full-scale panel test setup. Since release and lockup loads were important, a full-scale solar array panel was built to simulate the stiffness and inertia of the flight panel. The solar array was simulated by a typical aluminum honeycomb panel design, sized to simultaneously match the bending stiffness and inertia of the actual solar array. This was critical in being able to use the test data to correlate with the analytical model. Flight-quality hinges and struts were used. No attempt was made to use worst-case springs during qual testing. The springs that were used in the qual tests were close to nominal. To account for spring variations, the analytical model was correlated to the test results, and then the model was used to extrapolate to worst-case performance. The hinge line was aligned vertically to eliminate gravity effects on deployment. The test fixture had its own spherical off-load hinges (located outboard of the SADM hinges) to which the panel was attached. Therefore, the off-load hinges supported the full panel weight and prevented the SADM hinges from carrying any gravity-induced side load. The hinge lines of the test stand hinges and the SADM hinges were aligned with tooling to be co-linear. The SADM hinges were mounted to a graphite/epoxy panel on one side, to simulate the thermal expansion characteristics of the spacecraft, and to an aluminum plate on the other side, to simulate the thermal expansion characteristics of the solar array. Full-scale deployment tests were conducted at ambient and at qualification hot/cold temperatures. Figure 7 shows a chamber that was built around the hinge line to facilitate hot and cold development tests. The strut was not expected to be thermally sensitive, so it was left at ambient temperature. Figure 8 shows the solar array panel in the deployed position following a functional test.

The test fixture was equipped with many real-time computer-compatible instruments. A load cell was used between the hinge and the panel to measure the torque required to rotate the panel during the hinge friction and wire harness tests. A rotary potentiometer was used to measure the panel deployment angle. A strain gage bonded onto the RVD shaft was used to measure torque in the RVD. The shaft torque was of concern because of the 8° deadband between the hinge boss and the damper shaft. A load cell in line with the strut was used to measure lock-up load. All torque, angle, and force data were recorded and viewed "real time" on a Macintosh computer running the LabVIEW[1] software. All instrumentation was for the test only; there is no provision for measuring torque or angle during an on-orbit deployment.

---

[1]LabVIEW is a trademark of National Instruments Corporation.

Several important facts were learned about the components as a result of development testing. Some of these led to design changes before qual testing. Figure 9 shows a plot of the wire harness torques. These torques were acceptable and no changes were made to wire harness routing. However, the electrical power group asked that a change be made to the power cables, so it was re-tested and found to be an insignificant change relative to the wire harness torques.

First, it was discovered that the strut was resisting deployment at the end of travel. In the original design, the bending stresses in the bent section when the strut was stowed against the spacecraft were high enough to cause localized yielding at the edges of the strut. This yielding changed the strut output torque characteristics so that it resisted, instead of aided, deployment at the end of travel. This resulted in a negative torque margin and the panel would not deploy properly. The strut thickness was decreased from 0.406 mm (0.016 in) to 0.305 mm (0.012 in) to reduce the peak bending stresses. Reducing the stresses eliminated the yielding and resulted in a strut torque that always aided deployment. Figure 10 shows a plot of the strut output torque before and after the design change. The thinner material reduced the tensile strength and buckling force slightly, but the margins were still acceptable.

Second, the location of the spring mandrel pin on the hinges was changed slightly to wind up the torsion springs by an additional 15° for increased torque output. This was done to increase torque margin without redesigning the springs. The unique design of the spring end and spring mandrel pin allowed a cost effective way to increase torque by re-drilling only one hole. It should be noted that the spring design was initially sized with extra stress margins in case such a design change needed to be implemented. At the same time, the location of the mandrel pin was moved axially along the spring mandrel to reduce the coil-to-coil rubbing on the torsion spring. This reduced the hinge friction as a percentage of the spring torque. It was also found that the MoS_2 dry film (on the springs) was tending to gall and deposit on the soft aluminum of the spring mandrel, thus causing extra resisting torque. The hinge mandrel was subsequently hard anodized to reduce this effect. These changes to the hinge were made quite easily because the hinges were designed to allow changes such as this without major impacts to the design. Figure 11 shows a typical plot of the torsion spring and hinge friction torques before and after the design change.

Finally, it was discovered that the RVD did not rotate when the core temperature was below -40 °C. Initially, the vendor advertised that the RVD would operate at temperatures as low as -54 °C. However, the damper has a steel vane shaft and an aluminum case with very little clearance between the vanes and the case. Due to differential thermal contraction at cold temperatures, the case shrank down onto the vanes and prevented rotation. After this was learned, a heater and thermocouple were added to the RVD to prevent the temperature from going below -36°C before and during deployment. The power consumed by this heater did not significantly affect the spacecraft power budget. After this change, the cold qualification temperature for the RVD was increased from -54 °C to -36 °C. The survival temperature range (-64 °C to 81 °C) was not affected. In addition, it was found that the RVD damping rate was sensitive to both temperature and applied torque, as shown in Figure 12. This did not

adversely affect system performance, but was important to know for analytical performance predictions.

Following the development tests, a qualification test program was completed. Figure 13 shows the test flow. The test stand shown in Figure 6 was placed in a large thermal/vacuum chamber for the hot and cold thermal/vacuum tests. A feed-through was available for connecting the data acquisition system to the sensors on the hardware. Figure 14 shows the deployment time history for the ambient, hot, and cold tests.

All qualification tests were successfully completed and the SADM hardware is now flight qualified.

Analysis

The deployment analysis of the SADM covered two main areas: torque margin and deployment dynamics. Figure 15 shows the torque margin for the qual springs (which produced close to nominal spring torque) and for the worst-case springs. This shows that the margin is above the requirement of zero even for the worst-case springs. A computer simulation of the solar array panel deployment was developed to predict worst-on-worst release and lock-up loads. Figure 16 shows a schematic of the deployment system as it was modeled. The system was modeled using EZDYN, a general purpose, multi-body dynamics analysis code developed at Lockheed Missiles and Space Company. The model included component test data to predict system performance. It also included the capability to create a worst-on-worst combination of parameters to predict maximum loads. The outputs from this model were the following: damper shaft load, deployment time, and lockup loads. Figure 17 shows a typical time history of the panel deployment angle from both test and analysis data. This test data was from the baseline ambient deployment test. The damper shaft load was the critical load for release. The model predicted a worst-case damper shaft load of 50.8 N•m (450 in-lb), compared with a shaft yield capability (from destructive test data) of 112 N•m (990 in-lb). It also predicted a panel lock-up load of 600 N (135 lb). The strut axial strength was tested (destructive test data) to over 7500 N (1700 lb) so it was capable of surviving the maximum lock-up load of even an undamped deployment.

Conclusion and Lessons Learned

A lightweight deployment mechanism applicable to a spacecraft with low cost of production and installation goals has been designed and tested. The mechanism has passed all qualification tests and met all requirements. The following lessons were learned during this process:

- Perform adequate development testing to characterize all components *early* in the test program. Vary as many parameters as possible to get a "gut" feel as to how the mechanism performs and what parameters are really driving its performance.

- Take the time to characterize individual components of torque or force at temperatures. This alone can save enormous re-qualification costs when hit with last minute design changes. (e.g., introduction of "last minute" cable harnesses)

- Don't start out locked into a "point" design. Design components that can easily be upgraded or modified. Keep design options open as long as possible. A design that is on the "hairy" edge during the development phase of a program is probably going to be a "loser."

- Don't automatically trust vendor claims of component performance. Test them yourself. Take an early look at potential vendor's test capability and test methods to ensure that they are acceptable for your needs.

- Create an analytical model to predict worst-case performance, because one cannot usually test with worst-case components.
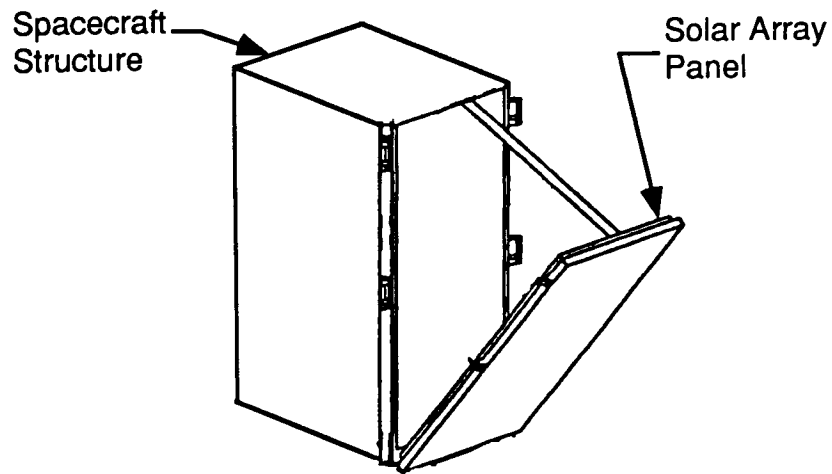
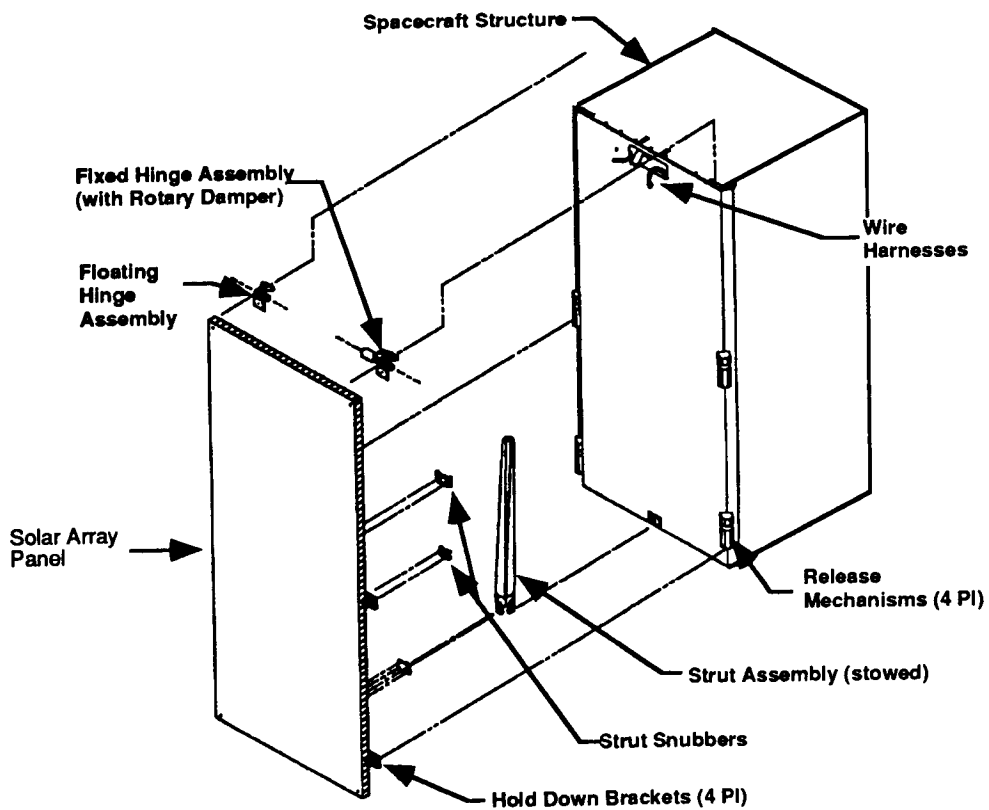**Figure 1. Solar Array in On-Orbit Configuration**

**Figure 2. Solar Array Deployment Mechanism Components
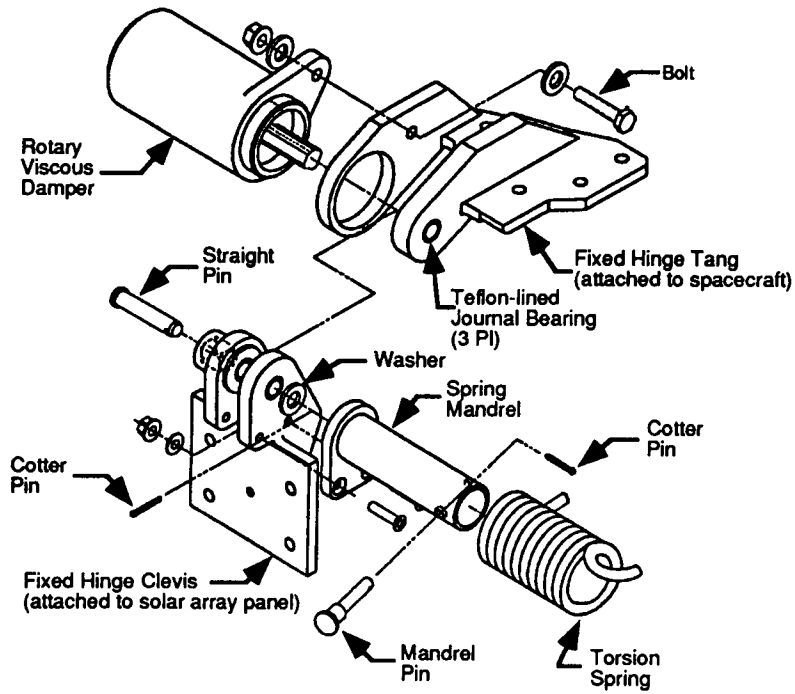(Note: Drawing is rotated 180° from Figure 1)**

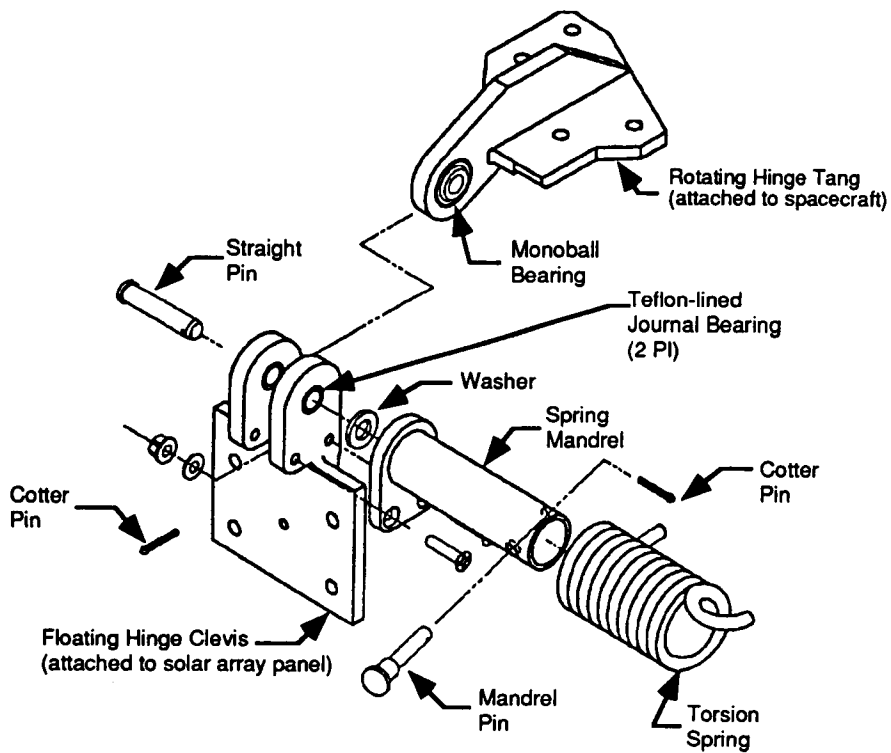Figure 3. SADM Fixed Hinge Assembly (Stowed Configuration)

Figure 4. SADM Floating Hinge Assembly (Stowed Configuration)

Product/Process
Improvement

NASA P/N 1025-9270

Rear viewport
to inspect fill
process

Single fastener
installation

Shaft alignment
accomplished
with precision
pilot boss

Bearings bonded
into place with tool
to decrease process
variability

Unique-sided shaft
cannot be installed
improperly

Visual reference
for reset position

Lockheed P/N ISME080
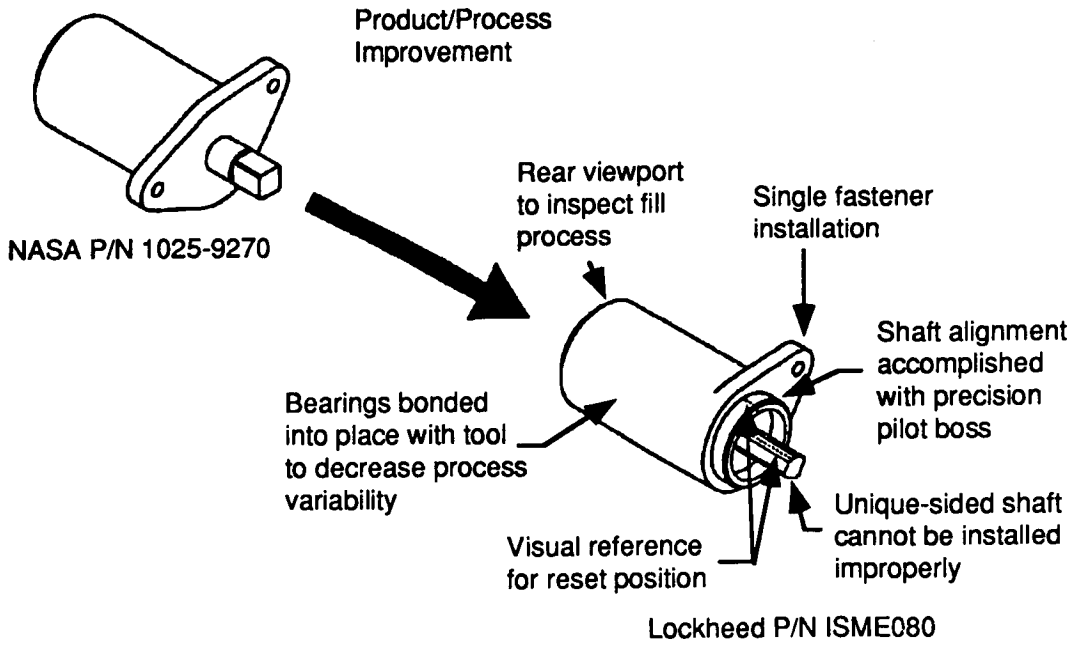
Figure 5. Rotary Viscous Damper Improvements

Solar Array Panel Inertia and
Stiffness Simulator

Potentiometer

Strut Load Cell

Real Time
Data
Acquisition
System

Graphite/Epoxy
Panel

SADM Hinges
(2 PL)

Off Load
Bearings
(2 PL)

Hinge Line
Load Cells
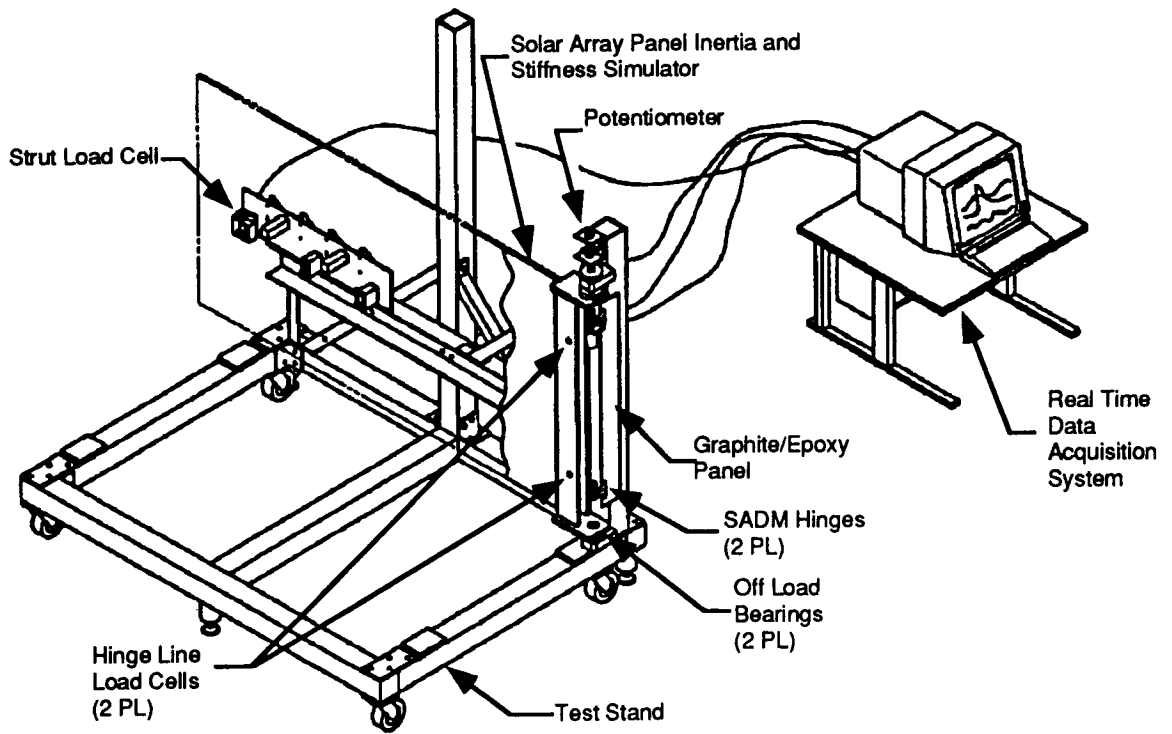(2 PL)

Test Stand

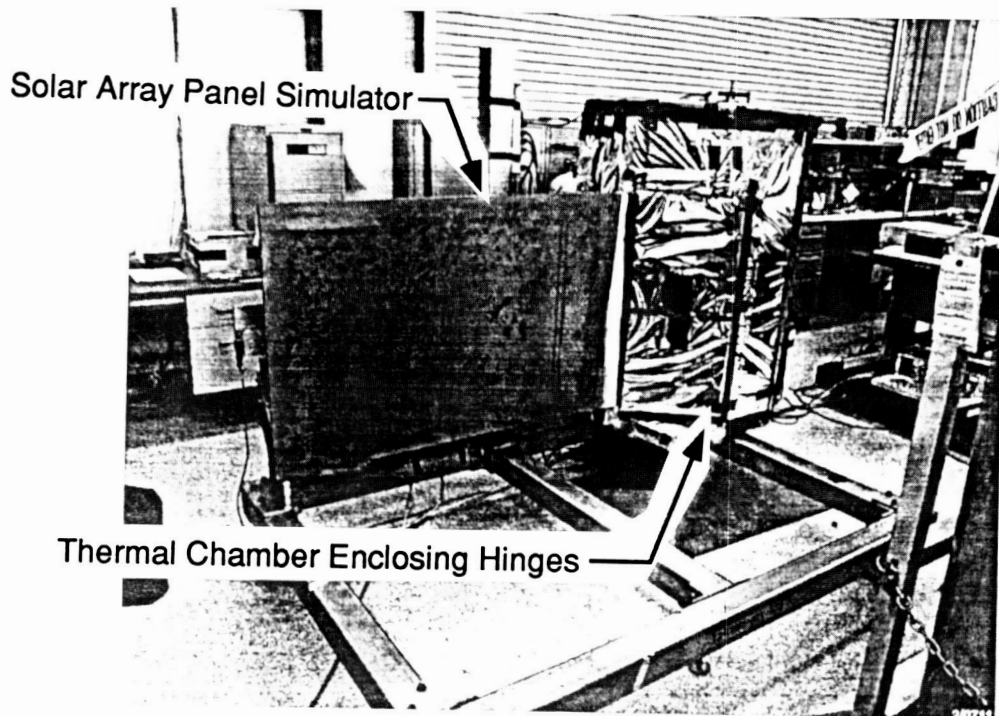**Figure 6. SADM Deployment Test Setup**

Figure 7. SADM Development Test
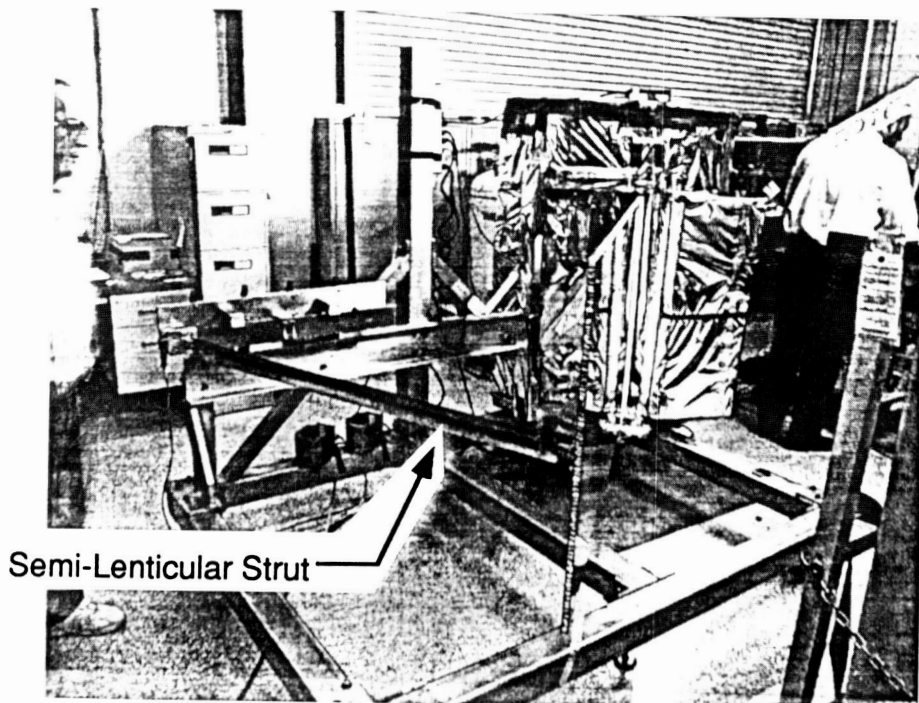
Figure 8. Solar Array Panel in Deployed Position

Figure 10. Strut Torque from Development Tests
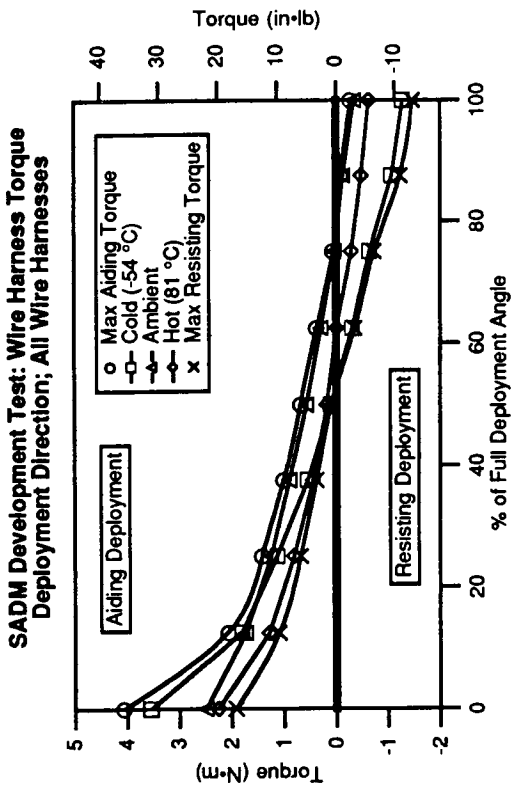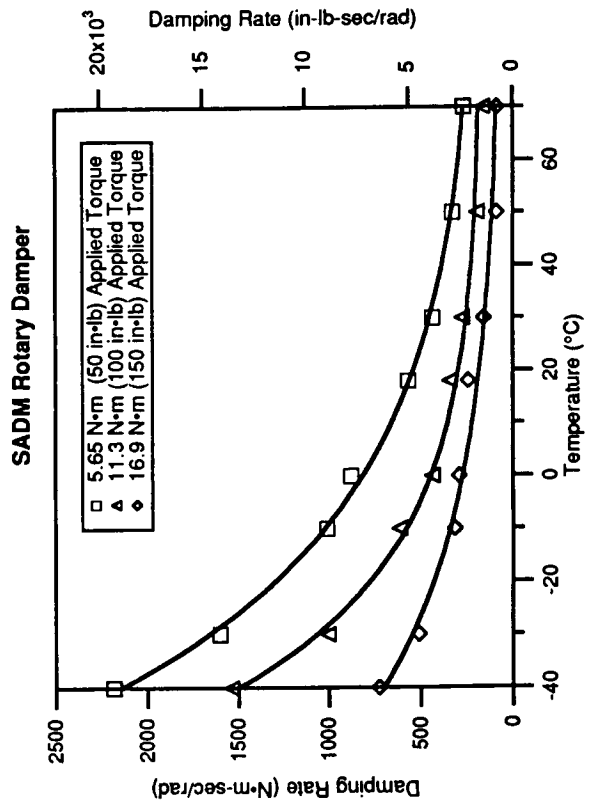

Figure 12. Rotary Damper Characteristics

Figure 9. Wire Harness Torque from Development Tests

Figure 11. Spring Torque and Hinge Friction

90

```
┌──────────┐   ┌──────────┐   ┌──────────┐   ┌──────────┐   ┌──────────┐
│ Torsion  │   │ Strut    │   │ Wire     │   │ Baseline │   │ Random   │
│ Spring   │──▶│ Torque   │──▶│ Harness  │──▶│ Ambient  │──▶│ Vibration│──┐
│ Torque   │   │ Test     │   │ Torque   │   │ Functional│  │ Test     │  │
│ Test     │   │          │   │ Test     │   │ Test     │   │          │  │
└──────────┘   └──────────┘   └──────────┘   └──────────┘   └──────────┘  │
                                                                          │
┌─────────────────────────────────────────────────────────────────────────┘
│
│   ┌──────────┐   ┌──────────┐   ┌──────────┐   ┌──────────┐
│   │ Second   │   │ Cold     │   │ Hot      │   │ Third    │
└──▶│ Ambient  │──▶│ Thermal- │──▶│ Thermal- │──▶│ Ambient  │
    │ Functional│  │ Vacuum   │   │ Vacuum   │   │ Functional│
    │ Test     │   │ Functional│  │ Functional│  │ Test     │
    │          │   │ Test     │   │ Test     │   │          │
    └──────────┘   └──────────┘   └──────────┘   └──────────┘
```

Figure 13. SADM Qualification Test Sequence

Figure 14. SADM Deployment Test Results

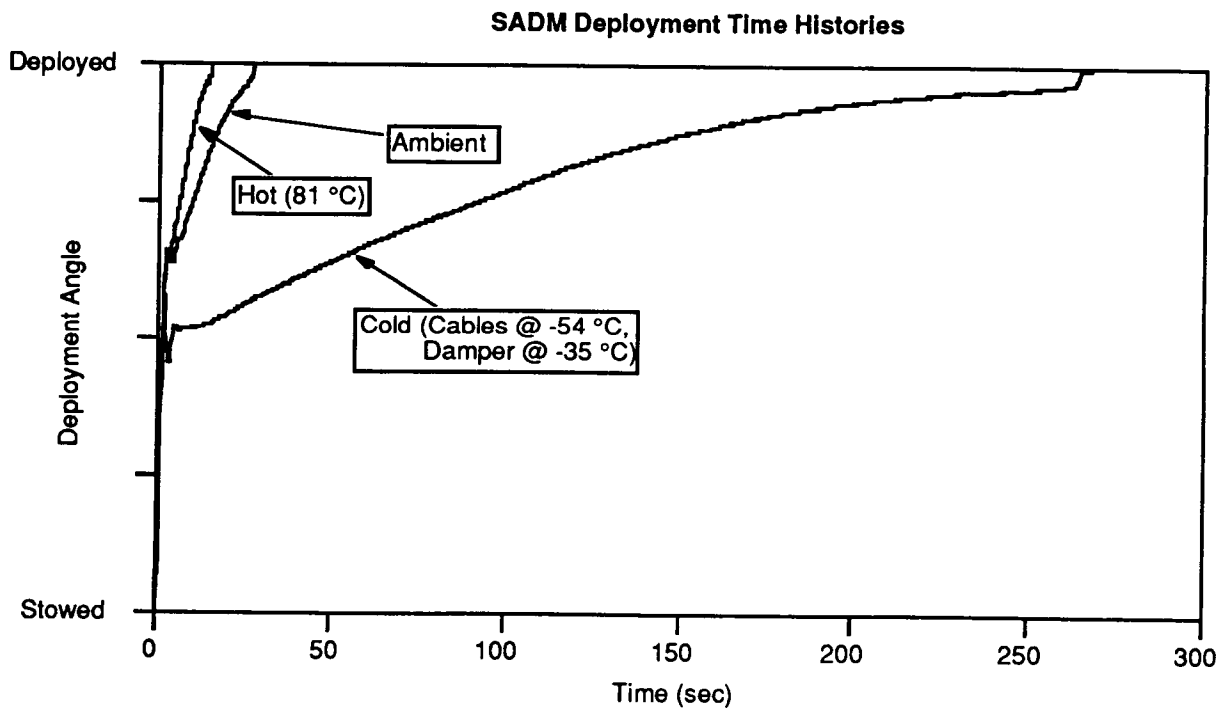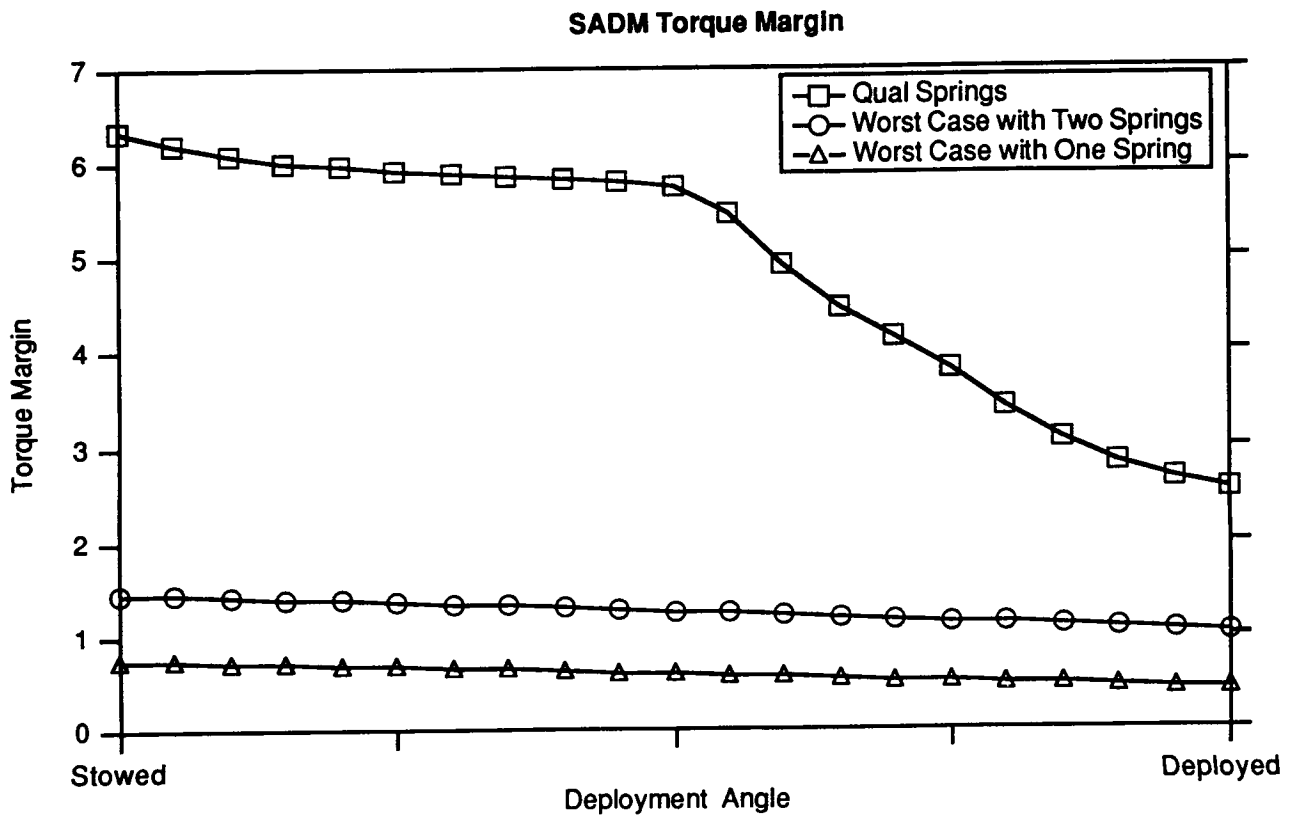**SADM Torque Margin**

Figure 15. Torque Margin with Qual Hardware and Worst Case Predictions
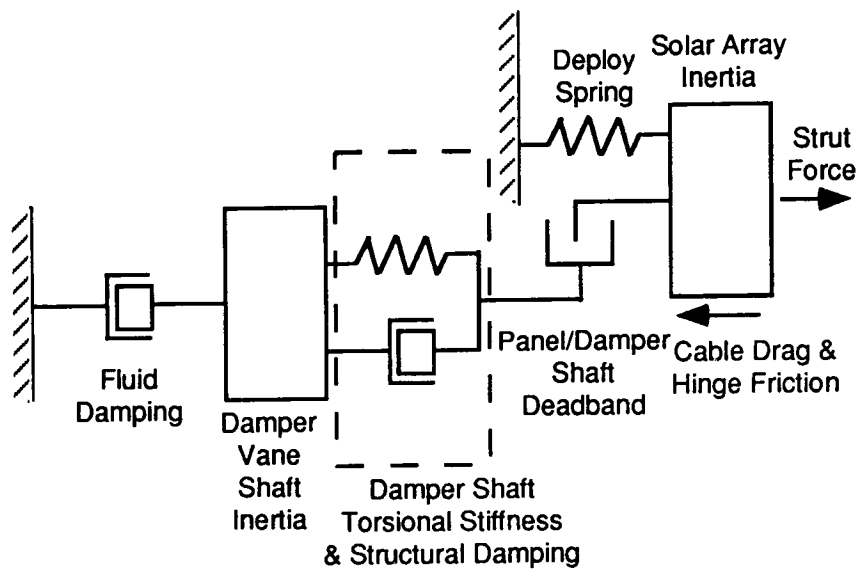

Figure 16. SADM Analytical Deployment Model

Changing Paradigms:

Manufacturing vs. Fabricating a High Volume

Hold Down and Release Mechanism

Daryl Maus* and Doug Monick*

Abstract

A detailed description of the Hold Down and Release Mechanisms designed for a 70+ constellation of spacecraft. The design is reviewed to understand the practical implications of severely constraining cost.   Strategies for adapting the traditional aerospace design paradigm to a more commercial, cost driven paradigm are discussed and practical examples are cited.

Introduction

Starsys Research Corporation (SRC) manufactures caging, hold down and deployment mechanisms for spacecraft. SRC is providing the Hold Down and Release Mechanisms (HDRM) for a 70+ constellation of satellites scheduled for launch starting in 1996. SRC will be providing over 1000 HDRMs for this program. Prior to this our largest build of mechanisms was 12.

The large scale commercialization of space is introducing a new paradigm. Commercial manufacturing exists in a paradigm that is one or even two orders of magnitude different than current spacecraft manufacturing. A latch that cost $10,000 must be built for $1,000. Manufacturing times that were measured in weeks must now be measured in days yet, the constraints of reliability, mass, environment and structure remain every bit as rigorous and in some cases are even more demanding.

Design, development and manufacture of the HDRM mechanism practically illustrate the change in thinking SRC had to incorporate as we made this shift. The initial conceptualization of a mechanism typically includes layout drawings and analysis. To this we added a detailed costing and weight matrix. Every option was rigorously evaluated not only for its direct cost impact but for secondary impacts such as assembly time, inspection time, reject rate (non-conformances cost a lot of money), handling time, and testing required.

Qualification hardware have been delivered. Flight hardware will be delivered May 1995 . The first launch is scheduled for 1996.

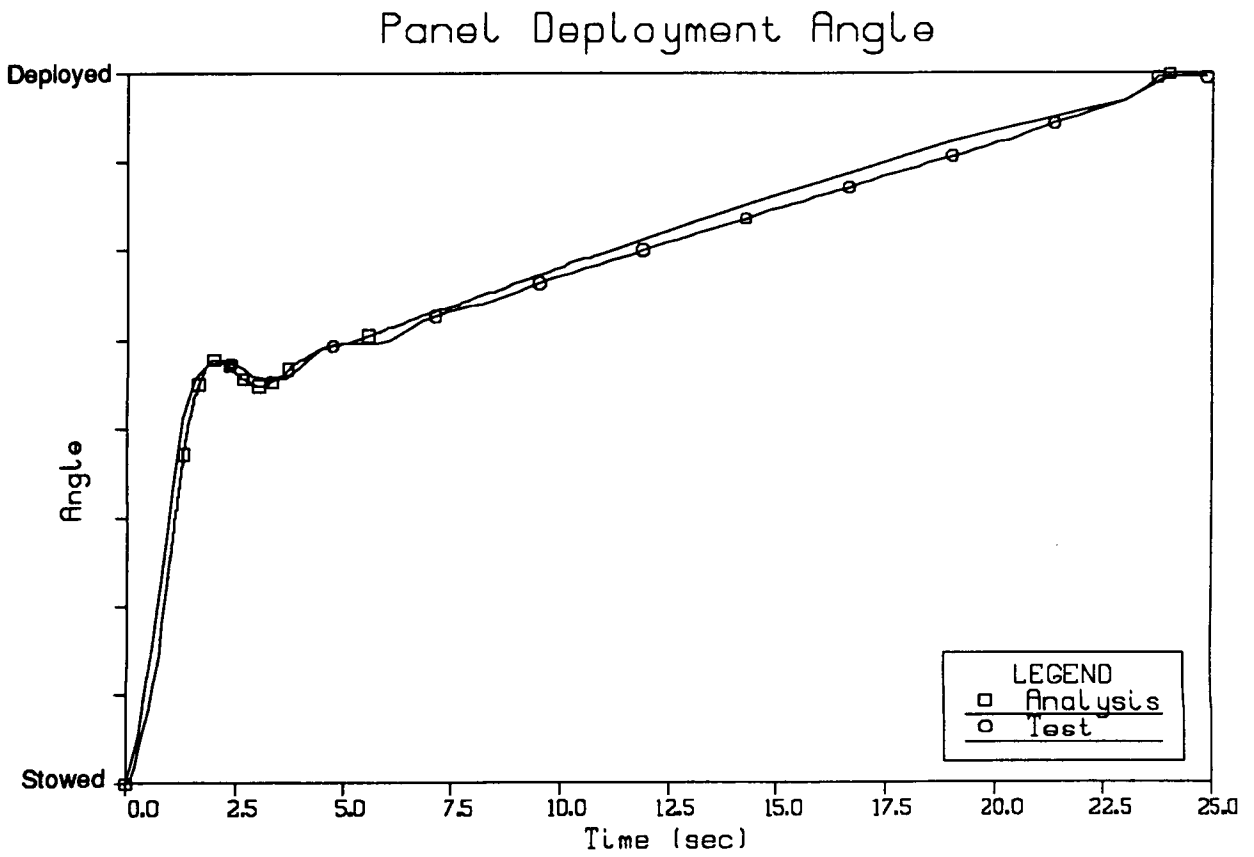*   Starsys Research Corporation, Boulder, Colorado USA

Panel Deployment Angle

Figure 17. Solar Array Panel Deployment (Ambient)

Hold Down and Release Mechanism (HDRM) Description

PRE-LOAD LEVEL ESTABLISHED BY
OPTIONAL PANEL BRACKET SPRINGS,
ALLOWING "FACTORY SET" PRELOAD

NORMAL TOLERANCE STACK-UP
ACCOMODATED BY ADJUSTABLE
FEET

EACH MECHANISM CAPABLE OF
RELEASING MULTIPLE
COMPONENTS (2 SHOWN)

LATERAL TOLERANCE
STACK-UP ACCOMODATED
WITH ADJUSTABLE SHEAR
CUP

SHOWN LATCHED WITH
OPTIONAL PANEL BRACKETS

SHOWN RELEASED

PIN FREE TO ROTATE
FOR ALIGNMENT WITH
LEVER ARM SLOT

ACTUATOR DRIVES PIN TO THIS
POSITION RELEASING CAM ARM
AND ALLOWING CAM TO ROTATE

PARAFFIN ACTUATOR IS
POWERED TO RELEASE
MECHANISM

LATCH IS SHOWN PRIOR TO
ACTUATION

LATCH IS SHOWN AFTER
ACTUATION (UNLATCHED)

FULLY REDUNDANT LATCH IS RELEASED BY
ENERGIZING BOTH ACTUATORS, RELEASE
OCCURS WHEN EITHER ACTUATOR EXTENDS

FLEXIBLE METAL BAND (2X)
CARRYS LOADS IN THE
RELEASE DIRECTION ONLY

CAMS ARE PREVENTED FROM ROTATING
BY THE LEVER ARM, WHICH IS FIRMLY
HELD BY THE RELEASE PIN, WHICH
TRANSLATES FROM THE ACTUATOR OUTPUT

CONNECTED TO STOWED
COMPONENT

CONNECTED TO STOWED
COMPONENT

SEPERATION PLANE

RELEASE CAMS

TORSION SPRING DRIVES CAM
ROTATION AFTER LATCH
RELEASE (ONE OF TWO SHOWN)

TABS ARE PREVENTED FROM
RELEASING BY THE NARROW
GAP BETWEEN THE CAMS

CONNECTED
TO RELEASE
COMPONENT

CONNECTED
TO RELEASE
COMPONENT

CAM ARM SHOWN IN
RELEASED POSITION

ROTATION OF CAM INCREASES
GAP BETWEEM CAMS RELEASING
BOTH TABS

GAP INCREASES

96

HDRM Subsystem - Latch
Actuator - SRC EH-1540, 445 N (100 lbf) maximum output, .64 cm (.25 in) stroke
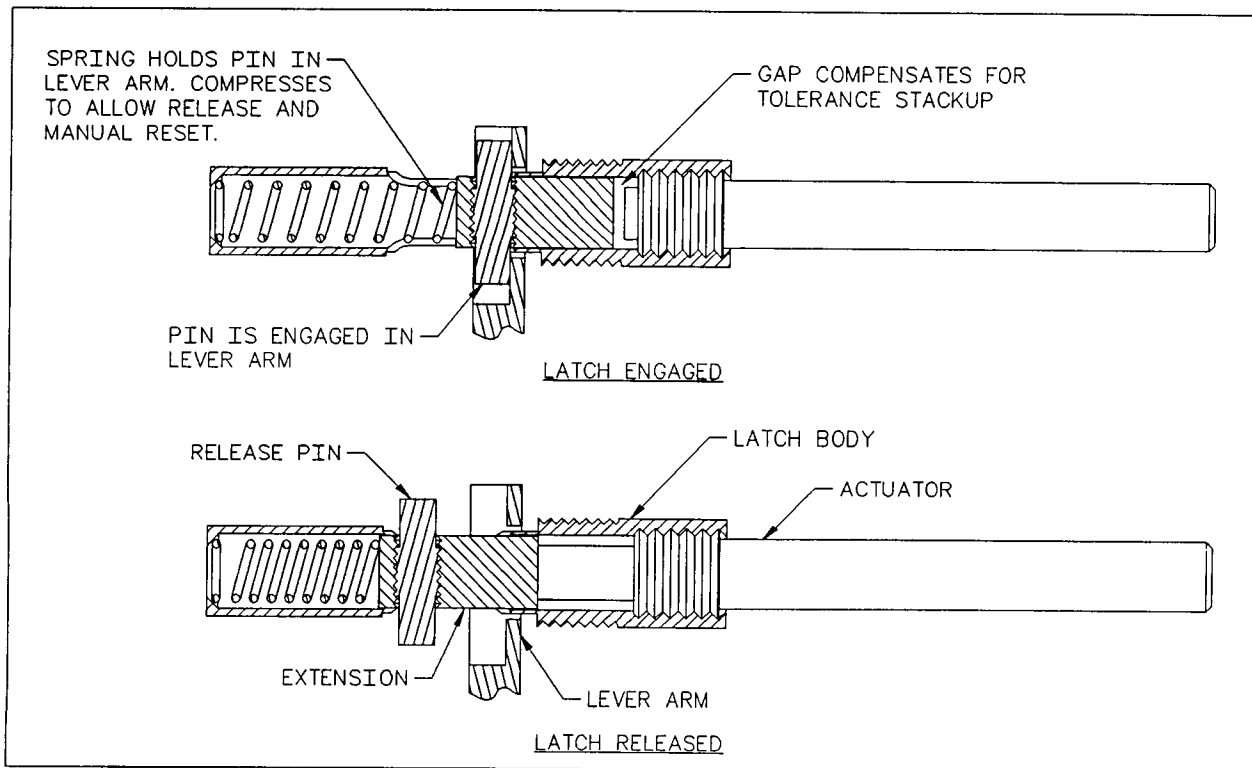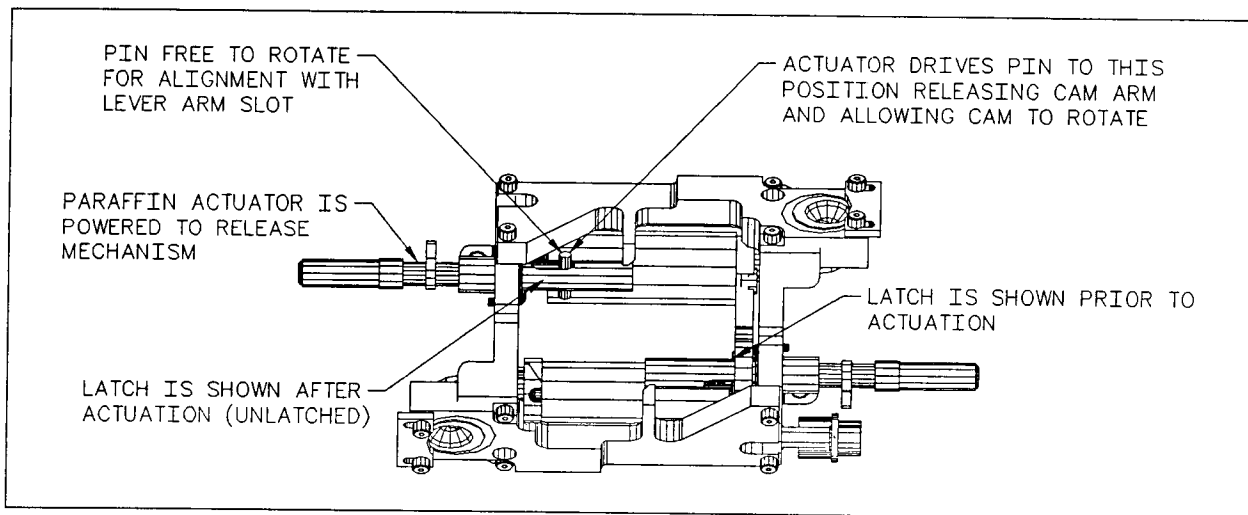Extension - Ultem 1000
Latch body - 6061 aluminum for low loads, 6AL-4V titanium with Tiodize for high loads
Release pin - Nitronic 60, Tiolube coating
Spring - 302 stainless steel
Lever arm - 6AL-4V titanium
Cam - 6061 aluminum for low loads, 6AL-4V titanium for high loads, Tiodize coating

PIN FREE TO ROTATE FOR ALIGNMENT WITH LEVER ARM SLOT

ACTUATOR DRIVES PIN TO THIS POSITION RELEASING CAM ARM AND ALLOWING CAM TO ROTATE

PARAFFIN ACTUATOR IS POWERED TO RELEASE MECHANISM

LATCH IS SHOWN PRIOR TO ACTUATION

LATCH IS SHOWN AFTER ACTUATION (UNLATCHED)

SPRING HOLDS PIN IN LEVER ARM. COMPRESSES TO ALLOW RELEASE AND MANUAL RESET.

GAP COMPENSATES FOR TOLERANCE STACKUP

PIN IS ENGAGED IN LEVER ARM

LATCH ENGAGED

RELEASE PIN

LATCH BODY

ACTUATOR

EXTENSION

LEVER ARM

LATCH RELEASED

HDRM Subsystem - Bracket

Tab - 6061 aluminum for low loads, titanium for high loads, Tiodize & Tiolube coating
Band pin - 303 stainless steel
Release band - 254,000 psi Elgiloy
Band attachment - 6AL-4V titanium
Band clamp - 6061 aluminum
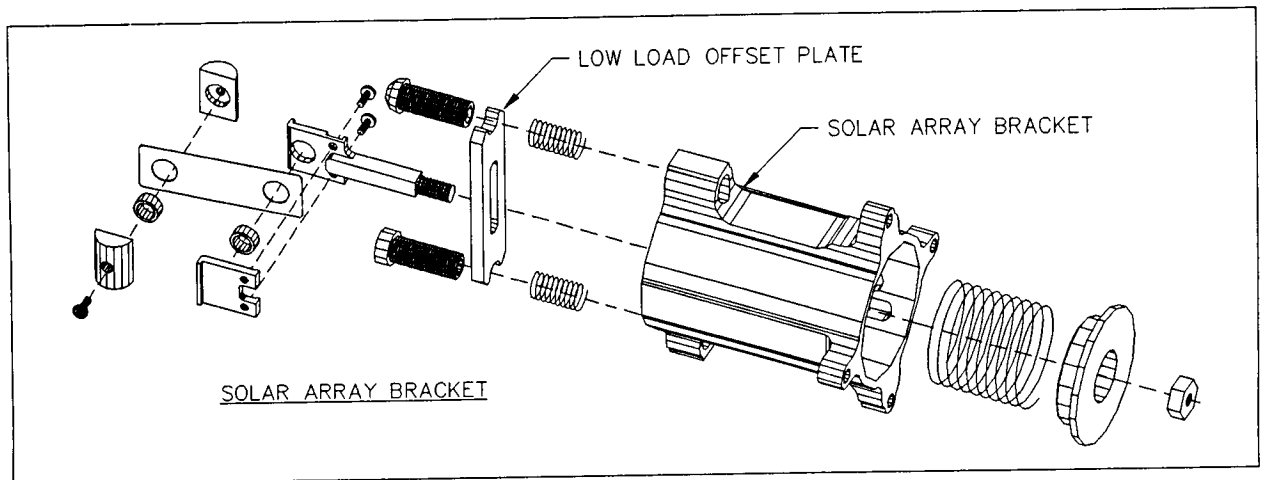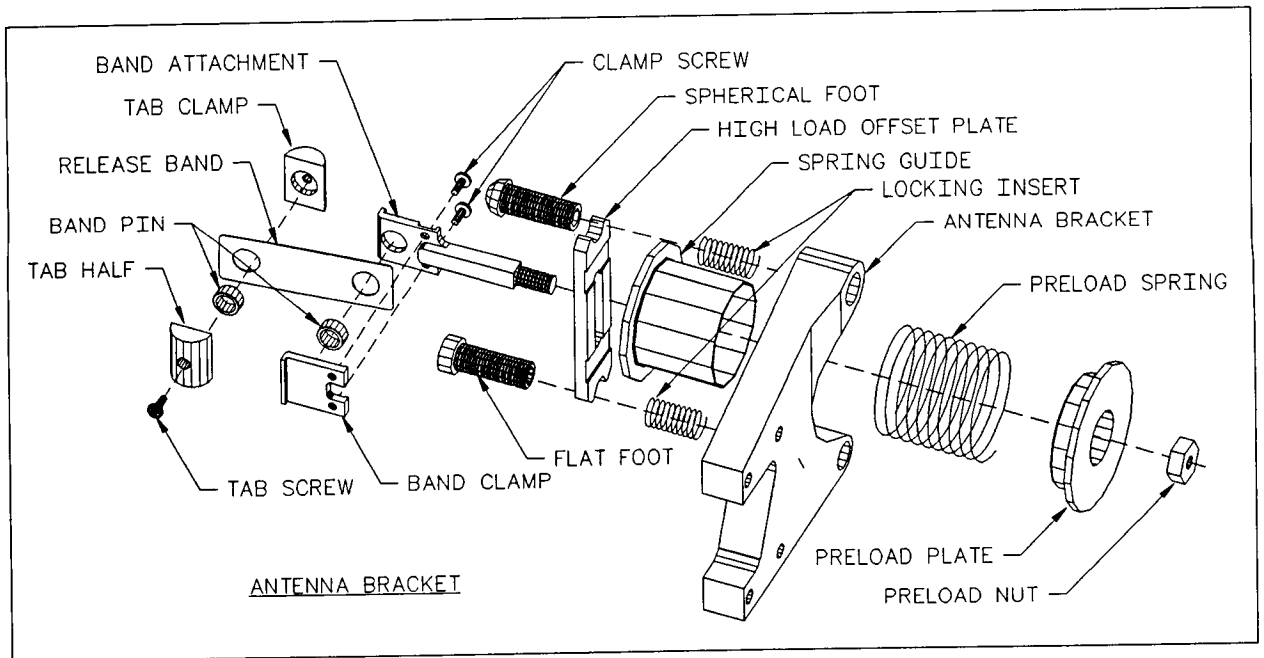Preload plate - 6061 aluminum
Spring - 17-4 stainless steel
Spring guide - 6061 aluminum (antenna bracket assembly only)
Offset plate - 6061 aluminum for low loads, 6AL-4V titanium for high loads
Bracket - 6061 aluminum extrusion
Feet - 6AL-4V titanium Tiodize and Tiolube

ANTENNA BRACKET

SOLAR ARRAY BRACKET
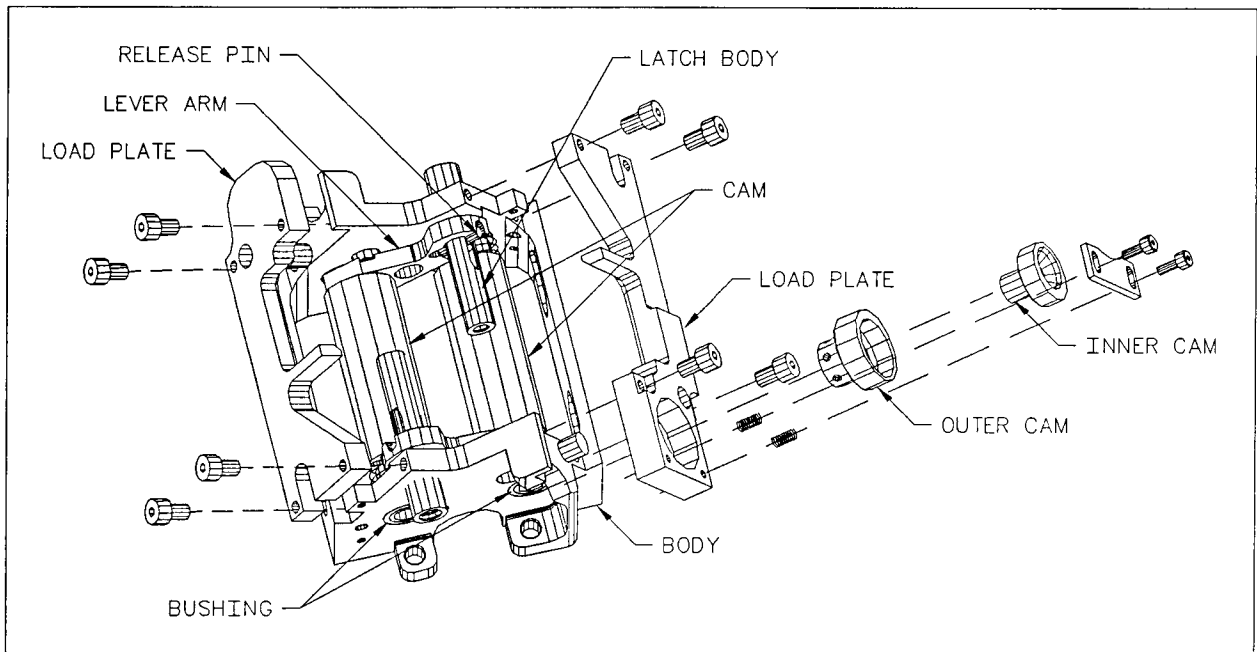
HDRM Subsystem - Body
Inner cam - 6061 aluminum, hard anodized
Outer cam - 6061 aluminum
Load plate - 6061 aluminum for low loads, 7075 for high loads, hard anodized
Body - 6061 aluminum extrusion
Bushing - 303 stainless steel, PTFE lined

HDRM Requirements

Interchangability
Provided by a design with minimal tolerance stack and a low spring rate. Bracket preload is set "at the factory" rather than on the spacecraft. Latches are inspected for final tab interface.

Positionability (± .15 cm (.060 in) lateral, ± .25 cm (.100 in) normal)
Provided by double-eccentric cams and screw adjustment of the interface spherical feet.

Kinematic freedom and restraint
Lateral restraint is provided by a spherical foot in a spherical socket. Normal restraint is provided by a flexible metal band with pivoting attachment points. A second foot restricts rotation in the axis normal to the spacecraft axis. The attachment is free to rotate about the normal and spacecraft axis.

Restraint - (3.18 KN (715 lbf) x2 axial, 3.09 KN (695 lbf) x2 lateral and 2.36 KN (530 lbf) x2 normal)

Motion and loads are restrained by a spherical foot in a hemispherical cup. The preload is restrained by redundant cams that capture multiple tabs allowing a single latch to restrain two brackets.

Release - (2.6 KN (585 lbf) x2 preload)

Provided by an HOP powered latch at the end of a lever arm attached to a moveable cam. The latch kinematics create approximately a 15:1 mechanical advantage thereby allowing a low input force to release a high force.

Multiple releases (20 minimum)

The cam and tab are round with the radii (.95 cm (.375 in) and (.71 cm (.281 in)) chosen to limit hertzian stresses. The latch pin and lever arm are made of high strength materials (Nitronic 60 and titanium) and have radiused interface points. Parts are coated with dry film lubricant (Tiolube).

Resettability

To reset the latch, the cams have a hex socket that allow a hex driver to return them to the latch position. The actuator spring resets the paraffin actuator and allows a ramped feature on the lever arm to rest the latch. To reset the bracket, a removable rest tools allow manual compression of the preload spring in the brackets and are removed after the bracket is engaged in the release latch.

Reliability (>.999)

100% of the components critical for release are redundant. Two actuators operate two release latches opening two cams. Rotation of either cam releases both tabs. All elements critical to restraint are limited to simple, high margin components.

Stiffness (3.85 KN/mm (22 klb/in) axial, 7.0 KN/mm (40 klb/in) lateral and normal)

Structural requirements are stiffness driven. Aluminum was chosen for it's stiffness to weight ratio and cost. FEA was used to optimize the shape of the structural elements.

Mass (14 kg (31 lbm) for 16 HDRMs)

The latch design is compact and uses a minimum of parts. The HOP actuator weighs 10 gm and provides 445 N (100 lbf) of force.

Strength driven parts are light-weighted extensively. The cams have 6 holes through them, the spherical feet are hollowed out, and the band pin is a tube.

Stiffness driven parts are 42% of the overall weight. The predominant material used is aluminum. Body and bracket shapes were chosen for stiffness and are optimized with FEA.

Load driven parts are 27% of the overall weight, titanium is used extensively for these parts. Metal bands provide a flexible couple at 1 gram each. Crest springs provide a 60% weight savings over die spring and 15% over belleville washers.

Fasteners
Fasteners are used only to secure parts, mechanical features carry loads. Uralane and Nylok are used to secure all permanently locked fasteners. Helicoils are used to secure user adjustable parts.

Cost strategies

Common elements
The initial goal was to have one latch for all requirements. As the customer's design evolved significantly different requirements forced a hybrid approach to commonalty.

Latch body
Because the satellite design placed the solar panels over the antenna panels different latch heights were required. The same placements of components were used and the additional length was applied outside of the functional area. The height difference was further exaggerated to improve stiffness in the higher loaded and higher stiffness (shorter) antenna latch body.
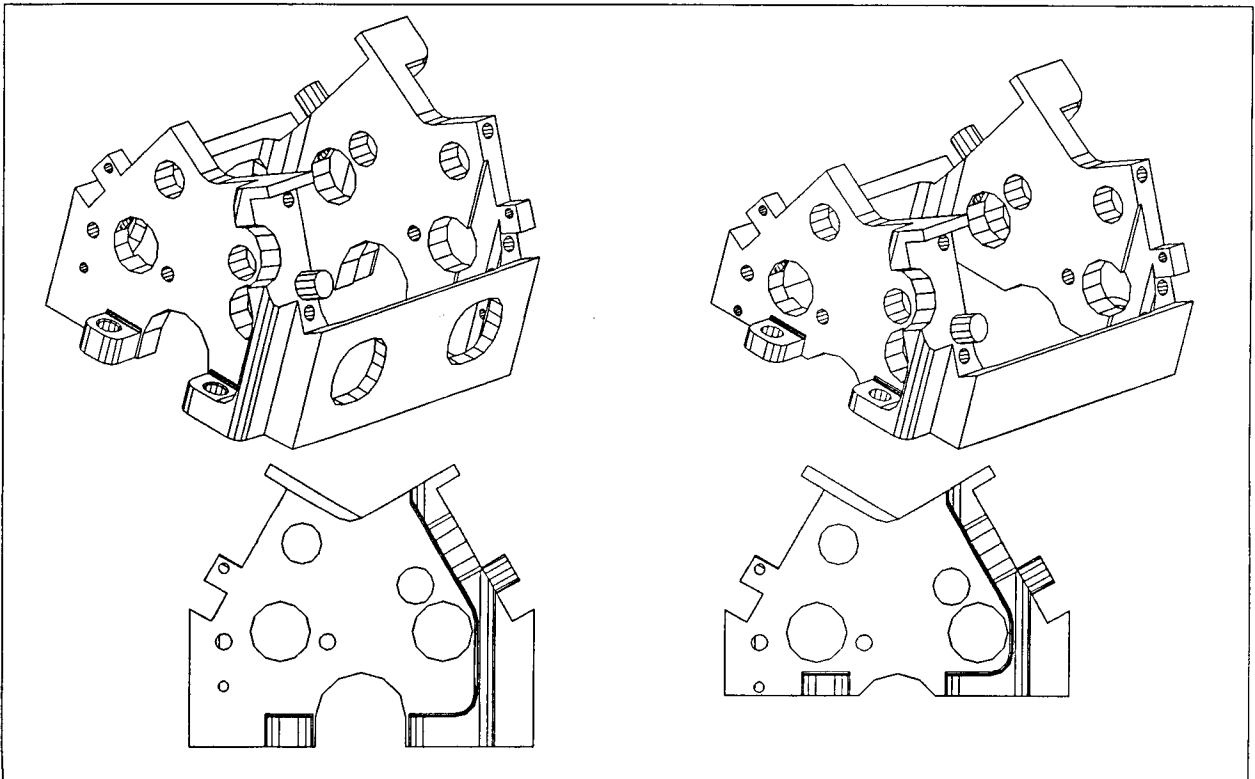
Cams and tabs

The preload requirement for the solar array HDRM is 734 N (165 lb) and for the antenna panel it is 2600 N (585 lb) or three times higher. The strength of titanium is three times higher than aluminum. Therefore, the part design for the cam and tab in the higher load latch could be the same as for the low load latch with the only change in material, from aluminum to titanium.

CAM SCREW HOLE

LIGHT WEIGHTING HOLES

RESET TOOL INTERFACE SOCKET
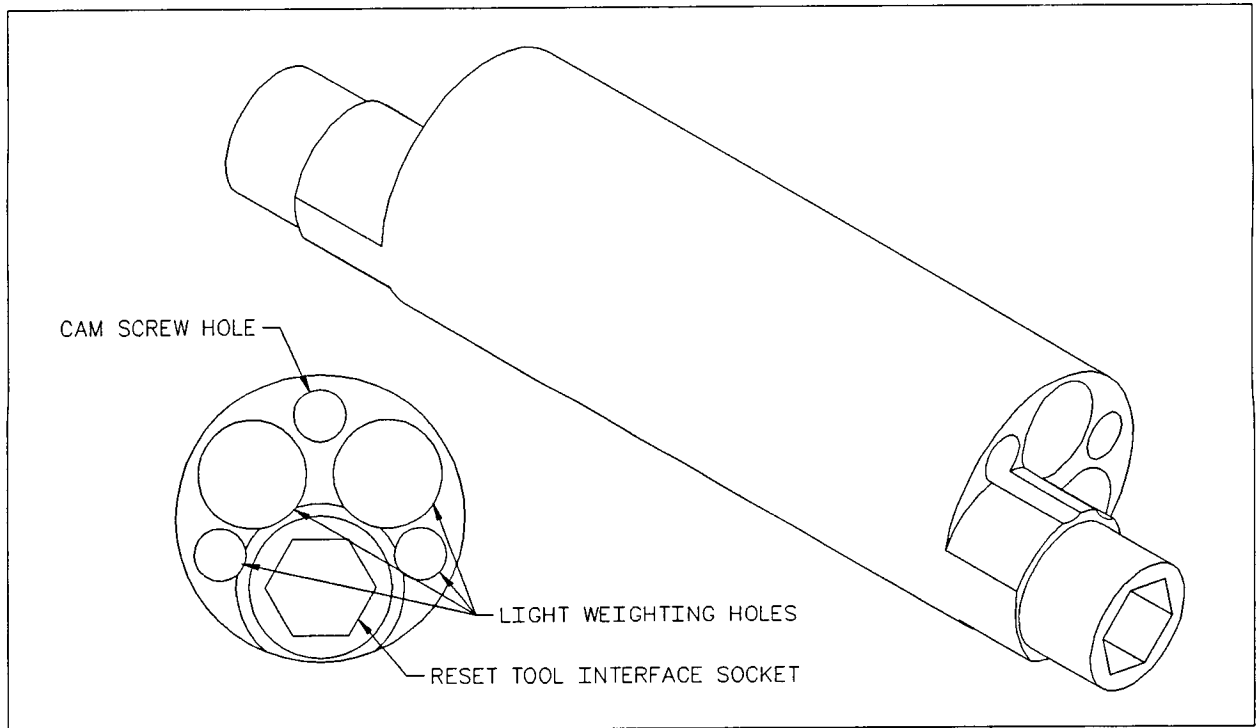
Fabrication costs and methods

Traditionally mechanisms at SRC are built around precisely machined parts. We explored many other methods used for fabricating parts.
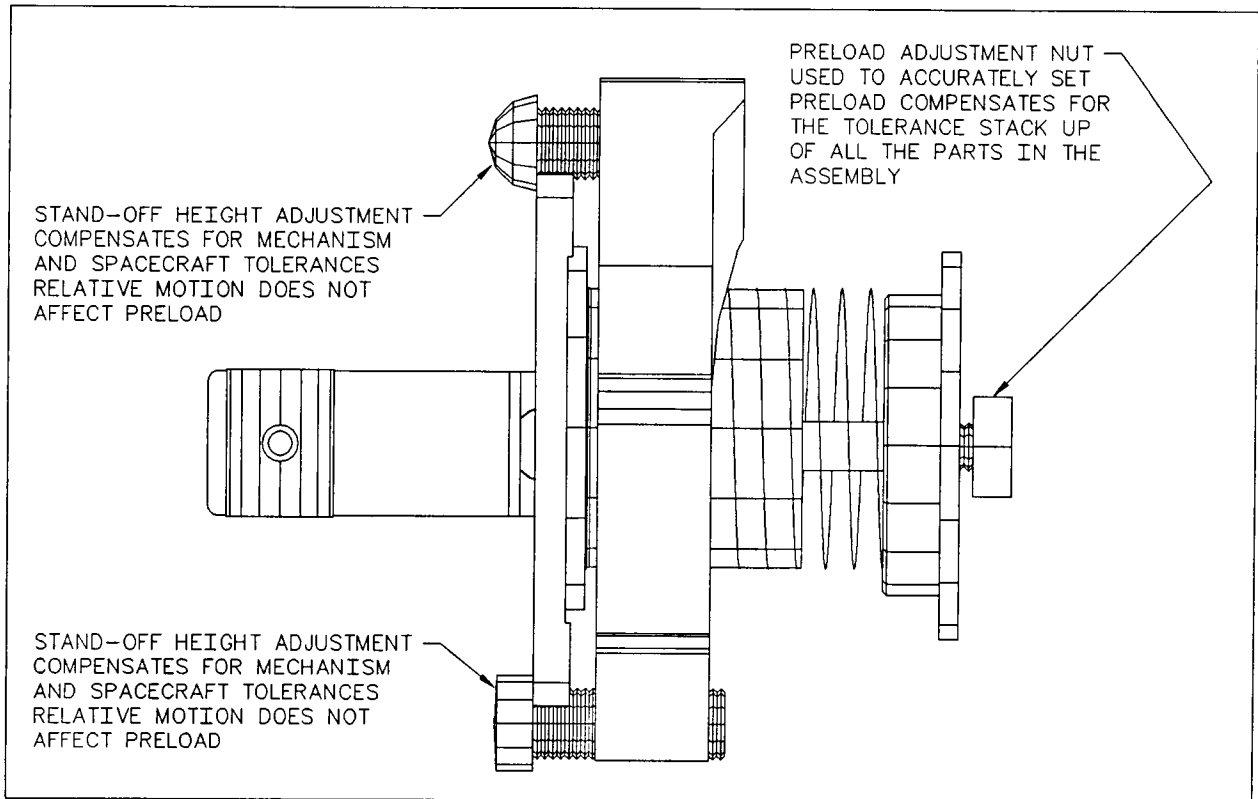
Supplier involvement

Our part designs were reviewed extensively by suppliers. Their comments and suggestions were employed whenever possible. This involvement started at the concept and layout stage so the design could evolve toward lower cost parts.

Customer involvement

In our relationship with our customer, requirements and design changes were reviewed for their cost implications. Dogmatic requirements were examined for their purpose and were frequently negotiated to reduce costs.

Tolerances
Lower tolerances directly lower cost and open the possibility of alternate methods of fabrication, such as using extrusions rather than machining from billets. Designing to limit the total number of parts in a stack up allows higher tolerances. Designing in an adjustable feature allows higher tolerances in associated parts.

PRELOAD ADJUSTMENT NUT
USED TO ACCURATELY SET
PRELOAD COMPENSATES FOR
THE TOLERANCE STACK UP
OF ALL THE PARTS IN THE
ASSEMBLY

STAND-OFF HEIGHT ADJUSTMENT
COMPENSATES FOR MECHANISM
AND SPACECRAFT TOLERANCES
RELATIVE MOTION DOES NOT
AFFECT PRELOAD

STAND-OFF HEIGHT ADJUSTMENT
COMPENSATES FOR MECHANISM
AND SPACECRAFT TOLERANCES
RELATIVE MOTION DOES NOT
AFFECT PRELOAD

Materials
At SRC the first choice for a high strength plastic is Envex, which was initially specific for the Extension. Envex is very costly, after a careful review of properties and cost Ultem was specified at 1/2 the material cost.

Extrusions
From the beginning of the design major parts were examined for the feasibility of using extrusions. The cost of an extrusion die is under $1500. In quantities as low as 100 parts this cost can be recovered from just the material saved and of course the machining cost reduction is even higher.

EXTRUSION

FINISHED PART

EXTRUSION

FINISHED PART
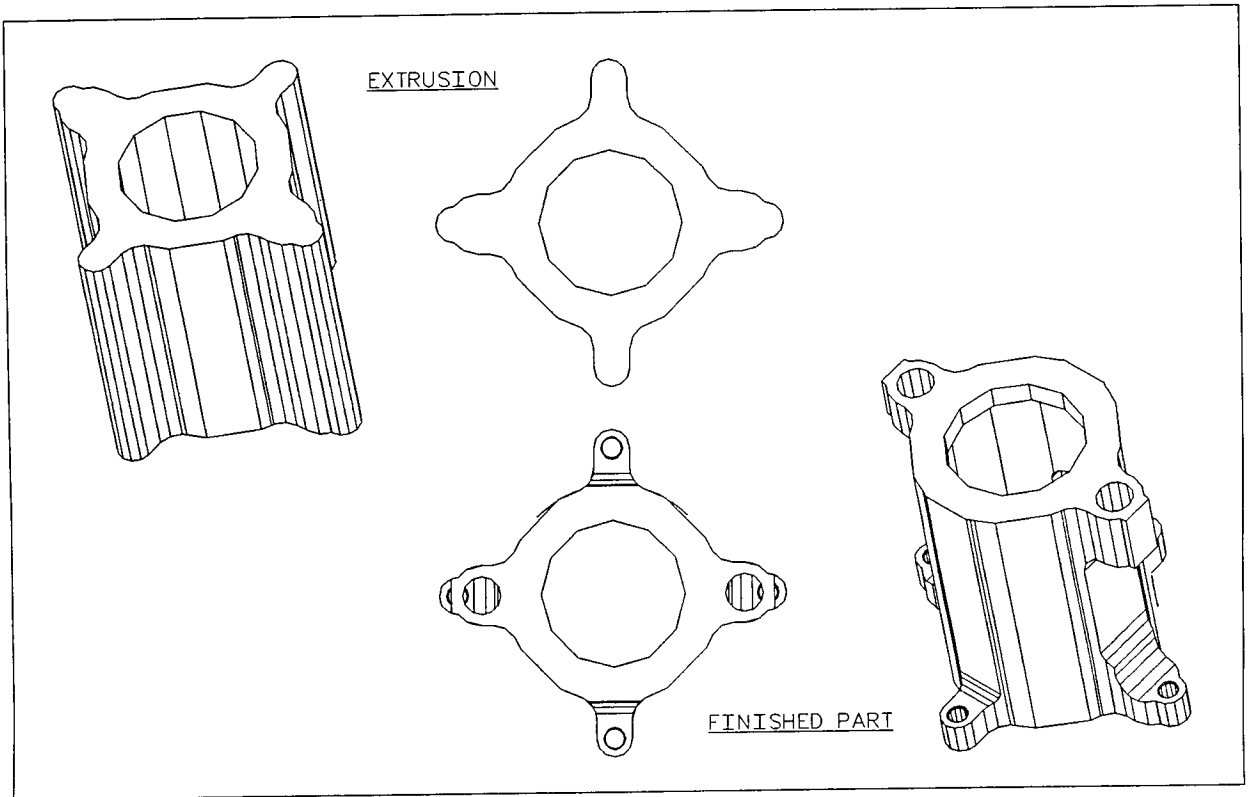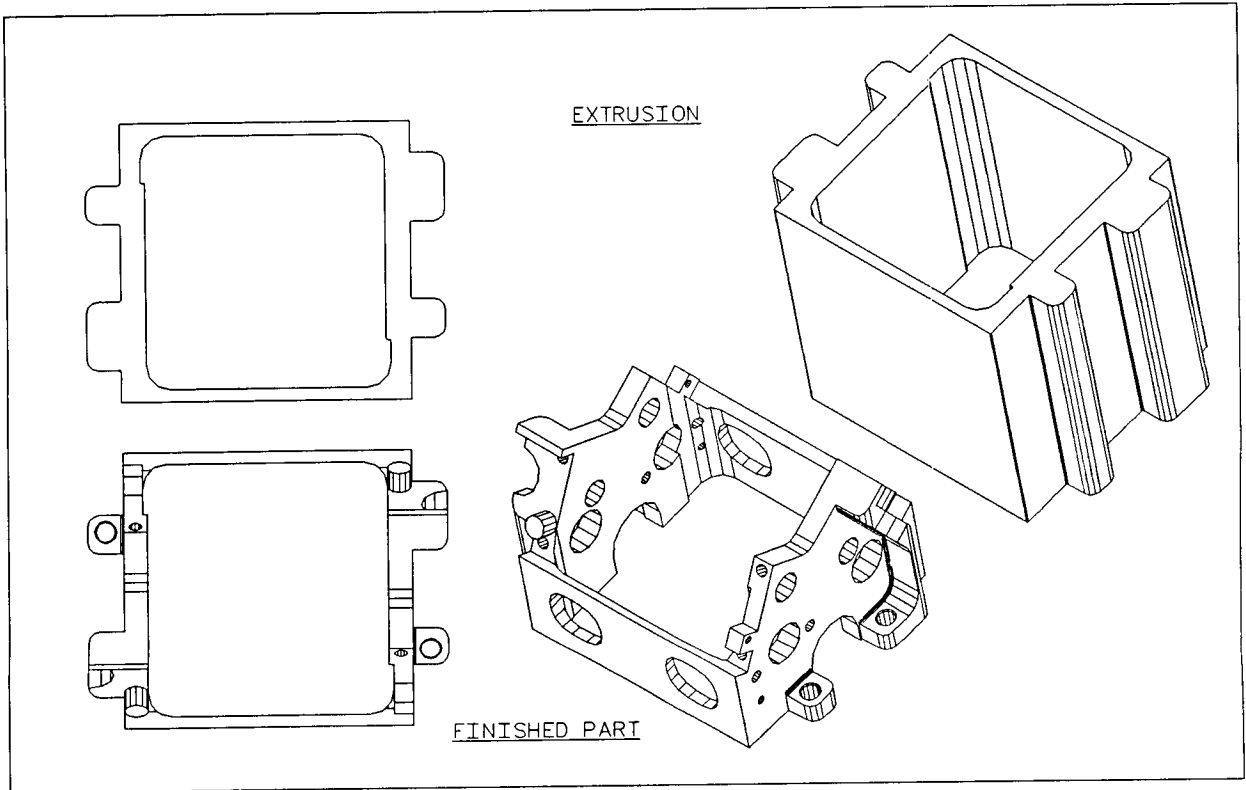
Standard "off-the-shelf" parts and shapes

Other than fasteners we usually design and fabricate most parts. The Thomas Register and component catalogs were consulted extensively. Parts were designed to use available stock and standard stock tolerances. The initial actuator heater was custom and with high volume still cost $70. A thorough search of standard heaters identified a stock heater that would work with slight modification of the actuator design. It cost only $9.84. The electrical connector is mounted on a stock standoff that costs only 25¢.

Keeping it simple

Since simplicity and reliability have such a strong correlation we always try to keep it simple. The mechanism utilizes a flexible metal band attached at both ends with a pin that allows rotation. this system allows 5 degrees of freedom and restrains in one axis. An equivalent toggle system would required more parts, be more sensitive to dimensional variation and cost more.

Limiting part count is one way to keep it simple. But, to limit costs this approach had to be expanded significantly, all the way to total setup count and total feature count. The more setups a part requires, the more labor intensive it becomes. The more dimensions on a part, the more time it takes to fabricate. Eliminating sharp corners on the cam clamp eliminated a second machining setup and lowered the fabrication cost by 20%.

Price determines cost

This is perhaps the biggest change in thinking required for ourselves and our industry. Traditionally we start with our costs add them up and come up with price. It is very different to start with the price and work backwards to determine the cost of each system and ultimately what the cost of each part must be. This seemingly backward approach to developing costs is what drives costs lower.

Negotiating

Setting a cost goal works. It worked for our customer with us and it worked with our suppliers. The cost goal set by our customer initially seemed impossible. But, after we accepted the challenge and applied our creativity amazing opportunities were identified. When we set aggressive cost goals with our vendors they surprised us with their solutions.

Understanding the source of costs

While we understood that some materials cost more than others and some materials are harder to machine than others we had to refine this understanding. We asked questions such as; Which features are harder to machine than others? What is the shape of a tolerance/cost curve?

Assembly
Assembly costs a lot and especially as part costs are lowered the percentage of cost attributed to labor becomes very significant. Designing parts for ease of assemble is critical. Extensive input from manufacturing was used in developing the design. In fact, our assembly documentation was developed concurrently with the design to allow assembly process to help dictate design.

Fixtures
Group discussion between engineering and manufacturing allowed us to identify operations where fixturing could significantly reduce assembly time. Discussions with suppliers identified tooling they could build to lower the unit part cost. Discussion with inspection personnel identified functional gages that could speed inspection. The use of actual parts in the fixtures lowered the cost to develop and build the fixtures.
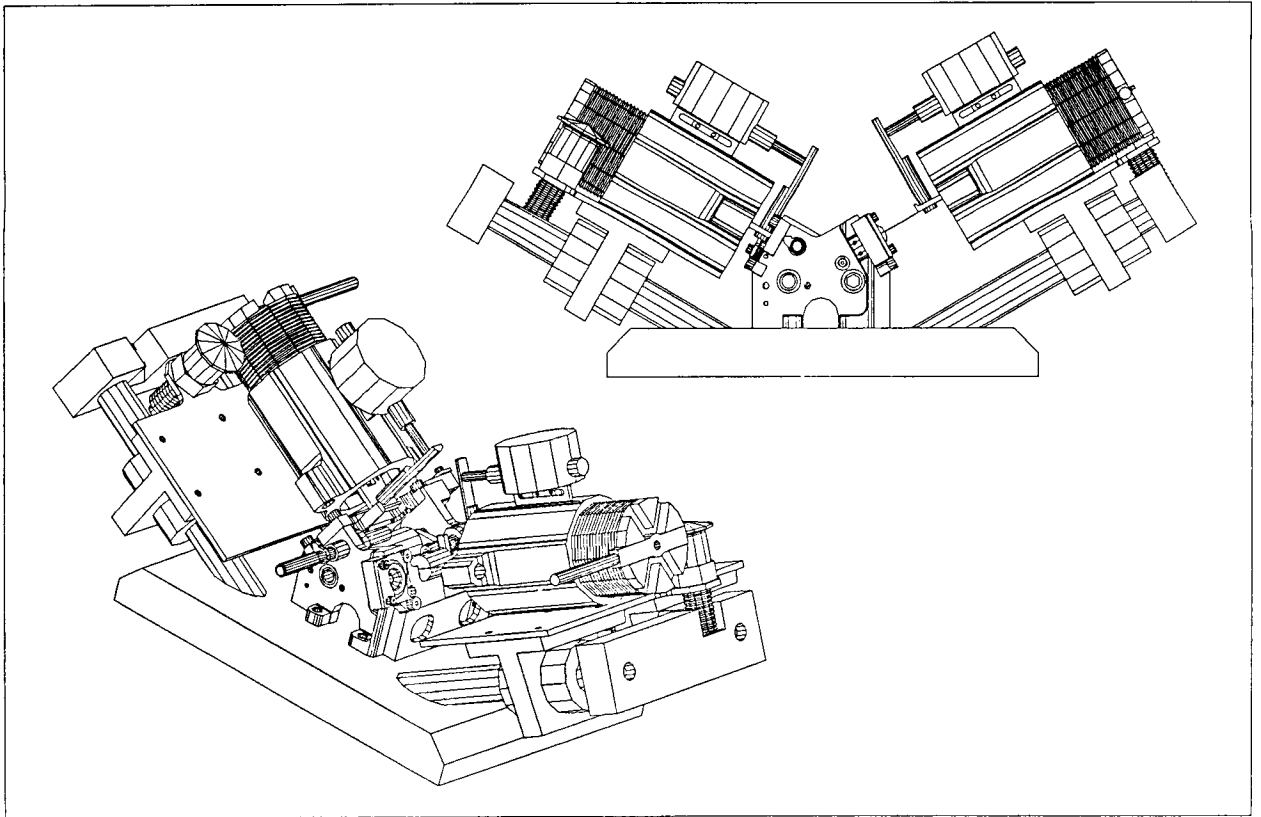
Design evolution

Phase one - Concept
The original design concepts had numerous complex parts. Each part and each system was conceived without fully considering the whole device. This initial design proved the approach and created the structure to begin optimizing the design. In the metaphor of the forest and the trees each tree was planted and the forest created.

Phase two - Simplification
Now it was time to look at the forest as a whole and integrate it. The design was refined, part functions were combined, part interfaces simplified and the value added by each part or feature was evaluated. The design was finalized and prototyped. But, as initial testing begin we realized some problems had been overly simplified and others ignored entirely.

Phase three - Refinement (Complication)
Customer requirements changed, some for the better, most for the worst. Fortunately, experience had taught us to allow for this in the design and no major changes were required. However, new and varying requirments challenged our approach to commonality and required creative solutions.

Extensive testing pointed to problems that were not adequately resolved, structures that were overly lightweighted and new kinematic interactions identified. Materials had to be changed, webs added to strengthen weak sections and features added to parts to improve clearances. As a result, mass and cost were added back to the design. On the other hand, a better, more refined, understanding of the design and kinematics allowed some parts to be simplified further, reducing mass and cost.

Examples
The solar array bracket was originally made with a thinner walled extrusion and had a stiffening ring inserted in the end to stiffen the tubular structure. After, building a prototype and understanding the real costs involved in such an approach, the bracket wall thickness was increased to the ring inner diameter and then machined to remove the excess material. This approach was identified in the beginning but was assumed to be more costly, our experience taught us differently.

In order to lower weight and cost, a guide to keep the preload spring located on the antenna bracket was eliminated. As loads rose and envelope shrunk the position of the spring became an issue. A feature was added to the offset plate to locate the spring end and a spring tube was added to the antenna bracket assembly to eliminate "caterpillaring" of the spring.

A word about changes
Make changes carefully. Last minute changes to correct a local problem can sometimes have far reaching effects on a complex system. Changes should be thought out as carefully as the original design was thought out. We changed the length of the release band to reduce the stroke of the preload spring and thereby reduce the shock at release. This change altered the complex trajectory of the exiting tab allowing it to impact the latch body. This impact effectively bent the latch body on the high load latches.

What we learned about changing our paradigm to include cost

Lots of inputs
Designers are used to balancing varied requirements and evaluating trades. Adding unit cost to the list of requirements is not inherently difficult. However, creating and

evaluating cost input and developing experience with costs requires effort. On a large design effort, assigning support personnel to concurrently monitor cost, source suppliers and participate with the development team can be a practical solution.

Simple tools
Creating and maintaining a part level cost budget, much like a mass budget, is a simple practical tool for meeting cost objectives. A part information summary was maintained for each part. It listed all suppliers, their price quotes, lead times, issues and suggestions.

Elegance = Reliability + Low Cost
There might be a belief that lower cost means lower reliability. It is our experience that high reliability actually results in low cost if the approach to reliability is driven by simplicity. "Keeping it simple" supports both reliability and cost. An elegant design is one that accomplishes as much as possible with as little as possible. Therefore, an elegant design inherently costs less. Time invested in an elegant design will result in lower costs.

Conclusion

Adding severe cost constraints to mechanism design extends the demands placed on a designer. The proven approach of acquiring knowledge, conducting research and experimenting work with the requirement of cost as it does with all other requirements. For the accomplished designer cost is the final frontier.

/ 9 9 5 ⁻ 1 2 0 8 4 8

4o5435
22p.

The Clementine Mechanisms

William Purdy[*] and Michael Hurley[*]

Abstract

The Clementine spacecraft was developed under the "faster, better, cheaper" theme. The constraints of a low budget coupled with an unusually tight schedule forced many departures from the normal spacecraft development methods. This paper discusses technical lessons learned about several of the mechanisms on the Clementine spacecraft as well as managerial lessons learned for the entire mechanisms subsystem. A quick overview of the Clementine mission is included, the mission schedule and environment during the mechanisms releases and deployment are highlighted. This paper then describes the entire mechanisms subsystem. The design and test approach and key philosophies for a fast-track program are discussed during the description of the mechanisms subsystem.

The mechanism subsystem included a marman clamp separation system, a separation nut separation system, a solar panel deployment and pointing system, a high gain antenna feed deployment system, and two separate sensor cover systems. Each mechanism is briefly discussed. Additional technical discussion is given on the marman clamp design, the sensor cover designs, and the design and testing practices for systems driven by heated actuators (specifically paraffin actuators and frangibolts). All of the other mechanisms were of conventional designs and will receive less emphasis. Lessons learned are discussed throughout the paper as they applied to the systems being discussed. Since there is information on many different systems, this paper is organized so that information on a particular topic can be quickly referenced.

Clementine Mission With Mechanism Activities Inserted

The Clementine satellite (Figure 1) was designed to map the lunar surface in many wavelengths and to do an asteroid flyby. The satellite was launched January 25, 1994 on a Titan IIG rocket from Vandenburg Air Force Base. The Clementine space vehicle was separated from the Titan approximately 45 minutes after launch via a pyro marman clamp release and four balanced kickoff springs. Clementine was in a Low Earth Orbit (LEO) for approximately 1 week. During the week in LEO, the star tracker covers were opened several times and the spacecraft was oriented based upon the star tracker readings. Also, all the satellite systems went through health checks to verify their proper operation. The satellite was then oriented and spun-up to approximately 60 rpm for the solid rocket burn that began the transfer orbits to the moon. The solid rocket burn took place on February 2, 1994, this burn put Clementine in a transfer orbit approximately 60-80% of the way to the lunar orbit.

After the solid rocket burn the spacecraft was spun-down and the solar panels were deployed shortly afterwards. Approximately 16 hours after the solid burn, the main sensor cover was opened and the interstage and solid rocket case were separated

---

[*] Naval Research Lab, Washington, D. C.

from the satellite (Figure 1) via a pyro release of eight separation nuts and four balanced kickoff springs. The high gain antenna feed was then deployed. A 490 N (110 lb) liquid propellant thruster was used to make the remaining burns for lunar transfer orbit changes and lunar insertion. Clementine spent 26 days transferring from LEO to a lunar orbit, the final lunar orbit was achieved on Feb 21, 1994. Note the staging of the solid rocket and the 490 N thruster significantly increased the allowable satellite weight that could attain a lunar orbit. The next seventy days were spent mapping the moon, 100% mapping of the surface was achieved. Clementine was scheduled to begin the transfer orbits for the asteroid Geographous in early May but the mission was ended due to a software failure.

Some significant miscellaneous information about Clementine. The total space vehicle weight was 16,020 N (3600 lb), with the following breakdown: 11,125 N (2500 lb) was the solid rocket, 445 N (100 lb) was the interstage, 2,225 N (500 lb) was propulsion fuel and oxidizer, and 2225 N (500 lb) was the dry satellite. The entire satellite was on a very tight weight budget as a 2225 N (500 lb) spacecraft had to perform a very complex mission. The five sensors on the satellite were a Ultra Violet/Visible Spectrum camera, a Long Wave Infrared camera, a Near Infrared camera, a LIDAR laser ranging system, and two star tracker cameras. The satellite design began in April, 1993, giving only 22 months for design, manufacturing, integration, test, and launch. The satellite was sponsored by Ballistic Missile Defense Organization, the sensors were supplied by Lawerence Livermore National Laboratory, and the satellite, integration, and mission operations were done by the Naval Research Laboratory.

List Of The Clementine Mechanisms Systems

1. Marman clamp and kickoff spring system at Titan II/spacecraft interface (Figure 1).
2. Separation nuts and kickoff spring system at satellite/interstage interface (Figure 1).
3. Solar array release, deploy, and pointing system (Figure 2). This system used frangibolts for array release, springs for deployment, and a stepper motor for pointing.
4. High gain antenna feed release and deployment system (Figure 3).
5. Main sensor cover system (Figure 4). This system was driven by a paraffin actuator.
6. Two star tracker covers systems (Figure 4). These systems used paraffin actuators.

Mechanisms System Approach And Key Philosophies

To begin any project all the necessary mechanism subsystems must be identified and their purpose in the mission completely understood. The following Clementine examples illustrate this: 1) Is the purpose of the sensor cover to keep out debris, light, or both?, 2) What data is the high gain antenna needed for and when? Next the major design requirements must be understood. **It is extremely important to understand the purpose of each mechanism and to be involved in the iterative process of defining the requirements** to assure that unnecessary and difficult requirements are not placed on the design since there is not enough time to meet these unnecessary requirements. For Clementine, high reliability was a requirement, redundancy was not - redundancy was determined on a system-by-

system basis and was incorporated only where it significantly improved the design. Besides avoiding unnecessary requirements, being involved in this process of determining the design requirements improves your design as your understanding of the system is much more complete.

The long-lead items, such as actuators and motors, must be sized and ordered very early in the design process. On our 22-month schedule, mechanisms that had lead times up to 15 months, including contract preparation, had to be ordered just three months into the design process, at which time the spacecraft design was still very immature. **Ordering these long-lead components with high functional margins was critical to our success**. Having high margins on critical, long-lead items allows the mechanisms to meet evolving requirements without needing to change critical components, thus allowing the program to continue on schedule. Further, high margins on driving components gives a robust design that greatly improves reliability. Specifying high functional margins enabled us to get through the development process without any major redesigns, which was crucial to meeting our schedule. As a rule of thumb, all actuators and motors were designed with a 3:1 ratio of driving to known opposing forces. It is not acceptable for evolving requirements or the discovery of unanticipated loads during testing to stop the entire program.

Understanding which components to put high margins on is extremely important. Long lead time items and/or driving components such as actuators are a must. Since these components only make up a small part of the system, the weight penalty is very small, yet the increased reliability and level of tolerance for changes or problems later is greatly improved. For example, to use a solar array drive motor "one size larger than necessary," or in our case, a motor that gave a 3 to 1 driving torque margin, only increased the motor weight by 0.45 kg each. However, had we discovered that we needed a larger motor (i.e., if array size increased) the entire program would have missed the launch window as the motors took 15 months to design, build, and test. This does not mean that all the components in a subsystem have high margins, on a weight-critical program this is not possible. Weight savings is obtained primarily from reducing the margins on the structural components of the mechanism. These structural components can be verified by testing to the maximum required load and, if they fail, can be often be modified as quickly as 1-5 weeks if necessary. The reliability of these components was kept high by testing them to qualification-level loads.

Early prototype testing proved to be extremely valuable. As soon as a design concept firmed up, a prototype was made and tested or more appropriately played with. Early prototype testing, even with very crude prototypes, proved very valuable. This testing often uncovered problems easier to recognize in hardware than in 2 or 3 dimensional drawings. Additionally, many subtleties of the mechanisms quickly became apparent in prototypes. The prototypes always greatly improved our understanding of how the system really works. The problem catching and understanding gained from the cheap, crude prototypes greatly improved the final designs and prevented many costly and schedule impacting mistakes.

The reliability of the mechanisms relied on 1) good engineering understanding of the system requirements and environment, and 2) on

rigorous qualification and acceptance testing. Design analysis included hand calculations, Roark and Young stress calculations, and TK Solver math models of the various systems. Finite element modeling was neither necessary nor useful except for the analysis of the marman clamp rings. A rigorous testing program was a major reason for the success of the mechanisms. The goal of a thorough testing program is to uncover all of the problems, and potential problems, on the ground where they can be solved. We performed our qualification testing in an informal manner although we tested the mechanisms very rigorously, often testing them to their functional limits. Our acceptance tests were taken to protoflight levels and included lengthy burn-in testing. The acceptance testing uncovered many minor and a few major flaws which we repaired before delivering the mechanisms for spacecraft integration. This rigorous testing provided us with a very high confidence in the reliability of our mechanisms upon delivery for spacecraft integration.

Furthermore, thorough testing gives a deep understudying of how the system works and what its subtleties are. This understanding can be invaluable during flight operations. For example, during a one-time lunar pass involving rapid temperature changes, the main sensor cover switch opened for ten minutes and then closed. Fortunately, during thermal testing we had found that the cover would bow causing the microswitch to open during periods when one side of the door was heated rapidly. This warping was due to the temperature difference between the outside and inside door surfaces that the poorly conducting door would temporarily support. Having seen this behavior in testing allowed us to quickly explain this unusual telemetry and kept us from disrupting the mission.

A Note On Primary Satellite Structure For Weight Critical Programs

It is important to realize on weight-critical programs that the loads requirements passed down from the launch vehicle are typically the results of a **3 sigma** situation, in other words results are inflated so that the actual launch loads will be less than predicted loads **99.7%** of the time. Further, combinations of loads that do not even occur at the same time are often used as design load case. The mechanical system manager of the satellite should truly understand the assumptions and method used to derive the design load cases to assure that an impossible situation is not becoming a driving design requirement. See the marman clamp section for more information.

Marman Clamp Separation System

The marman clamp separation system is shown in Figure 5. This system was used between the Titan II and the Clementine space vehicle (Figure 1). The clamp release was done via two explosive bolts, 180 degrees apart for redundancy. Balanced kick-off springs were used to separate the two vehicles and tension springs were used to restrain the clamp after release. The clamp design was very weight efficient totaling only 36 N (8 lb) and supporting a maximum line load of 32,280 $^{N}/_{m}$ (184 $^{lb}/_{in}$) over a 1.067 m (42 in) diameter, which corresponds to a launch vehicle combined load case of +3g tensile, ±2.2g lateral. The clamp was tested to 125% of this load case. The clamp preload was 16,020 N (3600 lb). The highlightable features of this clamp include the lightweight design, the joint design, and finally the trunnion design. In

developing this design, several other marman clamp designs were researched, the best design features were taken from these clamps and implemented on the Clementine clamp. All of the following comparisons are made against the designs that were researched.

The number one way to reduce weight is to choose a reasonable preload. First, the maximum line load around the ring is calculated based on the worst launch vehicle load case, which is conservative (see the next paragraph). Clamp preloads are sized to prevent gapping of the joint when the maximum predicted line load is applied all around the joint, a case the clamp never experiences. Additionally the required preload to prevent this gapping is typically greatly padded. This padded preload number is then increased again to allow for preloading errors. The above is a perfect example of how margin is added on top of margin producing tremendously conservative design loads. The preload that is determined as necessary to prevent gapping is the driver for sizing all of the clamp components and often the rings also. So for weight savings, it is very important to choose a reasonable preload. However, unless extremely weight critical, leave a ±25% tolerance on your preload to avoid the need for a very tedious installation procedure.

This next paragraph may sound like an exaggeration to make a point, but it is an actual example of how design loads can get out of control if not well understood and monitored. The original load case that the marman clamp was designed to was a +3g axial tension load superimposed on a ±3.5 g lateral load. Each of these loads independently (+3g axial and ±3.5 g lateral) is a 3 sigma (0.3% probability of happening) launch vehicle load case that in reality do not even occur at the same time. In addition, a finite element model was made of the interstage and the recommendation made that a stress concentration factor of 1.5 be applied to the maximum line load as well as an 8% model uncertainty factor. Finally, the clamp was going to be tested to 125% of the design load. Had we actually used these loads, the marman clamp would have been designed to handle loads 4 times the maximum expected loads (99.7% probable loads) and 8 times the actual predicted flight loads. The clamp was not designed to these loads. The clamp was designed to a +3g tension combined with a ±2.2g lateral load case and tested to 125% of this load case.

Once reasonable design loads and a preload have been selected, the marman clamp can be significantly lightweighted by reducing the high margins often put on the strap and the shoes, each of which account for approximately 40% of the clamp weight. Specifically, the strap margins are typically in the 3-6 range for ultimate strength; I found 2.5 to work fine (Note: all my margins are defined as Material Strength / Stress). Also, try to hold the same strap margin all the way around including rivet sections, around the trunnions, etc. It does no good to have one section of the strap stronger than the rest. The strap material was 301 corrosion resistant 1/2 hard steel. The marman clamp shoes were designed with a margin on yield of 3.0 which is lower than the typical margins of 4-8. Since the shoe load is much higher for the shoes located under the trunnions, significant weight can be saved by designing and optimizing an aluminum 7075-T7 shoe at the non-trunnion locations and using titanium shoes under the trunnions (Figure 5). Our surface preparation involved hard anodizing the aluminum shoes and rings, Tiodizing the titanium shoes, and dry lubing all the shoes

with Tiolube 460. We found no galling and always had clean separation between the shoes and the rings. Finally, **do NOT reduce the margin on your separation bolt below 2 times the nominal preload** and keep it even larger if you anticipate the satellite weight may increase significantly. Reducing the margin on the bolt saves little weight and is very high risk in that it is a long lead item that is very difficult to change. Also, there is a significant increase in bolt tension as load is applied to the joint, this increase in bolt load is directly related to the joint design which is discussed in the next section. Bolt load should only increase 10-15% with a good joint design. The Clementine separation bolt only had a margin of 1.5 over the nominal preload. While the design did work, the low margin caused much suffering, requiring tremendous effort in developing a careful preload procedure and two static load tests.

As with any preloaded joint, the joint design greatly affects how the clamp carries applied loads. NRL has traditionally used a joint that is gapped between the outer surfaces of the rings so that the rings rest on the inner surfaces (Figure #6A). **Locating the gap between the outer rings gives a much stiffer, linear joint which reduces the applied load that the clamp must carry as well as increasing the satellite's natural frequency on the launch vehicle.** The benefit comes from providing a load path that does not have to take a circuitous route around the outer rings. While the analogy is not perfect, comparing a marman clamp joint in a pure tension load case to a bolted joint in a pure tension load case gives tremendous insight (Figure #6B). The well-designed bolted joint has a low bolt to joint stiffness ratio, around 1 to 5, so that as tension is applied and the bolt is stretched, the joint relieves by approximately 80% of the applied load so that the bolt only has to carry 20% of the applied load. The same is true for the marman clamp joint; the stiffer the joint and the better the load path, the more the joint relieves when it is in tension and therefore clamp carries less of the applied load. Looking at the cross-sections and load paths shown in Figures 6A and 6C, it can easily be seen that the joint with the gap between the outside ring surfaces (6A) provides a much better load path and is much stiffer.

In fact, the first design iteration had a gap of only 0.254 mm (0.010 inch) between the outside surfaces, and this gap closed at approximately 60% of full preload as the lower ring rolled. The resulting joint contacted at both the outer and inner surfaces, but the inner surfaces were only preloaded to approximately 60% instead of 100% of the full preload. During static loads testing, this joint proved to be non-linear causing the clamp to carry a large percentage of the applied load which it was not designed for. The problem was corrected by increasing the gap size between the outer ring surfaces so that these surfaces did not contact when preloaded, thus preloaded the inner surfaces to the full preload. **The improved joint stiffness is easily seen in the results of the static loads tests. Figure 7 shows the increase in the marman clamp strap tension as a function of applied tensile load across the joint.** The graph shows the that the joint that was properly gapped and preloaded is linear and stiff, minimizing the percentage of applied load that the marman clamp needs to carry. On the other hand, the joint with the gap that closed at 60% of the preload is nonlinear and forces the marman clamp to carry a much larger percentage of the applied load. As could be anticipated, the biggest increase in slope (tension in

strap / applied tensile load) occurs at approximately 60% (20,000 lb on Figure 7) of the applied load that the preload was designed to support.

Traditionally, the marman clamp and separation bolt designs do not account for any increase in the marman clamp loads once preloaded, however, extremely high design margins are put on all the components. This maybe explained by the fact that marman clamp joints are usually gapped between the inner ring surfaces (Figure 6C), making them highly nonlinear and therefore very difficult to predict and design. **Designing a stiffer joint greatly improves the joint behavior and allows one to confidently reduce the extremely high design margins**.

The increased natural frequency of the satellite that results from the improved joint design (Figure 6A) should not be understated. In fact, the stiffer joint was originally designed because a soft marman clamp joint caused the satellite's first mode on the launch vehicle to be below the launch vehicle requirements. The program that made this design improvement was in no way weight critical, the change was driven completely by the system's natural frequency.

Trunnions have received a bad reputation by some as there was once a problem with trunnions putting the separation bolt in bending and causing it to fail. **Trunnions make for a very compact and clean design and do not put the bolt in bending if properly designed.** The correct and incorrect trunnion designs are shown in Figure 8. The free-body diagrams show that the bolt load must go into the trunnion on the bolt side of the trunnion's center to give a self-correcting system. If the bolt load goes into the trunnion on the far side of the trunnion's center, the system is unstable in the sense that any misalignment will continue to worsen. Increasing misalignment in the unstable design will only be prevented by increased bolt bending that eventually either reaches equilibrium or breaks the bolt.

Finally, some thoughts on when and what of the above to implement on a marman clamp design. The proper joint design that has the gap between the outer ring surfaces (Figure 6A) should always be done, it is a far better design. Also, if trunnions are used, the load should be put into the trunnions on the bolt side of the trunnions' centers (Figure 8) so that bolt bending is prevented. The decisions that are much more program specific include what to use for design loads, whether to trim margins, what preload to select, etc. If your program is not weight critical, it is not worth fighting launch vehicle design load requirements. Launch vehicle design loads are a major interface issue, so simply designing to the worst load case makes things go much smoother, however, understanding the level of conservatism in the load cases is still important. Also, designing the clamp to accept a large tolerance on the preload, ±25% or more, will greatly simplify your installation procedure. A good installation procedure must always be developed, however, if the preload must be obtained very precisely (±10%). Developing this procedure becomes very time consuming and tedious. While a large error tolerance on the preload is desirable, a high nominal preload may not be desirable. Often high nominal preloads, in terms of a preload that gives high margins on gapping, are mistakenly thought to be conservative. The whole reason for designing preloads to prevent gapping is to maintain the joint stiffness, however, high clamp preloads often cause serious ring rolling problems which greatly

reduce joint stiffness. Preloads should be sized to prevent gapping for whatever the design load case is, but excessively padding the nominal preload should be avoided. Finally, the design of the rings must be done in conjunction with the marman clamp design to assure both a good joint design and that the rings are stiff enough to prevent ring rolling problems.

Separation Nut Separation System

The separation system between the Clementine satellite and the interstage (Figure 1) was done with eight separation nuts and four kickoff springs. A 9.5 mm (3/8 in) separation nut was located between each satellite longeron and the interstage ring. The preload of each nut was 15,575 N (3500 lb). The eight separation nuts provided far more preload than necessary, but provided a good load path and were in stock at NRL. The separation velocity between the vehicle was 0.458 $^m/_s$ (1.5 $^{ft}/_s$) and was achieved via balanced compression springs. Each kickoff spring was in its own canister and was balanced in terms of energy and preload prior to being installed on the spacecraft.

Solar Array Deployment and Pointing Mechanisms

The Clementine spacecraft had two solar array wings, each about 1.3 m by 1.3 m (4 ft by 4 ft) and weighting about 60 N (14 lb) per wing (Figure 2). Each of these array wings had four folding hinges and two release joints. The arrays were pointed at the sun by stepper motors with harmonic drives. The hinges were conventional designs using vespel bushings, stainless steel hinge pins and latch pins. The release joints used the Frangibolt non-explosive release mechanisms. Clementine was the first flight for the Frangibolt, which is produced by TiNi Alloy Inc. in San Leandro, Ca.

While the solar array mechanisms were mostly conventional, we learned several lessons in developing them under the tight schedule. We built one array wing without solar cells to be devoted entirely to mechanisms testing which served us very well in meeting our development schedule. **We performed a large amount of testing to ensure that impact loads were acceptable so that we could keep our functional margins as high as possible.** We found that the impact loads were not excessive because we built a fair amount of compliance into the arm between the array and stepper motor and because of structural damping during impact.

Isogrid structural composite was the original array substrate early on in the program for a variety of reasons. The isogrid uses a flat panel with triangular reinforcing ribs on the backside and can provide stud mounting locations at each node between triangles. All structural attachments must be made at these nodes which severely limits the design flexibility of the hinges and attachments as they can only have triangular bolt patterns of a given size. It was surprising how much of our design was affected by the isogrid pattern. For example, the triangular shape and size of the frangibolt mounting plate caused us to change the shape of the sensor cover door, which caused us to change the layout of the main sensor bench. Further, all isogrid attachment points must be identified before the isogrid is laid-up, thus making the isogrid very difficult to adapt to almost any design change. Honeycomb panels with

aluminum core and graphite facesheets were finally used because in addition to the above problems the isogrid was not capable of being manufactured to the flatness required for a solar panel.

The first usage of the frangibolt went quite smoothly since it was developed on the ARTS program (Presented in 28th AMS). Integrating the frangibolt into a spacecraft forced us to learn how to use it properly. Our first issue was that the arrays were used to generate power while they remained stowed for the week the spacecraft was in earth orbit. With the sun on the solar panels they stabilized at 100°C. The frangibolt actuators had to be kept below 70°C to keep them from actuating and releasing the array prematurely. This thermal control was accomplished mounting the actuator on the spacecraft side of the interface using an aluminum plate to heat sink the actuator to the relatively cool spacecraft. A poorly conducting titanium interface plate on the solar panel was used to block the heat flow from the hot panel. This scheme kept the actuator at 44°C while the solar panel was 100°C and the spacecraft was 30°C.

The major lesson we learned with the frangibolts is that they should not be driven with a widely fluctuating bus voltage. We learned this lesson for all heat actuated mechanisms and it is discussed later in the paper. The last thing we learned about the frangibolts was the importance of following a good installation procedure. It must be a point of discipline to ensure that the actuator has been compressed before it is installed and that a notched bolt and the proper hardened nuts and washers are used.

High Gain Antenna Deployment System

The Clementine high gain antenna system is shown in Figure 3. This antenna system was very simple in design. The driver for deploying the antenna feed was two pairs of carpenter springs. The antenna feed was held in the stowed position via a preloaded cradle. A paraffin actuator was used to release the feed by driving a structure that pulled a pin. Once the pin was pulled kickoff springs under the cradle gave the system a large kickoff torque in a region where the carpenter springs are relatively weak.

The carpenter springs were made out of SAE 1095 strip steel, hardened and tempered. These springs were simply 2.54 cm x 0.0114 cm (1.0 in x 0.0045 in) tape measures purchased directly from the factory with no paint or markings; the cost was $25 per hundred feet. During the year prior to flight, several materials for carpenter springs were looked at, but the more we played with our tape measure prototype, the more obvious it became that they were fine for the job. The only disadvantage to the SAE 1095 is that it is prone to corrosion. On Clementine, this problem was minimal as the total time from flight assembly of the antenna feed to launch was 4 months. The springs were, however, lubricated with Braycote 601 to help resist corrosion and frequently inspected. On future programs, we would use Elgiloy, a corrosion resistant alloy with very high yield strength that is not prone to corrosion. Also, Elgiloy is manufactured in strip form and can be specified to have rounded edges which is important as the edges are under very high stress.

117

The antenna system was tested in a similar way as the sensor cover systems as all these systems were driven by paraffin actuators. This testing is discussed in the next section. One on-orbit lesson learned, which goes for all paraffins, is fight to get a temperature telemetry point for each paraffin actuator. **This temperature telemetry is invaluable for predicting the behavior of the paraffins in different and sometimes unexpected on orbit environments.**

Sensor Cover Systems

The Clementine satellite had a main sensor cover used over the primary suite of sensors and two star tracker covers. These covers are shown in Figure 4. The purpose of the sensor covers was to protect the optics from debris and solar radiation. Both types of covers employed a labyrinth seal to keep debris out of the optics areas. The covers were driven open with paraffin actuators, a latching mechanism was used to hold the covers open, and torsion springs drove the covers closed when the latch was released. The main sensor cover was designed and manufactured at Starsys Research in Bolder, Co. The main sensor cover was presented at the 28th AMS.

Often, neither the performance of a particular type of seal nor the sealing requirements are well quantified. In order to solve this problem, Starsys Research developed prototype seals and tested them by placing protoflight covers in a chamber, engulfing it in swirling flour using compressed air, and then quantifying the amount and size of the particles that got by the seal. Flour was chosen as the debris simulator because it has a range of particles from 0.51 mm (0.020 in) to less than 0.0254 mm (0.001 in) diameter. **This flour testing proved a very effective, as well as a cheap way, to evaluate various seal designs.** The protoflight labyrinth seal performed far better than expected. The good sealing performance of the labyrinth combined with the zero breakaway forces to open the cover and good design flexibility made the labyrinth seal the clear choice for our application. The flour testing was so effective that it was also used to evaluate the performance of the star tracker labyrinth seal. Figure 9 shows the before and after appearance of a prototype star tracker flour test.

An often difficult requirement to obtain is the cleanliness requirement of the seal. The sensor people often know they want their optics "clean" but do not have a good quantification of this. **The flour testing was invaluable for agreeing on a required seal cleanliness or performance level.** Since the flour test was a significant over-test due to the use of swirling, compressed air coupled with a large amount of flour, and since the seals only let 1 or 2 particles of 0.0254 mm (0.001 in) or less through, the seals were considered more than adequate and the entire issue was put to rest.

Before testing any of the paraffin-driven systems, a baseline characterization of the system's performance was done. This characterization involved characterizing the system's position and actuator temperature as a function of time. A performance characterization run was then done after every major test, such as random vibration and life cycling, and compared against the baseline performance. **This method of comparing the before and after performance was excellent for spotting and troubleshooting any cover**

system degradation as well as for verifying that the cover was operating properly and ultimately ready for flight. Figure 10 shows the baseline characterization curve for the main sensor cover. Note that for position and temperature to be repeatable functions of time, a consistent voltage and a consistent starting temperature for the paraffin actuator must be used. The starting temperature for the actuator should be well above the ambient temperature, we used 40°C, and is best achieved by heating the paraffin to a temperature above the desired starting temperature, turning the actuator off and letting it cool, and finally turning the actuator on when the desired starting temperature is reached. The baseline curves were all averages of three characterization runs. Finally, it is important to realize the baseline curves are specific to each individual paraffin actuator.

One important lessen we learned was that voltages above 34 volts should be avoided when using paraffin actuators. During the testing of the sensor cover one of the actuators had a heater circuit open due to overheating while being operated at 36 volts. This problem was exposed on the main sensor cover and may or may not be seen on other paraffin actuators because it is a heat transfer problem that resulted from a somewhat unique combination of factors. These factors included the main sensor cover paraffin actuator being designed for 150% higher power than typical paraffin actuators to increase stroke and maintain speed, the external load being relatively high, and finally being operated at 36 volts. Starsys does not recommend that the paraffin actuators be used at 36 volts, their testing as well as NRL's showed all such overheating problems could be eliminated by limiting the voltage to 34 volts.

Heat-Actuated Mechanisms In General

Clementine was NRL's first extensive use of heat-actuated mechanisms, specifically Frangibolts and paraffin actuators. As such, we learned much about integrating them into a spacecraft. Upon learning these lessons we were very happy with their characteristics and performance.

A voltage range of 24 to 36 volts is a brutal range for heat-driven devices leading to an extremely difficult heater design. The power is a function of the voltage squared which means that the heater must withstand two and a quarter times the power at 36 volts than it must withstand at 24 volts. Additionally, the heater must withstand applied mechanical stresses in both the Frangibolt and paraffin actuators. We feel that the spacecraft system design would be better served by reducing the heater supply voltage fluctuation to about ±2 to ±4 volts depending on the particular application. Note that limiting the operating voltage range greatly reduces the performance scatter of the devices making them much easier to characterize and predict on orbit.

Other lessons learned included discovering the need to protect the heat-driven mechanisms from accidentally being turned on during spacecraft integration and testing, specifically during software testing and debugging. Two flight star tracker paraffin actuators were destroyed because software accidentally turned them on for 8.5 hours, driving the covers against "remove before flight" hardware. Also we found that you have to be careful not to provide heat sinks to the actuators. For example, we once put a thermistor mounted on a small aluminum block on a paraffin actuator to

measure its temperature. The aluminum block acted as a heat sink and prevented the paraffin actuator from reaching its full stroke. Finally, routing power through redundant microswitches that opened when the paraffin actuators reached the end of their travel and when the Frangibolt released the solar panels, provided good fault protection with a low impact to reliability.

Conclusions

1. Understanding the purpose of each mechanism in the mission and being involved in defining the requirements is critical to assuring that unnecessary and difficult requirements are not placed on the design.

2. Ordering long lead components with high functional margins is critical on a fast track program. Further, high margins on driving components greatly improves a system's reliability and ability to adapt to changing requirements while costing little in terms of added weight.

3. Early prototyping and rigorous developmental and acceptance testing was one key to the success of the Clementine mechanisms.

4. Marman clamp joint designs can be significantly improved by locating the gap in the rings properly (Figure 6A). The proper gap location stiffens the joint which reduces the percentage of applied load that the marman clamp must carry and increase the satellite's natural frequency on the launch vehicle.

5. Paraffin actuators proved to be excellent drivers for sensor covers and frangibolts worked well for solar panel deployment. Both paraffins and frangibolts have the advantages of being lightweight, compact, capable of repeatable use (that is the .flight component can be tested and then flown), and neither have any safety issues.

6. Heat-actuated mechanisms should be powered by supply voltages varying by only ±2 to ±4 volts depending upon the particular application.

7. The labyrinth seals proved to be a good technique for moderate cleanliness requirements. They provided excellent mechanical reliability and very good cleanliness.
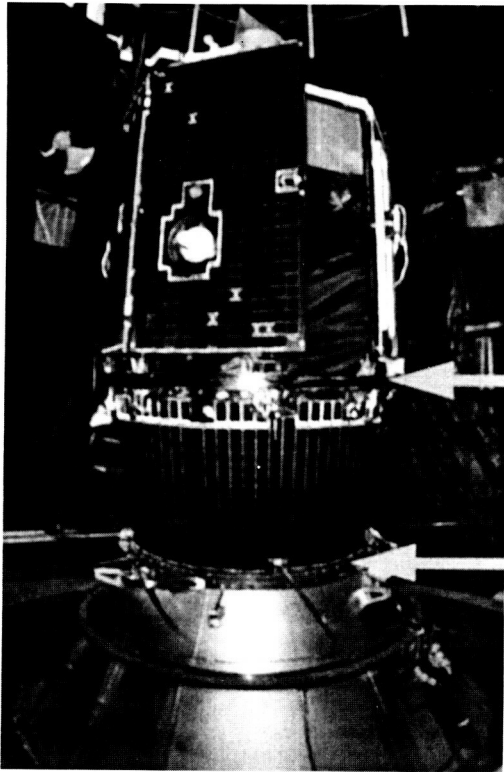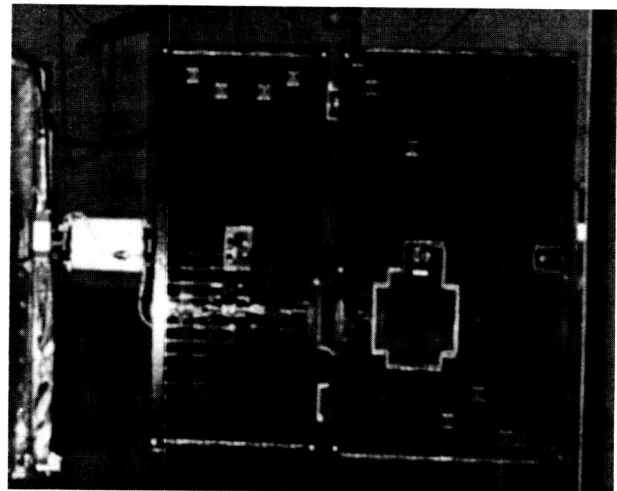
Satellite / Interstage
Separation Plane
(8 Separation Nuts)

Space Vehicle / Titan II
Separation Plane
(Marman Clamp)

Figure 1: Clementine Satellite On Titan II
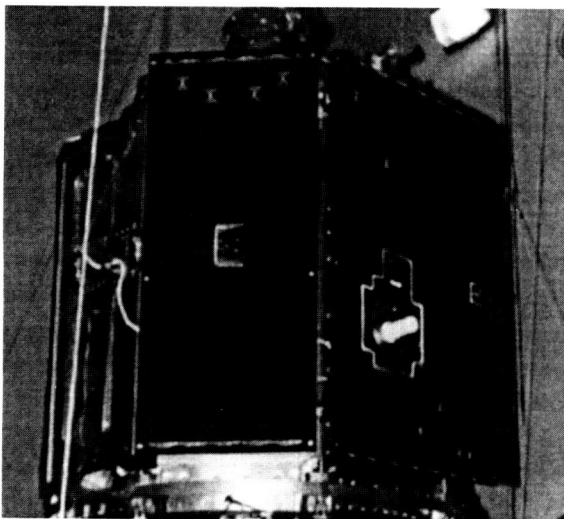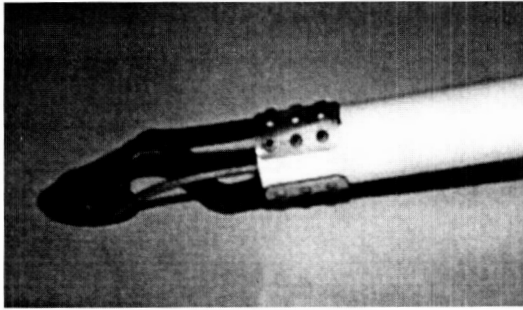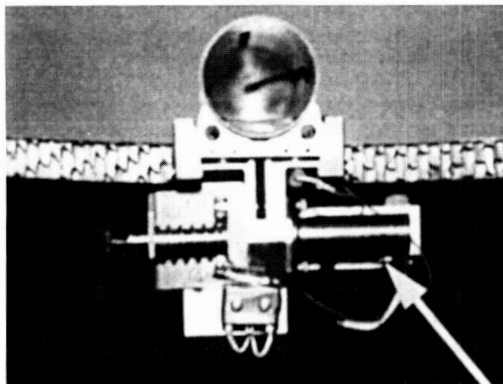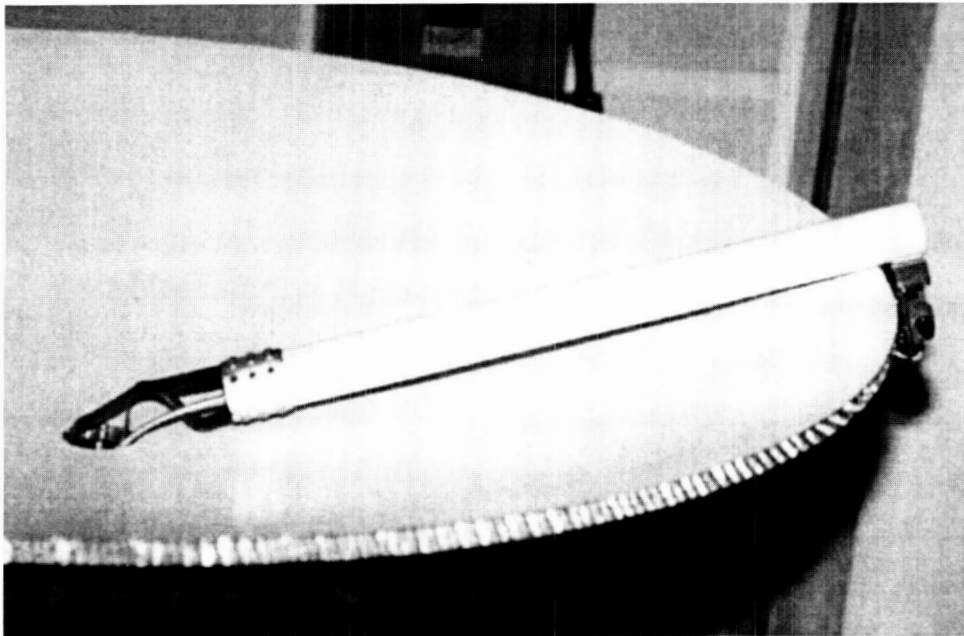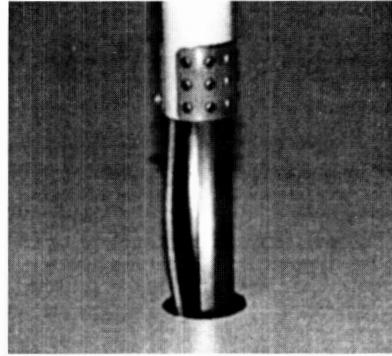

Stowed Solar Panels (1 of 2
Wings Shown)

Deployed Solar Panels (1 of 2
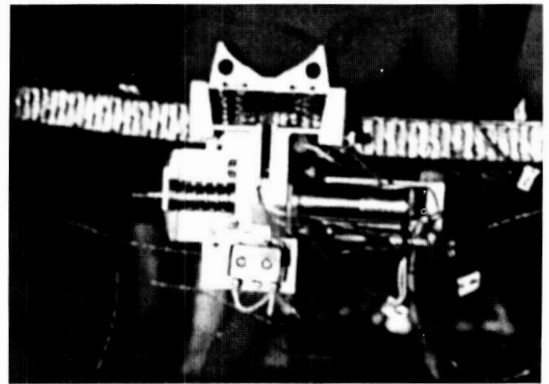Wings Shown)

Figure 2: Stowed & Deployed Solar Panels

Feed & Cradle In Stowed Position   Feed & Cradle In Deployed Position

Paraffin Actuator

Figure 3: Clementine High Gain Antenna System

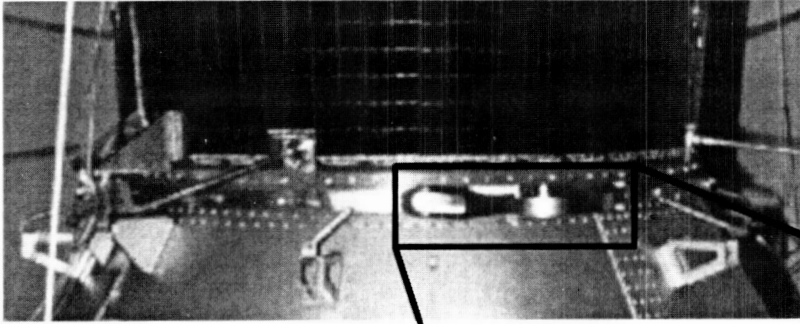# Sensors Included LWIR, NIR, LIDAR, & UV/Vis
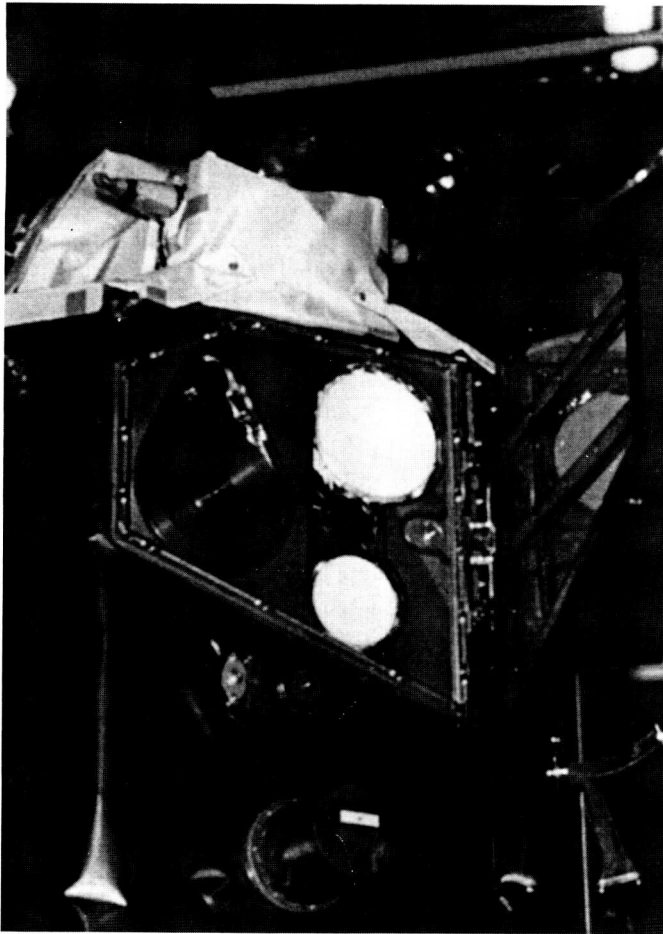
Main Sensor Cover On Satellite

Both Systems Used Paraffin Actuators With A Latch To Hold The Covers Open & Springs To Drive Them Closed
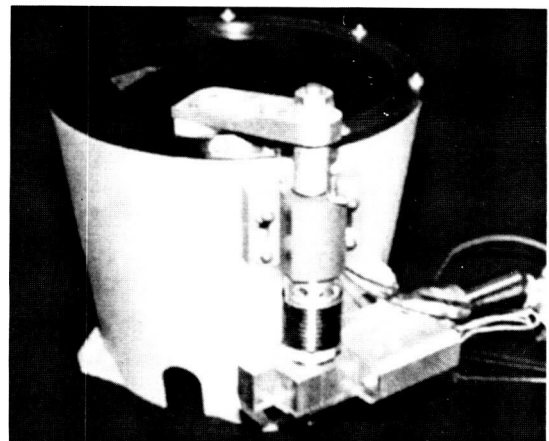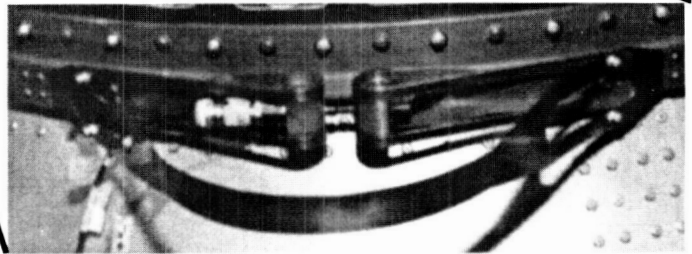

One Of Two Star Tracker Covers

Figure 4: Clementine Sensor Cover Systems

Marman Clamp On Titan Adapter (Lower) & Clementine Interstage (Upper)
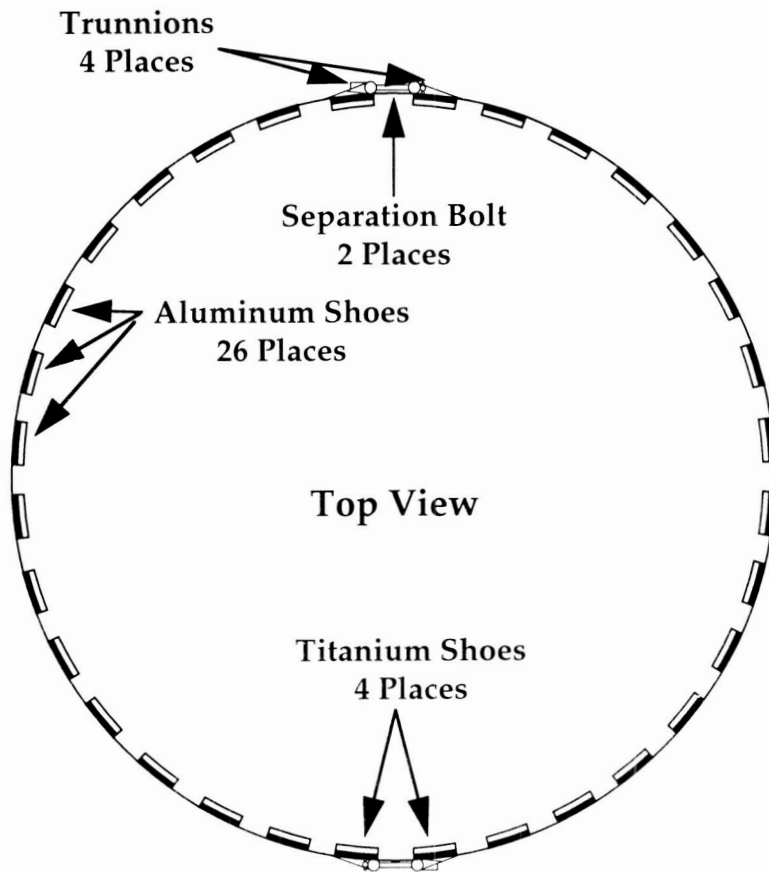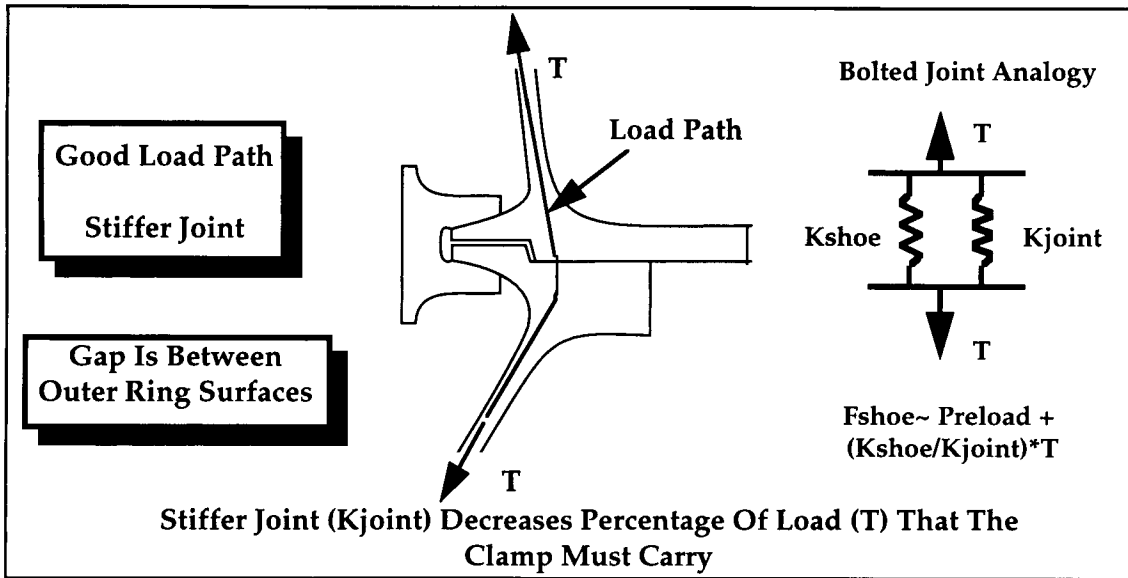
Separation Bolt & Trunnions

Trunnions
4 Places

Separation Bolt
2 Places

Aluminum Shoes
26 Places

Top View

Titanium Shoes
4 Places

Figure 5: Marman Clamp System

Good Load Path

Stiffer Joint

Gap Is Between Outer Ring Surfaces

T

Load Path

T

Bolted Joint Analogy

T

Kshoe   Kjoint

T

Fshoe~ Preload + (Kshoe/Kjoint)*T

Stiffer Joint (Kjoint) Decreases Percentage Of Load (T) That The Clamp Must Carry

Figure 6 A: Improved Marman Clamp Joint Design

T

Kbolt   Kjoint

T

Fbolt= Preload + (Kbolt/Kjoint)*T

T= Applied Tensile Load
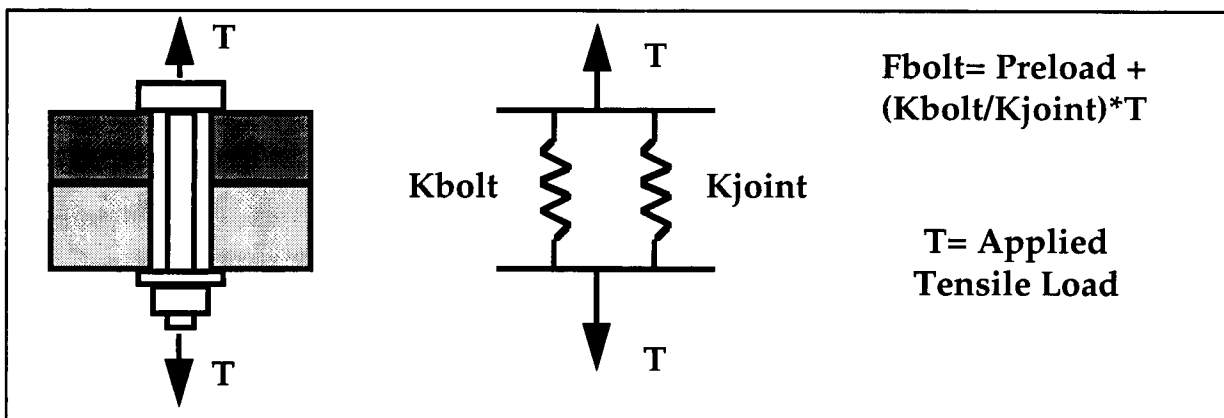
Figure 6 B: Bolted Joint In Tension

Poor Load Path

Soft Joint

Gap Is Between Inner Ring Surfaces

T

Load Path

T

Bolted Joint Analogy

T

Kshoe   Kjoint

T

Fshoe~ Preload + (Kshoe/Kjoint)*T
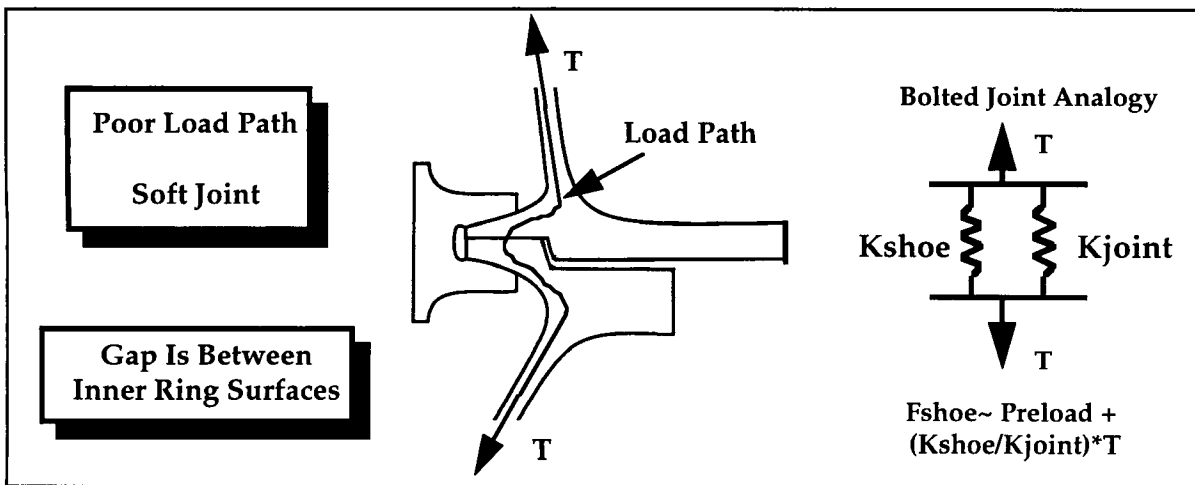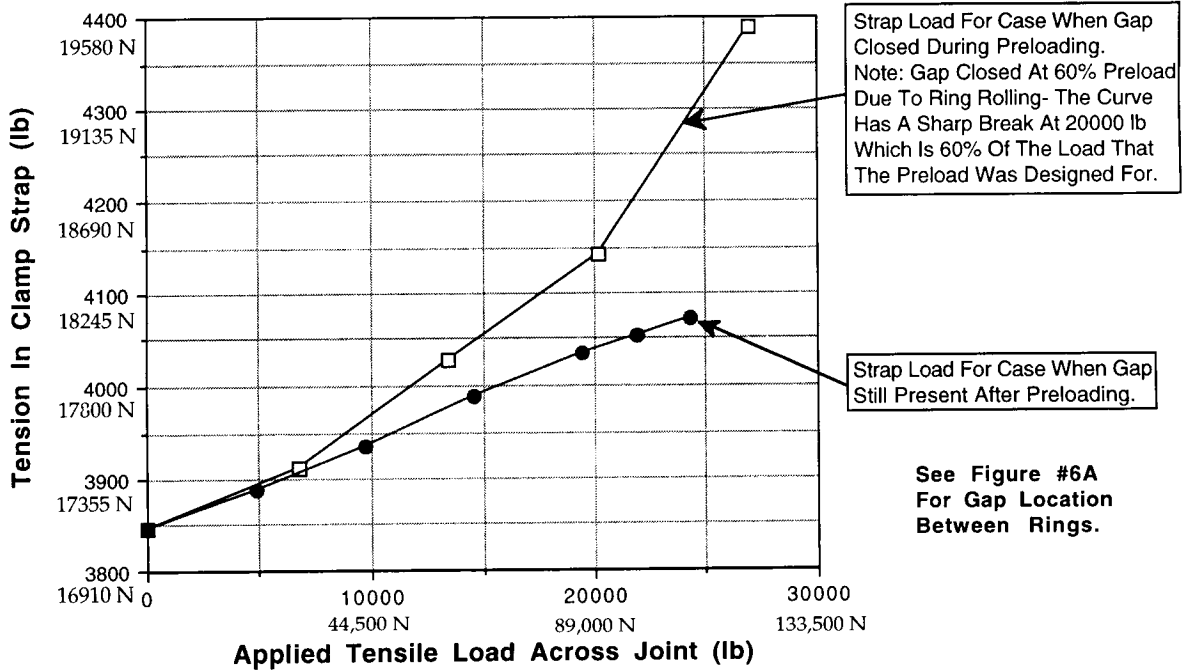
Figure 6 C: Traditional Marman Clamp Joint Design

Figure 7: Marman Clamp Strap Tension Vs Applied Tensile Load
For An Open Gap and Closed Gap Joint
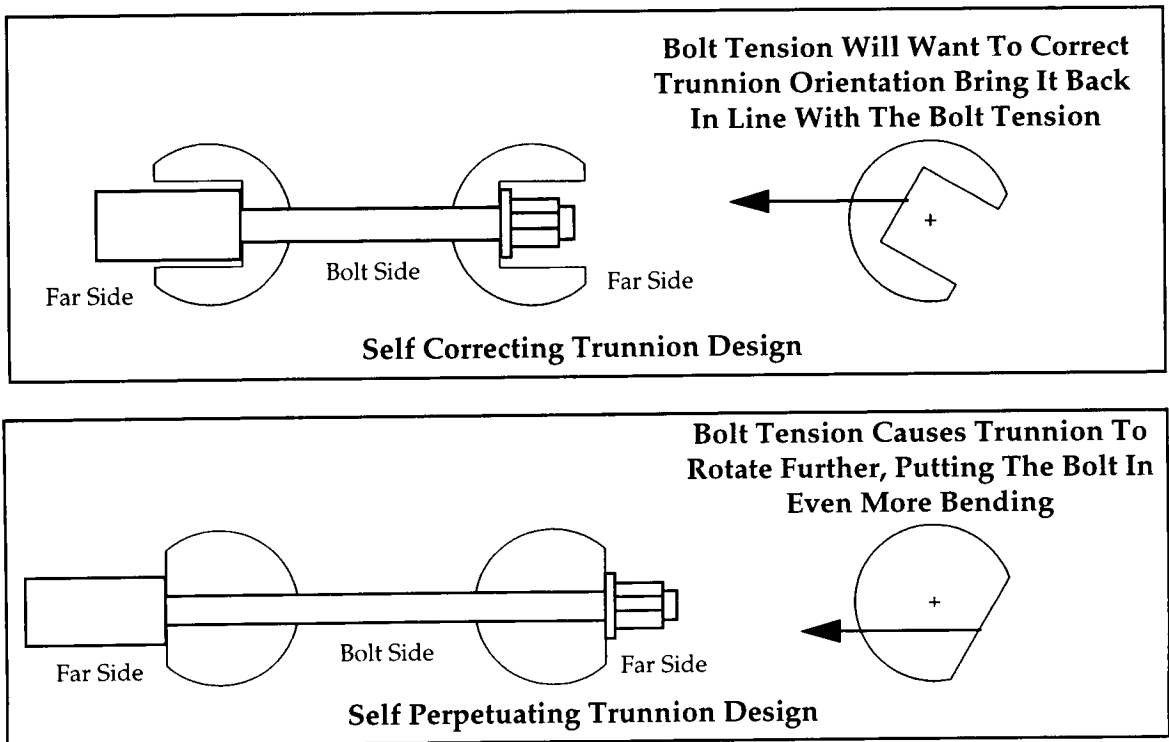
Figure 8: Trunnion Design & Free Body Diagrams
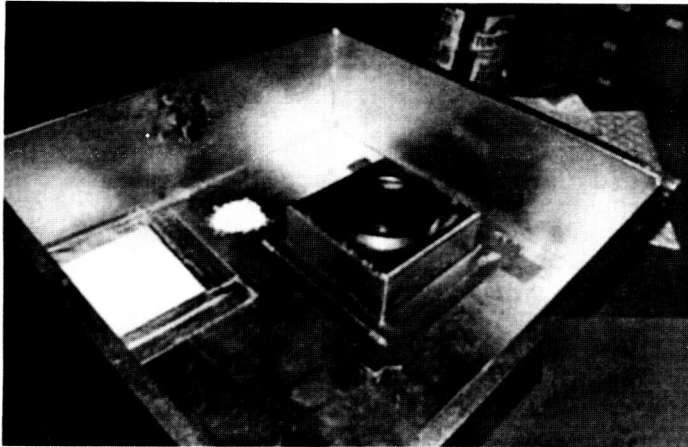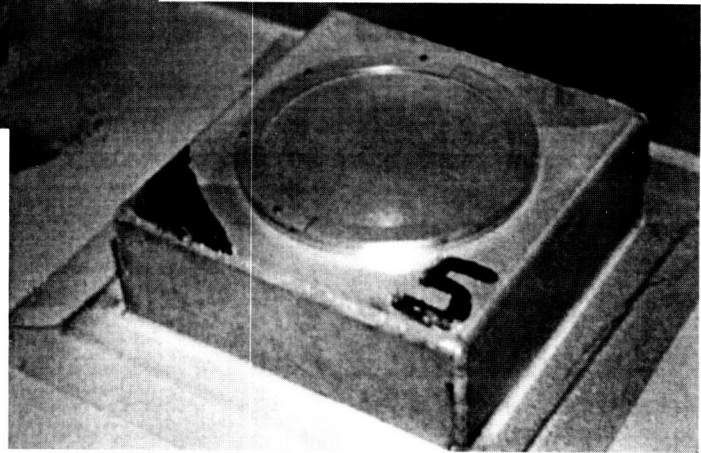
Prototype Seal After Testing

Setup Before Testing

Figure 9: Prototype Star Tracker Cover Flour Testing
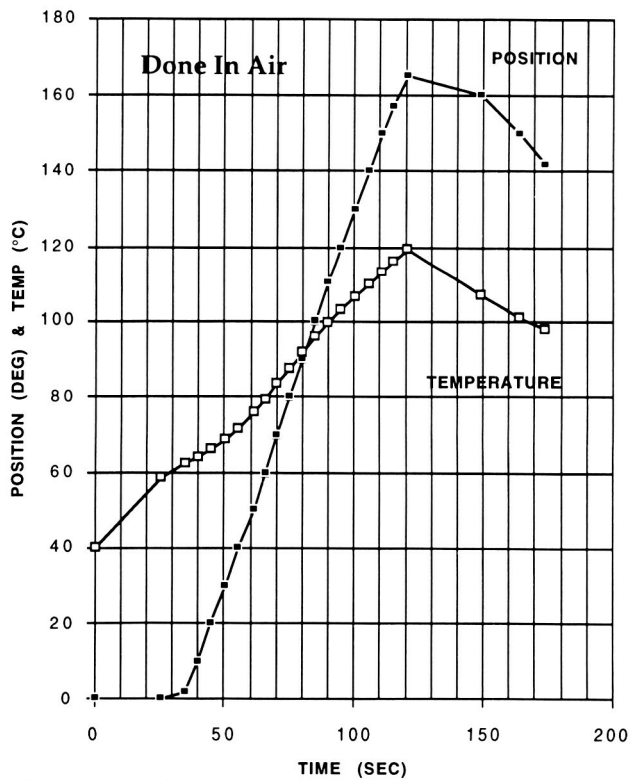
Figure 10: Baseline Performance For Opening Main Sensor Cover

Session Chair: Phil Olikara

Low-Cost Tubular Antenna Deployer for WISP-2

Robert M. Warden*

Abstract

A new tubular boom deployment mechanism has been designed, built, and flown as part of the second Waves In Space Program (WISP-2) through Cornell University. For this program, two booms were needed to form a dipole antenna but existing units were found to be too complicated and costly. A low-cost alternative was developed which combined flight-proven tubular boom technology with a new support and deployment mechanism. The simplicity of this new design was a major factor in providing a highly reliable and cost-effective system.

Mission Description

The WISP-2 experiment was launched from Wallops Island, VA on July 22, 1993 onboard a Black Brant X rocket. The 750-second experiment reached an altitude of 500 km and covered a distance of 500 km before burning up on its return to the atmosphere. Shortly before the apogee of the flight, the payload separated into two units to form a transmitter and a receiver. Onboard the transmitter unit, the two tubular booms deployed out of opposite sides of the spinning spacecraft to form a 40-meter dipole antenna. The three main instruments onboard measured electrical, magnetic, and particle properties. Data from these instruments verified that the booms deployed successfully.

Description

The new boom deployment mechanism, shown in Figure 1, was designed to contain and support the stowed antenna during launch and then enable the antenna to deploy on command. The mechanism consisted of three main components: the base, the tubular boom antenna, and the stowage spool. Deployment in space was initiated by actuating a pin-puller. The first part of deployment was controlled by the geared kick-off feature as shown in Figure 2. The boom continued to self deploy and once it was fully extended, the spool simply flew off the end. Because this was a non-orbital flight, restrictions on generating space debris did not apply.

Each assembly measured 10 by 13 cm on the base by 13 cm tall. The mass of the mechanism (excluding the tubular boom) was 0.86 Kg. The 20-meter-long tubular boom was 0.45 Kg and the Kapton insulation was 0.05 Kg for a total system mass of only 1.36 Kg. Four clearance holes were provided to mount the unit to the spacecraft.

---

*AEC-Able Engineering Co. Inc. Goleta California

The Base

The main part of the base structure was made by bolting two rectangular side plates onto a square base plate to form a simple "U" section. The sides and base were made out of 12.7 mm (0.5 inch) stock Delrin plate which had several advantages. This material was readily available, easy to machine, inexpensive to purchase, and provided good electrical insulation.

The relatively thick section of material allowed the use of oversized screws which could be threaded directly into the plastic plates without the need for threaded inserts. Typically, 10 to 15 threads were engaged which provided a good margin over the required strength. A thread locking compound was used to hold the screws in place. Slots were machined into the side plates which supported the stowed spool during launch and guided the spool out of the mechanism during the first part of deployment. Contained within the thick side plates were two spring-loaded plungers which provided an initial push on the spool away from the base.

The geared kick-off feature also held the stowed boom in place during launch. A short section of gear rack was mounted to each side plate. A rocker plate, with two single toothed sections of rack attached, was sandwiched between the two side plates. The spool was captured in the base by the rack on one side of each spool gear and the single gear tooth on the other. The rocker plate was held in place by a small pyrotechnic pin-puller.

A flanged aluminum post was attached to the base plate. The root of the boom was attached to and supported by the post. Electrical attachment to the boom was provided by a single tapped hole in the flange.
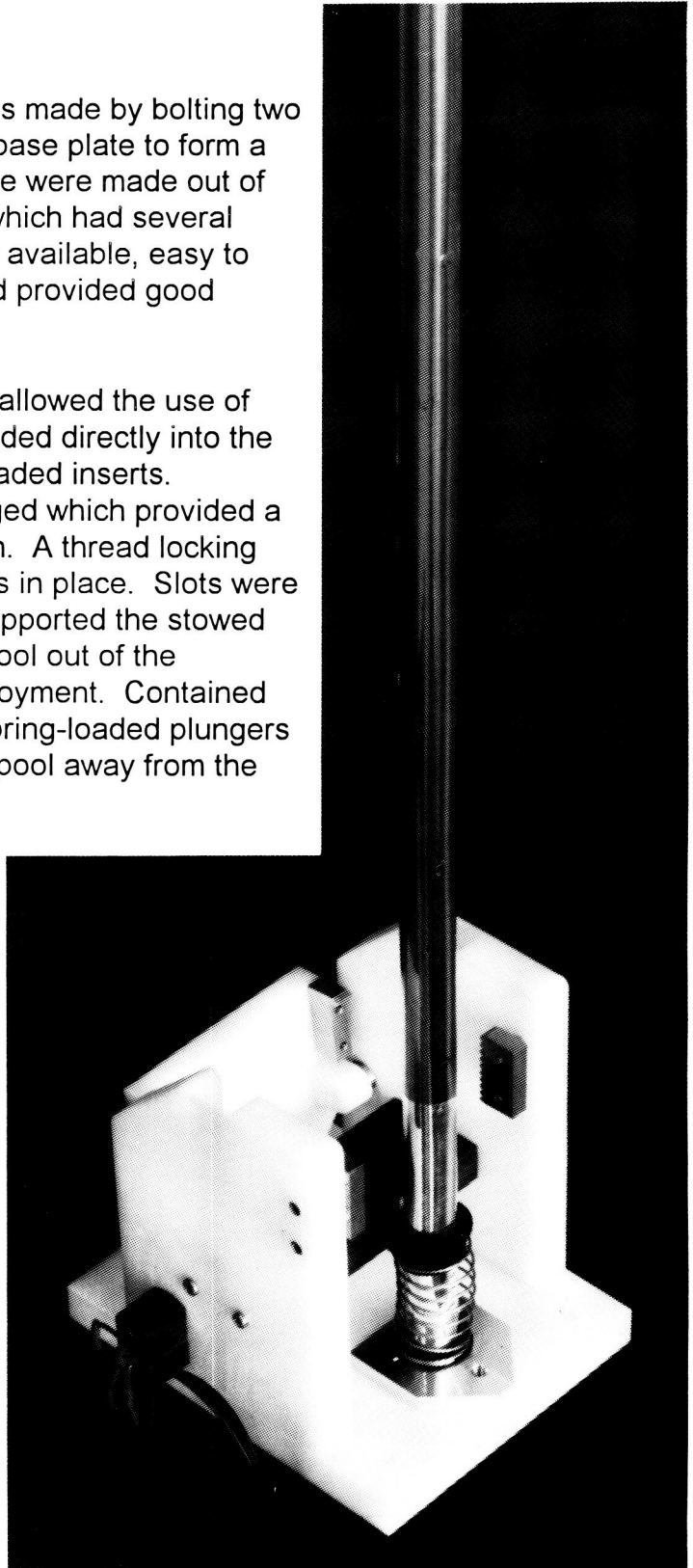

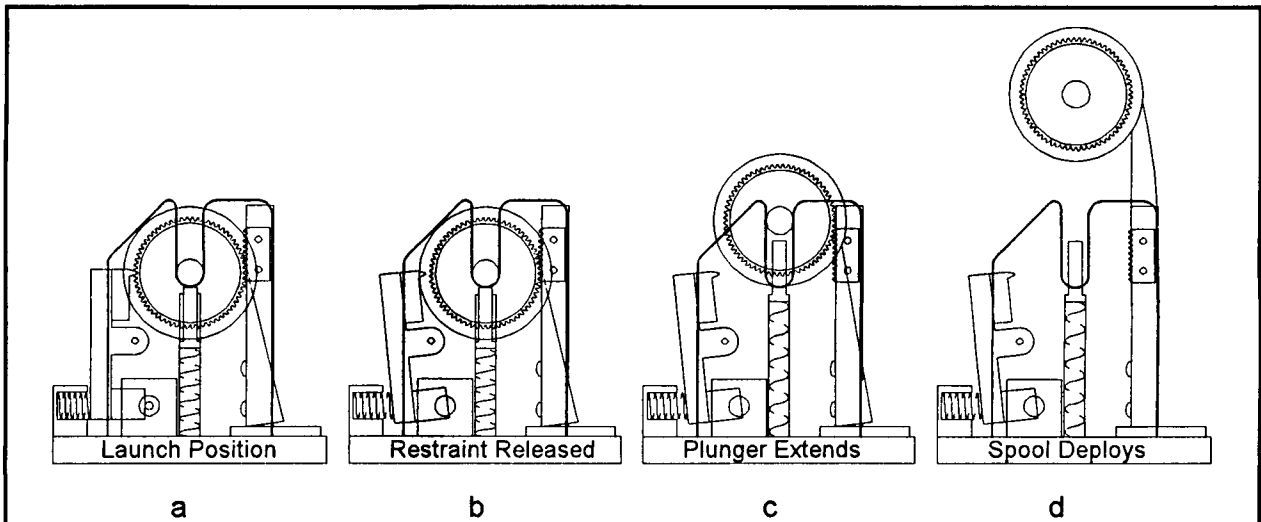**Figure 1. Mechanism With Boom Deployed**

Figure 2. Initial Deployment Sequence

a. In the launch position, the stowed boom on the spool was captured by the geared kick-off feature.

b. Once in space, a pyrotechnically actuated pin-puller released the launch restraint mechanism which allowed the spool to unwind and deploy the boom.

c. Two spring-loaded plungers provided the initial force to push the spool away from the base. The rack and gear forced the spool to rotate as it moved up the guide slots.

d. The guide slots directed the deploying spool away from the base. The initial deployment sequence took less than 1 second. The time to deploy the entire 20-meter boom was less than 10 seconds.

Tubular Boom

The antenna element for this program was specified to be a self-deploying tubular boom, 14 mm diameter by 20 meter long, made of silver-plated, beryllium-copper strip. A supply of surplus boom material was obtained which was made by Fairchild and flown on the RCA SOOS program as gravity-gradient booms. The design of the tubular boom antenna dates back to the 1960s and was the subject of various papers presented in the 2nd, 3rd, and 4th Mechanisms Symposia.

The tubular boom was stowed by being manually flattened and rolled up onto a small, lightweight spool. Once in space, the spool unwound so that the boom formed into a 20-meter-long tube. A high degree of confidence was achieved by using this existing boom stock which had been used successfully in previous flight programs.

The first half of the antenna (closest to the spacecraft) was required to be covered with an insulating Kapton film. This was easily achieved by the application of standard adhesive-backed Kapton tape to the boom. Other modifications to the existing booms were that they were trimmed to length and holes were made at the base for attachment.

The Spool

The boom was rolled up on a spool in a way which provided very good packaging and support during launch. The inner part or the flanged sides of the spool were based on existing designs which have a slight taper toward the middle which forces the boom to peel off the spool in a controlled manner. Critical wear surfaces of the aluminum flanges were hard anodized which was essential to the smooth deployment of the boom.

A spur gear was added to each end of the spool as part of the geared kick-off feature. The pitch diameter of the gear was designed to be the same as the outer diameter of the stowed boom. A Delrin knob was also added to each end of the spool to register it in the guide slot in the base.

Testing

Development and testing of the design was limited to verifying the deployment mechanism since the tubular antenna and spool design had already been proven by flight experience. Short sections of boom material approximately 3 meters long were used to test the mechanism. A spacer was added to the spool to represent the missing 17 meters. The unit was then deployed many times in various conditions including vertically upwards, vertically downwards, horizontal, with and without Kapton tape applied. Most of the deployment kinematics were developed with these tests.

Two flight units were then loaded with short booms which were sent to Cornell for vibration testing. Each unit had a 3-meter boom loaded onto the spool and a non-flight pyrotechnic pin-puller integrated into the launch restraint. One of the booms was covered with Kapton tape and the other was left bare. After the test, the units were returned to ABLE where they were mounted upside down and deployed by actuating the pin-puller.

The final flight assembly was then made with the full-length flight booms loaded onto the spools and the flight pin-pullers integrated into the launch restraints. The units were then shipped to Cornell and integrated into the spacecraft. The deployable booms and mechanisms were then visually inspected for any abnormality. This visual check out was the final verification of the units.

Problem Areas

Three problems were encountered in the development of the new deployer design:

1. The root strength of the boom was found to be inadequate for the spin-up phase of the mission. The attachment of the inboard end of the boom was critical to its overall strength. The first design allowed the root to twist which reduced the bending strength of the boom. A translating collar was added which moved into position as the boom deployed to lock the root in place. This greatly improved the root attachment of the boom which was then able to meet the bending strength requirements.

2. The use of Kapton tape was a simple and effective method for insulating the boom, however it did have an adverse affect on the boom deployment. The tape was applied when the boom was in a flat condition and this prevented the boom from achieving its deployed tubular shape. A tool was made to add small longitudinal slits to the film which then allowed the boom to deploy normally.

3. The pyrotechnic pin-puller was held in place by a small Delrin clamp. After the firing of the test units, a small crack was observed in the side of one of the clamps. An examination of the problem showed that when the pin-puller was actuated, it expanded in the area of the clamp which caused the crack. No adverse effects were found due to the crack but new clamps were installed for the flight units and no further action was taken.

Conclusion

The tubular boom deployment mechanism has been shown to be a reliable and inexpensive alternative to older systems. Throughout ground testing and the flight mission the mechanism proved to be quite dependable. The success of the boom deployment mechanism was largely due to keeping the design simple and by using standard materials and fasteners whenever possible.

/ 9951 20852

4054 27 5p

Ultra-High Resolution, Modular Optical Angle Encoder for Space-Based Opto-Mechanical Applications

Holger Luther*, Paul Beard*, Donald Mitchell**, and William Thorburn**

Abstract

A 27-bit optical encoder using a novel patent pending technology has been developed by the MicroE Development Center of BEI Sensors & Systems Company and tested by the Sensor Systems Group (SSG) Inc., in a positioning and stabilization mirror assembly (PSMA) designed and constructed under a grant from the Marshall Space Flight Center. Test results verified performance within the specifications of the PSMA.

Introduction

The high cost of space-based scientific missions and the limited funds environment make it absolutely necessary to design space-based sensor hardware such that it is lighter, less costly, and outperforms the previous generation of space resident hardware. Thus there is a great emphasis on the development of new materials with greater specific strength, smart materials, and most importantly ultra-high resolution sensors that are small, lightweight, and robust. Whereas previous generation angle sensors featured resolutions on the order of microradians, sensors for future space missions must extend that capability by an order of magnitude and maintain that capability over an extended time in space.

In 1994, SSG received a Small Business Innovative Research grant from the Marshall Space Flight Center to design, construct, and test a single-axis PSMA. The purpose of the project was to demonstrate the feasibility of constructing large aperture, ultra-high resolution scanning and pointing mirror assemblies that have sufficient bandwidth to substantially attenuate satellite platform base motion errors affecting the line of sight (LOS) of optical remote sensors while also capable of pointing that LOS over a range on the order of ±30 degrees in object space. This precise angular positioning was achieved by employing an interferometric encoder from BEI MicroE. The PSMA requirements for the encoder performance are given in Table 1.

Encoder Design

The MicroE encoder utilizes diffraction from a radial grating to generate interference fringes which are detected and then processed yielding the high resolution electrical output. Its light source is a commercially available laser diode as used in CD players. The laser output is collimated by a miniature lens assembly and then apertured, before passing through a transmissive phase grating deposited on a 69.85 mm (2.75 in) diameter glass disk. Light diffracted from the grating falls into discrete orders, with the grating geometry chosen such that the zeroth and even orders are suppressed while energy in the first order beams is maximized. Without the zero order diffraction, there

---
* SSG, Inc., Waltham, MA
** BEI Sensors & Systems Company MicroE Development Center, Needham, MA

exists a region beyond the third orders in which the first orders overlap and create an interference pattern with a nearly sinusoidal spatial intensity distribution. This high fidelity/high resolution pattern is the basis from which the encoder output is derived. A photodiode array located in that region converts the optical signal into four current amplitudes, which correspond with the spatial distribution of the interference pattern. These four photodiode current channels have a sinusoidal time dependence in the presence of a constant rotation of the disk supporting the grating. This concept is equally applicable to transmissive and reflective gratings. Since the above region of interference is typically on the order of 2.5 mm deep, there is no critical requirement for alignment of the detector array with the encoder disk. Moreover, it is shown that the spatial wavelength of the interference is independent of the laser wavelength, thus making the encoder's metrological accuracy only a function of the grating constant of the phase grating on the encoder disk.

This encoder weighs ounces as opposed to many pounds typical of high resolution geometric encoders, and the encoder can be installed and aligned in a matter of minutes in comparison to the hours spent aligning conventional modular encoders with less than half of the resolution of the MicroE encoder.

PSMA Design

A prototype MicroE two read station encoder was fabricated and installed in the high resolution PSMA . The PSMA was designed to feature a silicon carbide lightweight mirror with an aperture of 15.24 cm x 22.86 cm (6 x 9 inches), an angular range on the order of ±2.5 shaft angle excursion and servo system bandwidth greater than 60 Hz. The mirror shaft of the PSMA is suspended on two Bendix flexures and is driven by a BEI-Kimco rotary actuator designed for SSG. The prototype PSMA, shown in Figure 1, contains a magnesium alloy mirror which has a moment of inertia that is comparable with the SiC mirror. The PSMA was integrated with the encoder at MicroE's facility and tested at SSG on a pneumatically suspended optical bench. Figure 2 shows the MicroE encoder on the PSMA drive shaft. The digital signal processor (DSP), which interpolates the angular position of the encoder disk using the sine and cosine quadrature signals from the encoder analog signal conditioning electronics, is embedded in the Motion Engineering, Inc. DSP-200 digital servo control board. The DSP-200 board is capable of supporting an 85 Hz servo loop bandwidth.

Performance Tests

Performance of the MicroE encoder technology was first measured prior to the integration of the PSMA. Accuracy of the interpolated bits are dependent on the fidelity of the sinusoidal signals within each cycle. To determine this interpolation accuracy, the output of a similar MicroE encoder was compared against a Hewlett Packard dual frequency laser michelson interferometer and a Heidenhain LIP 402 A interferometric grating based encoder. The michelson interferometer is far more sensitive to environmental fluctuations, such as minor beam path turbulence, than the grating-based interferometers; because of this, the MicroE accuracy was not successfully measured using the michelson as the standard. Comparisons of the Heidenhain and the MicroE were successful, and the results are shown in Figure 3.

Relative error in terms of linear motion was ±14 nm peak to peak. The error profile provides clues as to the source of the error, with some of it due to the Heidenhain and some due to the MicroE, as indicated by their characteristic error signatures. Accuracy can be improved significantly with tighter adjustments to the signal gains and offsets.

While the position output of the encoder provides important information on the PSMA performance, it is the motion of the mirror itself in the integrated system that in the final analysis is the primary object of interest. To that end the mirror deflection was measured with an electronic autocollimator — a Moeller-Wedel ELCOMAT 2000. This instrument has resolution of 0.24 µrad in both x and y axes, while its dynamic range is 0.56 degree.

Important to an optical sensor is the PSMA's ability to point the sensor's LOS repeatedly in any commanded orientation, and the PSMA's jitter amplitude as a function of that angular orientation. Accordingly, two test regimens were formulated. The first consisted of recording a number of samples of the position as reported by the servo system and the autocollimator at the mirror's home position, after which it was deflected by an incremental step of some 50,000 counts where again multiple position reports were sampled. This procedure was then repeated over the entire field of the autocollimator. Since that is small in comparison with the total deflection angle of which the PSMA is capable, the entire procedure was repeated at initial positions of ±2.5 degrees. The second test involved commanding the mirror to repeatedly execute a step on the order of 0.25 degree starting at a number of initial positions near the home position and at about ±2.5 degrees. After each step, the mirror position, as reported by the servo system and the autocollimator, was recorded.

Results and Conclusion

Table 2 summarizes the test results. The top five entries list the results of the first test. It is seen that both the servo system noise and the mirror point accuracy improved after the PSMA was installed on a pneumatically isolated optical bench. No evidence of a consistent bias error was found in these data sets. The last six entries list the results of the repeatability tests. It is seen that the optical accuracy is on the order of 1.5 times the ELCOMAT's LSB. It is therefore reasonable to conclude that the PSMA's pointing repeatability exceeds the resolution limit of the ELCOMAT. Again it is not possible to discern any substantial contribution to the repeatability error by the servo system at the ±2.5 degree mirror positions. Results confirm that the encoder met the PSMA system requirements including absolute accuracy.

Table 1. Performance Goals of the MicroE Encoder

Performance Parameter	Magnitude
Resolution [1]	0.047 μrad
Angular Range	±2.5 degree
Repeatability (over 10 min)	0.2 μrad
Accuracy	±2.0 μrad
Electrical Output	32 bit parallel word

[1] 12 DSP-based interpolation

Table 2. Summary of Marshall SFC PSMA Bench Tests

Date	Ang. Range (degree)	Noise/Jitter[2] (rad rms)	Accuracy (μrad rms)	Remarks
08/08/94	-0.26 to 0	0.126	1.164	Small Bench, Foam Rubber Pad
08/08/94	0 to +0.26	0.257	1.251	Same
8/18/94	-2.64 to -2.12	0.034	0.795	Large Bench, Air Support, Foam Rubber
8/18/94	-0.26 to + 0.26	0.034	0.679	Same
8/18/94	2.12 to 2.64	0.033	0.776	Same

Date	Ang. Range (degree)	Step Size (degree)	Repeatability (μrad rms)	Remarks
8/10/94	-0.26 to +0.26	0.13	0.340	Small Bench, Foam Rubber Pad
8/10/94	-0.26 to +0.26	0.26	0.291	Same
8/24/94	2.14 to 2.66	0.26	0.388	Large Bench, Air Support, Index Table, Foam Rubber
8/24/94	-2.4 to -1.88	0.26	0.388	Same
8/25/94	-2.4 to -1.88	0.26	0.437	Same
8/30/94	1.88 to 2.4	0.26	0.388	Same

[2] Accuracy Data: Moeller-Wedel Autocollimator ELCOMAT-2000 (LSB 0.243 μrad); Jitter noise limit of seismic environment ~ 0.034 μrad rms.
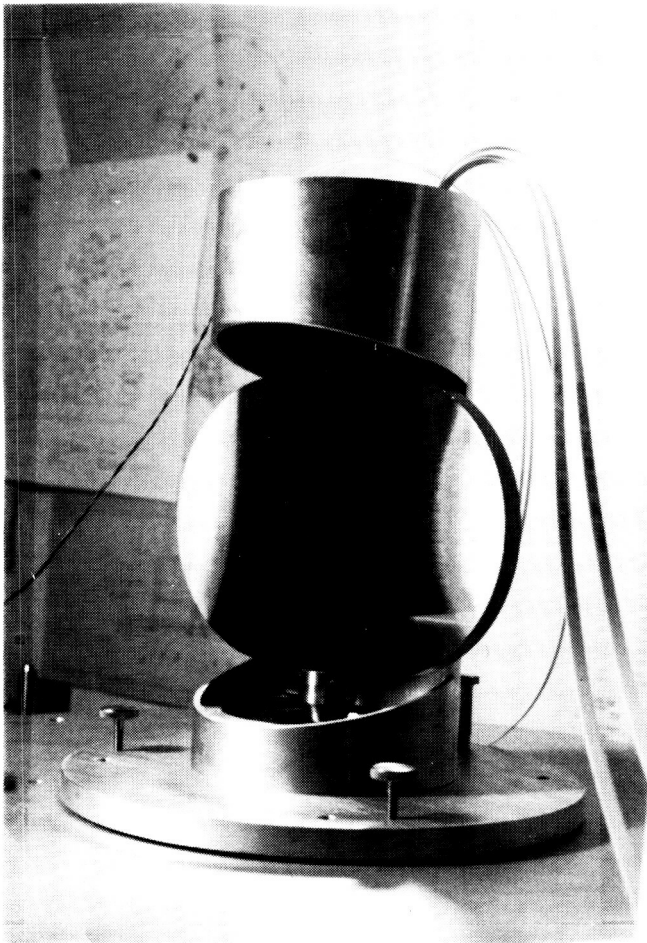
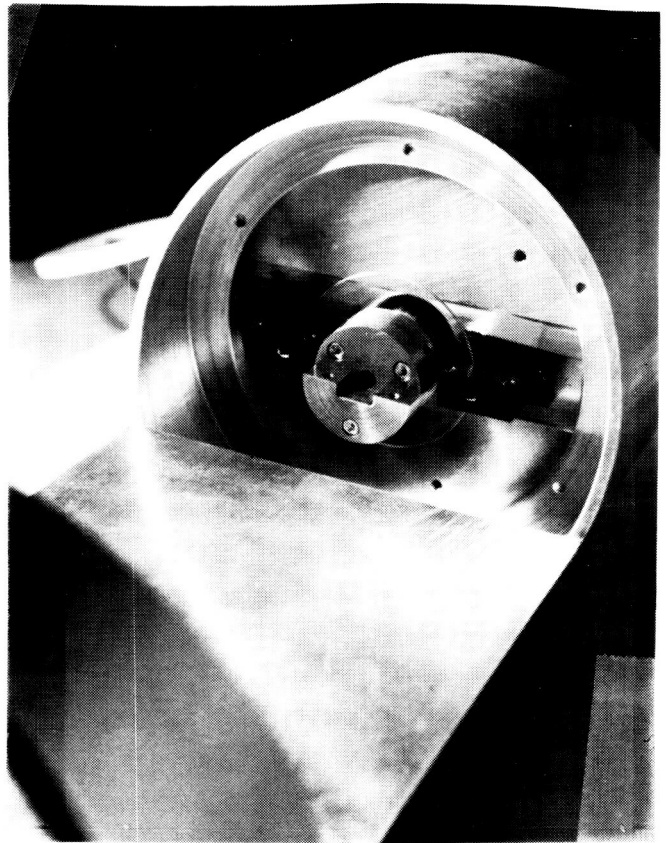**Figure 1. Marshall Pointing and Stabilization Mirror**
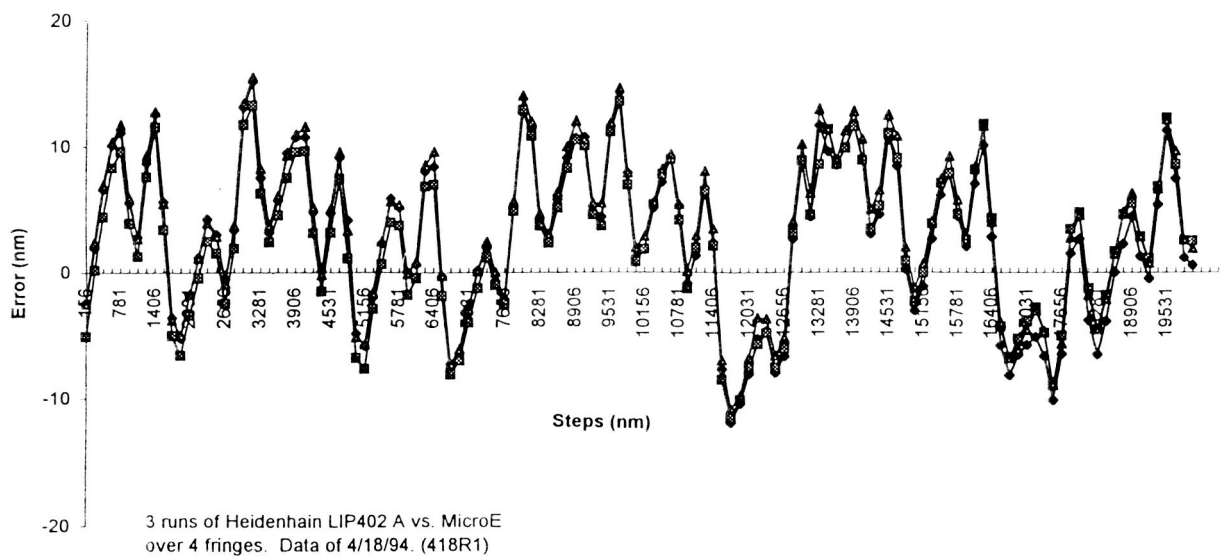

Figure 2. MicroE Encoder Installed in Marshall PSMA

3 runs of Heidenhain LIP402 A vs. MicroE over 4 fringes. Data of 4/18/94. (418R1)

Figure 3. MicroE vs Heidenhain Encoder: Interpolated Error

140

High Performance Stepper Motors for Space Mechanisms

Patrick Sega* and Christine Estevenon*

Abstract

Hybrid stepper motors are very well adapted to high performance space mechanisms. They are very simple to operate and are often used for accurate positioning and for smooth rotations. In order to fulfill these requirements, the motor torque, its harmonic content, and the magnetic parasitic torque have to be properly designed. Only finite element computations can provide enough accuracy to determine the toothed structures' magnetic permeance, whose derivative function leads to the torque. It is then possible to design motors with a maximum torque capability or with the most reduced torque harmonic content (<3% of fundamental). These later motors are dedicated to applications where a microstep or a synchronous mode is selected for minimal dynamic disturbances. In every case, the capability to convert electrical power into torque is much higher than on DC brushless motors.

Hybrid stepper motors operation in space mechanisms

Hybrid stepper motors are brushless synchronous motors usually dedicated to open-loop applications. They naturally generate controlled movements in position and speed. The usual applications are mainly for deployment, orientation, accurate pointing or positioning mechanisms (e.g., solar panels, antennas, optical devices). They are also an answer to classic motorization problems, as at average speeds (a few hundred rpm) there is no need for an angular or speed sensor, or a complex electronic driver. These motors can either be used in direct drive mechanisms or associated with a gearbox.

Their specific characteristics are required in numerous high performances space mechanisms :
- High incremental resolution (i.e., 0.3° full step) enhanced by microstep command possibilities.
- Very high torque capability per power unit (Motor Constant in $N \bullet m/\sqrt{W}$) and per mass unit (I_m in $N \bullet m/\sqrt{W}/kg$).
- High angular stiffness thanks to the natural high number of poles (up to 300).
- Excellent positioning accuracy and stability on steps and microsteps.
- Possibility of open loop continuous rotation at very low speeds (down to 0.001 rpm) and with a good instantaneous stability. The type of command is then "synchronous," with sinusoidal phase currents.

Moreover, special efforts must be done when designing these motors, such as :
- Research for a minimal torque harmonic content for very smooth movements (displacements of large inertia or micro-gravity experiences).
- Minimization of the motor parasitic torques (magnetic friction and detent torque) for improved positioning performances.

---

* SAGEM, Paris, France

Hybrid stepper motors design

Hybrid stepper motors (Fig. 1) produce a torque, which has a general expression of:

$$T = \frac{N_R}{2} \sum_{i=1}^{2p} F_i^2 \frac{\partial P_i}{\partial \theta_e} \qquad (1)$$

Where N_R : Number of rotor teeth.

e : Electrical angle $= N_R \theta_m$.

m : Mechanical angle.

F_i : Magneto Motive Force under pole i.
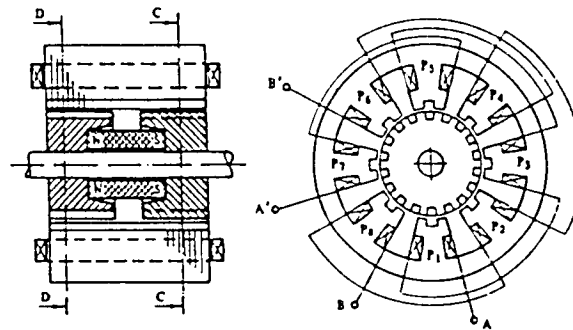
P_i : Air gap permeance under pole i.

Figure 1 - Hybrid stepper motor

$P_i = P(\theta_m)$ is the permeance function. It characterizes the possibility offered to the magnetic field to go through the air gap more or less easily. This is done according to the relative position of the rotor and stator teeth: P_i is maximal for aligned teeth, minimal for misaligned teeth.

$P(\theta_m)$ is of period $\frac{2\pi}{N_R}$ and can be written as a Fourier series. The relation (1) sets the tight link between the torque and its harmonic content and the permeance harmonics $(P_0, P_1, P_2,...)$.

This approach has been synthesized from the equivalent circuit diagram of a standard two-phase motor [1]. Simple analytical relations have been established between torque and permeance harmonics for a One-Phase-On mode. The same calculations for the synchronous mode $\left(F_i = F_0 \sin\left(\omega t - \frac{i\pi}{2}\right)\right)$ give a similar expression:

$$T = N_R \left[\begin{array}{l} -2\dfrac{F_0 \varnothing_m P_1}{P_D} \sin(\theta_e - \omega t) + F_0^2\left(\dfrac{2P_1^2}{P_D} - P_2\right)\sin(2(\theta_e - \omega t)) - F_0^2 P_2 \sin(2(\theta_e + \omega t)) \\[2mm] -6\dfrac{F_0 \varnothing_m P_3}{P_D} \sin(3\theta_e + \omega t) - 4P_4\left(F_0^2 + \dfrac{2\varnothing_m^2}{P_D^2}\right)\sin(4\theta_e) - 10\dfrac{F_0 \varnothing_m P_5}{P_D}\sin(5\theta_e - \omega t) \end{array} \right]$$
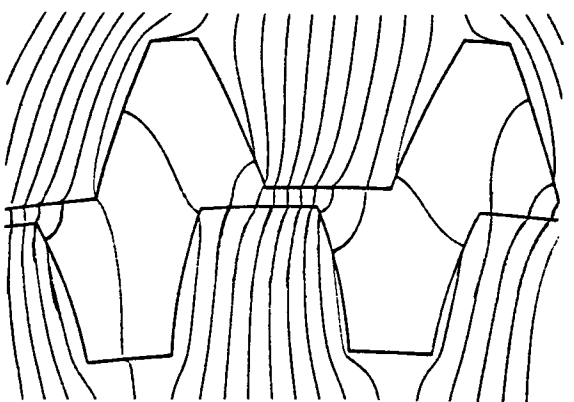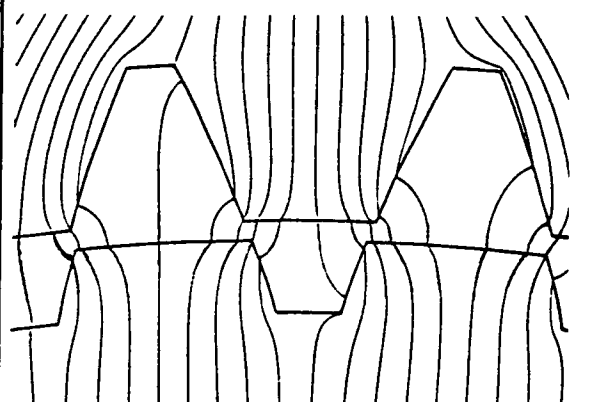
with: $\varnothing_m$: Magnet magnetic flux.
          P_D : $4P_o + P_m + P_r$
          P_m : Magnet permeance.
          P_r : Rotor leakage permeance.

The maximal motor torque implies a maximal ratio $\dfrac{P_1}{P_D}$. This ratio depends on the teeth geometry (P_o, P_1), on the magnet geometry (P_m), and on the rotor magnetic leakage (P_r). The torque harmonics are defined by the harmonic content of the air gap permeance. This one is completely defined by the teeth geometry, the teeth sizes compared to the air gap, and by the teeth magnetic saturation level.

Air gap permeance calculations

Simple analytical models have been proposed for the air gap permeance calculations [2]. Even though they can be improved mainly by taking into account the natural difference between rotor and stator tooth pitches, they are not accurate enough; the fundamental harmonic accuracy is not better than ±10% and the harmonic content they generate has nothing to do with the actual values.

Only finite element computations can give accurate values for $P(\theta_m)$, and will do so even if the teeth are highly saturated [3]. The toothed structures geometry optimization

Toothed structure A : High torque $N_R = 50$ - Airgap = 0.12 mm	Toothed structure B : Low torque harmonic content $N_R = 50$ - Airgap = 0.15 mm
$P_o = 4.241$ $P_1 = 0.839 = 100\ \%$ $P_2 = 0.008 = 1.0\ \%$ $P_3 = 0.021 = 2.5\ \%$ $P_4 = 0.000 = 0.0\ \%$ $P_5 = 0.000 = 0.0\ \%$	$P_o = 4.978$ $P_1 = 0.620 = 100\ \%$ $P_2 = 0.004 = 0.6\ \%$ $P_3 = 0.002 = 0.3\ \%$ $P_4 = 0.000 = 0.0\ \%$ $P_5 = 0.000 = 0.0\ \%$

is then possible according to different design purposes. (See the table with air gap permeances in 10^{-5} H/m. The stator is the same in the two cases.)

Parasitic torque

The parasitic torque is defined as the torque required to rotate the unpowered motor at low speed. This characteristic can be important when two motors are integrated on the same axis for total redundancy. This parasitic torque includes :

- The very well-known detent torque, written according to [1] or relation (2) with F_o = 0:

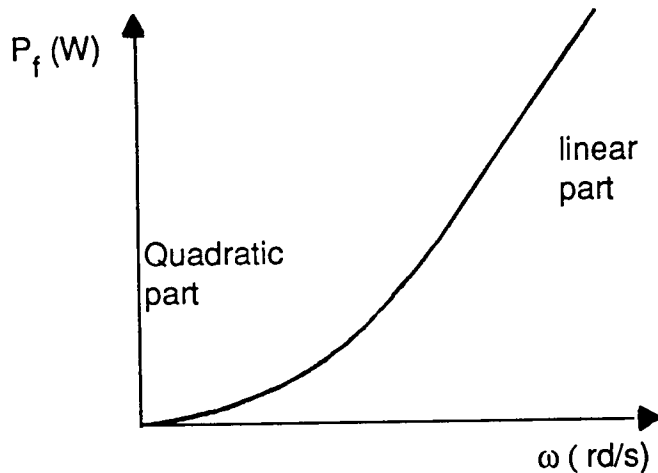$$T_d = -8P_4 \frac{\varnothing_m^2}{P_D^2} \sin(4\theta_e)$$

This fourth harmonic torque depends on the fourth harmonic permeance (P_4) and on the square value of the permanent magnet magnetic flux ($\varnothing_m^2$). These two parameters are defined when designing the motor.

- A torque related to the hysteresis phenomena inside the magnetic circuit which includes two components:

- • A "dry friction" component, $T_f = -\text{Sign}(\dot{\theta}) \cdot T_f$, which does not depend on the rotor angular position.
- • A component coming from the magnetic remanence effects in the toothed structures, especially when they are highly saturated, given as:
  $T_p = -T_p \sin(\theta_e + \gamma)$. γ is a phase shift with the torque created just before the currents have been switched off. T_p and γ depend on the "magnetic history" of the motor magnetic circuit which is linked to:
  - The magnetic materials characteristics (B(H) cycles, permanent magnet type).
  - The phase current relation versus time.
  - The rotor dynamic position $(\theta, \dot{\theta})$.

Modelling and evaluation of T_f and T_p are quite difficult to establish [4]. Materials with thin B(H) cycles and low levels of magnetic induction will contribute to lower their amplitudes. They will also lower the torque capabilities per mass unit.

Finally, at higher rotation speeds, the well-known iron losses have to be taken into account. Their experimental shape is the following:

Figure: Graph with P_f (W) on vertical axis and ω (rd/s) on horizontal axis, showing a "Quadratic part" and "linear part".

Results

SAGEM has designed a complete range of stepper motors for various space mechanisms. Their holding torques are from 0.2 N•m up to 6.0 N•m for an electrical power between 2 W and 10 W. The numbers of steps are the standard 200 steps/revolution and also 360 and 1200 steps/revolution for high-resolution applications. The SAGEM stepper motors are generally proposed in a frameless configuration for an optimized mechanical integration inside the mechanisms. An annular shape is offered for large outside diameter motors. Magnetic and mechanical modular designs have been selected. It's now possible to create new motors, with different lengths, from a basic magnetic structure. Housed configurations with bearings are also available, as well as redundant windings.

The most important electromechanical performances are presented in Figure 2. They have been measured on motors designed for:
- High torque (Application A)
- Low torque or speed harmonic content (Application B).

The first motors (A) have:
- A very high capability to convert the electrical power into static torque per mass unit: I_m can reach 0.6 to 0.8 $N•m/\sqrt{W}/kg$. It is between 3 and 6 times higher than the best DC brushless motors characteristics.
- A positioning accuracy better than 3% of the step angle (Peak to Peak) in the following conditions: step to step mode, no load conditions, back and forth rotation. Positioning repeatability and stability are one order of magnitude lower, around 0.5% of the step angle under similar dynamic approach conditions.

The second motors (B) offer:
- Lower torque capability per mass unit (-15% to -20% for I_m).
- A very low torque harmonic content (<3% of the fundamental), roughly without 3rd and 4th harmonics (<1% each).
- A low speed harmonic content in synchronous mode (<15% of the nominal constant speed). The fourth speed harmonic is the most important one (between 5% and 8%). It can be canceled by adding a third harmonic component in the phase currents according to well-known techniques.

Acknowledgments

References

1. Kuo, B. C. Torque components of hybrid PM step motors - Incremental Motion Control Systems and Devices. 1984.
2. Kuo, B. C. Permeance models and their applications to step motor design - Incremental Motion Control Systems and Devices. 1986.
3. Huard, S. R. and C. K. Taft. A finite element lumped parameter model for 1.8° stepping motors - Incremental Motion Control Systems and Devices. 1990.
4. Jufer, M. Hysteresis effect on the hybrid step motor statical and dynamical behaviour - Incremental Motion Control Systems and Devices. 1989.

Figure 2. Performance of some SAGEM Stepper Motors

	References						
	21PP61	23PP43	23PP63	35PP81	57PP41	57PP81	57PP82
Number of steps/rev. (step angle)	200 (1.8°)	200 (1.8°)	200 (1.8°)	360 (1°)	1200 (0.3°)	1200 (0.3°)	1200 (0.3°)
Basic application	A	B	A	A	B	A	A
Outside Diameter (mm) * Inside Diameter (mm) * Length (mm) * Total mass (g) *	53 10 22 180	59 10 40 525	59 10 40 525	88 55 25 320	155 94 30 1400	155 94 30 1400	155 94 44 2400
Holding torque (Nm) ** Power (W) Angular stiffness (Nm/rd)	0.16 2.0 8	0.34 1.4 17	0.40 1.4 20	0.60 5.2 54	2.4 8.2 720	3.0 8.2 900	5.5 10.0 1650
Total parasitic torque (Nm) Detent torque (Nm) Sum of the first ten torque harmonics (% of fundamental)	< 0.012 < 0.004	< 0.015 < 0.003 < 3 %	< 0.030 < 0.010	< 0.040 < 0.015	< 0.060 <0.005 < 3 %	< 0.10 < 0.01	< 0.20 < 0.01

Electromechanical ratios :
    Nm / kg
    Nm / √W
    Nm / √W / kg
	0.84
	 0.11
	 0.63
		0.63
		 0.29
		 0.55
			0.93
			 0.34
			 0.64
				1.87
				 0.26
				 0.82
					1.75
					 0.84
					 0.60
						2.15
						 1.05
						 0.75
							2.30
							 1.74
							 0.72

Open loop performances : No load positioning accuracy (deg. max. Peak to Peak) Low synchronous speed (rpm) Sum of the first ten speed harmonics (% of fundamental)	0.05°	0,01 to 1 < 15 %	0.03°	0.03°	0,001 to 1 < 15 %	0.02°	0.01°

*   In frameless configuration
**   Without magnetic saturation effects

1995-120852 405737

5p.

Development of a Miniature Actuator/Controller System

Scott P. Stanley[*]

Abstract

Development of new products is often hampered or prevented by the cost and resource commitments required by a traditional engineering approach. Schaeffer Magnetics, Inc. identified the potential need for a miniature incremental actuator with an integrated controller but did not want the development to be subject to the obstacles inherent in the traditional approach. In response a new approach - the Pathfinder Engineering Program (PEP) - was developed to streamline new product generation and improve product quality. The actuator/controller system resulting from implementation of this new procedure is an exceptionally compact and self-contained device with many applications.
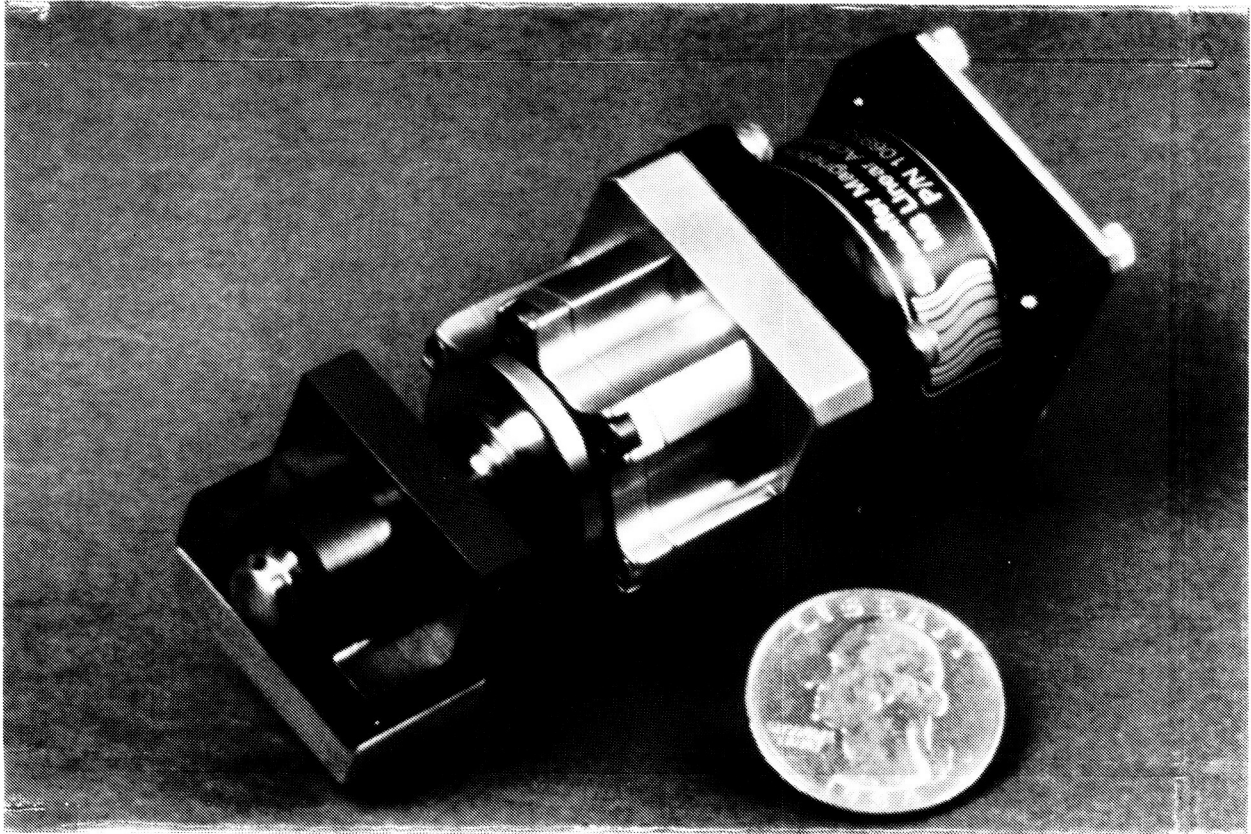

Figure 1.   Schaeffer Miniature Incremental Actuator

[*] Schaeffer Magnetics, Inc., Chatsworth, CA

Introduction

Schaeffer Magnetics, Inc. has for many years produced a line of rotary incremental actuators coupling small angle stepper motors with harmonic drive speed reducers in a coaxial arrangement. Controllers for the actuators have also been a staple Schaeffer product. Recently, a potential need was identified for miniature rotary and linear actuators with minimal control requirements. However, the application base was fairly narrow and did not necessarily warrant the cost of a traditional development program. In response, a new development scheme was utilized in an effort to achieve technical advance at minimum cost, yielding a substantially higher return on internal funding than with the traditional "mainstream" approach. The result of this effort, shown in Figure 1, was a small Schaeffer stepper motor coupled with a miniature size M8 harmonic drive from Harmonic Drive Systems, Inc., to produce a tiny 67.3 mm (2.65 in) long by 28.58 mm (1.125 in) square rotary incremental actuator. A self-contained electronics package was then developed complementing the compact size and low weight of the actuator.

Development Process Description

The challenge was to develop hardware faster, at less cost, with equal or improved quality. Due to the lack of a contracted development program and the need to optimally utilize internal funds, the traditional serial approach of design, analyze, review, fabricate, assemble, test, then iterate was rejected. Instead, a more informal yet still controlled development process - the PEP process - was developed and utilized which allowed early validation of designs with minimum cost. Conceptual drawings were generated with just enough detail to fabricate parts, then redlined as required for real-time improvements or corrections. Key members of the development team including both engineering and operations personnel were allowed to make changes which would enhance the performance or producibility of the unit, resulting in a design acceptable to all departments while minimizing bureaucratic delays and expenses. Only a single copy of each drawing was produced to maintain control of all redlined changes. This ease of modification enabled the initial fabricated design to be mature since inputs from all contributing departments were incorporated in a very rapid, inexpensive manner.

For the electronics, the engineer was provided only general goals of small size and ease of control. With inputs from other members of the PEP team, a compact workable design was breadboarded in just a few days.

Since hardware is available very early in the program, the PEP process allows validation of fabrication, assembly, and test techniques at the early stages of a program rather than at the end when little schedule (and perhaps budget) is available. The cycle of design/analyze/redesign/reanalyze is short-circuited, leading to economy and short fused deliveries. Redlines are incorporated after testing and data review with the assurance that the drawing revisions will be the last required and not just one iteration in a long series.

Actuator Description

The miniature actuator is a logical extension of the Schaeffer Magnetics rotary incremental actuator product line, but utilizes the miniature M8 harmonic drive in combination with a two-phase 90° stepper motor. A single cylindrical samarium-cobalt magnet is used and the rotor inertia is only 2.0 g·cm². The motor can be operated at any step rate between 0 and 80 steps per second. The rotor is supported on each end by annular contact ball bearings and drives the wave generator input of the harmonic drive via an Oldham coupling. The harmonic drive speed reducer is used because of its high ratio in a small package, torsional stiffness, accuracy, and lack of backlash. The 50:1 harmonic drive gear ratio results in an output step size of 1.8°. The M8 miniature harmonic drive is only 20.5 mm (0.807 in) long and the flexspline outside diameter only 20 mm (0.787 in). The motor stator is bonded in a 6061 aluminum housing to improve heat transfer. The output housing is fabricated from titanium 6Al-4V with 440C stainless steel output bearings for stiffness and load capacity. The bearings in the prototypes are wet lubricated, the specific lubricant selection being dependent on temperature range and load/life requirements. The unit is sealed against debris contamination and vented to outside pressure via labyrinth seals. The actuator is exceptionally light, weighing less than 0.23 kg (0.5 lbm). Since the actuator uses design, fabrication, and assembly practices borrowed or adapted from the Schaeffer heritage actuators, the M8 actuator system is fully flight capable with approved materials and processes. Figure 2 shows the dimensions of the actuator in mm (in).
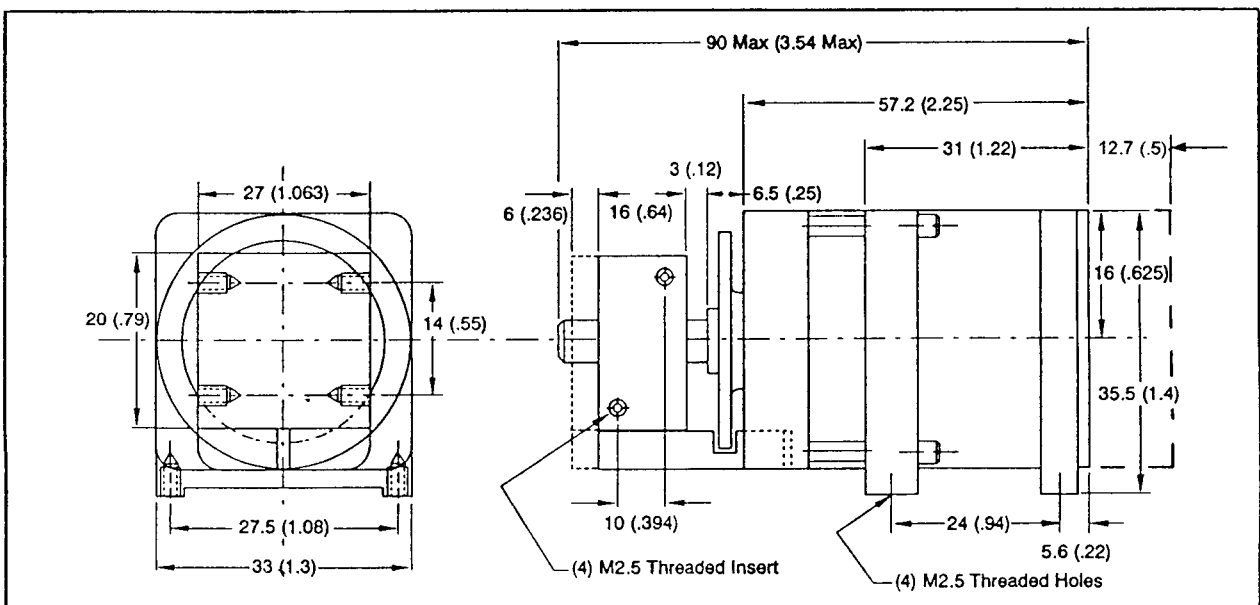

Figure 2. Miniature Type M8 Linear Actuator

Two prototypes have been developed, one rotary and one linear. The rotary actuator is capable of delivering 0.45 N·m (4 in·lb) of torque with a 12 volt input at a maximum output speed of 2.513 rad/s (24 rpm). The linear model of the actuator is identical to the rotary but is equipped with a lead screw and nut on the output resulting in high linear

149

force for the package size and fine resolution. The prototype has an output step of 0.010 mm (0.0004 in) with a total stroke of 35.1 mm (1.38 in), with other step sizes and strokes easily accommodated. Maximum speed is 0.30 mm (0.012 in) per second. Output force is a substantial 111 N (25 lbf). Non-jamming stops have been included so that the actuator can be driven through the full range of motion without damage.

Electronics Description

The miniature and self-contained electronic control unit mounts to the back or side of the actuator, following the unit contour with an envelope of 28.6 mm (1.125 in) square by 12.7 mm (0.500 in) deep. The module has been developed to adhere to strict high-reliability spaceflight standards with regards to design, manufacture, and test. All components are Grade 1 per MIL-STD-975 with one exception covered by a source control drawing. With simplicity of design and operation an important goal, the device requires only power and a direction command.

The electronics can be configured for two or three-wire operation. In the two-wire configuration, reversing the power polarity to the leads reverses the actuator motion in a manner similar to a DC brush motor but the unit operates at a pre-selected fixed rate. This arrangement also simplifies the driver since the controller only requires on/off power switching and not a linear drive circuit. In the three-wire configuration, the easiest to control, two leads are for power while the third controls direction. The prototype unit is configured for 13 volts maximum input which results in approximately an 11 volt output to the actuator. Total power dissipation is approximately 4 watts at 12 volts nominal input. Due to the power steering diodes and their associated voltage drops, the two-wire configuration is slightly less efficient than the three-wire system. The electronics can be easily modified to accommodate far higher input voltages depending on the required performance of the actuator. An optoisolator can also be ·incorporated to isolate direction command power return from actuator power with the addition of a fourth wire.

An internal regulator provides 5 volt power for the logic circuits enabling operation from a single voltage source. The unregulated bus voltage goes directly to the drive circuits. The unit can also operate directly from batteries which offers intriguing advantages for remote applications, including minimal power and control requirements and excellent EMI resistance. The linear regulator circuit offers high reliability without EMI generation or custom magnetics, and comparable power consumption to other types of converters.

An oscillator circuit generates the step rate. The rate can also be externally provided at the cost of additional control complexity. The design incorporates a precision timer integrated circuit and a temperature compensated capacitor to limit temperature and end of life rate variation. A crystal oscillator can be easily incorporated for enhanced step rate accuracy.

The motor state sequence generator converts the step and direction inputs into a sequential series of four repeating states required by the two-phase motor. A change in direction command reverses the sequence to the motor. The system always powers

up in a legal state and if a transient condition is encountered the unit would immediately recover to a legal state after conclusion of the event.

Level shifting and bipolar switching are functions performed by the motor drive circuits which receive the low voltage, low current motor phase commands from the state sequence generator and amplify the voltage and current to the levels necessary to drive the motor. The output section is a two-phase, four-leg, H-bridge inverter which drives the two motor windings in bipolar mode. Two diodes are provided across each leg of the inverter to suppress the back electromotive force generated by switching current to an inductive load.

Applications and Optional Configurations

Since the actuator/controller system can be controlled with respect to direction, position, and speed, there are numerous potential applications in either its linear or rotary form. The design was originally conceived as a cage mechanism or pin puller for deployment mechanisms offering controlled reversible motion and synchronous operation of multiple actuators, replacing one-shot pyrotechnic devices or other slow reacting linear motors. Due to its small size, the unit can also be utilized in focusing applications within cameras or other optical instruments. Other possibilities include use as door openers or small antenna pointing mechanisms.

For a biaxial configuration, the actuator housing is designed to bolt directly to the output flange of another actuator without an intermediate bracket for maximum weight savings. The design easily adapts to incorporate position feedback devices, including encoders, potentiometers, and resolvers. The stepper motor winding can be modified to match system power parameters and redundant motors can also be provided. A brushless DC motor can also be easily substituted for the stepper.

Conclusion

Improvements can and have been made in the traditional serial approach of engineering development programs. Using the Pathfinder Engineering Program (PEP) enabled Schaeffer Magnetics to develop a new product - a miniature incremental actuator/controller system with a promising market niche - at an investment of resources significantly less than typically associated with new product development.

Acknowledgments

Martin Lochte, Electronics Design
Ruben Nalbandian, Actuator Mechanical Design

Basic Space Payload Fastener

J. M. Vranish[*] and Stephen Gorevan[**]

Abstract

A new basic space fastener has been developed and tested by the GSFC. The purposes of this fastener are to permit assembly and servicing in space by astronauts and/or robots and to facilitate qualification of payloads on earth prior to launch by saving time and money during the systems integration and component testing and qualification processes. The space fastener is a rework of the basic machine screw such that cross-threading is impossible, it is self-locking and will not work its way out during launch (vibration proof), it will not wear out despite repeated use, it occupies a small foot print which is comparable to its machine screw equivalent, and it provides force and exhibits strength comparable to its machine screw equivalent. Construction is ultra-simple and cost effective and the principle is applicable across the full range of screw sizes ranging from a #10 screw to 2.5 cm (1 in) or more. In this paper, the fastener principles of operation will be discussed along with test results and construction details. The new fastener also has considerable potential in the commercial sector. A few promising applications will be presented.

Introduction

A new basic space fastener has been developed and tested by the GSFC. The purposes of this fastener are to permit assembly and servicing in space by astronauts and/or robots and to facilitate qualification of payloads on earth prior to launch by saving time and money during the systems integration and component testing and qualification processes. This fastener proves that one of the recurring problems prohibiting cost effective servicing and assembly of small structures on orbit can be solved in a reasonably straight forward manner. The fastener problem has long been overlooked and underestimated. To perform servicing on orbit, it was essential that the fastener be resistant to cross-threading; either by astronauts whose hands must be covered by large gloves which are not optimal for fine assembly or by robotic or machine means which, in the current art, are even less so. Also, the fastener must be able to resist the vibrations inherent in launch both from the standpoint of the huge forces and impacts involved and in terms of the natural tendency of all screws to back out during vibrations. At the same time, the device must be nearly as simple, efficient, cost effective and compact as the common machine screw.

The Problem

The two main deficiencies of the classical machine screw are: 1) That it has a propensity to back-out during vibrations and 2) That it is easily cross-threaded by astronauts wearing gloves and even more so by current state-of-the-art robots.

The reason machine screws back out during vibrations is inherent in the basic helix of the screw thread. Experience and tests have repeatedly shown that a screw backs out

---

[*] Electromechanical Branch, NASA Goddard Space Flight Center, Greenbelt, MD
[**] Honeybee Robotics, Inc, New York, NY

because of the shearing, or side to side motion of the two members the screw is joining together. This motion creates a formidable counter torque on the screw helix which tends to back out the screw. Current preload spring washers such as wave spring washers and lock washers actually enhance the problem by maintaining screw helix contact with the nut helix even as the screw backs out.

The reason cross-threading of machine screws is such a problem for astronauts and robots in space is inherent both in terms of the clumsiness of the robots and the gloved astronauts and the fine threads of machine screws. The classical approach has been not to perform servicing. However, in instances where it must be performed, screw threads are made very coarse, so that they cannot be cross-threaded. Because this makes them back out easier under vibrations, a highly frictional set of mating cones is installed at the top of the male screw and the female member it screws into. However, the course thread means that very large torques are required to obtain relatively modest preload forces. The large friction forces associated with the mating cones further reduces the preload forces (or alternately, requires larger input torques). This is especially problematic when one is attempting to unfasten the screw on orbit. These very large holding frictional forces are very unpredictable, and even dangerous, on orbit. Accordingly, they require very large and powerful tools to provide an acceptable margin of safety.

Principles of Operation

The strategy of the new basic space fastener was two pronged [1]. On the one hand, it was decided to prevent cross-threading by leaving the nut attached to the machine thread at all times so as to permit large preload forces with modest preload torques and then to shape the outside of the nut such that it acts as a coarse fastening system whose sole purpose is to join the mating members together. This strategy involved shaping the hole into which the nut was to be inserted in such a way as to perform as part of the coarse fastening system. On the other hand, it was decided to prevent the screw from backing out under vibration by prohibiting relative motion between the screw and the nut. It was further decided to do this by bottoming the outside of the screw thread against the outer wall of the nut thread.

Figure 1 [2] shows pictures of the test hardware which worked following the strategy outlined above. Figure 2 [2] shows line drawings of the same device in a manner that is useful in illustrating how the device works.

To solve the problem of making the thread of the screw bottom against the outer wall of the nut thread, it is necessary to alter the nut thread so that it has flats on its outer thread. This, in turn, is accomplished by machining a few thousands of an inch off the thread die used to form the nut thread. This, however, leaves the screw in an interference fit with the nut. Accordingly, a split is cut in the nut and two thin spring sections are formed in the nut wall. Thus, the nut can expand around the screw and the screw threads can bottom on the outer wall of the nut thread. The nut also acts as a form of lock washer that preloads radially so that the lock washer function does not tend to aid in backing the screw out during launch vibrations.

It is clear from Figures 1 & 2, how the outside of the nut and the inside of the fixture into which the nut fits mutually, act together to form a coarse fastening system that cannot

cross-thread. As the screw, with attached nut, is turned gently in a counterclockwise direction as it is inserted into the hole, the screw and nut drops down into the hole. Once down into the hole, the counterclockwise motion must stop because the nut is stopped by the end of the screw shaft. At this point, the screw is turned clockwise, the nut turns with it and positions itself so as to ensure the interference with the irregularly shaped hole necessary for fastening. The nut then travels upwards to perform the preload and fastening functions. The unfastening process has the reverse sequence of that involved in fastening.

Hardware and Test Results

Test results are summarized below [2]. As can be easily deduced from the data, the tests were highly successful against a very difficult standard, MIL-STD-1312-7A (10/19/84), Method 7. Three evaluations of the concept were developed during a Phase I SBIR performed by Honeybee Robotics, Inc. The third evolution is the definitive one to date. It was a miniaturized version, based on a #10 machine screw. The test breadboard was preloaded with values of 6.8 N•m (5 ft•lbf), 20.3 N•m (15 ft•lbf) and 47.5 N•m (35 ft•lbf). In each case the system was subjected to vibration in accordance with the above mentioned MIL-STD and in each case it passed the entire test with no measurable loss of preload. In comparison with Spiralock, used in Shuttle Engines for vibration resistance, the Basic Payload Fastener is equally vibration resistant; but will undoubtedly prove to produce a significantly larger preload force for the same input torque with much less radial loading and wear. This is because the Basic Space Fastener loads only lightly on its outer screw diameter and more heavily on its upper screw surface (in the classic machine screw manner), where as, the Spiralock [3] loads heavily on its outer screw diameter. Also, Spiralock is vulnerable to cross-threading so is not a serious candidate for on orbit servicing by astronauts or robots.

The Ramifications of The Solution - NASA and Industrial

This fastener has the potential to become the standard space fastener for nearly all NASA's space operations. The device is essentially immune to vibrations, is resistant to wear and so can be reused many times without degradation of performance, and provides a strong preload force for a modest input torque. It can self-align and fasten despite significant initial errors in alignment, without cross-threading. Therefore it is suitable for use by robots or astronauts for on orbit replacement missions. The commercial potential is enormous. There are many examples such as aircraft component fasteners, engine mounting bolts, bolts in motorcycles, automobiles, military tanks, tracked and wheeled vehicles, and lug nuts on automobile wheels. Any application involving screws and nuts can be performed using this system.

Development Plans

Development plans center mainly on simplifying the device, for remaking and testing it using the materials and conditions that it must employ in order to be used in the earth orbit/space environment and making it more cost effective for NASA needs. In addition to this, the optimum geometry will be revisited, and robotic operations will be taken into consideration. This will involve considerably more detailed and extensive analysis and testing and modifications than performed thus far. Also, the enormous potential and requirements of industry will be kept in mind.

Summary/Conclusions

A promising and innovative general usage space fastener has been proven in concept to the very difficult standard of MIL-STD-1312-7A (10/19/84), Method 7. This fastener has the potential to become the standard space fastener for nearly all NASA space operations. The device is essentially immune to vibrations, is resistant to wear and so can be reused many times without degradation of performance, and provides a strong preload force for a modest input torque. It can self-align and fasten despite significant initial errors in alignment without cross-threading, thus being suitable for use by robots or astronauts. The commercial potential is enormous. There are many examples such as aircraft component fasteners engine mounting bolts, bolts in motorcycles, automobiles, military tanks, tracked and wheeled vehicles, and lug nuts on automobile wheels. Any application involving screws and nuts can be performed using this system. Future work will concentrate on more extensive and thorough testing, analysis and development to simplify and make this device even more cost effective and useful.

References

1. Vranish, John M., Invention Disclosure, *Basic Space Payload Fastener*, submitted to GSFC patent office 1/20/95.

2. NASA SBIR Phase I Final Report, Contract # NAS5-38022 *"A Vibration Resistant Telerobotic/EVA Astronaut Compatible Fastener For Small/Medium Sized Payloads"*, June 10, 1994, Honeybee Robotics, Corp.

3. Advertising Brochure, Courtesy of *Spiralock,* Detroit Tool Industries, Madison Tech Center, 25219 Dequindre Road, Madison Hgts., MI 48071-0629.
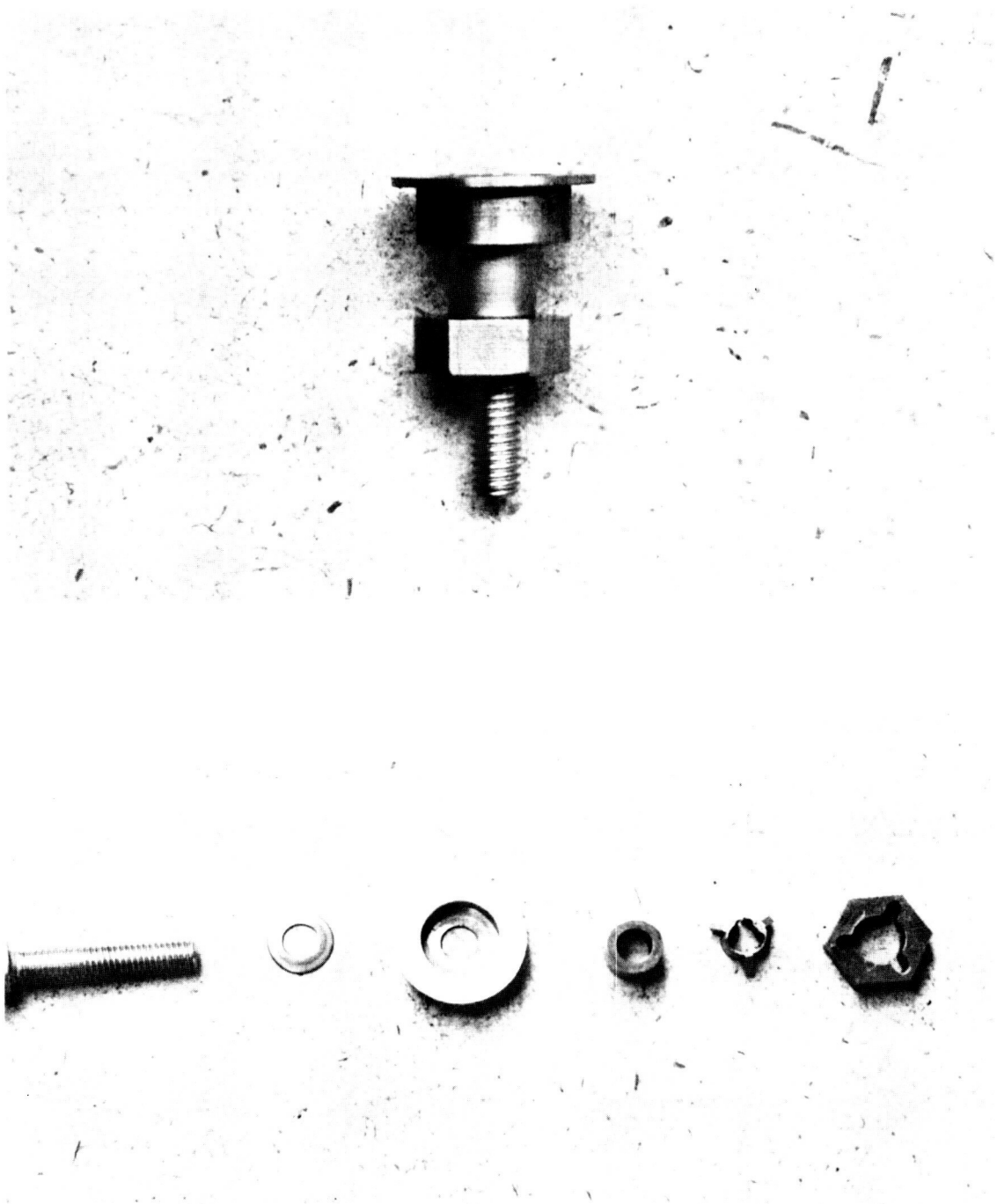
Figure 1

Phase 1 #10 fastener. Top, assembled system, and below,
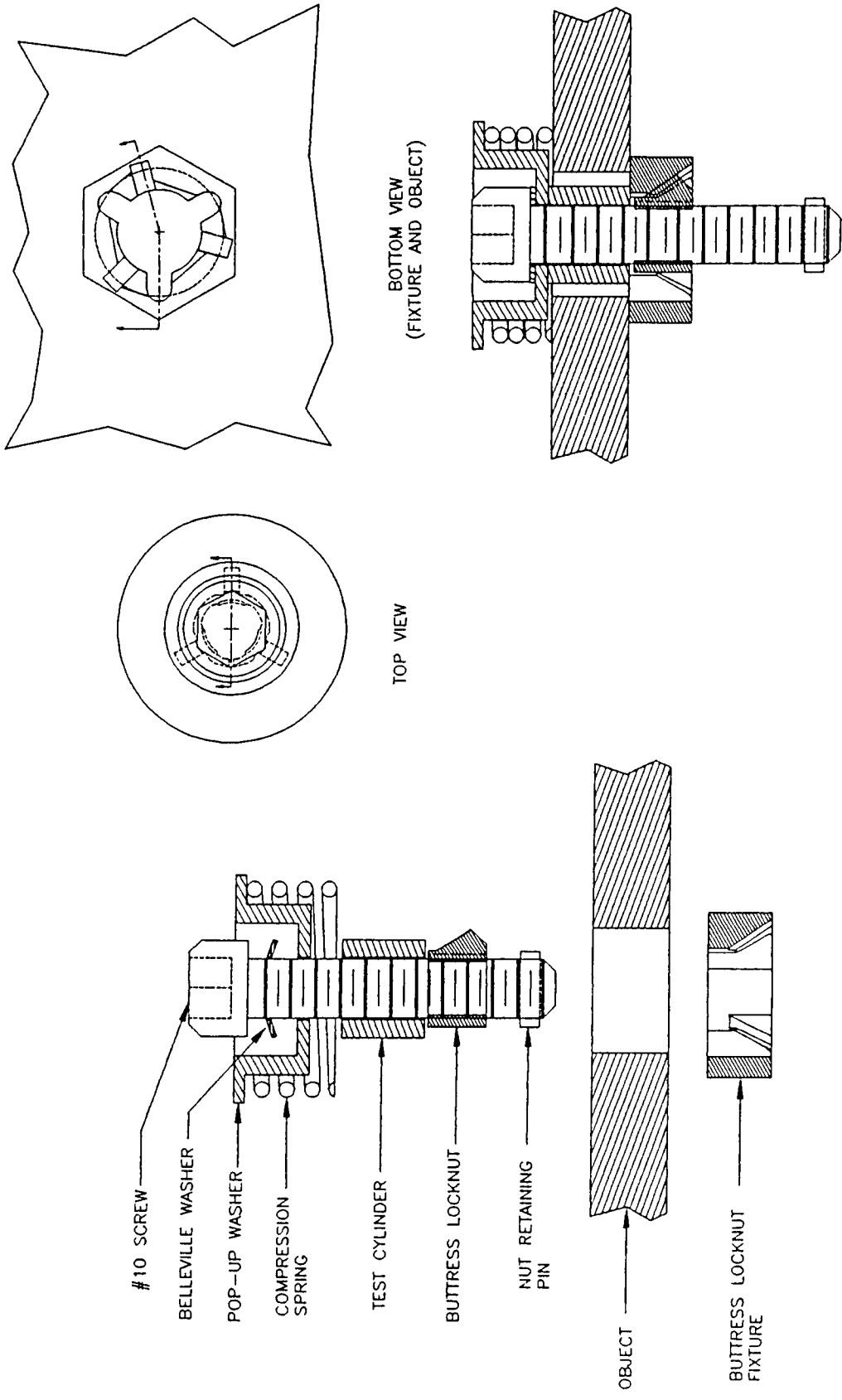system elements. The split buttress locknut is second from right.

BOTTOM VIEW
(FIXTURE AND OBJECT)

PRELOADED AND COUPLED SYSTEM

TOP VIEW

#10 SCREW

BELLEVILLE WASHER

POP-UP WASHER

COMPRESSION
SPRING

TEST CYLINDER

BUTTRESS LOCKNUT

NUT RETAINING
PIN

OBJECT

BUTTRESS LOCKNUT
FIXTURE

FIGURE 2: EVA/ROBOTIC COMPATIBLE PAYLOAD FASTENER
BREADBOARD 3 TEST CONFIGURATION.

157

Non-explosive Actuation for the ORBCOMM™ Satellite

Anthony Robinson*, Craig Courtney**, and Tom Moran**

Abstract

Spool-based non-explosive actuator (NEA) devices are used for three important holddown and release functions during the establishment of the ORBCOMM™ constellation. Non-explosive separation nuts are used to restrain and release the 26 individual satellites into low earth orbit. Cable release mechanisms based on the same technology are used to release the solar arrays and antenna boom.

Introduction

Non-explosive actuators are electro-mechanical devices that use miniature wire-wrapped spools to hold and release applied loads. The spools are made of two matched halves which are held together by the circumferential wire wrap. A mechanical advantage system allows the spool to restrain external loading on the actuator. When release is required, a low voltage and a current of 4.5 amperes is applied across a link wire on the spool. This signal causes the link wire to break and release the wire wrapping on the spools. The spools separate and the mechanical system releases the external loading on the actuator. NEA technology has been used in numerous launch and satellite programs to pull pins, push pins, and release tension loads.

Satellite Holddown And Release

The first ORBCOMM™ production launch is scheduled for early 1995. An air-launched Pegasus launch vehicle will carry two disc-shaped satellites that are stacked together within the Pegasus fairing. Three subsequent launches, scheduled for 1996, will carry payloads with eight stacked satellites.

Each satellite in the stack of eight is attached to the adjacent satellites or, in the case of the bottom satellite, to the Pegasus launch vehicle. The separable joint (Figure 1) between the satellites is established by three load bearing bracket assemblies spaced at 120° from each other and mounted on hard points on adjacent satellites. The load-bearing brackets are fabricated from aluminum-beryllium alloy (AlBeMet™) and the perimeter walls of the satellite ring are fabricated using AlBeMet™ face skins over an aluminum honeycomb core. The bracket flanges house a pair of shear fittings, compression springs, and a Model 9421-2 non-explosive separation nut.

The shear fittings (cups and cones) are match bonded during production so the satellites are perfectly mated when stacked together for launch. The satellite joint is secured by using a bolt and the Model 9421-2 separation nut to preload the cups and cones together. Lateral axial launch loads are reacted by this cup and cone

---

* Orbital Sciences Corporation, Dulles, VA
** G&H Technology, Inc., Camarillo, CA

arrangement. The cup and cone fittings are machined from titanium and have a hard coat of electroless nickel to prevent surface galling.

The satellite stack is required to have a minimum natural frequency of 20 Hz. The brackets on the satellite rings produce three stiff columns when bolted together and the most recent tests have shown a stack frequency of 21 Hz. A tension preload on the bolts and separation nuts and the match mating of the cup and cone interfaces prevents gapping. As the bolt head can experience a prying load, a larger 9.52 cm (0.375 inch) bolt is used to react these moment loads. The bolt shank is turned down with a 6.35 mm (0.25 inch) thread diameter to mate with the separation nut. The bolt also has an anti-galling coating.

The bottom satellite in the stack carries the maximum load. This load is induced following the release of the Pegasus during launch from a L-1011 aircraft and the subsequent release of the vehicle strain energy. The maximum bending load seen at this interface is 15,591 newton-meters (138,000 inch-pounds). Qualification testing on the structure produced 20,336 newton-meters (180,000 inch-pounds) at the joint and resulted in an axial load of 22,240 newtons (5,000 pounds) in the separation nut and bolt. The separation nut was also destructively tested by application of an axial load of 31,360 newtons (7,000 pounds).

During flight, the payload fairing is removed and the satellites are individually placed into orbit. An electrical command causes the separation nuts to actuate and release the attaching bolt without causing shock of sensitive payload boxes. The three NEA separation nuts on a satellite-to-satellite joint must fire simultaneously to prevent excessive tip-off rates. Each nut must actuate and release within 5 milliseconds of those adjacent to it. The bridge wire characteristics of the separation nuts ensures a minimum dwell time and a tip-off rate well within the design limit of 0.0087 radian/second (0.5 degree/second). The released bolt is contained within a bolt catcher that is integral to the cup portion of each satellite's top brackets

Small calibrated compression springs within the cups are used to push the satellite away after release. The spring preload is adjusted by a compressive nut and the imparted energy provides the correct orbital spacing.

Each ORBCOMM™ satellite has a mass of 42.75 kilograms (95 pounds). The satellite-to-satellite bracket joint assemblies contribute a mass of approximately 2.16 kilograms (4.8 pounds). This is considerably less than the estimated 4.5 to 5.4 kilograms (10 to 12 pounds) that would have been required by clamps and other frangible joints. For a stack of eight satellites, the ORBCOMM™ design results in a mass savings of approximately 18 kilograms (40 pounds).

This satellite holddown and release system has been thoroughly tested to verify its flight readiness. The joints survived all testing and measurements of the source shock from the separation nuts were well within limits.

Solar Array Holddown And Release

After a disc-shaped ORBCOMM™ satellite achieves orbit, another non-explosive actuator is used to open its twin solar panel arrays. The solar panels are hinged to the satellite structural rings and, when stowed, form the top and bottom exterior surfaces of the satellite. During flight and orbital positioning, a Model 8036-100 dual cable release mechanism (Figure 2) restrains two cables that are fastened to the center of the arrays with an adjustable nut. The mechanism uses a NEA spool assembly to restrain and release the ball ends of the cables. The Model 8036-100, which is rated for tension loads up to 445 newtons (100 pounds) from both cables, places an 89 newton (20 pound) preload on the panel, causing a concave deformation of its surface. A cup and cone arrangement, similar to that used on the satellite separation joints, is used with the NEA release mechanism to absorb shear loading. The cable tension prevents gapping between the satellite and the solar array panel. Adjustable axial snubbers are bonded to the backside of the solar panel at four hard points and urethane edge snubbers are used to prevent the edges of adjacent panels from touching while in flight. This system is designed for a first mode static frequency of greater than 30 Hz.

When the Model 8036-100 mechanism receives a command signal, the spool mechanism is actuated and releases the cable ends. Total release time for the mechanism is less than 20 milliseconds and actuation occurs with minimal imparted shock. The solar panels are manufactured from a 6.35 mm (0.25 inch) thick aluminum honeycomb core and 0.127 mm (0.005 inch) graphite epoxy face skins. When preloaded, this panel deforms to a slightly concave shape. When the NEA is actuated, the panel springs open to supply the kick-off force needed to initiate deployment. Small shear-viscous-damped hinges powered by torsion springs deploy the panels to their final position.

Antenna Holddown And Release

The ORBCOMM™ antenna is comprised of a four-segment, deployable boom assembly onto which an array of VHF and UHF quadrifilar helical antennae are mounted. The antenna elements are fabricated from S-glass mesh enabling it to be stowed into a very tight volume. The stowed antenna (Figure 2) is held in the spacecraft until the outboard solar panel is released. Upon release, the antenna bundle is deployed 180 degrees away from the vehicle using a constant force, negator-driven hinge assembly which is shear-viscous-damped to minimize end of travel impact loads. A Model 8036-200 NEA single cable release mechanism holds the antenna bundle together by fastening the fourth boom segment to the first boom segment with a preload of 89 newtons (20 pounds). When a command is received, the NEA spool actuates and the mechanism releases the cable. This frees the bundle and the flexible springs on each boom deploy the segments. The release occurs with minimal imparted shock.

Summary

Non-explosive actuators are used to holddown individual ORBCOMM™ satellites and release them into orbit, to holddown and deploy the solar panel arrays, and to restrain and deploy the antenna. Extensive testing demonstrated that they will reliably holddown

the required loads and simultaneously release them with low transmitted shock and no debris or pollution. The resulting designs resulted in an overall mass savings over comparable methods of holddown and release.
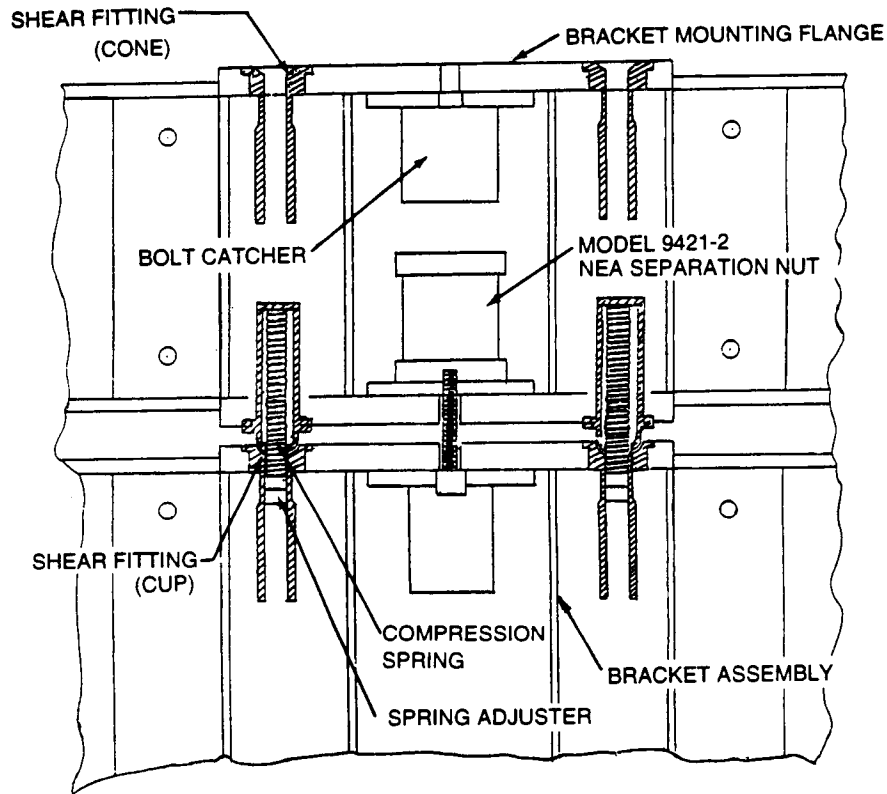

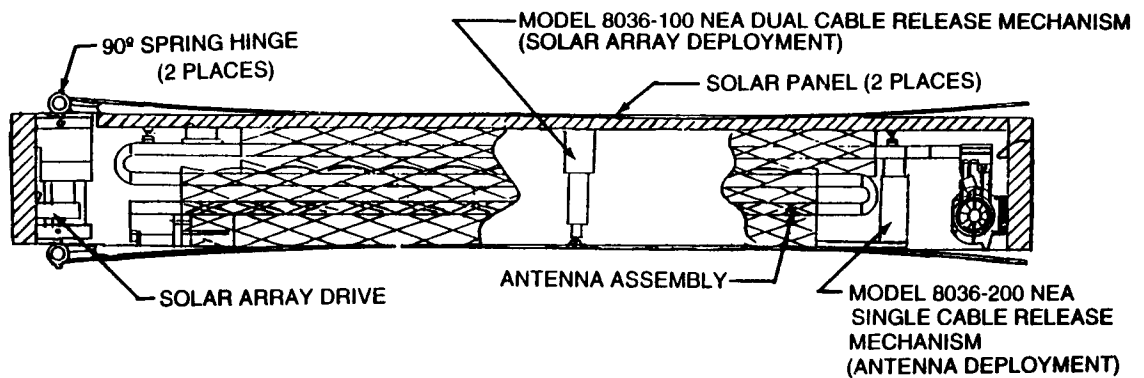FIGURE 1   - ORBCOMM™ SATELLITE-TO-SATELLITE JOINT

FIGURE 2   - SIDE VIEW SECTIONAL - ORBCOMM™ SATELLITE

Development of a High Force Thermal Latch

William D. Nygren*

Abstract

This paper describes the preliminary development of a high force thermal latch (HFTL). The HFTL has one moving part which is restrained in the latched position by a low melting temperature or fusible metal alloy. When heated the fusible alloy flows to a receiving chamber and in so doing at first releases the tension load in the latch bolt and later releases the bolt itself. The HFTL can be used in place of pyrotechnically activated spacecraft release devices in those instances where the elimination of both pyrotechnic shock-loading and rapid strain-energy release take precedence over the near instantaneous release offered by ordnance initiated devices.

Introduction

Many different types of nonpyrotechnic spacecraft release mechanisms have been developed and qualified for flight. However, as Table 1 shows, there are no simple, resetable, 44500N (10,000 lbf) devices which offer slow strain energy release.

Table 1. Low Shock Release Mechanisms

Type	Maximum Force (N)	Slow Strain Energy Release	Resetable Without Disassembly	Complexity
motor driven	6,500	yes	yes	high
frangible link	40,000	no	no	moderate
memory metal	6,700	no	no	low
paraffin	4,450	no	no	low
thermal knife	700	yes	no	low

The use of fusible metal alloys as the working "fluid" for a rotary damper was presented in the 26 Aerospace Mechanisms Symposium. Therefore, the possibility of using a fusible alloy as the working "solid" in a release mechanism seemed somewhat credible and so a simple test was developed to determine the load carrying capability of a candidate fusible alloy as well as any potential difficulties in sealing the molten alloy against leakage.

Figure 1 shows the test setup. A Hollow cylinder of the solid alloy was machined and placed in the space between a double piston and one side of an internal ledge on the surrounding cylinder. The cylinder was threaded at both ends so that its attachment to the holder could be easily reversed after stroking. In this manner the device was easily reset without requiring compressive loading. An eutectic alloy of bismuth and

---

* Martin Marietta Astronautics, Denver, Colorado

tin was chosen for its melting point of 138°C which was well above normal spacecraft qualification test temperatures and yet not so high as to require a great deal of energy to melt. With only thermal conductance under consideration, aluminum was chosen for the cylinder to readily conduct heat to the fusible alloy, and titanium was chosen for the piston to block conductance away from the alloy. The cylinder was wrapped with nichrome heating tape and the whole device was placed in a creep rack which could apply up to a 21300 N (4800 lbf) load.
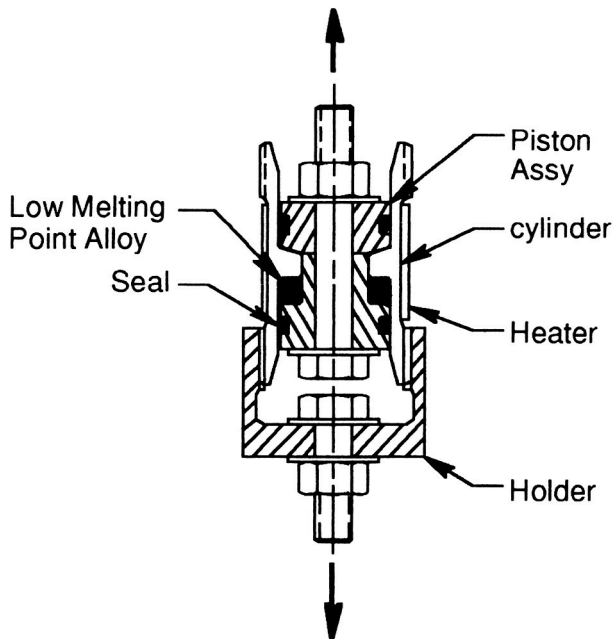
Figure 1. Initial Test Setup   Figure 2. Development Unit
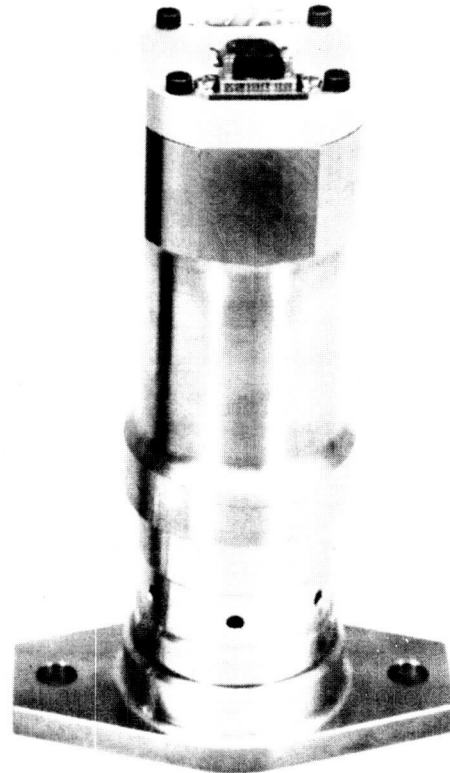
Initial results were promising. The assembly would stroke when heated with only a 20 pound applied force and would apparently hold 21,400 N (78.6 MPa internal pressure) at temperatures up to nearly the 138°C melting temperature of the alloy. The time to stroke was approximately 9 minutes with an input power of 30 Watts. The o-ring seals appeared to work as desired. Next, an elevated temperature (70°C) creep test was initiated which immediately showed that the piston was moving 50 microns (.002 inch) per day. Upon disassembly extrusion of the alloy in the 64 micron (.0025 inch) radial clearance between the piston and cylinder could be observed.

The solution to this problem was first to eliminate the clearance at non-operating temperatures with an interference fit between the piston and cylinder; and second, to choose materials with a large difference in coefficient of thermal expansion (CTE) so that there would be a radial gap or orifice for the alloy to flow through at the

operational or melting temperature of the alloy chosen. A new piston was fabricated from Invar 36 with a nearly zero CTE (1.1µ inch/inch/°F) with a room temperature interference of 25.4 microns (.001 inch) at the cylinder dia and 12.7 microns (.0005 inch) at the throat dia. This arrangement worked very well including a 30 day creep test at 70°C with only a 5 micron (.0002 inch) total movement.

Materials

After an attempt to increase internal pressure by simply increasing the throat dia. of the piston lead first to yielding of the original 6061 cylinder and later to the fracture of its "beefed up" 7075 replacement (upon heating), it was realized that greater attention had to be paid to material selection--in particular high temperature yield strength--and that a finite element model of the piston and cylinder would be required to accurately predict stresses and deflections. The finite element analysis showed that the piston and cylinder deflections were counteracting the interference fits. Which meant that stiffness was also a critical parameter. Table 2 lists the primary material candidates according to CTE and other key parameters

Table 2 Material Properties

Material	Coefficient of Thermal Expansion 10^{-6}m/m/ C	Thermal Conductivity W/m/ C	Modulus of Elasticity 10^4MPa	Yield Strength (20°C) MPa	Yield Strength (200°C) MPa	Yield Strength after cooling MPa
6061-T6	24.5	173	6.8	276	207	248
7075-T7651	24.3	164	7.1	469	193	276
2219-T87	23.9	145	7.2	386	221	338
2618-T61	22.9	156	7.4	372	283	377
W2F.20A-T6	19.3	122	10.4	420	310	
17200-AT	17.5	119	12.8	972		
17-4 PH	11.0	19	19.6	1172	1006	
Ti-6AL-4V	9.4	9	11.0	931	648	
Inco 902	7.6	15	18.6	931		
Invar 36	2.0	10	14.1	276		

2219-T87 aluminum was chosen for the cylinder for its availability and its strength after exposure to high temperatures. This exposure comes mainly from reheating to reset the device during ground test. W2F.20A-T6 which is 2618 aluminum reinforced with Al_2O_3 also looks very promising with its high modulus <u>and</u> high CTE. Inco 902 or Ni-Span-C which is an iron-nickel alloy like Invar but with much higher strength so it was chosen for the piston in spite of its higher CTE.

Development Unit

Figure 2 is a photograph of the development unit. This device has successfully completed 28 functional cycles (18 of which were at the 44500 N level), a 3 axis random vibration test (16.5 Grms),and a 4 cycle thermal-vacuum test (-40°C to +65°C).

The actuation times were 450 seconds from -40°C and 225 seconds from +65°C with 138 Watts of input power. The development unit used a redundant element foil heater which could be safely operated at the 200 watt level out of vacuum.
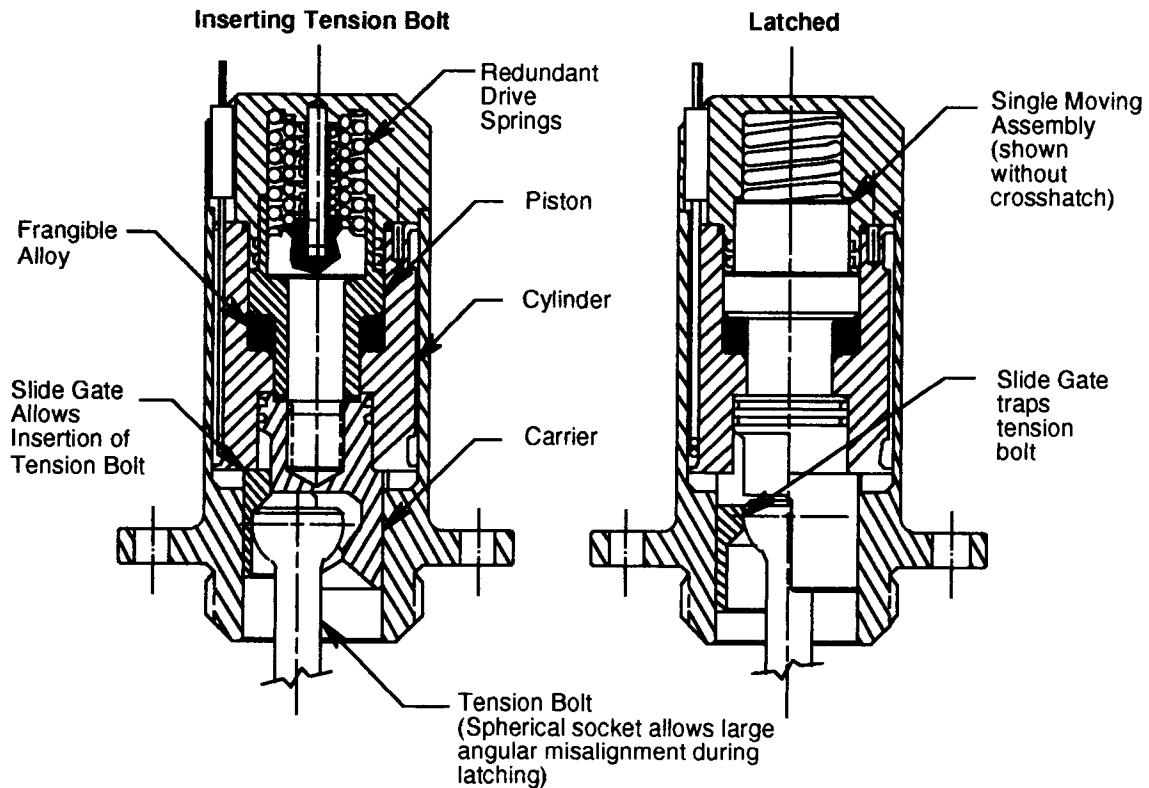

Figure 3 HFTL Cross Section

Two interesting phenomena occurred with the development unit. First, the behavior of the alloy changed from that of a eutectic or single melting point mixture to that of a noneutectic mixture with a slushy stage from 138°C to 175°C. Apparently, when liquefied under stress a lower melting temperature phase is forced out first leaving a non eutectic mixture behind. While too vigorously resetting the mechanism some of this non eutectic mixture was forced by the Teflon o-rings which allowed its composition to be investigated. Second, while the device will hold 44500 N at room temperature and at 65°C has a creep rate of only 145 microns/year (.0057 inch/year) it will stroke 1.4 to 1.7 micron per cycle if cycled between 65° and -40°. This may be a stress relieving phenomenon.

Qualification Unit

Based on desire to simplify the HFTL design plus decrease the operating time (which in turn decreases the total energy required to operate the device) the following changes were incorporated into the qualification unit's design. First, the tension bolt and carrier were changed to MP35N from 17-4 and beryllium copper so that the whole device could be downsized. Second, the foil heater was replaced with a cable heater which can deliver up to 400 watts input power with both circuits powered (see figure

165

4). Third, a frangible alloy of lead and bismuth with a lower melting point of 124°C has been chosen to replace the tin-bismuth alloy used in the development unit. Concerns have surfaced associated with the phenominum of liquid metal embrittlement (LME) and in this reguard, most tables show liquid tin to be more of a concern than liquid lead when in the presence of aluminum. In the new design the choice of anodizing vs. nickel or chrome plating for LME protection will be investigated. On the piston side of the problem, a central bolt which never comes in contact with the frangible alloy provides tensile backbone for the mechanism. Finally, a spring loaded slide gate was added to the design which allow easy insertion of the tension bolt prior to tensioning.

Figures 3 and 4 show the internal workings of the qualification design which should be somewhat selfexplanatory. The drive springs are incorporated so that even if the tension load in the bolt goes to zero, the drive springs will over come the o-ring drag and completely stroke the piston/latch. The device is reset by first reheating the alloy to liquefy it and then pushing the carrier and drive springs back to their initial position with a tool that mounts the HFTL housing.

Conclusion

The HFTL is a simple one critical movement device which can hold and gently release large tension loads. This capability comes at the expense of a somewhat large power requirement but one that is well within the capabilities of the batteries on today's large spacecraft.
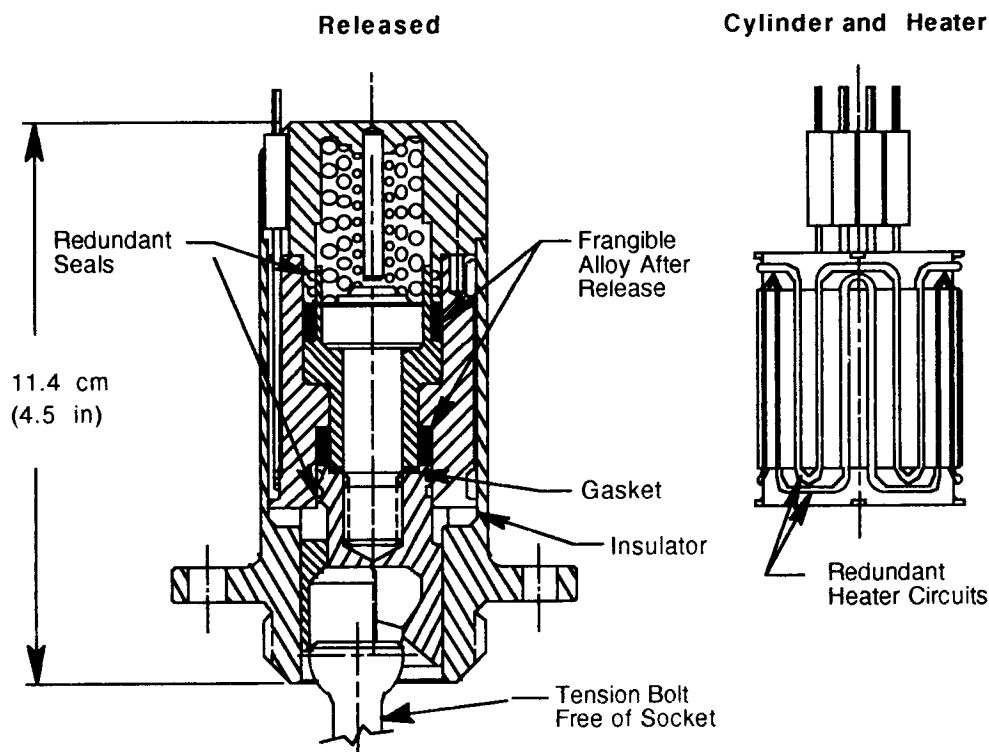
Figure 4. Released Configuration

A Rotating Arm Using Shape-Memory Alloy

Phillip P. Jenkins[*] and Geoffrey A. Landis[*]

Abstract

NASA's Mars Pathfinder mission, to be launched in 1996, reflects a new philosophy of exploiting new technologies to reduce mission cost and accelerate the pace of space exploration. One of the experiments on board Pathfinder will demonstrate the first use in space of a multi-cycle, electrically-activated, shape-memory alloy (SMA) actuator. SMAs are metal alloys which, when heated, undergo a crystalline phase change. This change in phase alters the alloy lattice-constant, resulting in a change of dimension. Upon cooling, the alloy returns to its original lattice formation. Wire drawn from a SMA contracts in length when heated. The reversible change in length is 3%-5%. The wire used in this actuator is a nickel-titanium alloy known as nitinol.

Introduction

Previous planetary missions have relied heavily on radioisotope thermal generators (RTG) for electrical power. Although RTGs have proven to be a reliable power source, they are expensive and politically less appealing than solar power. Mars Pathfinder, NASA's first Mars lander since the Viking-2 mission, will be solar powered. Mars offers a unique challenge to solar array designers. Since the Mars atmosphere contains large amounts of dust, the effects of dust settling onto solar panels must be considered in sizing solar arrays. Projections of power loss due to dust buildup vary from 20% to 90% over the course of a 2 year mission [1]. Unfortunately, very little data is available on the settling properties or optical opacity of Mars dust.

Among other things, Pathfinder will conduct a series of experiments to measure Mars environmental effects on solar arrays. One of these experiments [2] will measure the optical obscuration created by dust settling out of the atmosphere on to a solar cell. In what is an elegant and simple experiment, a solar cell is protected by a removable cover glass. During the course of the mission, the cover glass is occasionally moved from in front of the solar cell and the short circuit current (Isc) of the solar cell is measured. Comparing Isc with and without the cover glass in place will yield a direct measurement of the optical density of the dust that has settled on the cover glass, plus the optical density of the cover glass itself. The effect of the cover glass can be subtracted out by baseline measurements made before any appreciable dust has accumulated on the cover glass.

The design for the experiment had to meet several operational constraints: 1) a power budget of five watts for 10 seconds per day, 2) power distribution is limited to 5 volts DC up to 1 amp current, 3) short circuit protection, 4) a minimum of one square centimeter detector area, 5) a total footprint of 41.0 mm x 13.7 mm, 6) a mass not to exceed 16 grams, 7) must complete at least seven cycles on the Martian surface. The

---

[*] NYMA Inc., NASA Lewis Research Center, Cleveland, OH 44135

current working prototype uses 0.522 amp, and has a mass of 7 grams. Several actuator designs, including motors, solenoid actuators and various nitinol configurations, were tested. The present design was chosen for its simplicity and low weight.

Mechanical Configuration

The actuator consists of a rotating arm to which a cover glass is attached. The arm is approximately 3.5 cm long and must rotate 32° to completely uncover the solar cell. Figure 1 shows a top view schematic. The arm is attached to an axle which is free to rotate. A SMA wire is anchored to the axle and to a stationary point 3 cm away. The nitinol wire is heated resistively by passing a DC current through the wire. The wire heats up and contracts, pulling on the axle, which then rotates the arm and cover glass. When the current to the wire is shut off, the wire expands and is returned to the rest position by a flat spring in a "bending beam" configuration. Figure 2 shows a side view of the actuator. Figure 3 is a photograph of prototype hardware.

The axle was machined from 7075 aluminum and uses a bushing fabricated from a MoS_2-impregnated polyimide (SP-3 Vespel from Dupont). The return spring, which is also used as an electrical brush, was fabricated from 38.1 µm (0.0015 in) thick, 1095 high carbon steel. The spring was plated with copper, nickel and gold and afterward annealed at 190°C for 24 hours to prevent hydrogen embrittlement. The actuator is powered by a 150 micron diameter NiTi alloy (nitinol) wire with a 90°C transition temperature. Several different nitinol compositions, with varying transition temperatures were tested. The 90°C wire chosen was based on empirical testing of the device under the expected operating conditions. The manufacturer of the wire is Dynalloy Inc. of Irvine, California.

The mechanical leverage developed by the moment arm of the axle at the SMA attachment compared to the 3.5-cm rotating arm is about 36:1. When the arm is fully rotated, the SMA wire must supply a force of approximately 137 grams (1.34 N) to overcome the resistance of the return spring. This is well below the manufacturer's maximum recommended recovery force of 330 grams. The 3-cm-long nitinol wire contracts approximately 5%, giving about 1.5 mm of usable motion. The rotation of the axle requires a 0.6 mm contraction of the wire. By choosing the operating force conservatively and using less than the full contraction of the wire, the mechanism offers positive and robust action over a wide temperature range.

Operation and Electrical Configuration

The Mars Pathfinder consists of a lander and a small, autonomous, six-wheel rover vehicle. Once the lander is situated on Mars, it releases the rover. The rover has its own independent power system and on-board computer that controls rover functions including all experiments. It is also equipped with a transceiver for communicating with the lander. The "dust cover" experiment (also known as part of the "material adhesion experiment" or MAE) is situated on the front left corner of the rover. Figure 4 shows the rover and the position of the dust sensor.

The experiment requires that the rotating arm fully remove the cover glass from in front of the solar cell. The rover energizes the actuator, waits a predetermined time, and then measures the solar cell. No feedback signal is available from the actuator to tell the rover that the cover glass is in the fully rotated position. Although a feedback signal could easily be incorporated into the actuator, the rover computer has a very limited number of data channels available for the experiment. A qualitative feedback signal is obtained by comparing the solar cell Isc with and without the cover glass. The cover glass itself will attenuate the light by 7%. Therefore a qualitative measure of whether the cover glass has been removed is obtained by measuring at least a 7% increase in Isc when the cell is uncovered.

The mechanism actuates on a switched power supply of 5 Volts DC provided by the rover power system. The current through the SMA wire is limited using a single resistor. This is not an ideal condition. Since the SMA action is thermal in nature, the ambient temperature plays an important role in determining how much current will be required to activate the rotating arm. With a fixed power supply, the operating current must be set high enough to heat up the wire at the lowest expected operating temperature. For temperatures above the minimum, the wire will heat up more quickly and rotate the arm faster. If the wire is allowed to overheat (due to an excess of current for a relatively long time), the SMA will permanently deform and destroy the actuator. The actuator has an operating range of -50°C to 0°C. This is a large enough range that the time required to rotate the cover glass can vary from 6 to 0.5 seconds. If the rover has no feedback signal to tell it when the actuator is fully rotated, it must rely on ground-based testing of the actuator characteristics as a function of temperature to anticipate how long the actuator will take to fully rotate. In addition, the rover must have available an ambient temperature measurement at the time the actuator is used. The only other alternative available is to narrow the operating temperature range, and allow the actuator "on time" to remain constant. In summary, in order to optimize the operating range of the actuator, either the current through the wire or the "on time" of the actuator must be variable. Otherwise, a fixed current and fixed "on time", reduces the actuator's operating temperature range.

Considerations for the Mars Environment

The operating temperature of the actuator on Mars is expected to vary from -40°C to -10°C at a pressure of 8 Torr CO_2. Ground testing indicates that the main heat loss mechanism of the wire is by conduction through the mechanical and electrical connections. It was found that operation was highly dependent on the thermal conductivity of the mechanical connections of the wire. For a SMA actuator to operate at low temperatures, it is important that the wire heats up uniformly. The ends of the wire must be mechanically strong and offer good electrical contact. It is nearly impossible to have a good electrical contact without having a good thermal contact. If the ends of the wire are thermally anchored to cold mechanical connections, they will require more current to heat up to the transition temperature than does the middle of the wire. The extra current required to heat the ends of the wire will overheat the middle of the wire, causing it to fail. If possible, it is best to design the mechanism so that the mechanical connection is separate from the electrical connection, so that the

mechanical anchor for the wire can be made thermally insulating to allow the wire to heat up more uniformly. Figure 5 shows the operating current of two actuators; one with thermally insulated mechanical connections and the other with thermally conducting connections. Using insulated connections decreases the current necessary to heat up the wire and extends the operating range of the device. The flight actuator uses Mylar to reduce the thermal conductivity at the mechanical connection point. While the active portion of the wire is 3 cm long, the total wire length is approximately 4.5 cm long in order to physically separate the mechanical and electrical connections. Tests done at Mars temperature and pressure conditions have verified operation of the actuator over a temperature range of -50°C to 0°C.

Summary

A shape-memory alloy powered rotating actuator has been designed and fabricated for use on Mars. This actuator uses thermally insulated mechanical connections to achieve a more uniform heating of the SMA, reducing the operating current and extending the operating range. This will be the first multi-cycle, SMA actuator used in a space application.

References

1. Landis, Geoffrey A. "Dust Obscuration of Mars Solar Arrays." *45th Congress of the International Astronautical Federation* , IAF-94-380 (Oct. 9-14, 1994) Jerusalem, Israel.
2. Landis, Geoffrey A. and Dennis Flood. "Solar Distribution and Dust Obscuration Sensor." Presented at the MESUR Science Definition Team Meeting, Nov. 5-6, 1992, Jet Propulsion Laboratory, Pasadena, CA.
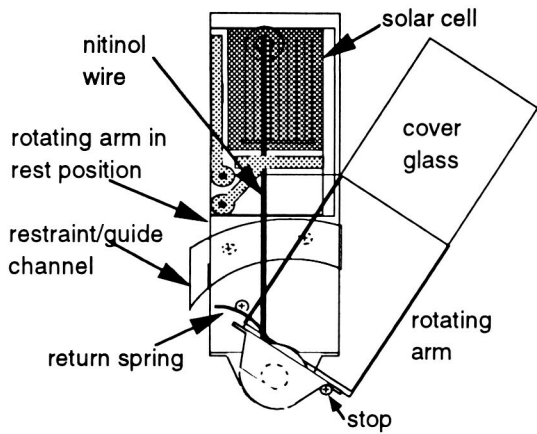
Figure 1) Top view of actuator.
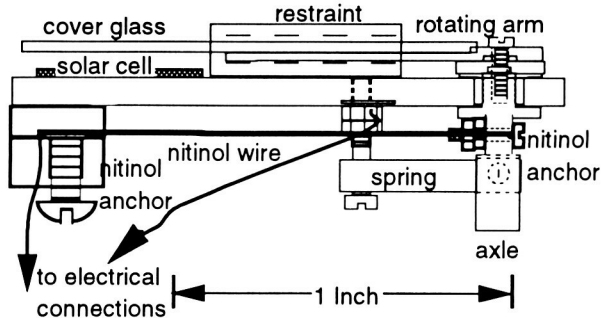
Figure 2) Side view of actuator.
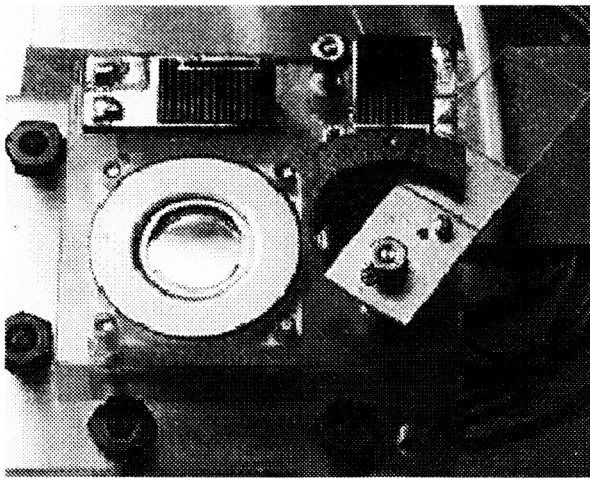
Figure 3) Photograph of the prototype material adhesion experiment. Actuator is on the right side, in the deployed position.
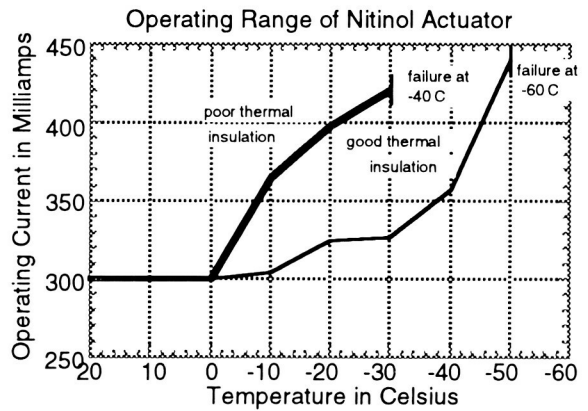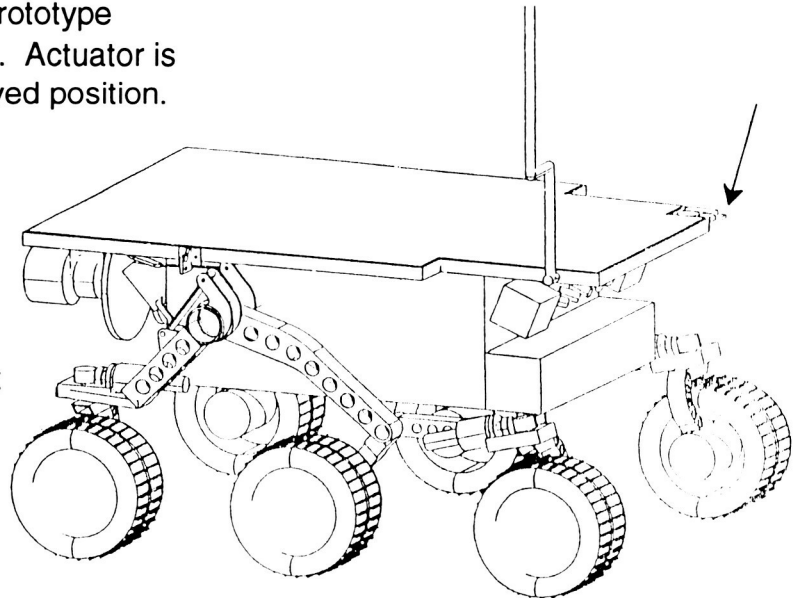

Figure 5) Insulation of mechanical connections improves operating range.

Figure 4) Pathfinder rover showing the location of the material adhesion experiment (MAE).

Retrofitting a Fine-Pointing System to Satellite Optics

Robert O. Woods*

Abstract

This paper describes a system added to an existing satellite-borne telescope design for the purpose of compensating the boresight errors that had been observed in earlier flights of similar instruments. Those errors had been found to be caused by thermal distortion of the spaceframe. This retrofit design was subjected to severe volume restrictions because it was fitted into an already tightly-packaged instrument envelope. It was found practical to improve the basic design by converting a redundant structure into a statically-determinate one. It was also possible to use portions of the mechanical actuation system to facilitate the position encoding needed for computer interfacing.

Introduction

Pointing information for this optical system is obtained from a star sensor that is located at some distance from the instrument itself. Thermal distortion occurs in the intervening structure, leading to boresight errors. These errors have been investigated by ground reference and found to be a reproducible function of the diurnal and annual cycles. It is possible to characterize this error with enough precision to permit uploading a protocol that controls a fine positioning system and removes the error at its source. In the case described here, it was necessary to input corrections having a resolution on the order of one arcsecond and a net excursion of approximately one half degree of arc. During an initial evaluation of the design problem, it was thought that a second electronics package would be required in addition to a substantial increase in the volume of the existing envelope. This would have caused a major dislocation because of the limited "real estate" available on the satellite platform, and because of the need to negotiate with numerous other experimenters whenever a change in geometry took place. To avoid these complications, it was taken as a design objective that any additional systems be entirely contained within the existing envelope. It was found that this was, in fact, possible.

The Basic Structure

The skeleton of the existing system is shown in Figure 1. It is a beryllium structure comprising a frame within a frame and having a square "footprint" on the mounting platform. The structure had been designed as two discrete entities in order to allow manual boresight adjustment of the telescope during its initial assembly. This feature provided an existing interface at which to input relative motion between the optical elements and the parts of the structure that were "grounded" to the spaceframe. The square cross section is clearly not optimum for a precision pointing system because it

---

* Intelligent Systems and Robotics Center, Sandia National Laboratories, Albuquerque, NM

is redundant. The geometry had been dictated by space constraints, being the only available volume on the satellite platform at the time of initial design. The square cross section did, however, have one intrinsic advantage. It was found to provide an already existing pair of orthogonal axes which could be used for X-Y pointing of a telescope. The structure also had what is, in effect, a universal joint at each of the four supporting corners. These ("monoballs") had been incorporated in the original design to minimize the distortion of the structure that would be caused by joint moments.

Pointing Modification

Two-axis pointing was accomplished by choosing one of the four support points as the only fixed "ground," locking the diagonally-opposed support point during launch and releasing it in flight, and placing actuators on the remaining two corners to move them normal to the plane. This is indicated conceptually by the sketch in the lower right-hand corner of Figure 1. It can be seen that if the upper right corner of the square is held at a given elevation and the lower right corner raised or lowered, rotation will occur about the horizontal axis. A similar rotation can be obtained about the vertical axis by motion at the upper left corner. The lower left corner is unsupported.

A study of the interior of the existing design revealed that the only sizable empty volumes were in the spaces immediately above the four monoball universal joints. This suggested that, if these spaces were to be used, each actuator would have to be extremely compact or each would have to be divided into two separate functional units. The latter course proved to be practical and, in fact, it was later found to be convenient. The approach that was ultimately chosen is shown schematically in Figure 2 where much of the detail is devoted to the position pickoff arrangement. This proved to be more challenging than the motion itself. Each actuator consists of two parts that are mounted at opposite ends of a lever. Each lever spans an edge of the square. Motion is accomplished by a stepper motor, which drives a lead screw through a gear train. This moves the long arm of the lever via of a pair of ball bearing nuts that have been spring loaded to eliminate backlash in the overall assembly. The shorter arm of the lever is shown in Figure 2 as being between a pair of bearings, the left one being the fulcrum and the right connected to "ground." This drawing is conceptual. In fact, the short arm of the lever is so small that it is really embodied by an eccentric mounted in the bore of a large fulcrum bearing. This can be seen by comparing Figure 2 to Figure 3. The latter shows the actual hardware as it was installed in the instrument. Specifications of this retrofitted system are as follows:

Angle increment per step:	1.1 arcsec
Total angular excursion:	0.43 degree
Number of steps (Full travel):	1408
Movement per step (At end of short lever):	914 nm (36 μin)
Net Travel (At end of short lever):	1.32 mm (0.052 in)
Total Lead Screw Revolutions (Full travel):	22
Total Motor Revolutions:	176

Since the system operates in a closed loop, determining the true location of the positioner to feed back to the onboard computer is a vital part of the operation. Not only is accurate position data needed, these data must come from absolute position encoders that will not be rendered useless in the event of a computer upset. Position encoding was incorporated by converting the leadscrew arrangement into an analogy of a mechanical micrometer. In both, a small deflection is measured by determining the angular position of a screw in its rotational cycle and interpreting this data in the light of knowledge regarding the specific pitch of the screw in which the angle data are taken. This concept was put into practice using a pair of encoders, which involved the Gray code [1] for digital output. One encoder was placed on the long lever arm and served to determine where the ball nut was in relation to the leadscrew. This gave a coarse indication of position. Fine position was indicated by an angular encoder attached to the lead screw. A "hardware" constraint influenced the design of the encoders. Only specific flight-qualified semiconductor components could be used in the light emitting diode/phototransistor pair that is used to provide digital position data. This led to a fairly bulky assembly. Pickoffs took the form of the sector encoder and rotary encoder set shown in Figure 2. The sector encoder may also be seen in Figure 3; the rotary encoder is not visible, being enclosed by the leadscrew housing in this figure. The stepper motor which turns the leadscrew advances 45 degrees per step. This, driving through a gear ratio of 8:1, gives 64 steps per revolution of the screw. The arrangement was chosen to make binary arithmetic easier. The pitch of the leadscrew is 1.27 mm (0.050 in) and the resolution of the coarse encoder is on the order of 80% of this distance.

A complication in using a pair of digital encoders in this fashion is the mechanical backlash and other accumulations of tolerances guarantee that when the coarse encoder changes state, it cannot be guaranteed do so every time at exactly the same transition indicated by the fine encoder. The problem of seaming together the outputs of two encoders in the presence of mechanical hysteresis has been discussed in an earlier publication [2]. Briefly, we have shown that as long as the hysteresis can be kept within calculable limits, unambiguous data can be generated and evaluated with the help of an onboard computer.

The Launch Lock

A mechanism that is fundamental to the operation of the system, but which is functioned only once during the flight, is the launch lock that constrains one corner of the square. The design of this component, too, had to satisfy a number of constraints -- not the least of which being that it had to fit into a volume only a little larger than the featureless column that supported the original assembly. In addition, it was required that it be able to lock the structure wherever it happened to be within its range of adjustment during manual boresighting, and to do so without perturbing that adjustment. The first constraint was satisfied by creating a linear assembly using a long gearhead motor that had a relatively small diameter. The latter requirement was met by creating a collet assembly, much like a lathe collet, which would grasp a cylinder attached to one corner of the moveable structure. The arrangement is shown in Figure 4. The bottommost component in the drive train is a DC motor with a gearhead. This, and the rest of the assembly, is housed in a beryllium column that

matches the thermal expansion coefficient of the balance of the structure. The motor drives a screw that incorporates a ball thrust bearing. The screw and bearing are combined into a single component so that the only external loading is the torque which turns it. This minimizes the tendency of the assembly to be deflected axially during operation and allows the collet to grasp a pin without perturbing its axial adjustment. Rotation of the screw causes steel balls to move in inclined races and opens or closes the jaws of the collet. The pin, which is grasped by the collet and which serves to fix one corner of the square during launch, runs in a linear ball bearing. When the collet is opened, this pin is completely free to move in an axial direction. Position of the nut -- and hence the state of the collet -- is monitored by micro switches that sense both limits of its travel. In order to make the collet clamping force adjustable from outside the assembly, this radial force is generated by a screw-adjustable collar surrounding the housing. The collet and ball assembly are run at a very high stress level. For this reason, the collet is made of 18 Ni maraging steel hardened to RC 57. The cylindrical pin which it grasps is 440C CRES hardened to RC 55. Since maraging steel is not resistant to corrosion, the collet assembly is gold plated.

Lubrication

Throughout, an effort was made to use sputtered molybdenum disulfide as a lubricant wherever possible, particularly on the ball screw and main bearings. This was done because of the proximity of the entire mechanism to optical components that would be degraded by off-gassed lubricants. In the case of the DC motor, use of a solid lubricant was not possible. The motor was therefore packaged in such a way as to provide only a very labyrinthine path to the outside and was lubricated with Braycote 600.

References

1. Gray, H. J., et al. "An Analog-to-Digital Converter for Serial Computing Machines." *Proceedings IRE*, 41, no. 10, 1462-1465.
2. Woods, R. O. "An Autonomous, Closed-loop Pointing System for use with Satellite Optics." *SPIE Proceedings*, 817, no. 08
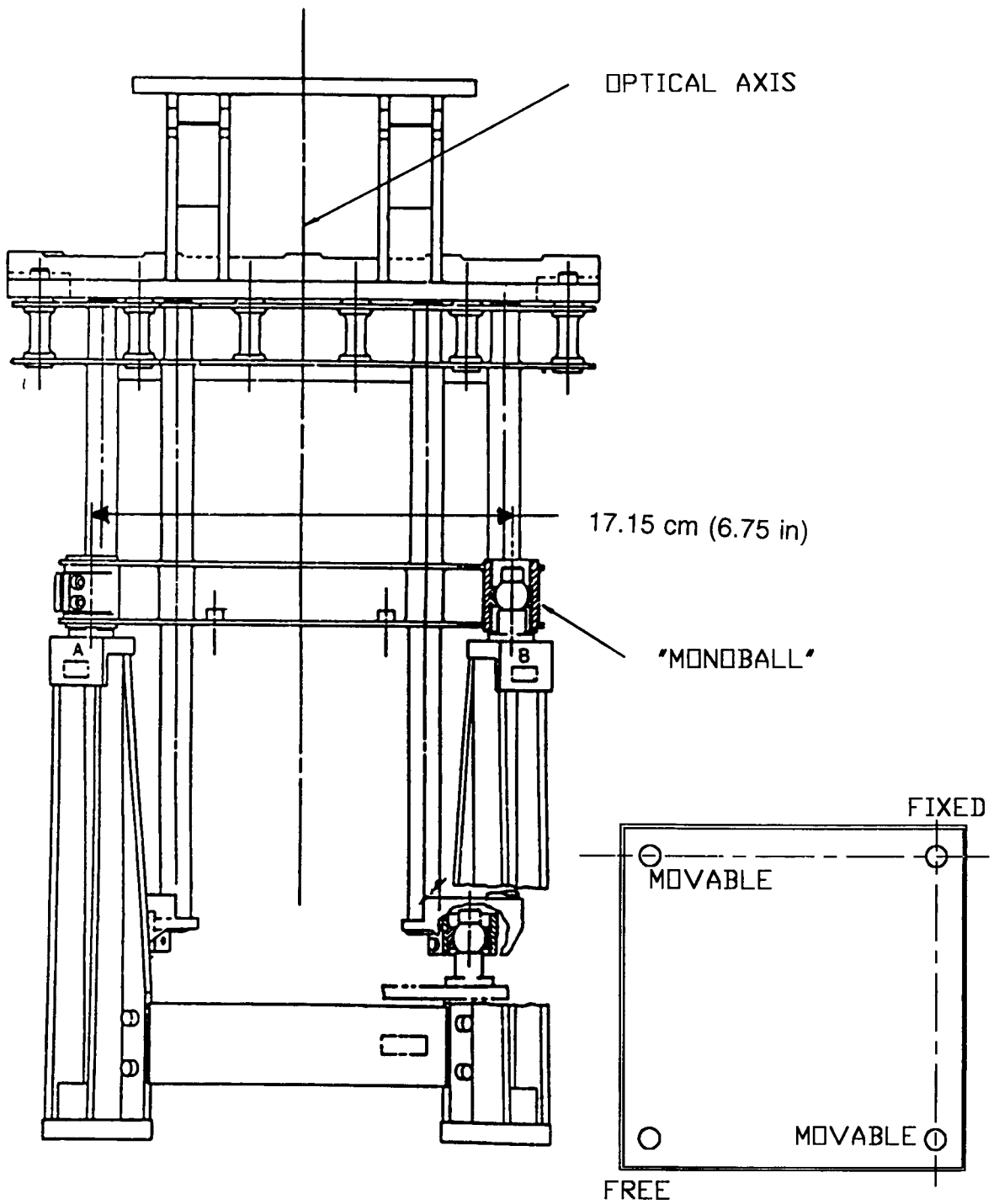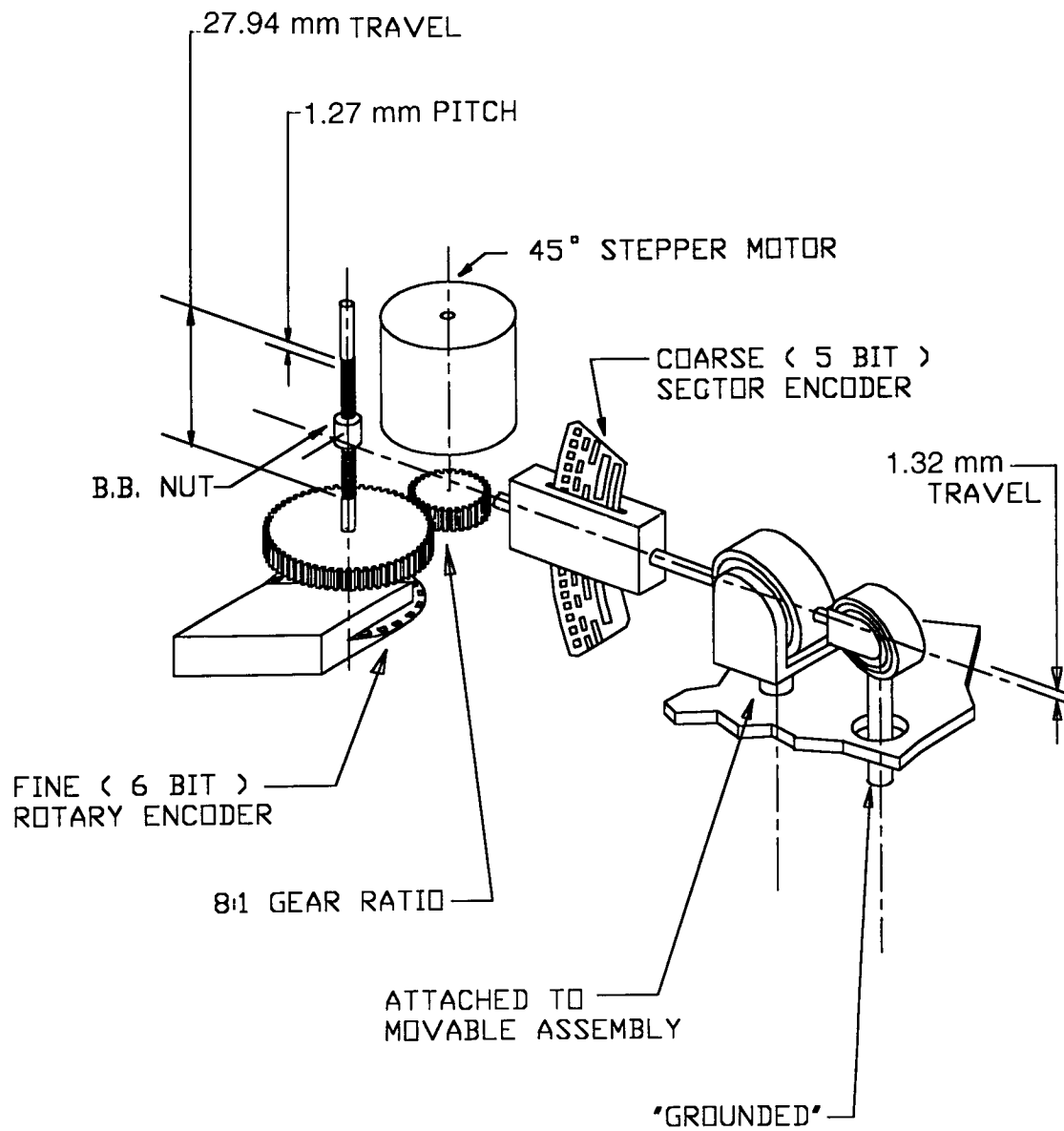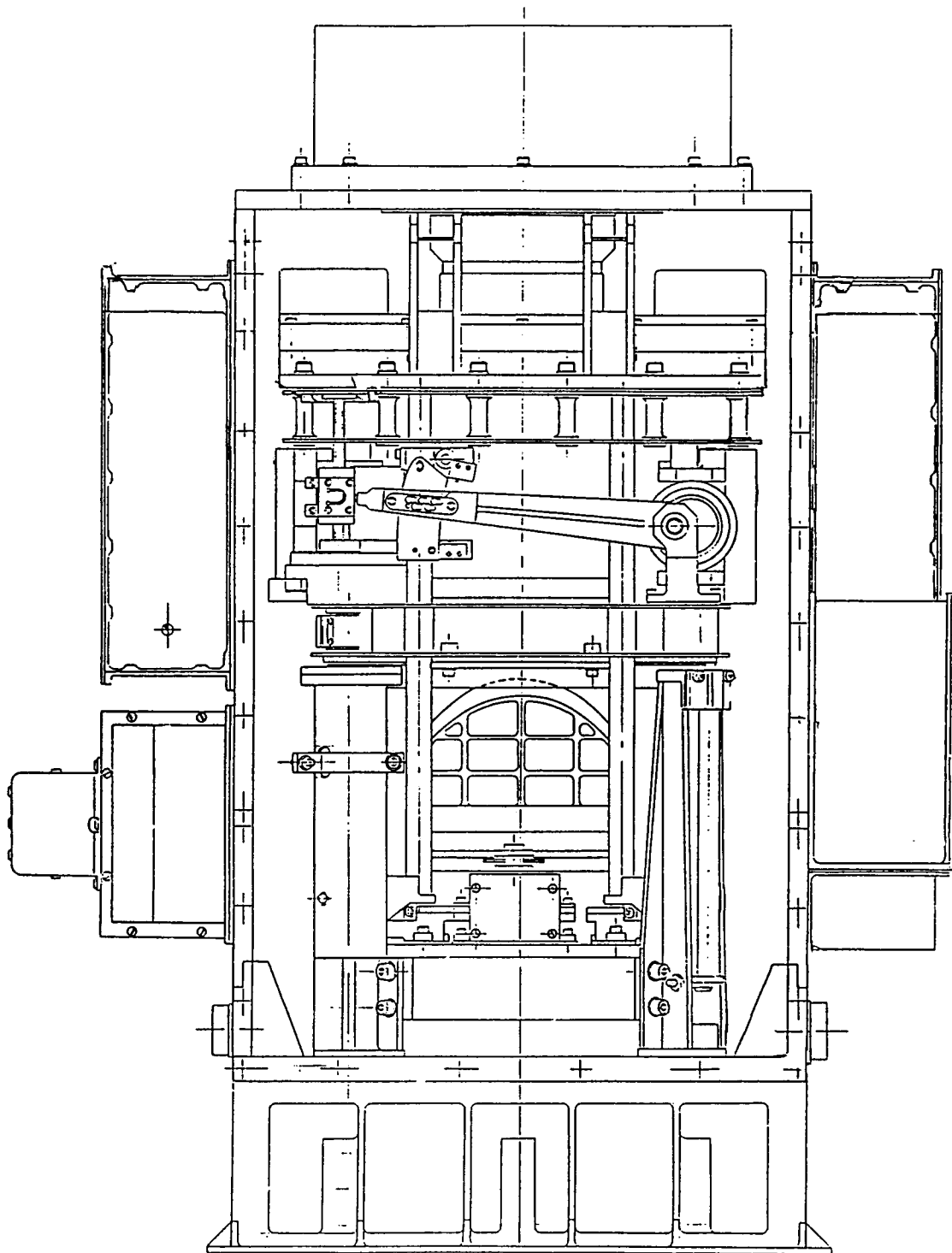
Figure 1. Original Frame

27.94 mm TRAVEL

1.27 mm PITCH

45° STEPPER MOTOR

COARSE (5 BIT)
SECTOR ENCODER

1.32 mm
TRAVEL

B.B. NUT

FINE (6 BIT)
ROTARY ENCODER

8:1 GEAR RATIO

ATTACHED TO
MOVABLE ASSEMBLY

'GROUNDED'

Figure 2. Actuator Concept

Figure 3. Actuator As Installed

CYLINDER

LINEAR BALL BEARING

COLLET

SCREW

D.C. MOTOR
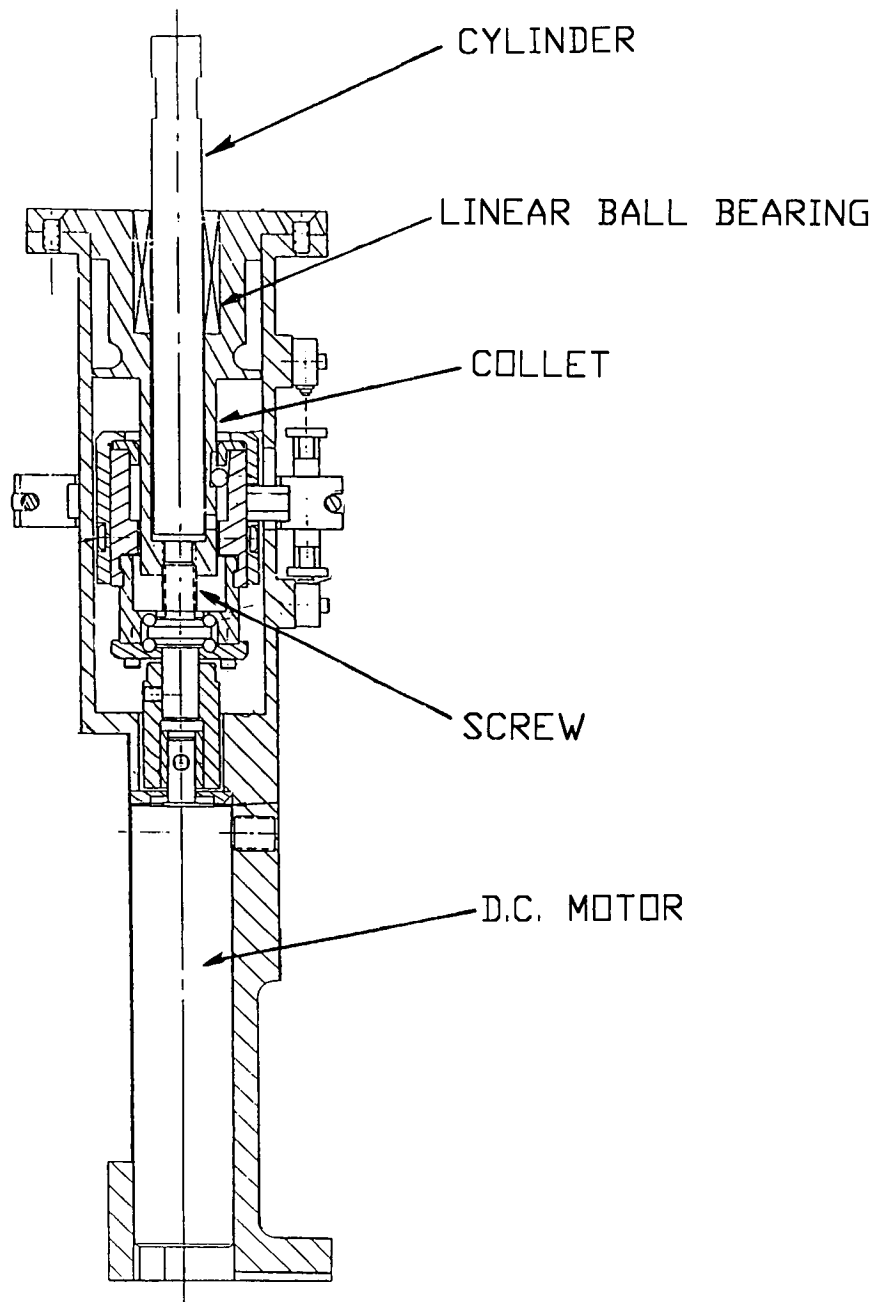
Figure 4. Launch Lock

Electromechanical Rotary Actuator

S. P. Smith* and W. J. McMahon*

Abstract

An electromechanical rotary actuator has been developed as the prime mover for a liquid oxygen modulation valve on the Centaur Vehicle Rocket Engine. The rotary actuator requirements, design, test, and associated problems and their solutions are discussed in this paper.

Introduction

This electromechanical rotary actuator, shown in Figure 4, has been successfully developed as the prime mover for a liquid oxygen valve. The unit is required to provide angular positioning of the liquid oxygen flow control valve on the Centaur Vehicle Rocket Engine. The application requirements are stringent. The unit must operate fully at cold temperatures and during vibration.

The unit was designed to meet specific customer needs. The design is fully developed, qualified and has flown on at least three missions (6 units). Design, performance, and qualification test problems are presented.

Design Requirements

The rotary actuator is required to modulate the flow of liquid oxygen (LOx) during rocket engine firing in order to optimize the fuel consumption. The application environment is severe; extreme cold temperature operation due to the close proximity of -184°C (-300°F) LOx and high, sustained vibrational loading due to rocket engine operation. The application requirements/unit capabilities are listed in Table 1.

Table 1 - Rotary Actuator Performance Requirements

Weight max.	2.08 kg (4.6 lbm)
Supply Voltage	28 VDC
Stall Current max. (supply limited)	0.45 A
Winding Resistance Phase to Phase	48 Ω
Output Rotation	2.44 rad (140 deg)
Step Size	0.32 mrad (0.0187 deg)
Running Torque @ 28 VDC & 0.13 $^{rad}/_s$	11.3 N•m (8.33 ft•lbf)
Unpowered Holding Torque min.	2.26 N•m (1.66 ft•lbf)
Operating Temperature Range	-64°C to +76°C (-83°F to +169°F)
Random Vibration Level	22.6 Grms

* Honeywell, Inc., Electro Components, Durham, NC

Mechanical Design

The rotary actuator consists of a three-phase small-angle stepper motor, a Harmonic Drive gear reducer, a duplex bearing pair, dual-ganged instrumentation potentiometers, and associated hardware all mounted in an appropriate housing. The actuator envelope is given in Figure 1. A layout of the device is given in Figure 2.

Motor

The motor is a three-phase, 1.5-degree stepper having a wound stationary member and a permanent magnet rotating member. The motor current was limited by the customer-supplied electronic controller. The motor parameters are given below.

Table 2 - Motor Parameters

Resistance - Phase to Phase	48 ± 10% Ω
Inductance	16 ± 30% mH
Running Torque @ 10.4 rad/s	2.4 N•mm (3.5 in•oz)
Voltage Range	22.5 to 32 VDC
Current	0.44 A

Gear Train

The 80:1 gear reduction is accomplished with a Harmonic Drive device which consists of a wave generator as the input member, a circular spline as the fixed member and a flex spline as the rotating output member.

Instrumentation

The actuator has two potentiometers that provide position feedback. The potentiometers sense the actuator output position by providing a voltage signal proportional to output position. The potentiometers are driven directly by the output shaft through an anti-backlash coupling. Characteristics of the potentiometer are:

Potentiometer Parameters	
Resistance	5000 ±10% Ω
Linearity	0.5% absolute
Power Rating	1.25 W

External visual shaft position was also provided for purposes of integrating the actuator with the valve. Shaft position is given by a scale graduated in 0.017 rad (1 deg) increments.

Bearings

The actuator output shaft rotates on a pair of 440C stainless steel preloaded ball bearings. The bearings are mounted in a face to face arrangement. This mounting is preferred in cases where the housing operates at a higher temperature than the shaft

and has a lower moment of stiffness. The lower moment of stiffness helps reduce radial loads induced by the actuator onto the valve shaft. The motor rotor is mounted in stainless steel shielded ball bearings.

Mechanical Stops

Adjustable mechanical stops were provided for purposes of integrating the actuator with the valve. The stops are external and independently adjustable in increments of 0.017 rad (1 deg). The stops are capable of withstanding the full actuator torque without damage to the unit.

Heater

Because of the connection to a liquid oxygen valve, the unit was mounted to the valve through a thermal isolator (not shown). A heater was provided to keep the unit within the required operating temperature. A hermetically sealed thermostat was used to close the heater circuit when the unit temperature dropped below -17.8°C (0°F).

Materials

Because the unit is mounted to a LOx valve, failure of the valve seal could allow LOx into the actuator. As a result, the housing and shaft material were chosen for LOx compatibility. The housings are made from 6061-T6 aluminum. The shaft and Harmonic Drive are made from 304L stainless steel.

Lessons Learned

During the development and qualification tests several problems occurred which required corrective action. The most significant of these were encountered during the vibration and thermal cycling tests, where the actuator was required to meet functional performance requirements. The investigations and the corrective actions were complicated by the arrangements of the tests, since thermal cycle testing always followed vibration. An important corrective action for a problem exposed during thermal cycling was actually caused during vibration. Listed below were the significant lessons learned during the Development and Qualification Testing.

a)   Motor current limit

Since the motor current is limited by an electronic controller and not the motor winding resistance, the developed motor torque remains constant over temperature. The customer required that the current limit be bracketed within ±10%, meeting the minimum torque requirement at minimum current and voltage, and not exceeding a maximum of 33.9 N•m (25 ft•lbf) at maximum current and voltage. Extensive testing at cold temperature was required to determine the minimum current value required to compensate for the variation in internal friction with temperature and still meet the performance goals.

185

As part of the cold temperature study, several motor and actuator parameters were characterized. The drag torque of all rotating components in the actuator were quantified and assessed for impact on the motor torque producing capability. This study was done at ambient conditions and at various temperatures down to -67.8°C (-90°F). The viscosity of the bearing and geartrain lubricant (Bray 601 grease) increased significantly at the colder temperatures, which resulted in an unacceptable increase in bearing and geartrain drag torque. These increases were anticipated during the design stage but the actual increases were higher than expected. The drag torque of the output bearings and seal, nearly doubled over the temperature range. The rotor and harmonic drive wave generator bearing drag, likewise, increased 300% over the temperature range, and was dependent on rotor speed. Since the drag torque of components on the output side of the geartrain is decreased by the gear ratio, the effect on the motor rotor is small. If drastic decreases in drag were to be obtained, they had to come from the input side of the geartrain, i.e. motor rotor and harmonic drive bearings.

Significant improvement in the input drag torque was obtained by changing the lubrication from grease to oil. The type of lubrication for the rotor and harmonic drive bearings was changed to oil (Bray 815Z) and testing was repeated. A reduction in the motor drag torque greater than 50% was realized with oil as the lubricant. Still, further improvements were necessary in order to gain margin for qualification testing. It was discovered that by controlling the amount of oil in the wave generator bearing (the largest contributor to drag) the necessary improvements to performance were attained. Two other changes were implemented at the same time, which were minor in drag reduction as compared to the lubrication change. The seal's outside diameter was reduced by 0.127 mm (0.005 in) to lessen the circumferential force on the output spline. This change amounted to a potential 5% decrease in motor drag. The other change was to position a bearing grade material between the wave generator and the aluminum rotor shaft, where the two components previously contacted each other.

b)   Potentiometer cover standoff fracture.

The potentiometer cover is removable and is attached to the actuator body via two standoffs. During vibration the standoffs fractured at the base of the thread. The cover was loosely fitted to the housing at the interface which allowed the cover, with the standoffs and fasteners rigidly attached, to move during vibration. This movement, increased the loading at the undercut of the standoff's thread to the point where it exceeded the material strength and fractured. The cover, standoffs and fasteners fell from the unit as an "assembly".

This problem was corrected by revising standoff installation torque to fit the material strength and bonding the cover to the housing.

c)   Potentiometer resistance variation.

The dual-ganged potentiometer is connected in parallel for telemetry information during flight. The previous valve actuator, using basically the same potentiometer, was tested in this same parallel arrangement. For this actuator, the customer wanted

to measure the output of each cup of the potentiometer to ensure that the redundancy of the potentiometers were still intact. In resistance variation testing of the potentiometer (the unit is powered, but not stepped), the response of each cup of the potentiometer was measured during vibration. The proper potentiometer response during the vibration would be to show no variation in the voltage (resistance) output. The limit for resistance variation, however, was 300 ohms.

During the qualification vibration testing, one cup of the potentiometer measured well within the 300-ohm limit, while the other cup showed ever increasing resistances as the level and vibration time increased. A test performed in the parallel arrangement, as done previously, would have indicated a resistance variation of less than the 300 ohms. Instead, the variation in the affected cup was shown to be clearly erratic. The cause of the erratic variation was found via X-ray and in the subsequent potentiometer teardown. One of the three wipers which contacted the circumferential element had broken off, leaving the two other wipers to contact the element. The wiper assembly was found to have nicks and dents, where the wipers were adjusted and trimmed. The wiper which broke off, fractured at an unintentional trim crease. Later, after discussing the matter with the potentiometer vendor, it was discovered that the wiper assembly was a new, cost saving, better linearity, precious metal stamping, which had been introduced into the potentiometer several years prior to this date. They informed Honeywell that the stamping had failed to live up to all of the expectations and that the wiper assemblies were now fabricated from precious metal wire as was done previously.

It was reassuring to know that the assemblies would no longer fracture, however, resistance variations in potentiometers remained a problem. Typically, one cup of the potentiometer would have excessive variation, while the other was within specification. Because the potentiometer had so many variables that could affect the resistance variation (bearing/shaft clearances, bearing preload, wiper pressure on the element, axial play, material resistivities, etc), the potentiometer vendor was directed to screen the potentiometers using the same test technique as would be employed on the end item actuator. The resistance variation limit for the potentiometer, tested alone, was reduced to 40% of the end item acceptance test limit to account for response magnification when mounted on the unit.

d)   Rotor shaft bearing shoulder

After the qualification level vibration testing, the unit failed to meet the required speed and torque load points. Disassembly of the unit revealed excessive wear on the rear rotor bearing shoulder and outside diameter. The vibration time and level had deformed the bearing shoulder, shifting the position of the rotor shaft greater than 0.254 mm (0.010 in). The rear of the rotor contacted the output side bearing mount, input rubbing against output, increasing the input drag torque to excessive levels.

The aluminum rotor shaft construction has slots machined along the axis of rotation, which transfer torque from the motor to the Harmonic Drive coupling. These slots reduced the shaft area moment of inertia and stiffness. Consequently, during vibration the shaft flexure contributed to the wear and degradation of the shaft bearing shoulder.

It was further discovered that the reduced stiffness of the rotor shaft was responsible for some of the problems seen in thermal cycling. Evidence of rubbing contact between the motor rotor and the stator had been seen on the qualification unit after the initial cold temperature failure.

The problem of the bearing shoulder was corrected by inserting a high strength steel spacer between the bearing shoulder and the rotor shaft shoulder. Figure 3 shows the revised rear motor bearing configuration. The spacer has two tabs that are machined to tightly fit the slotted shaft. The purpose of these tabs is to stiffen the rotor shaft and limit its deflections.

The potential for rotor and stator contact was decreased by the addition of this spacer. However, inspection of parts revealed a high runout condition in the rotor assembly. The condition was due to the manufacturing tolerance buildup of several parts in the assembly. The corrective action for this condition was to machine (grind) the rotor assembly as an assembly. The changes also resulted in more consistent motor performance during thermal cycling.

e)   Potentiometer signal noise.

During the qualification testing, the unit was required to undergo a temperature / humidity test. In this test the unit is subjected to high moisture levels for extended periods of time (hot and humid Florida climate). After the temperature/humidity test, the unit was subjected to a final Thermal Vacuum Test. The first temperature extreme was the cold temperature limit -63.8°C (-83°F). While monitoring each cup of the potentiometer, testing at this cold temperature produced erratic signals from one of the potentiometer cups. The other cup showed nominal behavior at cold temperature, and both functioned properly at warmer temperatures.

This problem was caused by the influx of water vapor (humidity) into the non-hermetically sealed potentiometer. This was corrected by vacuum baking the actuator after all unit acceptance tests in order to drive off any excess moisture. The bake cycle prevents moisture from condensing and freezing on the potentiometer elements and causing the electrical noise. Special handling instructions and storage in nitrogen purged packaging were added to the actuator assembly procedure to promote the humidity free state until the actuator is ready for the customer's installation.

Each of the above problems were sequentially identified during the qualification testing and were successfully corrected. The rotary actuator was tested for a total of 40,000 rotational cycles for a nine (9) cycle mission simulation.

Conclusion

The rotary actuator was designed, built and tested to satisfy specific customer requirements. The missions requirements included working conditions of high level vibration, rapid temperature/pressure changes and extreme temperature levels. The testing program verified the unit's capability to meet the challenging mission requirements. The unit has been successfully used on at least three launches.
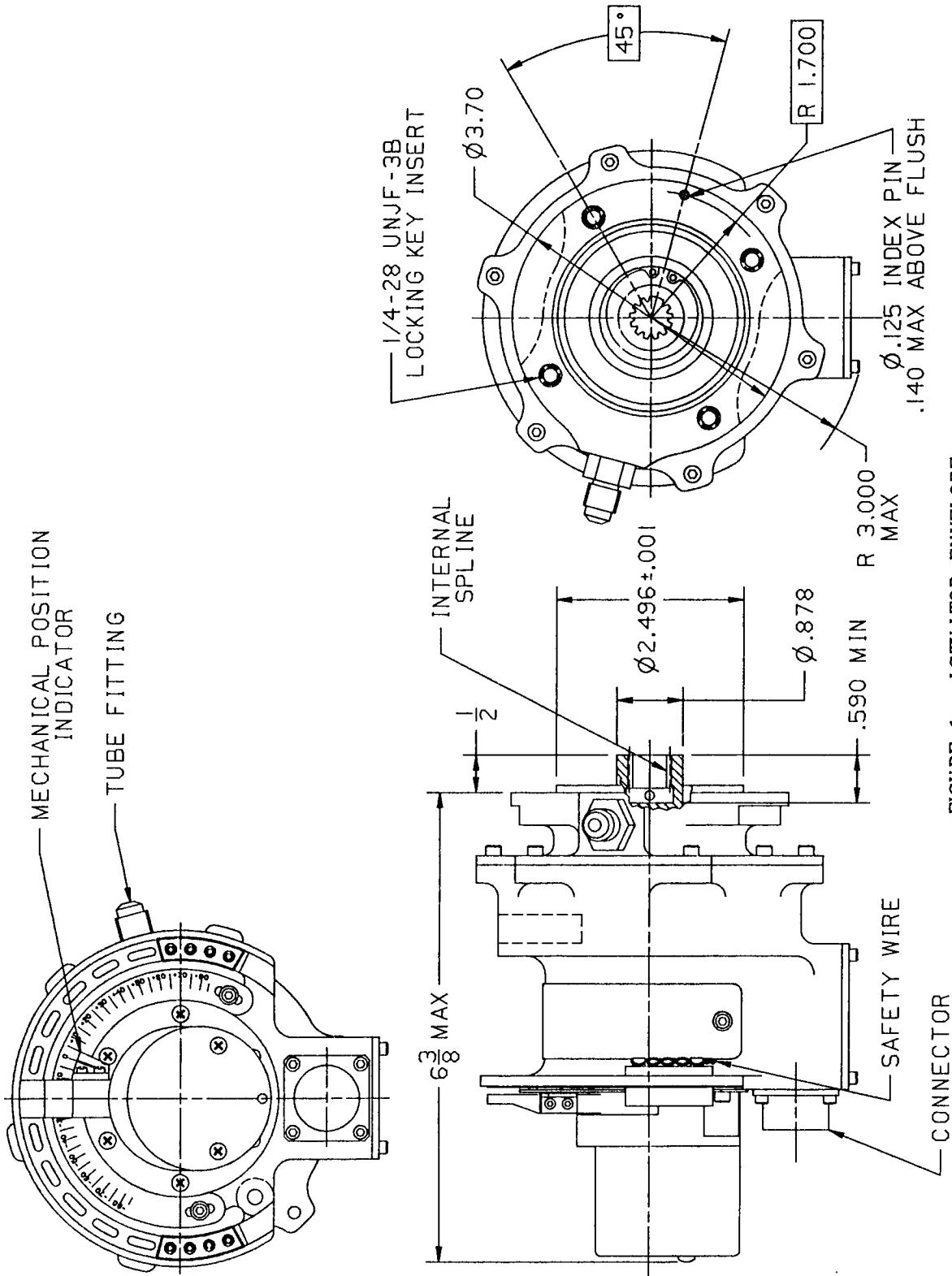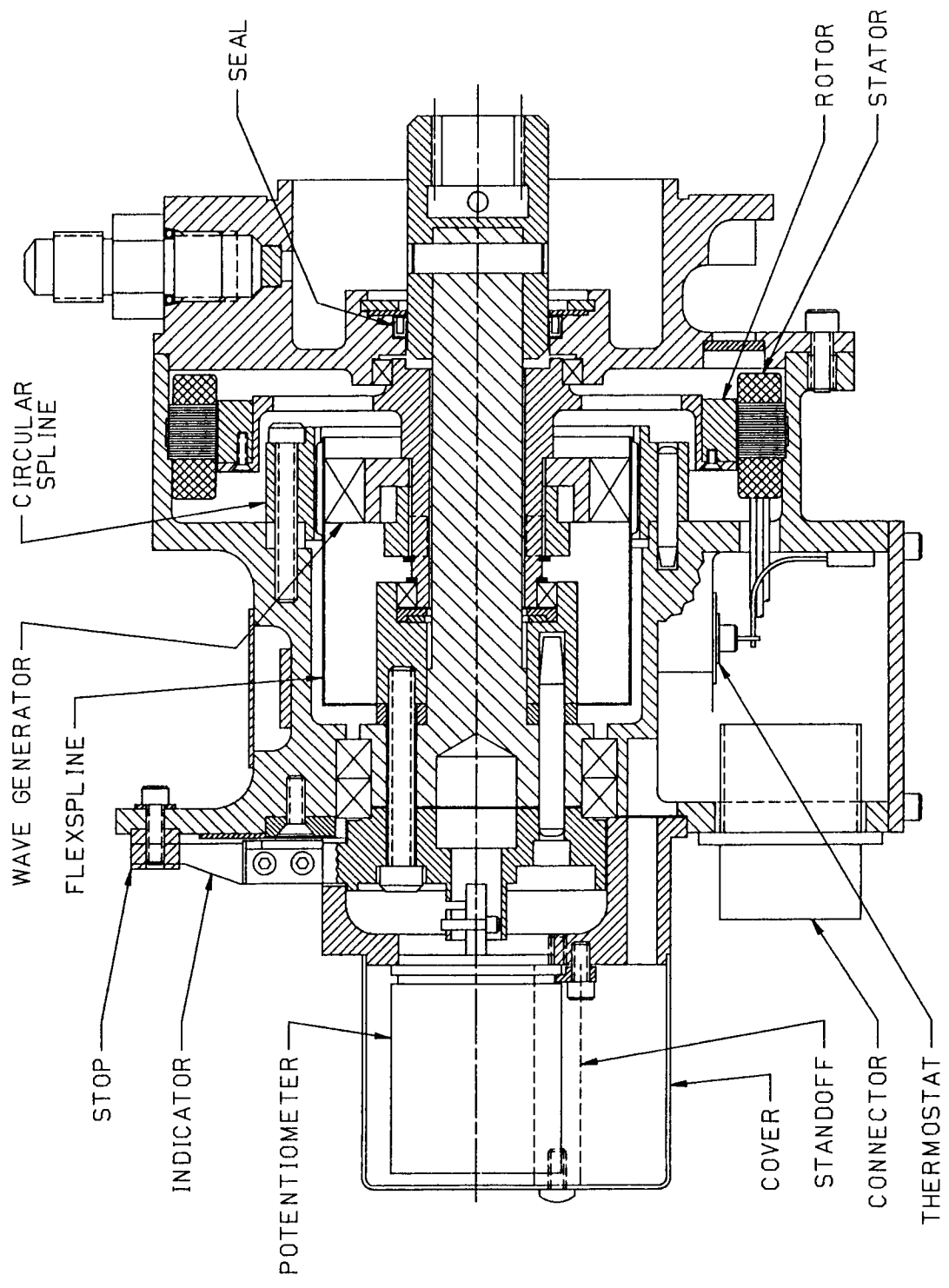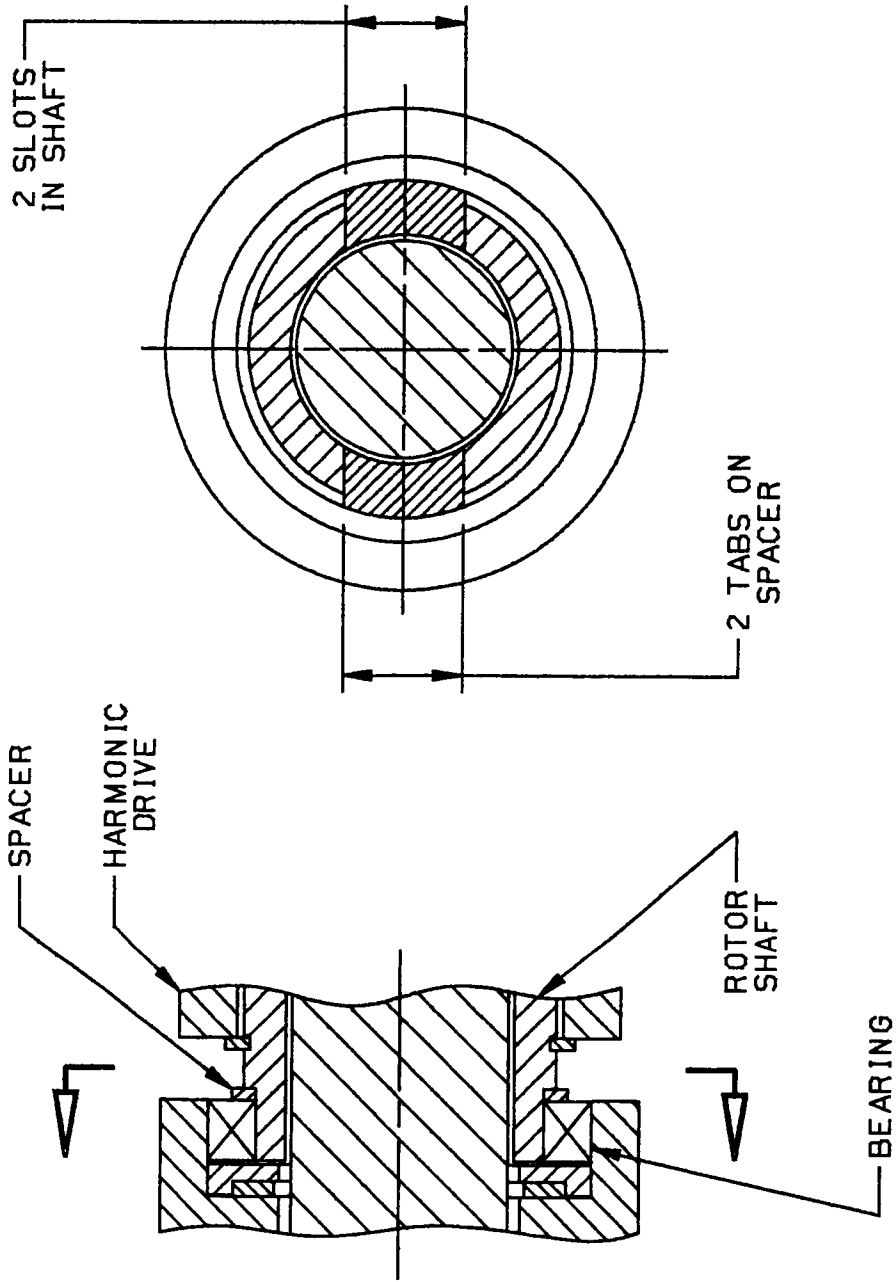
FIGURE 1. ACTUATOR ENVELOPE

45°

R 1.700

Ø3.70

1/4-28 UNJF-3B
LOCKING KEY INSERT

Ø.125 INDEX PIN
.140 MAX ABOVE FLUSH

R 3.000
MAX

INTERNAL
SPLINE

Ø2.496±.001

Ø.878

.590 MIN

$\frac{1}{2}$

MECHANICAL POSITION
INDICATOR

TUBE FITTING

$6\frac{3}{8}$ MAX

SAFETY WIRE

CONNECTOR

189

FIGURE 2. ROTARY ACTUATOR PN 2961041

2 SLOTS IN SHAFT

2 TABS ON SPACER

SPACER

HARMONIC DRIVE

ROTOR SHAFT

BEARING

FIGURE 9. ROTOR SHAFT DETAIL

191
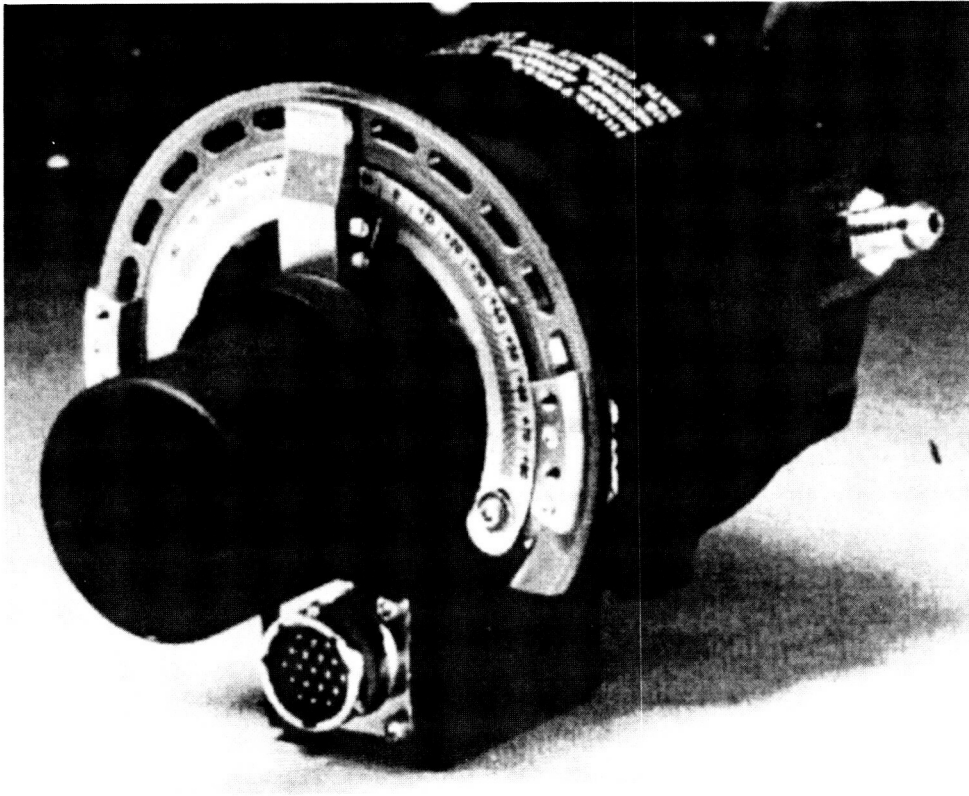
FIGURE 4. ROTARY ACTUATOR 2961041

/ 995/20f59

405765 /5p.

Design, Development and Testing of the X-Ray Timing Explorer High Gain Antenna System

Javier Lecha*, Claudia Woods*, and Minh Phan*

Abstract

The High Gain Antenna System (HGAS), consisting of two High Gain Antenna Deployment Systems (HGADS) and two Antenna Pointing Systems (APS), is used to position two High Gain Antennas (HGA) on the X-Ray Timing Explorer (XTE). A similar APS will be used on the upcoming Tropical Rainfall Measuring Mission (TRMM). Both XTE and TRMM are NASA in-house satellites. The salient features of the system include the two-axis gimbal and control electronics of the APS and the spring deployment and latch/release mechanisms of the HGADS. This paper describes some of the challenges faced in the design and testing of this system and their resolutions.

Introduction

The XTE spacecraft will be launched late in 1995 on a Delta II expendable rocket. The primary mission objective is the study of broad-band spectral and temporal phenomena associated with stellar and galactic systems. To provide a high scientific data rate communication linkage between the spacecraft, the Telemetry and Data Relay Satellite System (TDRSS), and the Ground Tracking Stations, the spacecraft employs two HGAs. Each HGA is stowed during launch, deploying into its operating configuration after the spacecraft finalizes its orbit. Each HGADS utilizes spring/damper hinges, aluminum booms, and pyrotechnic pin puller release mechanisms to stow and deploy each HGA. The function of the gimbal is to track TDRSS and to transfer 2.287 GHz radio frequency (RF) data across the moving interface, maintaining less than 1.5 dB insertion loss through the gimbal. The Gimbal and Solar Array Electronics (GSACE) provide control, commands and telemetry for the gimbal and the solar array drives.

Antenna Pointing System Description

The two-axis gimbal is shown in Figure 1. Each axis is driven by an actuator having a stepper motor with incremental position sensing and absolute home and endpoint reference sensing. The gear reduction is accomplished using a Silk Hat type harmonic drive, in which the mounting flange flares outward to accommodate a larger center hole for harness feedthrough. The 200:1 drive provides 0.0075 degree output motion per motor step. Each actuator has a minimum of 45 N•m of unpowered holding torque.

To accommodate both the XTE and TRMM missions, the X axis cable/harness wrap, shown in Figure 2, is designed to pass 76 shielded #22 and #24 gauge wires and two 4.88-mm-diameter, low-insertion-loss RF cable assemblies through the rotating interface with minimal stress, wear and torque. The rotation range is ±100.5 degrees and the envelope is 184 mm outer diameter and 62 mm in length. The cable wrap was

---

* National Aeronautics and Space Administration, Goddard Space Flight Center, Greenbelt, MD

designed to be modular for accommodation of future missions. For XTE and TRMM the harness is divided into 5 bundles each encased in an outer jacket; one motor, two encoder, and two thermal system bundles. Each bundle and RF cable passes through the 25-mm-diameter throughhole and spirals into its own annular compartment, completely separated from the next harness by a 1-mm-thick plate which forms the bottom of the next compartment. At either end of the cable wrap are caps which provide 0.76-mm-wide labyrinth paths to exclude particulate contamination. Each harness bundle or RF cable is held in place by Uralane 5753, potted into grooves at the rotor entrance and housing exit, and moves in a planar spiral between the two grooves. Prior to assembly, each harness and RF cable is wrapped around a 76-mm mandrel and heated overnight to 70° C to pre-form it into a spiral shape. The Y axis cable wrap is similar to the X axis, but passes fewer wires.

The primary function of the GSACE is to position the two HGAs and the two solar array panels. To minimize cost and complexity, the actuators to be driven are almost identical. The XTE spacecraft attitude and orbital position, along with other required orbital data, is supplied to the Attitude Control System (ACS) computer in the Spacecraft Data System (SDS). The ACS computer determines the desired pointing information and provides this input to the GSACE over the 1773 bus. The key components in the fully redundant GSACE are the MIL-STD-1773 interface and the ACTEL gate arrays. The GSACE was designed in modules to facilitate testing of the gimbals and the solar array. As shown in Figure 3, the box contains a 1773 remote terminal module, primary and redundant modules for the solar array drive, and primary and redundant modules for each of the HGAS systems. Each drive module consists of two Printed Circuit (PC) boards, one of which provides two totally independent paths of 24 volt regulation (one for each motor), as well as motor drive electronics (low power MOSFET). The other PC board contains the command decoding, telemetry buffers, position sensing logic, encoder interface, motor sequencer, and housekeeping logic.

High Gain Antenna Deployment System Description

Both HGADS are shown in Figure 4 in their stowed and deployed configurations. The Upper High Gain Antenna Deployment System (UHGADS) consists of a single linkage boom, a spring/damper base hinge assembly, four snubber/kick-off spring assemblies, and two cone and V-guide combinations of release mechanism assemblies. The boom rotates 94.35 degrees about its base hinge during deployment.

The Lower High Gain Antenna Deployment System (LHGADS) consists of a double linkage boom assembly, a spring/damper base hinge assembly, a spring/damper elbow (boom-to-boom) hinge assembly, four snubber/kick-off spring assemblies, and three cone and V-guide combinations of release mechanism assemblies. It also has a cable to synchronize the rotation the of two linkage booms 135 degrees about their hinges during deployment. The cable moves on a pulley built in to the hinge assembly.

The three hinge assemblies on the XTE HGADS are based on the same design principles. The differences are in the interface and deployment rotating angles. Each assembly is powered by a set of five constant spring leaves. Each set generates about 8.5 N•m of torque. To minimize the deployment impact force at the end of boom travel,

194

a viscous rotary damper is used for dynamic damping. Heaters, thermostats, and multiple layer insulation blankets provide each damper with active thermal control. A torsional-spring-loaded latch is employed in each hinge to provide positive mechanical locking in the deployed configuration. The locking latch also provides additional working energy to the assembly during the last five degrees of rotation. Primary and redundant potentiometers coupled to the rotating shaft of each assembly provide deployment telemetry. A cut-away view of an assembly is shown in Figure 5.

The differences between the three release mechanism assemblies are in the interface and number of degrees of freedom. The main components on each are the housing, the tension/release rod with conical end, redundant release jaws, and two pyrotechnic pin pullers. In the restraint configuration during launch, the tension/release rod is held in place by the two jaws, which are in turn held in place by the two pin pullers. In normal operating mode, both pin pullers are actuated by a pair of pyros to release the two jaws, which release the tension/release rod. Once the rods on all release mechanism assemblies are free, the hinge assemblies rotate the booms into their deployed configurations. Mechanical redundancy ensures that the successful actuation of either pin puller will release a jaw and thus the tension/release rod. Each pin puller is powered by a single pyro (pressure cartridge) having double bridgewires for electrical redundancy. A cone and V-guide release mechanism assembly combination is used for each deployment system to minimize the induced launch and thermal loads on the deployment systems. A release mechanism assembly is shown in Figure 6.

The snubber/kick-off spring assembly, shown in Figure 7, provides overall system stiffness at the stowed configuration, as well as extra kick-off energy at the beginning of the deployment process. Each snubber kick-off spring assembly provides approximately 26 N of deployment (kick-off) force. The position of the four snubber kick-off assemblies are selected to provide maximum stiffness of the HGADS.

HGAS Qualification Testing

Qualification testing included pointing, electromagnetic interference and compatibility, vibration, thermal vacuum, deployment, range of motion, and threshold torque.

One of the challenges to the testing program was the development of a gravity (G) negation system which allows economic and efficient deployments of the two HGAS without the costly and time consuming optical alignment operation usually required for each test. The primary function of the HGADS G-Negation System is to null the gravity force on the system during deployment tests. It is comprised of three assemblies; the honeycomb table, the air pad assembly, and the active air piston suspension assembly.

The honeycomb table provides the required flat and level surface for the air pads. Its features include adjustments for local flatness and table height, overall table leveling, light weight, and flexibility of size and configuration. It is also relatively inexpensive to fabricate and assemble. Each table module is made of a 1.2 m x 2.4 m honeycomb panel, a support structure, 15 flatness adjustment mechanisms, and an overall table

leveling mechanism. The honeycomb panel is commercial, readily available at various distributors around the country. The table support structure is a welded Aluminum 6061 frame which includes 15 pads with flatness adjustment mechanisms for mounting the honeycomb panel. Each of the four table legs has overall table leveling and height adjustment (both coarse and fine) mechanisms. The total weight of each honeycomb G-negation table assembly module is about 311 N. Multiple honeycomb table modules can easily be joined in various configurations to meet the demand of the complex test configurations of other spacecraft deployable systems.

The main function of the air pad (or air bearing) assembly is to provide the necessary lift to minimize travel friction for the deployment systems. Air pad assemblies are very compact and light weight, have high but efficient lift, and are self aligning. Each air pad is about 76 mm in diameter and has a center air feed through a custom-made spherical bearing which provides self alignment. The air-pad surface is coated with a layer of dry lubrication. An extensive development program optimized the air pad size, weight, lift, and air flow efficiency. Multiple air bearings can be combined to provide greater lift for supporting the deployment tests of larger or heavier deployable systems.

The active air piston suspension system provides a constant negative gravity force and actively compensates for high and low points on the surface of the G-negation table. Previous air pad G-negation systems required a critical optical alignment operation for each test set up to ensure that the deployment system is precisely parallel to the surface of the table throughout the deployment path. The active air piston suspension system was designed to relax the parallelism requirement (tolerates up to 6.35 mm), eliminating the need for alignment for each test set up. A simple mechanical air flow closed-loop feed back system is used. The system has a built-in load cell and can be easily adjusted to compensate for gravity for various deployable system weights. Figure 8 shows an active suspension air pad assembly.

.The active suspension air pad, the flexible and light weight honeycomb table, and the overall design of this G-Negation system have enabled the economic and efficient performance of the qualification and acceptance testing program on the HGADS.

Actuator Life Testing

The original actuator included a Silk Hat type harmonic drive comprised of a 304L stainless steel (SS) flex spline, 17-4 PH SS circular spline, and 440C CRES wave generator bearing. Based on successful heritage using Pennzane 2000X oil with 7% lead napthenate by weight on harmonic drives using these materials, this same oil/additive combination was chosen to lubricate the gear mesh, the flexspline bore, and all of the bearings and phenolic retainers. As most of the previous data had been accumulated on Cup-type harmonic drives, a life test of an actuator was performed. The results of this life test demonstrate the value of early life testing of mechanisms at the component level. It is fortunate that a life test was performed in time enough to recover with minimal impact to the overall program schedule.

The qualification actuator underwent all required environmental testing. It then accumulated 1,250,000 degrees of output travel, 1.25 times the expected XTE mission

life. The stepping pattern simulated operation: a tracking motion of 0.0026 $^{rad}/_s$ was swept ±10 degrees 13 times followed by a slew at the maximum speed of 0.026 $^{rad}/_s$ to both ends of travel. The thermal vacuum chamber was cycled every 3 to 4 days between 0°C and 40°C. The actuator passed all post-life test functional tests, including threshold voltage. Upon disassembly of the unit, a large number of metal particles were found in the flexspline bore and teeth, as well as particles that migrated elsewhere. There were two heavily gouged lines in the flexspline bore where it contacts the wave generator bearing outer diameter. The lines ran the entire circumference of the bore, located approximately at the bearing corners (Figure 9). Except for some darkened lubricant in the gouge marks, the rest of the bore surface looked dry. The bearings had no visible particles inside and their lubricant looked good: all surfaces were wet and undarkened with a good meniscus at the contact. It was also noticed that the wave generator bearing had moved approximately 2.5 mm axially inward, drawn toward the diaphragm end of the flexspline. The gear teeth also showed excessive wear. The most severe wear was near the location of the wave generator bearing outer corner (nearest the gear end of the flexspline), where the teeth were only about half their original thickness. The wear grew progressively less in both axial directions. The teeth were wet with lubricant, but some of it was darkened.

A detailed investigation determined this information:

1. The Cup type harmonic drive which spawned most of the heritage assumptions had a flexspline made of drawn 304L SS tubing already half hardened through cold working (no longer available). The still relatively soft 304L flexspline was further hardened using proprietary processes that did not significantly affect the dimensions. This process is not available to the manufacturer of the Silk Hat type harmonic drive. Consequently, the flexsplines used were very soft for a gear application using space lubricants.

2. The wear mark for a Cup type harmonic drive is generally a single wear path near the edge of the splines, a faint mark where run-in occurs and a deeper mark further in where operation occurs. None of the experienced harmonic drive consultants had ever seen a two path wear mark such as had occurred. Later tests using different materials showed the same two path pattern. The phenomenon is not completely understood.

3. The 440C wave generator bearing had many inclusions on the outer diameter surface and the corners were chamfered instead of rounded.

4. A torsional stiffness greater than 13558 $^{N \cdot m}/_{rad}$ (120,000 $^{in \cdot lb}/_{rad}$) was originally requested. The qualification actuator stiffness was 28246 $^{N \cdot m}/_{rad}$ (250,000 $^{in \cdot lb}/_{rad}$). This higher stiffness may be a life limiting factor. It was determined that stiffness could be as low as 9039 $^{N \cdot m}/_{rad}$ (80,000 $^{in \cdot lb}/_{rad}$) and maintain acceptable performance.

5. The Cup type harmonic drive has a shoulder to limit the axial motion of the wave generator bearing. The original Silk Hat design had no such shoulder.

It was decided to pursue two parallel paths. The first was to test a redesigned Silk Hat drive and the second to test a T-Cup type harmonic drive design, similar to the Cup

design except that the output flange first turns inward and then flares outward to accommodate a larger throughhole. Included in each specification was a one hour each direction run-in at 178 $rad/_s$ in transmission fluid. The parameters of each design are:

Redesigned Silk Hat

- 4340 vacuum melt flex spline, Rockwell hardness between 34 and 38.
- 17-4 PH SS circular spline, Rockwell hardness between 28 and 32.
- 52100 steel wave generator bearings, outer diameter Rockwell hardness of 57 to 60.
- 13558 $N{\cdot}m/_{rad}$ (120,000 $in{\cdot}lb/_{rad}$) ±30% stiffness, agreement to work to low end.
- Addition of a shoulder at the wave generator inner race to limit axial motion.
- Could not get rounded corners on wave generator bearings - straight chamfers.

T-Cup

- 15-5PH SS flex spline.
- 15-5PH SS circular spline, melonited for additional hardness.
- 440C CEVM SS wave generator bearings, with radius.
- Desired low stiffness, but could not get tight tolerance; stiffness ranged from 15818 to 39544 $N{\cdot}m/_{rad}$ (140,000 to 350,000 $in{\cdot}lb/_{rad}$).
- Bearing shoulder.

The lower stiffness harmonic drives of both the redesigned Silk Hat and the T-Cup showed some evidence of a small varying amount of backlash as received. In the present case the amount was acceptable for the program requirements.

The two designs were first tested against each other at ambient pressure and temperature with a reversing load, ±20 degrees travel at 0.026 $rad/_s$ over a total of 500,000 output degrees. At this point in time, production of a grease version of the Pennzane, Rheolube 2000, had matured. Based on previous experience with harmonic drives and other lubricants, it was decided that the grease version might be more successful than oil at the flexspline bore and gear mesh. Therefore, Rheolube 2000 with 3% lead napthenate by weight was used in the gear mesh and on the flexspline bore and wave generator outer diameter. The bearing internal lubrication scheme remained unchanged. The redesigned Silk Hat tested had a stiffness of 11298 $N{\cdot}m/_{rad}$ (100,000 $in{\cdot}lb/_{rad}$). After the test, its mesh looked good with plenty of grease evident, but the grease on the bore had disappeared. The surface felt somewhat oily but no film was evident. Other than the lack of oil, the bore looked fine. There was a two band pattern but it was a very light burnish (like a run-in mark), and there was no darkened oil. The first T-Cup design tested was one of very high stiffness, 39770 $N{\cdot}m/_{rad}$ (352,000 $in{\cdot}lb/_{rad}$). After 500,000 output degrees, the lubrication in the flexspline bore was extremely dark brown and analysis showed the presence in the oil of many 0.127 micrometer (5 micron) flat particles of 15-5PH SS. The grease at the ends of the teeth was darkened but was normal within the mesh.

Based on the poor performance of 100% grease at the flexspline bore (disappearance of grease on the Silk Hat and severe darkening on the T-Cup), the lubrication at the

bore was changed to a 50/50 grease/oil slurry with a grease dam outside the contact area. The gear mesh was lubricated with 100% grease. The redesigned Silk Hat was relubricated and accumulated a subsequent 1 million output degrees. The bore and bearing outer diameter came out looking nicely wet with only slightly darkened oil (as the test was done in atmosphere, depletion of antioxidants may have caused the darkening). The gear mesh had an ample supply of grease of a good oily texture and there was no visible wear on the teeth. The lubricant was slightly darker at the teeth edges than in the mesh. The two band burnish marks had become slightly more prominent, but there was no serious wear. A lower stiffness T-Cup, 17626 $N{\cdot}m/_{rad}$ (156,000 $in{\cdot}lb/_{rad}$), was also tested with a 50/50 slurry at the bore. After 1 million output degrees, the lubricant in the bore was slightly darkened but oily in texture. The mesh lubricant was also slightly darkened but oily, being somewhat darker at the edges of the teeth. There was no evidence of tooth wear. This harmonic drive also had a two band burnish pattern corresponding to the wave generator bearing corners, but the marks were extremely light and the original machine finish was still evident.

The decision to use the redesigned Silk Hat drive was based partly on the ease of retrofit and partly due to the difficulty of manufacturing low stiffness T-Cups. The final design implemented a 50/50 grease/oil slurry at the flexspline bore and all grease in the gear mesh. The qualification actuator was rebuilt using the same Silk Hat used in the ambient testing (relubricated) and this actuator was put through the original thermal vacuum life test. The gear mesh and the grease looked very good. The grease was oily in texture and only very slightly darkened. The bore had a nice oily film which was also nearly its original color. There was no evidence of a change in the two banded burnish marks. The unit was relubricated and closed up in order to accumulate the required travel for TRMM. It has presently accumulated 7 million output degrees out of the required 10 million with an inertial load in an argon purge at room temperature.

Radio Frequency (RF) Cable Wrap Life Testing

From the start there was a concern about the flexing of the RF cable assembly. To maintain the low loss performance of the assembly the manufacturer recommends that the bend radius be kept to greater than 25 mm for any flexing portion. In order to meet the range of travel and outer diameter requirements, the largest minimum bend radius possible is 38 mm. An extensive life test program was started to investigate the effect of this type of flexing. A cable was mechanically flexed for 80,000 cycles, a cycle being a sweep to both ends of travel and back (±100.5 degrees), at least four times the maximum life requirement of XTE or TRMM. The test fixture is shown in Figure 10. The test was run at ambient for the first 1000 cycles, 60° C for the next 24,000 cycles, and -10° C for the final 55,000 cycles.

Before and after cycling, the RF cable was subjected to visual (magnification X10) and X-Ray inspection, and insertion loss, voltage standing wave ratio (VSWR), time domain reflectometry (TDR), and DC resistance testing. The insertion loss, VSWR, and TDR tests characterize the cable's performance as well as the integrity of its shielding. A 50-ohm load placed at one end of the cable measured VSWR periodically during the test as well. There was no significant change in VSWR over the 80,000 cycle test or in the pre and post insertion loss, VSWR, TDR, and DC resistance measurements.

The most interesting results were seen in the X-Ray inspection. Figure 11 shows a section of cable under X-Ray prior to cycling. The shielding is wrapped helix fashion such that every inch of cable is covered with 2 to 3 layers of silver plated copper foil, which appears in the X-Rays as a very thin helical line as marked by the arrow. When a portion of the shielding begins to spread apart, the X-Ray shows it as a broader helical line. Figure 12 shows a portion of cable after 80,000 cycles. The arrow shows the location of the tightest bend radius. The cable to the left of the arrow was not bent as tightly. It can be seen that at the tight radius position the shielding wrap has begun to spread apart. The level of shielding at this point was still one to two layers at all places, which is enough to maintain the cable performance. No evidence was found of center conductor migration or crinkling.

Visually, the only evidence of some degradation in the cable was the appearance of some small dark spots between the weave of the outer mechanical braid. This also appears mainly in the areas of tightest flexing and is believed to be wear debris buildup from either the mechanical braid or the shield. There was also some wear debris of the outer Teflon jacket that came from the cable rubbing both against the flat fixture surface and against itself. The amount of debris was not excessive and was deemed acceptable. The outer jacket was not worn through in any location, nor was there any evidence of dents, kinks, or bent pins.

A subsequent test to 40,000 mechanical cycles was done on one RF cable in flight-like hardware, followed by a 40,000 cycle test of two RF cables and all of the harness bundles in flight-like hardware. The temperature was continuously cycled between 60°C and -10°C, soaking for one hour at each temperature. Approximately 70 thermal cycles were accumulated. The results were similar to the above except that there was less broadening of the helix pattern under X-Ray and less debris generated.

Harness Wrap Life Testing

To satisfy the size and motion requirements, the harness bundles had to be less than 8 mm in diameter. They also needed an outer covering which would remain flexible over the temperature and motion range. Three tests were run to determine a suitable candidate for Life Testing, using the same fixture as for the initial RF cable test. The temperature was cycled between -10°C and 60°C and the pressure was ambient.

The first test used a netting type material called EXPANDO to jacket a bundle of twisted shielded pairs. At 20,000 cycles, tears had developed in the jacket, and at 27,500 cycles torn fragments of the weave were interfering with other layers of the spiral. The test was stopped. The second test case was a Viton heat shrink tubing over the bundle. The harness rotation at room temperature looked smooth. At cold and hot temperatures however the harness experienced continual hangups which stalled the 50 N•mm stepper motor. At the cold temperature, the harness spiral shrunk inward against the rotor piece, causing an inward force which increased torque as the motor tried to pull away from the tightest position. At the hot temperature, the spiral expanded against the outer wall, causing an outward force which increased torque as the spiral neared its fully unwrapped position. The test was discontinued at 13500 cycles.

The primary candidate had four shielded, polytetrafloroethylene (PTFE) covered bundles surrounded by an outer PTFE jacket. The harness reached 80,000 cycles without incident and periodic visual checks showed the behavior of the harness to be well defined and smooth. There was no significant change in maximum torque over cycling. The torque ranged from 16 N•mm to 24 N•mm over the temperature range before and after the 80,000 cycles. There was some PTFE debris, but at an acceptable level. The outer jacket had developed two very small holes and had a few flattened spots. Inspection showed no penetration of the inner PTFE jackets. There was no change in electrical performance, which included milliohm resistance and dielectric withstanding voltage.

The performance of the PTFE jacketed harness was deemed acceptable for the XTE/TRMM life and it was chosen for flight. Five harness and two RF cables were next cycled in flight-like hardware to 40,000 mechanical and 70 thermal cycles (Figure 13). Post test inspection found no degradation of electrical performance or holes in the outer jackets. Some PTFE debris was evident but minimal.

Gimbal Life Testing

A life test of a fully functional flight-like gimbal with equivalent inertia load is presently underway. The test is being conducted under vacuum conditions and the gimbal temperature is cycled between 5°C and 37°C. The X axis only is being rotated in a pattern representative of on orbit operation. The life test will be stopped periodically to do threshold and pull-in rate testing. After the accumulation of the XTE life, the X axis actuator will be removed and partially disassembled to ascertain the health of the unit. It will then be reassembled and continue until the TRMM life has been accumulated.

Conclusion

Testing is the key in every mechanism. Early Life Testing of mechanical components can uncover unforeseen problems while there is still flexibility for change. Keeping testing in mind during the design is also important. The GSACE modular design made the HGAS testing very time and cost efficient. Thorough and timely test planning can reduce overall schedule, as is shown in the case of the HGADS G-Negation system.

RF CABLE
ASSEMBLIES

CABLE/HARNESS
WRAP ASSEMBLY

ACTUATOR
MOUNTING FLANGE
HARDSTOPS

ACTUATOR
OUTPUT FLANGE
HARDSTOP

-Y Y-AXIS +Y

ACTUATOR
OUTPUT FLANGE
HARDSTOP

-X X-AXIS +X

HARNESS

CABLE/HARNESS
WRAP ASSEMBLY

ACTUATOR
MOUNTING FLANGE
HARDSTOPS
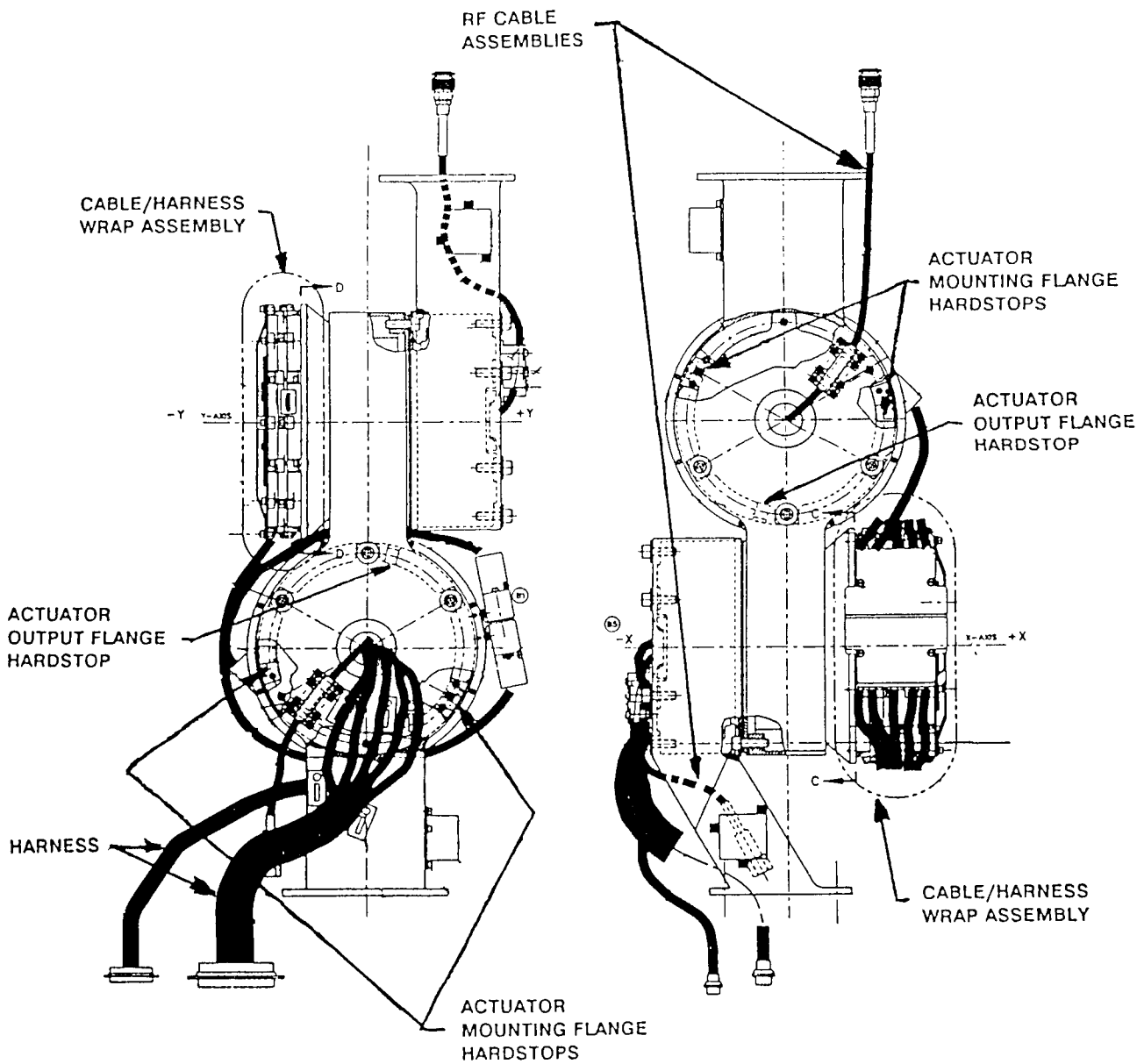
Figure 1. Two Axis Gimbal - XTE Configuration

202
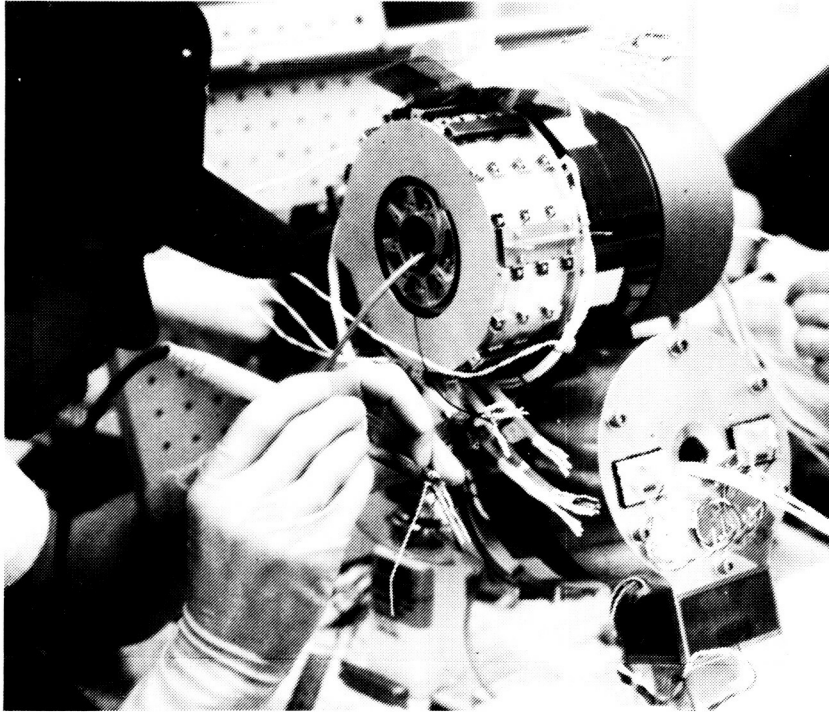
Figure 2. Gimbal Cable/Harness Wrap Assembly
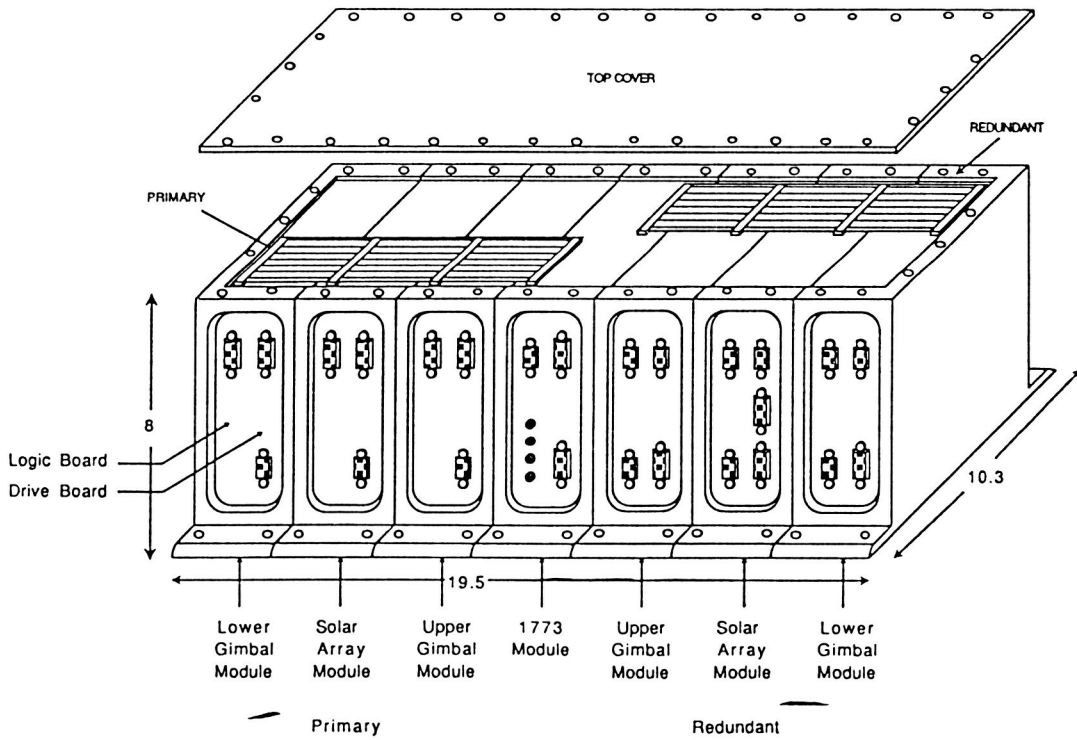
Figure 3. GSACE Electronics Box
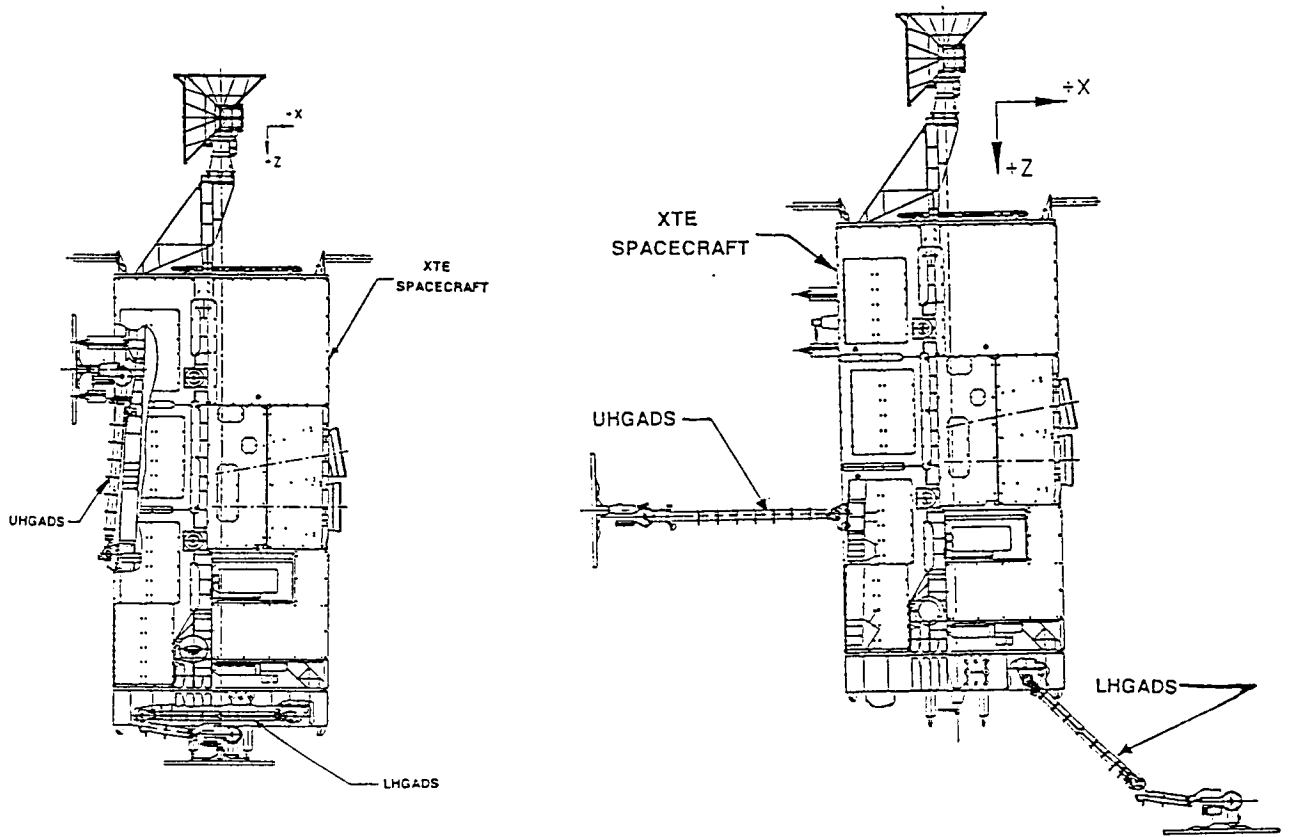
HGAS at Stowed Configuration   **HGAS at Deployed Configuration**

Figure 4. XTE Spacecraft
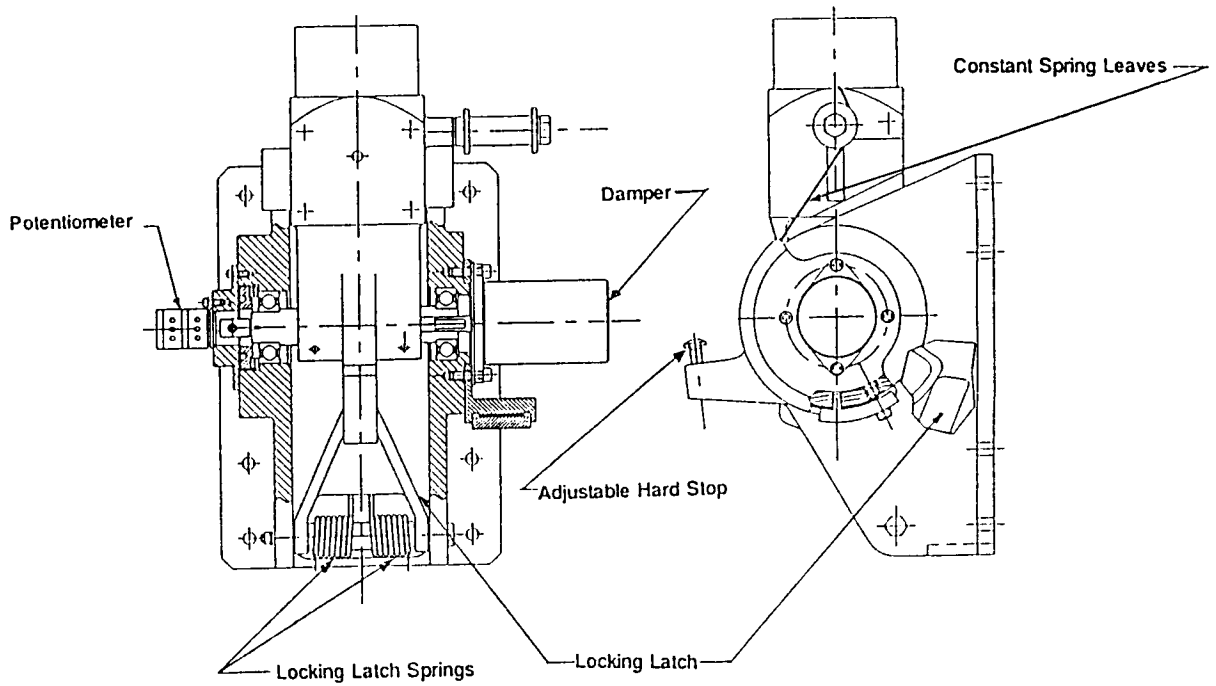
Figure 5. UHGADS Base Hinge Assembly
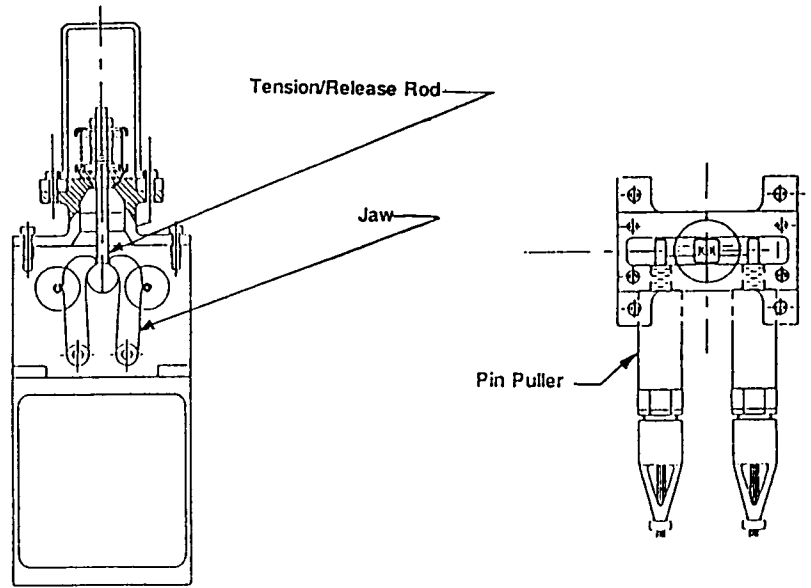
Figure 6. Release Mechanism Assembly
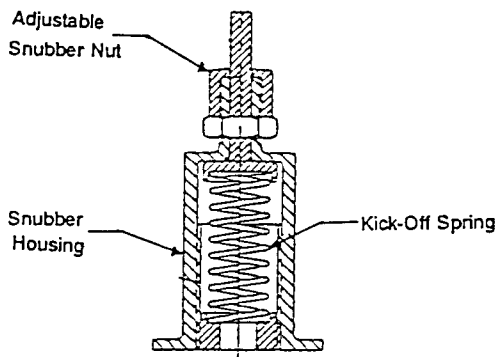
Figure 7. Snubber/Kick-off Spring Assembly
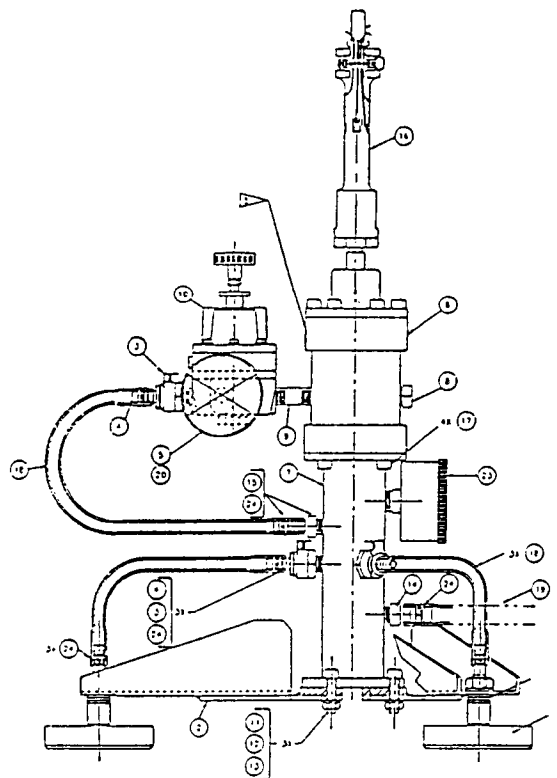
Figure 8. Typical Air Pad and Air Active Suspension Assembly

Figure 9. Harmonic Drive Flexspline After First Lifetest
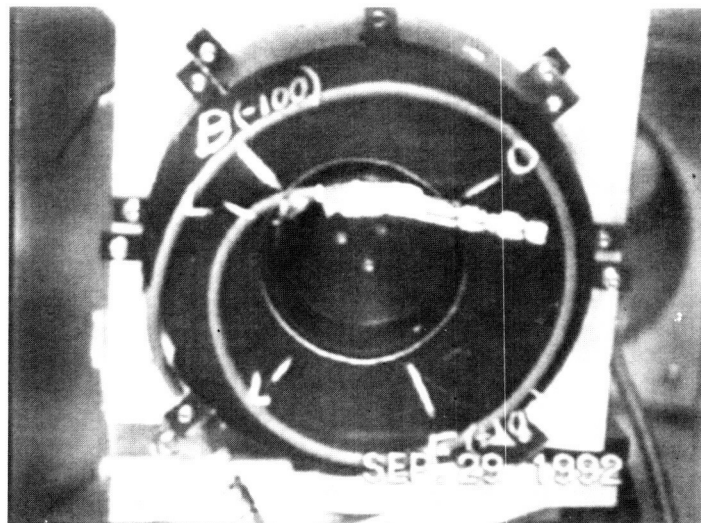
Figure 10. RF Cable Lifetest Fixture
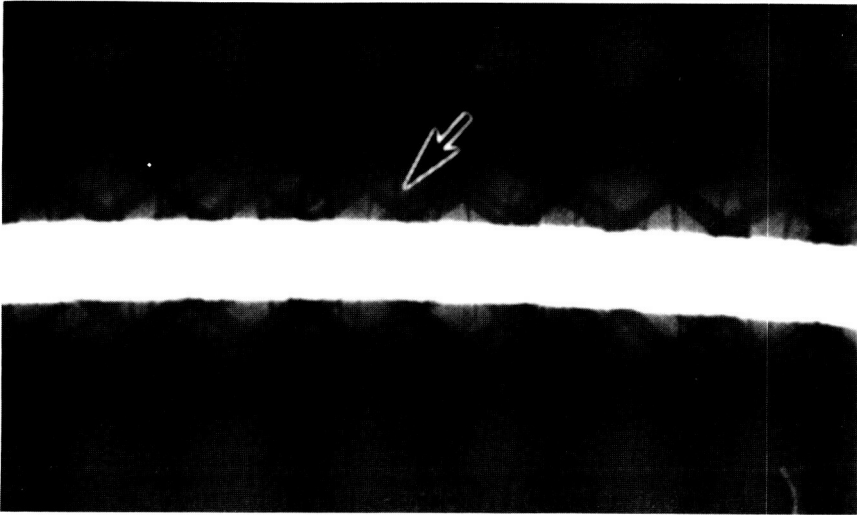
Figure 11. Pre RF Cable Lifetest X-Ray
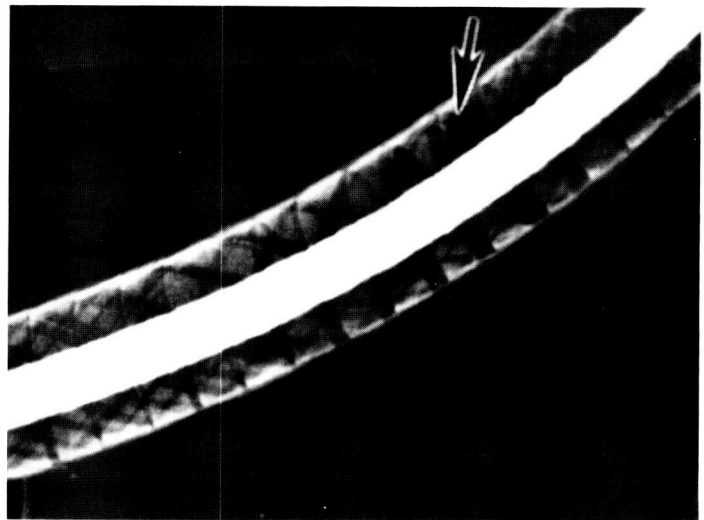
Figure 12. Post RF Cable Lifetest X-Ray
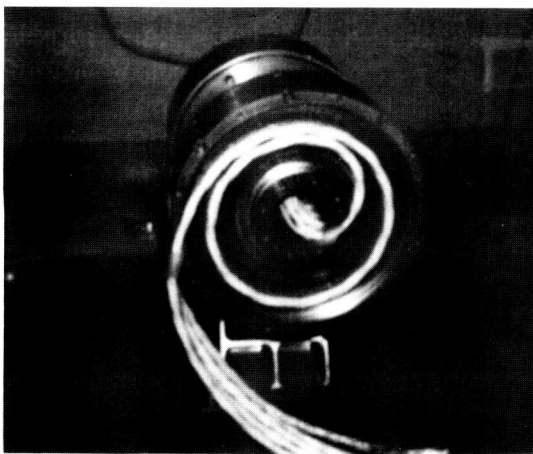
Figure 13. Final Harness Wrap Lifetest

The Solar X-ray Imager Vacuum Door Assembly

Donald H. McQueen, Jr.*

Abstract

This paper discusses the design and development of the Solar X-ray Imager (SXI) vacuum door assembly (VDA). Rationale for the type of mechanism, seal, and prime mover is covered. An overview of the testing performed is included.

Introduction and Background

The SXI is a satellite-based x-ray telescope. SXI will monitor solar activities so that resultant magnetic disturbances can be forecast for earth sooner and more accurately. SXI is launched on an Atlas II vehicle and is mounted on the solar array boom of the Geostationary Operational Environmental Satellite - M (GOES-M). GOES-M is an existing design, so SXI must perform within GOES-M resources. This limits SXI severely in redundancy, size, and mass. These are dominant factors in the design of the vacuum door assembly.

SXI is a class C instrument. NASA applies class C requirements to a payload that is generally of medium priority, and does not involve any possibility of human injury if the payload should not function as designed. Class C requirements leave much to engineering judgment, including level of testing and type of testing. As a class C instrument SXI is designated a protoflight instrument, which means the project has no dedicated qualification unit. All qualification and acceptance testing are done on the flight (or protoflight) system.

SXI requires a vacuum door because of a sensitive camera component (a micro channel plate, or MCP). This component can only be operated safely at a pressure of $1.33 \cdot 10^{-7}$ kPa (10^{-6} torr) or less. The vacuum door contains a window used in ground testing of the camera. In this ground testing, ultraviolet light illuminates the camera to determine the charge coupled device health before launch. The door remains closed during ground operations to preserve a protective environment for the camera MCP. A ground command opens the vacuum door on orbit after sufficient time for instrument and satellite outgassing.

The operational requirement of the vacuum door is a one time actuation on orbit. The door's purpose is to protect the camera from the ground environment and from on-orbit outgassing of the instrument. The only requirement for reset exists for ground testing. The mechanism is low profile to fit within the space envelope available. The envelope is approximately 50 x 13 x 178 mm (2 x 0.5 x 7 inches). The mass requirement is 0.454 kg (1 lb). Maximum power available is 10 watts. The window must transmit ultra violet light. The door must seal so that ground support equipment can pump down the camera housing to 1.33×10^{-7} kPa (10^{-6} torr). The design outlined below was chosen

---

* George C. Marshall Space Flight Center, Huntsville, AL

to provide the most simple and lowest cost mechanism that would perform the task reliably within the requirements stated above.

The limitations of the available GOES-M resources and the designation of SXI as a class C instrument dictated the design philosophy taken for this mechanism. This mechanism is a simple, rugged, relatively low cost design. No redundancy was incorporated other than the redundant heater elements of the paraffin actuator. Care is taken to use proven and already qualified elements wherever possible. The mechanism is tested thoroughly at the component level before system integration.

Basic Design

The mechanism can be divided into three different areas: the prime mover, the latch, and the carriage. Each interacts with the other to successfully open the door. The prime mover applies force to the latch. The latch restrains the carriage system when the door is closed, and applies opening force to the carriage system when the prime mover is energized. The carriage system for the door/window assembly of the mechanism is a slider-crank mechanism. Figure 1 shows an exploded view of the device.

The prime mover applies the opening force to the latch, which applies force to the carriage assembly. The prime mover selected for this application is a paraffin actuator. A power supply applies voltage to the actuator heaters. The paraffin goes through a change of state (solid to liquid). The paraffin applies hydrostatic pressure to an output pin. This particular paraffin actuator (or linear motor) outputs 222 N (50 lb) nominally, requires 10 watts, and is approximately 56.7 g (0.125 lb) in mass.

The latch of this design performs two functions. A cut out in the latch captures a pin in the carriage assembly. The latch restrains the door in the closed position. The latch also transfers the opening force of the prime mover to the carriage assembly (see Figure 2). An extension spring provides reset force for the actuator and latch.

The slider- crank mechanism was chosen for the carriage system. The profile of movement for this mechanism is low and fits in the required envelope (see Figure 3). The initial movement of the door is normal to the sealing surface; thus the seal loading reacts through the carriage system. A torsion spring actuates the carriage after de-latch. The torsion spring attaches to ground bracket and the input link. The design has liberal clearances so that no thermal expansion problems are encountered.

The VDA uses a gask-o-seal design for the primary seal. The material is viton (fluorocarbon). The crown height is 0.38 to 0.51 mm (0.015 to 0.020 in). The VDA utilizes the gask-o-seal design for several reasons. The door would have to be reset on the ground, and if this operation were to be remote the seal would have to be reusable (i.e., elastomer). The gask-o-seal is molded in place and can be formed in various shapes. The high contact stress generated when the gask-o-seal is compressed reduces overall permeability of the seal material. NASA has a long history of use and a high confidence level in the gask-o-seal design.

Development Testing

A development model was fabricated in December of 1993 (see Figure 4). This model was fabricated to test the basic design and to test seal material compatibility. The development unit underwent functional, vibration, and thermal vacuum tests. The functional tests were performed at room temperature and ambient pressure. The device operated a total of 40 cycles. The device was checked for leakage regularly to determine the effect of seal or mechanism wear. No significant changes in ultimate leak rate were recorded during these tests. A random vibration test was performed at the expected flight levels. Functional tests and leak checks were performed before and after. No anomalies occurred.

The VDA experienced trouble in the thermal vacuum test that resulted in design changes. The actuator and heater arrangement for the development model proved to be inadequate for this application. The actuator was low cost, low mass, and had high output force. However, the heater arrangement (externally mounted) was inefficient and the paraffin seals (shaft seals) were inadequate for cleanliness requirements. The design also lacked adequate instrumentation to signal the open position. The lack of these features resulted in long actuation times at cold temperature, contamination of the device through paraffin leakage, and damage to the device because of actuator "overstroke."

In addition to the problems discussed above, the lack of a remote control for door reset proved to be troublesome. The lack of a reset system lengthened the down time on thermal vacuum testing. The test chamber had to return to ambient temperature and pressure to reset the door by hand. This changed the time between cycles from a few minutes to a few hours.

Seal testing was an important part of development testing. Seal testing included outgassing/ contamination tests, ultimate leak rate tests (comparative), and compression effect on ultimate leak rate. Two different seal materials were tested for contamination per MSFC-SPEC-1443. MSFC-SPEC-1443 outlines testing procedures to determine material compatibility with optical systems. The two materials of study were a butyl rubber compound and a viton (fluorocarbon) compound. The viton was chosen because the leak rate was very similar to the butyl and the viton was much more compatible with optical systems. A test was conducted to find the effects of seal compression on ultimate leak rate. The results showed a considerable effect for the first 0.20 to 0.25 mm (0.008 to 0.010 in) of compression, but not much effect for the last 0.13 to 0.18 mm (0.005 to 0.007 in). From this series of tests come the determination of seal material and nominal compression of the seal for minimal loads reacted through the assembly.

Engineering Model

The next VDA to be designed and fabricated was the engineering model (EM). The EM design incorporated changes to alleviate some of the problems described in the last section. A new paraffin actuator that fit the design requirements more closely was

selected and procured. A sensor was added to the VDA to signal door actuation. A remote reset feature was incorporated for ground operations and testing.

The paraffin actuator chosen for the EM showed three improvements from the development model actuator. The EM actuator heaters are internal to the actuator and are in direct contact with the paraffin. The cavity in which the paraffin resides is hermetically sealed using a boot seal. The EM actuator has a shear disk arrangement that limits the output force to approximately two times the nominally rated output. Figure 5 shows the EM actuator installed on the developmental vacuum door.

The sensor added to the EM vacuum door assembly was a military standard sub-miniature switch. The switch is hermetically sealed. Exposed surfaces are stainless steel. The sensor is used on orbit to determine when to discontinue power to the actuator.

The remote reset feature was added to aid in ground testing. The return arm of the mechanism attaches to the input link of the carrier system. A flexible shaft actuates the return arm. The flexible shaft penetrates the optical bench of the telescope assembly and connects to a rotational feed through in the test chamber wall.

Engineering Model Testing

Some of the same testing was conducted on the development model and EM vacuum door assemblies, but with different objectives. As an engineering model, this unit was meant to unofficially qualify the design of the VDA. In the development program, changes are expected; and the results influence fundamental design decisions.

The EM vacuum door underwent four tests at the subsystem level: random vibration, thermal vacuum, thermal cycle, and life cycle tests. The random vibration test was conducted to the levels shown in Table 1. A functional test before and after (and leak checks) were the pass/fail criteria for the test. A twenty-four cycle thermal test was conducted in conjunction with a thermal vacuum test. These tests proved survivability and functionality at the expected flight temperatures. The criteria for these tests are shown in Table 2. The test program included life cycle testing to prove the ruggedness and durability of the design. The EM vacuum door operated approximately four times the expected duty cycle of the flight unit. The life cycle test had a duration of sixty cycles. The life cycle count included operations required for other tests.

The test program for the EM VDA was very successful. However, EM testing found one deficiency. During the thermal vacuum test, the operator left power engaged to the paraffin actuator longer than design parameters specified. This error resulted in the fail safe of an actuator and damage to the vacuum door. There are two reasons for the incident described above. The system level (i.e., the control circuit or operator) should have shut the device down before any damage was done to the mechanism. In the event of a system failure, the paraffin actuator should not have had enough output to damage the latch mechanism. One positive result of this incident is that the actuator did not release contamination even after being pushed well beyond design limits. Two changes will be implemented: 1) an automatic cut-off in the control logic of the SXI

system, and 2) the de-rating of the paraffin actuator to a 111 N (25 lb) nominal output instead of the original 222 N (50 lb) nominal output. Even if the control circuit fails, the actuator will fail safe before any harm. This is less important on orbit, since the door operates only one time. However, if a failure of this type occurs during testing it is necessary only to replace or refurbish an actuator rather than replace and re-qualify the whole VDA mechanism again. There is also less risk to the camera since the door could be closed again to protect the camera while actuator change out is accomplished.

Conclusion

The Solar X-ray Imager vacuum door assembly is a simple, low cost, reliable mechanism. The basic design is three very familiar mechanisms integrated to one device; a four-bar mechanism, an inclined plane, and a hydraulic actuator. Even during a "failure" in testing, the door has never failed to meet the overall objective - to open when commanded and provide a high vacuum seal when closed. The test anomalies experienced were partially due to deficient test set-ups and procedures. However, some valuable insight resulted from those failures. Because of this insight, design changes resulted in a more reliable unit.

Table 1   Random Vibration Test Environment

Y AND Z AXIS

FREQUENCY (Hz)	ACCELERATION SPECTRAL DENSITY (G^2/Hz)
20	0.005
100 - 160	0.5
200	0.05
2000	0.00158

OVERALL = 8.05 Grms

X AXIS

FREQUENCY (Hz)	ACCELERATION SPECTRAL DENSITY (G^2/Hz)
20	0.008
80 - 600	0.125
2000	0.00158

OVERALL = 9.77 Grms

Table 2   Thermal Test Environment

TEST	TEMPERATURE (°C)	NO. OF THERMAL CYCLES
THERMAL CYCLE	+36 / -53	24
THERMAL VACUUM	+36 / -53	3

Window Cover

Hinge Pin

Window Frame

*Carrier Link

*Driver Link

*Bracket

*Torsion Spring

Bearing*

Pin, Carrier/Bearing*

Actuator

Cover Plate

Pin, Carriage Assembly*
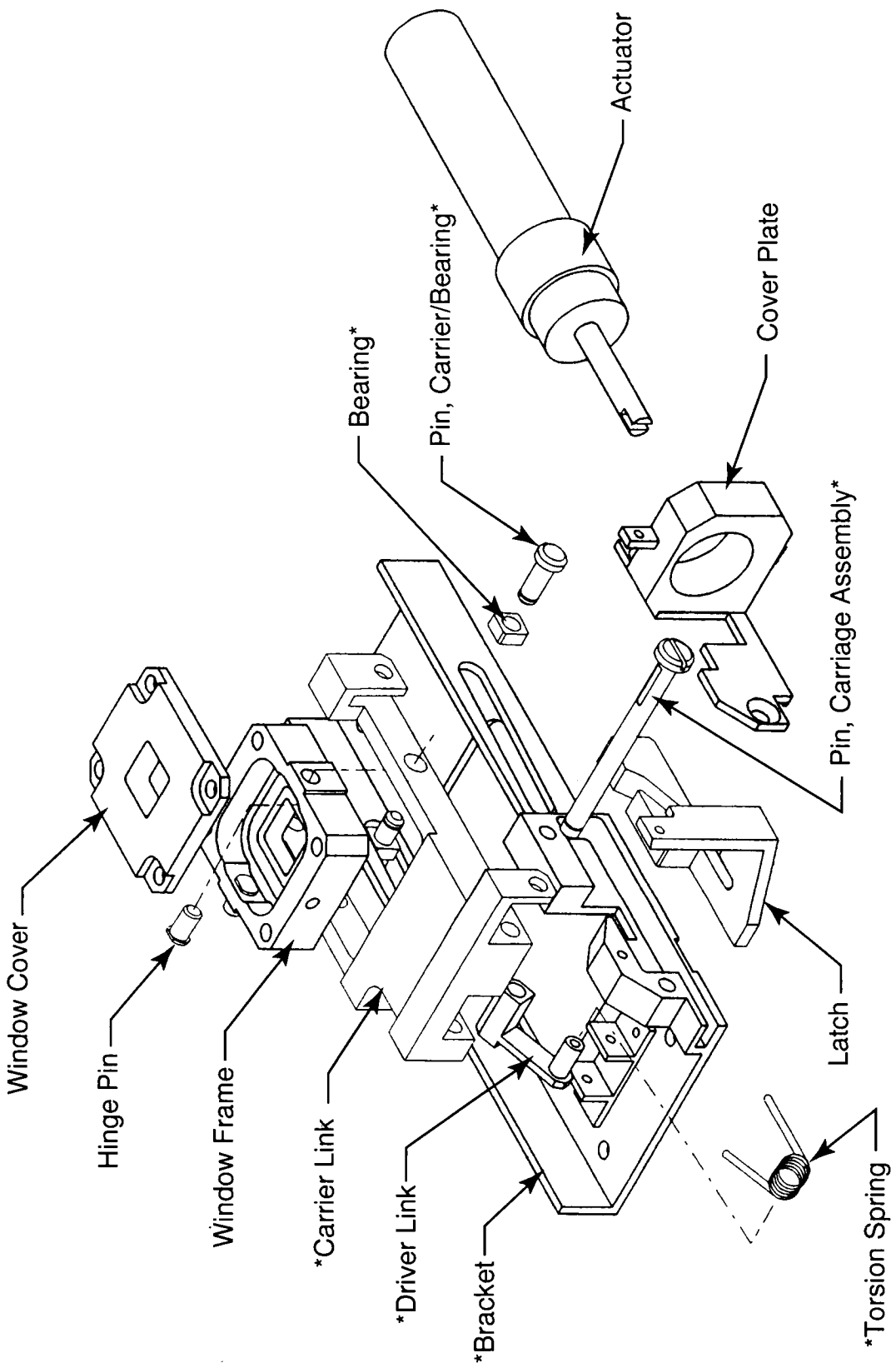
* These Elements Form The Carriage Assembly

Latch

Figure 1

213

Carriage Assembly

Latch

Pin

Bracket
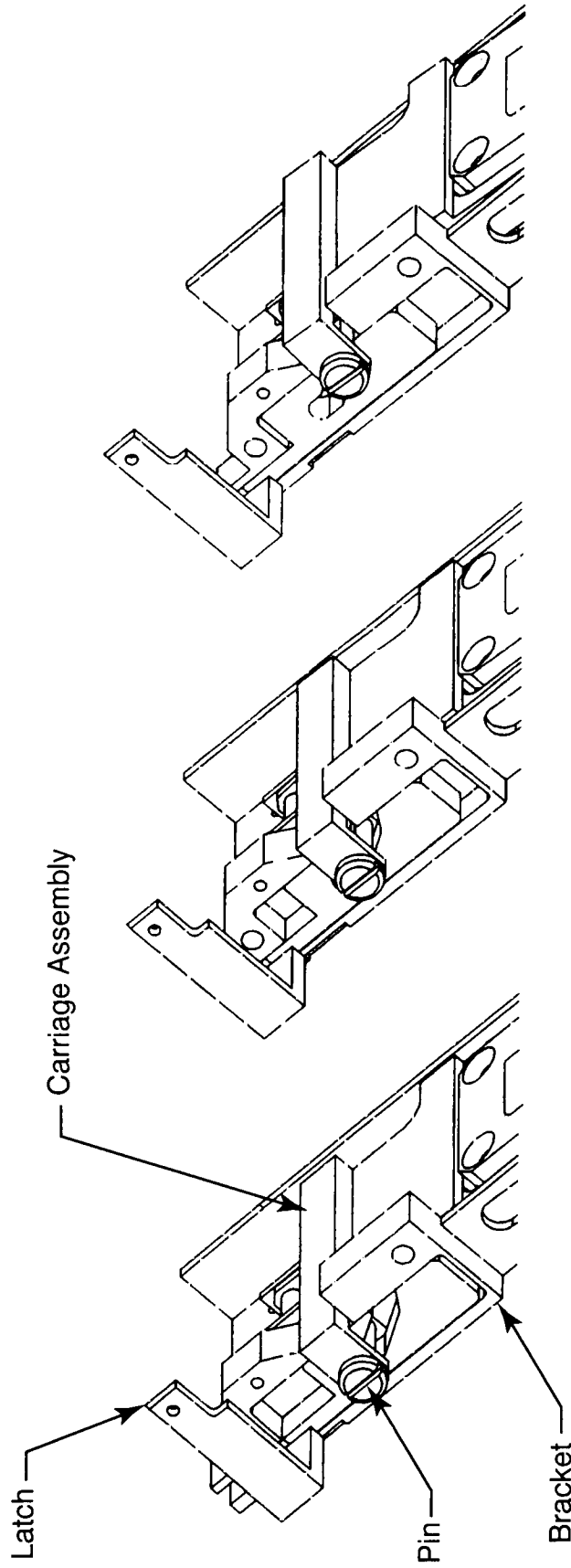
Fully Locked

Unlocked

Figure 2

(For illustration, the actuator and cover plate have been removed)

214

Unlocked

Half Open

Full Open
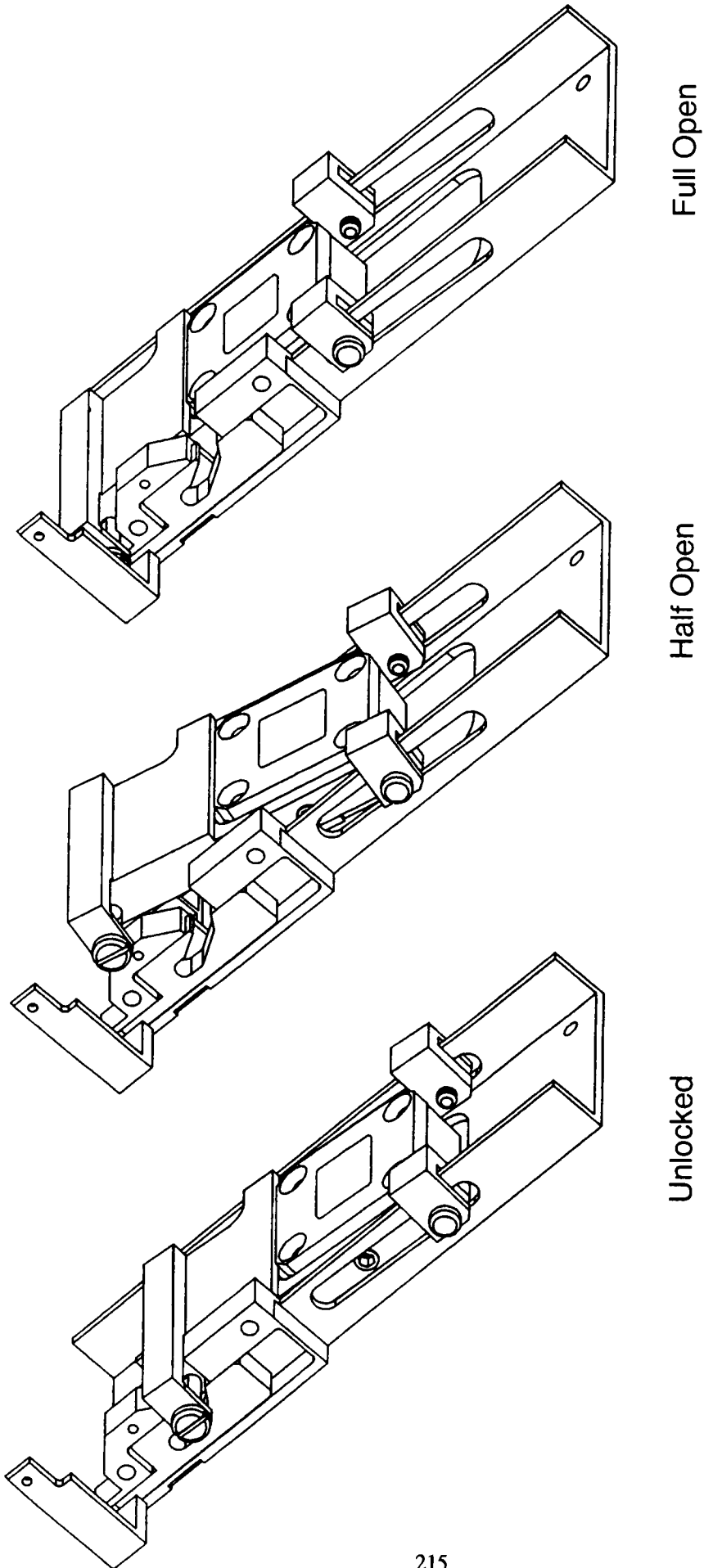
Figure 3

(For illustration, the actuator and cover plate have been removed)
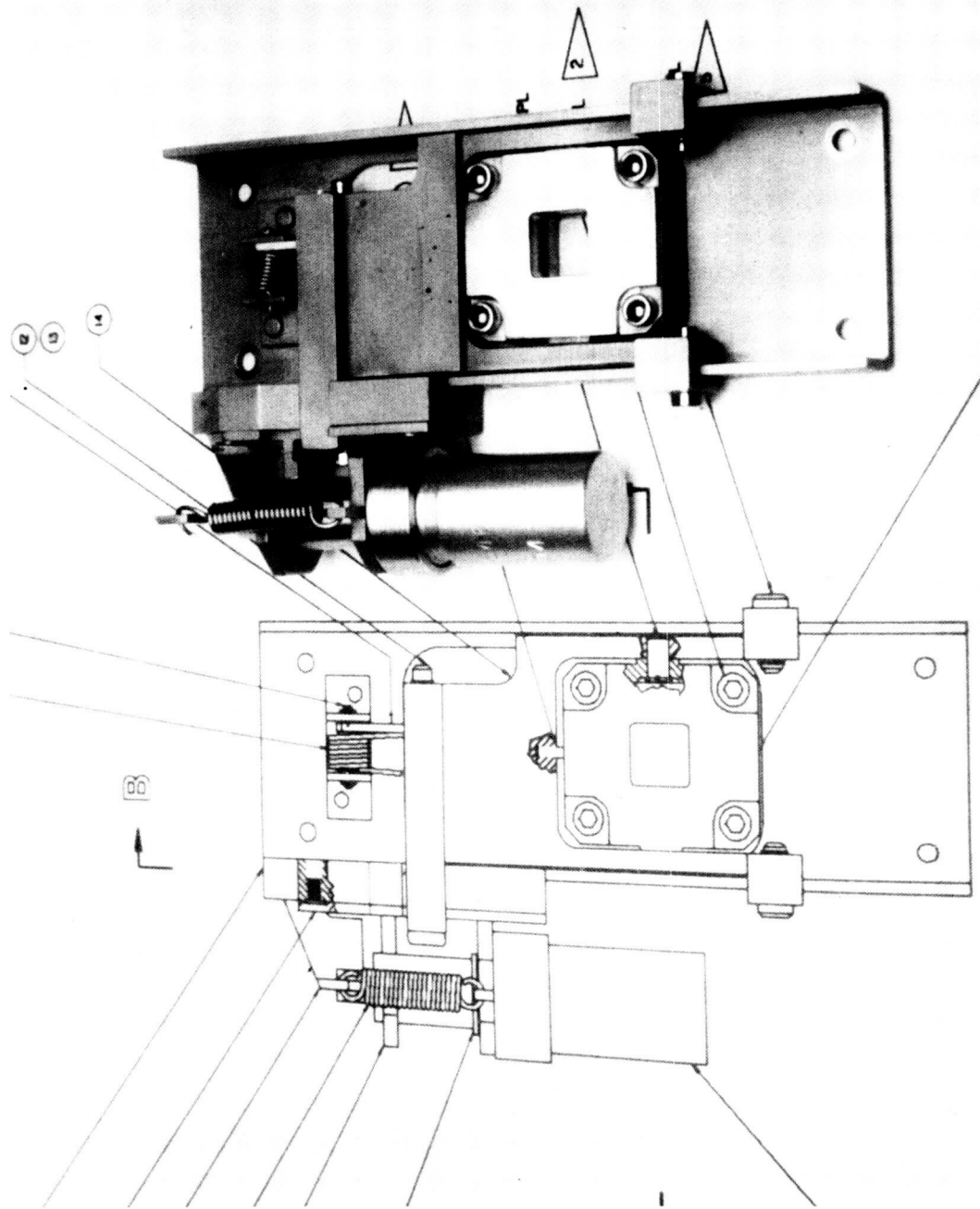
The Vacuum Door Assembly Development Unit

Figure 4
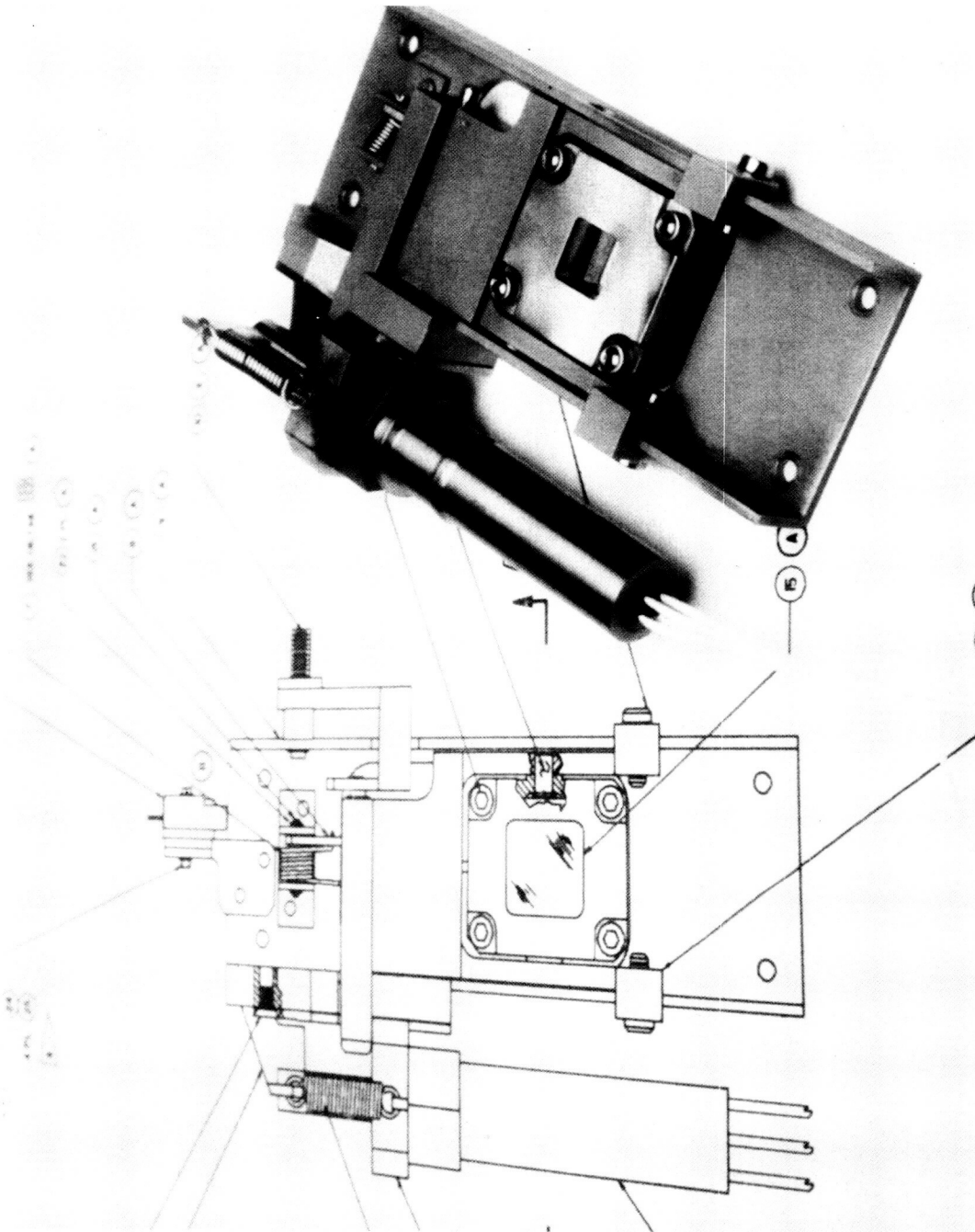
The Vacuum Door Assembly Development Unit With Eng. Model Actuator

Figure 5

Session Chair: Kornel Nagy

/995/20821

405773
/7p.

Special Features of the CLUSTER Antenna and Radial Booms Design, Development and Verification

G. Gianfiglio*, M.Yorck*, H.J. Luhmann*

Abstract

CLUSTER is a scientific space mission to in-situ investigate the Earth's plasma environment by means of four identical spin-stabilized spacecraft. Each spacecraft is provided with a set of four rigid booms: two Antenna Booms and two Radial Booms. This paper presents a summary of the boom development and verification phases addressing the key aspects of the Radial Boom design. In particular, it concentrates on the difficulties encountered in fulfilling simultaneously the requirements of minimum torque ratio and maximum allowed shock loads at boom latching for this two degree of freedom boom. The paper also provides an overview of the analysis campaign and testing program performed to achieve sufficient confidence in the boom performance and operation.

1. Introduction

The CLUSTER mission is part of a cooperative scientific research program between ESA and NASA for the investigation of the plasma interactions in the Sun-Earth system. The mission relies on four identical spin-stabilized spacecraft being placed in nearly identical high eccentric polar orbits. CLUSTER will observe in unprecedented detail magnetic and electric interactions between the Earth and the Sun by performing in-situ spatial and temporal plasma particle and electromagnetic field measurements. Each spacecraft is provided with a set of four booms: two Antenna Booms (AB's), each carrying a S-Band Antenna, and two Radial Booms (RB's), to place the two Flux Gate Magnetometers on one boom and the WEC 6 experiment on the other far enough from the spacecraft body to allow for undisturbed scientific measurements. The two RB's and one AB, are located on the +X side of the satellite. The other AB is accommodated on the -X side of the satellite (Figure 1). Both the RB's deploy in a plane perpendicular to the spacecraft spin axis, and each AB deploys in a plane parallel to the spacecraft spin axis. The CLUSTER mission is a "first" for ESA in that it requires the delivery of four identical spacecraft for simultaneous launch (in a double stack configuration) on the first qualification flight of the ARIANE 5 launcher. For the boom mechanisms, this has meant a series manufacturing, assembling, integrating and testing of 20 booms: 2 Structural Models (SM), 2 Qualification Models (QM) and 16 Flight Models (FM).

Because of the limited resources available to the CLUSTER program, at the start of system definition phase it was investigated whether the required functional performance of the boom mechanisms could have been achieved by utilizing hardware of proven design with existing space qualification. The outcome of this investigation resulted in the CLUSTER boom mechanism design baseline being derived from the radial boom flown on ULYSSES and to assume the CLUSTER booms were qualified by similarity with ULYSSES. Based on these assumptions, the

---

* European Space Agency, Noordwijk, The Netherlands

subsystem design phase was eventually started, though different and more stringent (than ULYSSES) requirements were specified to the boom mechanisms. Unfortunately, at the end of the subsystem design phase, the results of the first development tests revealed that the specific CLUSTER requirements could not be fulfilled with the assumed boom baseline design. Consequently, several design improvements were developed and implemented with the aim to recover this unexpected and critical situation. However, the introduction of these changes imposed the need for requalification and, therefore, a dedicated verification program encompassing both analysis and test was established and urgently commenced to acquire sufficient confidence in the CLUSTER booms' performance and operation.

2. Mechanism Requirements and Design Description

2.1. Mechanism Requirements
Among the CLUSTER requirements applicable to the booms, those which have significantly affected and driven the mechanism design are the:
- Electro Magnetic Cleanliness (EMC) requirements;
- Mission environmental and operational requirements;
- Static Torque Ratio (STR) requirement;
- Strength requirements;
- Structural frequency/stiffness requirements;
- Thermal requirements;
- Allocated resources.

EMC requirements. Due to the CLUSTER specific mission objectives the booms must be clean from both the electrical and magnetic point of view. Therefore, all boom external surfaces (including the thermal insulation) have to be electrically conductive and eventually grounded. In addition, the use of magnetic material is forbidden.

Mission environmental and operational requirements. During launch, the booms have to withstand the mechanical loads induced by the ARIANE 5 launcher in its first qualification flight. Upon separation from the launcher, a 45 day transfer orbit phase is foreseen, during which the booms will be subjected to a severe thermal environment induced by the wide range of expected Solar Aspect Angle (SAA). Once in their mission operation orbit, long eclipses (more than 4 hours) will be experienced. From an operational point of view, it is envisaged to release the +X AB immediately after launch and the other three booms once the Mission Operation Phase is reached. Both RB's are released after the -X AB is deployed.

Static Torque Ratio (STR) requirement. During boom deployment, available actuator forces/torques shall exceed by a factor of 2 the worst case predicted resistive forces/torques. No kinetic energy is to be taken into account. The following design factors have to be furthermore applied to the component of resistive forces/torques:

- Friction: 3.0[a]
- Hysteresis: 3.0[a]
- Harness: 3.0[a]
- Inertia: 1.1

222

• Spring Stiffness: 1.2

a These design factors can be reduced to 1.5 if relevant data for resistive contribution are obtained from test measurements.

Strength requirements. The booms must withstand the worst case combination of both mechanical and thermal loads that can be experienced during the required lifetime. Two worst cases are identified as the mechanical loads induced by the launcher and the combination of thermal and mechanical shock loads at boom release, deployment and latching. Stress analysis has to demonstrate that a positive Margin of Safety exists even after the application of a design factor of 1.5 for yield and 2.0 for ultimate. In addition, mechanical testing must demonstrate that neither structural failure nor boom performance degradation occurs when the flight loads are factored by 1.1 for acceptance and 1.25 for qualification. The launcher induced loads were derived from the coupled load analysis with the ARIANE 5 launcher. However, due to the experimental nature of the first ARIANE 5 launch, large uncertainty factors were applied leading to a Quasi-Static-Load factor of 33 g applicable for both the Radial and Antenna booms. The derivation of the shock loads at the moment of latching was performed by means of deployment analysis (see paragraph 3.1).

Structural frequency / stiffness requirements. To avoid dynamic coupling with the launcher, minimum natural frequencies of 75 Hz and 100 Hz are established for the RB and AB structures, respectively, in the stowed configuration. These frequencies were used to design the boom tubes, hinges and hold down brackets.

Thermal requirements. The booms must operate without any performance degradation within the specified acceptance temperature limits (the qualification temperature range is 20° C wider):

| AB | -130°C / +115 °C -15°C / +65 °C | Non Operating[1] Operating[2] |
| RB | -130°C / +115 °C -20°C / +80 °C | Non Operating[1] Operating[2] |

[1] Non Operating = pre-deployment and deployed.
[2] Operating = release, deployment and latching.

These limits were derived by means of flight temperature predictions employing the CLUSTER Comprehensive Thermal Mathematical Model and after application of temperature uncertainty margins. The required temperature range for the deployment operation will be achieved, if necessary, by an appropriate attitude maneuver.

Allocated resources.
A total mass of 30 kg is allowed for all the four booms. There is no power available except at boom release for the pyro actuators, and only a limited amount of telemetry channels are available to monitor boom temperatures (thermistors) and final deployment status (end-switches).

2.2. Mechanism Description

The RB is a two Degree of Freedom (DoF) system consisting of two tubes (each about 2300 mm long), two hinges, two hold-downs, their support brackets and one Inner Hinge (IH) support bracket (see RB stowed configuration in Figure 2). Additional features are:

- IH bracket interfacing with the IH support and holding the male side of the latch device;
- IH fitting holding the female side (redundant spring) of the latching device;
- Inner boom CFRP tube, 50.2 mm diameter and 1.1 mm thick;
- Two inner sleeves, properly shaped, nesting on the hold-down device and mating with the corresponding ones of the outer boom;
- Outer Hinge (OH) inner boom fitting with latch device (male side);
- OH outer boom fitting with redundant latch springs (female side);
- Redundant kick spring in the OH;
- Outer boom CFRP tube, 50.2 mm diameter and 1.1 mm thick;
- Two outer sleeves, properly shaped, nesting on the hold-down device and mating the corresponding ones of the inner boom;
- Fittings to accommodate the supported experiment sensors;
- Redundant AMPEP bearings (self-lubricated bushes) at the IH and OH;
- Single layer thermal protection of aluminized Kapton (Nomex scrim reinforced) striped with Kapton ITO tape.

Boom fittings, hinges, bearings, hold-down and hinge supports are made from Titanium alloy. In launch configuration, the two boom elements (inner and outer arm) are kept in position by two hold down clamps, which at deployment are pyrotechnically released. The clamps are subsequently driven into a latch position by a redundant spring drive system. Boom separation, deployment and latching in orbit is driven by the centrifugal forces generated by the spacecraft spin. Once both RB's are deployed, their tip to tip distance amounts to about 13 m.

The AB design is similar to the RB, except the single hinge/tube mechanism is about 1600 mm in length. During launch, each AB is clamped in position by a simple hold down mechanism (pre-loaded bolt pressing two V-shaped brackets together) located at the tip of the boom. Upon firing the pyro-nut device, the boom is released and driven by a redundant spring actuator, which rotates the tube by 90° and aligns the S-Band Antenna with the spacecraft X axis. In this position, the AB is positively latched by a redundant latch spring system which provides the required stiffness and positional accuracy. In order to comply with the CLUSTER-specified requirements, the original ULYSSES baseline design had to be changed. The design improvements implemented in the CLUSTER boom mechanisms are described in Table 1. They were mainly dictated by the mass/volume minimization constraint imposed by the CLUSTER mission and the need to:

- Increase the structural frequencies/stiffness of the booms in their stowed configuration;
- Decrease the components of the boom resistive torque contributions (e. g. hinge friction and harness) and increase the available actuator force/torque, such that sufficient STR can be achieved during the boom deployment;

224

- Increase the boom strength capability at the moment of latching.

As the RB is deployed by the centrifugal forces, the STR increases with the spacecraft spin rate. In order to fulfill the CLUSTER STR requirement, a spacecraft spin rate of about 20 rpm is needed. However, this would induce a shock load of about 10000 N•m at the RB IH. Obviously, the booms are not able to withstand such shock load. Critical items are the Titanium fitting/CFRP tube bonded joints. Therefore, the initial spacecraft spin rate must be decreased, thus impacting on the compliance with the STR especially at the end of the deployment. At this point, a large drive torque is required to engage the latch mechanism. However, due to the geometry and the mass distribution of the RB segments only a modest centrifugal force is available for latching.

To solve this problem and avoid a major re-design of the booms, a complex and unusual approach has been followed. First, a comprehensive analysis has been performed to determine the maximum allowable spacecraft spin rate at deployment start. Afterwards, for the determined spin rate, the available STR has been calculated. The aim was to demonstrate the baseline requirement was fulfilled at least in the first part of the deployment and at all possible stop positions. At these stop positions, which are function of the friction profiles assumed for each boom hinge, a spin-up maneuver is allowed to achieve the required STR. All analysis inputs have been verified and confirmed by test. However, the quasi-static measured torque profiles have been modified to take into account viscous effects, which have been also determined by test measurements. Finally, a special thermal conditioning phase has been planned prior to the deployment of the -X AB and the two RB's. As far as practical, a more benign thermal environment to the mechanism critical areas (hinges, harness and joints) after the rather long and severe transfer orbit phase will be provided. This will be achieved by tilting the spacecraft spin axis towards sun thus adjusting the SAA to the required value (presently predicted between 80° and 85°).

3. Verification Program

The verification of the Radial and Antenna Booms has been achieved by a combination of analysis and test. The rationale for this approach is the substantial difficulty to simulate, on ground, the in-orbit environment. Because of the RB size, it would be impractical and very expensive to release and fully deploy the booms under simulated space conditions in a thermal vacuum chamber. However, whenever possible, certain requirements have also been verified simply by test. To this purpose, specific acceptance criteria have been defined, in terms of overall resistive contribution and drive spring characteristics, to check the adequacy of the boom hardware at relevant stages of the assembly, integration and test program, both at subsystem and system level. These acceptance criteria have been also used as input for the deployment analysis in order to achieve a consistent verification.

3.1. Deployment Analysis
An extensive analysis campaign has been carried out in order to verify the boom deployment performance with respect to the applicable design requirements and check the effectiveness of potential changes and parameter sensitivity on the mechanism design. It encompasses:

- Shock load analysis (i. e. determination of boom bending moments at latching);
- Calculation of the STR during the boom deployment;
- Contingency analysis (i. e. definition of spin-up maneuvers);
- Sensitivity analysis with respect to deployment parameter variation.

The analysis has been performed by means of multi-body dynamic simulation. An appropriate software package has been used. The spacecraft and one RB have been modelled as rigid bodies connected by revolute joints, thus obtaining a two DoF deployment system representing the inner and outer arm of one boom. The related kinematic input has been derived by flight predictions, FE analysis or estimated on the basis on the data of the ULYSSES satellite. These data have been updated as soon as test data from the physical hardware were available. The resistive torque contributors have been factored according to the design requirements.

3.1.1. Shock Load Analysis
The centrifugal field of the spinning spacecraft provides the actuating forces / torques for the boom deployment. The initial spin rate is, apart from the friction in the hinges, the main driver for the shock loads induced in the booms during latch. The goal of the shock load analysis is therefore to define an appropriate initial spin rate for the boom deployment that is consistent with the allowable shock loads of the booms and other operational requirements. During latching, the arms of the booms are mainly stressed by a bending torque around the hinge axes. The latching loads are mainly function of the latching velocity, eigenfrequencies of the latched system and system inertia.

It is required to assume best case (minimum) friction in the hinges in order to calculate worst case shock loads. The lower the friction in the hinges, the higher the latching velocity of the booms. However, for a two DoF system like the CLUSTER booms, the eigenfrequency of the system changes depending on the order of latching of the various arms. Hence, assuming zero friction in the hinges does not always provide worst case shock loads. For the CLUSTER satellite, the highest eigenfrequencies have been found to occur when the inner arm latches first and the outer arm is close to the latch position. This latching configuration does not result when both hinges are frictionless, which is the case for a single DoF system.

Instead, the worst case has been found by varying the friction factors in each hinge independently. Figure 3 shows the IH shock loads as a function of hinge friction factor and initial spin rate for +Y RB for two cases. The target shock level (290 N·m), derived from the ultimate strength of the boom including safety factors, is shown as well. In, evaluating Figure 3, the following conclusions are drawn:
1.) The latching shock in the booms is linearly increasing with the initial spin rate for one particular latching sequence.
2.) The latching sequence changes from OH latches first to IH latches first when the initial spin rate is increased.
3.) The latching sequence changes at different spin rates depending on the assumed friction values.
4.) Assuming zero friction in both hinges does not provide worst case shock loads for all initial spin rates.

5.) The maximum allowable initial spin rate for the + Y RB has been found to be 4.1 rpm. For the -Y RB, 4.5 rpm is allowed.

3.1.2. Calculation of STR

The STR is calculated for both the inner and outer arm separately. STR>2 demonstrates the capability to continue the deployment in case of a boom stop position accounting for all unknown in-orbit conditions. The spin rate used to calculate the STR is based on the maximum allowable bending torque of the booms (see par. 3.1.1.). The STR has been calculated for the complete deployment range for both the inner and outer arm. It is shown for the +Y RB IH and OH in Figure 4 and 5, respectively. Figure 4 and 5 indicate clearly that the STR requirement is not fulfilled over the full range of deployment angle (grey shaded area). The values for the OH STR are higher due to the presence of the kick spring.

3.1.3. Contingency Analysis

In order to resolve the non compliance of the boom design with respect to the STR requirement, a contingency analysis has been performed with the aim to increase the spin rate and increase the deployment torque, thus to eliminate the original non compliance. An analysis for both the +Y RB and -Y RB has been run following the steps listed below:

- Identification of non compliance areas in the boom deployment range (see Figure 4 and Figure 5).
- Definition of possible stop positions, considering that either arm of the boom may have latched.
- Calculation of the spin rate necessary to increase the STR to 2.
- Consideration of the spin rate accuracy in the calculated spin rate (±0.1 rpm).
- Calculation of the latching shock for best case friction values.

In cases where the latching shock for the increased spin rate is below the target shock level, a spin up maneuver is considered acceptable. It has been demonstrated by analysis that the boom can be recovered and successfully deployed from a stationary position by increasing the spin rate without exceeding the target shock level.

3.1.4. Sensitivity Analysis

The resistive torque profiles as well as the actuating torques of the outer hinge kick spring have been measured for all QM and FM booms. The variation of the individual profiles has been subject of a sensitivity analysis. The goal of the investigation was to demonstrate that any variation of friction up to a factor of 6 in both hinges will not affect the successful deployment of both arms and not exceed the target shock level. The results are compiled in Table 2. The data in the fields indicate:

- The deployment sequence (O/I Outer hinge lathes first; I/O inner hinge latches first);
- The first number gives the inner hinge shock load in N•m;
- The second number gives the outer hinge shock load in N•m.

It can be seen that except for the friction factor of 6 in both hinges, one go release, deployment and latching is always accomplished. An investigation of the inertia uncertainty of the spacecraft at the time of deployment has also been performed. It has

been found that a 10% variation does not significantly influence the boom deployment behavior and latching shock magnitudes.

3.2. Testing Program
3.2.1. Subsystem-Level Testing

The boom testing program at subsystem level is based on Development tests, Qualification tests and Acceptance tests. The deployment tests were performed mainly at boom component and SM levels. turned out that with a mechanism design derived from the ULYSSES boom it was not possible to fulfill the CLUSTER specific requirements (see paragraph 2.2) and specific hardware acceptance criteria were also established (see paragraph 3.0). The Qualification and Acceptance test flow is in principle the same and, for the Radial Boom, is shown in Figure 6. Special attention was paid to the bonded joint sample testing, the thermal vacuum test and the functional performance test.

Bonded Joint Sample Testing. To adequately verify the strength capability of the CFRP tube/Titanium fitting bonded joints, a destructive sample testing campaign has been performed. Representative samples of both the 60 mm and 45 mm bonded joints have been first subjected to thermal cycling at more extreme temperature than those actually predicted and subsequently subjected to mechanical failure under representative temperature conditions expected at the moment of boom release. Based on the results of this sample testing program, a statistical evaluation has been performed to derive the allowable load for ultimate bending of the joints ("A Value" approach to achieve a probability of 99% with a confidence level of 95%). The results of this evaluation are summarized in Table 3.

Thermal Vacuum Test. The RB thermal vacuum test set-up is shown in Figure 7. Due to the limited space available in the test chamber, it was only possible to measure the friction of the IH. For the AB, full deployment and retraction has been tested. The tests for both the RB and AB confirmed the worst-case friction occurs at low temperatures and there is no significant difference between friction values measured at ambient and vacuum conditions.

Functional Performance Test. Because of adding the boom thermal conditioning phase (see paragraph 2.2.) and the thermal vacuum test results, the test verification of the basic performance of the mechanism has been performed at ambient conditions. Figure 8 shows a typical friction profile measured for the FM 3 RB. The simulation of the latching shock load has been also achieved in the frame of the functional performance test. All RB and AB QM and FM have successfully passed this test.

3.2.2. System Level Testing

The boom testing program at system level encompasses the following tests:
- Mass properties verification (prior to integration onto the satellite);
- Alignment checks in both stowed and deployed configurations (booms integrated onto the satellite) prior and after system environmental tests;
- Boom release, deployment and friction checks and latch spring proof load test, prior and after to system-level environmental tests.

- System environmental tests: mechanical (sine vibration and acoustic) and thermal vacuum tests.

In the frame of the boom release and deployment test, both the RB's and the AB's are checked with respect to the function of release and deployment. Pyro release is, however, performed, only after the environmental tests. Relevant measurements are carried out at ambient conditions.

Concerning the RB, gravity effects are compensated by means of two meteorological balloons filled with Helium (Figure 9). One of the balloons is fixed to the inner boom segment and the other to the outer boom segment at their respective mass center. The deployment of the booms is achieved by means of a small electrical motor propeller.

4. Conclusions

The key aspects of the design evolution of the CLUSTER booms have been presented. One of the major problems was caused by the assumption made during the system definition phase that the required mechanism design was of already existing qualification status. The design improvements implemented to fulfill the specific CLUSTER requirements have also been described.

The difficulties encountered to fulfill simultaneously the design requirements of the minimum STR and maximum allowed shock loads and the comprehensive analysis performed to determine the highest allowable spacecraft spin rate at the moment of boom release has been discussed.

To the authors knowledge, such combined extensive verification approach has never been applied to a conceptually simple two DoF system like the CLUSTER RB mechanism. Despite the problems encountered, the CLUSTER boom qualification has been successfully achieved at subsystem level (October 94) and confirmed at system level (December 94). All 16 flight booms have been delivered and integrated onto the CLUSTER satellites. The CLUSTER System AIV program is almost over since the FM 1, 2 and 3 satellites system environmental testing has been successfully completed and only the Thermal Balance/Vacuum test of the FM 4 satellite is still due. The CLUSTER launch is presently planned for end November, 1995.

5. Acknowledgments

This paper is based on the work performed by Sener, the CLUSTER Boom Subsystem responsible, and Dornier, the CLUSTER Prime Contractor, during the development, qualification and flight model production and testing phases. Significant support has been also provided by the ESA-ESTEC/YMM section. The authors wish to thank all their colleagues at Sener, Dornier and ESA-ESTEC who contributed to the preparation of this paper.

Table 1 Summary of AB/RB major design changes from ULYSSES design

Item	Design modification description	Purpose
RB	Hold–down (HD) and HD Support Bracket • rope element/pyro cutter device changed to Ti clamp/pyro nut device • support bracket cylindrical shape changed to conical shape	• increase eigenfrequency in stowed configuration • increase strength capability with respect to shock loads
AB/ RB	CFRP Tube • CFRP Tube lay–up optimized	• increase eigenfrequency in stowed configuration • increase strength capability with respect to thermal and shock loads
RB	CFRP Tube/Fitting joint • additional liner introduced inside the fitting in the glued zone	• increase strength capability with respect to thermal and shock loads
AB/ RB	Latch mechanism • latch mechanism stiffened / strengthened	• increase strength capability with respect to shock loads
AB/ RB	Hinge Bushings • clearance between shaft and bushing increased	• reduce overall friction profiles (increase STR)
AB/ RB	Harness • harness routing around hinges optimised by development test • AB harness shielding (Al tape) changed to mesh construction	• reduce overall friction profiles (increase STR)
RB	OH Drive Spring • short stroke spring (ca. 20 deg) introduced at OH	• change latching sequence (OH latches first) thus decreasing shock loads • increase STR at IH (OB help effect)
AB	Drive spring • pretension and stroke increased respecting the volume and shock load minimisation constraints	• increase confidence into succes–fully deployment start
RB	Contact surfaces • Ti/Ti contact sprayed with Everlube changed to Ti/Al Bronze (IB/OB) sprayed with Everlube	• avoid risk of cold welding

Table 2 Friction sesitivity analysis for +Y RB at 4.0 rpm

		Outer hinge friction factor						
		0	1	2	3	4	5	6
Inner hinge friction factor	0	O I 224 155	I O 278 125	I/O 275 38	I/O 261 22	I/O 237 20	I/O 210 25	I/O 176 28
	1	O/I 217 149	O/I 218 116	I/O 252 34	I/O 244 22	I/O 223 18	I/O 191 24	I/O 154 28
	2	O/I 210 143	O/I 209 111	I/O 233 35	I/O 224 22	I/O 207 17	I/O 172 23	I/O 126 26
	3	O/I 202 138	O/I 200 105	I/O 210 35	I/O 206 22	I/O 170 15	I/O 151 21	I/O 94 29
	4	O/I 193 133	O/I 192 98	I O 183 37	I O 181 22	I O 167 14	I O 127 20	I O 44 29
	5	O/I 183 127	O/I 181 91	I/O 138 40	I/O 152 22	I/O 141 12	I/O 96 20	I/O 32 61
	6	O/I 173 123	O/I 171 84	I/O 90 43	I/O 118 24	I/O 111 13	I/O 62 18	–

Table 3 Summary of statistical evaluation from bonded joint sample testing

Ultimate Bending Moment [Nm]	60 mm joint 7 samples	45 mm joint 8 samples
Min	978.1	741.5
Max	1355.8	1177.3
Average	1140	973
Standard Deviation	132.8	141.8
K_A	4.64	4.35
K_B	2.75	2.58
"A" value	523	356
"B" value	774	606
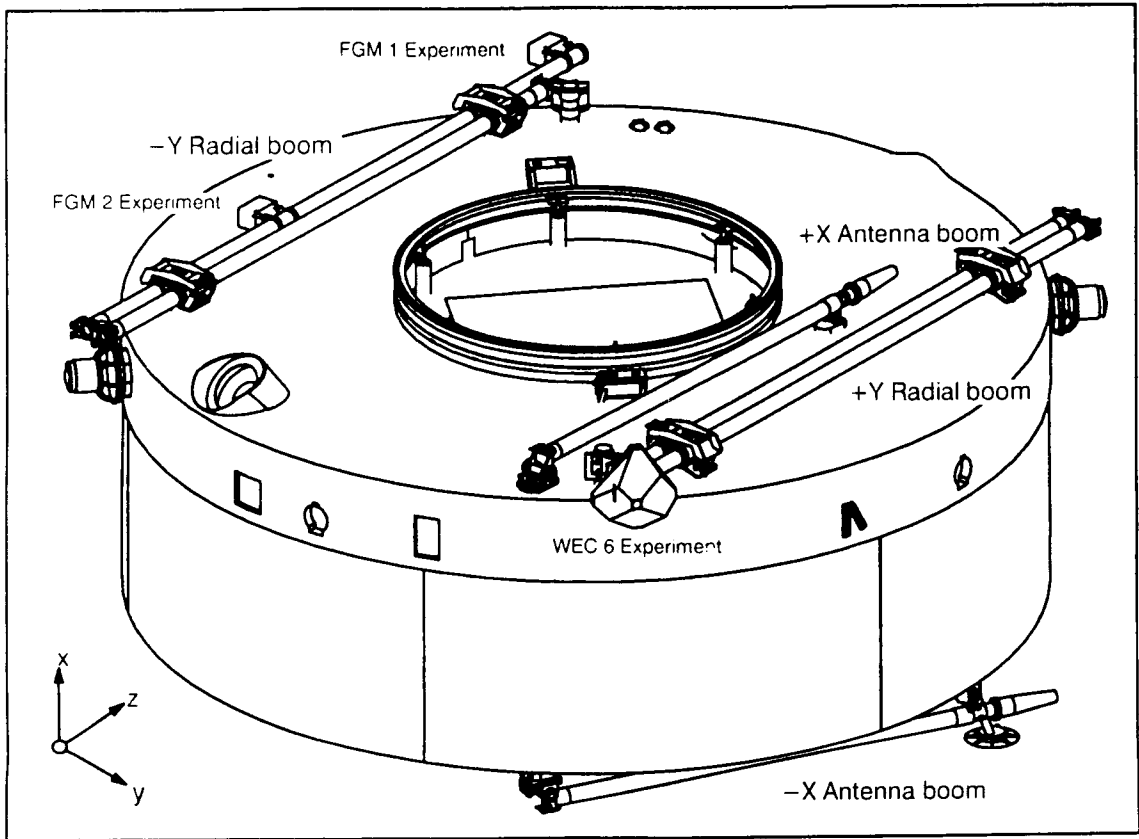
Figure 1 CLUSTER Satellite Configuration
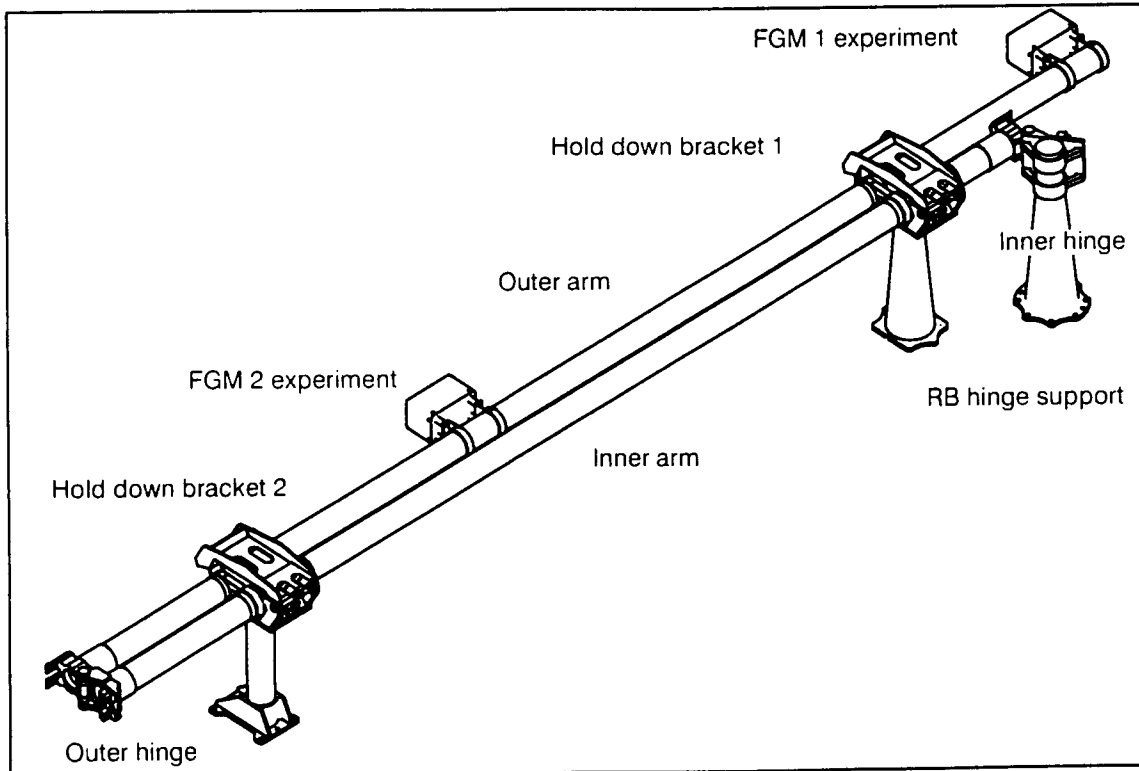
Figure 2 –Y RB Mechanical Arrangement
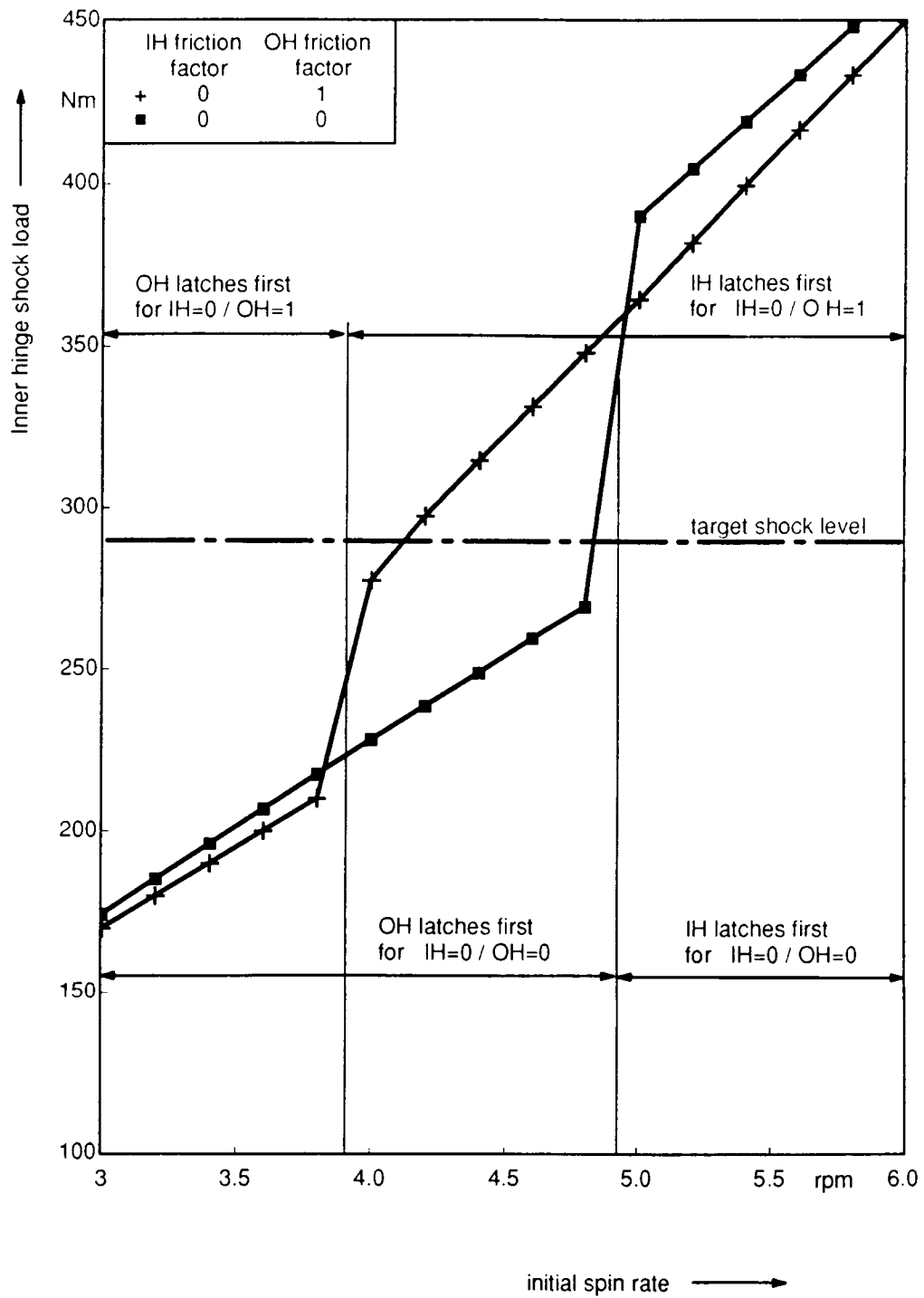
Figure 3 +Y RB Inner hinge shock load vs friction factor and initial spin rate
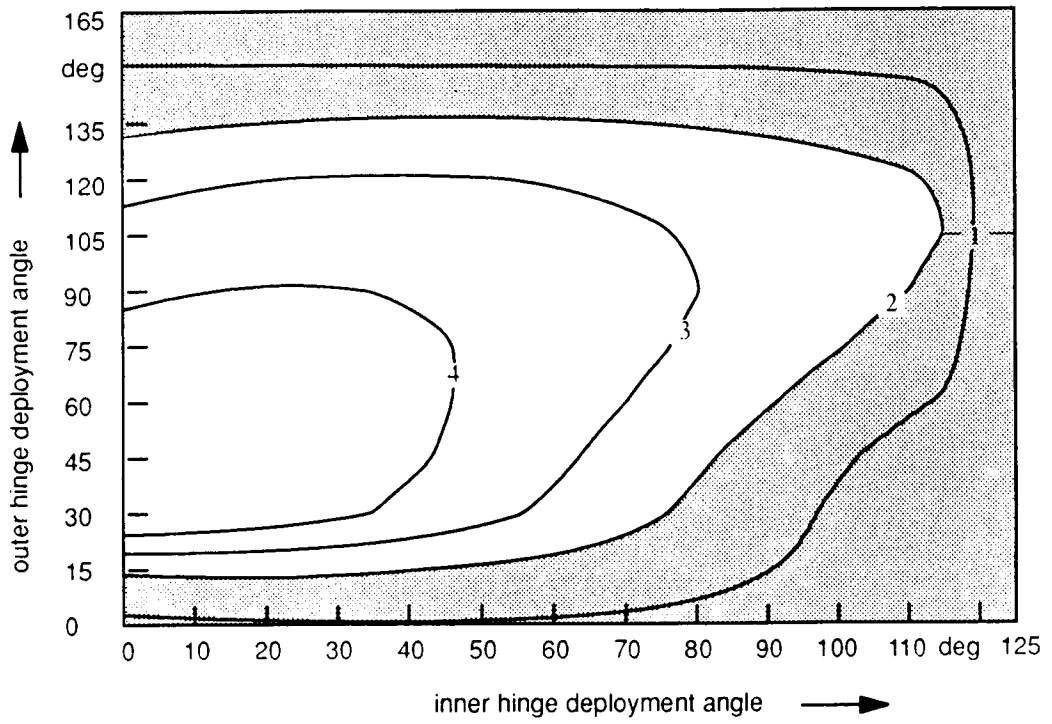
Figure 4 +Y Inner hinge torque ratio at 4 rpm
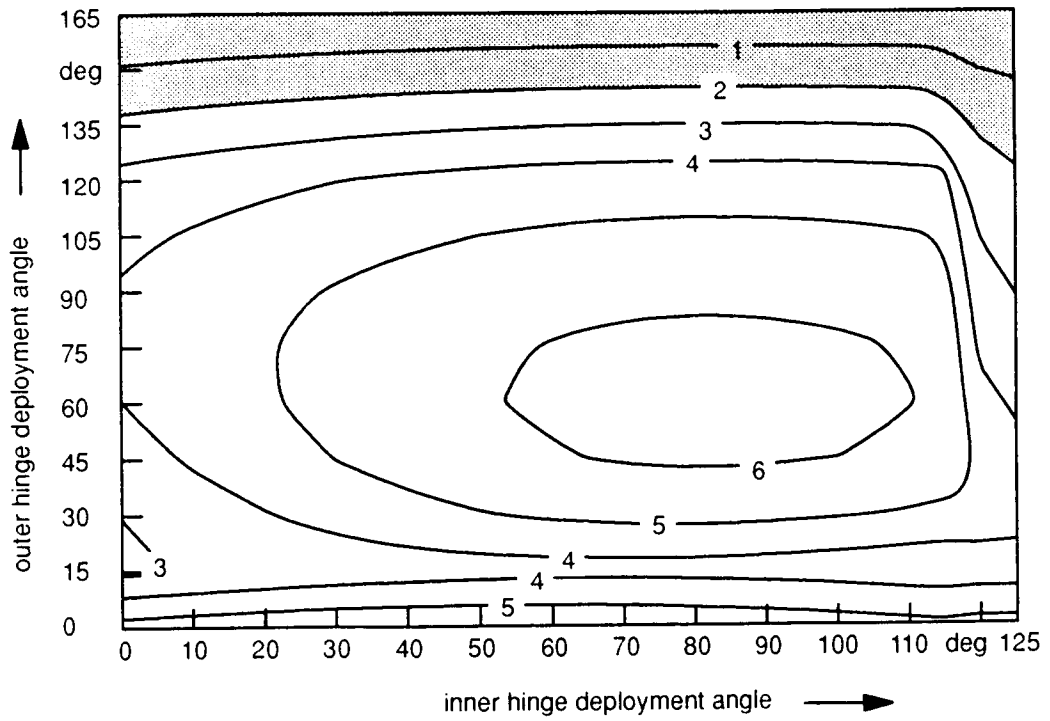
Figure 5 +Y Outer hinge torque ratio at 4 rpm

BOOM STRENGTH CAPABILITY

•Sample bending
test after TV cycling

•Boom acceptance bending
test (proof load at ambient)

Dimensions
Mass comp. level
Magnetic sniff

Harnes dimensions
Harness mass
Harness electrical performance

ASSEMBLY

Bush intgration

Shaft/Bush pair friction

Assembly/Adjustment

Latch spring sensitivity

Final adjustment
Harness installation

Bush screaning

Alignment rig

PHYSICAL MEASUREMENTS

Mechanical I/F
Electrical I/F
Alignment

Mass properties
total mass
CoM stowed
CoM deployed

Analysis

•CoM of supports
and hold downs
•Inertia properties

FUNCTIONAL PERFORMANCE

Analysis assumption
validation

Deployment analysis
prediction

Shaft friction in hinges
Latch spring friction
Hysteresis/Friction IH&OH
Microswitch performance
Release mech. performance
Latch mech. performance
Hinge shock capability
1st frequency deployed

ENVIRONMENTAL TESTS

Release / shaft friction check

Vibration test (3 axes)
resonance survey
sine vibration *
random vibration
resonance survey

Vibration fixture

Dimensions

Alignment

Vibration response

Release / shaft friction

Thermal vacuum cycling
Hysteresis/friction at ambient
TV cycling (4 cycles)
Pyrofiring at hot
Hysteresis in fourth cycle at
•hot qualification level *
•hot acceptance level
•cold qualification level *
•Vacuum ambient temp.
Hysteresis/friction at ambient

TV deployment devices

Dimensions

Alignment

FUNCTIONAL CHECK

Hysteresis/Friction IH/OH
OH spring characteristic
Latch check
Shock loads

PHYSICAL CHECK

Electrical check
Alignment check

* only QM

Figure 6 RB Test flow

Figure 7 TV test set up for RB
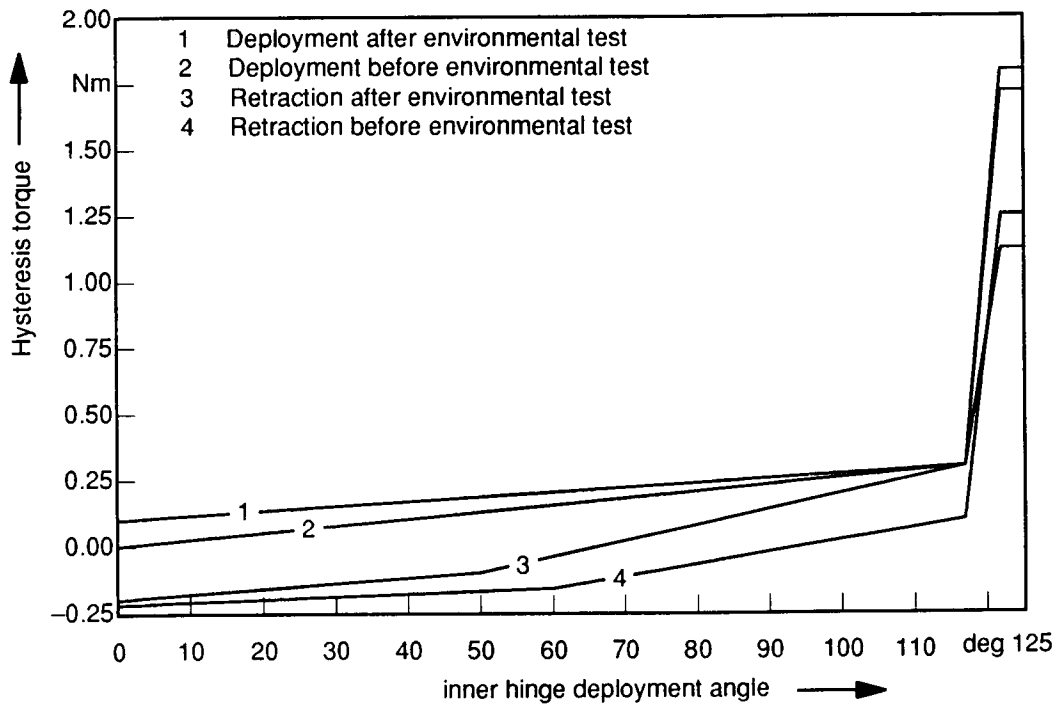
Figure 8 FM3 +Y RB Inner Hinge Friction Profiles

236
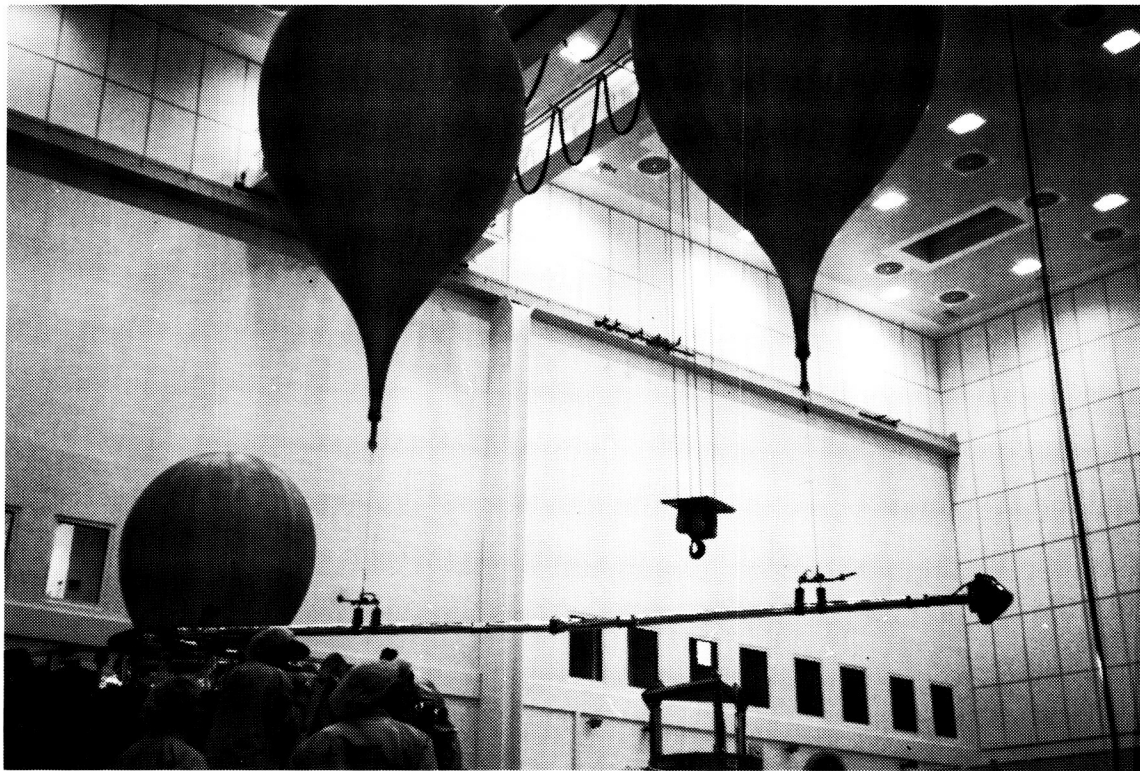
Figure 9 RB System level deployment test set up

/ 995/ 20 862

4 05 077

FORTÉ Antenna Element and Release Mechanism Design   */ 6 p -*

David J. Rohweller[*] and Thomas A. Butler[**]

Abstract

The Fast On-Orbit Recording of Transient Events (FORTÉ) satellite being built by Los Alamos National Laboratory (LANL) and Sandia National Laboratories (SNL) has as its most prominent feature a large deployable (11 m by 5 m) log periodic antenna to monitor emissions from electrical storms on the Earth. This paper describes the antenna and the design for the long elements and explains the dynamics of their deployment and the damping system employed. It also describes the unique paraffin-actuated reusable tie-down and release mechanism employed in the system.

Introduction

The antenna for the FORTÉ satellite for LANL/SNL is a log periodic antenna for detecting broadband electromagnetic pulses associated with natural and man-made events. The antenna elements are stowed for launch within and wound around a concentric stack of rings that separate one at a time as deployment proceeds. As each ring separates, four antenna elements are uncovered and whip out rotationally from the wrap position into the straight position. Extended, the antenna configuration is an array of four 10-element dipole antennas, orthogonal to each other as shown in Figure 1. Each antenna is held in position by a torsion spring that holds the root of the antenna against a stop.

The antenna uses an Astromast[TM] from Astro Aerospace Corporation to deploy the antenna and support it on orbit. The most challenging design problems were as follows:

1. To design antenna elements that assume a straight position after many months stored in a tight coil, and measure the straightness of the thin elements unaffected by gravity.

2. Analyze the whipping motion of the deploying antenna elements and damp the energy released from the antenna elements so that they are not damaged as they deploy.

3. Develop a reusable release mechanism to release the 4400 N (1000 lb) preload required for launch.

Antenna Element Design

The antenna elements vary in length from 2.45 m (96 in) to 0.55 m (21.5 in) and, when extended, must lie at 20 ±2 degrees above the base plane and at 90 ±2 degrees to each other. These criteria translate to the straightness requirement shown in Figure 2.

---

[*] Astro Aerospace Corporaton, Carpinteria, CA
[**] Los Alamos National Laboratory, Los Alamos, NM

For the long thin elements, this straightness is difficult to measure. Additionally, the elements must be capable of coiling onto a 291 mm (11.46 in) diameter cylinder without taking any permanent set. The following materials were initially investigated to find a high strain capable antenna element:

- Electrodeposited copper on fiberglass rods
- Electrodeposited silver on fiberglass rods
- Copper wire inside a fiberglass pultrusion
- Pultruded graphite epoxy rods

All of these were rejected except the graphite epoxy rods. The original design used graphite rods, 2.54 mm (0.1 in) in diameter. Graphite has the required stiffness, strength, and conductivity to perform as antennas and coil to the required diameter. However, creep tests showed that the elements took a permanent set after storage on the cylinder. The set was slight, but the straightness of the rods is sensitive to slight amounts of creep within the material. This creep translates directly to bow deflection in the rod. The amount of bow deflection allowed on a 2.45 m rod is 21 mm (0.84 in) in a weightless environment. Figure 2 shows the straightness required as the rods get longer in order to stay within the ±2 degree angle.

Several methods for measuring the bow were attempted. The thin rods were deflected 3 mm or so by every measurement system tried, however. One method involved supporting the rods on floats on a water table and measuring the deflection in the horizontal plane to minimize the effect of gravity. The rod tended to sag between the supports, so it was difficult to tell if the maximum plane of bow was parallel to the ground. Also, the results were not repeatable. This method nevertheless demonstrated that the graphite elements did not meet the straightness requirement.

Consequently, titanium spring wire Ti-3Al-8V-6Cr-4Mo-4Zr per AMS 4957 (modified) was tried. It has high strength and a stiffness between that of graphite and fiberglass rods and will not creep significantly in the stowed condition. The diameter was reduced from 2.54 mm to 1.52 mm (0.06 in) to reduce the stowed strain.

A new method was used to measure the straightness of the titanium wire. The wire was hung vertically and the plane of bow was oriented perpendicular to the axis of a jig transit placed 5 m (16 ft) to one side of the wire as shown in Figure 3. The bottom end of the wire was placed in a cup of water to quickly damp its motion (tape flags on the end also helped). The deflection was then measured from the bottom to the center and top of the wire, and the bow in the free state calculated according to the following equation from Timoshenko [1]:

$$b = y \left[1 + \frac{TL^2}{\pi^2 EI} \right] \tag{1}$$

Where: b = maximum deflection in free state
y = deflection under tension
E = modulus of elasticity

I = moment of inertia
T = tension load
L = length of member

This equation assumes the wire is weightless, tension is applied to the ends, and that the wire has an initial deflection in the free state. For this calculation, half the weight of the wire was used as the T (tension) value in the equation. This approximation was verified by finite element analysis rather than by deriving the exact equation.

Results of Design and Testing of the Antenna Element

A piece of titanium wire 2.9 m (114 in) long had a measured bow deflection after storage on a cylinder for 3 days of 7.3 mm (0.287 in). This wire was then laid on floats on the water table for 24 hours to allow it to recover without influence. The bow deflection then measured 4.1 mm (0.162 in). This met the requirements of the specification for the longest antenna element, and since the shorter elements have more tolerance, the straightness is acceptable. For margin in meeting the specification, the longest antenna elements were set at 1 degree beyond nominal as shown in Figure 2, since the wire will take a set in only one direction.

Analysis of the Antenna Elements

Mechanics of the Antenna Element Deployment

Two primary concerns exist when the antenna elements are released from the rings around which they are wrapped in the stowed configuration. The first concern is related to the stress in the element at different times during the release sequence. When the element root has moved approximately 90 degrees, it contacts a stop that prevents further rotation of the arm at the root. Thus the base of the element becomes a "fixed" beam with high initial velocity. As the element continues its motion, the stress at the root builds up to high levels. Stress also occurs in the element when the initial planar motion is forced into out-of-plane motion as the arm at the root starts to rotate. The inertia in the moving element resists motion that the arm is trying to enforce. The second concern is that the out-of-plane motion of the antenna may become excessive and allow the longest elements to strike the spacecraft.

Stress in the Element

A simple planar model is sufficient to show that the stress in the element may exceed yield when the arm at the root contacts the stop. It is first assumed that all of the stored potential energy in the element (in the stowed configuration) is transformed into rotational kinetic energy just before the stop is contacted. Using this velocity profile for the initial conditions (when it comes to a stop at the root) shows that the yield stress for titanium is exceeded.

When these calculations were performed for the graphite epoxy antenna elements, it was determined that for planar motion the ultimate stress would be exceeded and the elements would be expected to fracture. The expected stress for this simplified model is

independent of element length so it was convenient to verify the validity of the model by testing a deployment of the shortest element set. The test was performed in a vacuum chamber to eliminate the significant effects of air drag on the element after its release.

Results of the test were that the elements were not visibly damaged. Review of high-speed videos of the deployment showed that damage to the elements did not occur for several reasons. First, the motion of the element was not entirely planar. Significant energy is coupled into out-of-plane motion of the element. Also, because of the uncontrolled release of the elements from the canister, higher frequency short wavelength vibration modes in the elements are excited. Some of the original energy is retained in the deformation described by these modes. Finally, the assumption that the arm at the root of the element contacts a rigid stop is not completely valid. The stop and the area of the canister surrounding it have significant local compliance.

Antenna Motion

Review of the high-speed videos shows that out-of-plane motion of the antenna elements is large and may be critical since the longer elements can contact the satellite. This out-of-plane motion is caused by the 20-degree rotation of the arm at the element root, as each element rotates into its final 70-degree angle relative to the mast axis.

Modeling Antenna Deployment

Review of video from the tests led to the conclusion that a better model of the antenna had to be developed for accurately predicting its motion and associated stresses. The finite element (FE) computer code ABAQUS [2] was chosen for developing the model. ABAQUS is a nonlinear FE code that can easily handle the large motions and other nonlinearities associated with antenna deployment.

A single antenna element was modeled with 16 second-order beam finite elements. The antenna mast was modeled as a rigid cylindrical surface that the element could not penetrate as it deployed. This representation of the mast is important because the element unfurls and then wraps back up around the mast. It then reverses its motion and repeats this sequence several times until the initial stored energy is completely dissipated. If the mast were not represented in the model, the predicted element motion would be incorrect. The model includes the out-of-plane rotation of the antenna arm and the subsequent three-dimensional motion of the complete element. The stop that the element arm contacts when it reaches its final position is represented by a nonlinear rotational spring.

The simulation was started when the element was fully unwrapped and was positioned tangential to the ring to which its root was attached. It was assumed that at this point in time the element was perfectly straight and, therefore, all of its original stored strain energy had been converted to rotational kinetic energy of the element. It is also at this position where the motion of the arm about two axes starts. It rotates about the axis of the mast and also starts to swing the element 20 degrees from the perpendicular to the mast.

With the large motion, rigid contact surface representing the mast, and the nonlinear spring representing the stop, the FE model is nonlinear and requires small time steps to run through the deployment simulation. Several thousand time steps in the millisecond range are needed to simulate a few cycles of motion during the deployment sequence.

Predicted Stresses

Because of unknowns concerning the initial energy (velocity) of the antenna element at the start of the simulation, a parameter study was performed to determine how the stress in the element varies with the initial conditions. Figure 4 shows how the stress changes in the root of the element as the initial energy decreases. This presentation of the stresses is also useful for considering antenna response at later times. The nonlinear model is too costly to run for a full simulation, so the lower energy states were analyzed by modeling conditions as energy is gradually dissipated during the course of deployment. When the normalized stress is unity, the predicted stress in the element is at the yield stress for the titanium element. Therefore, when the two components of stress are combined, the element would deform plastically.

The results depicted in Figure 4 are not intuitive in that, for the component of stress perpendicular to the satellite (mast) axis, the stress is actually higher for a lower energy state. The stress is approximately 10 percent higher for a 75 percent energy level than for the full energy level. This can be thought of as the cyclic stress in this direction increasing during deployment for a few cycles of element motion and then gradually decreasing after that. This shows that the stress decreases in the element as the energy decreases. However, for the optimum case, the energy should be less than about 60 percent of the initial value.

Testing the response of the elements to determine whether they would permanently deform during deployment is difficult because of the effect of gravity. For vertical deployment where the antenna elements end up sloping downward, the effect of gravity subtracts from the bending stress. If the deployment is performed with the antenna in the opposite orientation, the effect of gravity adds to the stress and the elements would deform plastically.

Predicted Antenna Motion

The same parameter study discussed in the previous section predicted the antenna motion summarized in Figure 5. Here it can be seen that antenna element tip displacement toward the satellite initially increases with lower energy levels and then begins to decrease after 25 percent of the energy is dissipated. Motion away from the satellite increases as energy dissipates. Keep in mind, however, that the final tip location is approximately 0.84 m from the root location because of the 20-degree angle of the element relative to the mast.

The maximum motion toward the satellite exceeds the distance between the element and the satellite so the problem of the element tip contacting the satellite during deployment is a possibility. To illustrate this problem, Figure 6 shows the predicted position of the antenna at one point during its deployment without any energy

dissipating features present. Note that the antenna element would "brush" the base of the satellite and could damage solar cells located near the base of the satellite.

Minimizing Stresses and Displacements

To dissipate the released energy and thus minimize stress and motion, several hollow cylindrical beads were placed on each element. When the element unfurls, the beads slide outward and, as they accelerate, a portion of the element's rotational kinetic energy transfers to radial outward motion of the beads. Kinetic energy in the beads in the radial direction couples inefficiently into deformation of the element and decreases energy available to cause out-of-plane motion. Several short beads were required to allow the antenna element to wrap around the canister cylinder during the stowing operation.

The outward (radial) motion of the beads is arrested by a stop at the end of the element. Additional energy losses occur when the beads impact each other and the stop. There will also be some losses from friction between the beads and the antenna element.

Modeling Bead Motion

The effects of the bead motion were determined by using a simple model of a rigid rod (the element) with a sliding mass attached (the beads). For this model all of the beads on a single element were assumed to be contained within a single mass and friction was neglected. The coupled equations of motion for the system are

$$\ddot{r}(t) - \dot{\theta}^2(t)r(t) = 0 \tag{2}$$

$$[I_R + m_B r^2(t)]\ddot{\theta}(t) + 2\,m_B r(t)\dot{r}(t)\dot{\theta}(t) = 0 \tag{3}$$

where $r(t)$ is the radial outward motion of the bead(s) and $\dot{\theta}(t)$ is the rotational motion of the rigid rod (element). The mass of the bead(s) is m_B and the rotary inertia of the element about its base is I_R. For the remainder of this discussion the term "bead" is synonymous with the term "beads."

Some interesting features of these equations can be noticed. First, there is a damping term associated with the rotational motion and this is the product of the radial location of the bead, the radial velocity of the bead, and the mass of the bead. Second, if the initial location of the bead is too near the root of the element, it will accelerate slowly outward so that little energy transfers before the maximum stresses are experienced. Therefore, an initial location should be found that will maximize $r(t)$ and $dr(t)/dt$ before the element arm contacts the stop.

The equations are coupled and nonlinear and therefore have been solved numerically using the Mathematica software [3]. The numerical solution is valid until the bead reaches the end of the element. Several different bead masses were considered for the study. These masses were equal to 1.0, 0.5, and 0.25 of the total antenna element mass. After considering the energy transferred to radial motion of the bead for each

case, along with other factors such as the number of beads that could be conveniently packaged in the stowed antenna, the lowest mass of beads (0.25 of mass of element) was chosen. Doubling the mass of the beads decreased the energy by about 50 percent more.

The initial radial position on the element was set at 0.26 of the element length outward from the root. This position caused the bead to reach the end of the element at the same time the element arm contacts the stop. The required time for this motion is 0.238 second. Figure 7 shows the rotational velocity of the element as a function of time up to 0.238 second and Figure 8 shows the fraction of system energy that is converted to radial bead motion as a function of time. At 0.238 second, approximately 43 percent of the energy resides in radial motion of the bead. This amount exceeds the target of 40 percent discussed previously.

The ABAQUS FE model was modified in an attempt to simulate the bead motion during deployment. Because of the highly nonlinear nature of the bead sliding along the element, the simulation became too time consuming to simulate the motion until the bead reached the end of the element. However, the 70 ms of motion that was simulated verified the motion predicted by the simple rigid rod model discussed here.

ABAQUS was also used to determine the approximate response of the element with the mass of the bead located at its end after 43 percent of the energy had been dissipated. Results of this analysis showed that the maximum expected out-of-plane displacement of the tip of the element decreased from 1.14 m toward the satellite without the beads to less than 0.73 m with the beads present, which is an acceptable amount of motion.

Reusable Release Mechanism

This mechanism releases the FORTÉ mast on command from the ground and performs the same function as a pyrotechnic cutter for less cost, with less shock, and without teardown and replacement after test. It uses a Heat Operated Paraffin (HOP) actuator[1] rated at 222 N (50 lbf) push force for 3000 cycles for a stroke of 12.7 mm (0.5 in). The HOP actuator contains a paraffin that expands as it melts, and this is used to squeeze a stainless steel push rod out of a rubber boot. The actuator drive capacity is 222 N (50 lbf), however, with a safety factor of 3 applied, the maximum allowed release force is 74 N (16.7 lbf). The HOP is activated by running 28 V DC through redundant heaters at 10 W for approximately 60 seconds.

The preload that the actuator releases is 4400 N (1000 lbf). The ratio between the stowed and the release load is thus 60:1. A direct link system with a friction coefficient of 0.1 would require 444 N (100 lbf) to release this load, so a device with low friction or a long lever arm was needed, or a combination of these.

The final design uses a single roller to reduce friction as shown in Figure 9. In combination with this is a lever and drag link to maximize the release force and minimize the load on the roller. The contact surfaces are made of titanium with a yield

---

1 HOP actuator manufactured by STARSYS Research Corporation, Boulder, CO

strength of 1103 MPa (160 ksi) ultimate tensile strength, and a modulus of elasticity of 110000 MPa (16 million lb/in^2). High strength and a low modulus combine to maximize the contact stress capacity for a given weight and size.

The titanium is coated with electroless nickel to prevent galling. It has five moving parts not including the HOP actuator which is a purchased part. The force required to release the 4400 N load is approximately 31 N (7 lbf). The HOP actuator capacity has been rated upwards by test to 356 N (80 lbf), so the factor of safety on release for the completed design exceeds 11. The springs that are critical to operation are redundant. These springs prevent premature release during vibration and reset the HOP actuator after operation. The tie rod is attached to the mechanism by pushing the tie rod member inside the mechanism from the bottom and then pulling it back out which locks the tie rod into the ready position. Proper setup can be verified visually. The unit also has a safety pin that prevents premature operation.

This device has passed all qualification tests including vibration and thermal vacuum, and is set to be launched in 1995 with the FORTÉ spacecraft.

Conclusions

The FORTÉ antenna is a device conceived for a unique application. It combines a proven Astromast™ deployer with an antenna configuration developed by LANL/SNL. The antenna has passed all tests and the next step is integration into the FORTÉ spacecraft for launch in 1995.

References

1. Timoshenko. *Strength of Materials*. 3rd Edition, D. Van Nostrand and Company, pp. 54-56.
2. Hibbitt, Karlsson, and Sorensen, Inc., *ABAQUS Users' Manual Version 5.2*, Providence, Rhode Island (1992).
3. Wolfram Research, Inc. Mathematica Version 2, Champaign, Illinois (1992).

Antenna Spacing

9.66 m
8.54 m
8.05 m
7.99 m
6.84 m
6.09 m
5.21 m
4.18 m
3.00 m
1.61 m
0 m
−1.08 m

20° ±2°

Earth

Antenna Element Lengths

0.55 m
0.65 m
0.78 m
0.92 m
1.09 m
1.29 m
1.52 m
1.78 m
2.09 m
2.45 m (96.4 in)

Antenna elements
Extended mast
FORTÉ Spacecraft

Mast axis

.30 m (11.8 in)

Stack canisters

Antenna just released

Extended mast

Antenna root
Antenna element array #1

90°

±2°

Antenna element array #2

Deployment direction (~ 1 in/sec)

Coiled and stacked antenna

Antenna element array #4

Antenna element array #3

Figure 1. FORTÉ Antenna Deployment Schematic and Configuration After Fully Extended.

246
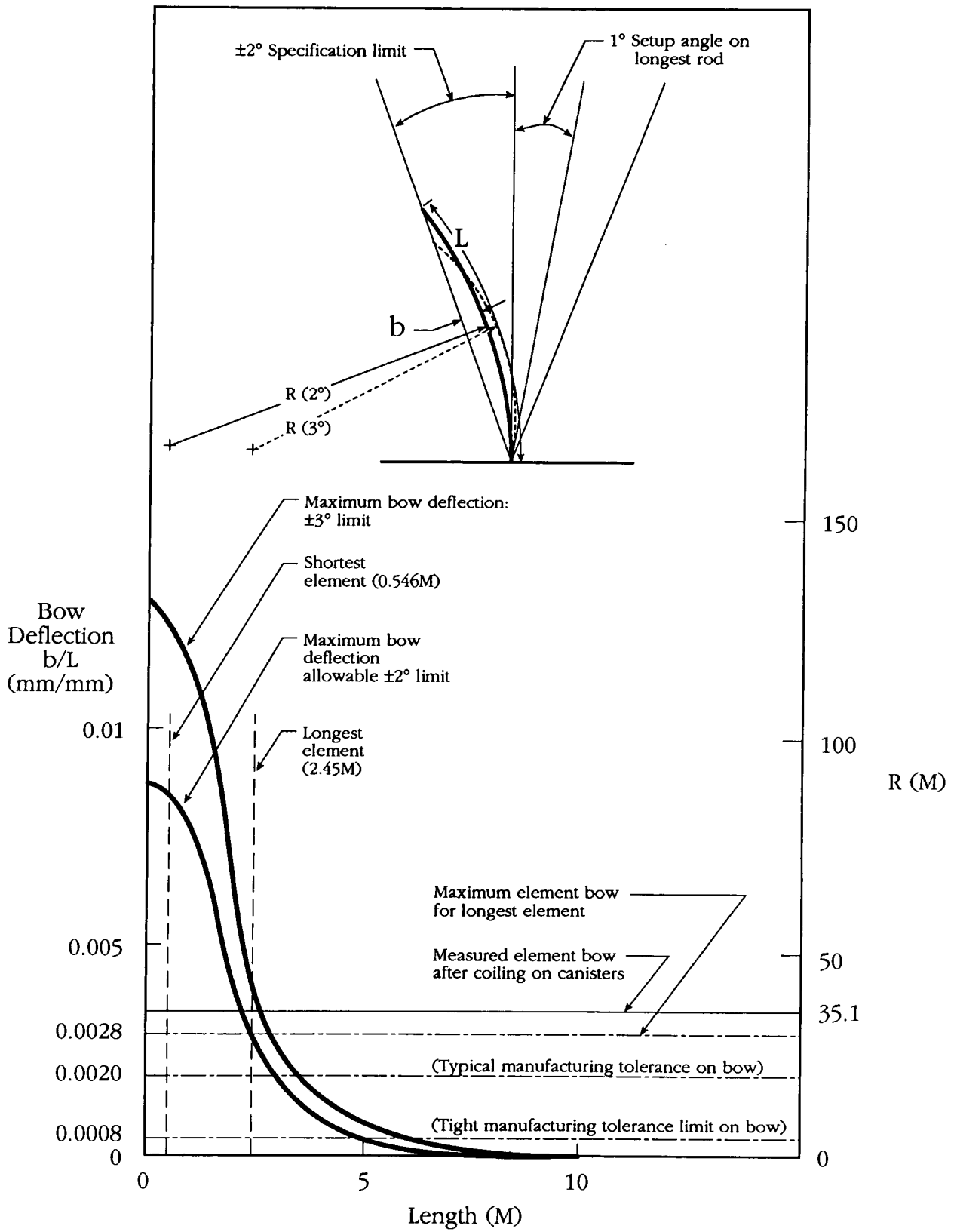
Figure 2. Required Straightness of Antenna Element as Length Increases and Setup Angle.
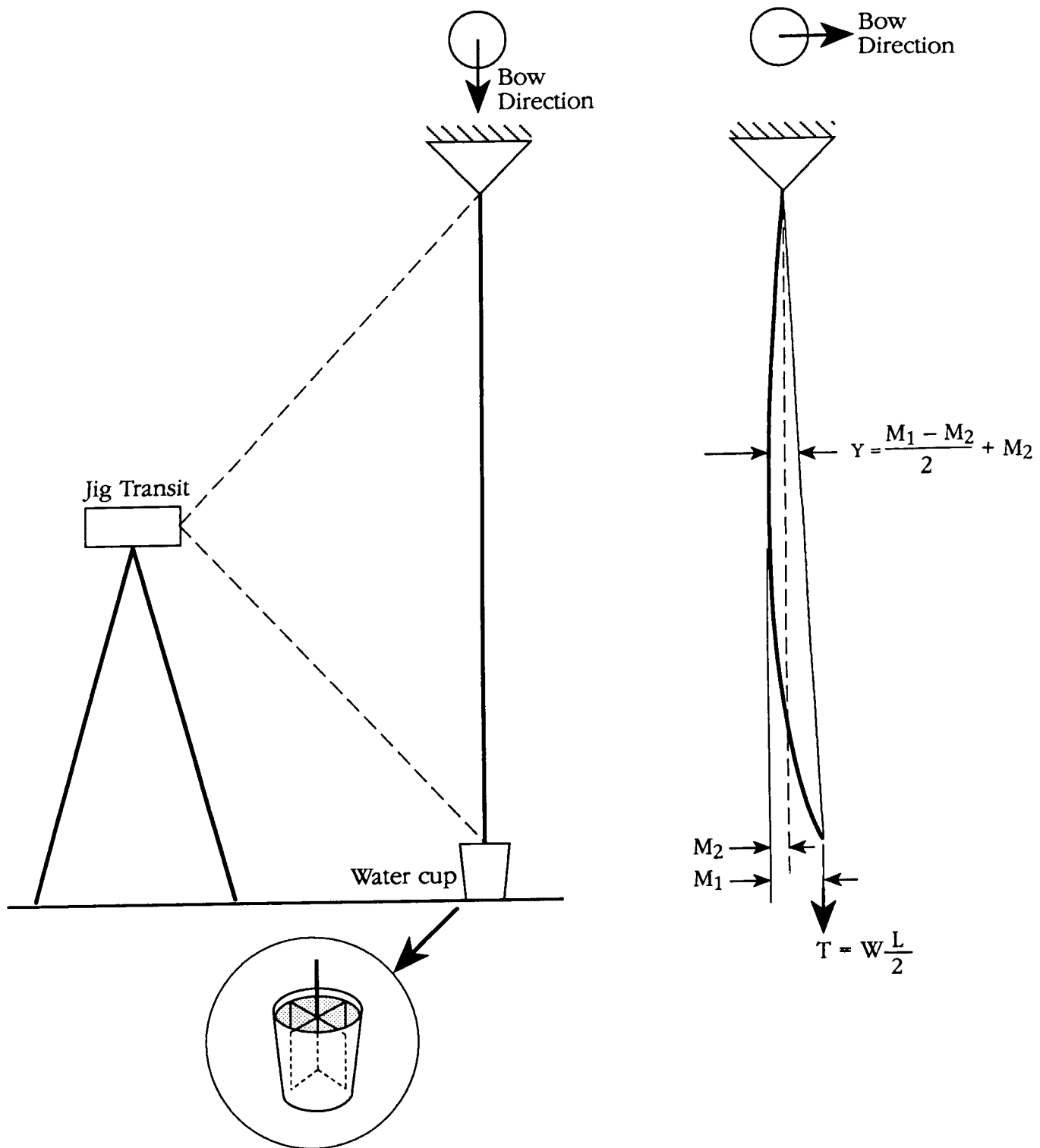
Figure 3. Measuring Bow Deflection of a Suspended Rod.
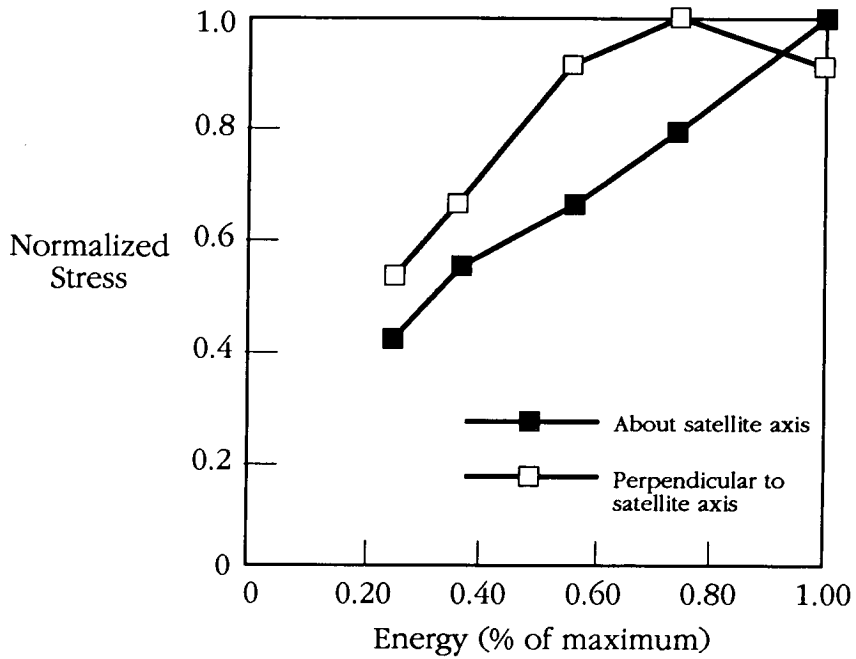
Figure 4. Maximum Bending Stress at the Root of the Antenna Element as a Function of Initial Kinetic Energy.
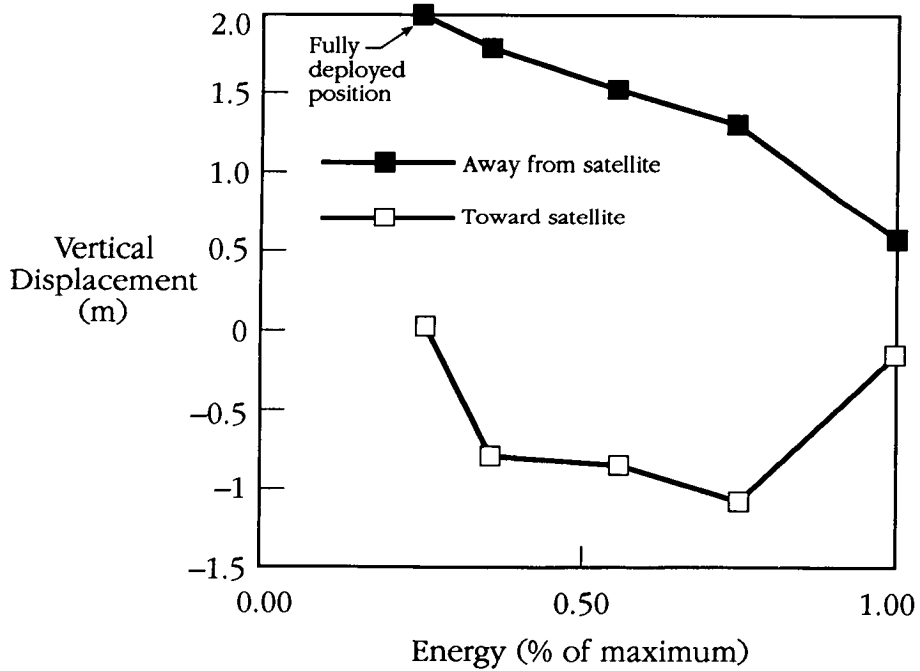
Figure 5. Maximum Vertical Displacement of Antenna Tip as a Function of Initial Kinetic Energy.

249

Side View   **Bottom View**

Final position of
antenna element.
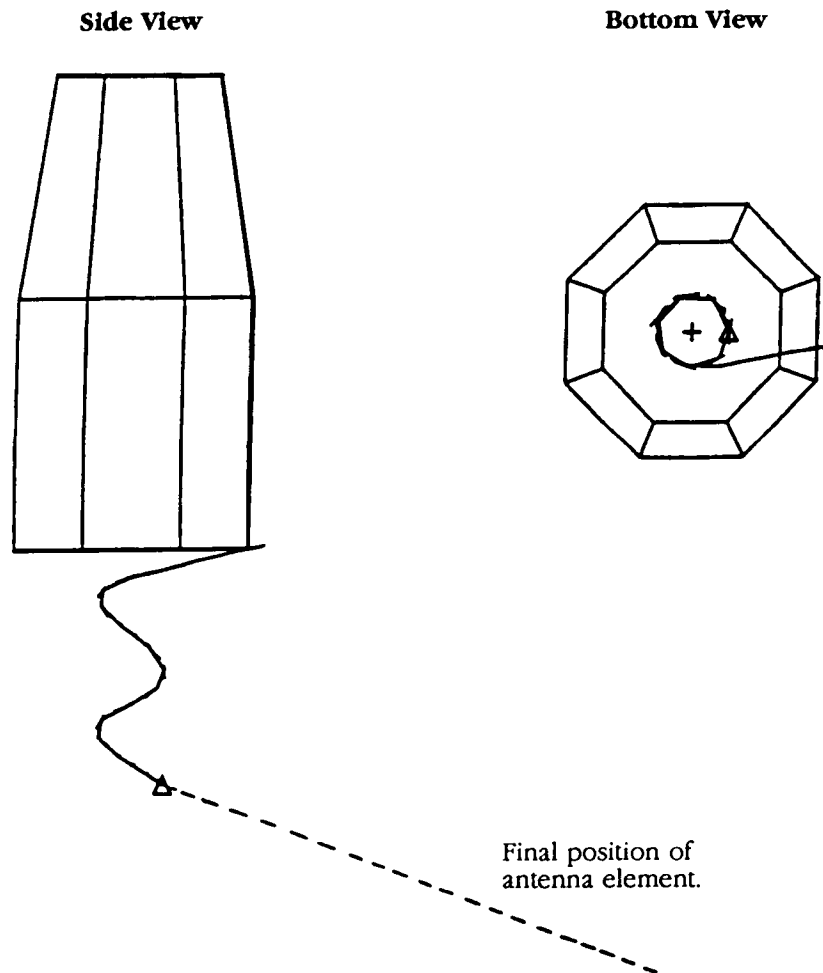
Element is shown contacting the bottom corner of the satellite.

Figure 6. Position of One Antenna Element at One Point of Time During
Deployment Without any Energy Dissipation Features Implemented.

250
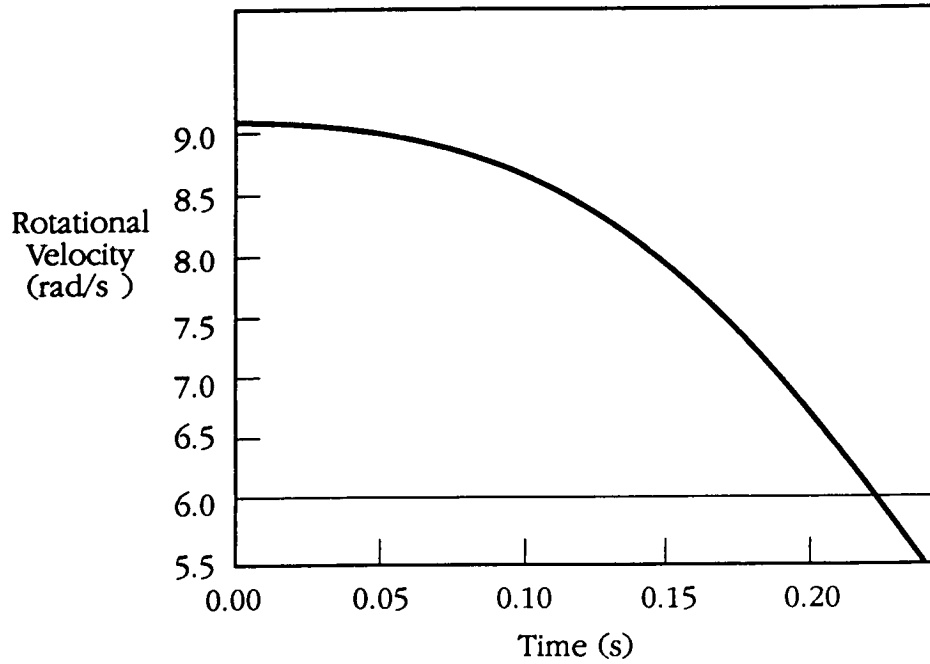
Figure 7. Rotational Velocity of Rigid Rod as a Function of Time.
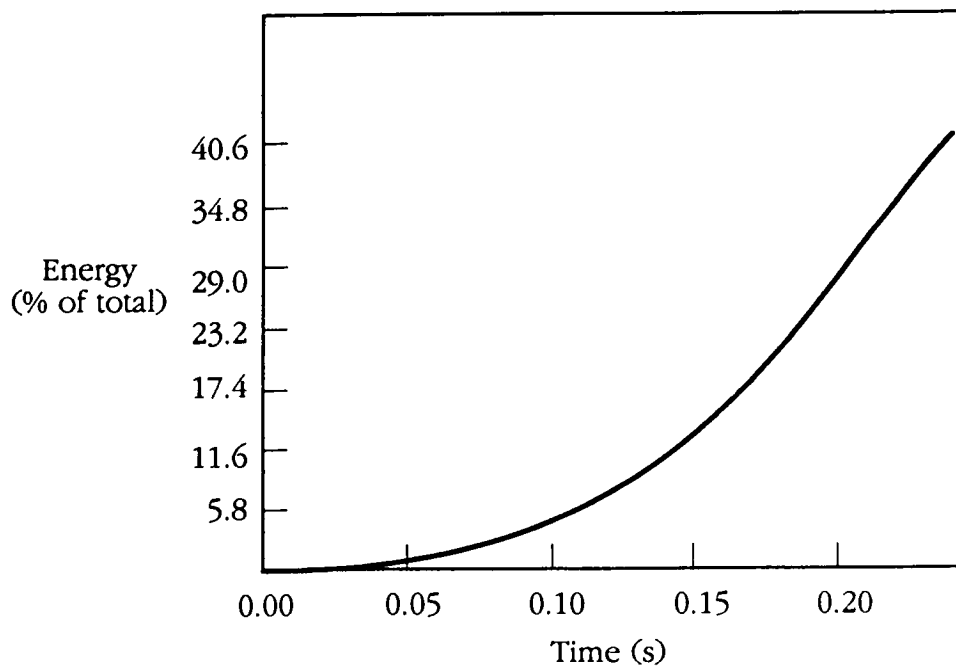
Figure 8. Percent of Total Energy Residing in Radial Motion of Bead as a Function of Time.
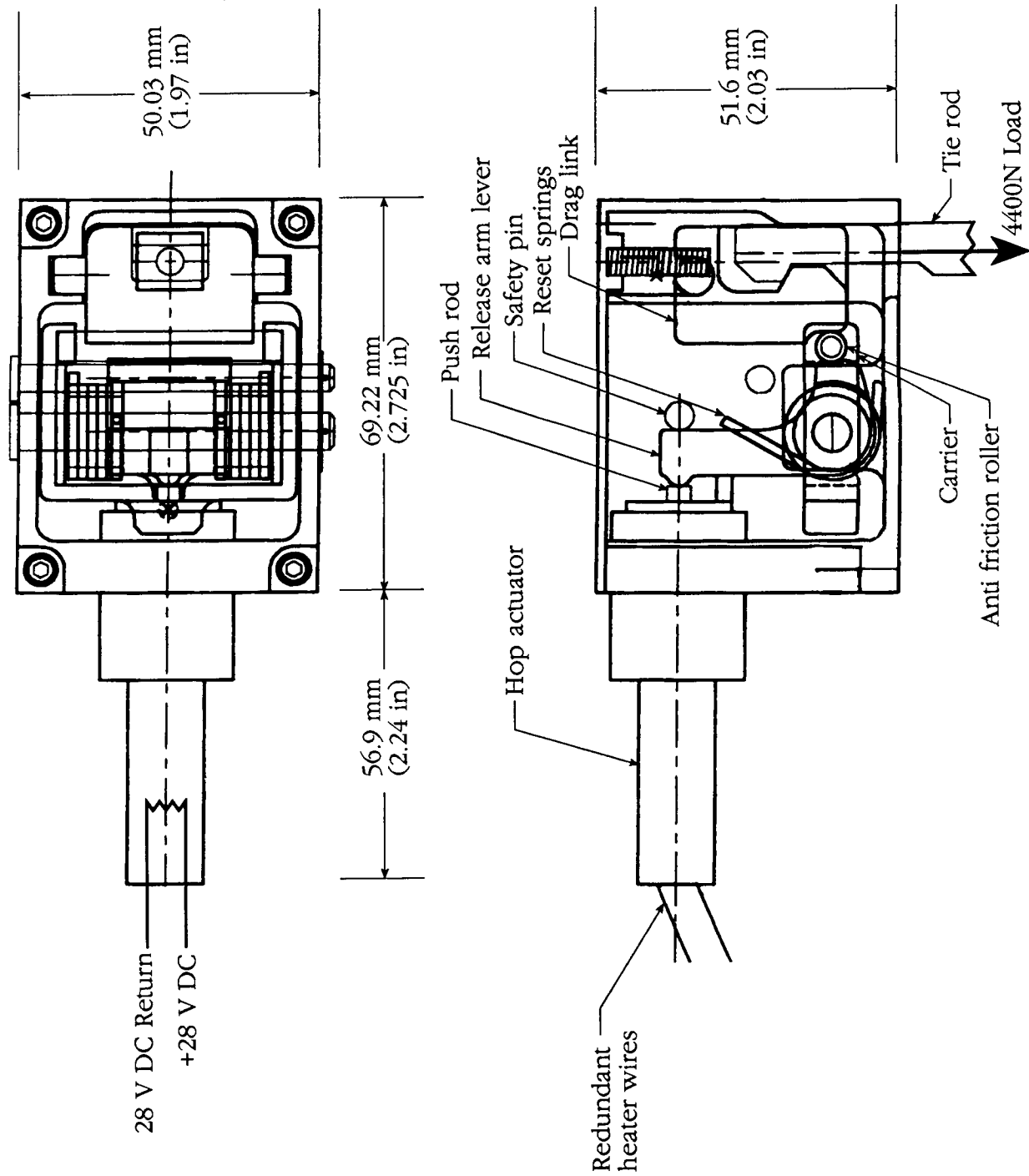
Figure 9. Schematic of the Reusable Release Mechanism.

50.03 mm (1.97 in)

69.22 mm (2.725 in)

56.9 mm (2.24 in)

51.6 mm (2.03 in)

28 V DC Return

+28 V DC

Push rod
Release arm lever
Safety pin
Reset springs
Drag link

Hop actuator

Tie rod

4400N Load

Carrier
Anti friction roller

Redundant heater wires

252

405758
14p.

Deployment and Retraction of a Cable-Driven Solar Array:
Testing and Simulation

P. Kumar* and S. Pellegrino*

Abstract

The paper investigates three critical areas in cable-driven rigid-panel solar arrays. First, the variation of deployment and retraction cable tensions due to friction at the hinges. Second, the change in deployment dynamics associated with different deployment histories. Third, the relationship between the level of pre-tension in the closed contact loops and the synchronization of deployment. A small scale model array has been made and tested, and its behavior has been compared to numerical simulations.

Introduction

Rigid panel solar arrays have been widely and successfully used for Low Earth Orbit missions with power requirements below 10 kW. Their ability to cope with many thermal cycles leads to a longer mission life, while simpler deployment mechanisms ensure reliable operation. In the standard design, for deploy-only missions, these arrays are deployed by a series of torsion springs located at the hinges. The motion of the panels is coupled by a series of synchronization elements, while a damping system attenuates the end of deployment shock. Typical deployment times are around 10 s. The design and analysis of such systems has been studied extensively [1-4].

Cable-driven arrays are used mainly for their retraction capability and to control end-of-deployment shocks more accurately. Typically, two continuous cables run over a series of pulleys connected to the hinges of the solar array. One end of each cable is connected to a motorized drum, whose rotation activates deployment or retraction. The principle of operation is illustrated in Figure 1. In Figure 1(a), a clockwise rotation of the drum shortens the overall length of the deployment cable and hence activates deployment: the angle θ increases from 0 to 90 deg. In Figure 1(b), a counterclockwise rotation of the drum shortens the length of the retraction cable and hence causes the solar array to retract, thus decreasing θ from 90 to 0 deg. Of course, the deployment cable needs to be lengthened during retraction and, for simplicity, the deployment and retraction cables can be wound on the same drum, but in opposite directions.

For example, a solar array with five full panels and a half-panel or a yoke has six degrees of freedom (dof), of which only one is controlled by the Deployment and Retraction (D/R) cables. The remaining five dof are eliminated by introducing five synchronization elements. A common type of synchronization element is the Closed Contact Loop (CCL), mounted alongside a panel and over two pulleys on either side of that panel. These pulleys are fixed to the outer panels, but are free to rotate relative to the inner one. Thus, the CCL couples the rotation angles of the two outer panels, provided that friction between cable and pulleys is sufficiently large. A chain of five CCL's will remove the five internal dof of the array, thus coupling the motion of panel 1

---

* Department of Engineering, University of Cambridge, Cambidge, U.K.

to that of the other panels. The remaining global dof, i.e. the rotation of panel 1 with respect to the spacecraft, is controlled by the D/R cable.
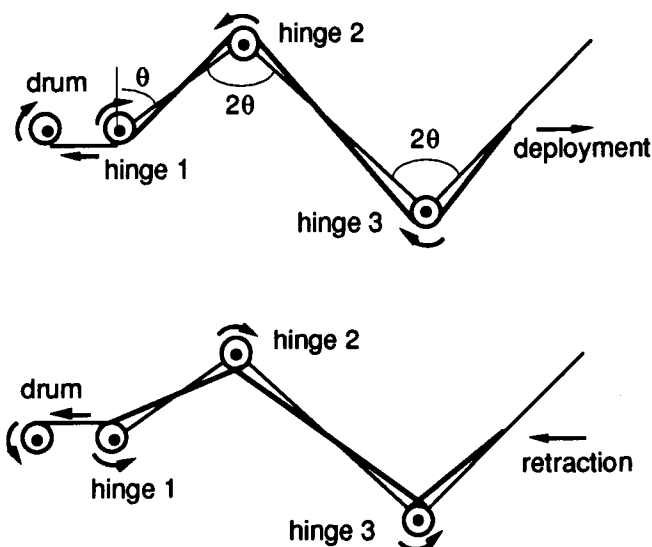
Figure 1. Operating principle of cable-driven arrays.

Ideally, each CCL should be highly pre-stressed to avoid slippage, and should also have high axial stiffness for total synchronization. However, a limit on pre-stress is imposed by the buckling load of the panels, while stiffness is limited by the need to control the thermal sensitivity of the system. Often CCL's are mounted in series with springs, whose stiffness is crucial to the dynamic behavior of the solar array.

The objective of this research is to study the D/R behavior of a cable-driven rigid-panel solar array. Three critical areas are investigated. First, the variation of D/R cable tension due to friction at the hinges. Second, the change in deployment dynamics associated with different deployment histories. Third, the relationship between the level of pre-tension in the CCL's and the synchronization of deployment. A small scale, model array has been made and tested, and its behavior has been compared to numerical simulations.

Experimental Setup

Model array
An accordion type, cable-deployed rigid-panel solar array has been set up. Its design, shown in Figure 2, is a simplified version of the Retractable Advanced Rigid Array used in the European Retrievable Carrier (EURECA) [5, 6]. The model array consists of one half-length panel and five full-length, 16 gauge (1.63 mm thick) Al-alloy panels. The panels are connected to each other and to horizontal brackets, bolted to a vertical plate, by continuous stainless steel shafts with radius r = 3 mm. All connections are through Al-alloy hinge assemblies, Figure 3(a), whose PTFE lined journal bearings have a friction coefficient μ = 0.15. Two multi-stranded steel cables, one for deployment and
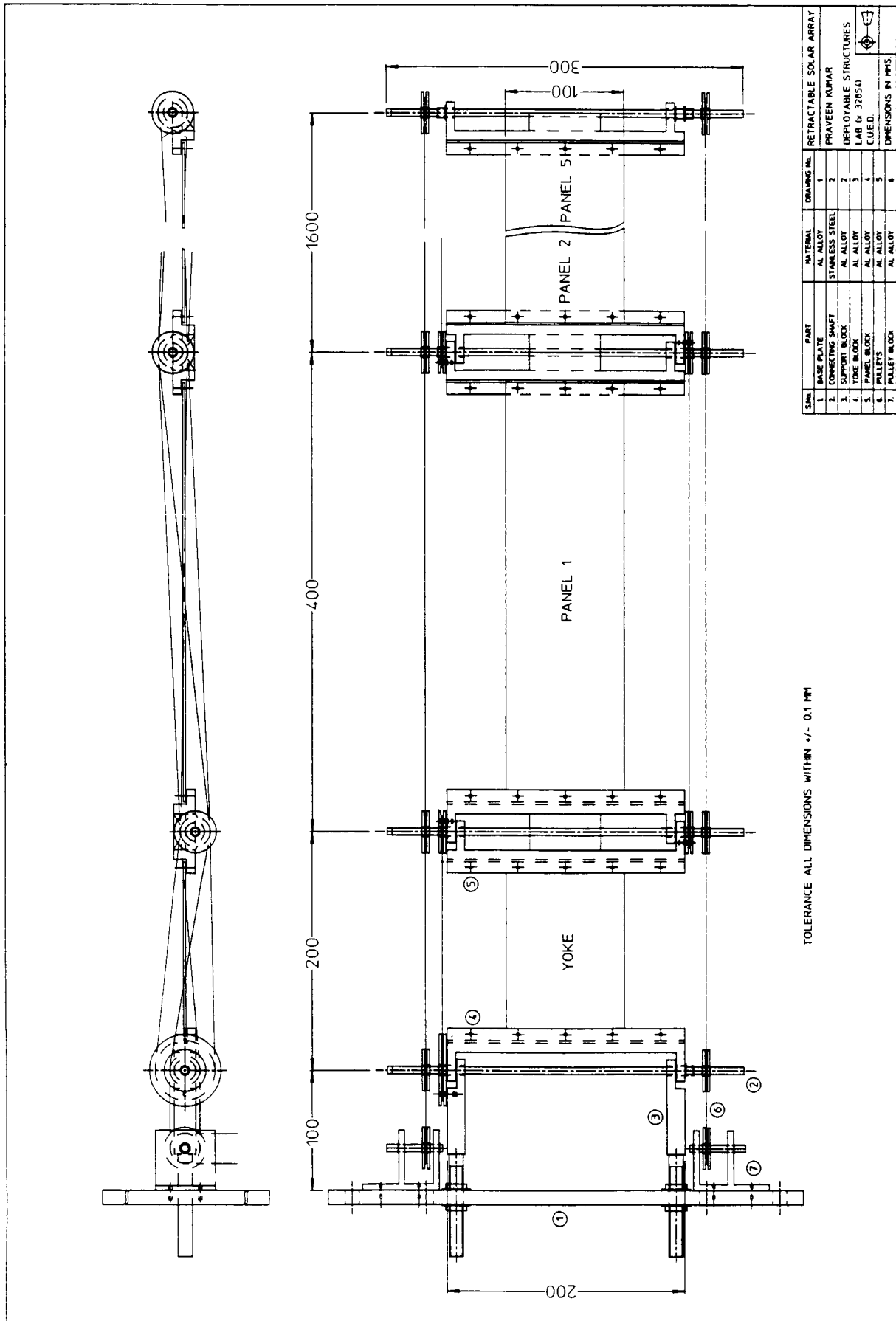
Figure 2. Schematic drawing of the model array.

S.No.	PART	MATERIAL	DRAWING No.
1	BASE PLATE	AL ALLOY	1
2	CONNECTING SHAFT	STAINLESS STEEL	2
3	SUPPORT BLOCK	AL ALLOY	3
4	YOKE BLOCK	AL ALLOY	4
5	PANEL BLOCK	AL ALLOY	5
6	PULLEYS	AL ALLOY	6
7	PULLEY BLOCK	AL ALLOY	7

RETRACTABLE SOLAR ARRAY

PRAVEEN KUMAR

DEPLOYABLE STRUCTURES
LAB (x 32854)
C.U.E.D.

DIMENSIONS IN MMS.

TOLERANCE ALL DIMENSIONS WITHIN +/- 0.1 MM
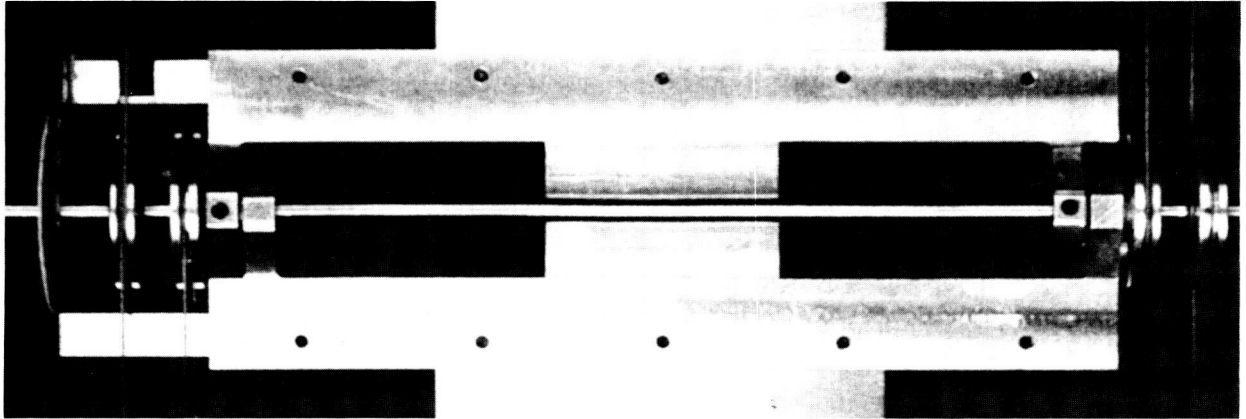
(a)
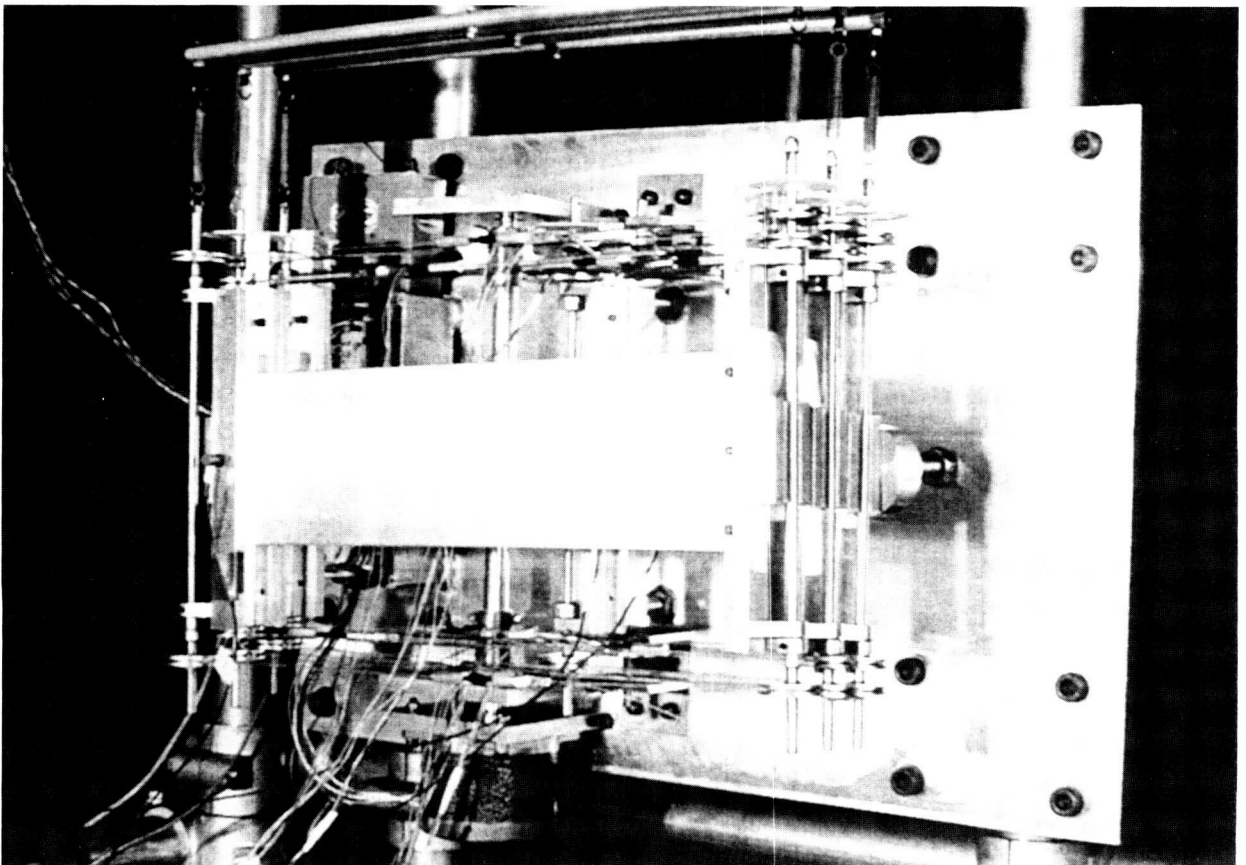
(b)

Figure 3. (a) Hinge detail. (b) View of array.

one for retraction, are mounted on either side of the panels. Each cable has diameter of 0.8 mm and breaking load of 54 N, and runs over a series of pulleys with radius R = 12.5 mm. These pulleys are mounted on the hinge shafts with the same journal bearings described above. The D/R cables are connected to a single drum, bolted to the vertical mounting plate shown on the left hand side of Figure 3(b). Five CCL's, each consisting of a multi-stranded steel cable in series with a soft spring, synchronize the motion of the panels. Each CCL applies a compressive axial force on the panel, whose magnitude is equal to double the pre-tension in the loop. The thickness of the panels is sufficiently large to avoid buckling, and yet the vibration of the array during D/R is appreciable. The total mass of the model array is 4.2 kg, mainly concentrated at the hinges. It is supported by a gravity compensation system consisting of three independent linear bearings running on horizontal rails. Each bearing is connected to two hinge shafts and has a mass of 0.1 kg.

Stepper Motor

Stepper motors offer many advantages over DC torque motors for space applications [7]. Particularly relevant to this study is their ability to follow accurately any prescribed D/R profile by simple open loop control. To eliminate positioning errors due to backlash, the motor has been connected directly to the drum, without any reduction gears. A well-known disadvantage of standard stepper motors without gears is the relatively large size of each step, a full revolution is usually divided into 200 steps, and hence one step corresponds to 1.8 deg, which results in a very irregular motion. However, each full step can be sub-divided into up to 256 steps using a microstepping drive, with the only disadvantage of reducing the available torque by up to 30%.

To estimate the maximum torque required from the stepper motor, the maximum difference between the tension in the deployment and retraction cables is required.

Assuming, for simplicity, a uniform tension F in the deployment cable, no tension in the retraction cable, and a uniform pre-tension S in all CCL's, the work done on the system must be equal to the energy dissipated by friction, for any small configuration change of the array. For a small rotation $d\theta$ of all panels, this gives

$$11 RF \, d\theta = 82 \, \mu r F \cos\theta \, d\theta + (44\cos\theta + 16)\mu r S \, d\theta \tag{1}$$

$$F = \frac{(44\cos\theta + 16)\mu r S}{11R - 82\mu r\cos\theta} \tag{2}$$

For r = 3 mm, R = 12.5 mm, μ = 0.15, S = 30 N and θ = 90 deg, Equation 2 gives

$$F = 7.2 \, N$$

Because there are no latches in this type of solar array, at the end of deployment the tension in the deployment cable has to be increased to 25 N to prevent hinge line gapping. Thus, with a drum radius of 10 mm a torque of 250 N•mm is required to deploy and pretension the array. Using a torque margin of 4, and an additional 30% for the microstepping drive, a final motor torque of 1.3 N•m is arrived at. Note that the motor torque requirement is linked to the final level of pre-tension of the array; the torque required for deployment is much lower.
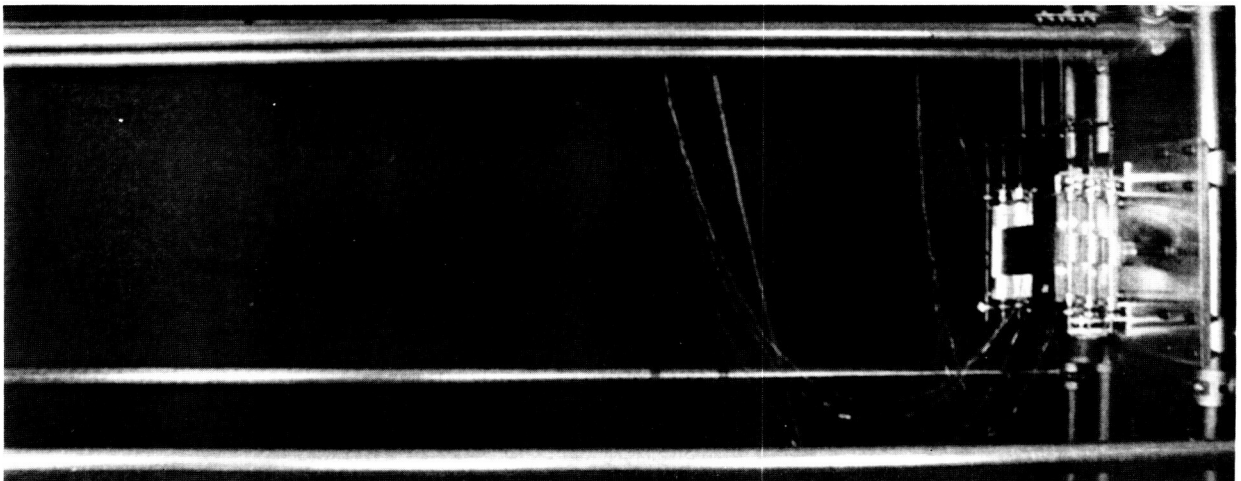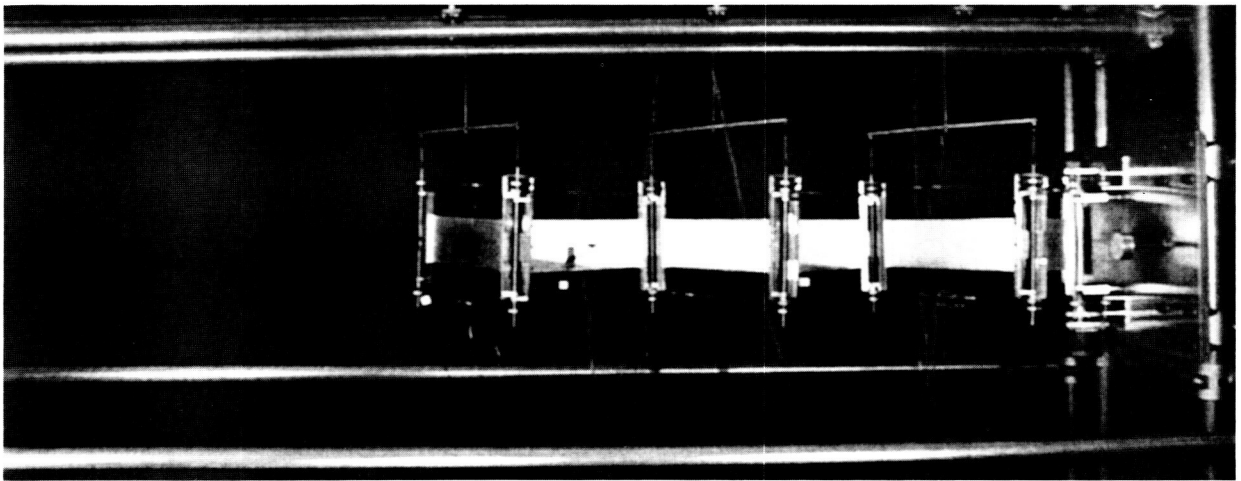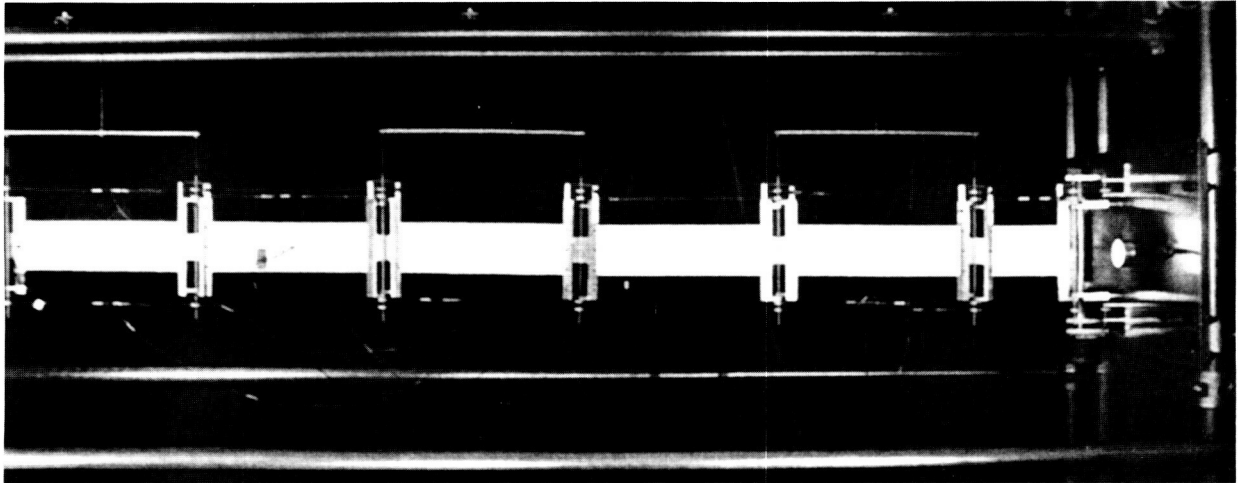
Figure 4. Retraction sequence.

A SMS 341-044 hybrid stepper motor has been chosen with a nominal torque capacity of 1.3 N•m @ 300 rpm. The motor is driven by a CMM 542 microstepping drive, set at 12800 steps/revolution and connected to a personal computer through a multi-function digital-analog converter board (Amplicon PC-30PGL). The board outputs a pulse each time the motor is required to turn through one step.

A constant angular speed of the drum is obtained by sending a series of pulses at a constant frequency, while a variable speed requires the pulse frequency to be varied accordingly. The drum rotation profiles that have been used in the experiments are shown in Figure 5. Note that the linear profile involves a sudden acceleration / deceleration of the array when the motion starts/stops, while the non-linear profile, a third-order polynomial with zero slope at the start and at the end is much smoother.
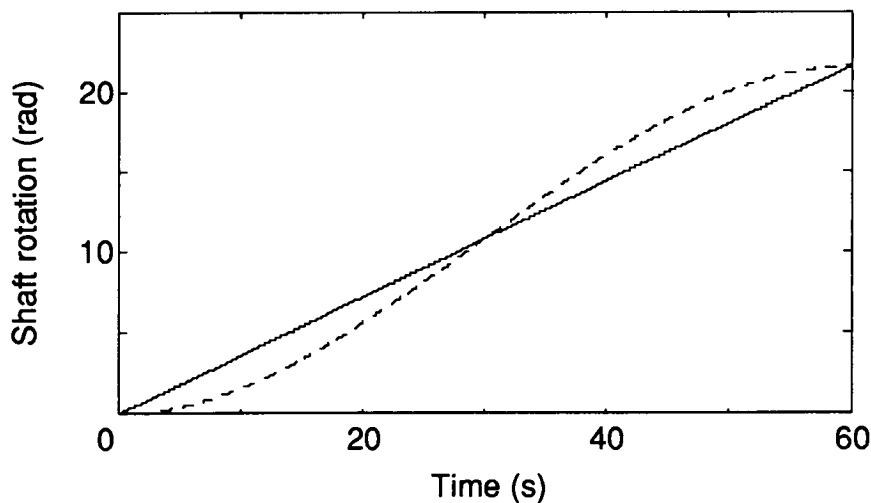
Figure 5. Linear and non-linear drum rotation profiles.

Instrumentation
The instrumentation of the model array includes three types of transducers. Strain gauges, glued on turnbuckles, measure the tensions D_{2_3}, D_{6_7}, R_{2_3}, R_{6_7}, respectively in the deployment and retraction cables, and between hinges 2-3 and 6-7. Pairs of strain gauges are mounted also on the CCL's between hinges 2-3 and 5-6. The torques applied by these CCL's respectively onto hinges 3 and 6 are obtained by multiplying the change of tension in each side of a CCL by the pulley diameter. These torques are positive if anti-clockwise. A Quartz Shear Mode ICP Accelerometer, mounted at the tip of the array, monitors vibrations. Finally, an angular dial gauge is attached to each hinge shaft, to monitor panel rotations.

Test Results

D/R tests have been performed for different drum rotation profiles, total deployment times, and CCL pre-tensions. This section presents a complete set of results obtained from a reference test, where the D/R time is T = 60 s, the drum rotation profile is a linear ramp, and S = 30 N. The behavior of the array during this test is compared to the

259

response when T = 30 s, when the rotation profile is non-linear, and when the CCL pre-tension is reduced to 15 N.

T = 60 s: Linear Ramp: S = 30 N
The results from the deployment test are shown in Figure 6. The tensions in the deployment and retraction cables, Figure 6(a, b), show very similar patterns. At the start $D_{2\_3} \cong D_{6\_7} \cong 3\,N$ and $R_{2\_3} \cong R_{6\_7} \cong 30\,N$. As the array starts to deploy, the cable tensions rapidly converge to $D_{2\_3} \cong 12\,N$, $D_{6\_7} \cong R_{6\_7} \cong 9\,N$, and $R_{2\_3} \cong 4\,N$. The tension in the deployment cable decreases from the drum towards the tip of the array, while the tension in the retraction cable increases. Finally, as the array reaches its fully deployed shape, the tension in the deployment cable quickly increases until the motor stops. The torques applied to hinge 3 and hinge 6 are shown in Figure 6(c), assuming that all synchronization torques are zero at the start. The torque applied by CCL_{2_3} is of greater magnitude and of opposite sign to that applied by CCL_{5_6}. There is no simple pattern in the variation of these torques, and no simple correlation between them.

The results from the retraction test are shown in Figure 7. The role of the deployment cable is similar to the role of the retraction cable in the earlier test. Hence, now $D_{2\_3} \cong 5\,N$ and remains approximately constant throughout, while D_{6_7} varies in the range 8-9 N. The tension in the retraction cable, though, increases steadily and $R_{2\_3} > R_{6\_7}$. Both torques applied by the instrumented CCL's vary with similar patterns and in the same range, approximately -100 to 0 N, but in opposite directions. CCL_{2_3} quickly drops to about -100 N·mm at the start and gradually increases, before dropping to about -150 N·mm towards the end of the test. CCL_{5_6} starts at zero and gradually decreases to -100 N·mm. As in the deployment test, these torques have been set equal to zero at the start; note that they are not zero at the end.

T = 60 s: Non-Linear Ramp: S = 30 N
Figure 8(a) compares the variation of D_{2_3} in the reference deployment test with the response obtained using the smoother drum rotation profile shown in Figure 5. The differences are quite small, and mainly due to the way the data is plotted. The tension builds up to its (approximately) steady-state value at a slower rate because during the first half of the test θ lags behind the reference test. Towards the end of the test, though, θ leads the reference test and hence the end-of-deployment tension increase occurs earlier. The two curves practically coincide if tension is plotted as a function of θ, instead of time.

The important difference between this and the standard test is that the shock loading of the array at the start and end of deployment is much lower. Figure 8(b, c) shows plots of accelerometer data taken at a constant sampling rate of 50 Hz. The 1 g acceleration peaks measured in the reference test have now been eliminated.

T = 30 s: Linear Ramp: S = 30 N
Halving the deployment time has no significant effects on D_{2_3}, but leads to larger shocks at the start and end of deployment.

(a)

(b)

(c)
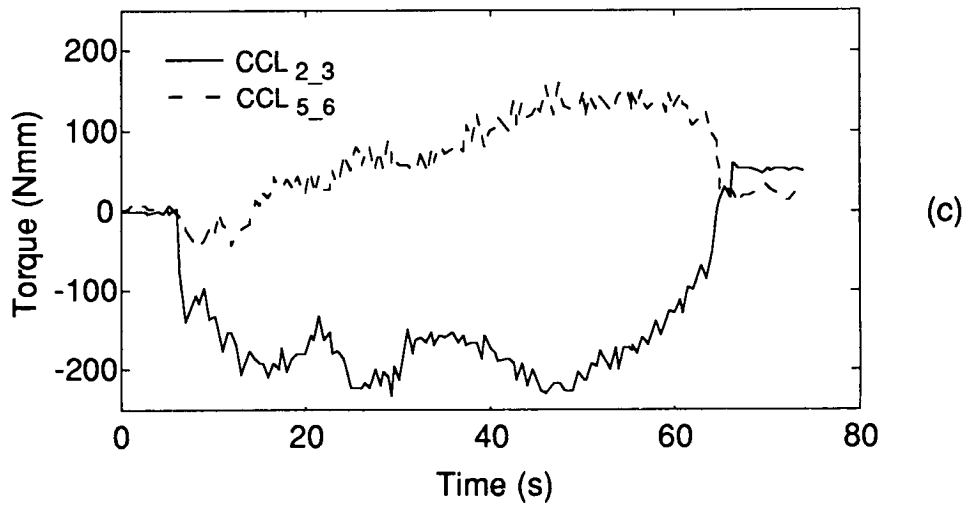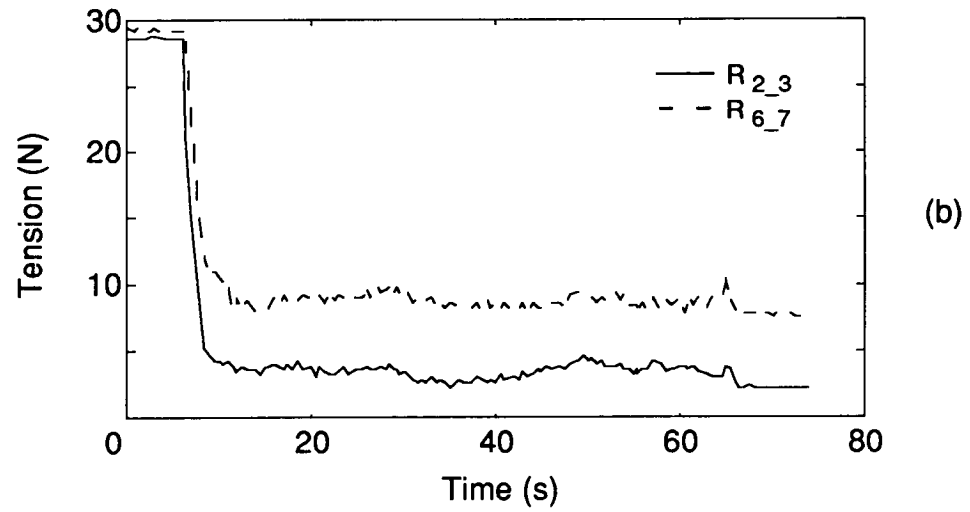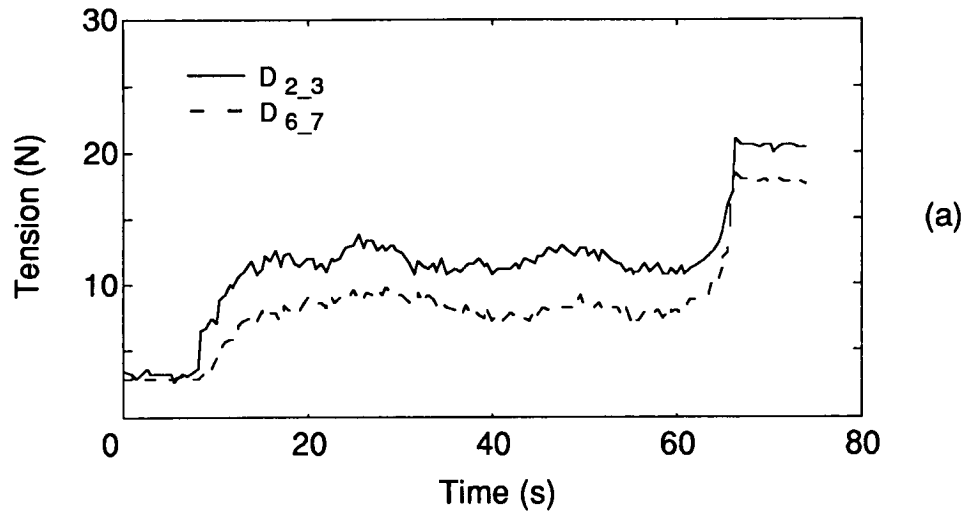
Figure 6. Deployment in 60 s, linear ramp.
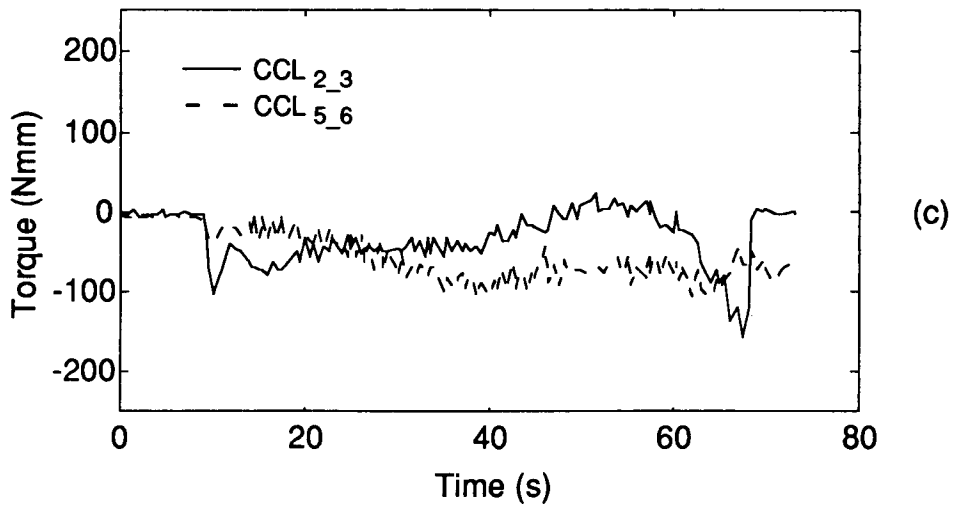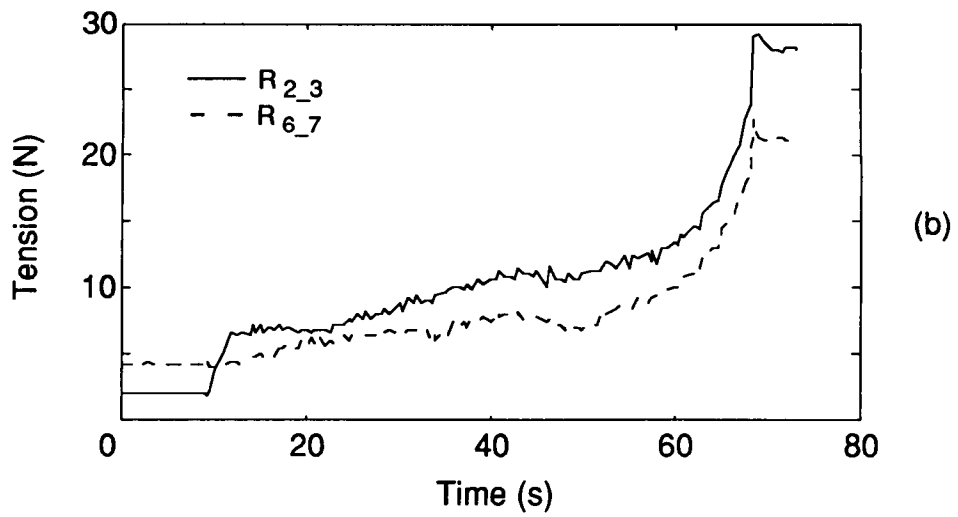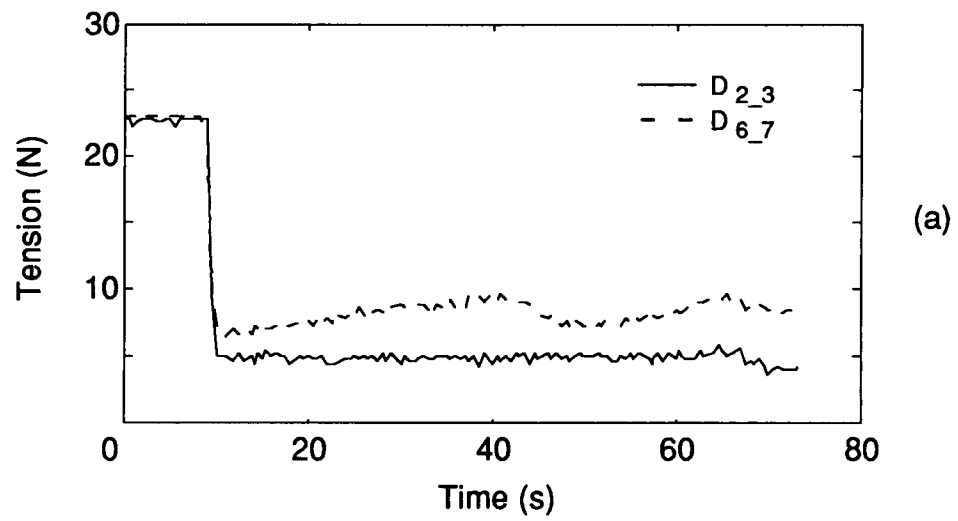
Figure 7. Retraction in 60 s, linear ramp.

(a)

(b)

(c)
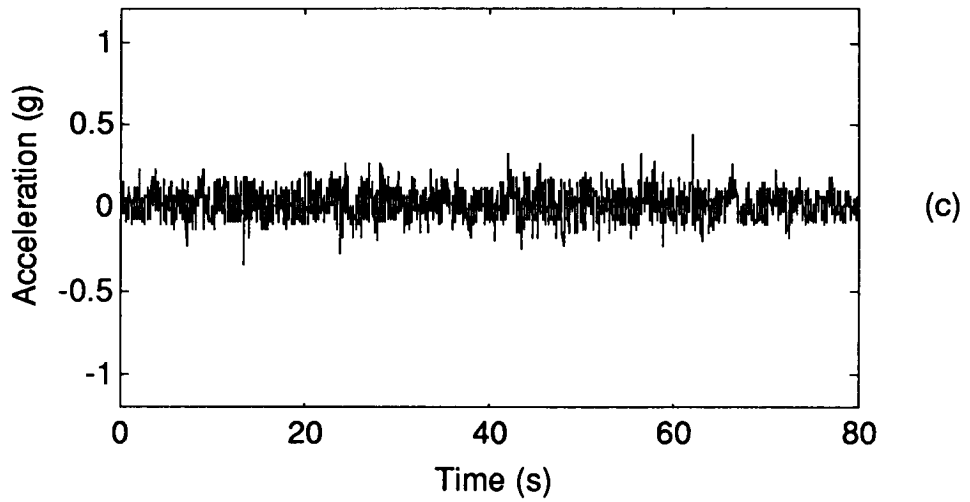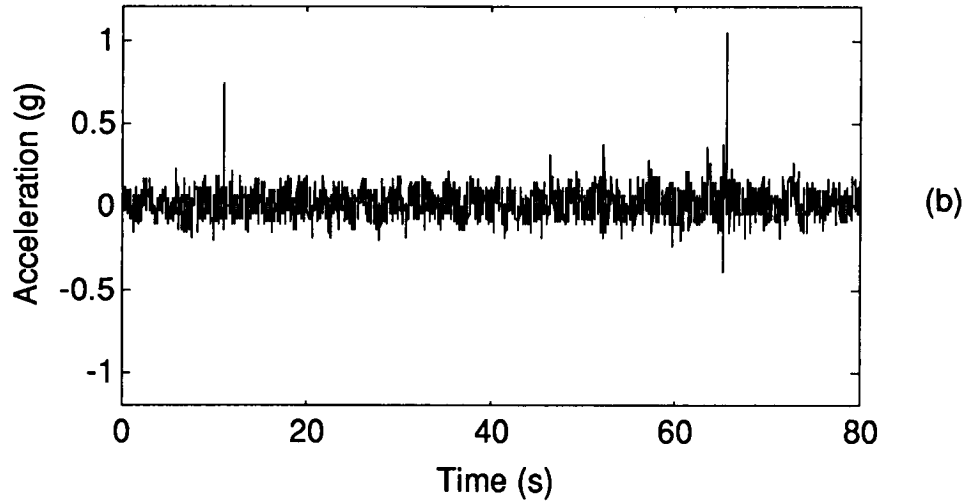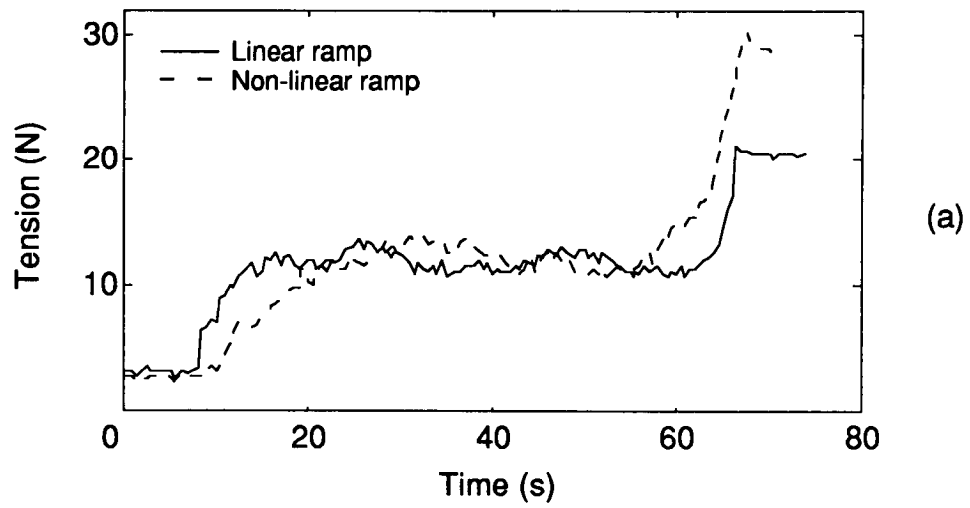
Figure 8. Comparison of linear vs non-linear ramp.

<u>T = 60 s: Linear Ramp: S = 15 N</u>
In the reference test there is good synchronization between different panels.
Figure 9(a) shows that all hinge rotations are within ±5 deg of their nominal values, i.e.
θ for hinge 1 and 2θ for hinges 2-6. If the CCL pre-tension is reduced to S = 20 N, the
array is still well synchronized. If the pre-tension is further reduced to S = 15 N there is
a substantial loss of synchronization, see Figure 9(b). Hinges 5 and 6 are now *lagging*
i.e. they have turned through an angle smaller than 2θ, whereas hinges 1 and 2 are
leading.
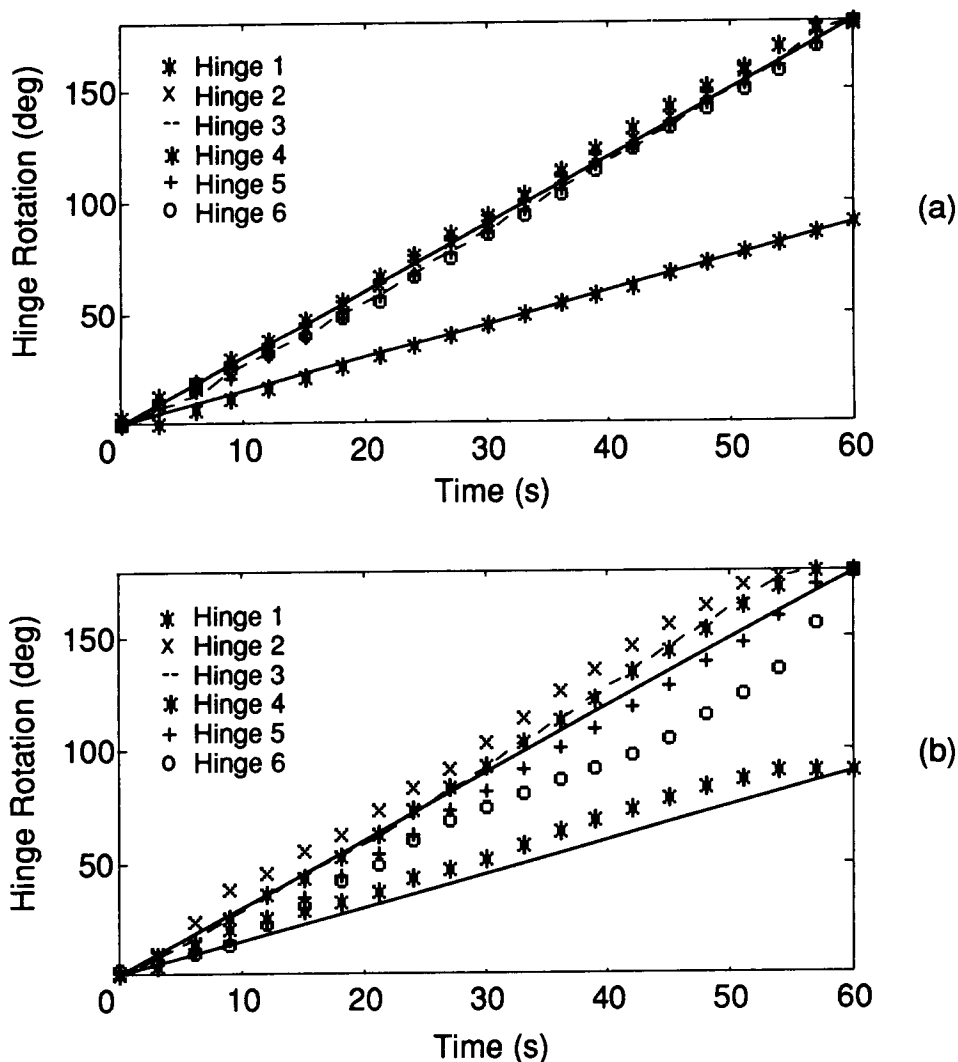
Figure 9. Hinge synchronisation for different CCL
pre-tension (a) 30 N; (b) 15 N.

264

Simulations

A model of the solar array has been set up using ADAMS [8], a multi-body dynamic analysis package which has been used for solar array deployment simulations [9].

The model consists of a two-dimensional chain of elements, connected by hinges. Each element simulates a panel, whose elastic properties are modelled by the stiffness matrix of a corresponding BEAM element. A frictionless pulley of radius R is connected to each hinge. The D/R cable is modelled using a SFORCE element, which applies a tangential force to the pulley connected to hinge 2. At any stage of the calculation, the magnitude of SFORCE is equal to the current length of the D/R cable, including the length wound onto the drum, less the initial length, multiplied by the axial stiffness of the cable. Synchronization between different panels is imposed by applying a series of torques to the hinges. Each torque is equal to the difference between the rotation angles of adjacent panels, multiplied by 2R times the axial stiffness of the cable. The effects of friction are simulated by applying frictional torques at all hinges.

A simpler, purely kinematic model of the array has also been developed, where five hinge rotations are coupled to MOTION GENERATORS.

Figure 10 shows a simulation of the retraction process, obtained from the kinematic model. Obtaining sensible results from the more complex dynamic model has proved quite difficult. If realistic values of the mass and stiffness properties are used, the calculations become very sensitive to initial conditions and small errors, and therefore it is impossible to achieve the correct motion. So far, the correct motion pattern has been obtained only from dynamic models with very low mass and stiffness.
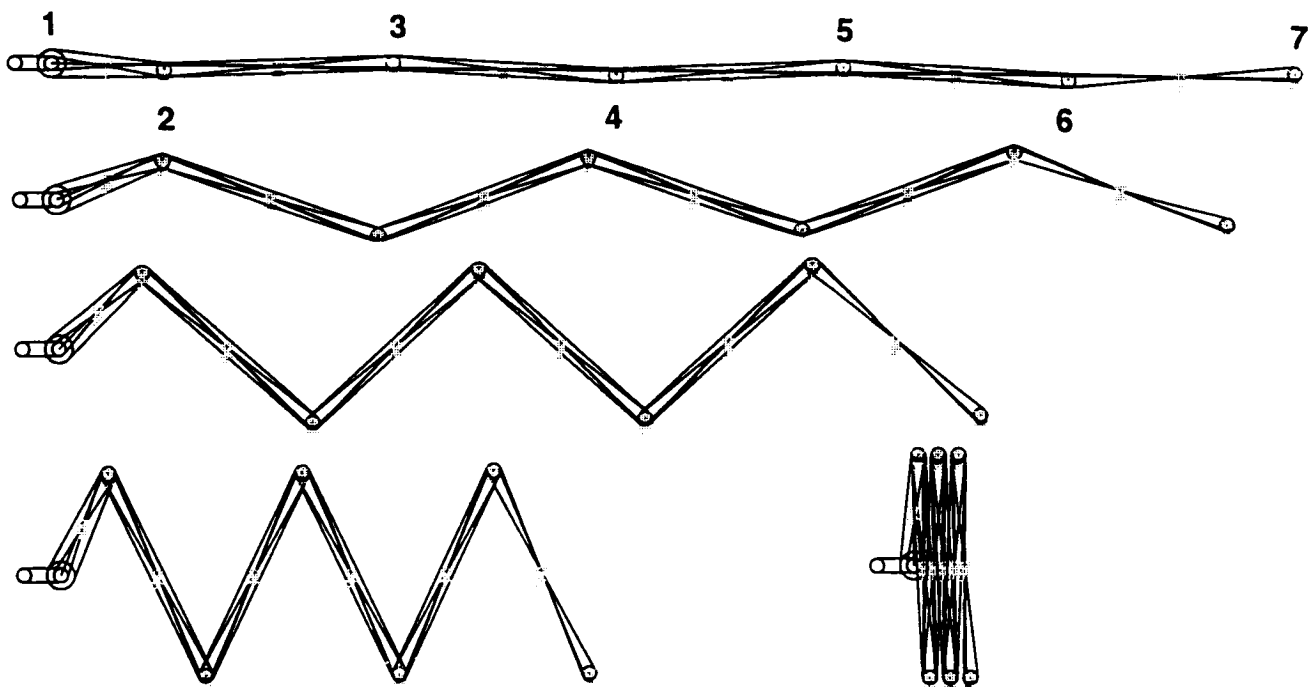
Figure 10. ADAMS simulation of retraction.

An alternative, quasi-static model of the array D/R process has been developed. It is assumed that all accelerations are sufficiently small to be negligible, and that limiting friction is reached simultaneously at all hinges. Therefore, tensions in the deployment cable can be obtained from a single value, e.g. D_{0_1}, while the tensions in the retraction cable can be obtained from R_{0_1}. These assumptions are believed to be reasonable in a simulation of a slow D/R process that neglects the initial and final transients.

During deployment, for any configuration of the array and for any given value of R_{0_1}, the forces and moments in each panel are related to the torques applied by the CCL's and to D_{0_1} by a non-linear system of equilibrium equations. A complete description of this analytical model will be published elsewhere. Figure 11 shows the predicted behavior of the array, obtained by solving the above system of equations for many values of θ, and for $R_{0\_1} = 6\,\mathrm{N}$ and $S = 30\,\mathrm{N}$.
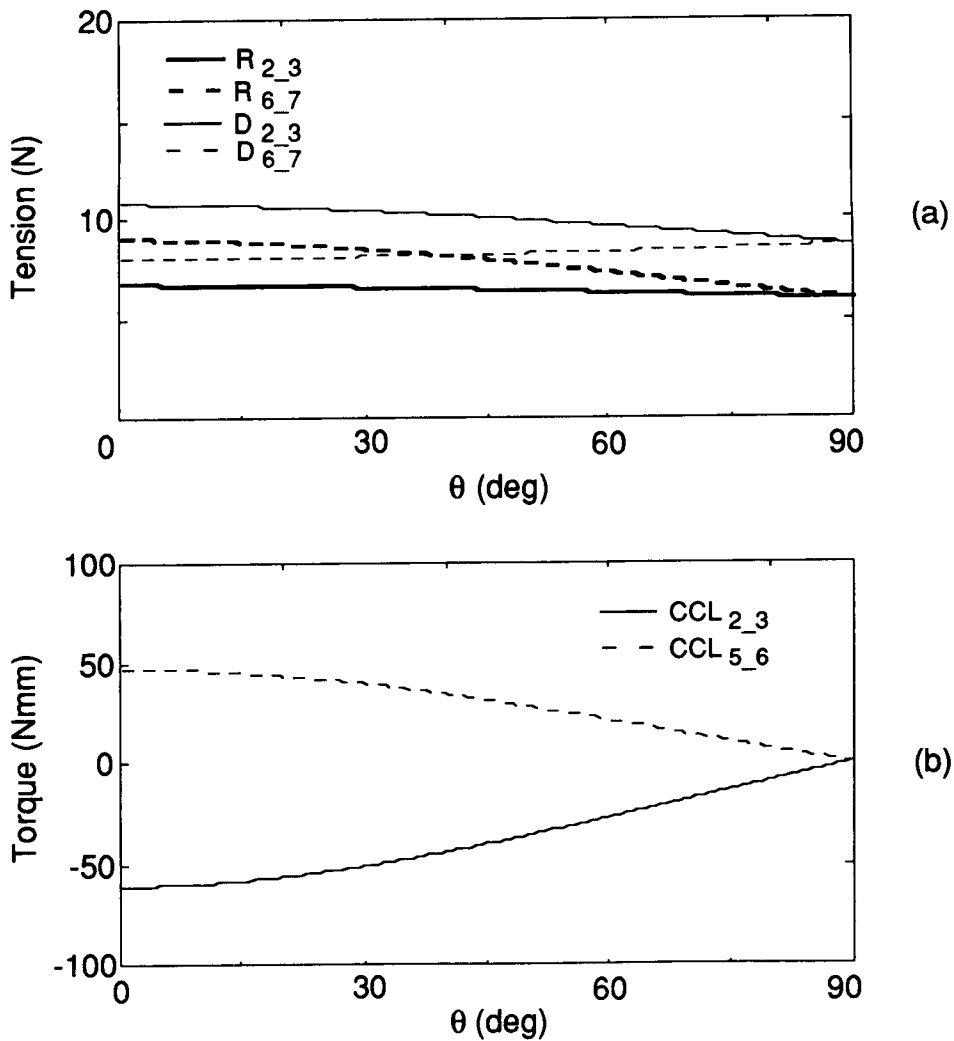
Figure 11. Analytical predictions of solar array behaviour during deployment.

A similar analysis of the retraction process has given almost identical results, but the tensions in the D/R cable are exchanged, and the sign of the CCL torques are reversed.

Discussion

The model array has shown, unexpectedly, significant differences in behavior between deployment and retraction. During deployment, the tensions in the D/R cables remain roughly constant, which is consistent with the simulation results. During retraction, though, the tension in the retraction cable steadily increases, which is not shown by the simulations. Also, significant differences have been observed in the variation patterns, as well as in the magnitudes of the synchronization torques applied by the CCL's. Thus, while there is a reasonably good correlation between the simulations and the torques measured during retraction, the agreement is poor for the deployment data. These discrepancies are not caused by inertia forces, neglected in the simulations, because almost the same response is measured when the array is deployed and retracted at much lower speeds. An alternative explanation is that in the present set-up there is an undesired coupling between array and gravity-compensation system, which is quite flexible. A stiffer system is being considered.

Acknowledgment

References

1.   Vorlicek, P.L., Gore, J.V. and Plescia, C.T. "Design and Analysis Considerations for Deployment Mechanisms in a Space Environment." *16th Aerospace Mechanisms Symposium* (May 1982), pp. 211-222.
2.   Wie, B., Furumoto, N., Banerjee, A. K. and Barba, P. M. "Modeling and Simulation of Spacecraft Solar Array Deployment." *AIAA Journal of Guidance Control and Dynamics*, 9, (1986), 593-598.
3.   Nataraju, B. S. and Vidyasagar, A. "Deployment Dynamics of Accordion Type of Deployable Solar Arrays Considering Flexibility of Closed Control Loops." *Proceedings of 38th IAF Congress* (1987).
4.   Celli, J., Lomas, N., Pollard, H. and Totah, N. "Intelsat VII Solar Array Electrical and Mechanical Design." *Proceedings of 13th AIAA International Communication Satellite Systems Conference and Exhibition*, (March 1990), pp 34-41.
5.   de Kam, J. "EURECA Application of the RARA Solar Array." *Proceedings of Photovoltaic Generators in Space* (October 1986), ESA, pp 105-114.
6.   Racca, G. D., Bongers, E. and Sebek, R. "Solar Array Mechanism Design and Performance." *Proceedings of EURECA Symposium*, (April 1994), pp 223-229.
7.   Hinkle, K. "Spacecraft Deployable Appendages." NASA Goddard Space Flight Center Report, May 1992.
8.   Mechanical Dynamics. "ADAMS Reference Manual Version 7.0." 1993.
9.   Roux, C. and Flament, P. "Solar Array Deployment Simulation Using ADAMS Software." *Proceedings of Second European Mechanisms & Tribology Symposium* (October 1985), pp 41-46.

/9957208664

4405791

Development of the Solar Array Deployment and Drive System for the XTE Spacecraft

Rodger Farley[*] and Son Ngo[*]

Abstract

The X-ray Timing Explorer (XTE) spacecraft is a NASA science low-earth orbit explorer-class satellite to be launched in 1995, and is an in-house Goddard Space Flight Center (GSFC) project. It has two deployable aluminum honeycomb solar array wings with each wing being articulated by a single axis solar array drive assembly. This paper will address the design, the qualification testing, and the development problems as they surfaced of the Solar Array Deployment and Drive System.

Introduction

The XTE spacecraft will be carried into orbit on a Delta II expendable rocket, and the solar arrays will remain folded until the spacecraft is off the Delta second stage. The two silicon-celled wings are comprised of three panels each, with a total array area of 17.88 m^2 (192.5 ft^2). Figure 1 shows the panels stowed and deployed. By a timer sequence on the spacecraft, the two wings are deployed by initiating the pyrotechnic pin pullers in the release mechanisms. Kick-off springs initiate the first motion to break the stiction and spring driven hinges with rotary viscous dampers carry the panels to their deployed positions minimizing the kinetic energy. Limited travel of ±90 deg was required to articulate the arrays, and this was accomplished with a solar array drive composed of a main hinge, a stepper motor based rotary actuator, and a rotary cable wrap to transfer power and sensor signals from the array.

Some of these mechanisms were an outgrowth of the devices designed for the COBE spacecraft. What was attempted early on in the preliminary design of the solar array and antenna deployment systems was to use the same or similar components not only between the two subsystems, but also between two spacecraft, namely XTE and the Tropical Rainfall Measurement Mission.

The qualification program progressed to a very late date before problems became evident, most notably unusual wear in the harmonic drive of the rotary actuator, G-negation imbalance during deployment tests, and honeycomb panel face sheet delamination of the flight solar array panels.

---

[*] NASA Goddard Space Flight Center, Greenbelt, MD

C-4

Component Descriptions

Solar Array Drive Assembly

The Solar Array Drive Assembly, or SADA, consisted the three main subassemblies: the Rotary Actuator, the Cable Wrap, and the Main Deployment Hinge. Figure 2 shows a cross section of this device.

The Rotary Actuator is a Schaeffer Magnetic's modified type 5 actuator with an output bearing from a type 6 drive, thus it was called a type 5 and 1/2. It is a three-phase, six-state stepper motor with a 200:1 reduction gear harmonic drive. The harmonic drive was a "silk hat" type with a pitch diameter of 6.35 cm (2.5 in). Materials for the harmonic drive are as follows: the flexspline is 304L stainless steel, the circular spline is 17-4 PH stainless steel, and the wave generator bearing is 440C stainless steel. The gear teeth and bearings were lubricated with Penzane 2000 synthetic hydrocarbon oil, with a 5% lead napthanate additive as well as an antioxidant. An internal rotary incremental encoder with three absolute positions provided position, velocity, direction of travel, and could be used in a closed or open loop mode. The encoder used pairs of light emitting diodes and photo transistors on several tracks. A circular disk with a punch-out pattern placed between the diodes and transistors provided the logic signals.

The Cable Wrap is a device in which individual hook-up wires have been sewn together to form two belts that spiral around a central reel. This two arm spiral wrap communicates 76 wires (mostly 20 gage) across the rotary joint, and in addition (in their own separate chambers) two twisted shielded pair wires for the coarse sun sensors on the arrays. The spiraling parts of the two belts are each 0.914 m (36 in) long and 6.35 cm (2.5 in) wide, with the inner diameter of the reel being 4.19 cm (1.65 in), and the outer diameter of the reel being 13 cm (5.12 in). The two main belts are separated by a sheet of 127 μm (0.005 in) thick Kapton, which greatly smooths the sliding friction between the two belts and their Dacron stitches. A "twill weave lock stitch" was used to sew the wires together. The reel and housing were aluminum with an anodized/Teflon coating. The cable wrap has a maximum travel of ±300 deg (where it either winds completely on the inner diameter or out on the outer diameter), but the designed use is between ±175 deg where it can operate in the "sweet spot" region of low friction. Maximum design travel is estimated by relationships written in Figure 2.

The Main Deployment Hinge bolts onto the output face of the rotary actuator, and rotates the wing 90 deg from the spacecraft body. It does this with constant torque spring laminates and a rotary viscous damper, kept warm with strip heaters and thermostats. A delay latch connected to the extension of the locking latch prevents the three panels from their final deployment until the main hinge has rotated the wing at least 85 deg. This hinge also carries the thrust launch loads of the outer solar array panel.

Panel to Panel Hinges

These hinges have spherical bearings to accommodate misalignments and distortions, and act as a redundant rotary path. These hinges are installed in pairs with one fixed, the other free to float along the hinge line. One hinge of the pair has a rotary viscous damper (same as the main hinge) and the other hinge has a rotary potentiometer for position telemetry.

Honeycomb Panels

The panels are made from 7075 T73 aluminum face sheets, 180 μm (0.007 in) thick. The overall panel thickness is 2 cm (0.787 in) and outside dimensions are 1.067 m x 2.79 m (42 x 110 in). The aluminum core density is 32 $kg/m3$ (2.0 $lb/ft3$) with a cell size of 4.8 mm ($^3/_{16}$ in). The FM123-2LVC adhesive was selected for its low outgassing qualities and history of use at the GSFC. The lowest density film was used. The panels have internal doublers and machined blocks. One side of each panel was insulated with 152 μm (0.006 in) of ED-3, a type of E-glass fiberglass.

Release Mechanisms

The retention/release mechanisms have at their heart pyrotechnic HiShear pin pullers with 6.35 mm (0.25 in) diameter pins that could retract with a 4003 N (900 lb) single shear side force. Three jaws hold a tension/release rod with a conical end, and two of the three jaws were restrained with pin pullers. Release can occur with the retraction of one out of the three jaws. The tension/release rods would compress a series of cones and vee guides, with preloads selected to allow expansion and sliding of the panels (Figure 3). The degrees of constraint were selected in order to isolate it from spacecraft generated loads which could damage the arrays. The cones and vees were made from titanium with a titanium oxide / Teflon coating, although upon reflection a better choice perhaps would have been aluminum with an aluminum oxide / Teflon coating to lessen the chance of galling and increase workability for shear pin installation. Braycote 602 grease was used liberally on the interfaces.

Qualification Program Overview

The qualification of the system consisted of components that had undergone testing, building up to a full assembly qualification test program. This included vibration, acoustic, ambient deployment, cold deployment, hot deployment, and torque margin deployment tests. In parallel to these efforts, life tests of the cable wrap, the actuator, and the SADA were performed to address the wear issues.

System Test Methods

The most interesting part of the test program was the full up deployments of the solar array wing. With G-negation consisting of a combination of airpads and counter weights, a full, uninterrupted, end to end deployment of all the hinge axes could be accomplished in one test in the same manner as the anticipated flight deployment.

Early in the program it was recognized that the air pad system would have to compensate for a hinge axis that was close but not perfectly parallel to gravity. If the solar array wing wanted to climb up hill during a deployment test due to an imperfectly

aligned hinge, the required change in potential energy would have to be supplied by the hinge springs. That of course was unacceptable because the springs did not have that much stored energy to spare, resulting in a loss of torque available to swing the wing out. Instead, the energy should be supplied by the airpad suspension system. The airpad assembly would have, in addition to the airpads, a cylinder/piston arrangement. Air pressure controlled by a regulator would float the piston and anything it had to support (such as a solar array) with a constant force. The rise or fall of the piston during the deployment could compensate for a misaligned hinge. What is necessary and easy to control is that the airpad table be very level. Figure 4 shows this arrangement. The constant force desired could be achieved by either multiplying the piston area with the air regulator pressure, or by monitoring the set of strain gages that was applied to the support tube between the piston and the load. This tube was made thin enough in order to make the strain a measurable amount. Swales and Associates, Inc., a local support contractor designed this air pad system.

Producing full deployments under thermal conditions posed a great challenge, and a compromise allowed a practical solution. The compromise was to simulate flight temperatures and gradients while in the stowed configuration, and to release thermal control just before and during deployment. This was accomplished with a thermal insulating box encapsulating the array, and was controlled by liquid nitrogen and heaters. Two thermal circuits helped to produce the desired gradients, although the magnitude of the panel to panel gradients were not achieved. When the bulk temperatures and gradients were sustained for some minutes, the thermal box lid was quickly removed and the pyro pin pullers were subsequently fired.

Torque margin verification was simply demonstrated by removing 50% of all hinge springs and timing the deployment. Each hinge line had two springs, and so removing one spring per hinge line produced the desired deficiency. The result was that the deployment took about twice as long, indicating that the Coulomb friction in the system was a small fraction of the spring force available. This demonstrated a torque margin greater than 2, and by implication of the deployment speed and a known damping rate, a much higher calculated margin can be said to exist.

Torque margin verification of the rotary actuator was done by a combination of test data and modeling. Since the device uses a 200:1 reduction gear, the margin to be concerned with in our case was the internal torque margin at the motor rotor. Since applying an internal brake force to "dial up the load" to measure torque margin was impossible, test data of the input friction vs temperature had to be measured and modeled instead. This was done on the qualification unit motor rotor and harmonic drive, lubricated with Penzane 2000 on a test stand. The temperature was varied from 50 deg C to -20 deg C. Schaeffer Magnetics provided this crucial data, which was incorporated into a GSFC-generated computer program called Mosim. The program could "dial up" this friction map to see the resulting effect of the dynamics of the rotor over different temperatures. With the solar array inertia tuned at 1 Hz, the program predicts a margin of 3 while at -5 deg C (Figure 5). What was interesting to note, since the harmonic drive error was also modeled, was that the 2 per revolution harmonic drive error produced a 1 Hz sinusoidal output at 120 pulses per second (PPS) superimposed onto the steady motion. This predicted result was clearly demonstrated

271

during testing with a tuned simulator bolted to the output flange. A very strong coupled response between 105 and 135 PPS resulted. The speed had to be within 10 PPS of the center frequency for the response to grow. Of course we needed additional confidence of Mosim's power to predict, and this was done by comparing the running torque vs speed test results, as well as matching the motor rotor ringing motion at temperature. This was accomplished in an indirect fashion by measuring the back EMF of the redundant motor windings while running at low speeds such as 10 PPS. Mosim would predict the voltage trace between two phases and a comparison made to test voltage data. Also the predicted current trace in one active phase could be compared to test data at low and high speeds such as 10 and 200 PPS. The characteristics to compare were the wave form shapes, frequency, amplitudes, and decay rate (low speed only). Additional tests to compare would be predictions of the threshold voltages at 28 and 200 PPS. Figures 6, 7, and 8 show some typical simulation results. It is of paramount importance that the effects of the drive electronics be incorporated into any simulation model of a stepper motor actuator, as the shape of the current pulses can have a drastic effect on the high speed torque capability.

Problems Encountered and Solutions

Harmonic Drive
Upon the completion of the rotary actuator qualification unit partial life test, no outwardly signs of deterioration could be detected by any of the tests designed to monitor health (threshold voltage, output torque). But when the unit was dismantled for inspection, it was discovered that a significant amount of wear had occurred in the harmonic drive, especially in the bearing to flexspline interface, which was unprecedented. The gear teeth were partially worn as well. The 304L flexspline inner diameter had galled with the 440C bearing outer race, the inner race had slipped down the wave generator plug, and the surfaces seemed to be dry of the original film of Penzane 2000 oil. Surely a number of things had gone wrong here. A number of theories were put forth, but of course nothing could be proven to satisfaction due to the constraints of time and money. But a few general intuitions could be stated; the 304L flexspline was too soft a material to be put directly into service under a minimal lubrication environment (as in typical spaceflight applications). Some form of breaking-in procedure to first work harden the surfaces would have helped. The 440C bearing was not of the vacuum melt material variety, and the outer race surface was rough looking and probably had inclusions and carbide particles on the surface. The inner race should have been locked into position with a shoulder machined into the wave generator plug to prevent the bearing from being swallowed further down the flexspline throat. The factory preload produced an unusually high torsional stiffness (between 28250 and 33900 $N \cdot m/_{rad}$ (250,000 and 300,000 $in \cdot lb/_{rad}$)) which would indicate that the bearing stresses were higher than normally seen in service. Also, the oil did not seem very inclined to wet the surface of the 304L flexspline, and would have benefited from a grease dam to keep what little was there on the contact surface. A combination of all these effects and probably others not imagined contributed to the failure.

The tested solution, given the time constraints, was to use the commercial grade AISI 4340 steel flexspline and 52100 steel wave generator bearing. Gold plating was

seriously considered to prevent possible corrosion of the 4340 steel, but was later rejected due to the concerns of the ability to properly gold plate, and the realization that if any corrosion occurred, it would be more cosmetic than damaging. The 52100 material was selected as a superior bearing, and under magnification had a much smoother appearance on the outer race/flexspline interface. The corrosion concern was considered minimal due to the high chrome content and the oil's antioxidant. A great effort was made to lower the preload such that the torsional stiffness would fall around 13560 $N \cdot m/_{rad}$ (120000 $in \cdot lb/_{rad}$), instead of the high values of the previous set. This meant careful grinding of the wave generator plug major axis. The plug was further modified by machining a shoulder to register the inner race, thereby giving a hard load path for the reaction to the walking forces which tend to draw in the wave generator when acting as a speed reducer. Also, the oil was mixed with the grease variation of Penzane 2000 (known as Rheolub 2000) to form a slurry. This was done as it was noticed that the grease alone did not seem to release oil to keep a surface wet after it was pumped out of the contact zone. The peanut-butter like consistency was just to thick for the application, and the oil alone was just too thin. Figure 9 shows the application of the different forms of Penzane on the harmonic drive. Initial testing was done in ambient conditions in order to quickly weed out the nonsolutions. Testing in ambient conditions was seen with some doubt, since the presence of oxygen could alter the results either way. The metals would benefit from oxygen in than any wear would expose fresh metal that could quickly gall if surface oxidation did not occur first, creating a ceramic layer separating the metals. The oil, on the other hand, would be stressed in the presence of oxygen, and in fact the oil turned darker and chemical analysis indicated some oxidation had occurred. Further testing in vacuum vindicated both the oil/grease slurry and the material combination.

G-negation

As stated earlier, a combination of airpads and counter weights were used to deploy a wing assembly. The more complicated components were by far the airpads, but the greatest problems occurred with the counter weights. This in part was due to deflections of the counter weight brackets, but was mostly due to panel deflections which varied with the deployment angle. With the springs disabled, measured values of counter weight unbalance exceeded 5.6 N·m (50 in·lb). This unbalance could shift from positive to negative maximums in as little as a 30 deg motion. Since this was over 150% of the spring force available, it presented quite a problem. The solution was to control the deflections of the panel by using an auxiliary hinge, which kept panel tip deflections to a minimum by constraining the vertical motion of the deploying panel to the stationary middle panel. The constraint loads would react in an in-plane direction of the middle panel, which is the stiffest load path, and therefore produce the least deflection. Balance error was reduced to 10% of the original error.

Release Mechanism Galling

The vee guide interface to the spacecraft (qualification unit) was knowingly installed with a slight misalignment in order to see if any galling of the two surfaces would occur during vibration, and if any such galling would hang up the deployment. The vee guides were titanium with an anodic / Teflon coating, and had Braycote 602 grease applied at the interface. Even though one of the spacecraft interfaces was a cone, there was much relative motion in the vee guide, with some displacements being on

the order of ±2.5 mm (0.1 in) during the in-plane sine vibration test. After the vibration test, an ambient deployment test was performed. The deployment first begins with the pyro shock followed by the four kick-off springs, each 22.2 N (5 lbf). Another source of potential energy was the panels themselves, as they were slightly bowed due to the preload of the snubbers. This preload would produce a reaction load of 311 N (70 lbf) at each release mechanism, bringing the total force to break contact after the pin pullers fired to 355 N (80 lbf). After the test, the vee guide contact surface was examined and the result was that a small area of the surface coating had been worn off on both mating surfaces, exposing bare titanium. A very small area inside that area (perhaps 1 x 1 mm) had a peculiar, porous surface texture, as if some micro welding and tearing had occurred. Whether the galling had resulted in a firm weld or a broken weld at the end of the vibration test, that could not be determined. However, with 355 N (80 lbf) and a pyro shock right at the vee guide, the resultant initial motion was quite aggressive, galled or not. The saving grace is that the flight units are shimmed to perfection to avoid any high contact stresses which are required for galling.

Honeycomb Panels

The qualification solar array wing had been exposed to the full engineering test qualification program without any structural problems. But the flight units, during their bake out at temperatures slightly above 100 deg C, delaminated over large areas where there were internal doubler sheets. The delaminations seemed to develop thru a low adhesion to the doubler and combined with a gas generated from the adhesive itself. The delaminated face sheet was blistered up in a permanently yielded condition, as if internally pressurized. The possibilities for the source of the problem seemed endless, such as contamination, tooling, handling, humidity, tolerance buildup, primer, and so on. The truly frightening aspect was that tap testing did not detect the problem of "light bonding." Sophisticated techniques such as pulse echo and air scanning failed to detect lightly bonded areas adjacent to the obviously failed spots which later were determined to be lightly bonded as well. There were too many layers in the solar array panel to image separately. The best interrogative method was to grind a small hole in the external face sheet, exposing the doubler underneath, and to push a dental pick into the adhesive between the two aluminum sheets. If the parts were lightly bonded, the metal skins would separate. If the dental pick could not be shoved into the adhesive layer without tearing the face sheet or bending the pick, then the adhesive was considered acceptable.

Since the failure occurred in three out of the six panels in virtually the exact same areas implicating tooling, tolerance, and process, the speculation on the cause narrows to the following argument. The process of handling this adhesive film included numerous thawing and refreezing cycles between use and storage. Together with high environmental humidity, the adhesive could have absorbed water from these types of exposure. In parallel, the mechanical tolerances had to be kept tight in order to prevent a low cure pressure situation, where the outer face sheet would have to arch down to make contact with the already assembled and cured internal doubler panel. If a thick caul plate (top tooling plate) was used, the autoclave pressure would have to deform it also as it bridged across the doubler panel. These conditions lead to low cure pressure locally over the internal doubler panel. Unfortunately the adhesive film is sensitive to this condition as it has a very low-flow

nature, a definite disadvantage of the adhesive. So, if the adhesive was poisoned by moisture and aggravated by low curing pressures, and trapped in a sheet to sheet bond where products of curing or outgassing water vapor had to travel sideways thru the adhesive layer, and not simply straight out into the vented honeycomb core, then "light bonding" should not be an unexpected result. Over the core away from the doubler panels, products of curing easily escaped into the vented core, and there were no bridging problems here, and so these areas did not suffer from the sensitive nature of the adhesive or moisture absorption.

The fix was to grind and strip all the lightly bonded areas and with a hand layup, apply custom cut face sheet material with EA9395 epoxy. To have prevented the problem all together would entail a close examination on the requirements to use of FM123-2LVC, the vendor's capability and successful history of using that product, and a high appreciation of the delicate and unforgiving nature of that film adhesive which requires expert handling.

Conclusions

Nothing should be taken for granted! Most of the areas we anticipated to be problems were not, and many unexpected areas became major problems. An entire subsystem such as a solar array deployment and drive entail hundreds of details, many of which take care of themselves. Lubrication and process controls of even typical everyday applications should never be taken as givens. Cheaper, faster will usually result in many details falling thru the cracks, and then it is a gamble whether these details take care of themselves, or not.
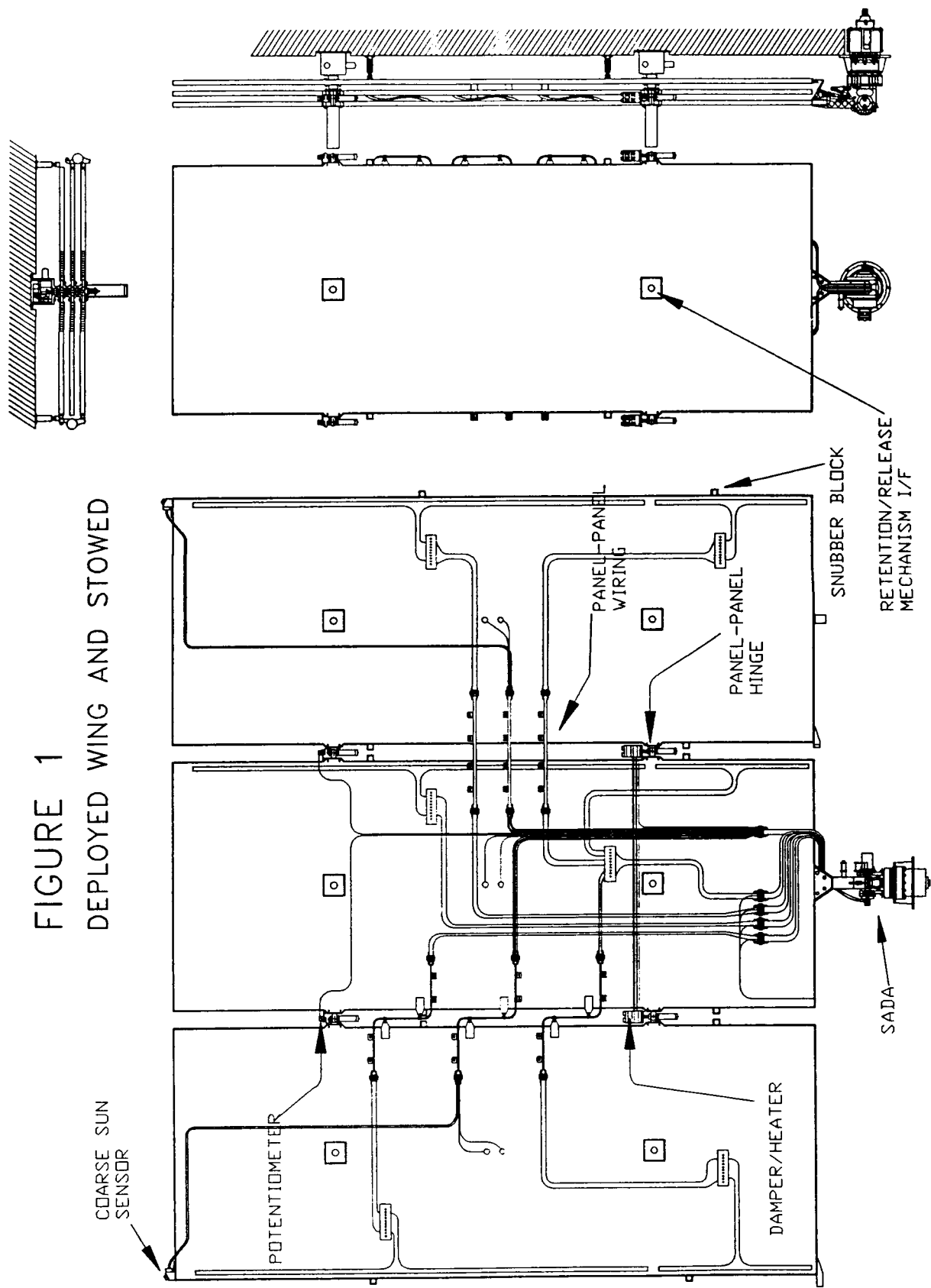
FIGURE 1
DEPLOYED WING AND STOWED

COARSE SUN SENSOR

POTENTIOMETER

PANEL-PANEL WIRING

PANEL-PANEL HINGE

SNUBBER BLOCK

RETENTION/RELEASE MECHANISM I/F

SADA

DAMPER/HEATER

276

FIGURE 2 XTE SADA

.005" KAPTON SEPARATOR

WIRE BELT

CABLE WRAP

LATCH

NEGATOR SPRING

DELAY DEVICE

THERMAL SHIELD

POTENTIOMETER

THERMOSTATS

VISCOUS DAMPER

ROTARY ACTUATOR, SMI TYPE 5 1/2

CABLEWRAP TRAVEL EQUATIONS:

NUMBER OF SPIRAL BELT ARMS = N
BELT THICKNESS = t
BELT LENGTH = L
INNER DRUM DIAMETER = D_i, OUTER = D_o

$a = N(t/D_i)\pi$

$b_i = \pi(N(t/D_i)/2 + 1)$

$c = (\pi/4)(D_o/D_i + 1) - L/D_i$

$b_o = \pi(D_o/D_i - (N/2)(t/D_i))$

$TURNinner = (-b_i + \sqrt{(b_i^2 - 4ac)})/(2a)$

$TURNouter = (+b_o - \sqrt{(b_o^2 + 4ac)})/(2a)$

HALF TRAVEL +/−, deg
$= 180(TURNinner-TURNouter)$

0 1 2 3 4 5 6
INCHES

FIGURE 3

XTE S/A RETENTION/RELEASE MECHANISM

SNUBBER / KICKOFF UNIT

PYRO PIN PULLERS, 2

S/A PANELS

VEE GUIDE I/F

BELLEVILLE
WASHERS, B0500-018S
5 COMPRESSED FLAT = 350 LBS

RELEASE
ROD
ASSY

JAWS, 2 MOVING
1 FIXED

30 deg CONE-CONE
I/F WITH .004 "RATTLE"

SURFACES "TIODIZED" AND LUBRICATED
WITH BRAY 602
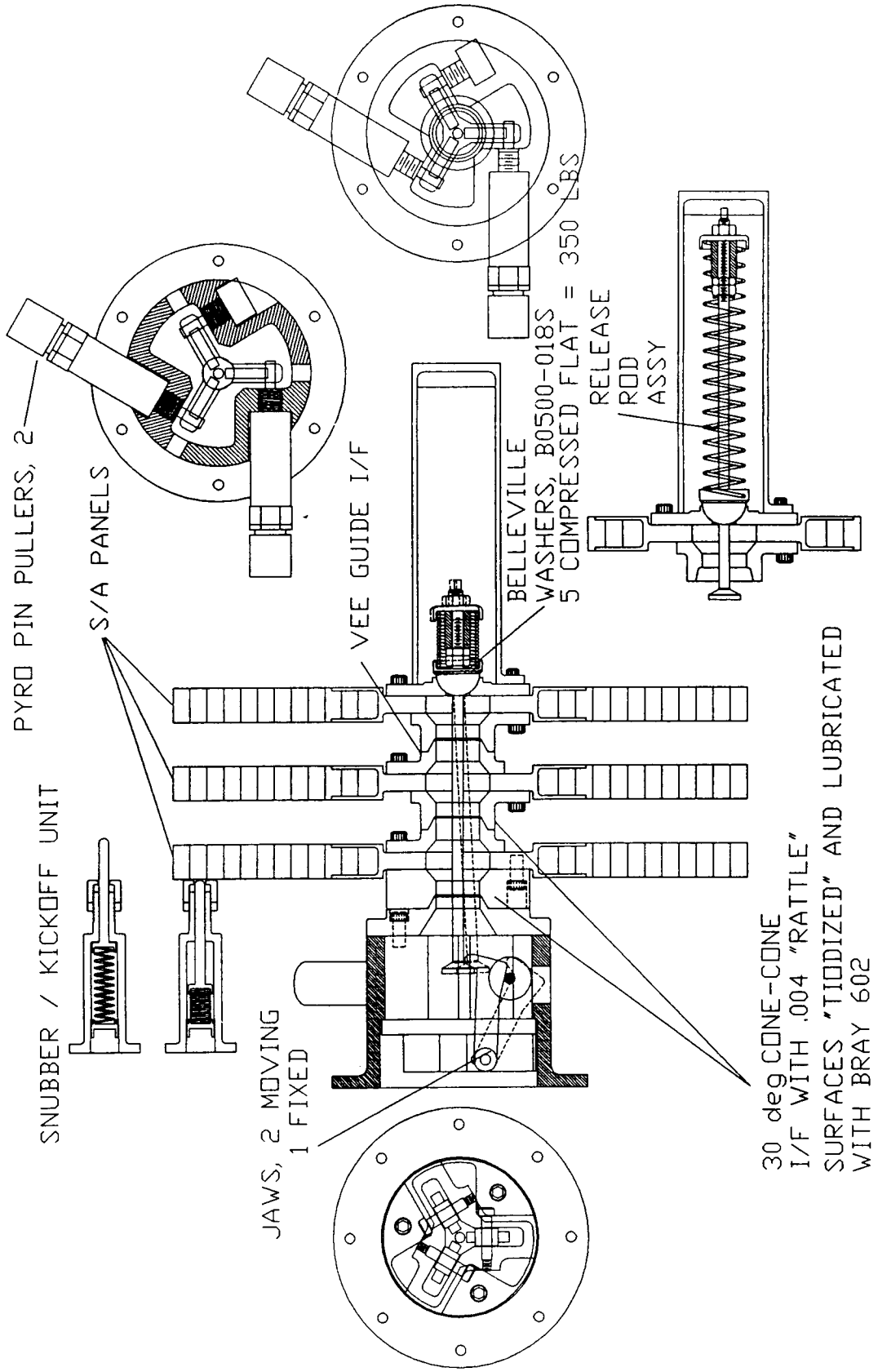
FIGURE 4

XTE S/A DEPLOYMENT
WITH AIRPADS
AND COUNTER WEIGHTS

XTE S/A
AIRPAD

PISTON

AIR SUPPLY

AIR PAD

SUPPORT TUBE

REGULATOR
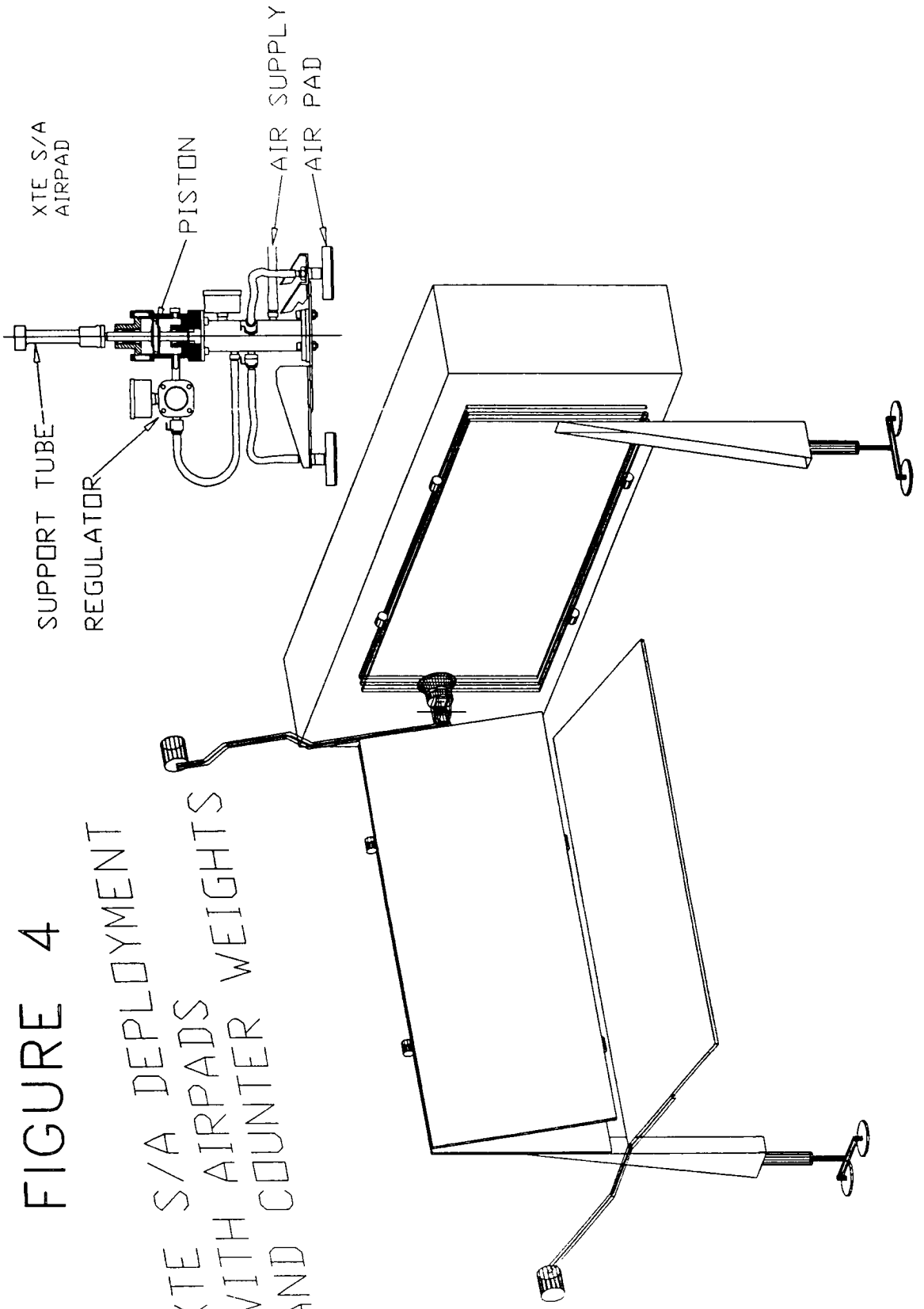
FIGURE 5

ROTARY ACTUATOR MODEL
DEFINITION OF VARIABLES
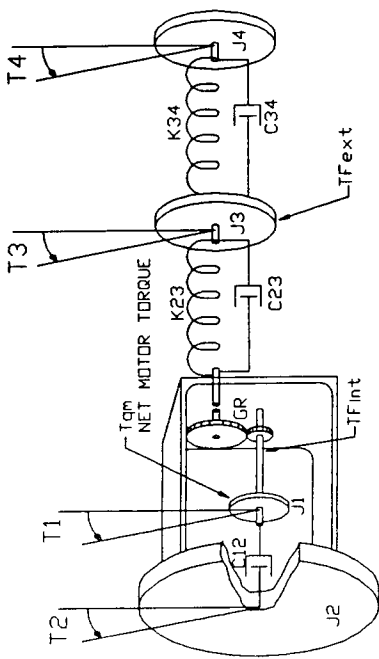
ROTARY ACTUATOR MODEL
DEFINITION OF COMPONENTS
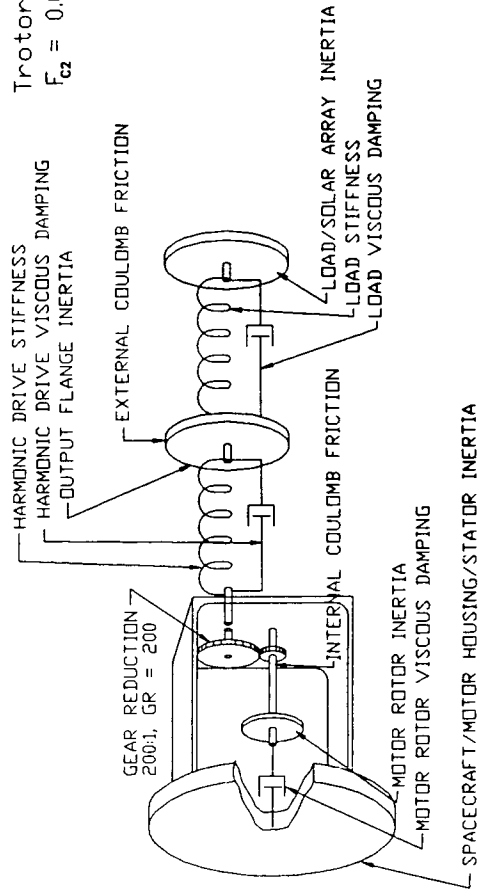
DIFFERENTIAL EQUATIONS

$$\ddot{T}1 = \{-K23*(T3-T2*(1+1/GR)+T1/GR - GearError)/GR$$
$$-C12*(\dot{T}1-\dot{T}2) - C23*(\dot{T}3+\dot{T}2*(1+1/GR) -\dot{T}1/GR)/GR$$
$$+Tqm - TFint\}/ J1$$

$$\ddot{T}2 = \{(K23*(T3-T2*(1+1/GR)+T1/GR - GearError)/(1+1/GR)$$
$$+C12*(\dot{T}1-\dot{T}2) + C23*(\dot{T}3+\dot{T}2*(1+1/GR) -\dot{T}1/GR)*(1+1/GR)$$
$$-Tqm + TFint + TFext\}/ J2$$

$$\ddot{T}3 = \{-K23*(T3-T2*(1+1/GR)+T1/GR - GearError) +K34*(T4-T3)$$
$$+C34*(\dot{T}4-\dot{T}3) - C23*(\dot{T}3+\dot{T}2*(1+1/GR) -\dot{T}1/GR)$$
$$- TFext\}/ J3$$

$$\ddot{T}4 =\{-K34*(T4-T3)$$
$$-C34*(\dot{T}4-\dot{T}3)\}/ J4$$

GearError = F_{c2}Sin(2Trotor) + F_{c4}Sin(4Trotor) + F_{c9}Sin(9Trotor)
Trotor = T1 - T2
F_{c2} = 0.00025 radians F_{c4} = 1/2 F_{c2} F_{c9} = 1/5 F_{c2}

INTERNAL FRICTION MODEL
AS FUNCTIONS OF SPEED, TEMPERATURE

TFint = A1*(PPS^A2)*10$^{(-A3*(TEMP + A4))}$

+ TFint @ AMBIENT, BREAKAWAY   in-oz

A1 = 0.55
A2 = 0.6
A3 = 0.021
A4 = 8.0
TFint @ AMBIENT, BREAKAWAY = 4 in-oz

PPS = PULSES PER SECOND, AT 1.5 deg PER PULSE
TEMP = TEMPERATURE @ DEG CENTIGRADE

HARMONIC DRIVE STIFFNESS
HARMONIC DRIVE VISCOUS DAMPING
OUTPUT FLANGE INERTIA
EXTERNAL COULOMB FRICTION
LOAD/SOLAR ARRAY INERTIA
LOAD STIFFNESS
LOAD VISCOUS DAMPING

GEAR REDUCTION
200:1, GR = 200
INTERNAL COULOMB FRICTION
MOTOR ROTOR INERTIA
MOTOR ROTOR VISCOUS DAMPING
SPACECRAFT/MOTOR HOUSING/STATOR INERTIA

T4
K34
C34
TFext
T3
J4
J3
NET MOTOR TORQUE
Tqm
GR
K23
C23
T1
J1
C12
TFint
J2
T2

Figure 6
Back emf trace

Y SCALE:
MAX BACK EMF VOLTAGE   18
VOLTS
2 volts/div

X SCALE:
MAX TIME   .5
0.05 sec/div

Figure 7
Current trace at 200 PPS

Y SCALE:
MAX CURRENT 1
AMPS
0.2 amps/div

X SCALE:
MAX TIME   .1
0.01 sec/div

Figure 8
Output Running Torque

FIGURE 9
HARMONIC DRIVE FIX

GREASE ON TEETH

FREE OIL ADDED TO BEARING 52100 BEARING

OIL IMPREGNATED RETAINER

4340 STEEL FLEXSPLINE

GREASE DAM

17-4PH CIRCULAR SPLINE

OIL/GREASE SLURRY

MACHINED SHOULDER

OIL FILM

Session Chair: Rick Abramowitz

Effects of Bearing Cleaning and Lube Environment
on Bearing Performance

Peter C. Ward[*]

Abstract

Running torque data of SR6 ball bearings are presented for different temperatures and speeds. The data are discussed in contrast to generally used torque prediction models and points out the need to obtain empirical data in critical applications.

Also, the effects of changing bearing washing techniques from old, universally used CFC-based systems to CFC-free aqueous/alkaline solutions are discussed. Data on wettability, torque and lubricant life using SR3 ball bearings are presented. In general, performance is improved using the new aqueous washing techniques.

Introduction

Torque prediction has been accomplished over the years using various models, followed by actual data at as close to application environments as possible. In space applications, this prediction becomes very critical.

Torque models don't vary that much. They include various combinations of three terms. First, a term for the mechanical drag torque, second, a term for retainer drag, and finally and most important, a term for viscous lube effects [1, 2, 3]. A typical model used in the bearing industry is equation 1.

$$T_t = \frac{\mu\, T^{4/3}\, d^{1/3}}{n^{1/3}\, \sin^{1/3} B_t} \frac{\left(1 - \partial^2\right)^{1/3}}{E^{1/3}}\left(K_t + \frac{P \cdot K_r}{d}\right) + S + L \tag{1}$$

where μ = friction coefficient (0.1 typical), T = thrust load, d = ball diameter, n = number of balls, B_t = contact angle, E = modulus of elasticity, ∂ = Poisson's ratio, K_t and K_r are contact ellipse functions ($K_t = 1.3$, $K_r = 0.11$ for 52% curvatures, P = pitch diameter, $S = 15000\, d^{2/3}/P^2$, and

$$L = 6800\, P^{5/3}\, d^{4/3}\, n^{2/3}\left(1 - \frac{d \cdot \cos B_t}{P}\right)^{2/3} \cdot (\text{inner ring speed})^{2/3} \cdot Q \cdot \left(\frac{\text{viscosity} \cdot \text{specific grav}}{100}\right)^{2/3}$$

The whole first term, the mechanical drag, is friction coefficient times thrust load times area. The second term, "S", is the retainer term, a function of ball size and pitch diameter. Finally, the term, "L", the viscous drag term is made up of bearing speed to the $2/3$ power, a lube quantity factor (Q) that equals one except when lube is starved (at which time it equals 0.4), and a lubricant property term that multiplies viscosity times specific gravity. In general, this model is dominated by the viscous drag term,

---

[*] MPB Corp., subsidiary of The Timken Co., Keene, NH

especially at higher speeds and higher viscosities caused by lower operating temperatures.

In Figure 1, the torque curves versus speed for the test bearing, SR6RHH7, are plotted for some of the lubricants tested in this work. It can be seen that increased torque follows increased viscosity and specific gravity, the dynamic viscosity, and then gets multiplied by speed. The nature of this investigation was to see how good these models are in light of the critical nature of space mechanisms.

In the second part of this paper, data on ball bearing performance such as low speed torque, steel wettability, and lubricant life in actual ball bearings are presented where the test variable is final assembly wash before applying lubricant. MPB's old Freon / aqueous / Freon dry system was compared to our new aqueous ultrasonic, rinse, air dry system.

Test Procedures and Results

Grease Testing

Actual torque results of the SR6RHH7 ball bearings were obtained using a variable-speed torque tester based on the same principles as the MPB RT2C, MIL-STD-206 running torque tester. The mechanical elements of the tester were put in an environmental chamber to obtain the temperature results. All bearings were run in for a pre-determined time and tests were repeated to ensure and demonstrate repeatability.

Bearings were lubed with the test greases to $^{1}/_{3}$ full. Speed was varied from 1000 to 5000 rpm and a constant 35.5 N (8 lb) axial load was used. Bearings were tested at 24°C (75°F), 1.7°C (35°F), -17.8°C (0°F), and -29°C (-20°F). The greases reported on here are:

Halocarbon 25-10M ----	polychlorotrifluoroethylene
Mobil 28 --------------------	clay thickened synthetic hydrocarbon base
Rheolube 2000 -----------	organic gel thickened synthetic hydrocarbon
Aeroshell 5 -----------------	clay thickened petroleum base
Mobilith SHC220 ---------	lithium soap thickened synthetic base
Braycote 803 RP ----------	perfluoroether

The results of the room temperature tests versus speed are shown in Figure 2. The torque curves are all under the model prediction and are quite independent of speed in this range. Only the heavy, low-viscosity Halocarbon reverses the trend.

The Mobil 28 and Rheolube 2000 appear close to predicted but are flat with respect to speed. It is possible the shearing of the lubricant is not so prevalent as predicted. It is also possible that another effect, not modeled, is lowering the torque with increasing speed, counteracting the lube shearing effect.

Figure 3 is a collection of traces from Mobil 28 greased bearings to illustrate bearing to bearing consistency. Also the independence of torque versus speed is quite graphic.

The bearings were run in for a minimum of 30 minutes eliminating any beginning grease distribution differences.

In Figure 4, the Mobil 28 viscosity change with temperature is put into the model, resulting in dramatic increases in torque predicted with lower temperature and higher speed. In actual tests, the second graph in Figure 4, the data do show an increase in torque at 1000 rpm due to the test temperature induced viscosity change. As speed is increased, however, torque is not affected and went down at 1.7°C (35°F) as speed increased. This poses a question, "Is the extra shearing force being offset by other mechanical effects, such as lube availability in the contact zones going to marginal, i.e., less lube sheared?" The torque traces in Figure 5 show this trend.

Also in Figure 4, the Rheolube 2000 data show similar results. It follows the model, increasing at 1000 rpm as the test temperature is decreased. Also, speed effects are negated or masked by unmodeled phenomena. Another interesting observation, shown in Figure 6, is the occasional chatter or hash, which is not predictable in a model.

The torque of Mobilith SHC220 grease is also shown in Figure 4. In this case, almost no sensitivity to speed and test temperature was found. It seems the dynamic character of a grease is not all in its viscosity and density. The nature of additives, blending and other factors are not modeled. Figure 7 contains the actual torque traces. The test was also run at -45°C (-50°F) where only torque hash was encountered. This grease was the best tested under the conditions imposed.

Finally, the base oil of Mobil 28 was tested under the same conditions as the greases to observe the effect of the thickener and additives. The amount of oil was obtained using a standard practice of flooding, then a centrifuge at 800 G's for 3 minutes. Figure 4 illustrates the torque is very similar to the grease. Other experience has shown that smaller instrument ball bearings or thin section bearings with small balls do show an increase in torque hash with grease versus oil.

Washing
In the washing experiments, a smaller, SR3R ball bearing was used. All bearing components were washed during manufacturing using distilled mineral spirits. These components were assembled into bearings, split into groups and assembly washed appropriately. The old system was Freon ultrasonic, aqueous ultrasonic, and Freon-based drying. The new system is aqueous ultrasonic, rinses, and air drying.

In the goniometer disc wettability tests, 440C stainless steel discs were washed in hexane after surface preparation. Then the discs were processed through the standard assembly wash that utilizes freon products or through the new assembly system that is aqueous-cleaning based. The standard oil drop angle was measured after fifteen minutes and after 24 hours. The old freon process gave oil drop angle of 8 to 9° while the CFC-free washed discs were at 4 to 6°; the new wash procedure is more wettable. These results did not change after 24 hours.

The ball bearing life test uses the following parameters and log normally distributed statistical analysis was applied to 37 freon-washed failures and 10 aqueous-washed failures.

> 440C rings and balls
> stainless ribbon retainer
> lubrication: 1000/1 hexane and Mil-L-6085 oil, starved or parched lube running
>   conditions
> test speed: 12,000 rpm
> test load: 13 N (3 lb) axial
> Failure mode -- lubricant breakdown quantified by bearing cartridge accelerometer
>   limit

Figure 8 represents the weibull data of the ball bearing life test. The circle data points represent the CFC-washed bearings and the triangles are the CFC-free washed bearings.

This test is an accelerated lubricant life tester for instrument bearings. Instrument bearings are usually lightly loaded such that lubricant breakdown or polymerization is the failure mode. The resulting associated torque increase causes bearing performance degradation. This tester is designed to accelerate that condition by limiting the available lubricant to just a thin, non-replenishable, partial EHD film.

The data show a L50 life of 4.74 hours for the new CFC-free washing system versus 2.25 hours for the old Freon-based system. Statistics say the data supports a conclusion of difference, that is, the new wash is better than the old wash at the 99 % confidence level.

The running torque tests were performed to MIL-STD-206 requirements on SR3R stainless bearings washed both ways. The tester used is manufactured by MPB and is an industry standard that measures torque at 2 rpm under a standard light load, using a transducer. The specimens were run lubed with a standard oil and also dry to pick up subtle effects. Results were statistically compared.

In the torque tests, four groups of ten bearings were torque tested. They were:

> CFC washed, oil lubed
> CFC washed, dry
> CFC free (aqueous) washed, oil lubed
> CFC free (aqueous) washed, dry

The first three groups showed no significant difference in the running torque levels and all averaged about 5000 μg·m (Figure 9). The fourth group, the aqueous washed, dry, was significantly higher with 99% confidence. In fact, the repeatability was also bad in this group as evidenced by a sample trace at the bottom of Figure 9. Here it is obvious the bearing is hanging up. Normally, one would not test bearings dry and it is not per the MIL STD to do so, but our experienced bearing people have historically always

used the "dry" mode for analytical reasons. Now, in this case, it seems the extra clean nature of the metal parts does not allow this.

Silicon nitride balls are quite popular in instrument bearings for their lubricant extending ability. It is reported that the dissimilarity of the ball and race materials inhibits interactions that cause lubricant breakdown [4, 5]. Some customers have asked if running silicon nitride ball hybrids without lubricant is possible and most suppliers have been reluctant to approve this.

This thought about the dry nature of CFC-free (aqueous) washed parts caused the following observation. Figure 10 shows the condition of ceramic balls in an SR3 full complement (no retainer) bearing after a running torque test at 2 rpm in the dry condition. The balls have scratched themselves while rubbing against each other. Further tests have proved that the washing in the old freon-based wash system eliminated the scratches, leading to speculation that there is a slight oil residue after freon washing. Introduction of a retainer, separating the balls, stops the scratching.

Conclusions

Grease Testing
1. In torque models, the lube term is dominant. For example, Mobil 28 at 1000 rpm at room temperature is 3.7 g·cm due to mechanical drag, 0.17 g·cm due to retainer drag, and 6.25 g·cm due to the lube term. And as speed increases or temperature decreases, it gets even more dominant. In the moderate speed and temperature range investigated here, this dominance is not evident.

2. Some greases are inherently more independent of speed and temperature changes than others of comparable viscosities and other modelable properties. In this testing, Mobilith SC 220 was the most independent.

3. This work will lead to an investigation of retainer type and grease amount in an effort to understand if either of these variables are affecting or negating the viscosity term.

Bearing washing performance
1. Based on the consistent results of goniometer angle, life tests, and torque tests, it is felt that the new aqueous-based assembly washing systems do not cause any degradation in bearing performance and may lead to enhanced lubricant life in some situations.

2. Torque perturbations and scratching of silicon nitride balls in the dry, full complement bearing condition suggests that aqueous washing may be eliminating a minor or thin film of some nature left behind by the old Freon-based cleaning system. The performance testing still indicates that this film was not beneficial to normally lubricated bearing performance.

References

1. Shaw, M. C. and Macks, F. "Analysis and Lubrication of Bearings," Mcgraw Hill, 1949, pp. 423-431.
2. Eschman, Hasbargen, and Weigard. "Ball and Roller Bearings; Theory, Design, and Application". John Wiley, 1985, pp. 201-215.
3. Gordon, K. "Calculating Bearing Torque," MPB internal publication, 1963, pp. 1-7.
4. Hanson, R. "The Effect of Advanced Material Technologies on Wear in Instrument Bearings". IBWG Symposium, Orlando, FL, 1987.
5. Wunch, F. "Grease Lubrication of High Speed Hybrid Bearings," International Rolling Element Bearing Symposium, San Diego, CA, April 1994.

Torque Model

Torque (gram - cm)

Speed (Thousands of RPM)

Grease	Viscosity
Halocarbon 25-10M	3.3
Mobil 28	62.3
Rheolube 2000	350
Aeroshell 5	400
Mobilith SC220	560
Braycote 803RP	450

Legend:
- ■ Mobil 28
- □ Mobilith SC220
- + Halocarbon 25-10M
- ✳ Aeroshell 5
- ✕ Braycote 803RP
- ▶ Rheolube 2000

Figure 1

Mobilith SC220

Torque (gram - cm)

Speed (Thousands of RPM)

Mobilith

Theoretical — Actual

Rheolube 2000

Torque (gram - cm)

Speed (Thousands of RPM)

Rheolube

Theoretical — Actual

Halocarbon 25-10M

Torque (gram - cm)

Speed (Thousands of RPM)

Halocarbon

Theoretical — Actual

Mobil 28

Torque (gram - cm)

Speed (Thousands of RPM)

Mobil28

Theoretical — Actual

Aeroshell 5

Torque (gram - cm)

Speed (Thousands of RPM)

Aeroshell 5

Theoretical — Actual

Braycote 803RP

Torque (gram - cm)

Speed (Thousands of RPM)

Braycote 803RP

Theoretical — Actual

Torque vs. Speed at Room Temperature

Figure 2

MOBIL 28 GREASE CONSISTANCY

SPEED-RPM

FIGURE 3

294

294 (handwritten, rotated)

Mobil 28 Base Oil

Mobil 28

Mobil 28 Model vs Temp.
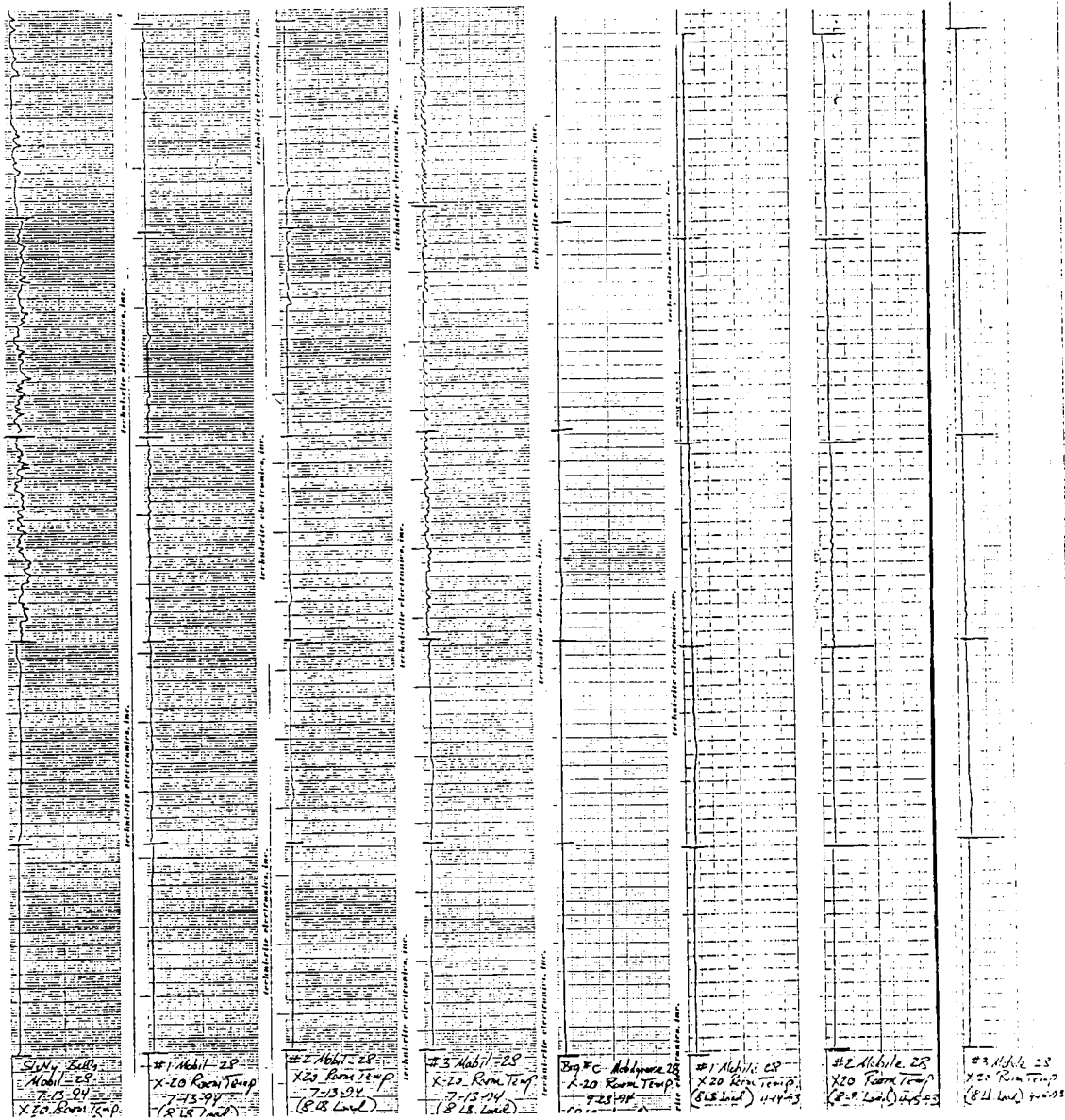
Mobilith SC220
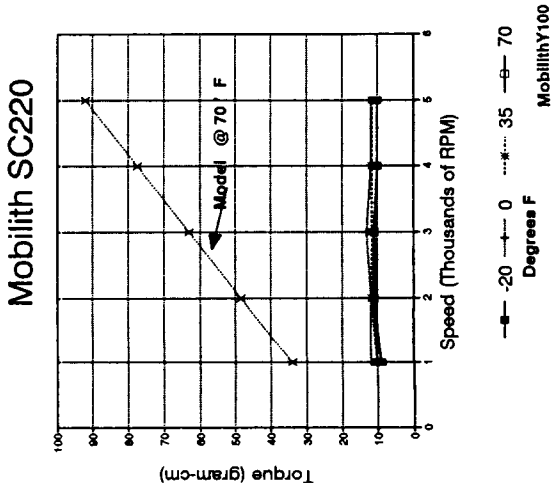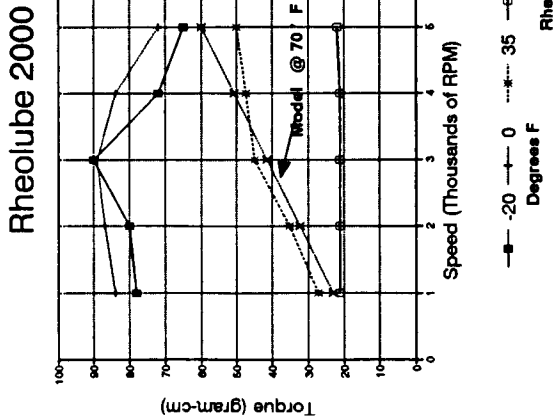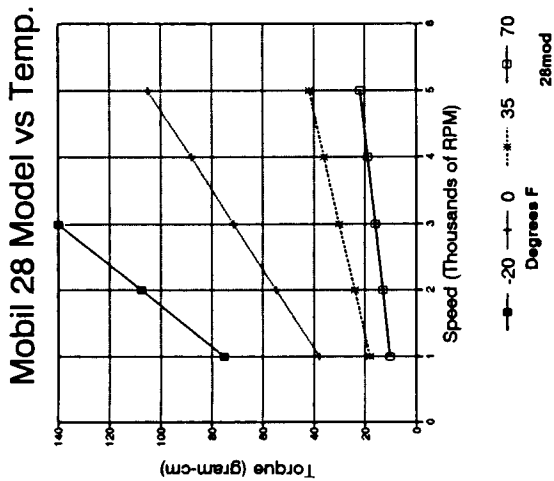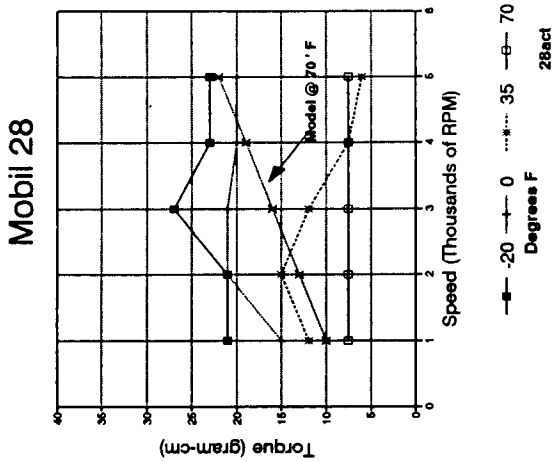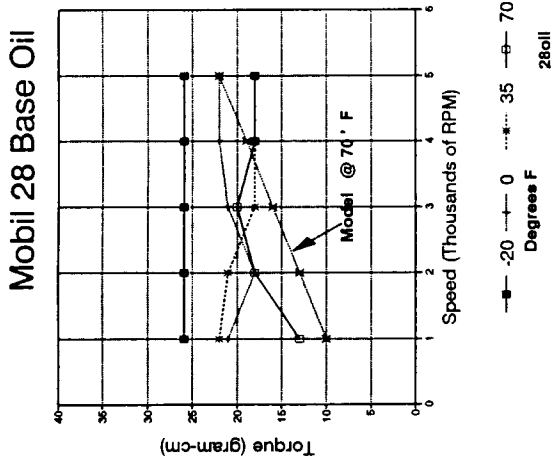
Rheolube 2000

Torque vs. Temperature

Figure 4

MOBIL 28 TORQUE VS TEMPERATURE
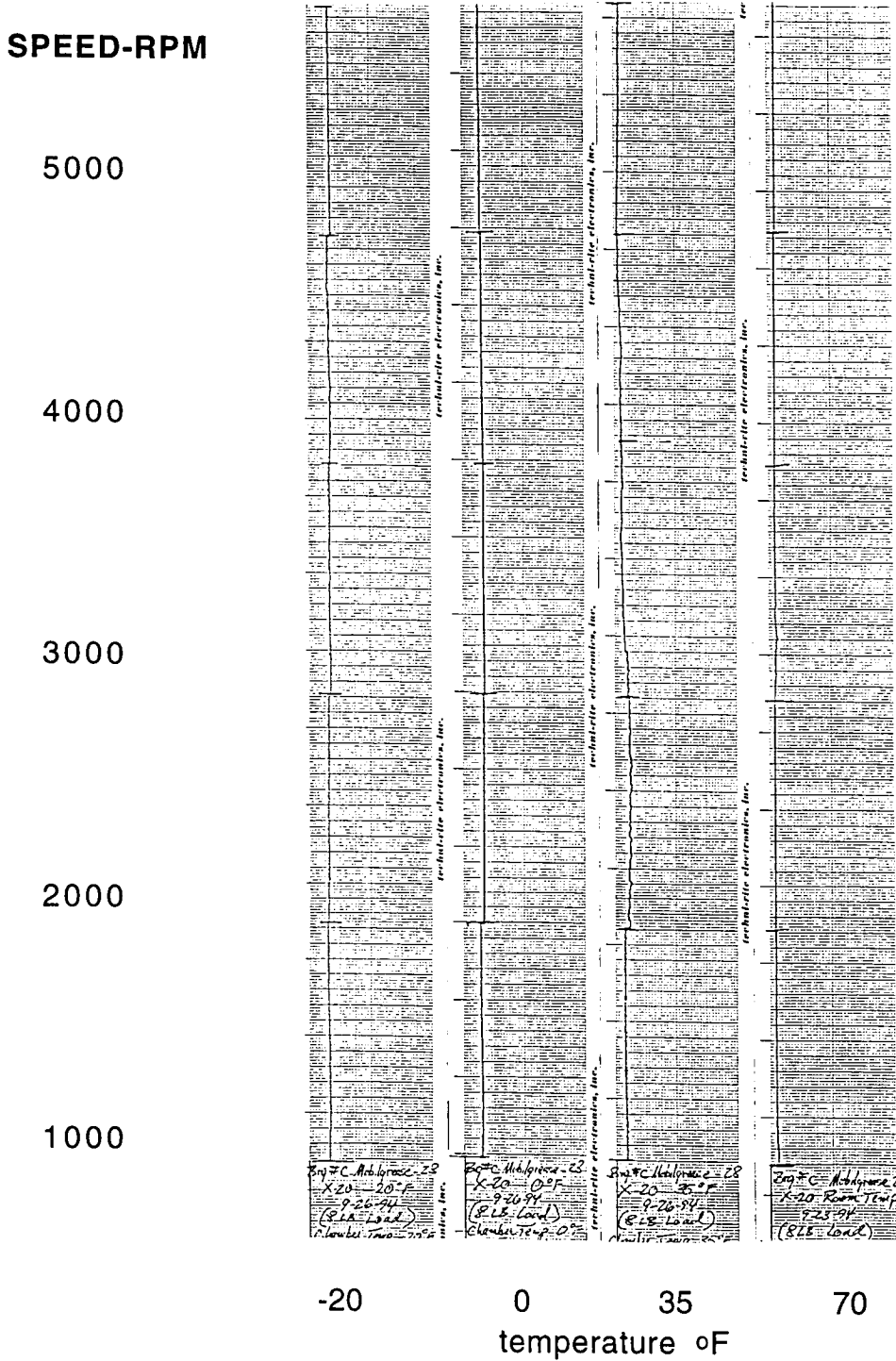
SPEED-RPM

5000

4000

3000

2000

1000

-20   0   35   70

temperature oF

FIGURE 5

295

RHEOLUBE 2000 TORQUE VS TEMPERATURE

SPEED-RPM

5000

4000

3000

2000

1000

-20   0   35   70
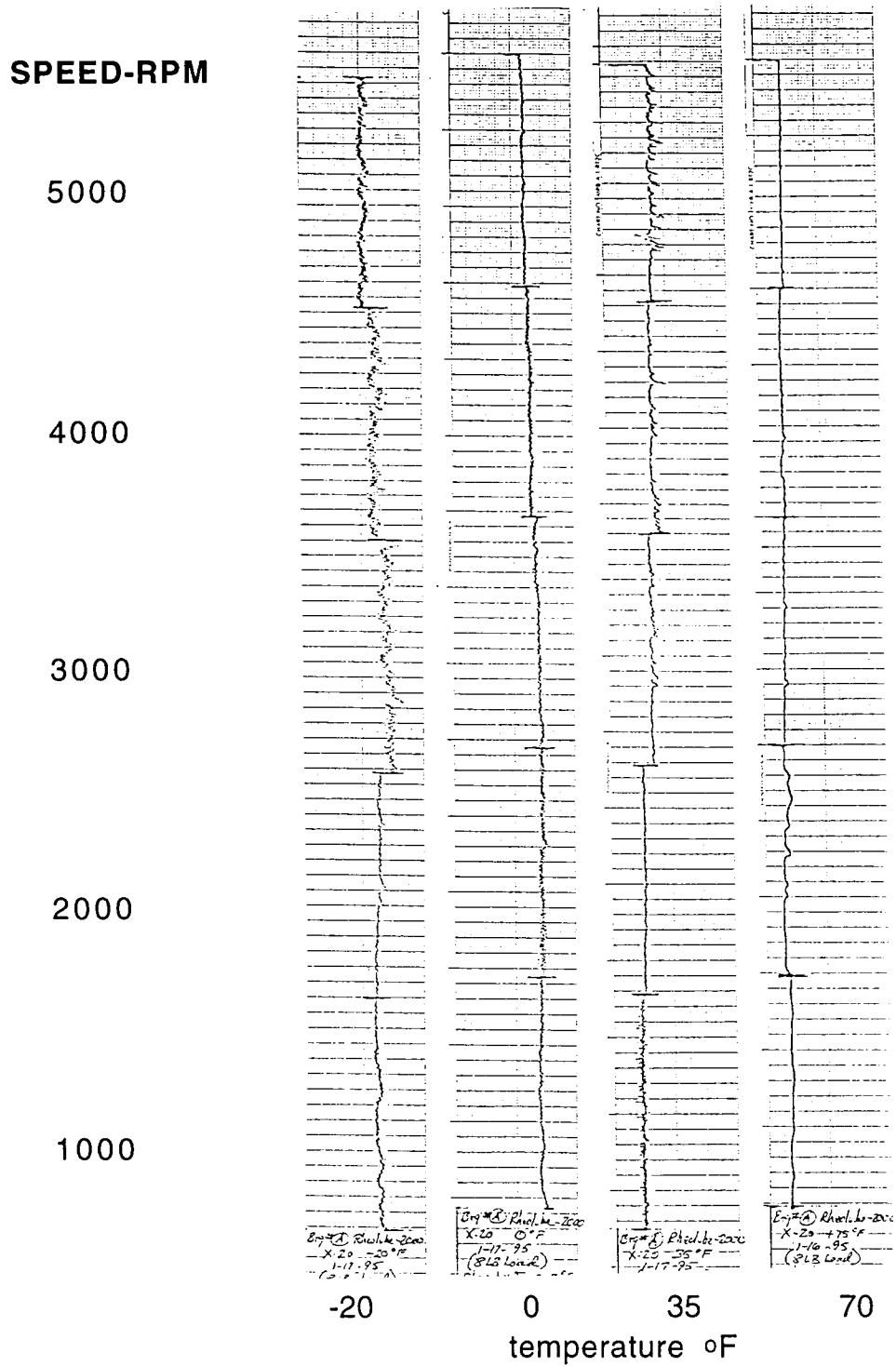
temperature oF

FIGURE 6

296

MOBILITH SC 220 TORQUE VS TEMPERATURE
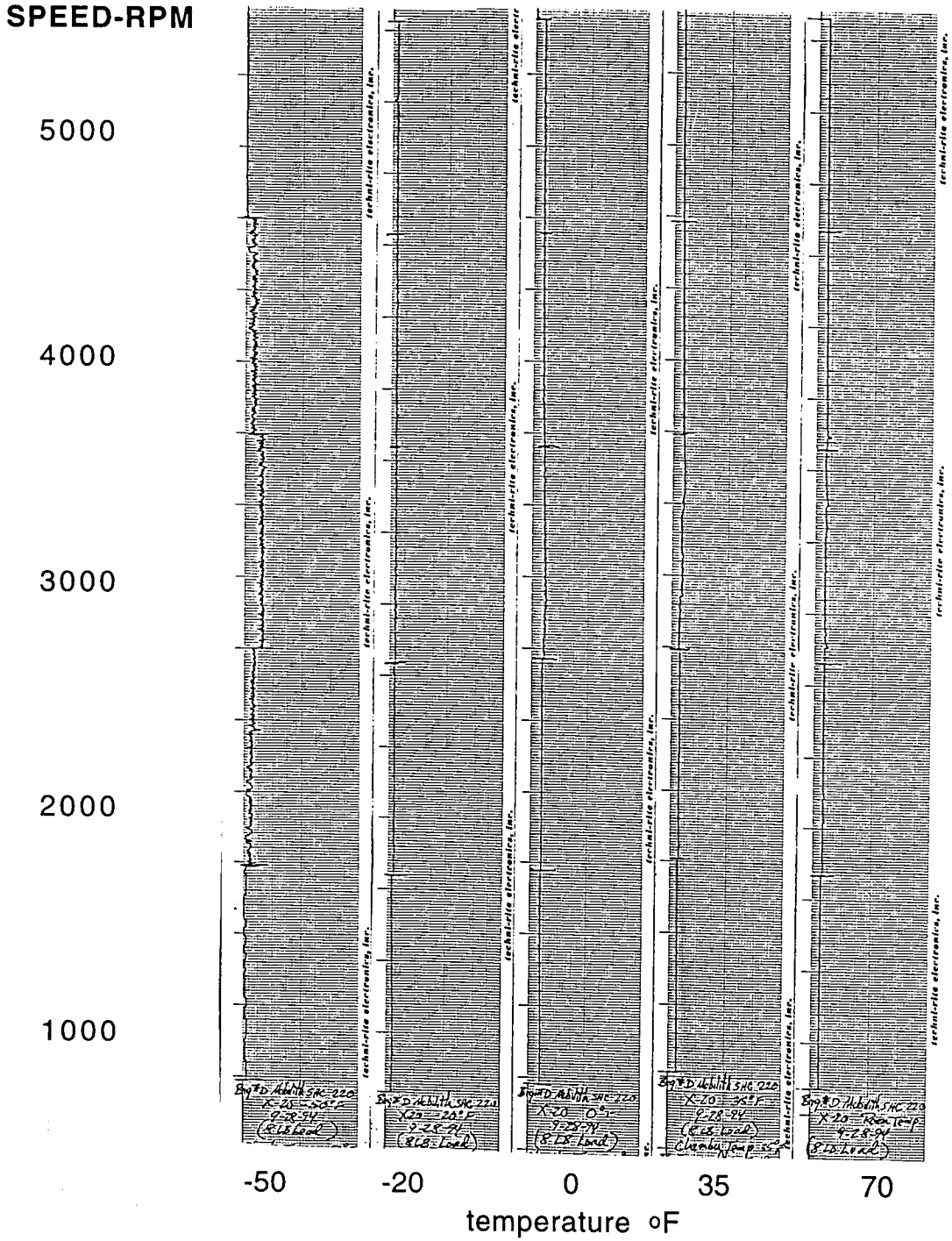
FIGURE 7

297

BEARING LUBRICANT LIFE TEST

CFC CLEANED BEARINGS (0) VERSUS CFC FREE CLEANED BEARINGS (Δ)
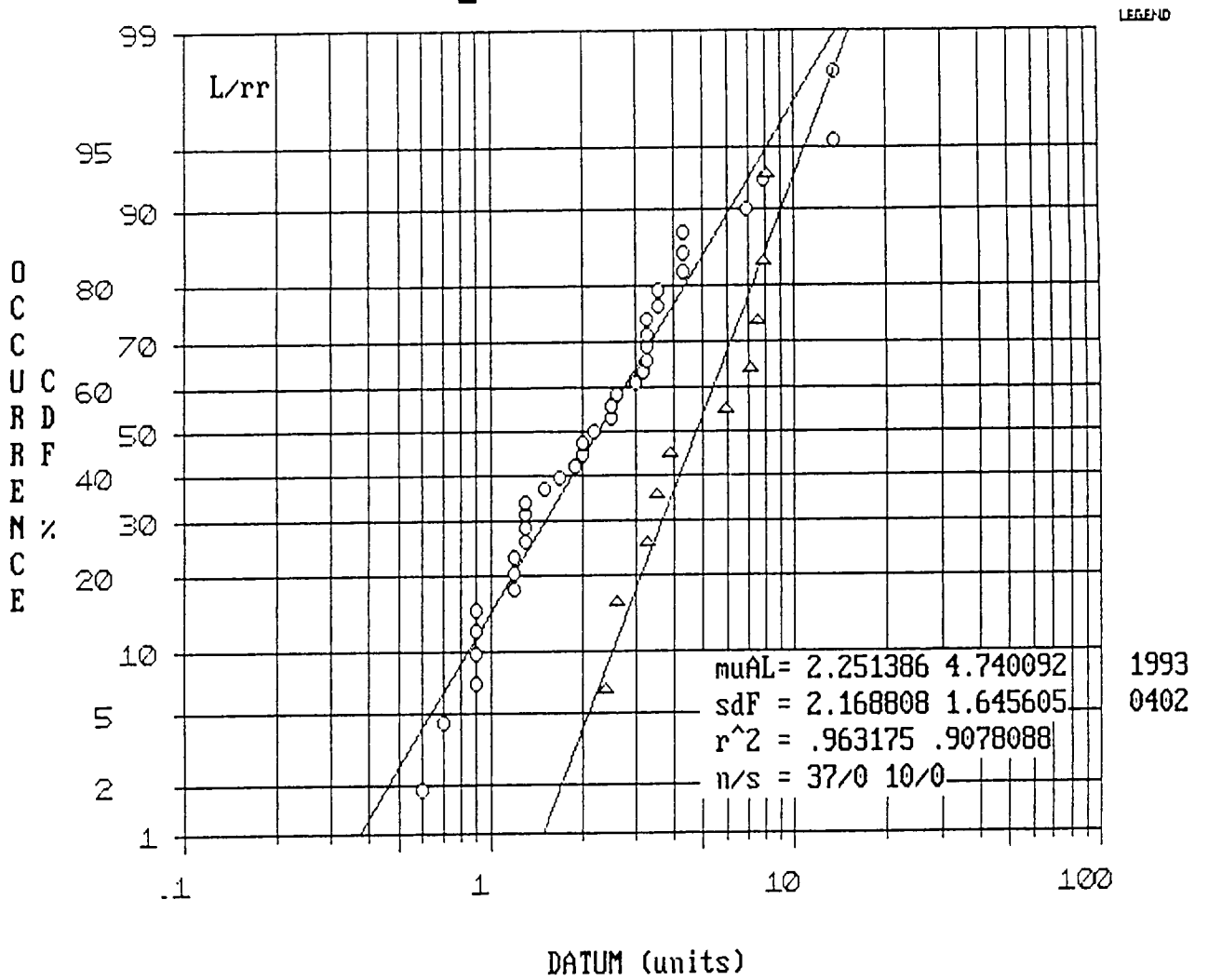
FIGURE 8

CFC CLEANED BEARINGS VERSUS CFC FREE CLEANED BEARINGS
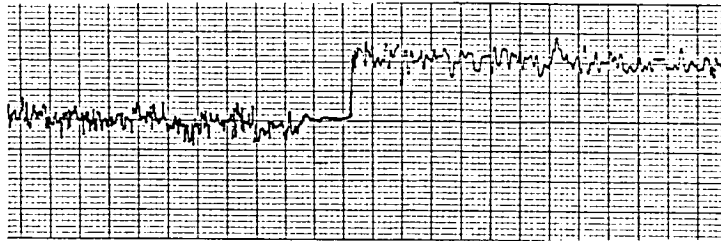
Old wash system -- Lubed
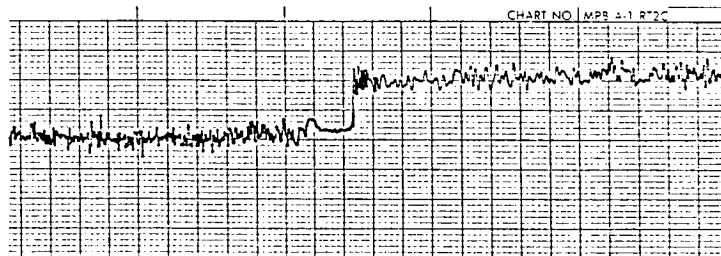
Old wash system -- Dry
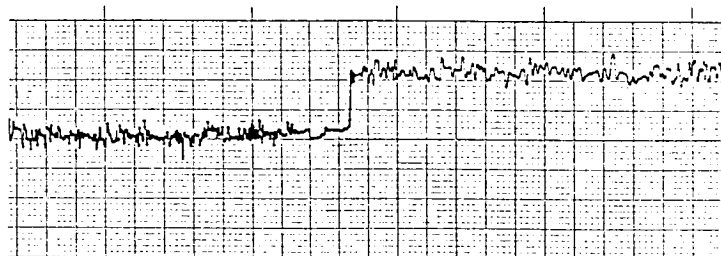
New wash system -- Lubed

New wash system -- Dry
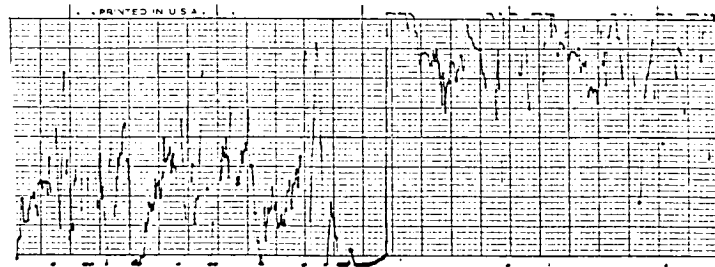
New wash system -- Dry
Sample of erratic behavior

FIGURE 9

CERAMIC HYBRID SR3 BEARING
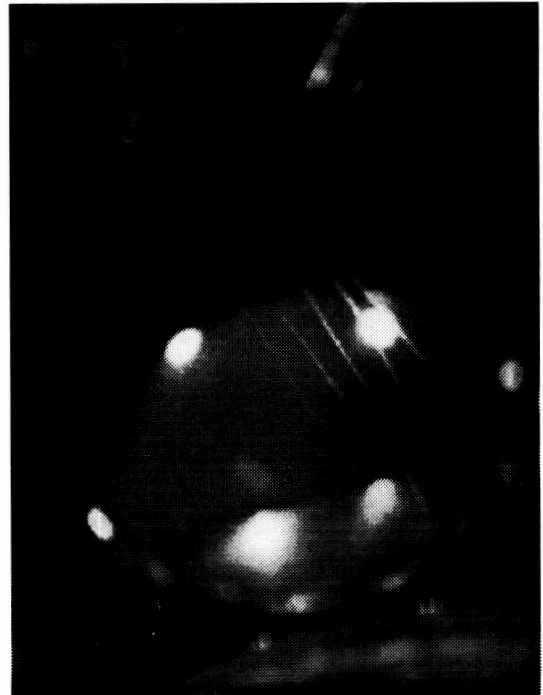
NEW WASH SYSTEM
CERAMIC BALLS SHOWING BALL TO BALL SCUFFING DAMAGE

FIGURE 10

300

/ 9 9 5 / 2 0 8 6 6

4 0 5 7 9 7
/ 3 p.

BALL BEARING VIBRATIONS
AMPLITUDE MODELING AND TEST COMPARISONS

Richard A. Hightower III* and Dave Bailey*

ABSTRACT

Bearings generate disturbances that, when combined with structural gains of a momentum wheel, contribute to induced vibration in the wheel. The frequencies generated by a ball bearing are defined by the bearing's geometry and defects. The amplitudes at these frequencies are dependent upon the actual geometry variations from perfection; therefore, a geometrically perfect bearing will produce no amplitudes at the kinematic frequencies that the design generates. Because perfect geometry can only be approached, emitted vibrations do occur. The most significant vibration is at the spin frequency and can be balanced out in the build process. Other frequencies' amplitudes, however, cannot be balanced out.

Momentum wheels are usually the single largest source of vibrations in a spacecraft and can contribute to pointing inaccuracies if emitted vibrations ring the structure or are in the high-gain bandwidth of a sensitive pointing control loop. It is therefore important to be able to provide an apriori knowledge of possible amplitudes that are singular in source or are a result of interacting defects that do not reveal themselves in normal frequency prediction equations.

This paper will describe the computer model that provides for the incorporation of bearing geometry errors and then develops an estimation of actual amplitudes and frequencies. Test results were correlated with the model.

A momentum wheel was producing an unacceptable 74 Hz amplitude. The model was used to simulate geometry errors and proved successful in identifying a cause that was verified when the parts were inspected.

INTRODUCTION

Vibration in spacecraft has always been of concern when considering component life and performance issues. Of particular concern is the effect on pointing accuracies of instruments that must perform despite emitted vibrations from other on-board devices.

---

* Honeywell Inc., Satellite Systems Operation, Glendale, Arizona

Momentum wheels provide momentum control for space vehicles. The wheel is supported by conventional ball bearings, which generate their own vibration due to normal manufacturing geometry errors and/or defects. To gain a better understanding of how these geometry errors and defects contribute to induced vibration from the bearings, a model was developed and applied to study these motions. This model is actually an extension of a static model developed to analyze mounted and operating preload, ball loading, and contact stresses.

MODEL DESCRIPTION

The **Motion Model** was developed as an analytical tool that could be utilized to predict bearing motion. If bearing motion could be predicted, then ultimately individual bearing parts could be matched to yield bearing assemblies (bearing pairs in the momentum wheel application) that produce minimal bearing motions.

The Motion Model is a quasistatic model that actually analyzes bearing motion in 512 (or less if desired) incremental steps as a static model. This number of steps was determined as sufficient to yield adequate frequency resolution over the frequency spectrum of interest (0 - 200 Hz). The data from these 512 steps is run through a discrete Fast Fourier Transform (FFT) Routine, developed by Dave Bailey, Honeywell Satellite Systems Operation (SSO), to yield a frequency spectrum of radial and axial amplitudes. The FFT Routine requires 2^n steps to generate a spectrum from the model data. The number of steps selected is divided by the number of inner ring (e.g., shaft) rotations. The number of shaft rotations input into the model represents the number of inner ring rotations that will bring the inner ring and balls back to their original starting position, taking into account nominal bearing geometry. For the 305 size bearing referenced in this paper, 19 inner ring (e.g., shaft) rotations are required.

Motions generated by the model include radial (designated k & v by the model) and axial (designated h) forces and deflections. Figure 1 shows the sign convention used.
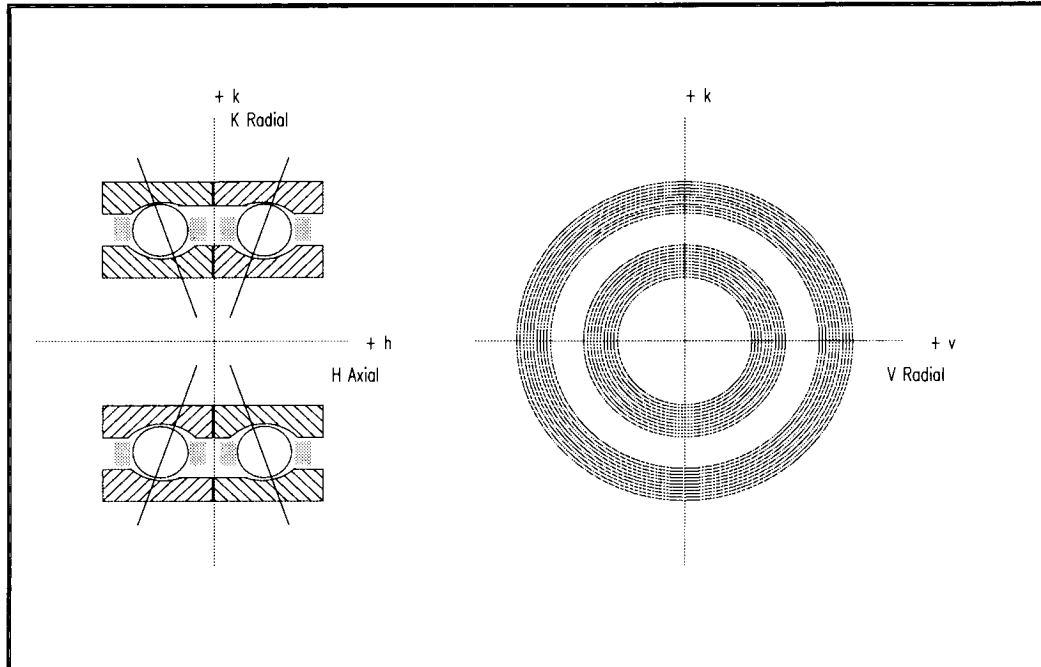
Figure 1. Motion Model Sign Convention

Model Input Description. Bearing nominal geometry, measured bearing geometry errors, and mounting interfaces are accepted as inputs into the model to predict shaft motions under 0 or 1g loading conditions. Bearing geometry is initially entered into the input file and is used by the model to determine preload. The following bearing geometry parameters are inputs to the model. Actual values for the 305 size bearing discussed in this paper are listed.

305 Size

Bearing outside diameter	62.0 mm (2.4409 in.)
Bearing bore	25.0 mm (0.9843 in.)
Preload (unmounted)	5.44 kg (12 lbm)
Free contact angle	13.66 deg
Bearing width	17.0 mm (0.6693 in.)
Race curvature	Proprietary
# balls	10
Ball diameter (nominal)	11.9 mm (0.46875 in.)
Ball pitch diameter	44.3 mm (1.743 in.)

Bearing geometry errors that can be input into the model follow:

    ✓   Race Node Eccentricities (defined as the number of points out-of-round)

Input Options - 1, 2, 3, or 4 Node
- Node 1 is a simple eccentricity, i.e., the bore axis offset from the race axis
- Node 2 is a 2 point out-of-round, i.e., oval shaped
- Node 3 is a 3 point out-of-round
- Node 4 is a 4 point out-of-round

Eccentricity values can be input for:
- Inner and/or outer radial eccentricity
- Inner and/or outer axial eccentricity

✓ Race Talyrond Data (radial only)
- Digitized data. A sample plot of a typical error data file is shown in Figure 2.
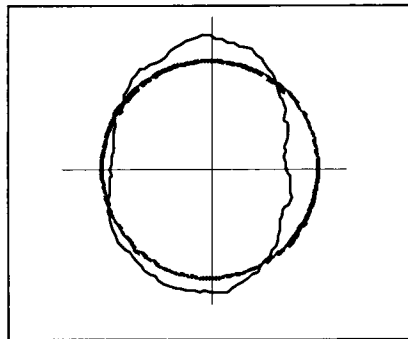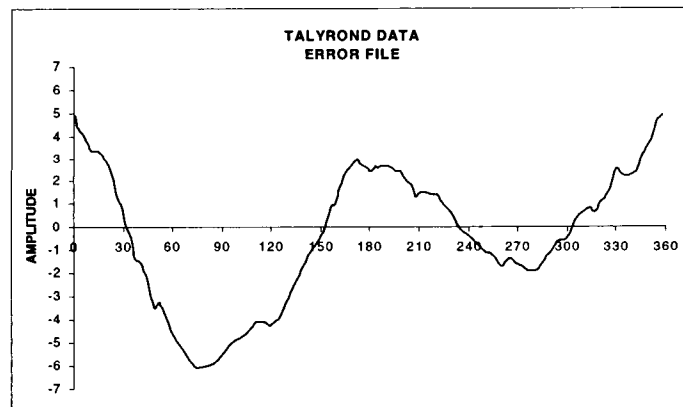
Figure 2. Talyrond Error Plot

✓ Contact Angle difference (row 1 versus row 2)

✓ Ball Geometry Errors
Size   Errors generally input as a random ball size deviation
            Specific ball size deviations can also be entered
Spacing   Errors input for biased cage applications

304

Program-generated geometry errors from previous error inputs, together with the measured Talyrond errors, are summed and input into the main model for the motion analysis.

In addition to the above inputs, the model will also allow the inner and/or outer rings to be "clocked" relative to each other. This clocking allows the model to analyze motions for various face-to-face alignments of the bearing rings. In addition, the effect of phasing the inner or outer ring radial eccentricities relative to the axial eccentricities at specified angles can be investigated.

Figure 3 is a sample input file[1] used by the Motion Model.

Motion plots are generated by the model and are shown as the number of steps versus deflection amplitude. Information that can be extracted from these plots includes not only deflection ranges but motion phase information amongst the three components. Figure 4 is an example of a motion plot.

In addition to motion plots, frequency spectrum plots versus radial and axial amplitudes can also be generated. Figure 5 is an example of a frequency plot.

Other plots that can be generated include force (N) and acceleration (g's) versus frequency.

MODEL VALIDATION

Validation of the Motion Model was an important first step towards gaining an understanding of how the model worked and determining what key bearing parameters needed to be included in the model. A program verification test matrix was therefore developed to review motion and FFT plots generated by the model and to ensure that the test cases agreed with expected results.

Analytical Test Matrix. The intent of the test matrix was to look at each bearing geometry error independently and combined, to review the motion and FFT output of each test case, and to determine if the output was as expected.

The analytical test matrix included:
- Perfect part geometries
- Radial and axial eccentricities for 1 node to 4 node geometry errors
- Ball size errors
- Ball spacing errors
- Two balls missing
- Shaft unbalance forces
- 0g (space environment) and 1g (ground environment) loading

---

[1] Inputs shown not specific to this paper.

```
?PROBLEM SET DESCRIPTION .....................................................|
61071gF3  -  VER 5.2 JULY 5,1991  RUN DATE 08/09/91
?DESCRIPTION ................................................................|
1G GRAVITY CASE - BIASED CAGE - OUTER CLOCKED 90   INNER EVERY 30 deg
?NO ROWS |?DF/DT/DB|?THRUST  |?RADIAL  |?APHA/MOM|? RPM   |? STEPS  |?CONTROL |
-2.       -1.        0.0       20.                2000.       512.   1.
?STRADDLE|?PRELOAD |?CASE    |?FMU-PRLD|?RATE    |?GAP     |?FLUSH   |?FILM    |
.6693     12.0      1.        .15                          -.000005
?FMUS    |?FMUL    |?FMUC    |?L-VIS CS|?L-QUAN  |?CLEAR   |?XRUN    |?NUSE    |
.07       .07       .07       140.      .13       .010
?SH TURNS|?SHAFT WT|?UNBAL   |?UNBA ANG|?ITER_TOL|?DIFF_CA |?VRADIAL |?TEST    |
19.       0.        0.        0.        .025      -.140
? ROW NO |?#-BALLS |?BALL DIA|?FREE CA |? E      |? FI     |? FO     |? BGAP   |
1.        10.0      .46875    13.66     1.743     .54       .55
?IR PRESS ?IR HD/D |?IR-DAM/D|?IR-WIDTH|?SHAFT ID|?BRG BORE|?IR-CLAMP|?IRC-FMU |
 .000200  .26       .26       .6693               .9843     100.      .1
?OR PRESS ?OR HD/D |?OR-DAM/D|?OR-WIDTH|? BRG OD |? HSG OD |?OR-CLAMP|?ORC-FMU |
-.00037   .26       .26       .6693     2.4409    5.        100.      .1
?E-SHAFT |?E-BRG   |?E-HSG   |?PR-SHAFT|?PR-BRG  |?PR-HSG  |DENSITY  |? DELR   |
32.E6     32.E6     32.E6     .32       .32       .30       .150
?TC-SHAFT|?TC-BRG  |?TC-HSG  |?OT-SHAFT|?OT-IR   |?OT-OR   |?OT-HSG  |? DELH   |
7.0E-6    7.5E-6    6.2E-6    80.       80.       70.       75.
---------ROW 1 GEOMETRY ERRORS (MICROINCHES) ---|RADIAL TO AXIAL DEG|IR RADIAL|
?NODE    |?IR RAD  |?OR RAD  |?IR AXIAL|?OR AXIAL|?PHASE IR|PHASE OR |?SHIFT   |
 1.        30.0      40.0      -30.0     30.0
 2.
 3.
 4.
?SHIFT IR|?SHIFT OR|          |         |?IR FILE  |?OR FILE  |
          90.                            IR721FX.RND OR520FX.RND
? NSIR   |? NSOR   |?BSIZE   |?        |?         |?         |
12.0      1.0       0.000005
-------------- BALL SPACEING ERRORS   (degrees) ----------------------
?BALL1 |?BALL2 |?BALL3 |?BALL4 |?BALL5 |?BALL6 |?BALL7 |?BALL8 |?BALL9 |?BALL10|

?BALL11|?BALL12|?BALL13|?BALL14|?BALL15|?BALL16|?BALL17|?BALL18|?BALL19|?BALL20|

-------------- BALL DIAMETER ERRORS   (micro-inches) ----------------
?BALL1 |?BALL2 |?BALL3 |?BALL4 |?BALL5 |?BALL6 |?BALL7 |?BALL8 |?BALL9 |?BALL10|

?BALL11|?BALL12|?BALL13|?BALL14|?BALL15|?BALL16|?BALL17|?BALL18|?BALL19|?BALL20|

----------ROW 2 GEOMETRY ERRORS (MICROINCHES) ---|RADIAL TO AXIAL DEG|IR RADIAL|
?NODE    |?IR RAD  |?OR RAD  |?IR AXIAL|?OR AXIAL|?PHASE IR|PHASE OR |?SHIFT   |
 1.        20.0      45.0      30.0      -30.0
 2.
 3.
 4.
?SHIFT IR|?SHIFT OR|          |         |?IR FILE  |?OR FILE  |
                                         IR672FX.RND OR353FX.RND
? NSIR   |? NSOR   |?BSIZE   |?        |?         |?         |
 1.0      1.0       0.000005
-------------- BALL SPACEING ERRORS   (degrees) ----------------------
?BALL1 |?BALL2 |?BALL3 |?BALL4 |?BALL5 |?BALL6 |?BALL7 |?BALL8 |?BALL9 |?BALL10|

?BALL11|?BALL12|?BALL13|?BALL14|?BALL15|?BALL16|?BALL17|?BALL18|?BALL19|?BALL20|

-------------- BALL DIAMETER ERRORS   (micro-inches) ----------------
?BALL1 |?BALL2 |?BALL3 |?BALL4 |?BALL5 |?BALL6 |?BALL7 |?BALL8 |?BALL9 |?BALL10|

?BALL11|?BALL12|?BALL13|?BALL14|?BALL15|?BALL16|?BALL17|?BALL18|?BALL19|?BALL20|
```

Figure 3. Model Input File
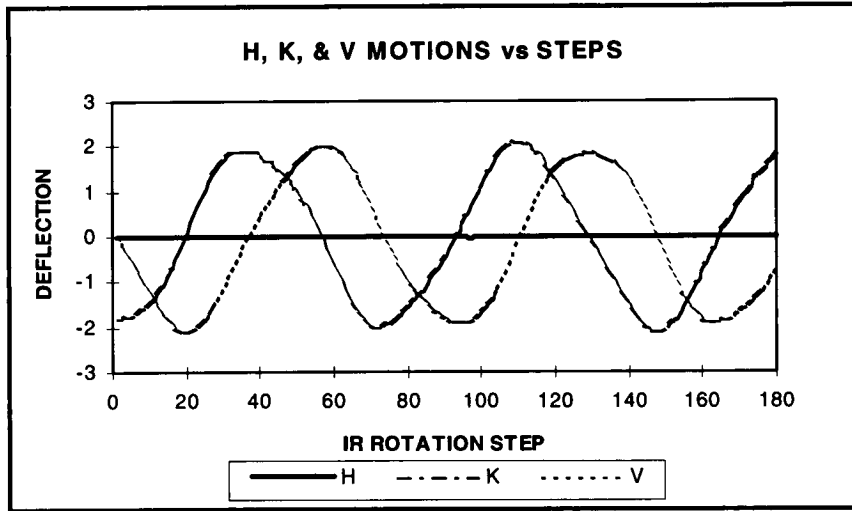
Figure 4. Motion Plot
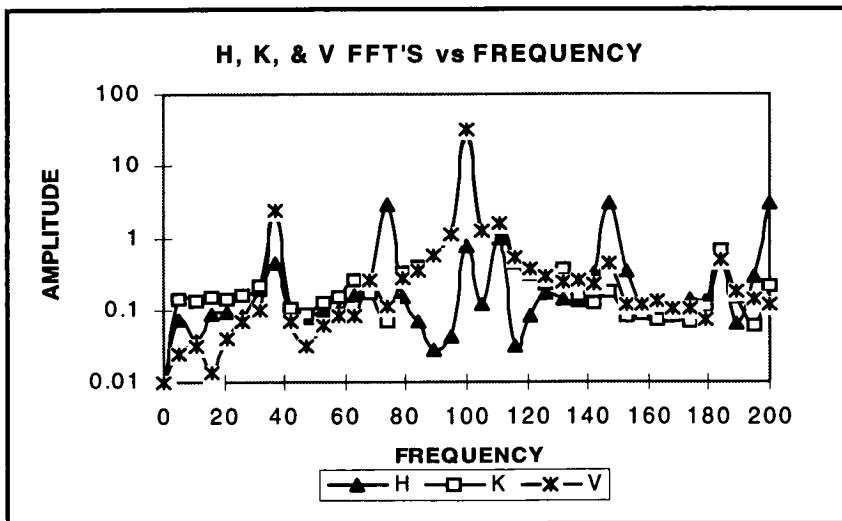
Figure 5. Frequency Plot

A total of 122 test cases were run and reviewed.

Several iterations of these test cases were completed because each iteration revealed additional model errors and identified model enhancements. Finally, all 122 test case results were considered acceptable and it was concluded that the model was valid.

Figures 6 and 7 are shown to illustrate the sensitivity of the model to inputted geometry errors. Figure 6 shows a frequency plot for a 0.10 μm (4 μin.) cosine ball size distribution error input; no other geometry errors were input. As expected, the model generated a disturbance at the ball group frequency, a 37 Hz peak of 0.10 μm (4 μin.) amplitude.

Figure 7 is an output plot for the same cosine ball size distribution and a 0.09 kg (0.2 lbm) shaft unbalance force applied. Note the motion response at the 100 Hz spin frequency.
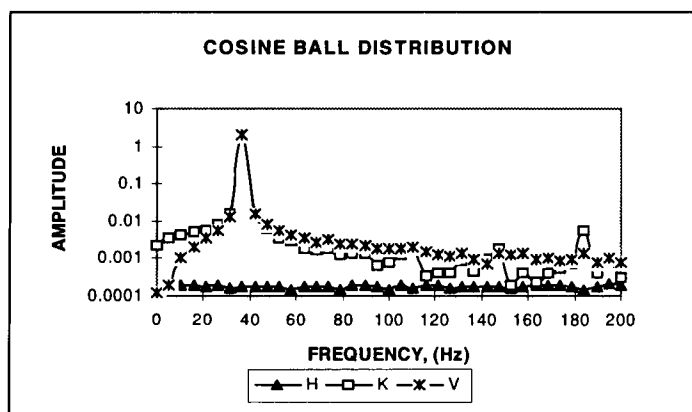
Figure 6. Cosine Ball Distribution
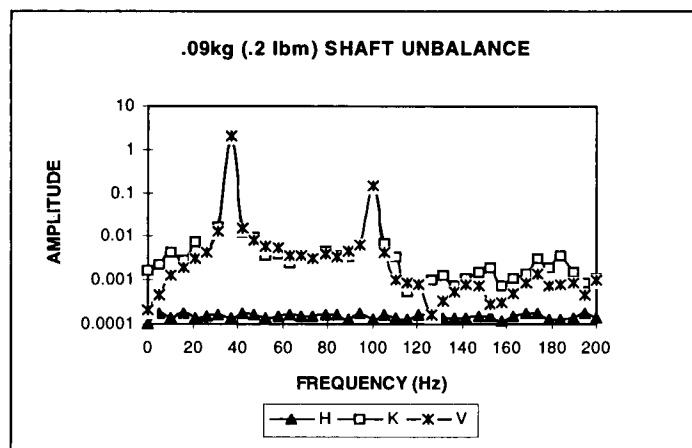
Figure 7. Shaft Unbalance

BEARING DISTURBANCES

Two frequencies have been identified as being of particular interest in the investigation of bearing disturbance effects on momentum wheels. These frequencies are 74 and 100 Hz. A momentum wheel was producing an unacceptable 74 Hz axial disturbance. The model was used to simulate geometry errors and identify a cause.

Frequency Drivers. The model was run using actual measured data from a 305 size bearing pair to investigate effects on bearing motion due to inner and outer ring clocking and phasing. This data included measured contact angle, face stickout, and bore diameter. In addition, axial runout and unmounted preload was input to the model for the bearing pair. Inspection data for each bearing ring (inner and outer) included race/bore radial runout and race radial roundness. Talyrond plots of the individual rings were digitized and converted to error files for the model. A ± 0.13 μm (± 5 μin.) random ball size error distribution was input into the model, which is the size variation specified for Anti-Friction Bearing Manufacturers Association (AFBMA) Grade 3 balls. Also, ball position errors were included to account for biased cage geometry effects.

Cases were run for 0g and 1g loading.

Table 1 lists the cases that were run in the model, the parameters that were varied, and the effect on the Model output.

Table 1. Actual Bearing Results

Case	Parameter Varied	Model Results
1 (0g) 2 (1g)	Inner rings clocked every 30°	Negligible change in amplitudes at all frequencies
3 (0g)	Same as above + Same size balls	Negligible change in amplitudes
4 (0g) 5 (1g)	Inner rings clocked every 30° for every 30° clocking of outer ring	Negligible change in amplitudes
6 (0g) 7 (1g)	Phase radial to axial inner ring ecc. 90° for every 90° phasing of radial to axial outer ring ecc. (row 1 only)	Negligible change in amplitudes
8 (0g) 9 (1g)	Shift row 1 rings +2.54 μm (+100 μin), row 2 rings -2.54 μm (-100 μin)	Large increase in axial amplitudes at 74 and 100 Hz

Results from these runs follow:

♦ Inner ring clocking has no effect on amplitudes
♦ Outer ring clocking has no effect on amplitudes
♦ Random ball size change has a small effect on amplitudes at 37 Hz
♦ Phasing of eccentricities has a minimal effect on amplitudes at 100 Hz
♦ Loading (0g versus 1g) has an effect on 100 Hz axial and 74 Hz radial components

In completing the model verification test runs, bearing disturbance frequencies, geometry error input, and the component drive (radial or axial), relationships were noted. Table 2 summarizes the relationship of these factors.

Table 2. Bearing Disturbances

Frequency	Disturbance Causes	Component
74 Hz	Ball size (random)	Radial/Axial
	Ball position (biased cage)	Radial
	Outer ring geometry combined with ball size variation	Radial
	Outer ring geometry combined with ball size and ball position	Radial/Axial
	1 large/9 small balls	Radial
100 Hz	Inner race axial eccentricity (node 1)	Radial/Axial
	Inner race radial eccentricity (node 1)	Radial/Axial
	Rotor unbalance force	Radial

From Table 2 it is evident that 74 Hz axial motion is controlled by ball group symmetry and/or outer race geometry.

Momentum Wheel Amplitude Prediction. The most likely cause of the 74 Hz axial bearing motion generated in the momentum wheel is outer ring geometry errors. One scenario that could cause this geometry error is the bearing cartridge "squeezing" the bearing outer ring. This squeezing is actually a two-point interference fit between the bearing cartridge and the bearing outer ring. It was theorized that the cartridge had possibly become egg-shaped (i.e., node 2 error) as a result of slots that were cut into the cartridge to accommodate other hardware. These slots could have stress-relieved the part, allowing the cartridge to deform and squeeze the outer rings of the bearings.

The outer ring squeeze was modeled as a 2 node radial geometry error in row 1 and row 2 of the bearing outer rings. Figure 8 shows the node 2 error relative to a "perfect" ring.
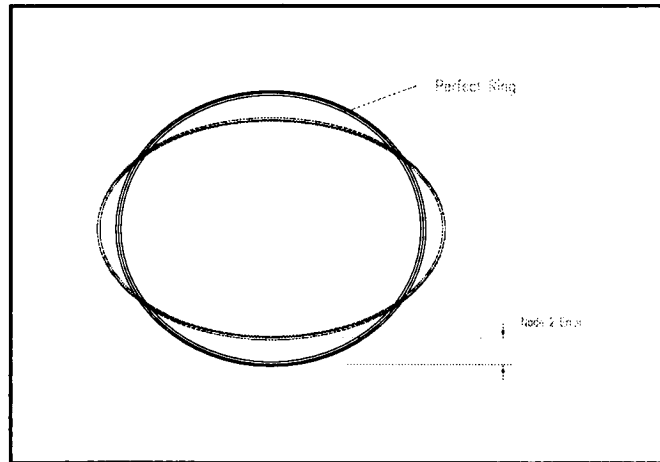
Figure 8. Outer Ring Node 2 Error

Bearing inspection data for the bearings mounted in the momentum wheel was used for geometry error inputs. These inputs, in addition to mounting and loading parameters, are as follows:

♦	Ball position error	biased cage
♦	Random ball size	±0.13 μm (± 5 μin.)
♦	Node 1 eccentricity	

	Row 1	0.76 μm (30 μin.) inner radial
		1.02 μm (40 μin.) outer radial
		0.76 μm (30 μin.) inner axial
		0.76 μm (30 μin.) outer axial
	Row 2	0.51 μm (20 μin.) inner radial
		1.14 μm (45 μin.) outer radial
		0.76 μm (30 μin.) inner axial
		0.76 μm (30 μin.) outer axial
♦	Talyrond data	digitized data
♦	Bore/Shaft interference	2.54 μm (100 μin.)
♦	Bearing OD clearance	9.40 μm (370 μin.)
♦	1g loading	

Several cases were modeled to compare the axial amplitudes for different node 2 error values. Cases were run with equal node 2 errors in both rows, 2x error in row 1 versus row 2, 3.81 μm (150 μin.) error difference in row 1 versus row 2, and 7.62 μm (300 μin.) error in row 1 versus row 2. These inputs are summarized in Table 3.

Table 3. Node 2 Error Inputs

Case	Node 2 Error μm (μin.)	
	Row 1	Row 2
Baseline	0	0
Row 1 & 2	7.62 (300)	7.62 (300)
Row 1 & 2	5.08 (200)	5.08 (200)
Row 1 & 2	2.54 (100)	2.54 (100)
Row 1 & 2	0.76 (30)	0.76 (30)
Row 1 & 2	0.38 (15)	0.38 (15)
Split Row 1 & 2	7.62 (300)	3.81 (150)
Split Row 1 & 2	5.08 (200)	2.54 (100)
Split Row 1 & 2	2.54 (100)	1.27 (50)
Split Row 1 & 2	0.76 (30)	0.38 (15)
Split Row 1 & 2	0.38 (15)	0.19 (7)
Split 150 μin	3.81 (150)	0 (0)
Split 150 μin	7.62 (300)	3.81 (150)
Split 150 μin	11.43 (450)	7.62 (300)
Row 1 only	7.62 (300)	0

Figure 9 shows the results of the 2 node geometry effects for each of the cases. Figure 10 is a plot of axial amplitude versus frequency.
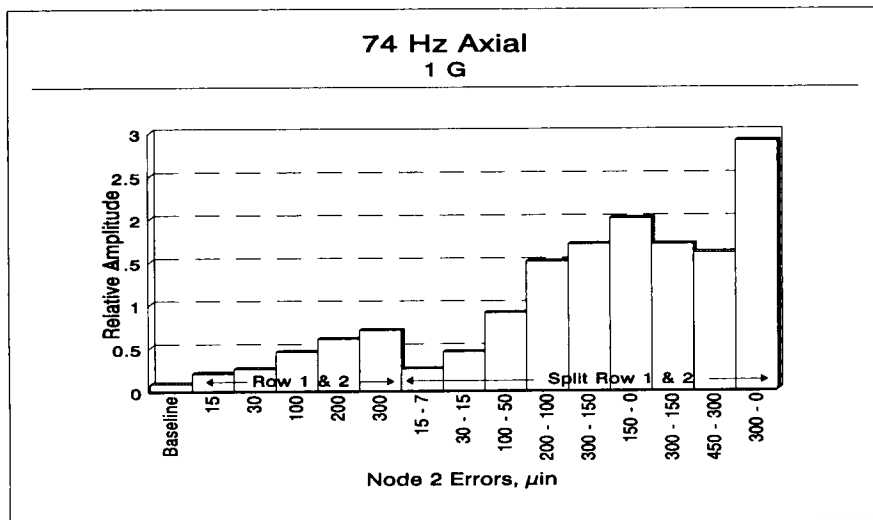
Figure 9. 2 Node Results
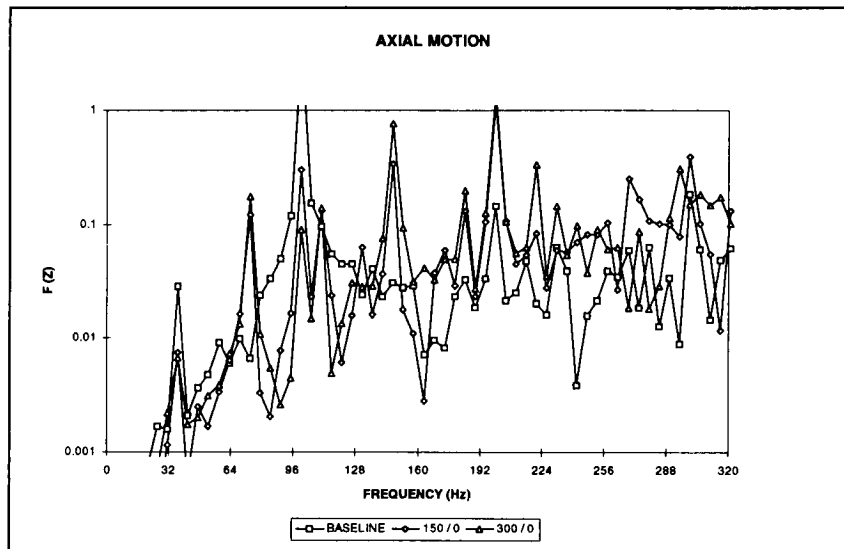
Figure 10. Frequency Plot

Axial motion is largest for the 7.62 μm (300 μin.) node 2 error difference in row 1 versus row 2. The cases where there is a 3.81 μm (150 μin.) difference in node 2 errors between row 1 and row 2 show a **decrease** in amplitude as the absolute values of the errors are increased equally for each row. This is expected because the spring rates of each bearing are increasing as the radial squeezing increases in both rows. As the difference in node 2 errors between rows increases, the axial amplitude increases. The cases where the node errors are equal in both rows have relatively low axial amplitudes, even for a 7.62 μm (300 μin.) error.

An interesting general result in pursuing the 74 Hz disturbance is that axial motions at 100 Hz are driven by external radial loads.

From this data, it was concluded that significant axial motion at 74 Hz can be generated by outer ring node 2 errors together with ball position and size errors, particularly when the error difference between rings is large [>2.54 μm (100 μin.)]; therefore, the next step was to inspect both cartridges from the momentum wheel.

TEST RESULTS

Parts Inspection. As a result of the model predictions for the possible source of the 74 Hz axial disturbance, the bearing cartridges were inspected on the momentum wheel producing the axial disturbance. One of the two bearing cartridges was found to be out-of-round. Measurements of the bearing outer ring and cartridge bore confirmed that there was an interference.

313

Wheel Test Results. A series of tests were conducted to verify that the out-of-round cartridge was indeed the driver. Frequency data was taken with the 305 bearing pair installed in the out-of-round cartridge and again with the bearings installed in a round cartridge. The test was repeated with the bearings installed in the out-of-round cartridge to check repeatability of the measurements. Frequency output data for the out-of-round cartridge is shown in Figure 11, while Figure 12 illustrates frequency data for the round cartridge. Note the significant decrease in amplitude at 74 Hz for the round cartridge.

These tests confirmed that the out-of-round cartridge did cause the outer ring to distort, generating the 74 Hz axial motion and producing over 3x the disturbance at 74 Hz than bearings installed in the round cartridge.
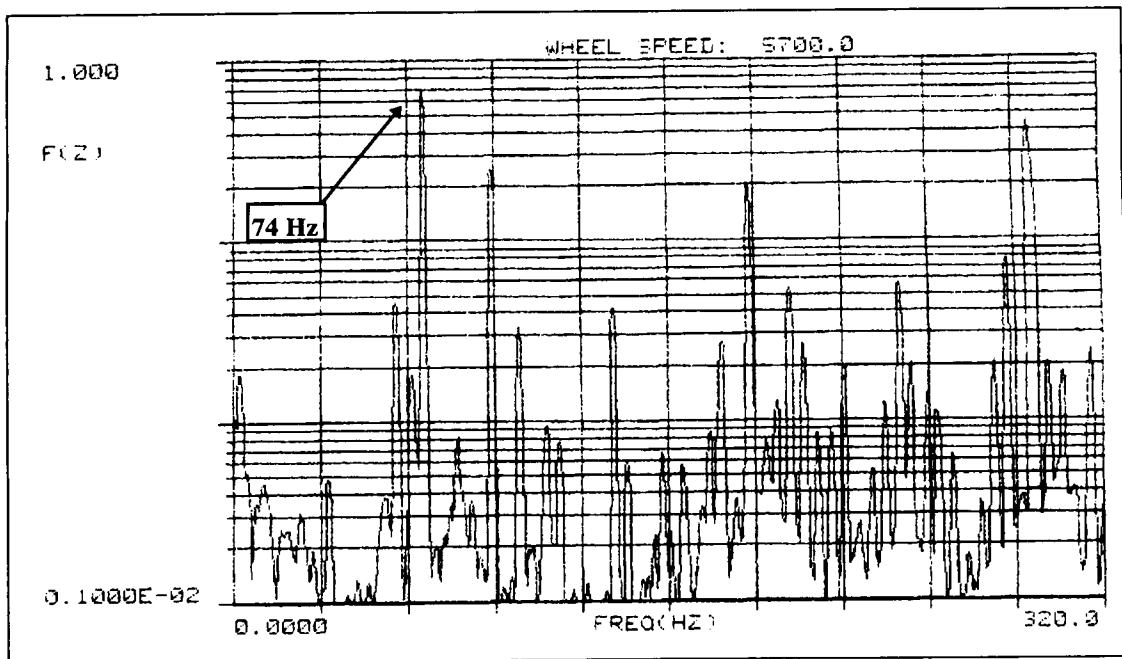
Figure 11. Out-of-round Cartridge
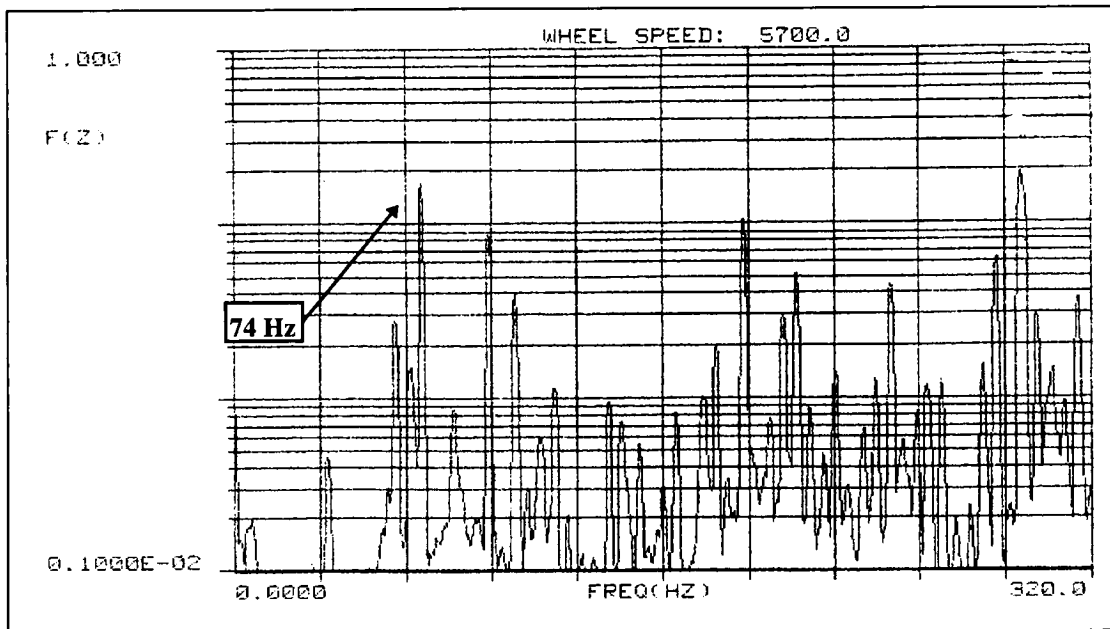
Figure 12. Round Cartridge

CONCLUSIONS

The quasi steady state model was successful in predicting the source of the 74 Hz axial disturbance. The effect of the cartridge out-of-round condition was the source of the undesirable motion. The bearing outer races that generated the 74 Hz disturbance were measured and found to have an interference with the out-of-round cartridge.

Placing the bearings in a round cartridge reduced the undesirable vibration. Placing the bearings back in the out-of-round cartridge reproduced the undesirable performance.

The Motion Model is a useful tool to predict bearing motion using theoretical or actual bearing geometric data.

315

A Cryogenic Scan Mechanism for use in Fourier Transform Spectrometers

Claef F. Hakun[*] and Kenneth A. Blumenstock[*]

ABSTRACT

This paper describes the requirements, design, assembly and testing of the linear Scan Mechanism (SM) of the Composite Infrared Spectrometer (CIRS) Instrument. The mechanism consists of an over constrained flexible structure, an innovative moving magnet actuator, passive eddy current dampers, a Differential Eddy Current (DEC) sensor, Optical Limit Sensors (OLS), and a launch lock. Although all the components of the mechanism are discussed, the flexible structure and the magnetic components are the primary focus. Several problems encountered and solutions implemented during the development of the scan mechanism are also described.

INTRODUCTION
CIRS OVERVIEW

The CIRS is a remote sensing instrument designed for the Cassini spacecraft which will be launched in October 1997. The primary science objectives of the CIRS are:
* To globally map the thermal structure, gas composition, hazes and clouds, and non-equilibrium processes of Saturn and Titan.
* To search for new molecular species in the atmosphere of Saturn and Titan.
* To globally map the surface temperature of Titan.
* To map the thermal characteristics and composition of the rings and icy satellites.
The CIRS will provide the highest resolution interferograms of Saturn and associated targets to date. The top view of the Optical Assembly (OA) and the instrument coordinate system are shown in Figure-1. The instrument consists of the following subsystems:

OPTICAL The optical system[1] consists of a Cassegrain telescope and three Michelson interferometers. The Mid-Infrared (MIR) and Far-Infrared (FIR) science interferometers provide for a spectral coverage from 7 to 1000 microns. The Reference interferometer (RI) provides signals used for instrument timing and data collection and control of the Scan Mechanism.

MECHANICAL The beryllium telescope assembly, 80K radiative cooler assembly, the relay optics and detectors, and scan mechanism are all mounted on the monolithic aluminum optical plate and constitute the OA. The OA is mounted to the spacecraft via a titanium mounting tube which provides pointing stability and thermal isolation. The scan mechanism is fastened and pinned to the OA on three coplanar mounting pads. The OA is designed to provide access to and alignment of all critical components.

ELECTRICAL The CIRS Electronics Assembly (CEA), is connected to the OA via a cryogenic cable which minimizes the thermal input between the warm CEA and the colder OA. The CEA controls all functions of the CIRS instrument: In particular the CEA contains the Scan Mechanism Electronics (SME). The SME performs the following

[*] Code 723, NASA Goddard Space Flight Center, Greenbelt, MD

major functions: phase-locked loop scan control, flyback control, engineering telemetry, unlatching control, and state selection of the mechanism. Describing the SME design constitutes the subject of another paper.

THERMAL The passive thermal design provides temperature stabilization at 80K for the MIR detectors and 170K for the rest of the OA. Heaters provide 0.1K per day stability of the 170K and 80K regions of the instrument. The main shaft of the SM must also meet this requirement.

MECHANISM Several mechanisms are utilized on the optical assembly; two cover release mechanisms, a calibration shutter mechanism[2] and the scan mechanism. The scan mechanism design, as with most instrument mechanisms, relates to all of the instrument subsystems.

FUNCTIONAL DESCRIPTION

The scan mechanism provides the optical alignment for the moving mirrors of the three interferometers. It provides precision linear translation of the retroreflector shared by the MIR/RI interferometers and the dihedral mirror for the FIR interferometer. The main shaft supports the retroreflector on one end and the dihedral on the other. Events are shown (Figure-2) which occur as the main shaft translates between its limits of travel. Motion of the main shaft modulates the incoming wavefronts of the interferometers to create interference between the fixed and moving arms. The data collected during a scan contains the amplitude and frequency content of the light collected by the field of view of the instrument. The scan mechanism has two main operational states; scan and flyback. When in the scan state, the mechanism translates in the -X direction. The main shaft velocity is precisely controlled by the phased-locked loop circuitry located in the SME. The mechanism continues to scan until given the flyback command from the Instrument Data System or until the end of scan OLS is triggered. Variable scan lengths are therefore possible. The majority of scans will either be short 0.4 mm scans or long 10.4 mm scans. The long scan is not centered on mechanism neutral (At the center of displacement where the spring forces are zero in the x axis). Skewing the long scan makes the average power dissipation equal for both long and short scans. In the flyback state, the mechanism translates in the +X direction at a rate approximately 20 times the nominal scan velocity. When the end flyback OLS is triggered, the mechanism begins scanning again. During the 4 year operational phase of the mission, the scan mechanism will continuously toggle between these two states.

HERITAGE

The CIRS is similar to the Infrared Interferometer Spectrometer (IRIS) instruments which flew on Voyager I and II. Similar mechanism concepts were implemented on each of these instruments, however, due to the stringent spacecraft limitations on mass and power, operating environment, and science requirements which provide for significantly broader spectral coverage and 10 times the resolution of previous missions, it is believed that the CIRS scan mechanism represents the state of the art design of a mechanism of this type.

MECHANISM OVERVIEW

The requirements, electromechanical design and operation, and testing of the scan mechanism are described. The scan mechanism design evolved over a two year period. Two developmental breadboard units where assembled and tested. Two engineering unit mechanisms which represent the flight design have been fabricated and tested. Two flight units are being assembled and tested.

REQUIREMENTS
The environmental and performance requirements listed below were developed at the Cassini Spacecraft[3] and CIRS instrument[4] levels directly from science requirements or engineering analyses. All testing and analysis of the engineering model scan mechanism indicate compliance with the following requirements.

SPACECRAFT LEVEL
- Survive the launch environment. Cassini will be launched on a modified Titan IV.
- Meet performance requirements while being subjected to spacecraft jitter disturbances. The reaction wheel disturbances represent the major disturbances during instrument operation. The effect of disturbances generated by other instruments will be minimized by scheduling observations and operation of other disturbance sources.
- All components to be insensitive 100Krad radiation environment
- Constitute < 2.5 nanotesla and < 10 nanotesla at 1 meter to instrument static and dynamic stray magnetic field budgets respectively. Meet AC stray magnetic field requirements.

INSTRUMENT LEVEL
- Contribute < 2.0 kg to instrument mass
- Fit into the OA and provide 160 mm metering distance between the vertex of the retroreflector and the apex line of the dihedral mirror. Allowable volume: X (134mm), Y (180mm), Z (165mm)
- Provide travel for variable length scans between 0.4 mm and 10.4 mm
- Dissipate an average of < 200 milliwatts @ 170K
- Operate for over 5 million fully reversing cycles over the 12 year mission
- Provide spring and actuator force constants which have < 5% deviation from linearity. This requirement was derived from analysis of the control system. Since all degradation effects are known, a minimum force margin of 50% is sufficient.
- Provide precision alignment and translation of the optical elements which have an allocated combined mass of 240 grams.
- Tilt of main shaft about the Y and Z axes to be < ±3 arcseconds under zero g, at 170K and throughout the entire scan. Repeatability between scans <0.15 arcsecond.
- Shear, defined as translation in the transverse Y and Z directions from nominal optical axis, to be < 6 microns under zero g , at 170K and throughout entire scan. Repeatability between scans < 0.5 microns.
- Allowable shear during ground testing to be < 18 microns throughout the entire scan.
- Provide a nominal scan velocity of 0.0208 cm/s.
- Provide for a minimum 69% scan efficiency for short scans and 95% for long scans.
- Control scan velocity to 5% (ZPD)/15% (elsewhere) rms in presence of disturbances.

318

ELECTROMECHANICAL DESIGN AND OPERATION

The top level assembly, each sub-assembly, and mechanism testing are summarized. The spring pair, actuator, outrigger/damper, launch lock, OLS, and compensation coil sub-assemblies form the top level assembly. The CIRS engineering model scan mechanism (Figure-3) cross-sectional view (Figure-4) depicts the major components of the scan mechanism top level assembly in the launch-locked configuration. The mechanism design has the following salient features:

- A flexible structure which supports the main shaft
- An innovative moving magnetic circuit with precision layer winding
- A Differential Eddy Current (DEC) sensor for analog displacement telemetry
- Passive electromagnetic dampers on both the main shaft and the outriggers
- Optical limit sensors (OLS) to provide end of travel indications
- Remotely resetable launch lock
- Compensation coil to minimize stray magnetic fields.

TOP LEVEL ASSEMBLY A spring pair assembly is attached to each end of the main shaft and to each end of the main housing. The outrigger shafts connect the spring pair assemblies. The main housing and the components referenced above constitute the flexible structure. The outrigger shafts pass through the outrigger dampers and are constrained only by the eddy current damping produced when the damping rings which are rigidly attached to each outrigger are translated through the radial magnetic field of the closed magnetic circuit of the dampers. The actuator magnetic circuit is contained between the two halves of the main shaft. The moving magnet configuration provides for minimal power dissipation on the main shaft and therefore minimal temperature increases of the main shaft occur during operation. Embedded within the main shaft is the bobbin assembly which is rigidly attached to the main housing. The bobbin assembly includes the DEC sensor windings, and the winding and single turn damping ring of the actuator. A tab is attached to the main shaft which triggers the OLS's directly after the end of long scan and at the end of flyback location. The launch lock constrains the mechanism whenever the mechanism is subjected to sizable vibration inputs. When unlatched, the main shaft is constrained by the tab of the launch lock and the endcap of the FIR spring pair assembly.

As the main shaft is displaced from mechanism neutral, the outriggers breathe in the radial direction and traverse half the displacement of the main shaft. This allows the springs to deform in almost pure bending. The mechanism can be viewed as three double four-bar-linkages each in parallel. In Figure-4, one of double four-bar-linkages is clearly visible. The load path goes from the inner springs which are rigidly attached to the main housing up to the outriggers and then down the outer springs which connect to the main shaft. A quick and fairly accurate method to calculate the axial stiffness of a mechanism of this type is to make an imaginary cut of one of the springs at the midpoint and impose a displacement condition. The flexible structure of the mechanism can now be reduced to a system of cantilever beams in series and in parallel with each other. The main housing, outriggers, and main shaft constitute the metering structure of the mechanism and are made of aluminum 6061 to match the OA. This ensures that gross misalignments between optical elements due to CTE mismatches does not occur.

319

This configuration results in a mechanism which has an extremely linear axial force versus displacement relationship, relatively high radial stiffness, minimal power dissipation on the main shaft, thermal stability and precision mirror positioning capability.

SUB-ASSEMBLIES

Spring Pair Assembly The spring pairs provide the support, alignment and guidance of the main shaft and outriggers. The spring pair assembly pictured in Figure-5 is the result of a precision matched machining and pinning assembly procedure. The assembly procedure ensures that the spring clamping surfaces are flat and coplanar to within 5 microns and that the spring lengths are all equivalent to within 5 microns. The assembly is fastened to the main housing, outrigger/damper assembly, and the actuator assembly. The design of the spring pairs allows for repeatable assembly into the top level assembly of the mechanism without the need to perform complicated and time consuming realignment procedures. The performance of the design is relatively insensitive to preloading of the clamping surfaces and is therefore insensitive to changes in bulk temperature of the components.

The assembly consists of 6 beryllium copper leaf springs, and the following AL 6061 T651 structural components: the endcap, outrigger components, clamp plates, and the mirror mount hub. The endcap and mirror mount hub are thermally cycled to ensure stability at 170K. All aluminum parts are black anodized. Fixture heat treating of the beryllium copper to the TH02 (half hard) condition enhances the physical properties, relieves residual stresses and flattens the springs. In the TH02 condition, beryllium copper has excellent fatigue and strength properties, relatively good thermal conductance, and good stability of the elastic modulus over the operating temperature range. The springs are 0.3 mm (0.010") thick, 28 mm (1.1") wide and 68mm (2.670") long. These dimensions provide the desired force constant (600 $^N/_m$), fatigue life (infinite: 10.5 ksi maximum bending stress), and radial stiffness.

Actuator Assembly The actuator assembly (Figure-6) provides mechanical force required to overcome the axial spring force and required to control displacement and velocity of the main shaft. It incorporates passive eddy current damping and position monitoring of the main shaft. This assembly is composed of three primary sub-assemblies; the moving magnetic circuit, the fixed bobbin, and DEC sensor assemblies.

<u>Magnetic Circuit</u> The moving magnetic circuit is divided into two symmetric halves. Each half consists of the inner housing, pole piece assembly, and axial magnet. The pole piece assembly is epoxy bonded with Stycast 2850/24LV and consists of the pole piece, sectioned radial magnet and a thin Carpenter 430F solenoid quality stainless magnet containment ring. The inner housings and pole pieces, machined from Hiperco 50a, provide a low reluctance magnetic path which completely encloses the air gap of the actuator and carries the flux of the SmCo 28 magnets. The magnetization directions of the axial and radial magnets are indicated in Figure-6. The magnets and Hiperco 50a components are sized to provide a maximum flux of 2 tesla within the magnetic circuit. This configuration results in the extremely linear current versus displacement relationship (Figure-9).

Bobbin The bobbin supports the DEC sensor, the actuator winding, and the main shaft damping ring. The bobbin is made of 6061-T651 aluminum which is black anodized to ensure non-conduction between the winding and the bobbin structure. The bobbin is rigidly attached to both endcaps by six integral legs which pass axially through holes in the inner housings and radial magnets. Grooves have been machined on each of the legs on one side of the bobbin to provide a path for the six wires which exit the actuator assembly. Two wires are carried on each leg. In addition, the bobbin has 61 parallel circular grooves precisely machined and located between the side walls of the bobbin. These grooves mimic a perfect layer of the winding. This precision layer winding has exactly 24 layers and 61 turns per layer of 32AWG magnet wire. The cross-section photograph (Figure-6) reveals its uniformity. The winding is encapsulated with Stycast 2850/24LV according to a vacuum/high pressure impregnation procedure which assures that no voids are present within the winding. The encapsulant is also used to secure the high purity copper damping ring which slides over the outer diameter of the bobbin. Passive eddy current damping of the main shaft works on the same principle as that of the outrigger dampers. The winding produced by this process is highly reliable, easy to wind, and approaches maximum achievable fill factor of copper within the air gap and therefore maximum actuator efficiency.

Differential Eddy Current (DEC) Sensor The DEC sensor provides an analog voltage output proportional to displacement of the main shaft. The sensor consists of excitation and pick-up windings which are coupled by two aluminum tubes which are integral to the main shaft halves. Windings are centrally located within the main shaft. The sensor operates differentially; one tube couples as the other decouples when the main shaft is displaced from mechanism neutral. The coupling between the excitation and pick-up coil induced by a 20 kHz excitation signal is demodulated and filtered with a standard LVDT signal conditioning chip to provide the analog output of the sensor. Linearity and resolution of the sensor is shown in Figure-10.

Actuator Parameters

Actuator constant (Ka), 170K	$5.0\ N/\sqrt{W}$	Actuator constant (Ka), 293K	$3.6\ N/\sqrt{W}$
Force constant (Kf)	$30.1\ N/A$	Damping	$17\ N/m/s$
Diameter (w/o shaft)	40.6 mm	Length	63.5 mm
Moving mass	272 g	Mass, fixed (w/o sensor)	74 g

Outrigger/Damper Assembly A single turn high purity copper damping ring is rigidly attached to the outrigger shaft and is in the air gap of the magnetic circuit (Figure-7). The magnetic circuit consists of a single SmCo 28 radial magnet and a closed Hiperco 50a low reluctance magnetic path. The circuit is designed to carry a maximum flux of 2 tesla. As the damping ring is translated through the radial magnetic field, eddy currents are generated. These currents create a force which is proportional to the velocity and in opposition to the direction of motion of the ring. The value of damping was determined by the control system model, the allowable volume, and the spring dimensions. The dampers are sized to provide critical damping at the resonance of the outriggers when located at the mechanism neutral position. The damping increases by a factor of ~ 1.9 at 170K due to decrease of resistance of the damping ring.

Launch Lock Assembly The housing, guide shafts, and yoke comprise the structure of the launch lock (Figure-8). Return springs located on both guide shafts provide the force required to reset the High Output Paraffin (HOP) actuator and maintain the yoke in the latched configuration during launch. Optical limit sensors are triggered when the yoke is displaced ~ 1.3 mm (0.05") from either end of travel of the yoke within the housing. The first OLS provides an indication that the yoke is in the proper unpowered location. The second OLS ensures that power is removed from the HOP prior to the yoke being driven into the hard stop which could damage the HOP.

In the locked configuration, the main shaft is displaced to the MIR end of travel and constrained in the axial direction by interaction of tabs located on the yoke and main shaft and by radial stops on the main housing (Figure-4). Motion of the outriggers is limited by snubbers. To unlatch, power is applied to the HOP actuator. The drive shaft of the HOP overcomes the 17.8 to 44.5 N (4 to 10 lb) return spring force and displaces the yoke ~ 12.7 mm (0.5") in the Y direction. This disengages the yoke and main shaft tabs. Once disengaged, the main shaft is forced to the mechanism neutral position by the flexible structure of the mechanism. After the second OLS is triggered and power is removed from the HOP, the yoke returns to its original unpowered position. The yoke tab now becomes the hardstop in the +X direction. To relatch, power is applied to the HOP driving the yoke in the +Y direction. The main shaft is then commanded to the MIR hardstop. Power is removed from the HOP and the yoke returns to the unpowered position, thus constraining the main shaft in the axial direction. The lock is therefore remotely resettable.

OLS Assembly The OLS's provide precision displacement information of the main shaft and the launch lock yoke (Figure-8). Each sensor consists of an LED and phototransistor pair secured by uralane in aluminum housings. Half of the aperture of the phototransistor is obscured by an aluminum structure. When the blocking tab crosses the aluminum edge, no light impinges on the detector. A relatively sharp transition occurs. Resolution is measured to be << 3 microns. This design utilizes the stability of the aluminum edge and a threshold circuit to determine the transition point. The OLS's are insensitive to relative motion between the LED and the phototransistor and to changes in their optoelectronic behavior after exposure to radiation.

Compensation Coil Assembly The compensation coil assembly (Figure-4) when energized counteracts the residual dynamic stray magnetic field of the scan mechanism. It consists of 25 turns of 26 gage lead wire. The coil polarity is such that as the drive current increases, the magnetic field of the compensation coil increases with an opposing field.

MECHANISM TESTING The engineering model scan mechanism has been extensively tested at the component, SM/RI subsystem, and OA levels to ensure compliance with requirements. Component level testing includes verification of mechanism parameters and performance. The axial spring and actuator constants, tilt, shear, and sensor outputs are some of the parameters which are measured at both ambient and 170K. Stray magnetic field and launch vibration testing occurs at this level. The SM and RI are also tested as a subsystem prior to integration into the OA. A dewar with optical quality windows was designed for both component and sub-system testing. Jitter sensitivity

testing is performed at the SM/RI subsystem level. System-level performance and environmental testing is also conducted during OA level testing.

PROBLEMS/SOLUTIONS

How should a mechanism be designed so that it can be repeatably assembled and disassembled and yield consistent performance characteristics? How can some of the inherent non-linearities of this type of mechanism be overcome? How could a linear actuator with permanent magnets be designed to radiate extremely low stray magnetic fields? These are just a few of the questions which required answers during the development of the CIRS scan mechanism. A description of these problems and how they were solved is now provided.

ASSEMBLY PROCESS

Since the flexible structure overconstrains the main shaft, it is important that care be taken to equalize the length of each spring to ensure that a snap through buckling behavior of the springs does not occur. Excessive buckling will cause increased non-linearity about the mechanism neutral position. The length of the main shaft and the three outriggers are critical to the tilt and snap performance of the mechanism as the main shaft is displaced from mechanism neutral. Spacers have been designed into the mechanism at both ends of the three outriggers and the main shaft to allow tuning of mechanism tilt and elimination of any snap through buckling behavior. The spring pair assembly procedure, careful measurement of all critical component dimensions, and lapping the adjustment spacers, the main housing, and outrigger interface surfaces ensure that the final assembly of the mechanism meets performance requirements. Measurements of current versus displacement and tilt versus displacement are made during the assembly process. Tilt sensitivity about the Y and Z axes versus displacement is shown in Figure-11. To illustrate the tilt sensitivity, a 200 gram unbalanced load was applied to the shaft during the measurement. Maximum tilt values of 2 to 3 arcseconds throughout the entire scan are readily achievable when the masses attached to each end of the main shaft are approximately equal. The actual masses of the optical elements are within 40 grams of each other. Acceptable tilt performance is a good figure of merit that the mechanism is assembled properly.

NONLINEAR CHARACTERISTICS

Although some aspects of scan mechanism performance indicated superior linearity in the axial direction, non-linear behavior related to translation of the main shaft in the axial direction is observed. Two major non-linearities inherent in the design which directly effect conformance to mechanism performance requirements are the changing radial stiffness and a shifting outrigger resonance.

RADIAL STIFFNESS VERSUS DISPLACEMENT The transverse stiffness of the flexible structure decreases as the main shaft is displaced from the neutral position of the mechanism. The structure is stiffest when all the springs are parallel to each other. The mechanism is said to shear under the influence of gravity. Shear of the main shaft under the influence of gravity as a function of displacement and increased loading of the main shaft is shown in Figure-12. Shear in the lateral direction to gravity does not deviate by more than 2 microns. The linear analysis conducted to design the original

323

developmental unit failed to accurately predict shear. After initial testing revealed unexceptable shear performance, an extensive mechanism parametric analysis was conducted. The major parameters involved were moving mass, power dissipation, mechanism volume, outrigger damping, radial and axial stiffness, and fatigue stress. The development unit was modified and the performance of the new spring design was verified. Early "breadboarding" of designs even when some heritage of a particular design exists is critical to successful delivery of a mechanism.

SHIFTING OUTRIGGER RESONANCE Another non-linearity inherent in a design of this type is that as radial stiffness decreases, the fundamental resonant frequency of the outriggers increases as a function of the displacement of the main shaft. The mechanism has a shifting resonance. Indicated in Figure-13 is the frequency response of the mechanism with increasing offsets of the main shaft from the neutral point. The outrigger resonance shifts from ~ 25 Hz at the neutral point to ~ 90 Hz near the end of travel. This is highly undesirable from a mechanism control point of view. The response of the mechanism to external disturbances is highly dependent on the resonant frequency of the outrigger. External vibrations are amplified and mechanism velocity variation performance can suffer when the frequency content of the external disturbances coincide with the resonance of the outriggers. As in previous mechanisms of this type, outrigger dampers were designed to reduce the effect of outrigger resonances and enhance control of the mechanism. The subject of jitter sensitivity continues to be a concern. The control of the mechanism operating in a "quiet" environment as achieved velocity variation of less than 0.5%. The transmissibility and quantification of disturbances through the spacecraft and instrument structures has been the subject of extensive analysis and testing. In addition to the subsystem SM/RI jitter testing, spacecraft level testing is scheduled.

ACTUATOR DEVELOPMENT
From the beginning of this project, there has always been a great deal of concern about meeting stringent magnetic field requirements without compromising performance. It was decided to first consult with commercial vendors of linear actuators to gain expertise to select the most promising configuration. Otherwise, all work was done in-house. Software was written to perform parametric studies so as to optimize all the actuator parameters. Magnetic field modeling was performed to predict performance and stray magnetic fields and to explore various approaches to minimizing stray fields. A major emphasis was placed on designing the actuator to have minimal stray magnetic field.

CONFIGURATION A study was performed by Northern Magnetics[5] to determine the optimal configuration for the actuator. A number of configurations were studied. A moving magnet type design was selected so that the heat generated by the winding could be easily sinked without the necessity for flexing thermal straps or power leads. A voice coil type design (no soft magnetic material associated with the coil) was selected to prevent radial actuator attractions. The selected configuration was expected to radiate minimal stray magnetic fields because the air-gap is nearly fully enclosed and the path for magnetic flux generated by the winding sees the high reluctance of the magnets, thus preventing excessive flux densities. Also, having the magnet material located away from the air-gap allows the flux to distribute very uniformly across the air-

gap (Figure-14) enhancing force constant linearity throughout the actuator displacement. The outrigger damper which has a radial magnet supplying magnetic flux directly across the air gap does not distribute flux as uniformly (Figure-14). This configuration is simple and adequate for the purpose of damping. However, if the actuator was designed to have a flux distribution like that of the damper, linearity would be degraded.

OPTIMIZATION An Excel spreadsheet program was written such that dimensional and material property parameters, force constant, and the force environment could be inputted. The output parameters are actuator constant, power, turns, wire size, resistance, current, force margin, damping, mass, etc. Using the Solver, an input value could be found to satisfy a desired output value. The program was used to examine the relationship between mass and power and look at other tradeoffs so as to best meet the requirements.

MAGNETIC FIELD MODEL A 2-D radially symmetric Boundary Element Model (BEM) was created using MAGNETO. With this model, better values for flux densities and actuator performance can be predicted. The BEM model can solve the flux distributions taking into account non-linear characteristics of the materials. Flux levels were of interest in the air gap (Figure-14) to predict force constant linearity and damping levels, in the soft magnetic material to minimize saturation which results in magnetic field leakage, in the magnets to see if operation was near the maximum energy product (BH) for minimum magnet volume. The BEM model was also used predict the magnetic field at 1 meter, but with questionable confidence due to the fact that those values are on the order of 10^8 smaller than the flux in the gap (Predicted values: 1.2 nT unpowered, 4.4 nT powered).

MAGNETIC FIELD IMPROVEMENT Magnetic field mapping was performed at the Spacecraft Magnetic Test Facility at GSFC using fluxgate magnetometers with the Earth's field canceled. The field shape resembles that of a dipole. A static (0 Hz, unpowered) level of 7 nanotesla (static spec: 2.5 nT @ 1 m for mechanism, 5 nT for instrument) was measured at 1 meter along the scan axis. However, powering so as to cause a full displacement results in a change in field of 23 nanotesla peak to peak (dynamic spec 10 nT p-p <10 Hz @ 1 m). The specifications were re-evaluated and it was determined that it would be beneficial reduce the level of dynamic magnetic field because of its effect on the Vector-Helium magnetometer on the spacecraft. A coil with 18 turns around the entire mechanism was connected in series with the actuator winding. Measurements showed that the dynamic magnetic field was reduced to 4 nT p-p. Due to dimensional constraints, the implemented compensation coil is smaller in diameter requiring more turns and is located asymmetrically.

CONCLUSION

The CIRS scan mechanism has achieved high precision linear motion for greater scan displacements than previously accomplished, necessary for high resolution infrared spectrometry. A uniquely designed moving magnet actuator with an integral coaxially located displacement sensor is incorporated into the scan mechanism. This actuator has high linearity, allows for temperature stability of the optical elements, and exhibits extremely low levels of stray magnetic fields. The actuator, dampers, and spring characteristics have been optimized and tailored to allow for superior controller performance so as to scan at very low velocities with minimal velocity variation. The CIRS scan mechanism is the result of extensive mechanical, optical, electromagnetic, and control system analysis and testing, consultation with fabrication and material experts, and the dedication of numerous hard working individuals.

ACKNOWLEDGMENTS

REFERENCES

1. P. Maymon, M. Dittman, B. Pasquale, D. Jennings, K. Mehalick, C. Trout, "Optical Design of the Composite Infrared Spectrometer (CIRS) for the Cassini Mission." SPIE Vol 1945, (1993), Pg 100-110.
2. A. Tyler, "Shutter Mechanism for Calibration of the Cryogenic Diffused Infrared Background Experiment (DIRBE) Instrument." 20th Aerospace Mechanisms Symposium, (1986), Pg 97-102.
3. NASA/JPL, "Cassini Orbiter Functional Requirements Book Environmental Design Requirements." Rev A, CAS-3-240 (Insert to 699-205 Cassini Orbiter Functional Requirement Book), (11 February 1994).
4. NASA/GSFC, "Cassisni/Composite Infrared Spectrometer Performance Requirements Document." CIRS-704-001 Rev B, (21 November 1994).
5. W. Hinds, M. Wilson, "Optimum Non-commutated DC Linear Motor." Northern Magnetics Technical Report N-101, (7 February 1992).
6. Munch et al., "Inductive Coupling Position Sensor Method And Apparatus Having Primary and Secondary Windings Parallel To Each Other." 5,036,275, (1991).
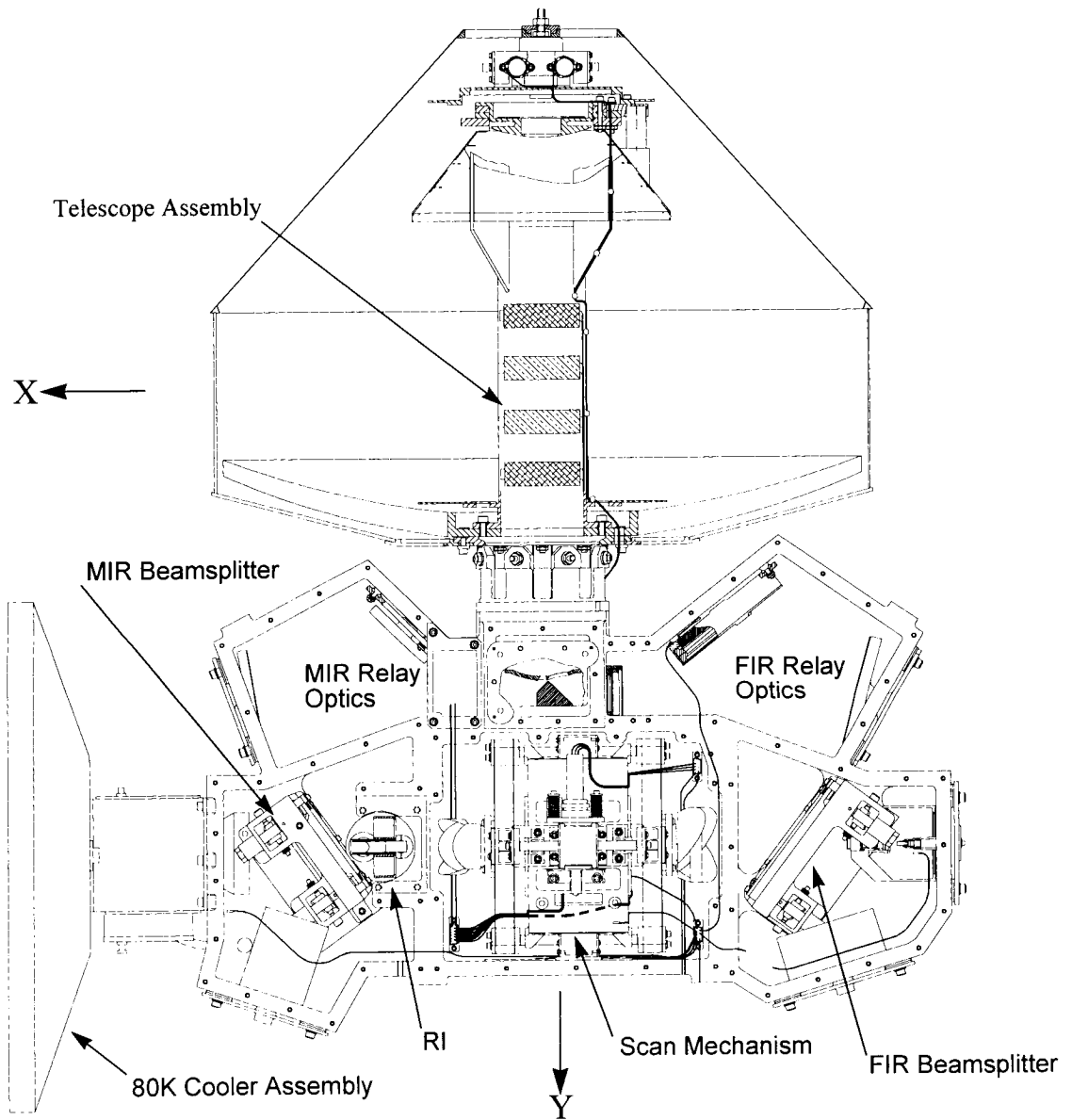
Figure-1 CIRS Optical Assembly
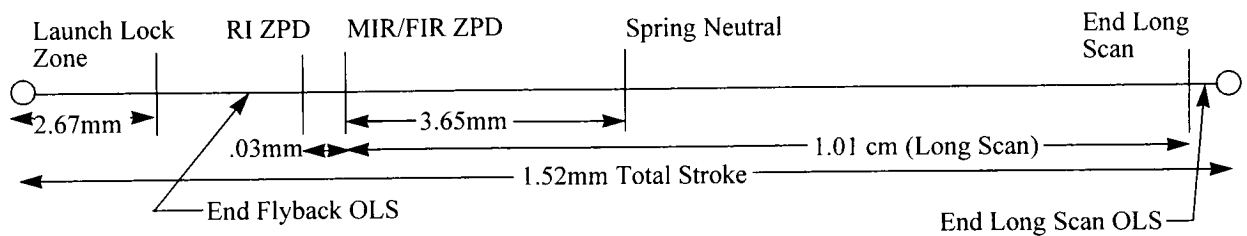
Zero Path Difference (ZPD)

Figure-2 Scan Mechanism Displacement

327
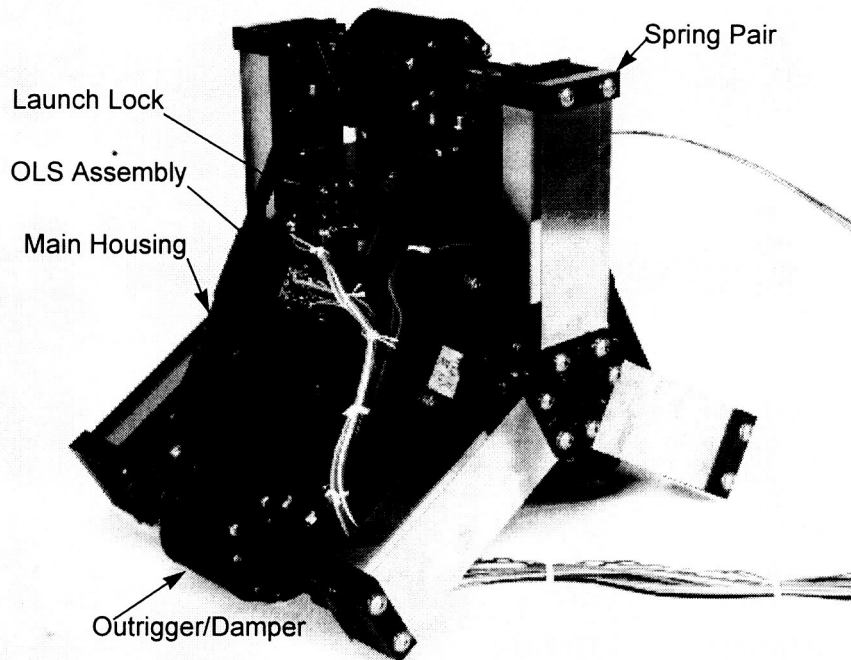
Figure-3 Engineering Model Scan Mechanism
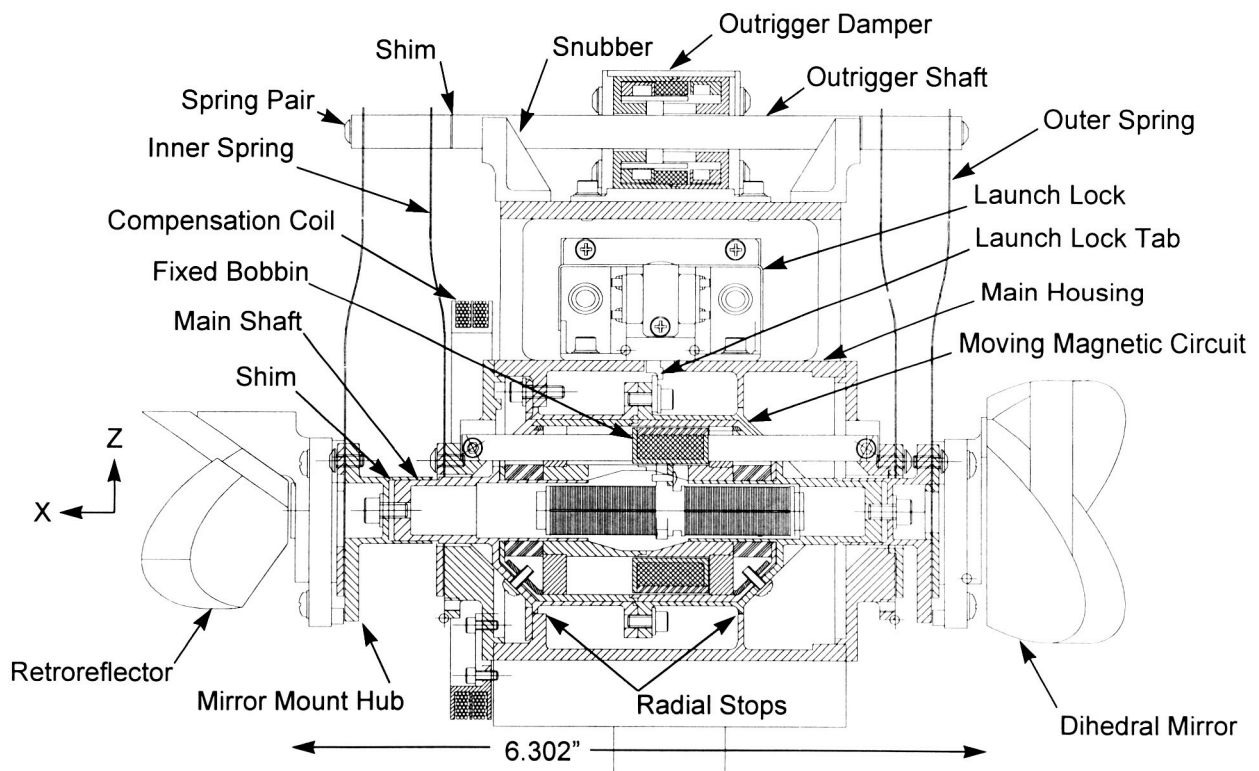
Figure-4 Scan Mechanism In Locked Configuration
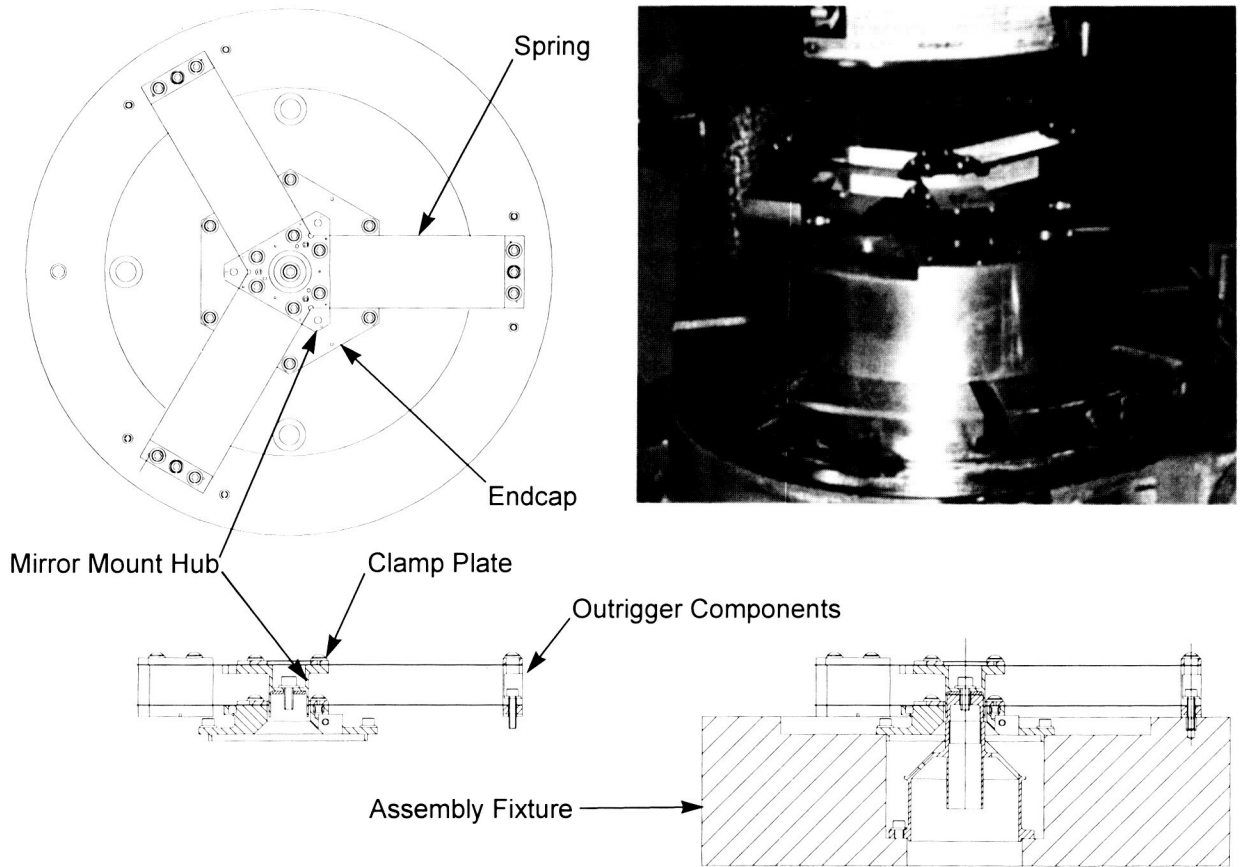
Figure-5 Spring Pair Assembly
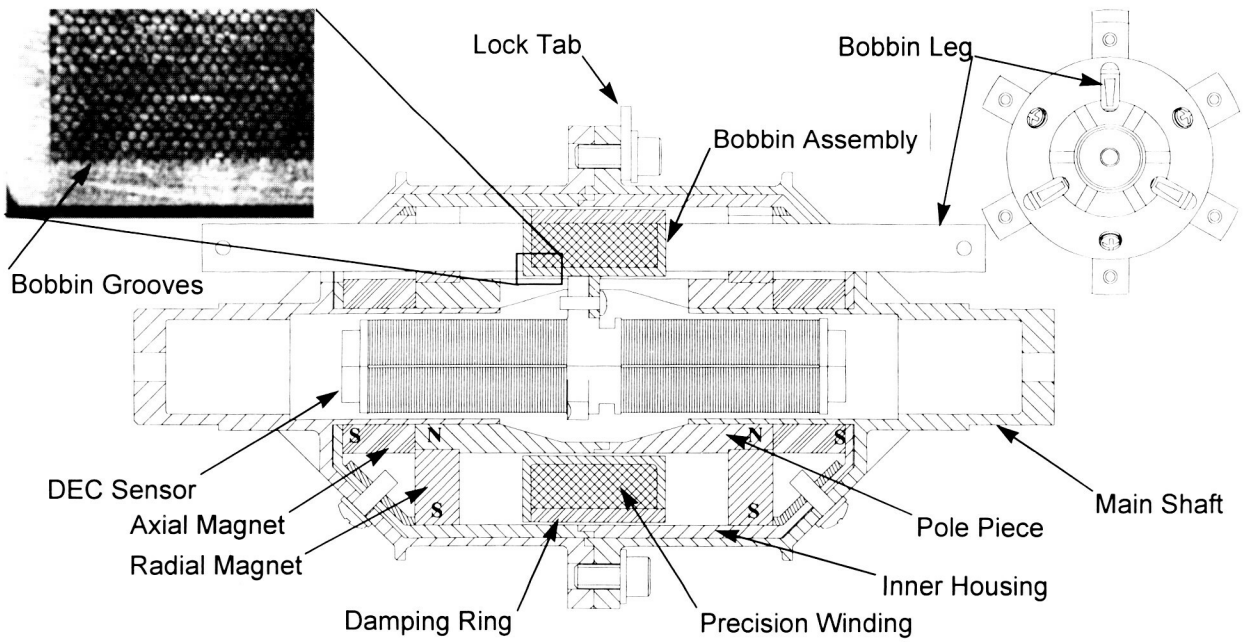
Figure-6 Actuator Assembly
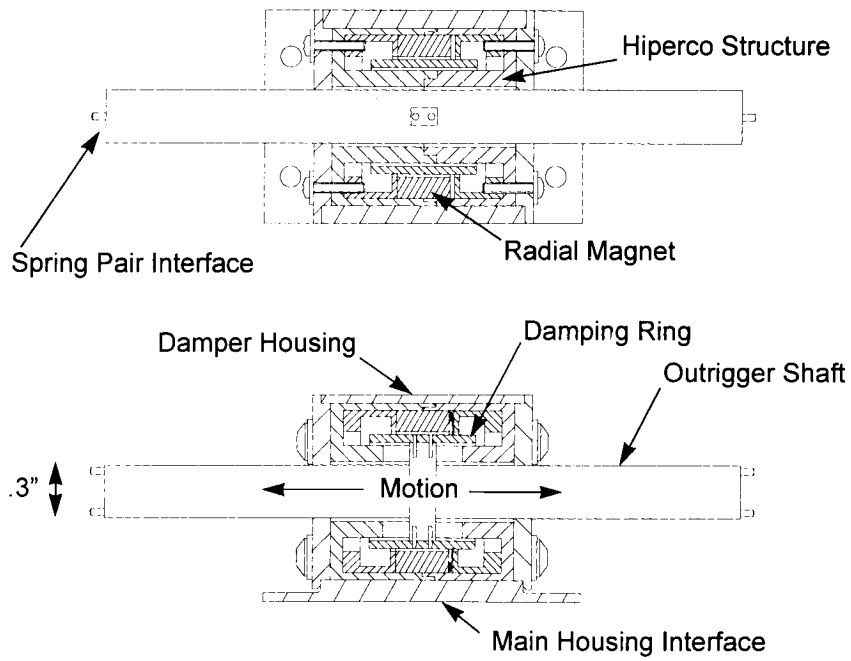
Figure-7 Outrigger/Damper Assembly

Launch Lock

Optical Limit Sensor
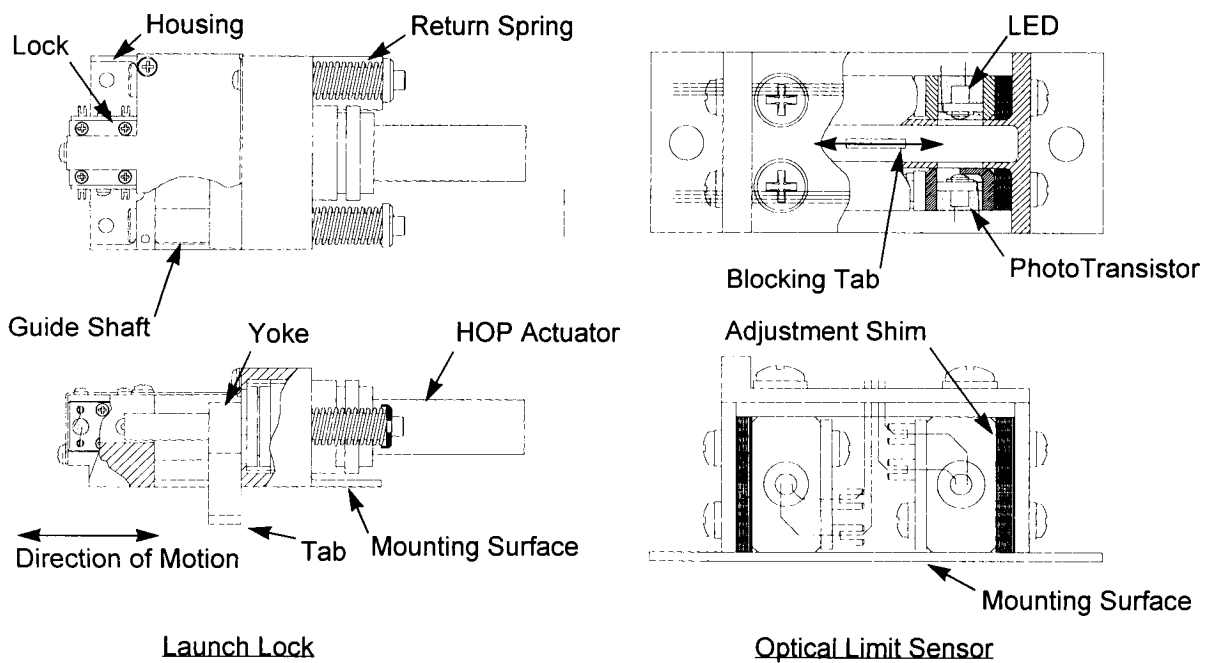
Figure-8 Launch Lock and Optical Limit Sensor Assemblies
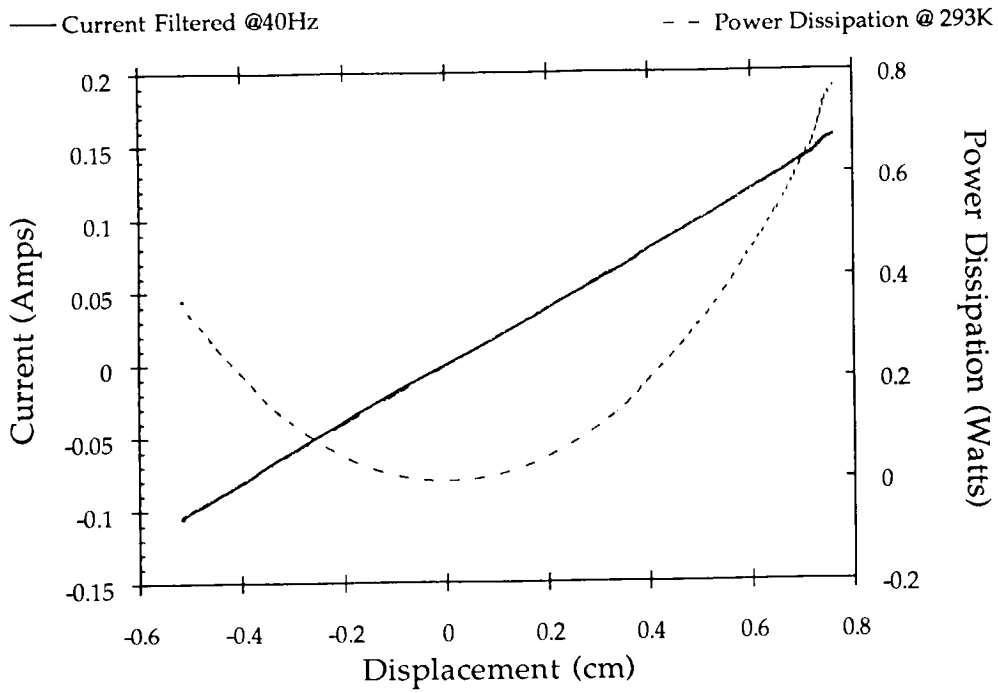
Figure-9 Current and Power versus Displacement

Displacement Range: ±7.5 mm
Nonlinearity: ±3%
Resolution: <1%
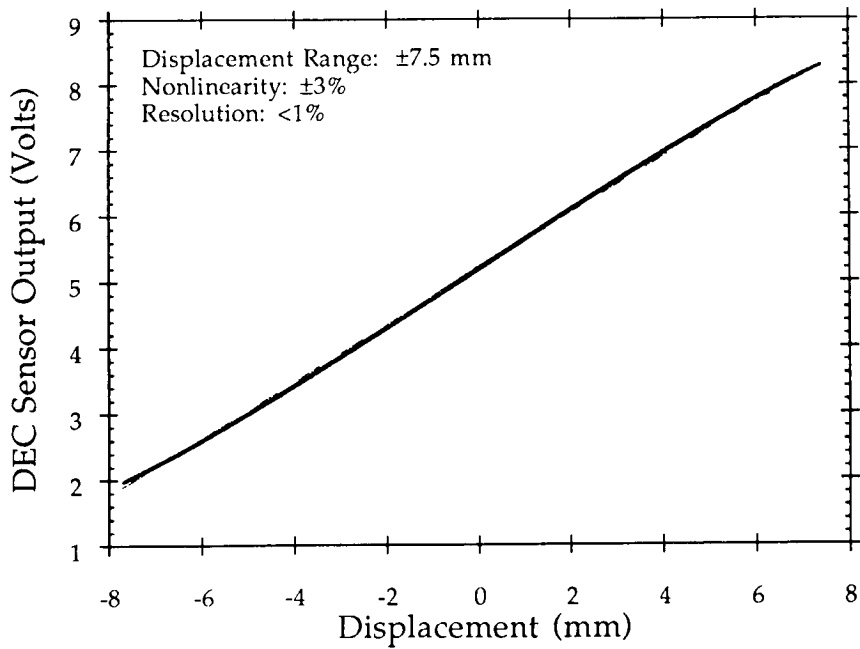
Figure-10 DEC Sensor Output versus Displacement

331

200 Gram Unbalanced Load
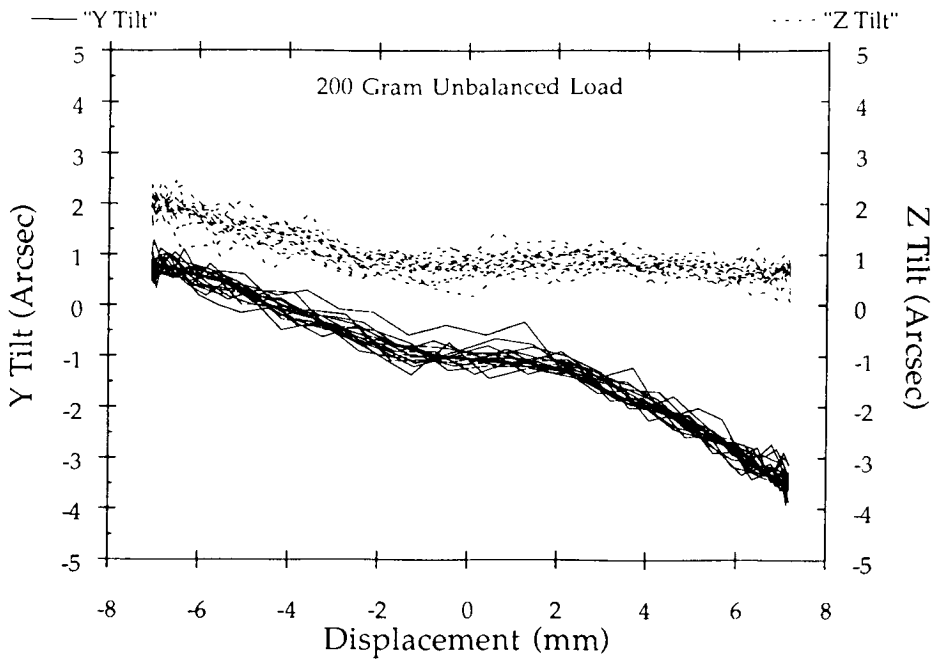
Figure-11 Y and Z Tilt versus Displacement

Z Shear Includes Sensor Gap
Actual Shear is Difference Between Values @
7 mm and 0 mm displacement (Larger gap
indicates shaft motion in gravity direction)

400 Grams

200 Grams

100 Grams
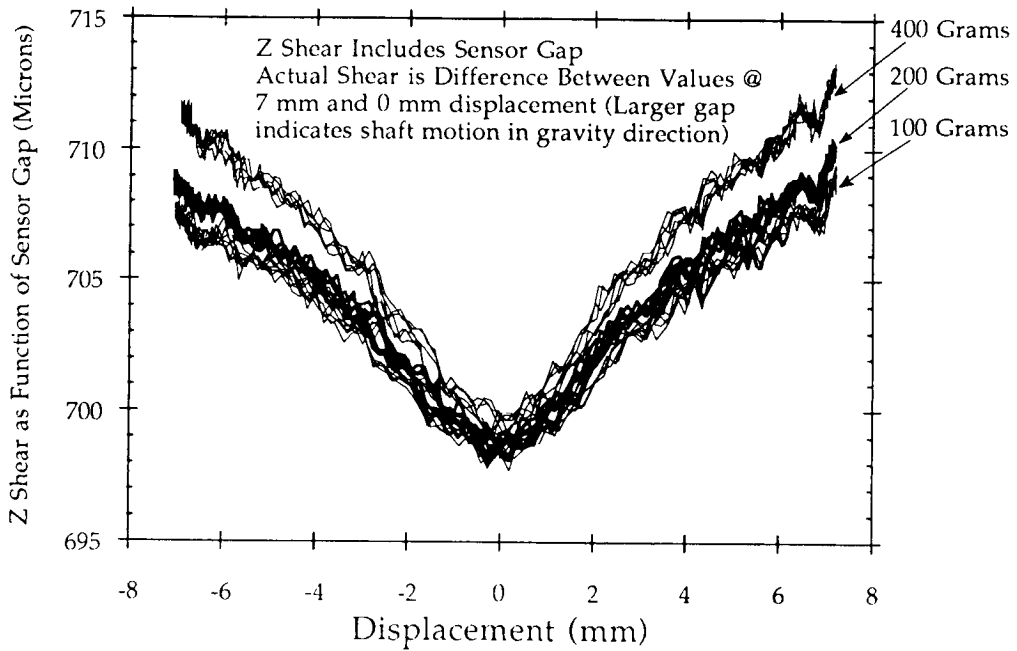
Figure-12 Shear Due To Gravity versus Displacement
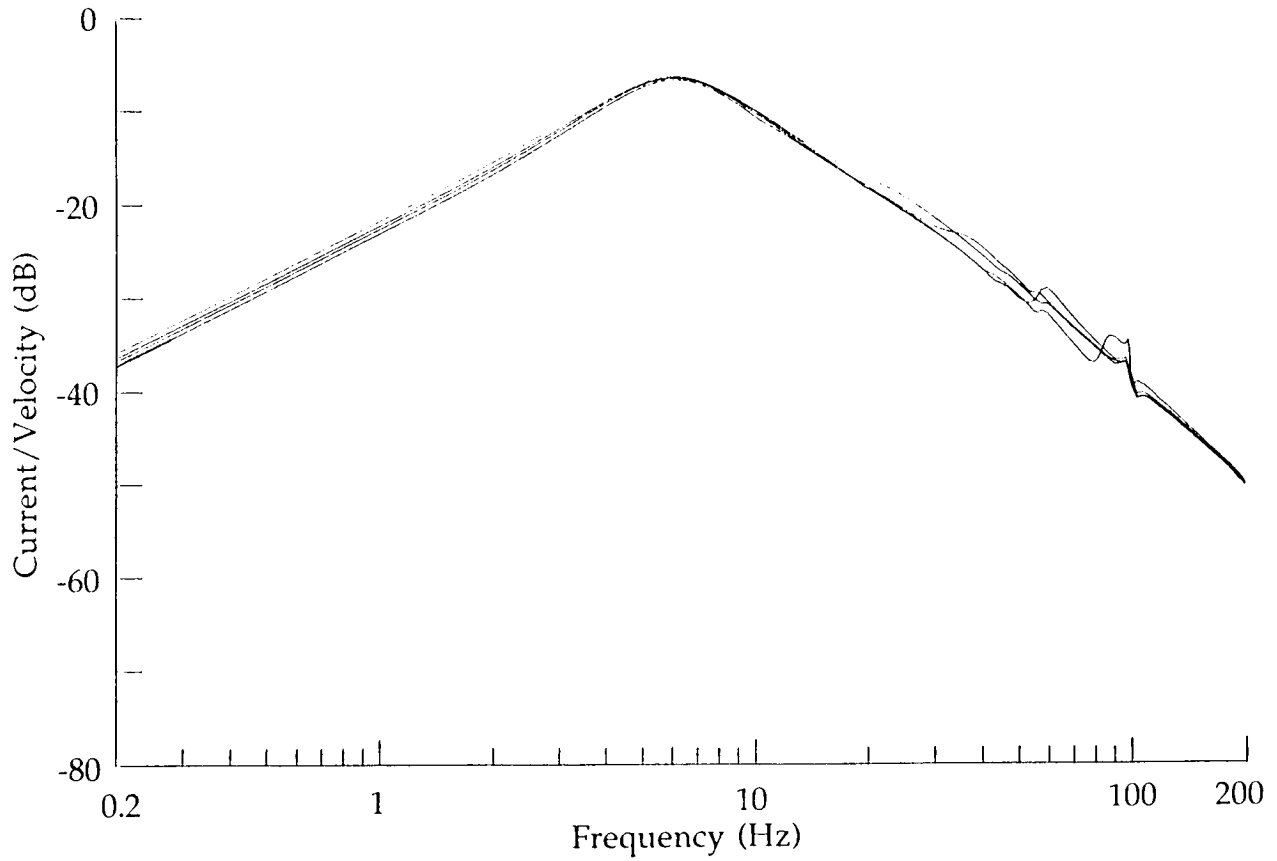
Figure-13 Mechanism Frequency Response
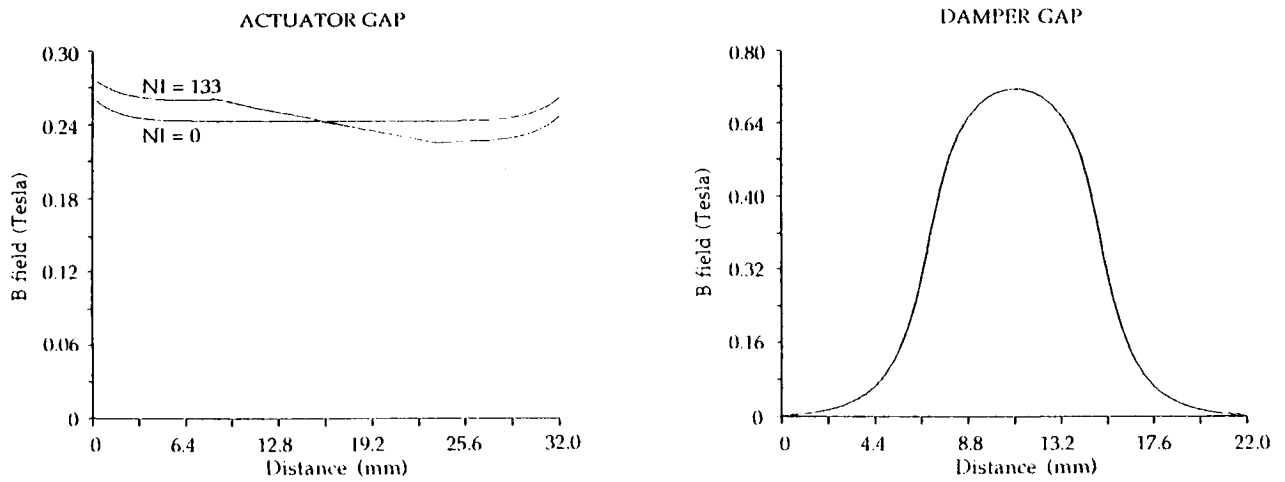
Figure-14 Magnetic Flux Models

High-Performance Reactionless Scan Mechanism

Ellen I. Williams*, Richard T. Summers* and Miroslaw A. Ostaszewski**

Abstract

A high-performance reactionless scan mirror mechanism was developed for space applications to provide thermal images of the Earth. The design incorporates a unique mechanical means of providing reactionless operation that also minimizes weight, mechanical resonance operation to minimize power, combined use of a single optical encoder to sense coarse and fine angular position, and a new kinematic mount of the mirror. A flex pivot hardware failure and current project status are discussed.

1.0   Introduction

The reactionless scanning mechanism replaces the earlier mechanisms designed to map thermal radiation from the Earth with the goal of weighing less and having higher performance. Built by Ball Corporation, Aerospace Systems Division, the new scanner system consists of the scanning mechanism and the servo drive electronics (Figure 1).

2.0   Mechanical Description

2.1 General Description.   The reactionless scanning mechanism is comprised of two legs, the Encoder Side Assembly (ESA) and the Flex Lead Side Assembly (FLSA), that support a yoke assembly mounted on bearings for coarse angular travel. Coarse angular travel is accomplished using a stepper motor. The mirror/mirror carrier (MMC) and reaction mass (RM) assemblies are within the yoke assembly. The MMC and RM assemblies are mounted on flexures to allow for fine angular travel over the scanning angle range. Scanning motion is accomplished using linear actuators mounted between the RM and the yoke assemblies. RM motion is transferred to the MMC through drive flexures that tie the two assemblies together. These drive flexures allow for out-of-phase motion of the two masses, which effectively cancels any generated forces and torques. During scanning, a brake is used to secure the yoke assembly. Angular position information for both the coarse and fine travel is obtained from an optical encoder referenced to one of the support legs (Figure 2).

The scanning mechanism is servo controlled by the control electronics that are mounted separately in an electronics box. The control electronics house the power supply, optical encoder processing electronics, servo electronics, and command and telemetry interface electronics. The control electronics operate from a 28 Vdc power bus.

2.2   Reactionless Scanner.   The scanning assembly is contained within a yoke assembly. It consists of the mirror, the kinematic mounts for the mirror, the mirror

---

* Ball Corporation, Aerospace Systems Division, Boulder, CO
** former employee of Ball Corporation, Aerospace Systems Division
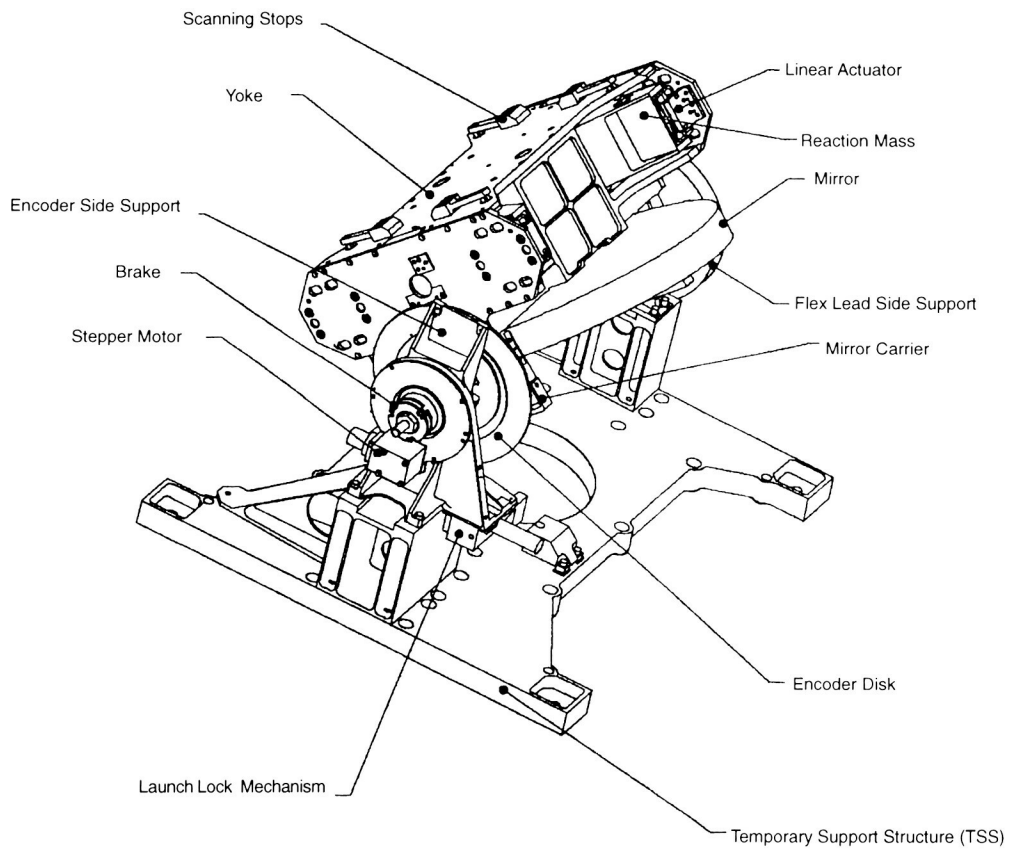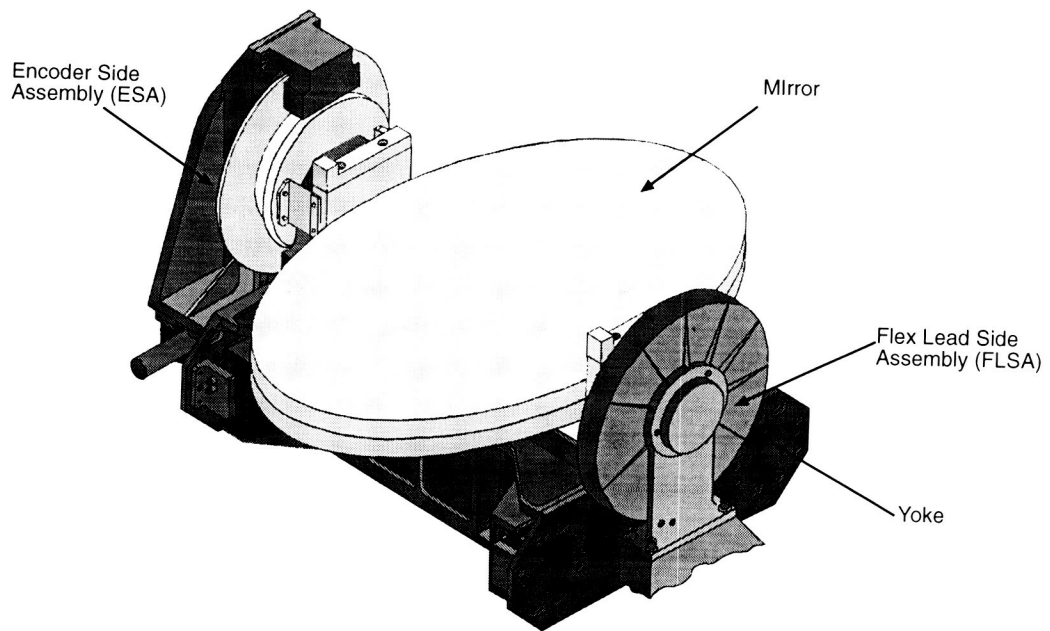
Figure 1. Reactionless scanner assembly, front and back views
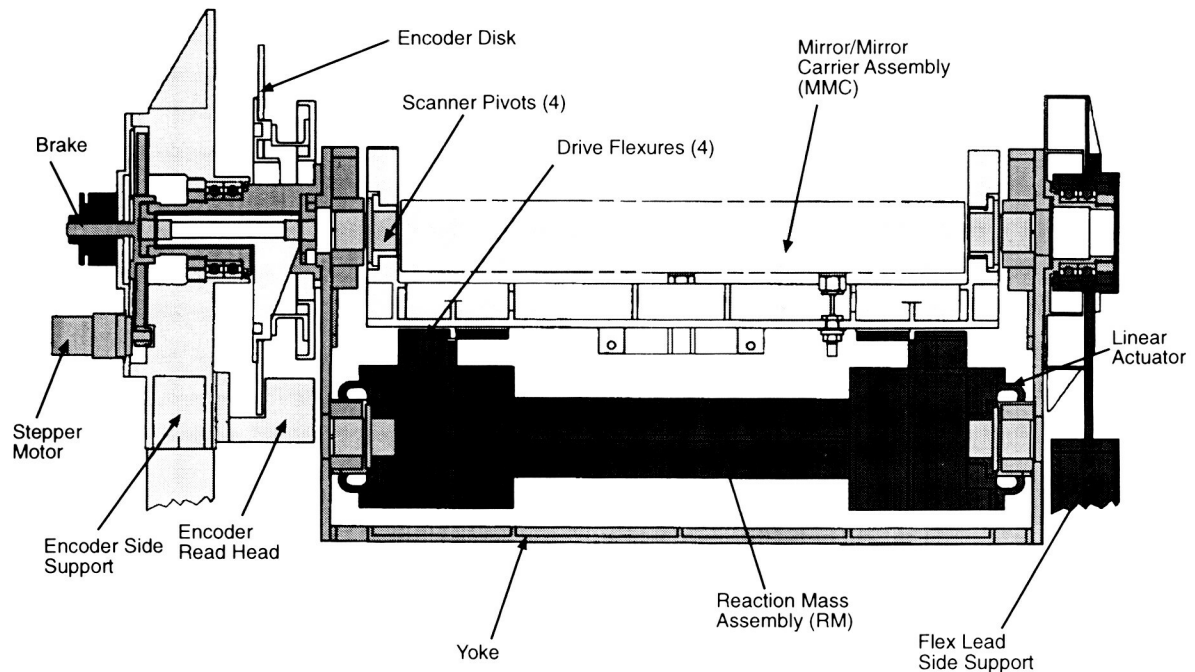
Figure 2. Reactionless scanner section

carrier, the reaction mass, the drive flexures, and the linear actuators (Figure 3).

<u>The Mirror.</u> The scanner system must be able to accommodate a 277.9 x 441.7 mm elliptical flat mirror with an aperture of $\geq$ 267.18 x 433.1 mm. The system aligns the pivot axis 15 mm behind the mirror surface and parallel to the minor axis of the ellipse within 0.05 mm. The mirror flatness must be maintained within 0.4 µm peak to valley and have a slope angle of less than 0.65 arc second over a broad range of thermal influences while subjected to high scanning torques. The surface roughness must be less than 0.005 μm_{RMS}.

The mirror has two halves, 17.53 mm thick each, of I-70 beryllium that are pocketed out to have a ribbed light-weighted structure. The two halves are brazed together, mounted on the back with kinematic mounts, and polished and coated for final performance. The coating of the mirror is a vacuum deposited gold with a specialized overcoat.

<u>The Mirror Carrier.</u> The MC is made from structural grade beryllium, S-200F, that provides the three-point kinematic mount for the mirror, the mounting for the driving flexures, and the pivot flexures for the scanning motion.

The kinematic mounts have two flexing elements account for the thermal growth differences of the structures. Figure 4 depicts the kinematic mounts. The Y-Flexure mount accommodates differential growth in the direction of the major axis of the mirror. The XY Stabilizer Post accommodates change in the minor and major axis plane of the mirror. The Post Mount is a stiff mount that does not flex. At two locations, the Y-

336
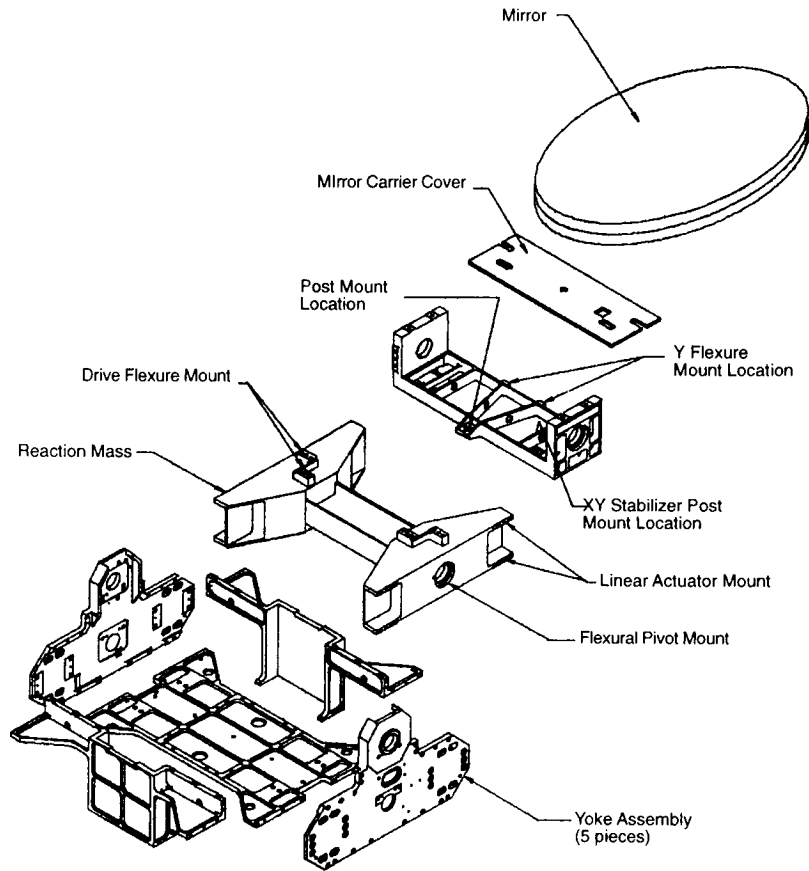
Figure 3. Reactionless Scanner
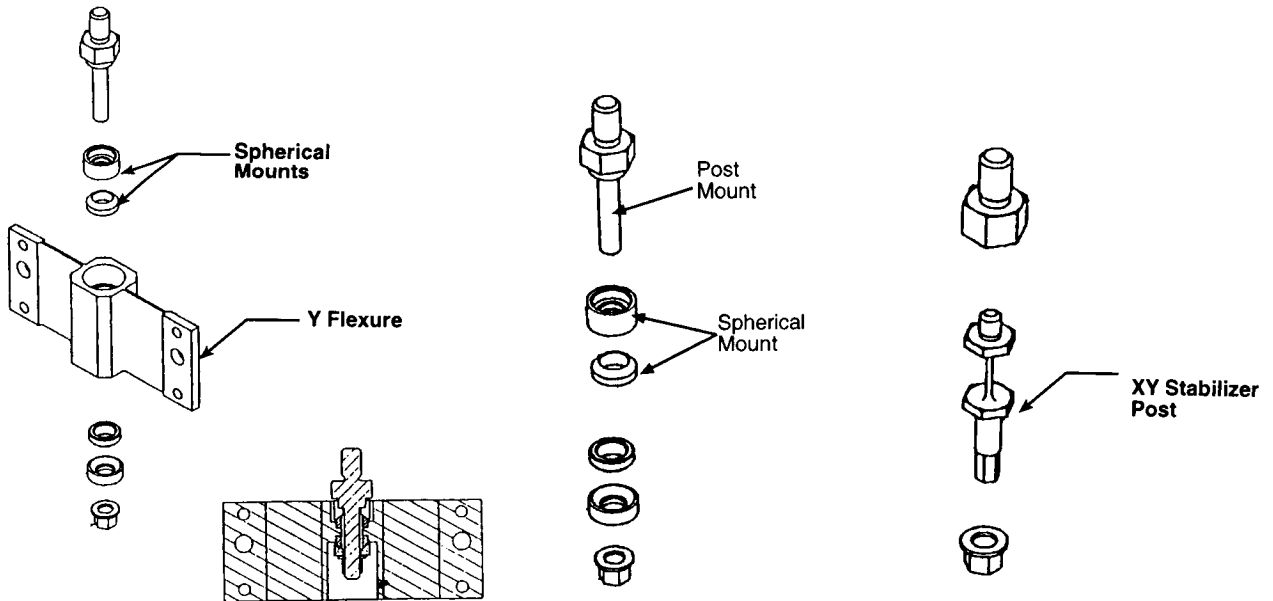
Figure 4. Kinematic Mirror Mounts

Flexure and the Post Mount, a spherical mount is included that accommodates alignment motion during assembly and is then torqued to levels that do not allow the spherical mount to move.

The Reaction Mass. During the scanning operation the RM moves in opposite angular motion to counteract the forces generated due to the MMC action. It also provides the mount for the linear actuators, the driving flexures, and an independent pivot axis (from the mirror scanning axis). Thermal effects from the actuator coils are also kept at a maximum distance from the mirror.

The RM structure consists of an I-beam crossbar that has two symmetrical members brazed to the ends. All the members of the RM are made from structural grade beryllium, S-200F. The I-beam is designed torsionally flexible. The two end members are stiff and place the linear actuators at a location that uses the linear actuator weight as an inertia match for the MMC thereby minimizing weight of the system.

The Drive Flexures. The MC and the RM are connected through a set of four drive flexures that behave as a set of frictionless gears. The drive flexures cause the two assemblies to rotate out of phase without backlash, hysteresis, rubbing or sliding elements, and associated reliability and contamination concerns. This design requires no lubrication.

All four drive flexures are identical and mounted in pairs with one in an 180 deg opposite orientation as shown in Figure 5. The flexure is an assembly of a titanium flexing blade with four mounting blocks. It is designed for 1.75 deg maximum deformation at each end and is designed for infinite fatigue life.

The Linear Actuators. The actuators consist of four efficient magnet/core structures mounted directly to the RM on equal moment arms. They are designed to input torque moments into the system with limited residual forces. The actuators are part of the RM and are closely integrated with the design of the RM itself. The stiffness, power, and weight requirements required optimization of physical size, weight, mounting radius, and motor constant to achieve the requirements. In addition, high reliability is an
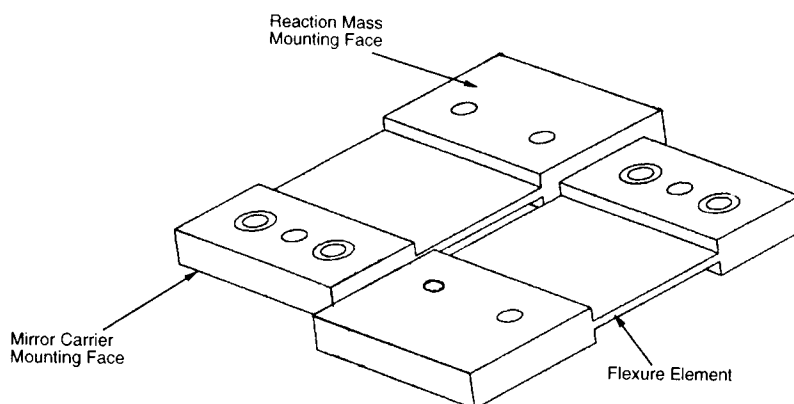
Figure 5. Drive Flexures

important design driver. The motor coils are mounted to the yoke so there is no direct conduction heat path to the mirror, and there are no moving leads. The reaction mass itself provides a shield against motor thermal radiation to the mirror's back surface.

The Flex Pivots. The MC and the RM are individually supported by flex pivots. The pivots must be designed to support all the loads developed during launch. These loads are considerable and are a major design driver. Each assembly has two flex pivots that create a pivot axis for the RM and a pivot axis for the MC. Flex pivots are a system of cross-bladed flexing elements that provide frictionless, lubrication free, and low hysteresis bearing with high radial and axial stiffness. The torsional stiffness was designed to optimize the power requirements.

The flex pivots are commercially made but have been available since the mid-1960's [1]. The standard commercial assembly, shown in Figure 6, consists of an outer cylindrical housing, an inner cylindrical housing, and three flex blades. During assembly, the blades are electron beam welded into the inner housing and the inner housing is electron beam welded into the outer housing. The outer housing is slotted to have a diametrical gap separating two outer cylinders. These two cylinders are then able to rotate relative to each other in opposite directions. The flex pivots that were produced for this project were customized for mounting interface, torsional spring rate, concentricity, radial stiffness, infinite life, and load carrying capability. The resulting pivot design incorporated a flange mount, a stiffer housing, and four blades oriented at 60 deg instead of 90 deg. The blade material was changed from the standard 420 SS to 422 SS to improve fatigue life.

Flexing Elements (3)
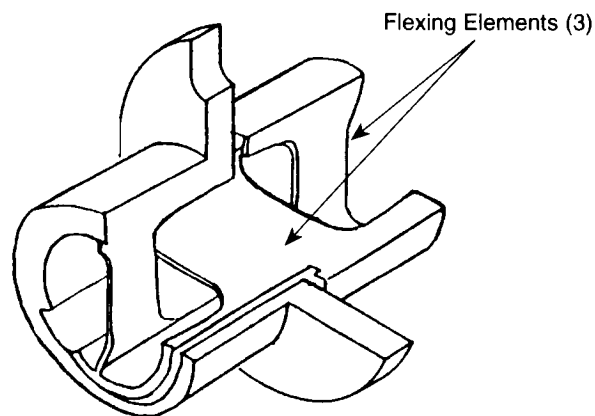
Figure 6. Flexural Pivots

The Yoke Assembly. The yoke assembly is a five-sided structure that contains the RM and MMC assemblies. The outer ends of the flex pivots that support the RM and the MC are mounted on the yoke assembly. The linear actuator coils are also mounted to the yoke assembly, thereby providing a heat path away from the mirror and also eliminating the need for electrical flex leads or bushings for the scanning operation.

339

The five panels for the yoke assembly are made of structural grade beryllium, S-200F. After initial assembly the final critical surfaces are machined including the bores for the flex pivots, 4 places, and the mounting surfaces and bosses for the support shafts.

2.3   Flex Lead Side Assembly.   The FLSA provides support for one half of the yoke assembly, contains the coarse angular travel bearings, houses the flex leads, and is axially compliant to compensate for material thermal differential between the satellite bulkhead and the scanner mechanism (Figure 7).
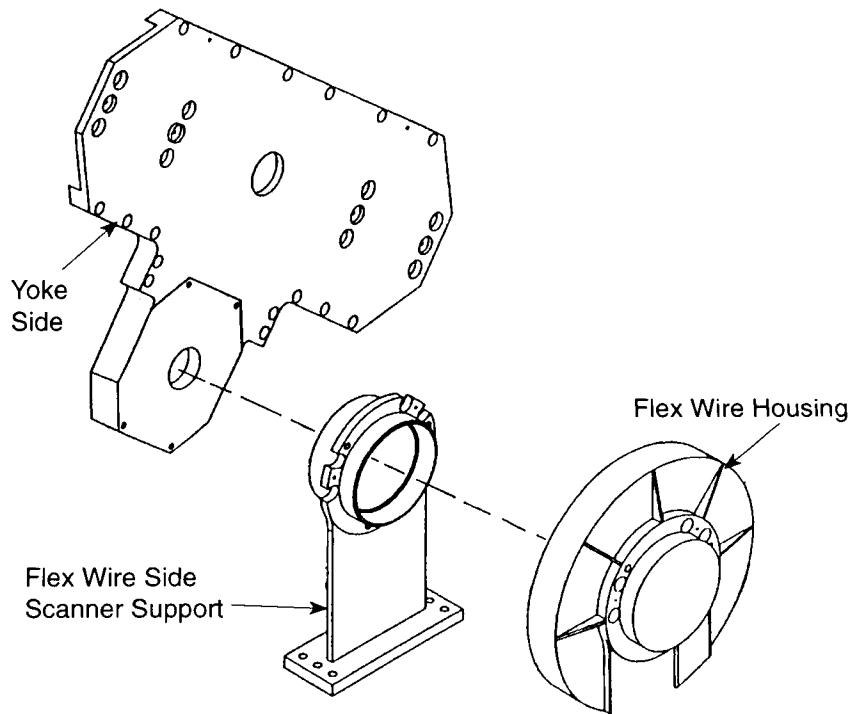
Figure 7. Flex Lead Side Support

There are four twisted shielded pairs (one for each linear actuator) and four thermistor wires that are routed from the yoke assembly to the FLSA. The flex lead housing provides 240 deg freedom of rotation for the flex lead ribbons.

2.4   Encoder Side Assembly.   The ESA is the main support for half of the yoke assembly, the coarse angular travel bearings, the drive gear and stepper motor for coarse angular travel, the brake, the encoder disk and spindle, the encoder read head, and the launch lock mechanism (Figure 8).

The Drive Gear and Stepper Motor.   The drive gear and the stepper motor drive the yoke assembly through 235 deg for coarse angular travel. The drive gear, made from titanium, has a slot integrated with a pin stop in the support to provide a known location stop at either ends of travel for the electronics servo control. The stepper motor is an Astro Instruments Corporation motor and provides system angular travel at a rate of 0.068 rad/s and requires less than 5 W.

340
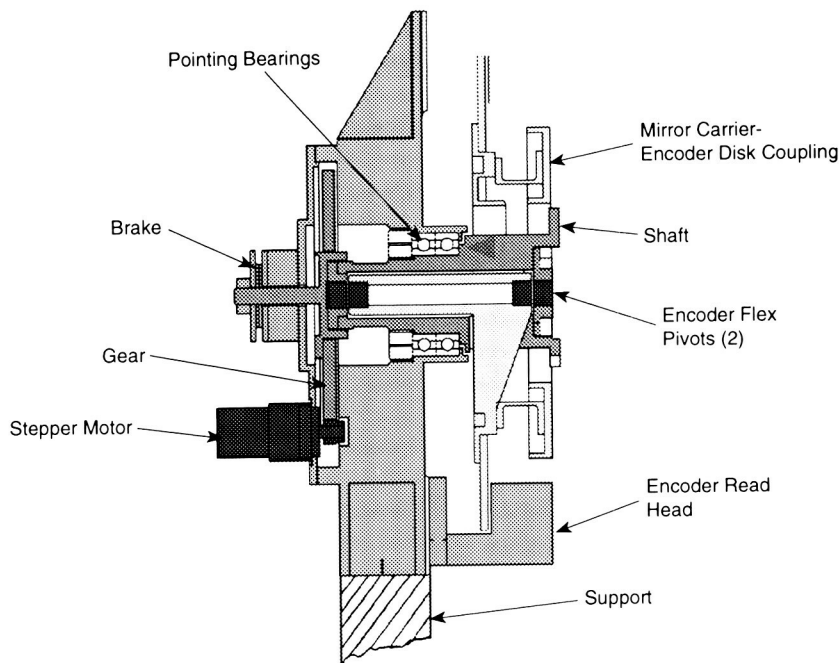
Figure 8. Encoder Side Assembly

<u>The Brake.</u> The brake is designed to hold the yoke assembly in zero gravity once the yoke is in position. It does not stop the yoke assembly during pointing operation (this is controlled by the stepper motor positioning). Due to low out-gassing, material control, low power requirements, and other aerospace design requirements, Ball is designing a brake for the system.

<u>The Encoder Disk, Spindle, and Read Head.</u> The mirror must be positioned during fast scan operation and also coarse pointed for calibration and launch lock. The mirror position must be known throughout the entire range of motion with a specified precision. The encoder is a 1.36 μrad per step encoder with the disk, read head, and electronic control board procured from Aerospace Controls Corporation and then mounted and calibrated on Ball parts. The disk is mounted on a spindle that is supported by flex pivots similar to but smaller than the flex pivots used for the MC and RM. The spindle is interconnected to the MC through an inverted box flexure coupling. The coupling allows transmission of MMC torsional motion, but isolates the encoder disk from translational motion. The read head is mounted directly to the support.

<u>The Launch Lock Mechanism.</u> The scanner mechanism is unbalanced and would rotate freely during launch, possibly damaging scanner components. The launch lock, designed by Starsys Research, consists of a paraffin actuator pin-puller that restrains the scanner rotationally during launch. A line-to-line contact is established between the launch lock pin and a feature on the yoke. The pin restrains the yoke in one direction while a feature on the launch lock body restrains it in the other direction. A small gap is allowed to prevent jamming during actuation.

In addition to the launch lock mechanism, snubbers are mounted to the yoke that prevent excessive structural deflection during launch along the rotation axis, which could damage the encoder. The high accuracy requirement for the encoder necessitate close mechanical tolerances between the read heads and encoder disk.

2.5 Reactionless Concept. Figure 9 shows the section view of the scanner and the components that make up the reactionless scanner mechanism. As previously described the MMC and the RM are mounted to the yoke assembly through flex pivots and interconnect to each other through drive flexures. The purpose of the drive flexures is to provide a frictionless gearing system between the RM and the MMC. As the RM rotates in one direction it pulls the MMC through the drive flexures causing the MMC to rotate in the opposite direction. The RM has two sets of linear actuators mounted outboard of the RM. If the rotational inertia of the MMC and the RM are equal and the drive flexures are centered between the two flex pivots, the scanner will operate without any reactions even though the actuators push on the yoke. Of course, this is only true if all the structure, including radial stiffness of the flex pivots, has infinite stiffness. In a real mechanism with mechanical tolerances and structural modes, reactions are generated. Therefore, a critical design goal is to increase the structure stiffness as much as possible which will minimize reactions as well as permit the design of a high servo bandwidth system to control the precision linear scan profile.
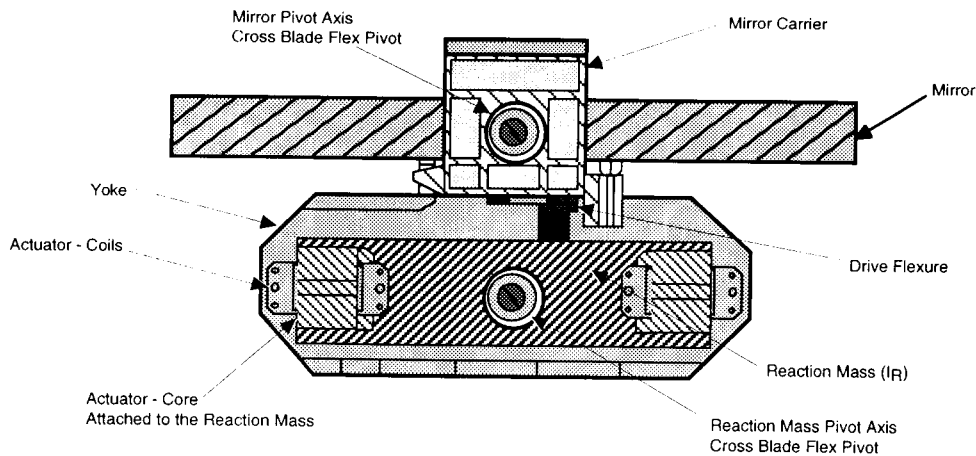
Figure 9. Reactionless Scanner Concept

2.6 Resonance Operation. As the flex pivot torsional stiffness is increased, the rotational natural frequency of the MMC and the RM will increase. The MMC and RM will oscillate sinusoidally when set in motion at a frequency determined by the torsional stiffness of the flex pivots and the rotational inertias of MMC and RM. If the desired scan profile is also sinusoidal, one could exactly match the mechanical natural frequency to the scan frequency. Once the system is set in motion, little power would be necessary to maintain the scan profile. Since the actual scan profile is nearly sinusoidal, an optimum mechanical natural frequency can be determined. Figure 10 shows a graph of computed power vs. scanner natural frequency. From the graph, the minimum power required is when the system mechanical natural frequency is 9.5 Hz.
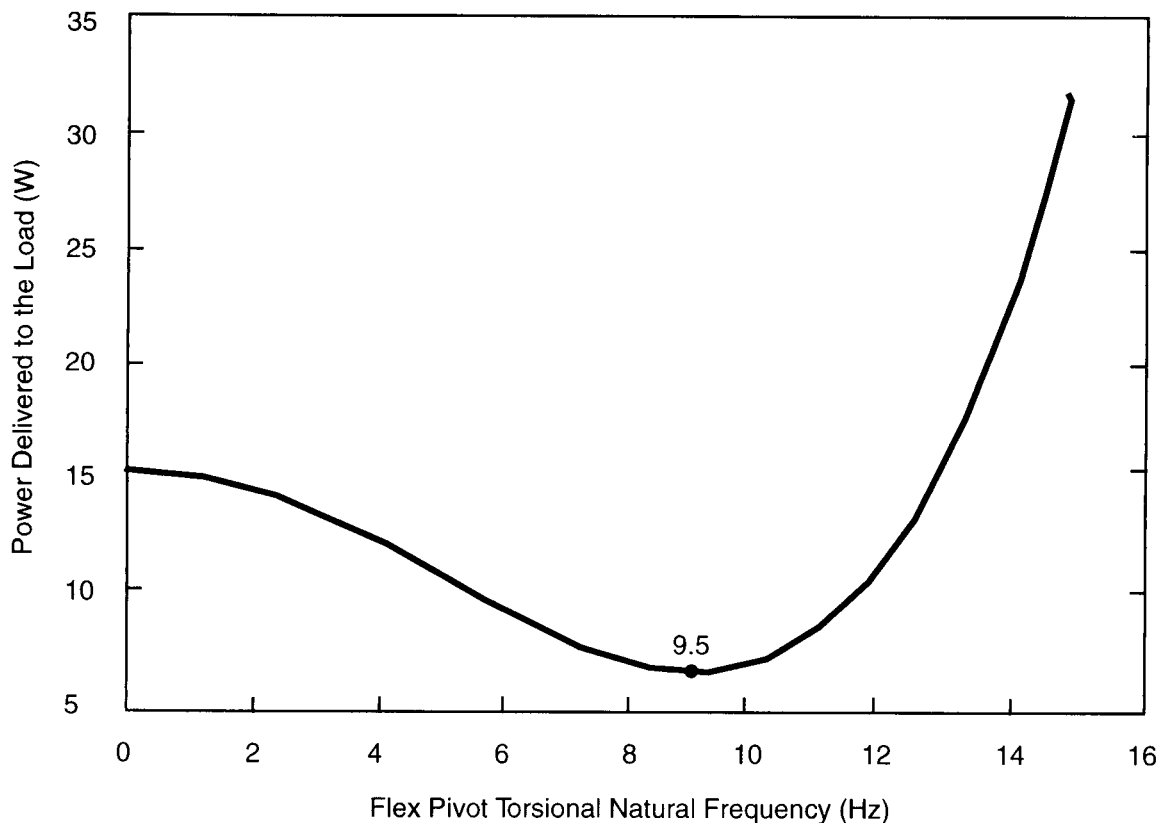
Figure 10. Mechanical Resonance Of *f*n = 9.5 Hz Is Optimum for the Application Scan Profile

3.0 Performance Design Goals

3.1 Performance Overview. All of the individual pieces and subassemblies were designed to meet a ≥500-Hz first mode resonance. The system must be able to scan the mirror with a flyback pulse and maintain an accurate positional readout. The mirror coarse points in a nominal nadir region and over 90° to a calibration position.

3.2 Mirror. The scanner may not have more than 6.4-μrad angular jitter. The polished, coated mirror is required to exhibit a nominal surface roughness of less than 50 Å and maintain a minimum reflectance of 98 percent in the 8 to 12-μm band at a 45–deg incident angle over an orbital lifetime of 5 years.

3.3 Scan Profile. Figure 11 shows the required scan profile of the mirror. The mirror must execute a linear scan profile within an angular range of ±1.71 deg (mechanical angles) with a desired precision of ± 15.0 μrad (3 σ) after 60 sec of observation mode initiation. Linear scan rate is required to be constant to within ±0.082 percent. Following the linear scan, the mirror executes a non-precision fast fly back. The total scan period will be 0.131 sec (scan cycle frequency will be 7.6 Hz).
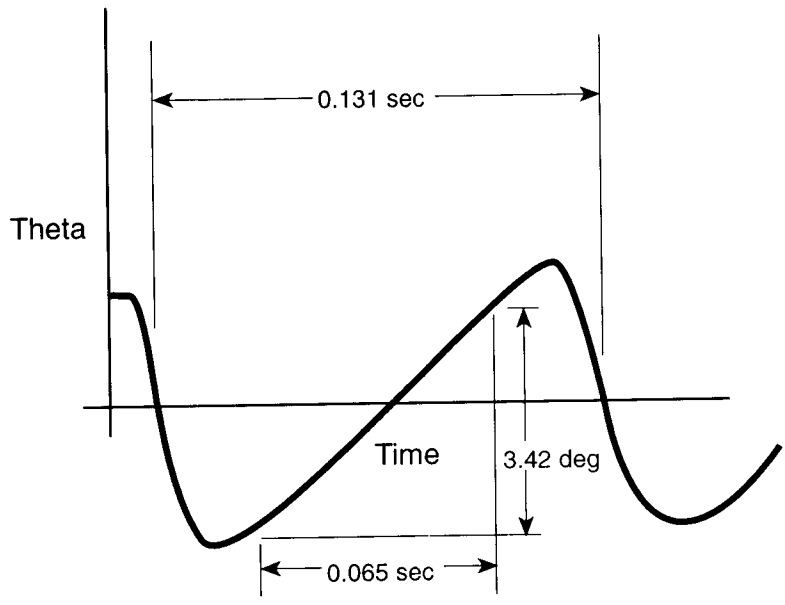
Figure 11. Scan Profile

3.4 Pointing Requirements. The mechanism must be able to adjust the scan position within a ±4.39 deg (mechanical angle) nominal range with a 0.00549 deg resolution. Also, to calibrate the system, the mirror must be able to rotate 90 deg from the nominal scan position to view a calibration black body. To launch the system, the mirror must rotate -135 deg. Therefore, the total angular travel of the mirror must be 225 deg (Figure 12).
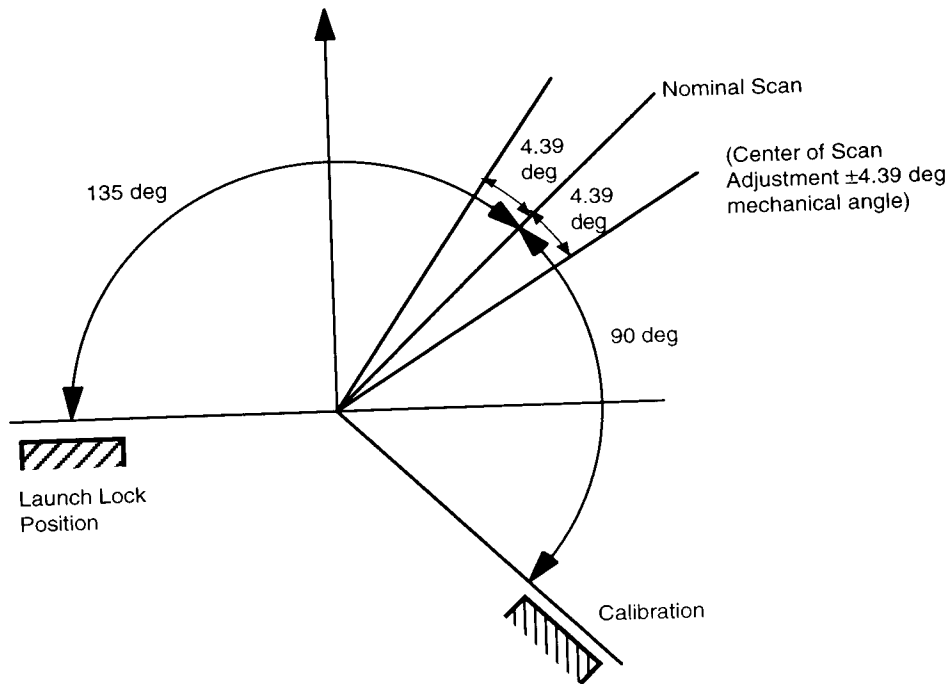
Figure 12. Pointing Range

344

3.5 Reaction Disturbances.
In order for the scanner not to disturb other instruments on the spacecraft, the scanner must operate with minimum reactions.

The rms force disturbance for any one axis for a bandpass of 1 Hz shall not exceed 0.2 N_{RMS} over the frequency range of 1 to 40 Hz and 0.13 N_{RMS} over the frequency range of 40 to 50 Hz. The total rms force over the frequency range of 1 to 50 Hz shall be less than or equal to 0.4 N_{RMS}. The power spectral density, PSD, for force disturbance is shown in Figure 13. Force disturbances shall be measured to 150 Hz.

The rms torque disturbance for any one axis for a bandpass of 1 Hz shall not exceed 0.01 Nm_{RMS} over the frequency range of 1 to 50 Hz shall be less than or equal to 0.02 Nm_{RMS}. The PSD for torque disturbance is shown in Figure 14. Torque disturbances shall be measured to 150 Hz. The impulse torque response as a result of stepper motor operation shall not exceed 0.038 Nms_{RMS} for a 10 second period.
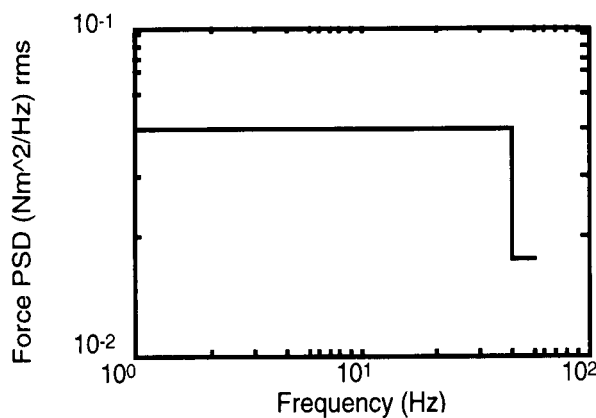
Figure 13. Force Disturbance PSD
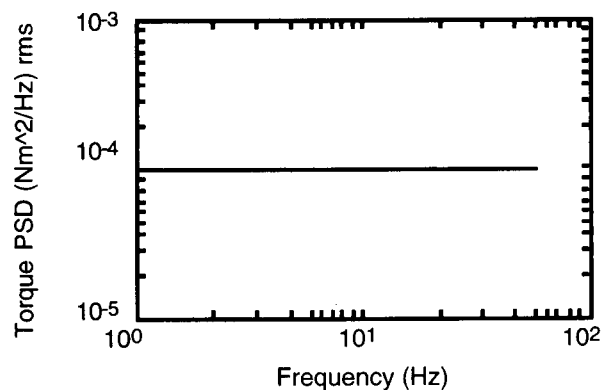
Figure 14. Torque Disturbance PSD

3.6 Mass and Power.
The total mass goal for the scanner, including electronics is less than 17.8 kg. Also, the total design power necessary to drive the scanner must be maintained below 30 W rms.

4.0 Flex Pivot Failure

A technical issue that required considerable effort to resolve was the failure of the flexural pivots during random vibration testing. The following is a discussion of the failure, the failure investigation, and the corrective action.

4.1 Hardware Failure.
A visual inspection following a 15 G_{RMS} Z-axis random vibration test of a prototype scanner revealed the outer blades of the flex pivots were cracked. Figure 15 shows a representative crack. The accelerometer data show that the initial failure occurred about 28 seconds into the test after full vibration level was achieved. The curves show that half-level random (7.5 G_{RMS}) produced no damage since there was not marked change in the frequency response from the scanner.

4.2 Failure Investigation and Analysis. The unit was disassembled and all of the pivots were inspected, showing that 12 of 16 scanner flex pivots cracked and 2 of 6 encoder mount flex pivots cracked and buckled. The pivots were sectioned (axially and longitudinally), micrographed, penetrant inspected, and hardness tested. A complete fractography was not possible due to damage of the fracture surface subsequent to failure. All failures occurred at the weld roots (typically the area of low strength). Sections of the weld showed porosity, inclusions, and lack of penetration. Figure 16 displays a prominent void in the weld and Figure 17 shows the weld penetration. Close inspection of the manufacturer's processes revealed potential problems in piece part cleanliness and weld consistency. Another source for weld integrity problems might have been the use of different material for the housing (420 SS) and the blades (422 SS).

The initial scanner NASTRAN model incorporated the pivots as uncoupled springs using manufacturer's data for material strengths, static load carrying capability and spring rate. This model indicated an acceptable margin of safety. The failure created the need for a highly detailed model of the flex pivot.

The overall scanner model incorporated the new detailed flex pivot model to determine the loads generated during random vibration. In addition, sample pivot material was tensile tested. The results indicated strength properties lower than originally believed. The results of the analytical model indicated a negative margin of safety of -0.05 for the flex pivots based on a worst case combination of loads and reduced strength properties. The aforementioned welding flaws compounded the negative margin of safety. The analysis results confirmed the test failure.

4.3 Corrective Action. Multiple paths to improve pivot performance were pursued to be used for the subsequent assemblies. The paths consisted of:

1. Modify the commercial design and processes to produce an acceptable pivot. Ball reworked the manufacturers' design to widen the weld base and reconfigure the blades to use the same housing and blade material. The manufacturer worked with Ball to improve their welding processes. Pivots were lengthened to accommodate weld samples from each pivot and tests were performed on each weld.

2. Negotiate with the customer to reduce the required vibration levels. Past experience has shown that as vibration envelope specifications flow down through multiple levels of contracts, margins often get added onto margins until the specification is difficult to achieve. Negotiations to review the original specification were worked with the customer.

3. Perform rigorous testing and establish selection criteria. Original testing was performed on inadequate fixtures. New fixtures were designed by Ball to provide adequate stiffness and precision.

Tests similar to those outlined by J.L. Olson of Hughes Aircraft Co. [2] are now performed at Ball using the latest technology. The following pivot characteristics are measured: radial stiffness, axial stiffness, torsional spring rate and geometric
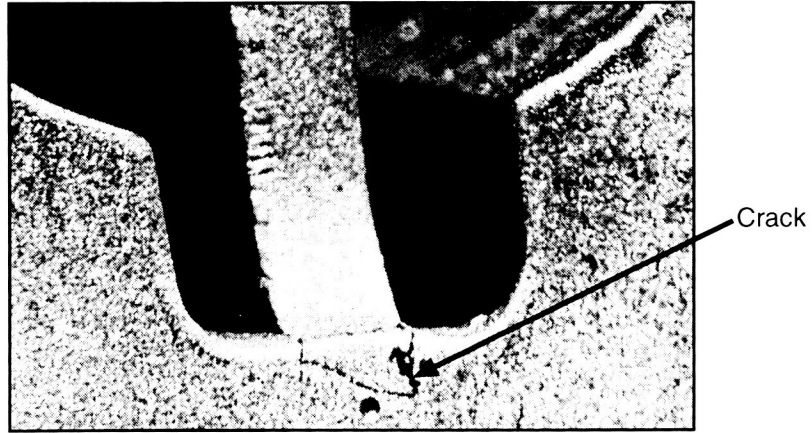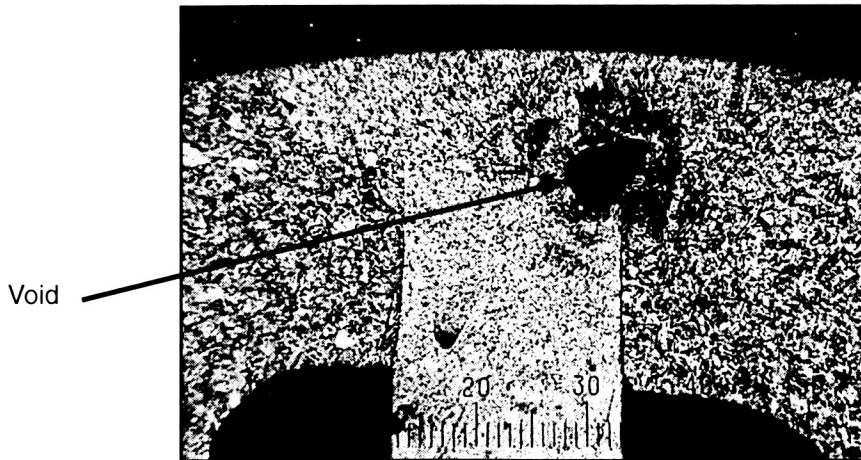
Figure 15. Representative Crack

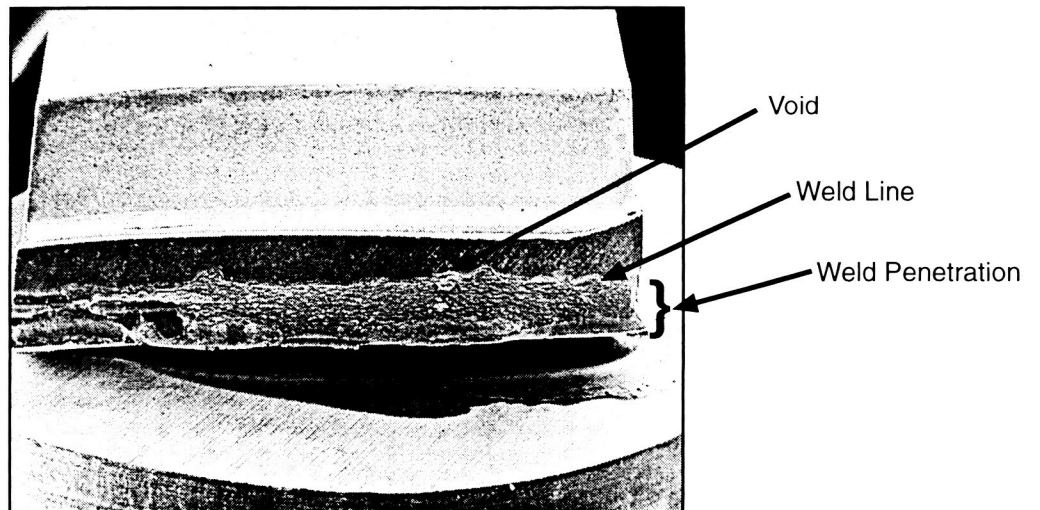**Figure 16. Weld Zone Along Crack (30X)**

Figure 17. Weld Zone With Prominent Void (12X)

decentering. A run-in test of 10^6 cycles is conducted to eliminate infant mortality. After completing run-in, the pivots are placed in matched sets exhibiting similar decentering patterns.

4. Design a new flex pivot concept.
The fully developed design is a "multi-spoke" configuration machined out of one piece of material, eliminating weld problems. System alignment is improved by ensuring pivot concentricity through one piece construction. The additional blades increase radial and torsional stiffness and provide more load carrying capacity. Final polishing produces blades that are without cracks or flaws and have minimal surface roughness. Pivot fatigue life and therefore system reliability increase as a result. The new flex pivot also improves system pointing accuracy by reducing geometric decentering. Better overall scanner system performance will be achieved through use of the new Ball flex pivot. Figure 18 is a photograph of the pre-polished pivot. Ball is currently seeking patents for this design.
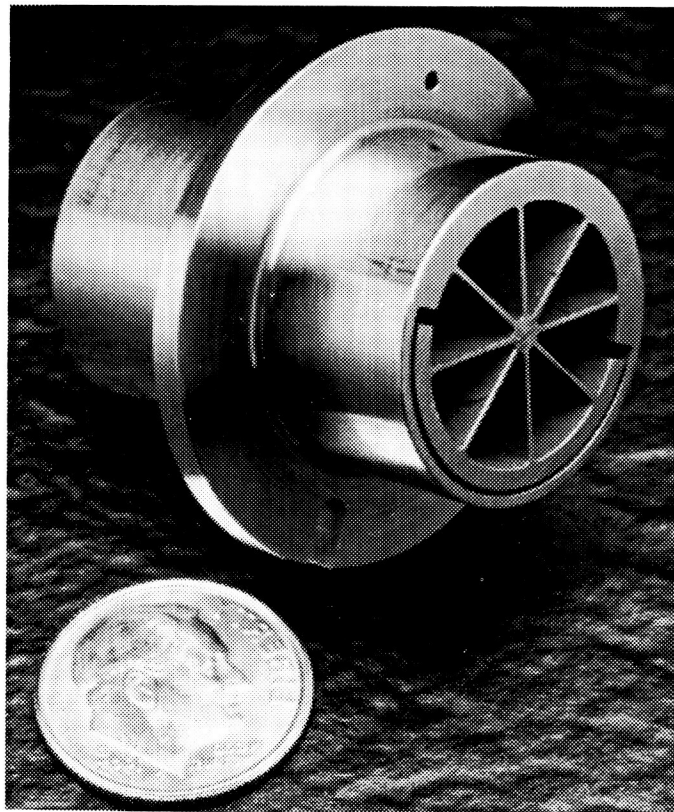
Figure 18. Pre-Polished Pivot

5.0   Program Status

The program was originally contracted to be worked in three phases. The first phase was to include an electronics breadboard and mechanical design development. The second phase was to include a proto-flight qualifying model and the third phase was to construct the flight acceptance model. The project is now in the final phase with an

additional effort added to the contract. Due to some failures and discoveries, discussed in Section 4.0, the second phase model has been returned to have the upgraded hardware and design changes incorporated and re-tested. The flight model, the third phase, has had the new design incorporated and the hardware is almost 100% fabricated.

One of the new flex pivot designs being developed by Ball is a leading contender for incorporation into the mechanism. Development pivots have been manufactured and have successfully passed extensive selection criteria. Ball is now fabricating 30 flight pivots.

6.0 References

1. Seelig, F. A. "*Flexural Pivots for Space Application.*" Bendix Corporation Fluid Power Division, Utica, NY, presented at the 3rd Aerospace Mechanisms Symposium.

2. Olson, J. L. "*The Evaluation of Flexural Pivots to Meet Critical Performance and Life Requirements.*" American Society of Mechanical Engineers, presented at the Design Engineering Conference & Show May 11-14, 1970.

7.0 Acknowledgments

Development and Testing of the
Rack Insertion Device

G. Scott Strickland[*]

Abstract

Installing and removing experiment racks in a Space Station Logistics Module will become a repetitive operation at Kennedy Space Center (KSC) in the near future. A Rack Insertion Device (RID) consisting of an Extendible Boom, End Effector, and Positioning Base is being developed for the task. This paper discusses the key elements of the RID's function and design. Prototype test results for the RID's Extendible Boom and End Effector are presented. Also discussed are future end effectors that will further enhance the RID's Space Station processing capability.

Introduction

Installing experiment racks in the Space Station's Logistics Module will be similar to putting together a ship in a bottle. The Logistics Module, shown in Figure 1, supports sixteen (16) racks in four different quadrants. It has a 2.44-m (96 in) diameter door on one end to simplify rack loading. The module opening reduces to 2 m (84 in) square when racks are installed. For installation, the 816.5-kg (1800 lb) rack must be inserted through the opening, then accurately positioned inside the module for connection. Complicating the operation are the lower, rear, rack-to-module interfaces being hidden from view. The remaining rack-to-module interfaces are two struts connected to the upper, front of the rack. A Logistics Module may be flown up to four times a year to re-supply Space Station, requiring integration of racks each time. Thus, installing and removing racks will become a repetitive process that requires ground support equipment (GSE) that is safe, reliable and time-efficient.

The Rack Insertion Device, shown in Figure 2, is being developed to take a rack out of its support dolly and install it in less than an hour. This will save days in the processing schedule for integrating Logistics Modules based on time-line comparisons with other concepts. The RID concept may also allow processing of multiple rack quadrants without rotating the module, further decreasing processing time. However, decreasing processing time was not the only goal of the RID concept. Limiting risk to flight hardware and personnel was a major priority. One early rack installation concept required technicians to push a rack into position on top of a roller floor, much like loading cargo containers into aircraft. A safe operation would depend on the technician's strength and coordination. KSC Design felt that eliminating man-handling of the rack and reducing GSE-to-GSE transfers of the rack would decrease risk. The RID concept provides positive control of the rack through-out the operation with a push-button control pendant. Also, the RID concept eliminates unnecessary rack transfers.

---

[*] McDonnell Douglas Space & Defense Systems, Kennedy Space Center, FL

Rack Insertion Device Operation

The RID will be operated in the Space Station Processing Facility at Kennedy Space Center. Prior to rack installation or removal, technicians remove the Logistics Module's door and install a GSE personnel floor. An integrated rack, sitting in its support dolly, is staged within the RID's reach. Figure 3 shows a typical rack installation sequence accomplished with the following steps:

Step 1: Rotate and lower the RID's Boom, aligning the End Effector with the rack sitting in its support dolly. Adjust the End Effector to compensate for minor misalignment, then connect it to the rack's GSE handling points.

Step 2: Take the rack's weight off the support dolly and disconnect it from the dolly (the dolly supports the rack in the same manner as the module). The End Effector pivots the rack about its on-orbit pivot location forward 30 degrees.

Step 3: Align the rack with the module's door using the Positioning Base to raise and rotate the Boom.

Step 4: Extend the RID's Boom, aligning the rack with its on-orbit module location.

Step 5: Translate the Positioning Base approximately 0.75 m (2.5 ft) and align the rack with its on-orbit pivot axis. The End Effector can compensate for misalignment and Boom deflection using its adjustment capability.

Step 6: Pivot the rack until it contacts the module support located at the lower, rear portion of the rack. Connect the upper struts and engage the pins, built into the rack, with the lower module support. The rack's weight is transferred from the Boom by adjusting the End Effector. The End Effector design prevents the RID from putting additional loads into the module.

After disconnecting the End Effector from the rack the Boom is retracted and Step 1 is repeated to install the next integrated rack. Rack removal requires the same steps performed in reverse.

The RID, as the concept evolved, has three main components: an Extendible Boom, End Effector, and Positioning Base. The Extendible Boom supports the rack as it is inserted into the module. The Boom not only provides positive control of the rack, it also eliminates the need to design the module for GSE/rack-handling loads. This aspect and the capability for multiple end effectors make the RID very adaptable to flight hardware design changes. The ability to change end effectors will also allow the RID to accomplish many processing tasks other than rack installation. Each end effector will have its own set of requirements and flight hardware interfaces. The End Effector for installing and removing racks in the Logistics Module connects directly to the rack GSE interfaces. It compensates for misalignment and prevents the Boom from accidentally putting loads into the module. The Positioning Base adds flexibility to the RID, providing three degrees of freedom to the Extendible Boom. The Base can raise, rotate and translate the Boom giving the RID the capability to pick a rack out of its dolly without additional transfers. The Base's rotation also allows integration of two Logistics Modules without repositioning the modules or the RID. A discussion of the key design elements for the Extendible Boom, End Effector, and Positioning Base follows.

The Extendible Boom

The RID's Extendible Boom is a critical component in the system. Requirements for the RID called for a boom that extended 8.2 m (27 ft) with a capacity of 1,814 kg (4000 lb). The Boom must handle a torque of 9,040 N•m ($8 \cdot 10^4$ lb•in) and a moment of 22,600 N•m ($2 \cdot 10^5$ lb•in) applied at the Boom's endplate. These requirements provide the Boom with the capacity to install Lab Module racks, should an end effector be designed to do so. The Extendible Boom must support these loads with minimum deflection. If the Boom's deflection is too great, the Positioning Base will constantly have to adjust the Boom's height while extending the rack into the module. Also, the End Effector will require greater adjustment capabilities to compensate for the Boom's deflection. Our goal for the design was to hold the change in Boom deflection to less than 25 mm (1 in) when the rack's weight is transferred from the Boom to the module. The Boom design must maintain minimum safety factors of two against yield and three against ultimate failure.

The Extendible Boom design, shown in Figure 4, includes three telescoping sections and a support structure. Each of the Boom's sections are weldments forming hollow, square tubes (see Figure 5). The material is ASTM A572 steel plate. Top and bottom surfaces of the square tubes were machined for the mounting of hardened bearing ways. The ways are chrome-plated and have a minimum Rockwell hardness of 71C as recommended by the bearing manufacturer. Two upper and two lower linear roller bearings, separated by 1.22 m (48 in), form a couple to support each section. Bearing reactions from the largest tube exceed 125,000 N (28,000 lb). The bearings have a coefficient of friction of less than 0.005 and allow the Boom sections to move quite easily, even when loaded. Originally all of the bearings were to be aligned with shim adjustment only. At the time of manufacture, a spherical mount for the upper bearings was designed to simplify assembly and ensure proper alignment with the hardened way. In addition to the main bearings, rollers react side loading and support the tubes when they are not loaded and are fully retracted. Each of the three Boom sections are actuated independently using a 3.81-cm (1.5 in) diameter ball screw and a stepper motor. The power and control cables are routed through the Boom's sections using separate flexible, metal conduits. Expandable bellows, installed over each section, prevent contamination of the cleanroom environment.

The support structure for the Boom's sections is a welded ASTM A572 steel frame fabricated using standard shapes. To minimize annual inspection requirements, critical welds were eliminated from the design. The support frame has built-in interfaces for the Positioning Base's four jacks to raise and lower the Boom. Two lead-filled counterweights totaling 7879 kg (17370 lb) are mounted on the back of the support structure. The counterweights prevent any upload on the lifting jacks. Linear bearings, mounted vertically on the frame, react side loads to the Positioning Base. The support frame was analyzed using finite-element techniques to ensure its integrity even if one of the four lifting jacks failed.

Rack Installation End Effector

The end effector is the interface between the Extendible Boom and flight hardware. The End Effector, designed to install and remove Logistics Module racks, must compensate for Boom deflection and RID misalignment with the module. Also, the design must prevent over-loading the module with the Boom. Manual operation of the End Effector is preferred, allowing the operator some "feel" as to whether the rack is being adjusted properly. Lastly, the End Effector must provide proper alignment between the rack's rear fittings and the module's interfacing support. This connection is hidden from view if there are racks on either side of the one being installed.

The End Effector provides five degrees of freedom to align the rack. Controls for the Extendible Boom are sensitive enough to align the rack along the module's axis (the x-axis). The End Effector's design concept, shown in Figure 6, uses a simple three-point suspension. Three points describe a plane and no matter where you move one of the points, a plane is still defined. The End Effector supports the rack interface plate at three points, using spherical bearings. The two lower support bearings are independently moved in the "y" and "z" directions. By moving these bearings together or independently, the rack can be adjusted with five degrees of freedom. These two bearings are located in-line with the rack's on-orbit pivot axis allowing the rack to pivot about that axis while supported by the End Effector. The rack's pivot points are not obstructed from the operator's view during installation. If the operator aligns the rack's pivot axis properly in the module, the rack is ensured of being properly aligned with the module's support fittings. Located on the rack's center-line is the third support bearing, connected to a screw jack for pivoting the rack.

The End Effector's two lower support bearings move in the y-direction, actuated by jack screws housed in the bearing's support arm. A ratcheting turnbuckle pivots the support arm providing bearing movement in the z-direction. The turnbuckles and jack screws provide fine adjustment of the support bearings, ±50 mm (2 in). To prevent damaging the module's support fittings with the RID the turnbuckles' design can support only a tension load. If the Boom is mistakenly lowered while the rack is in contact with the module's fittings, the turnbuckles will begin to collapse, alerting the operator of a problem. Only the weights of the rack and interface plate are applied to the module's fittings. This turnbuckle feature also helps the operator sense when the rack's weight transfers to the module.

Positioning Base

The Positioning Base, shown in Figure 7, supports the Extendible Boom and provides three additional degrees of freedom for the RID. The Base design can raise and lower the 15,875 kg (35,000 lb) Extendible Boom within a 2.75 m (9 ft) stroke. This allows the RID to attach to a rack sitting in its support stand on the floor then raise the rack to the module level. The Base can also rotate the Boom 365° to allow processing of two modules without moving or realigning the RID. Finally, the Base translates the Extendible Boom in the y-direction ±1 m (3.5 ft). This motion is necessary to position the rack inside the module. The mechanical systems required to achieve these movements are independent from each other. Each requires a level of structural

support. The three systems are stacked with the Jacking System on the top level, followed by the Rotation System and Translation System.

The Jacking System, shown in Figure 8, mounts on a steel support frame 20.3 cm (8 in) deep. A large enclosure surrounds the entire system to preserve the cleanroom environment. Four 27,000 kg (30 ton) acme screw jacks raise and lower the Extendible Boom. The off-the-shelf jacks have a 7-cm (2.75 in) diameter acme screw. There is a 4 to 1 safety factor against buckling for the highest loaded screw. The jacks have a 9:1 gear reduction built in and a 10:1 gear reducer connects to each jack to further reduce the motor torque required. Rather than a single drive motor, two servo-motors drive the four jacks, one between each forward and rear jack. Two motors were used for several reasons. Having two motors decreases the length of the transmission shafting required. This lowers the inertia of the system and decreases the potential for shaft wind-up. Also, having two motors with fail-safe brakes in the system eliminates a single-failure point. Should some portion of the Jacking System fail, such as a shaft or coupling, three jacks are still connected to a brake. Finally, the size and cost of a single servo-motor, large enough to drive all four jacks, was much greater than the two motors used.

The Base's Rotation System design, shown in Figure 9, can rotate the Extendible Boom and the Base's Jacking System 365°. To decrease inertia, the two smaller Boom sections must be retracted prior to rotating. However, that still translates into an inertia of 13,333 kg•m^2 (118,000 lb•ft•s^2). A large diameter roller bearing with an integral gear was our first consideration for the Rotation System. It became impractical because of the size and cost of the bearing required. The rotation bearing had to be mounted directly underneath the jacking screws to minimize the depth and deflection of the Jacking System's support frame. This required a bearing 4.25 m (14 ft) in diameter. The few manufacturers that were able to make such a bearing gave quotes of 70 to 100-thousand-dollars with a year's lead time. A much cheaper and equally capable system was designed using multiple components. Sixteen 7.6-cm (3 in) diameter yoke-style rollers mount directly below the jacking screws on the Jacking System's support frame along a 4.25-m (14 ft) diameter. The sealed rollers operate on hardened-steel ways mounted to the Rotation System's structural frame. Also mounted to the Rotations System's support is a 2.44-m (96 in) diameter spur gear with external teeth. The mating pinion mounts to the Jacking System's support frame. It provides a 14:1 torque reduction and rotates the frame when driven. Even with the large gear, the pinion starting torque required calculates to be 1,119 N•m (9,900 in•lb). A servo-motor drives the pinion through a 200:1 gear reduction. Cam-followers, rolling on the inside diameter of the spur gear, take care of side load. The power and control cables that route down to the next level are the only limitation to infinite rotation of the Boom.

The Base's Translation System, shown in Figure 10, moves the Extendible Boom as well as the Base's Jacking and Rotation Systems totaling about 36,300 kg (80,000 lb). The system comprises of linear bearings used with a rail and a ball screw actuator. Four linear bearings are equally spaced on two parallel rails. The linear bearings mount to the bottom of the Rotation System's structural frame. The ball screw provides controlled movement and mounts to the Translation System's structural support. The

ball nut bolts to the Rotation System support. The linear bearings' coefficient of friction being low, the ball screw's calculated starting torque is also relatively small, 11.5 N•m (100 in•lb). However, to reduce the system inertia a 10:1 planetary drive is used in conjunction with the drive motor. Also mounted to the Translation System's support are hand-operated lifting jacks. These jacks can lift the RID in order to place air bearings underneath. Air bearings are the means used to move heavy stands and equipment in the Space Station Processing Facility at KSC.

The Positioning Base's structural components, like the Extendible Boom's, are designed with safety factors of two against yield and three against ultimate failure. The Base is made almost entirely from standard structural steel shapes with the exception of the Rotation System's support frame. This frame will be fabricated from steel plate. Again, a finite-element program was used to solve for the loads in each structural member. Various different load cases, based on the many possible RID positions, were required to find the maximum loading in each member. Like the Extendible Boom, the Positioning Base was designed without any critical welds.

Controls

Computer-programmed stepper and servo motors drive all of the RID's powered systems. The use of this type of motor gives precise control of the mechanical elements and allows changing the travel speed and acceleration by modifying the drive program. It also allows future consideration for automating all or portions of the RID operation. However, the motors required greater care to match the mechanical system's inertia with the drive motor's rotor inertia. In fact, all of the motors were selected on this basis rather than torque or speed limitations. With the current design the operator controls the motors with a push-button pendant (see Figure 11). The pendant is located at the end of the Extendible Boom along with a separate emergency-stop pendant. A master control station, located on the Positioning Base, ·can also be used to control the RID. Redundant limit switches for all of the powered system's end-stops prevent over travel.

Prototype Testing

Fabrication of the Extendible Boom and End Effector was completed in June, 1994. Both items were proof-loaded at 125% of their maximum design load. The change in Boom deflection that occurs when the rack is removed from the End Effector, met our expectations. The net deflection was only 1.27 cm (0.50 in) which is well within the adjustment capability of the End Effector. The calculated deflections of the boom for various cases are shown in Table 1. The deflection at the rack pivot point is given which includes the torsional deflection of the Boom.

Table 1. Extendible Boom Deflections

Case	Weight	Torque Arm	Moment Arm	Def. @ Rack (Calc.)
125% Capacity	22.2 kN (5000 lb)	127 cm (50 in)	117 cm (46 in)	4.44 cm (1.75 in)
100% Capacity	17.8 kN (4000 lb)	127 cm (50 in)	117 cm (46 in)	3.75 cm (1.45 in)
End Effector w/Rack	13.3 kN (3000 lb)	58 cm (23 in)	88 cm (35 in)	2.13 cm (0.84 in)
End Effector w/o Rack	5.3 kN (1200 lb)	58 cm (23 in)	88 cm (35 in)	1.14 cm (0.45 in)

To prove that the RID concept could successfully install and remove a rack, a Logistics Module simulator, shown in Figure 12, was built. The simulator has very high-fidelity with the Logistics Module's rack mounting brackets and interior clearances (Figure 13). The dummy rack used for the test was modified to support 816 kg (1800 lb) and to mimic the actual rack's module interfaces. Without the Positioning Base, a support stand was fabricated to hold the Extendible Boom at the module opening's height. No vertical adjustment was provided. The support stand was equipped with rollers to provide horizontal translation like the Positioning Base. The dummy rack was installed on the End Effector using the facility crane. The first attempt to install the rack in the module simulator went very well with the installation taking just over thirty minutes. No alignment guides or sensors were required. Technicians are able to visually align the rack being installed using the adjacent rack's pivot points as a guide. The dummy rack has since been installed and removed over twenty times in the simulator without inciden (Figure 14).

To convert the Extendible Boom and End Effector into certified GSE, the designs must be put through a Critical Design Review. Prior to that review some changes will be made to the designs based on lessons learned during the prototype testing. The largest impact will be to modify the linear bearing supports for the Extendible Boom. The current design requires each tube section to be removed sequentially to access the bearings. Modifications will be made to simplify bearing replacement in case of a failure. Also, bearing ways will be added for the side rollers. It was first thought that the loads in these rollers would be negligible. As it turned out, the linear bearings have a tendency to find a groove that forces the tubes into the rollers, creating a much higher load. The rollers, bearing against the primered steel, cause flaking that could be a contamination issue. Modifications planned for the End Effector include providing a captured-screw connection for the rack and incorporating the "y" axis screw jacks into the support for greater module clearance. We also plan to add instrumentation to End Effector to measure the weight and cg of the rack. By incorporating weight and cg measurement into the End Effector, a number of operations and rack transfers are eliminated, further reducing processing time and decreasing risk to flight hardware. Prototype testing of the weight and cg components are on going.

Other End Effectors

Although the RID was designed to install racks, there are many processing tasks that the RID is capable of performing. Changing end effectors allows the RID to interact with different pieces of flight hardware. End effectors are being developed or considered to perform the following operations:
- Installation and removal of Lab Module and Node racks
- Installation and removal of the Logistic Module's large diameter door
- Opening and closing of the 1.27 m (50 in) hatch
- Late and early personnel access to the module
- Installation and removal of rack drawers/large components/replaceable units

Late and early personnel access to the module may be impossible without the RID. Alternative methods for the other above operations, not using the RID, require extensive amounts of GSE. Using the RID to perform the above operations will reduce the flight hardware processing time and GSE requirements.
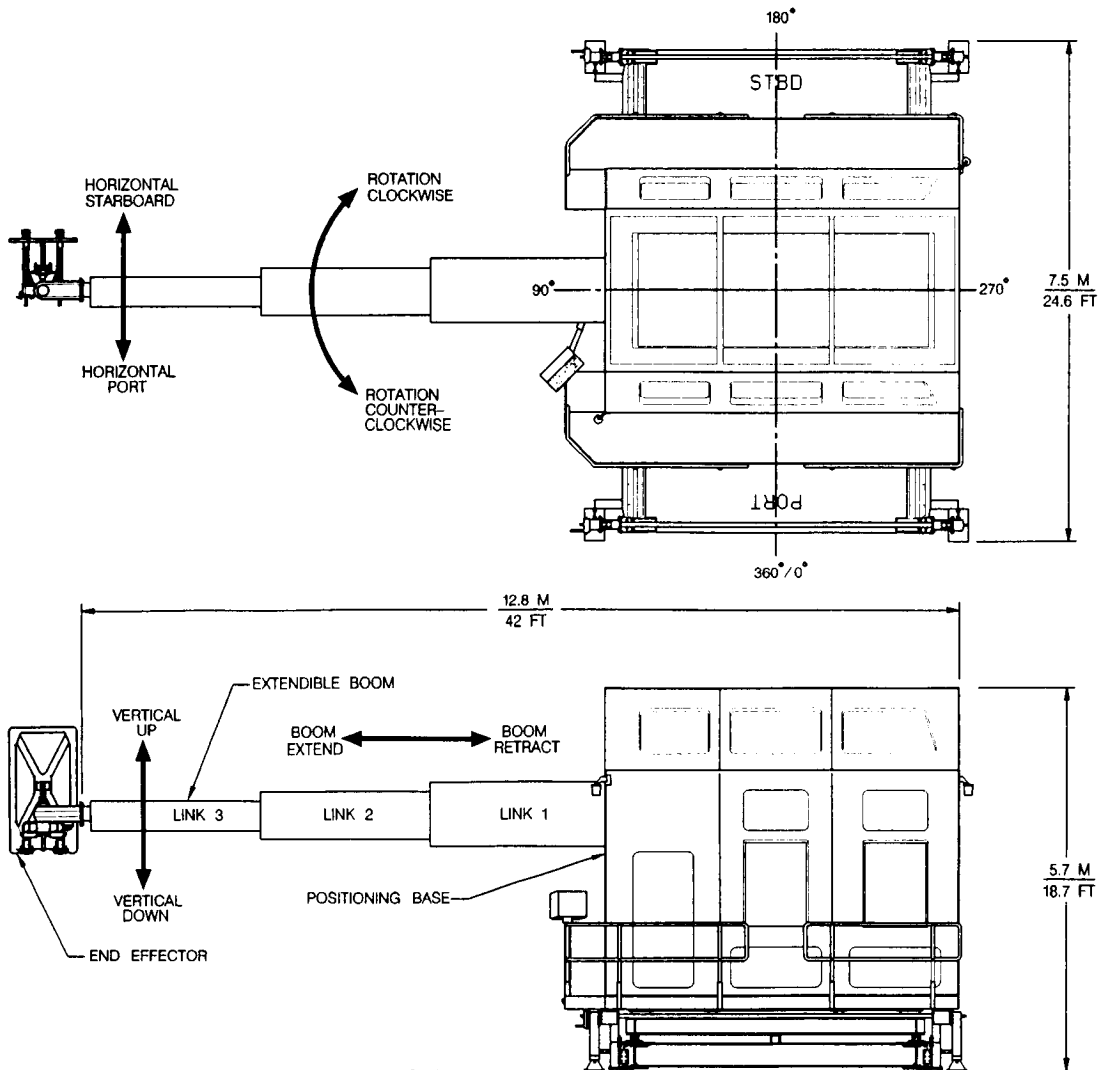
Conclusion and Summary

The Rack Insertion Device is scheduled to be activated in March, 1996. The Extendible Boom and End Effector prototypes have been thoroughly tested and are currently being converted to GSE. Their testing has proved that an 8.2-m (27 ft) long extendible boom can accurately and dependably position equipment the weight of a small car with the push of a button. Delivery of the Positioning Base is expected in August, 1995. Once the RID is complete, it will be one of the more expensive and complicated GSE systems at Kennedy Space Center. However, no other concept would have made the Logistics Module's rack installation operation as efficient or safe as the RID can. With the development of additional end effectors, the RID will become an integral part of Space Station processing.

Acknowledgments

Figure 1: The Logistics Module

Labels: EXPERIMENT RACK, LARGE DIAMETER DOOR

Labels: HORIZONTAL STARBOARD, ROTATION CLOCKWISE, HORIZONTAL PORT, ROTATION COUNTER-CLOCKWISE, STBD, PORT, 180°, 90°, 270°, 360°/0°, 7.5 M / 24.6 FT

Labels: EXTENDIBLE BOOM, VERTICAL UP, BOOM EXTEND, BOOM RETRACT, LINK 3, LINK 2, LINK 1, POSITIONING BASE, VERTICAL DOWN, END EFFECTOR, 12.8 M / 42 FT, 5.7 M / 18.7 FT

Figure 2: The Rack Insertion Device

STEP 1

STEP 2

STEP 3

STEP 4

STEP 5

STEP 6

Figure 3: RID Operational Steps

C-5

Top View

Jack Interface (4 Places)

Support Structure

Bearing Way (Typ)

Counterweight (2 Places)

Ball Screw (3 Places)

Linear Bearings

E-Stop

Cable Conduit (Typ)

Cross Section

Control Pendant

Stepper Motor (3 Places)
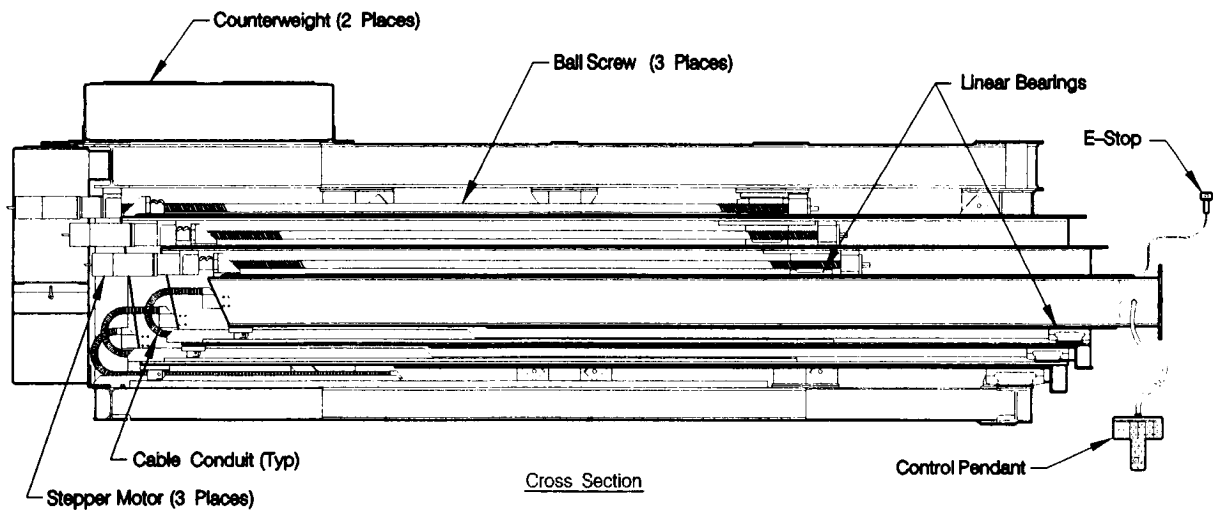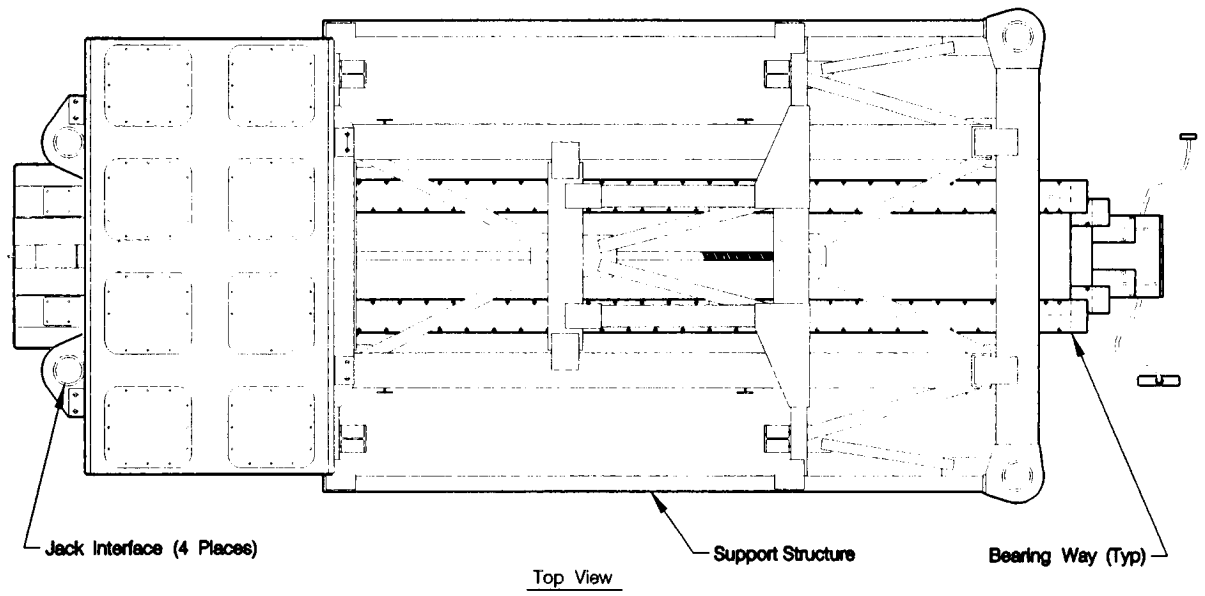
Figure 4: The Extendible Boom

Ball Screw (3 Places)

Support Structure

Linear Bearing (12 Places)

Side Roller (6 Places)

Boom Section 1
Boom Section 2
Boom Section 3
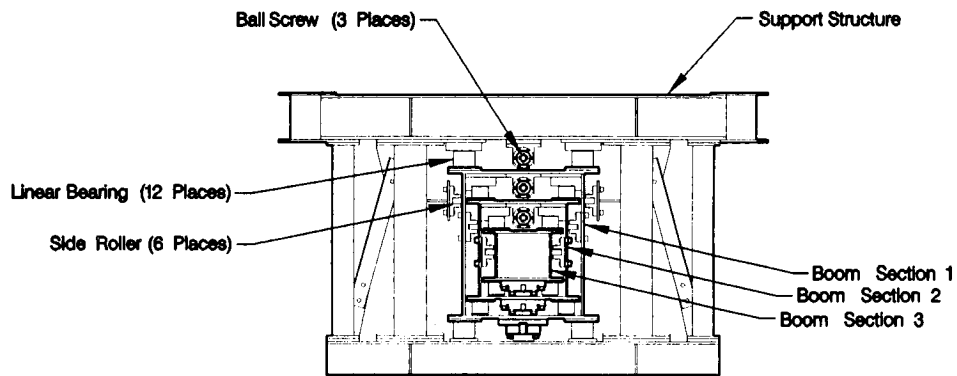
Figure 5: Tube Arrangement
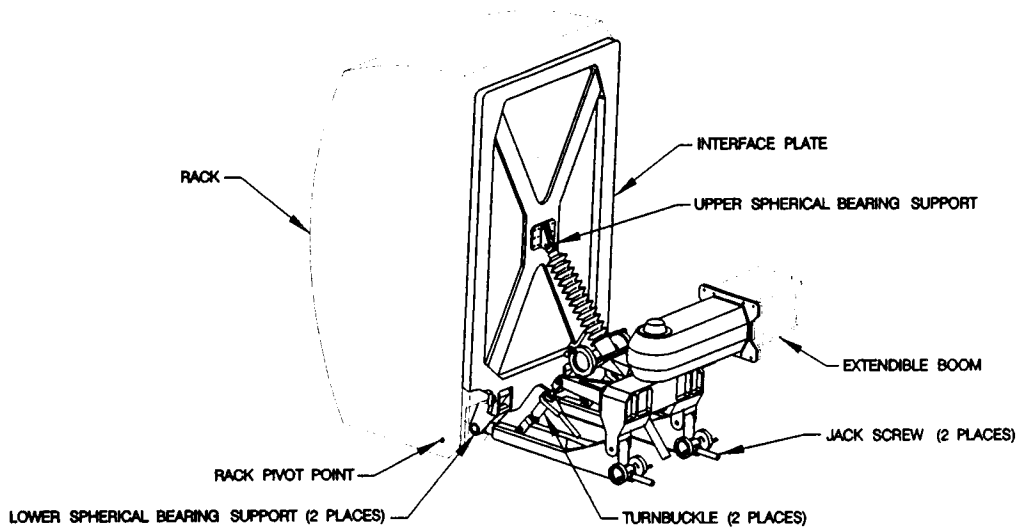
Figure 6: End Effector (Installed Position)

Labels in figure:
- RACK
- INTERFACE PLATE
- UPPER SPHERICAL BEARING SUPPORT
- EXTENDIBLE BOOM
- JACK SCREW (2 PLACES)
- RACK PIVOT POINT
- LOWER SPHERICAL BEARING SUPPORT (2 PLACES)
- TURNBUCKLE (2 PLACES)
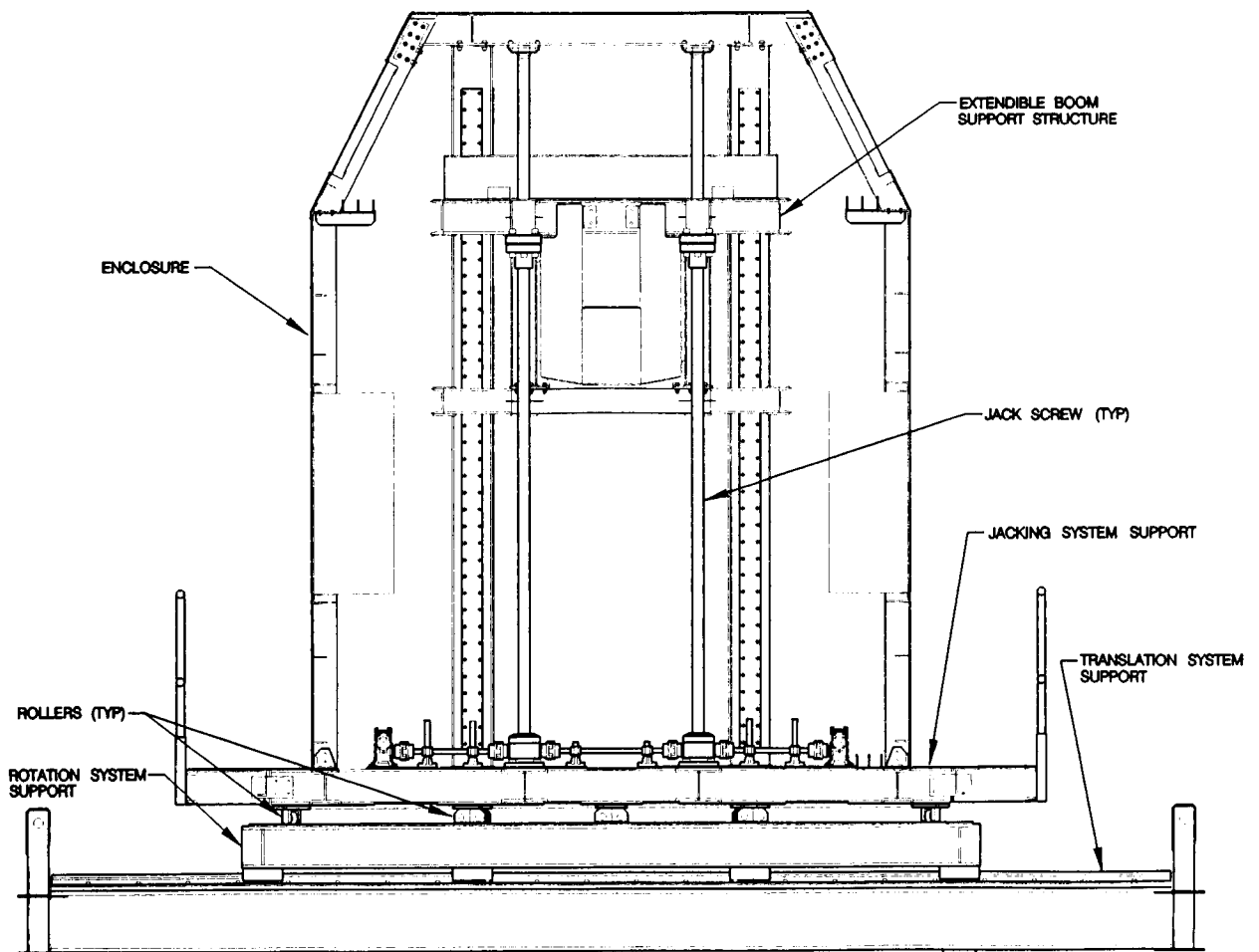
Figure 7: Positioning Base Cross-Section

Labels in figure:
- EXTENDIBLE BOOM SUPPORT STRUCTURE
- ENCLOSURE
- JACK SCREW (TYP)
- JACKING SYSTEM SUPPORT
- TRANSLATION SYSTEM SUPPORT
- ROLLERS (TYP)
- ROTATION SYSTEM SUPPORT
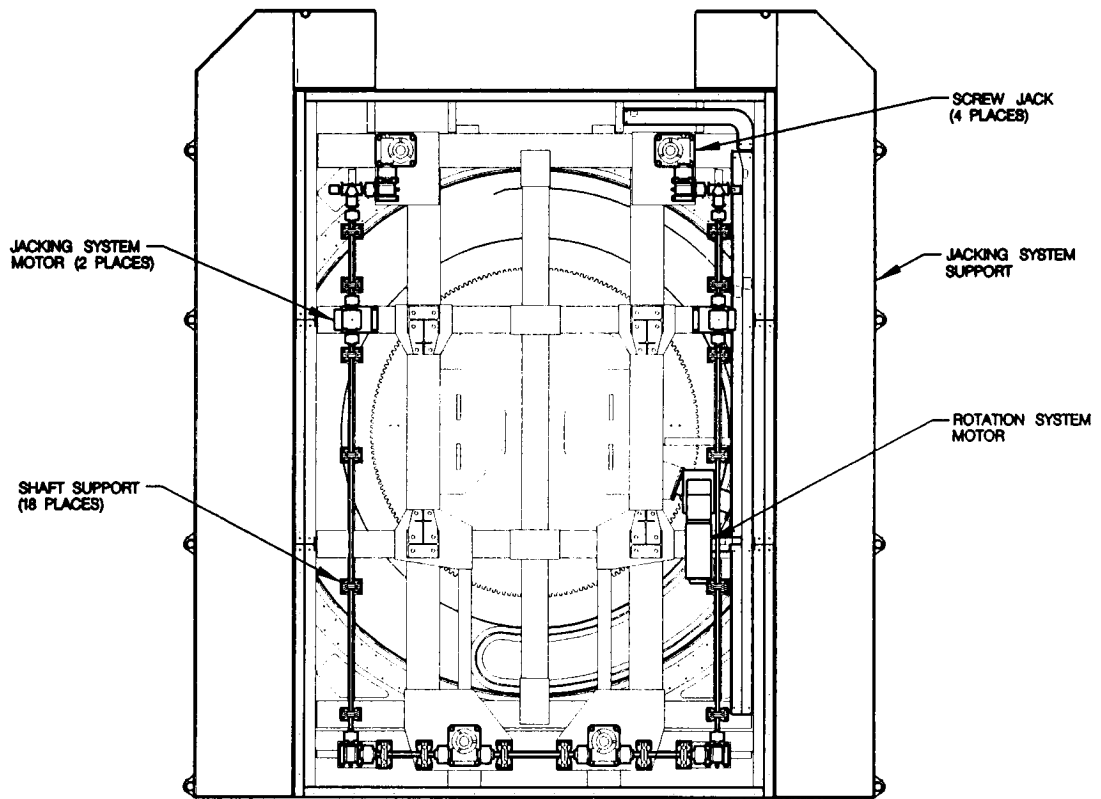
Figure 8: Positioning Base Jacking System
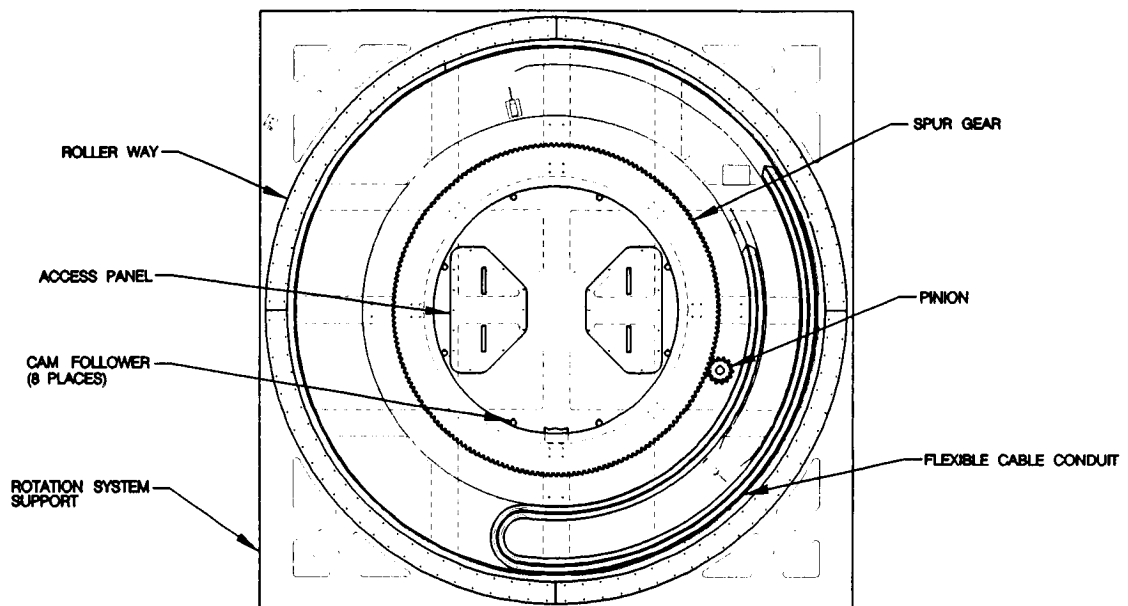
Figure 9: Positioning Base Rotation System

365
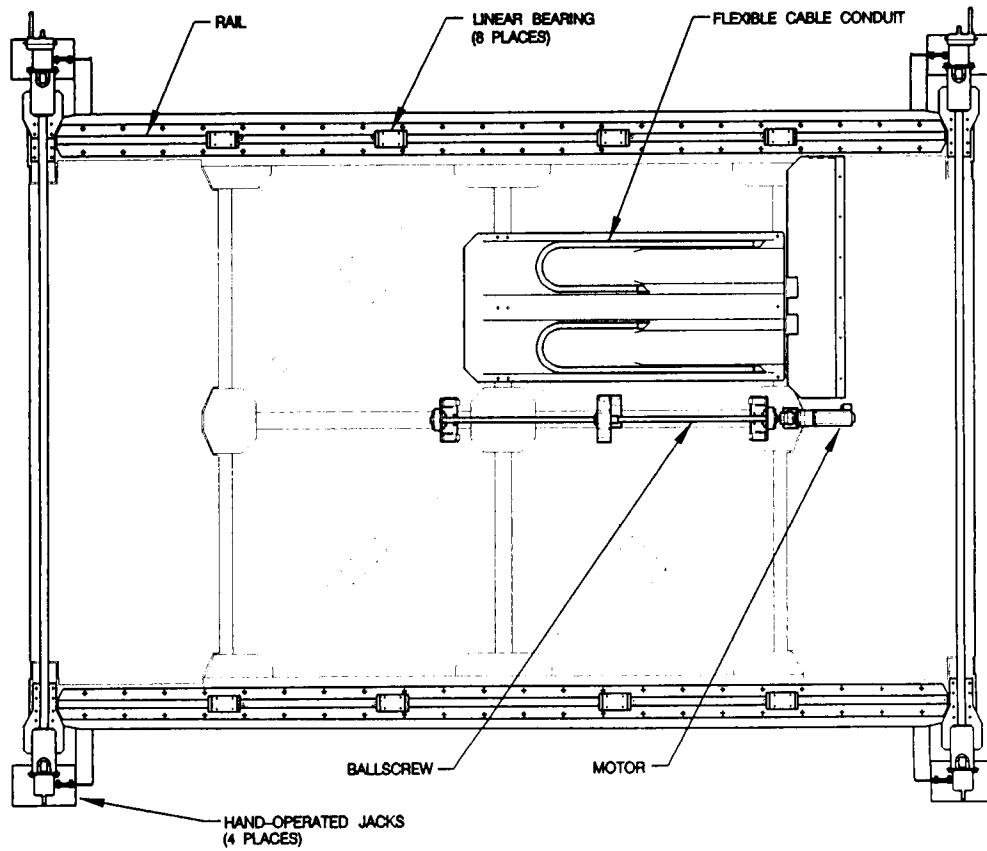
Figure 10: Positioning Base Translation System
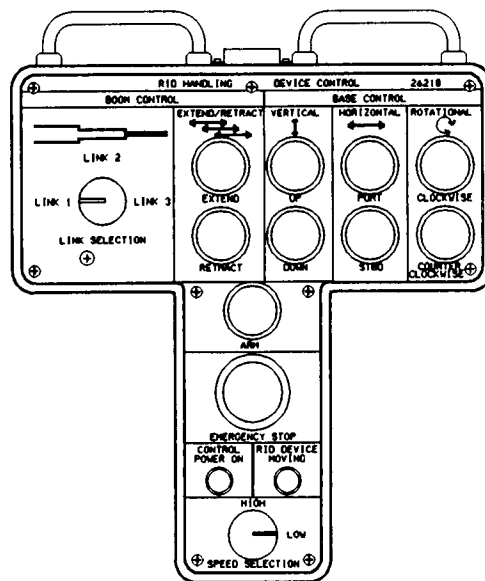
Figure 11: RID Control Pendant
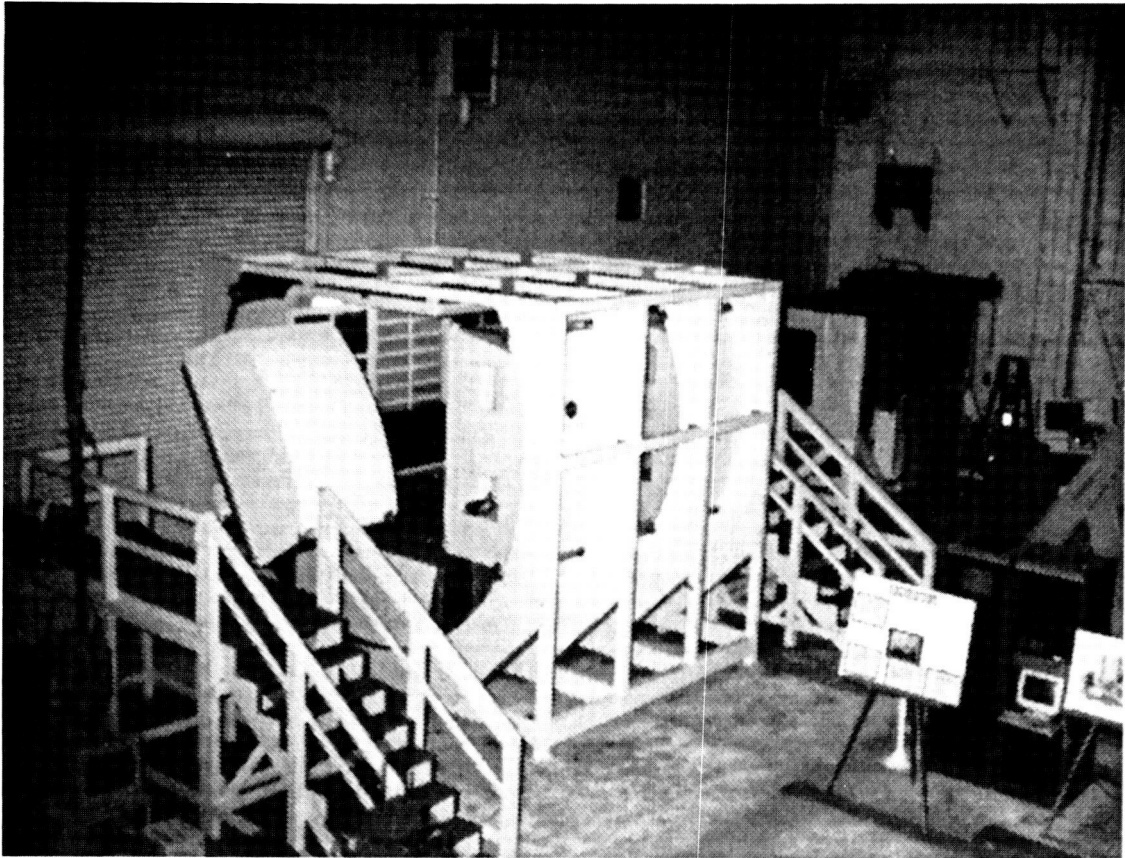
Figure 12: The Module Simulator With Boom Extended Through It
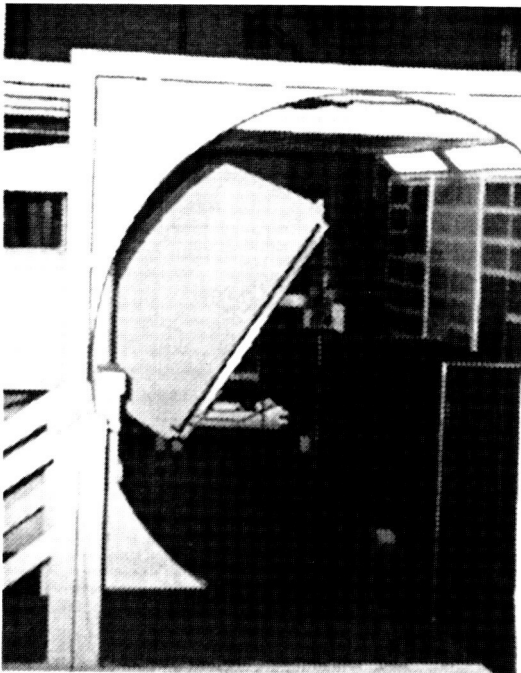
Figure 13: Rack Being Inserted by the Boom
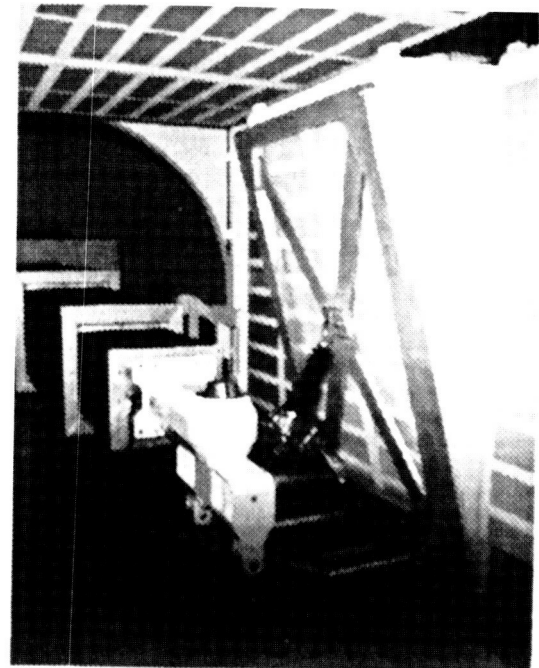
Figure14: Rack Being Installed

LINEAR PROOF MASS ACTUATOR

S. E. Holloway III
NASA Langley Research Center
Hampton, VA 23681-0001

ABSTRACT

This paper describes the mechanical design, analysis, fabrication, testing, and lessons learned by developing a uniquely designed spaceflight-like actuator. The Linear Proof Mass Actuator (LPMA) was designed to attach to both a large space structure and a ground test model without modification. Previous designs lacked the power to perform in a terrestrial environment while other designs failed to produce the desired accelerations or frequency range for spaceflight applications. Thus, the design for a unique actuator was conceived and developed at NASA Langley Research Center. The basic design consists of four large mechanical parts (Mass, Upper Housing, Lower Housing, and Center Support) and numerous smaller supporting components including an accelerometer, encoder, and four drive motors. Fabrication personnel were included early in the design phase of the LPMA as part of an integrated manufacturing process to alleviate potential difficulties in machining an already challenging design. Operational testing of the LPMA demonstrated that the actuator is capable of various types of load functions.

INTRODUCTION

With the development of large space structures, a means of control to eliminate vibrations induced into the structures by disturbances such as plume impingement, docking forces, and crew activity is desired. Also of interest is the ability to study structural behavior of a flight article in a terrestrial environment so that analyses can be verified prior to launch. Hence, it became necessary to design an actuator with multiple functions for spaceflight and terrestrial environments.

The actuator was to satisfy four major requirements: 1) Typically, space structures are extremely lightweight, and some structures can not support their own mass in a terrestrial environment; therefore, the actuator should be lightweight, yet rigid; 2) A major function of the actuator is to damp out vibrations, but equally as important is its ability to excite oscillations in a structure so that reactionary dynamics can be studied; 3) The actuator must be functional in spaceflight and terrestrial environments without being modified; 4) The actuator must perform in the gravity oriented axis and two axes orthogonal to the gravity axis. Together, the above requirements resulted in a challenge that, if successfully met, would contribute significantly to the design of lightweight actuators that could operate in gravity or zero-g environments. An actuator called LPMA was designed, fabricated, and tested that met the above requirements. As a result of this work and its inventive nature, U.S. Patent 5,150,875 entitled "Linear Mass Actuator" was granted on September 29, 1992.

DESIGN

To avoid replicating the deficiencies of previous actuators, a unique and original design was required. After an intense conceptual design phase, a linear mass actuator with a friction drive, powered by DC torque motors, was selected and subsequently called the Linear Proof Mass Actuator (LPMA). A photograph of the assembled LPMA is shown in Figure 1. Designing a friction drive system utilizing DC torque motors solved several
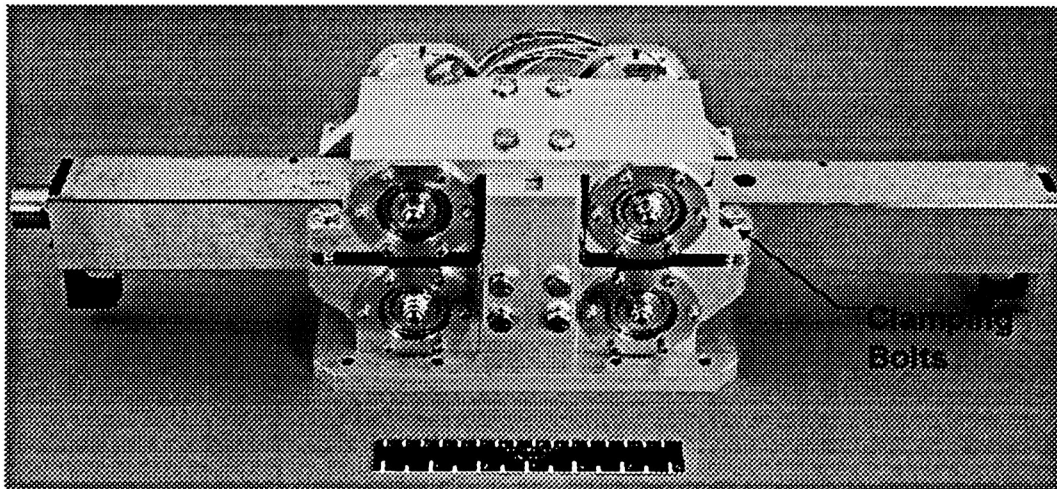

Figure 1. Linear Proof Mass Actuator (NASA Photograph L-89-2126)

problems of previous actuators. Several actuators possessed cogging problems because of gear drives while others were power limited by magnetic field drivers. The combination of DC torque motors and friction drive eliminated these deficiencies, yet the friction drive system requiring tolerances of 2.54×10^{-6} meters (0.0001 inches) created more challenges. The minute tolerances presented a difficult design and fabrication task. With the use of the American National Standards Institute's Dimensioning and Tolerancing document, ANSI Y-14.5M-1982, the difficult tolerancing task was accomplished.

As previously mentioned, the design consists of four major mechanical parts with the Mass being the most precise and critical, fifty-six smaller parts, and fasteners which are shown in Figure 2. The Mass weighs approximately 98 N (22 lb) which is roughly half of the total system weight. Sandwiched between four motor driven shafts, called Rollers, the Mass translates linearly to deliver a force. Friction contact between the Rollers and the Mass is the only drive mechanism. When the four clamping bolts (see
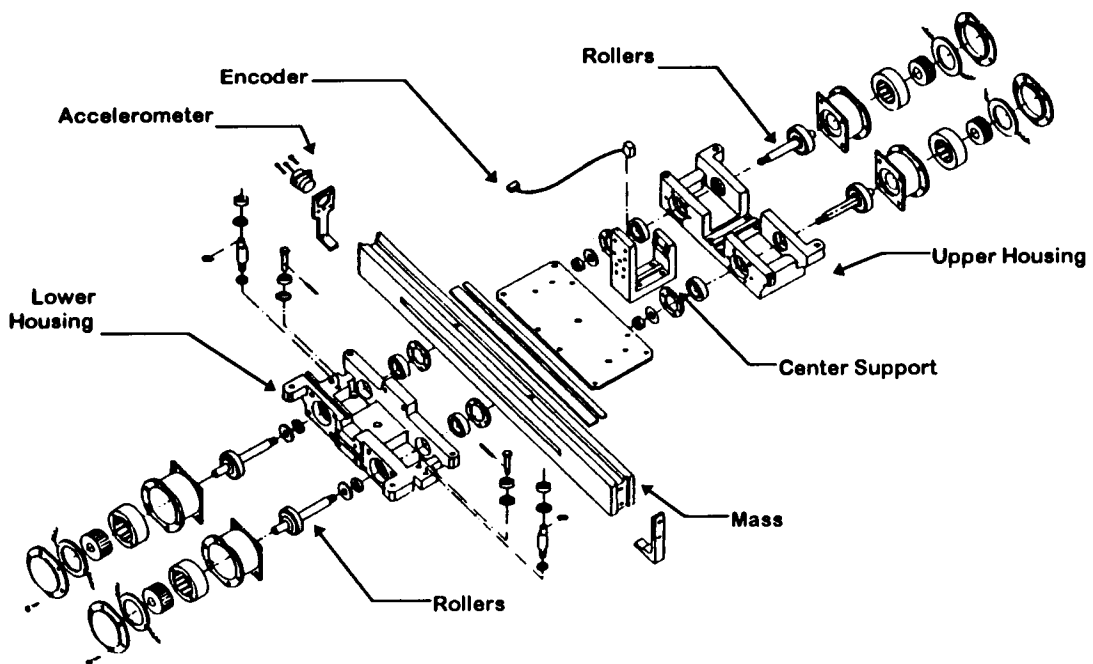
Figure 2. Components of LPMA (2)

Figures 1 and 3) are torqued, the Upper and Lower Housings spring about the Center Support which causes the Rollers to engage the Mass. After the Mass is engaged, an additional preload of 111 N (25 lb) gives the Mass/Roller interface the necessary friction to move the Mass without slipping. The clamping bolts are screwed into locking helical inserts to maintain the proper torque values. The top and bottom Motors, which drive the Rollers, counter-rotate to move the Mass one direction, then they reverse rotation to move the Mass the opposite direction. Figure 3 pictorially illustrates the functioning system. By deleting gears, belts, and hydraulics, this design resulted in improved performance because the Mass traveled in a smoother fashion with no cogging effects. Deleting belts eliminated a mechanism to compensate for decreased belt tension as the belt aged and eliminated concerns over belt breakage. Omitting hydraulics solved potential fluid leakage problems and removed a substantial weight penalty that was not desirable for spaceflight. As a result, the friction drive system for the Mass provides a smooth traveling linear actuator. Since the Mass and the DC Torque Motors determine the ultimate amount of force to be applied to a space structure, Newton's Second Law becomes the governing design equation.

$$F=ma$$

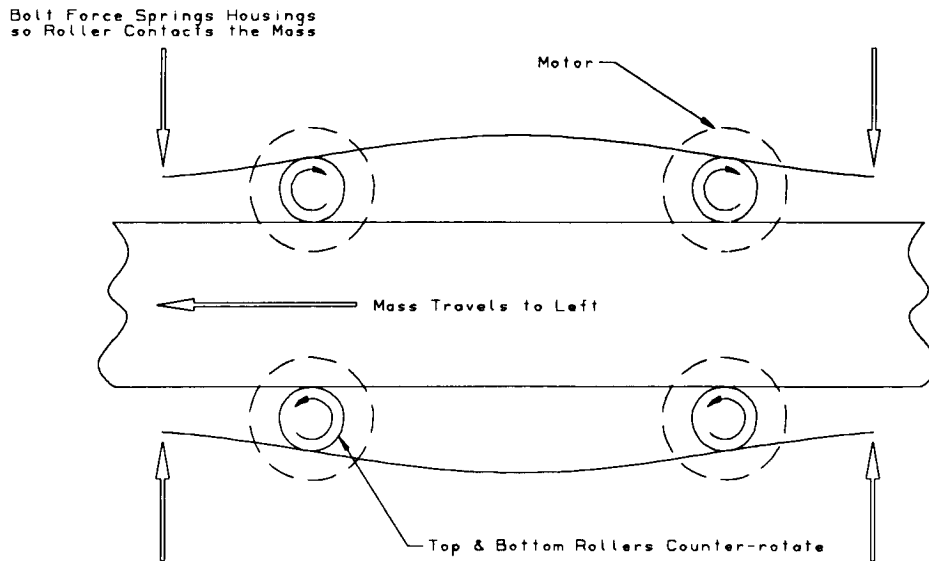Force Delivered = (mass of the Mass) x (Torque Motor Acceleration)

Figure 3. Schematic Representation of Actuator Operation

The actuator was then designed around the Motor-Roller and Mass interface. The length of the Mass determines the available stroke or distance of travel which maximizes the amplitude of motion. The volume of the Mass determines the mass which accelerates to produce the total available force. Therefore, after the Mass was sized, only the motors could vary the force by changing the acceleration.

The Mass is sized at 10 kilograms (22 lb), so when the assembly is oriented vertically, the LPMA delivers 30 N (6.75 lb) of force. When the LPMA is oriented horizontally, it possesses additional force capability which allows delivery of 128 N (28.78 lb). The full stroke of the LPMA is ±15 cm (5.9 inches) with a position resolution of 10 micrometers $(3.94 \times 10^{-4}$ in).

The LPMA can operate in four different modes. The first mode is a position mode where force is delivered to the Mass so the Mass may maintain its positon at the commanded position relative to the LPMA base. This mode is limited by an upper frequency limit which is a function of excitation amplitude and maximum available force. Figure 4 illustrates how the stroke, which is defined in decibels because of its compatibility with the controls analysis, varies with frequency. Stroke is defined in decibels as: db=20log(x/15), where x is the stroke length in centimeters. The second mode is a force mode which is limited at low frequencies by the stroke capability and excitation amplitude. Figure 5 illustrates how the forces vary with frequency. The force
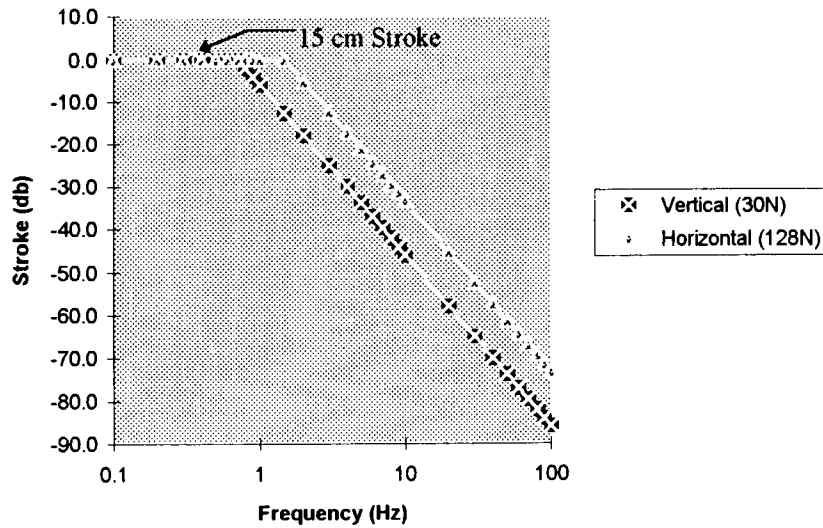
371

LPMA Stroke Curves

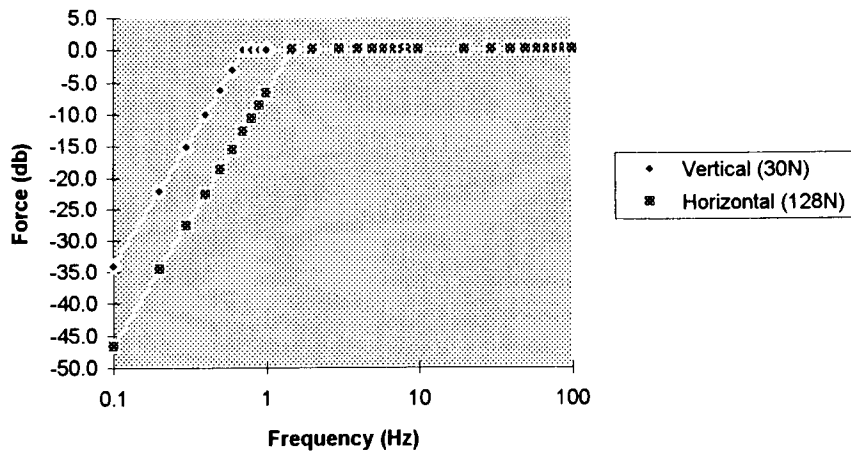Figure 4. Stroke Versus Frequency

LPMA Force Curves

Figure 5. Forces Versus Frequency

curves are again displayed in decibels because of their compatibility with the controls analysis. The third mode is a combination of the position and force modes which gives the LPMA increased performance across the frequency range. The fourth and final

mode is the velocity mode which is used in rare occurrences where constant velocity is required.

The friction drive concept requires a preloaded metal to metal contact between the Mass and the Rollers. This type of contact presents problems with galling and wear. To avoid galling,17-4 PH Corrosion Resistant Steel (CRES) heat treated to 496°C (925°F) to achieve a Rockwell Hardness of C47 was selected for the Mass, and 15-5 PH CRES heat treated to 538°C (1000°F) to achieve a Rockwell Hardness of C36 was selected for the Rollers (shown in Figure 6). The durability of 17-4 on 15-5 is considered very good and the heat treatments were chosen so that the Mass, which is very costly to produce, is much harder than the Rollers. Therefore, any detrimental wear will occur on the Rollers, which are much cheaper to replace.
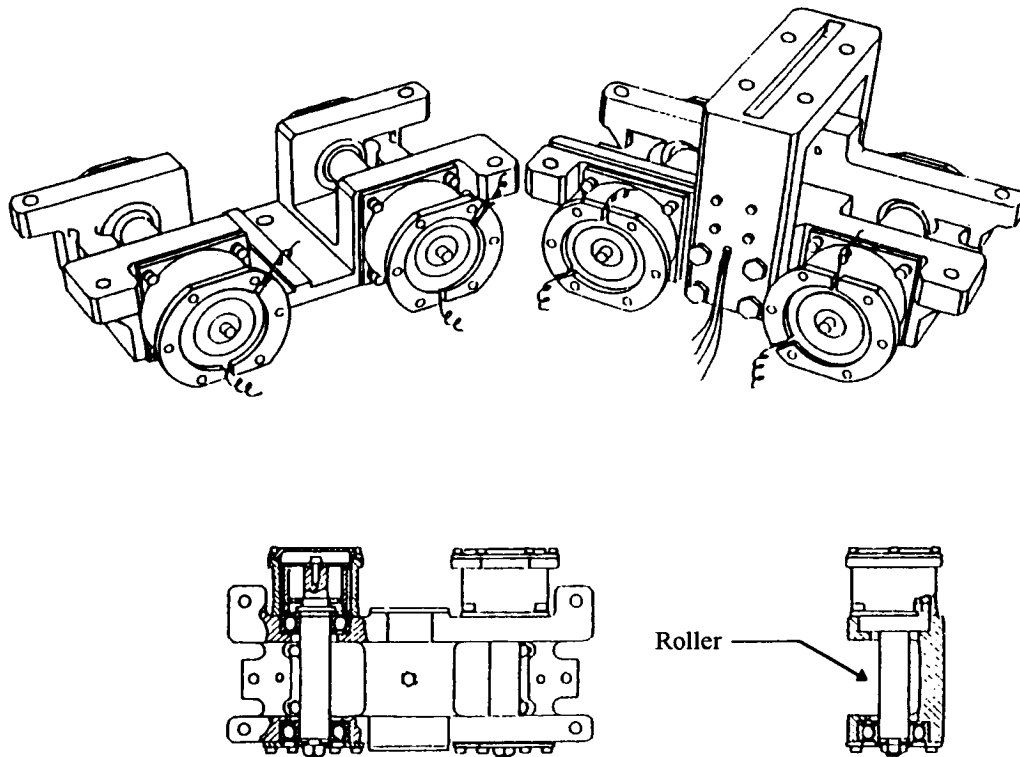
Figure 6. Lower Housing (Left) and Upper Housing (Right) (1)

ANALYSIS

The structural analysis of the LPMA consisted of a finite element model created using solid elements for the Upper Housing, Center Support, and Mass, beam elements for the Rollers, and spring elements for the Roller Bearings. The Lower Housing is more massive and obviously stiffer than the Upper Housing, so the Lower Housing was

assumed to be a rigid structure in this analysis. As a result, the modeling concentrates on the Upper Housing and its mating parts.

Because the LPMA relied on friction to drive the Mass, the Mass and Rollers necessitated a metal to metal non-slipping interface. The design requirements specified zero tolerance which ensures a metal to metal fit that is nearly impossible to manufacture; therefore, the parts were toleranced so the minimum tolerance was zero and the maximum tolerance between the Rollers and the Mass was 0.029 cm (0.0114 in). For any situation other than a perfect fit, a certain amount of bolt preload is necessary to clamp the Upper and Lower Housings, which contain the Rollers, to the Mass for engagement. The worst case preload of 15,123 N (3400 lbs) is required for the maximum tolerance of 0.029 cm (0.0114 in) to guarantee metal to metal engagement. Figure 7 illustrates the displacements and Figure 8 illustrates the deformations of the Upper Housing and Center Support under the 15,123 Newton (3400 lbs) preload assuming an infinitely stiff Lower Housing. The Von Mises stresses
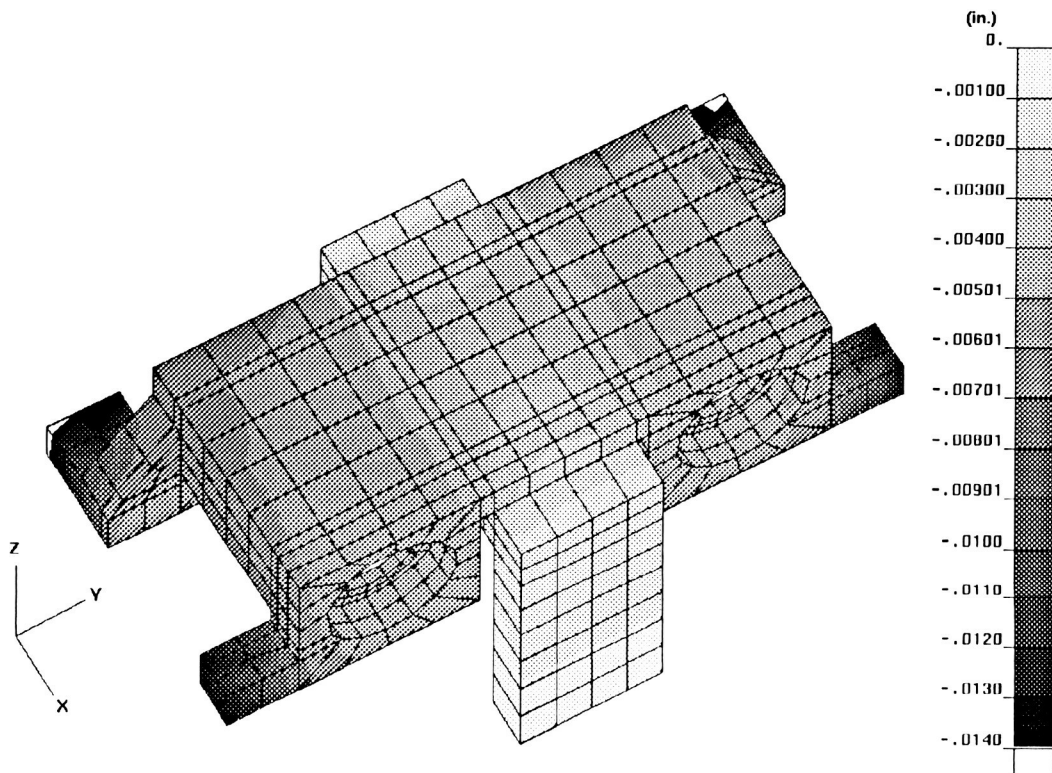

Figure 7. Upper Housing and Center Support Displacements for 3400 lbs Preload

for the Upper Housing were below the yield 241,325 kPa (35 ksi) of Aluminum 6061-T6 except at two bolt locations. The stresses at these bolt locations are artificially high because the bolt loads are applied as point loads. Figure 9 shows the stresses for the preload state indicating the higher stresses at the attachment feet of the Upper Housing. Detailed calculations at the bolt interface area indicate that the actual stress
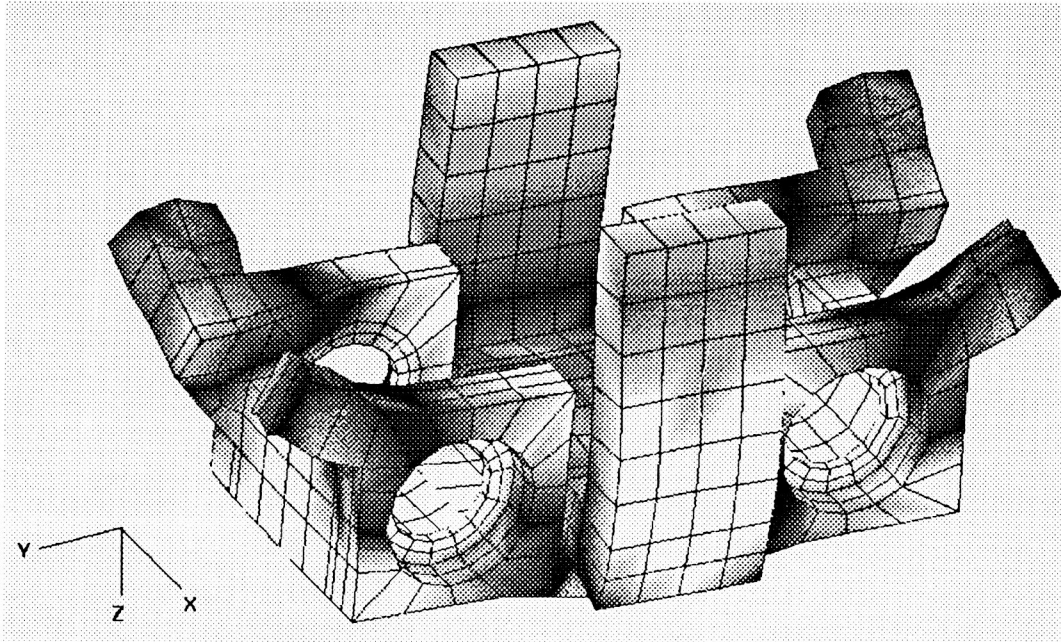
Figure 8. Upper Housing and Center Support Deformations for 3400 lb Preload
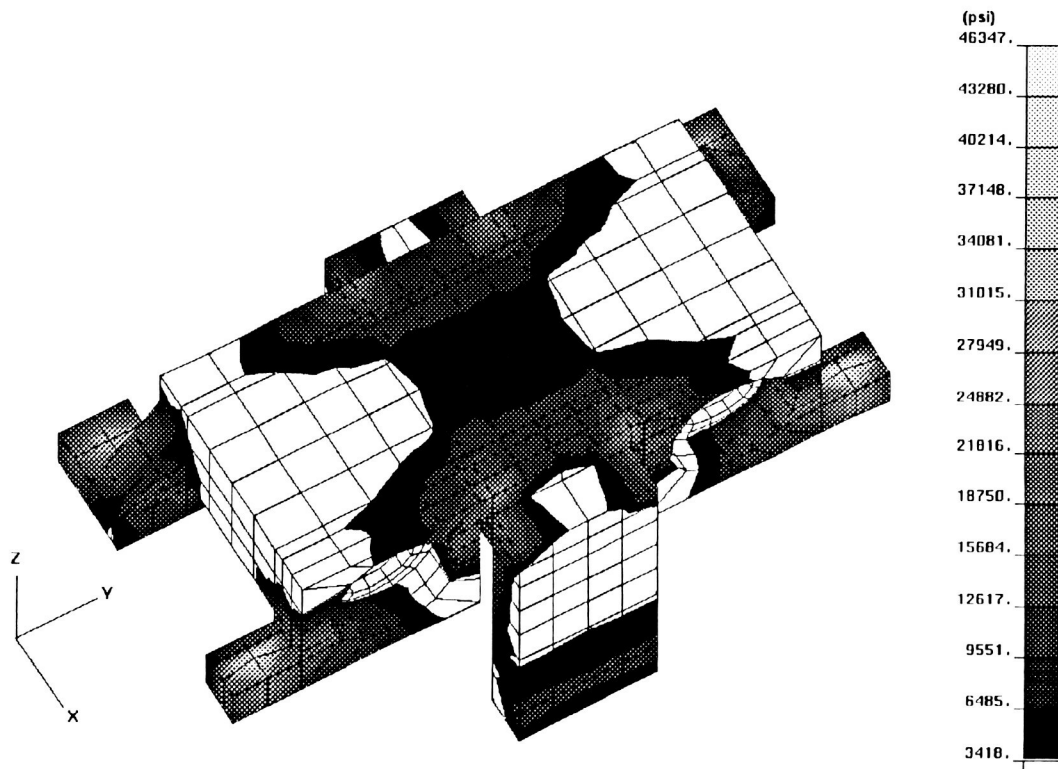

Figure 9. Upper Housing and Center Support Von Mises' Stresses for Preload Condition

was 166,859 kPa (24.2 ksi) compared to the artificially high stress of 319,0238 kPa (46.3 ksi) in Figure 9.

As mentioned previously, a metal to metal non-slip interface was the requirement for the friction drive to work. The analysis determined the bolt loads necessary for metal to metal contact. The Mass must deliver the maximum force without slipping on the Rollers. A conservative coefficient of friction of 0.3 was chosen versus the typical value of 0.58 for steel on steel. Using this extremely conservative value, only 111N (25 lbs) of additional bolt force were required to produce sufficient contact force, which produces minimal stresses in the rollers, for operation at maximum acceleration. As a result, a maximum load of 15,234 N (3425 lbs) was required to obtain a metal to metal non-slip interface for the LPMA for its worst case tolerance where the maximum gap existed between the Rollers and the Mass.

FABRICATION and ASSEMBLY

The philosophy of the program was geared to manufacturing one spaceflight engineering model and five subsequent spaceflight prototypes for ground testing. Utilizing spaceflight design and fabrication practices for the engineering models increased manufacturing costs. The project rationale demanded this philosophy so that a flight article only necessitated fabrication and flight qualification if an opportunity for a space mission became available.

One of the newest engineering phrases of the 1990's is "integrated product design." This is a concept where all disciplines involved in the final product work the task together from start to finish to produce a cheaper and higher quality product in a shorter amount of time. The LPMA project team practiced this philosophy from the start of the program in early 1986 to its completion in June of 1990. The Lead Fabrication Technician participated in the design phase recommending materials, tooling cuts, and design changes. The monetary savings were numerous and significant, and the model was produced quicker and cheaper than envisioned. As an example, to reduce the high costs of spaceflight fabrication, all small parts were purchased or machined simultaneously for all six assemblies prior to completion of the design of the Upper and Lower Housings. This course of action was risky because the possibility of scrapping hardware because of design changes to the housings existed; yet, the smaller pieces were simpler and less likely to change. The gamble paid off as the bulk machining of the smaller hardware pieces saved tooling costs because repetitive tooling set up operations were avoided. In addition to the fabrication time saved, Quality Assurance (QA) time to inspect the hardware was also reduced for the same reasons. As a result of project budget cuts, only two complete prototype assemblies were manufactured; therefore, four assemblies of smaller hardware became spare parts.

After assembling the engineering model, the Rollers were noticeably scored after a press fitting through the precision bearings. Using the integrated product design philosophy within the project team, a new assembly method was developed using the spare parts. The new process submerged the Rollers in liquid nitrogen for five minutes

to shrink the Roller diameters. The cold Rollers were assembled with the warm Barden Precision Bearings producing a loose fit. After insertion through the bearings, the Rollers warm up to their original dimensions which produce the desired interference fit, and the Rollers remain undamaged.

In order to ensure smooth travel and optimum performance, the Mass must be designed precisely and machined accurately within the miniscule tolerances provided. The Mass' design required an expert machinist for fabrication to hold the rectangular 56.6 cm (22.3 in) long piece of 17-4 PH corrosion resistant steel flat and parallel to 0.0002 cm (0.0001 in), so it would maintain frictional contact with the Rollers at all times.

TESTING

Due to low priority, the LPMA was developed over a period of approximately five years. The customers of LPMA finally established a drop dead delivery date for the hardware. This delivery date, coupled with the fact that the electronics/software design and fabrication lagged the mechanical development, left little time for testing. The only mechanical testing accomplished was that testing done while verifying the software and control system. Even through this limited testing, the LPMA demonstrated that the Mass would deliver forces by several methods over a frequency range of 0 to 100 Hz. The LPMA displayed capabilities to move in response to commanded displacements, velocities, or accelerations. The input curves could also simulate sinusoidal, step, and saw-tooth functions. Despite the limited testing, the LPMA proved this friction drive concept and was used at a ground test facility to be discussed later in this paper.

LESSONS LEARNED

Since the engineering model was intended to be a learning experience for subsequent prototypes, the project team was able to improve the design and fabrication deficiencies. Numerous improvements, which could be applied to future prototypes, were derived from the experience.

The first and most productive lesson learned was using the integrated product design philosophy. By integrating the lead fabrication technician into the design team, many problems were eliminated before they became problems. The engineer and fabrication technician frequently reviewed the design in a "Coyote Team" manner. Coyote Teams differ from "Tiger Teams" in that a Tiger team attempts a solution to an existing problem; whereas, a Coyote team searches for potential problems before they impact the work. Time and money were saved due to the technician's suggestions on material selections and tooling cuts on the hardware. He also offered a suggestion on the dimensional verification process of the housings and center support. Since aluminum alloy tends to warp after an abundance of machining, he suggested checking the dimensions while the parts were in their tooling fixtures. The warpage was very small but large enough to fail the QA inspection; yet, when assembled, torquing the fasteners

in the assembly eliminated the warpage. His suggestion saved the time and money of rework or a new set of hardware.

For spaceflight aluminum parts, anodization and chemical film are two widely used protection processes. Anodization offers good abrasion resistance while chemical films protect better against corrosion. Typical thicknesses of sulfuric anodization are 0.0001-.002 cm (0.00005-0.001 in) while chemical film thickness is zero. Sulfuric anodization was chosen for its inherent abrasion protection since many of the LPMA parts were metal to metal fits. One problem with sulfuric anodization was entrapment. It is common knowledge that the solution can cause problems in screw threads and inserts, and that the threaded holes should be protected from the solution. After anodizing the Upper and Lower Housings, a film of 0.1 cm (0.04 in) was measured in the bearing bore holes. The hole diameters were 4.7 cm (1.85 in) and entrapment was never envisioned in a hole this large. Figure 10 illustrates the area of entrapment. The parts had to be remachined to remove the excessive film and the protection process was switched to chemical film treatment which has zero dimensional change. So, for hardware with three place decimal tolerances, careful consideration should be given to choosing anodization over chemical film treatment.
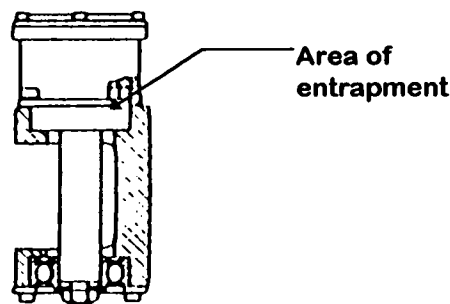

Figure 10. Area of Anodization Entrapment. (2)

The Roller and Mass interface was the most important interface of the actuator. Heat treatments were chosen to avoid galling and to ensure that excessive wear would not occur to the most expensive part, the Mass. The heat treatments were chosen using average values. After fabrication, it was discovered in MIL-HDBK-5, Metallic Materials and Elements for Aerospace Vehicle Structures, that each heat treatment has a range of hardness values for a particular temperature. As a result, it was possible for the Mass to be softer than the Rollers which was not desirable. Both parts were checked, and their intended hardness values were in a desirable range. To ensure that the Roller is always softer, the heat treatment should be changed to H1150 or H1150M, which yields hardness values no higher than C37 and C30, respectively.

After pressing the precision bearings on the Rollers, scoring was witnessed on the Rollers. The scoring would have a detrimental effect on the friction contact between the Rollers and the Mass, so a new installation procedure, which thermally decreases the Roller diameters by submerging them in liquid nitrogen, was utilized. While the

378

Rollers are still cold, they are inserted through the bearings with no contact. As the Rollers warm up, contact is achieved. For spaceflight, a better solution would be to redesign the Roller by stepping down the diameter where the Mass contacts the Rollers. As a result, the Mass height would increase by twice the radial decrease of the Rollers. This solution avoids the liquid nitrogen process which causes the Rollers to frost after installation, and the bearing lubricants may be contaminated from the melted ice.

An adjustable shaft with a bearing was located on the Lower Housing with the bearing running in a groove on the lower portion of the Mass to eliminate lateral motion created by tolerance stackup. The adjustable shaft was a cam by design so the full diameter of the cam was utilized at the maximum tolerance. After adjusting the cam on the assemblies, it became apparent that the cam should have been much larger in diameter to give a better feel for alignment adjustment. Figure 11 shows the cam which should have its diameter increased for better performance.
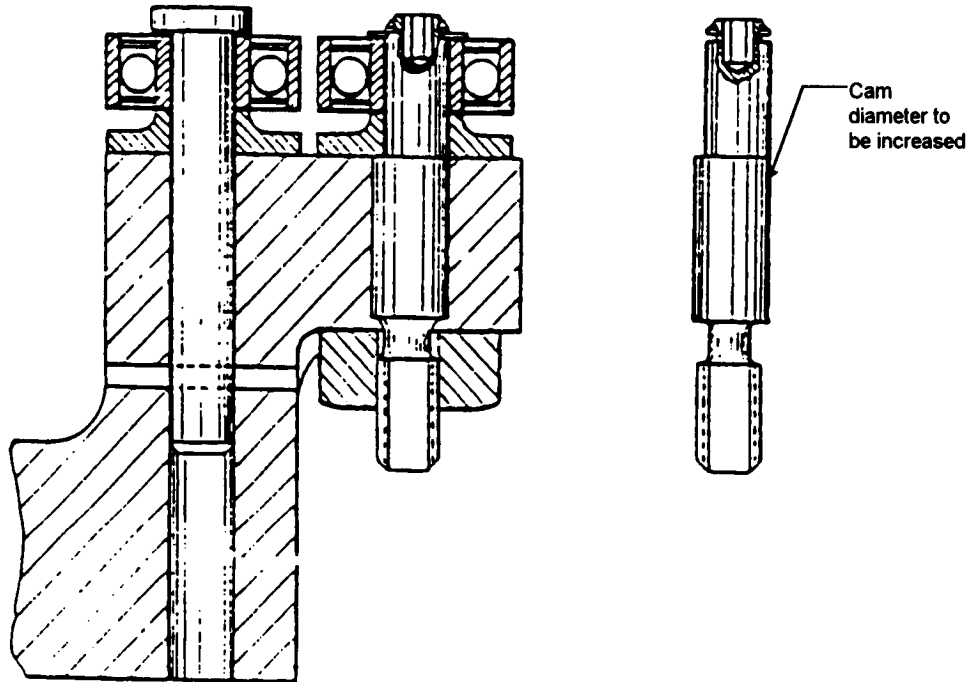

Cam
diameter to
be increased

Figure 11. Views of Cam and Cam Assembly. (1)

Another lesson learned pertains to using commercial parts. On the LPMA, the D.C. torque motor parts were supposed to be interchangeable which was a bonus because the LPMAs were designed for total interchangeability. After dimensionally checking the lot of twenty-four motors, it was documented that the motor parts were not dimensionally interchangeable. These commercial parts were verified early in the fabrication process which allowed time to re-bore the inner diameters of the motors so

379

that the whole set was completely interchangeable. As a result, commercial parts should always be verified for interchangeability despite the claims of product literature.

To acquire the flatness needed for the Mass to translate properly, a uniform flatness requirement of 0.0005 cm (0.0002 in) was needed on the Roller sides of the Mass. To accomplish this requirement, the Mass was fixed to a granite table where bluing ink was applied to one Roller surface. The surface was then hand-lapped with a 0.00038 cm (0.00015 in) flatness lapping stone until the ink was removed; thus, meeting the flatness requirement. Since new machines can achieve tighter tolerances, most hand operations of the past have become obsolete. Today's current machining technology brought the Mass within 0.002 cm (0.001 in) of the Mass' goal, so the lapping process was shortened by only having to remove 0.002 cm (0.0008 in) of material. As a result, the art of hand-lapping still had not lost its niche in today's high technology world.

CONCLUSION

The LPMA was used as a frequency exciter for a large space structures support fixture at the top of Building 1293 at NASA Langley Research Center. To ensure structural soundness of the support fixture, the LPMA was attached and operated to excite this instrumented fixture. By observing and comparing frequency responses of the fixture, the structural integrity was verified without the cost of load testing. As long as the LPMA is connected to the fixture, structural verification could be done by turning on its power.

ACKNOWLEDGEMENTS

I would like to acknowledge those who contributed to the design and analysis of the LPMA. Irby Jones conceived the mechanical design and Jim Miller conceived and engineered the electrical design. Vaughn Behun and Lewis Goodrich were instrumental in developing a preliminary design concept. Ed Crossley served as a consultant during final design, and he checked all mechanical design drawings. Calvin Davis, Lead Technician, directed the LPMA fabrication, and he contributed suggestions on material selections, tooling cuts, and assembly procedures which made the fabrication and asembly processes much simplier. Genevieve Dellinger completed the structural analysis using finite element model techniques. She created Figures 7,8, and 9 in this paper during her analysis. Without the contributions of the above, this paper would have not been possible.

REFERENCES

(1) Holloway III, S.E.: and et al.: U.S. Patent No. 5,150,875, "Linear Mass Actuator", September 1992

(2) Holloway III, S.E.: and et al.: "Technical Support Package for Tech Brief LAR-14352, Friction-Driven Linear Mass Actuator", May 1993.

/ 9 9 5 / 3 0 8 9 /

4 0 5 8 1 6
12 p.

Load Measurement System
With Load Cell Lock-Out Mechanism

Thang Le*
Monty Carroll*
Jonathan Liu*

Abstract

In the frame work of the project Shuttle Plume Impingement Flight Experiment
(SPIFEX), a Load Measurement System was developed and fabricated to measure the
impingement force of Shuttle Reaction Control System (RCS) jets. The Load
Measurement System is a force sensing system that measures any combination of
normal and shear forces up to 40 N (9 lbf) in the normal direction and 22 N (5 lbf) in the
shear direction with an accuracy of ±0.04 N (±0.01 lbf). Since high resolution is
required for the force measurement, the Load Measurement System is built with highly
sensitive load cells. To protect these fragile load cells in the non-operational mode
from being damaged due to flight loads such as launch and landing loads of the Shuttle
vehicle, a motor driven device known as the Load Cell Lock-Out Mechanism was built.
This Lock-Out Mechanism isolates the load cells from flight loads and re-engages the
load cells for the force measurement experiment once in space. With this highly
effective protection system, the SPIFEX load measurement experiment was
successfully conducted on STS-64 in September 1994 with all load cells operating
properly and reading impingement forces as expected.

Introduction

The Space Shuttle is maneuvered in space by RCS jets. These jets can produce
significant plume impingement forces on surfaces that may be in the path of the jet
plume. Among these surfaces are the solar arrays on the planned International Space
Station Alpha or the Russian Mir Station. Due to the uncertainties of the analytical
plume force predictions of the Orbiter RCS jets in the vacuum of high Earth orbit and
the lack of direct empirical measurements, a project called SPIFEX was created.

The SPIFEX project consists of a 0.343-meter (13.5 in) diameter by 10-meter (32 ft)
long boom with an avionics package and plume sensor array attached to one end. In
operation, the Orbiter Remote Manipulator System (RMS), robot arm, grapples the
other end of the boom providing power and communication and positions the plume
sensor array over an RCS jet for a data point firing. The plume sensor data is recorded
in the SPIFEX avionics for later downloading.

---

* Mechanical Systems Laboratory, Lockheed Engineering & Sciences Company, Houston, TX

A primary design factor for this project was minimizing cost. This factor led to no redundancy in the SPIFEX operational avionics or mechanisms. Three motor-driven mechanisms were used on SPIFEX: (1) a Two-Axis Drive to finely position the sensor array at the end of the boom, (2) a Lock-Down device to secure the Two-Axis Drive and sensor array for Space Shuttle launch and landing, and (3) a Load Cell Lock-Out Mechanism to isolate the Load Measurement System from Space Shuttle launch and landing loads. The Load Cell Lock-Out Mechanism is the topic of this paper.

Lock-Out Control System

The Lock-Out mechanism of the Load Measurement System is driven with a low-power DC gearmotor and with the end-to-end travel controlled by limit switch feedback to the SPIFEX avionics. Due to limited 28-VDC power allocation for SPIFEX, a low-power DC gearmotor with a high 4126:1 gear ratio and 13.5 N-m (120 in-lbf) peak torque permitted the use of a small 28-VDC relay drive with less than 1-Amp capacity. This combination provided a reasonable operation time of 15 seconds for the Load Cell Lock-Out to open or close. A DC motor was chosen to drive this mechanism because of the simplicity of the low-level control system and the simple open/close state of the mechanism. A high-level means of controlling the Lock-Out mechanism was provided from the SPIFEX avionics through a serial link to a Space Shuttle crew cabin laptop computer.

Load Measurement System

The purpose of the Load Measurement System is to measure the magnitude and to determine the direction of the plume force once the Load Measurement System is placed in the plume field. The Load Measurement System consists of two major components: a flat panel to catch the jet plume and an array of load cells to sense the plume force. The panel is called the Load Plate, and the load cell array is known as the Load Ring (Figure 1).

The Load Plate is a rectangular surface that provides a flat area to capture the impingement of the RCS jet in the plume field. The Load Plate has a honeycomb structure of aluminum. Woven graphite sheets are used for the plate close-outs for all sides. This method of construction provides the necessary stiffness for the Load Plate while minimizing its mass. The Load Plate minimal mass is required so that the Load Measurement System can be responsive to the brief plume forces. A natural frequency of 100 Hz or higher is required for the plate. The light-weight plate also prevents the load cells from being subjected to strenuous forces during the non-experiment phases.

The Load Ring has six uniaxial strain gage load cells arranged in a circular pattern. The load cells are installed with a universal joint at each end to form six struts between the Load Plate and the base structure of the Load Measurement System. This arrangement permits the Load Plate to have 6 degrees of freedom (DOF) movement

with respect to the base structure when lengths of the strut vary. In other words, once a force is applied on the Load Plate, the infinitesimal movement of the Load Plate can be detected by the reaction forces in the six struts. The reaction forces are the actual compression or tension forces sensed by the individual load cells within the struts.
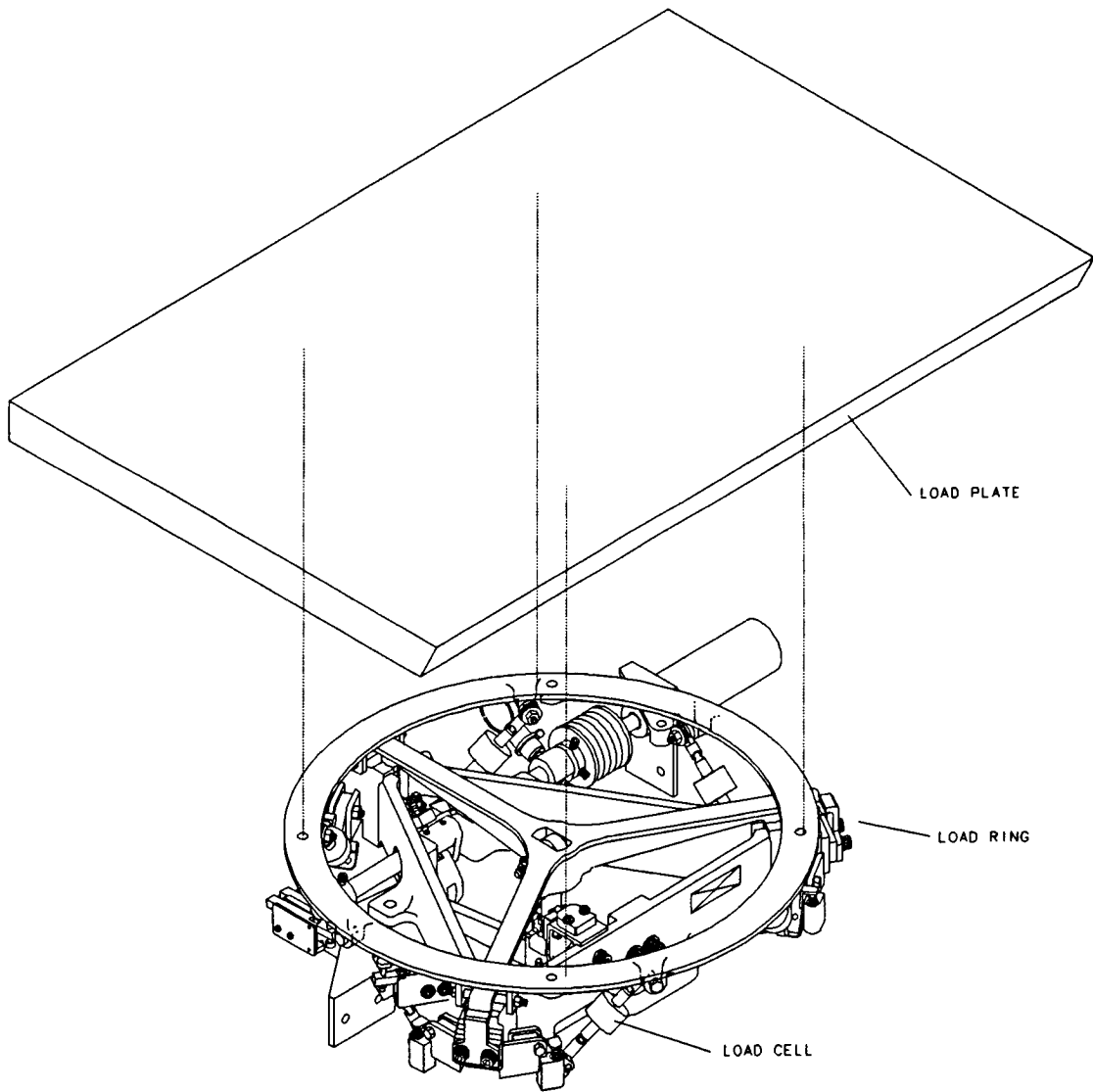

LOAD PLATE

LOAD RING

LOAD CELL

Figure 1. Load Measurement System

The universal joints at the load cell ends prevent a bending moment from being transferred and allow nothing but strictly axial load through the load cells. The six struts with universal joints form a statically determinant structure from which the total force exerted on the Load Plate can be derived from the individual axial forces in the load cells. Thus, the input force can be computed from the force readings in the six

load cells to yield three force components and three moment components of the applied force.

The Load Ring and the Load Plate are held together by several structural members as illustrated in Figure 1. A majority of these members are made from aluminum because of its light weight. A few members are made of stainless steel where large deflection is not desirable.

Force Calculation

To calculate the external force, **FX, FY, FZ**, and moments, **MX, MY, MZ**, acting on the Load Plate, the six load cell force readings are decomposed into component **x-y-z** forces using the **x-y** connection position of the universal joints and orientation of the load cells. The component forces are then summed into composite **X-Y-Z** forces acting on the Load Plate. The composite **X-Y-Z** moments acting on the Load Plate are calculated by summing the component forces times the distance from the axis of interest. The axis of interest is defined by the offsets, **Xoff, Yoff, Zoff**, from the Load Measurement System origin. The origin (0,0,0) is defined at the **x-y** center of the circle of load cell struts and the **x-y** plane that passes through the load cell upper universal joint pivot points. The resulting matrix equation is as follows:

$$
\begin{bmatrix} FX \\ FY \\ FZ \\ MX \\ MY \\ MZ \end{bmatrix} = T \cdot F - \begin{bmatrix} FXoff \\ FYoff \\ FZoff \\ MXoff \\ MYoff \\ MZoff \end{bmatrix}
$$

where **F** is the vector of six force readings of the load cells, and **T** is the constant matrix describing the Load Ring geometry. The matrix equation also shows where a static force or moment offset can be removed from the result. Refer to the notes at the end of this paper for the complete matrix derivation.

Load Cell Lock-Out System

The purpose of the Load Cell Lock-Out System is to provide an alternate load path for the system so that the force passing through the load cells from the Load Plate to the base structure can be minimized during the harsh vibration phase of launch and landing of the Shuttle vehicle. During this vibration period all load cells are isolated, or locked, for protection. The load cells then can be returned to the unlocked configuration for operation during the load measurement experiment.

The Load Cell Lock-Out system is an over-center mechanism driven by a DC gear motor (Figure 2). The upper end of each load cell is connected to the Load Plate via a universal joint. The lower end of a load cell is connected to a linkage, also, through a universal joint. In the operational, unlocked position, the linkage is spring loaded against a hard stop (Figure 3). The Load Measurement System is then subjected to plume forces for force measurement in this configuration, and all six load cells act as the primary load path from the Load Plate to the base structure.
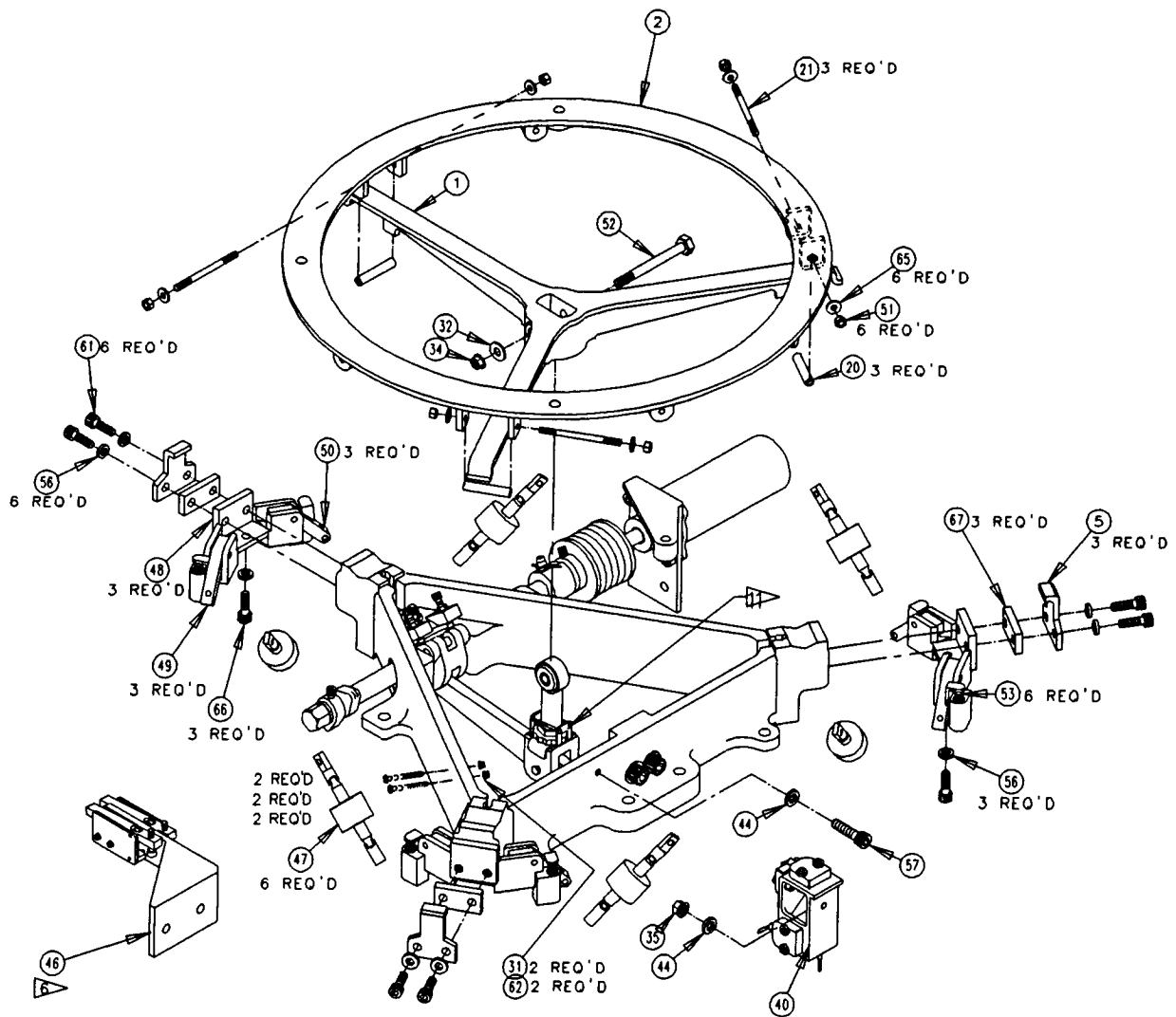
Figure 2. Load Cell Lock-Out Mechanism

Once in the non-operational locked mode, a set of three hooks reach up and clamp down the Load Plate to rigidize the plate to the base structure. In this configuration, the linkage at the load cell lower end compresses the spring to separate the load cell lower

end from the hard stop to minimize the load transferred through the load cells. The clamping hooks act as the primary connection for load transferred from the Load Plate to the base structure. When the Load Measurement System is returned back to the operation mode, these clamping hooks are completely separated from the Load Plate so that only the load cells are subjected to the energy transfer.
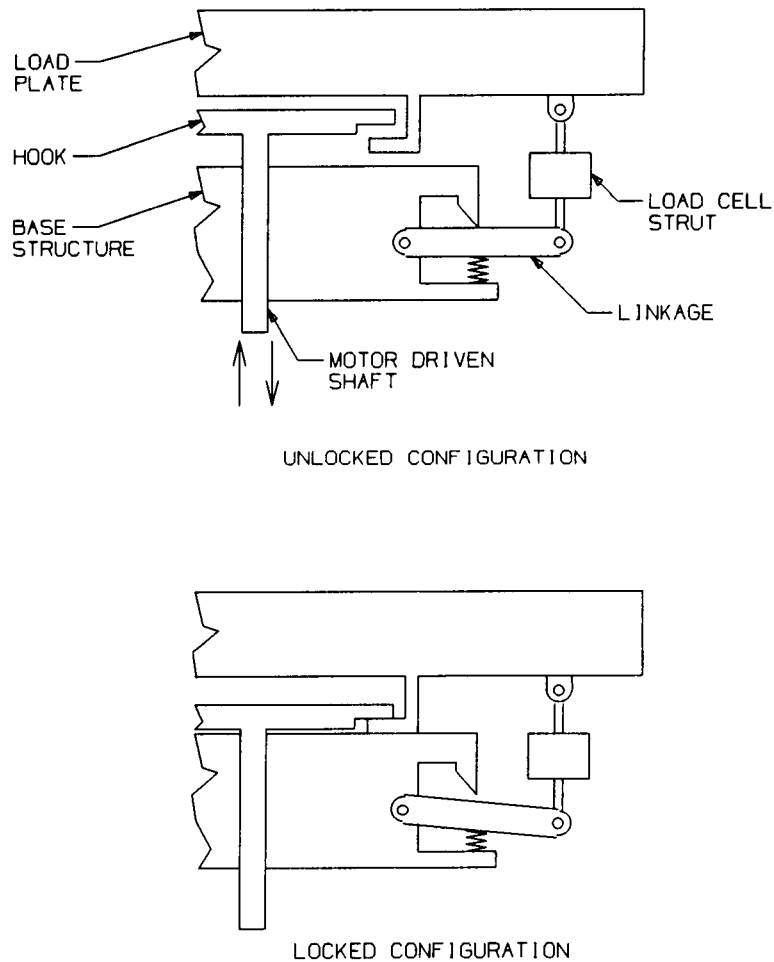

UNLOCKED CONFIGURATION

LOCKED CONFIGURATION

Figure 3. Load Cell Lock-Out System Schematic

Furthermore, the linkage springs are preloaded in such a way that when the load cells are compressed in the locked position, the spring compression force is equal to the load cell full-scale capacity. Therefore, the load cells measuring capability is maximized. The linkage spring system also provides a means of overload protection during the operation mode should the magnitude of the applied force exceed the spring preload. In this case, the spring is compressed, and the force magnitude passing through the load cell is confined.

All linkages and pivot pins in the drive system are made from stainless steel for higher strength. The DC gear motor has a high-ratio gearhead and is deactivated by limit switches once the mechanism is in a complete locked or unlocked state. Additional features include adjusting screws and a pip pin. Six spring adjusting screws allow the fine tuning of the spring preload at the linkages. Another six position adjusting screws provide the system with a means of alignment for the orientation of the Load Plate with respect to the base structure. The pip pin is used for quick disengagement of the motor from the shaft. This disconnection permits the mechanism to be manually actuated as desired using a standard 7/16 hex wrench.

System Performance on STS-64

The SPIFEX mission on STS-64 collected data for as many as 105 test points. Force measurement data were recorded in terms of voltage readings by the load cells and by their interpreted axial force in the individual load cells. All load cells were locked prior to payload installation and were not unlocked for the experiment, in orbit, until about eight weeks later. During the experiment, all six load cells were operational and reading forces properly. With the force magnitudes in all six load cells recorded, the composite force applied on the Load Plate can be calculated. A typical composite force of normal direction to the Load Plate is illustrated in Figure 4. The rectangular Load Plate has a dimension of 0.33 m by 0.51 m (13 in. by 20 in.). The force exerted per unit area can be easily obtained.
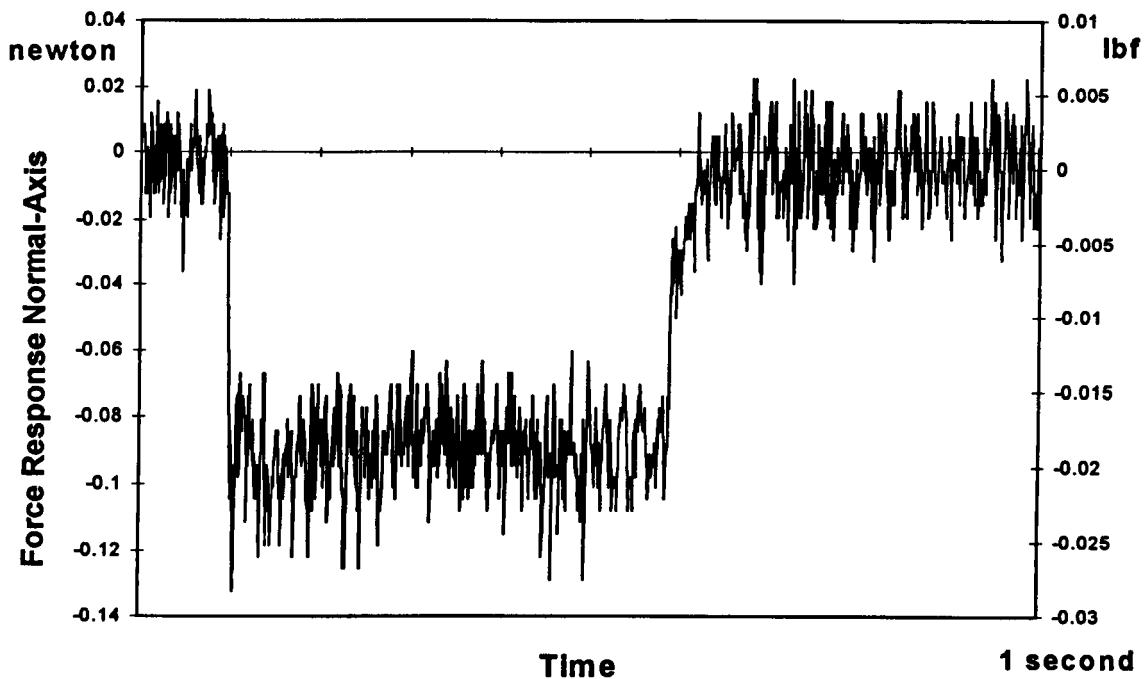

Figure 4. Typical Normal Composite Force Response

Conclusion

The design work of the Load Measurement System was begun in June 1992. The system design was then presented at the SPIFEX Preliminary Design Review in October 1992 and at the SPIFEX Critical Design Review in July 1993. Fabrication of two complete units (one qualification unit and one flight unit) was completed in March 1994. Photographs of the unit prior to installation on the SPIFEX boom are shown in Figure 5. The system was flown on the OV-103 (*Discovery*), STS-64 mission, in September 1994.

The Load Measurement System has successfully collected plume force data. All load cells endured the harsh environment of launch and landing conditions and were completely functional during flight and postflight. Preflight and postflight calibrations of the system indicate no degradation of the force measurement capability and its sensitivity. This fact illustrates that the load cells were efficiently protected by the Load Cell Lock-Out System and its Motor Controller.

The design of the 6-DOF force measurement platform utilizes only uniaxial load cells to measure all three force and three moment components as opposed to using complex multiaxis load cells. This concept can be adopted for various force torque measurement applications. The Lock-Out Mechanism idea can also be used to protect fragile instruments under severe conditions to ensure their functionality during the operating mode.

Acknowledgments

The authors wish to thank the SPIFEX team, which provided valuable support throughout the project.
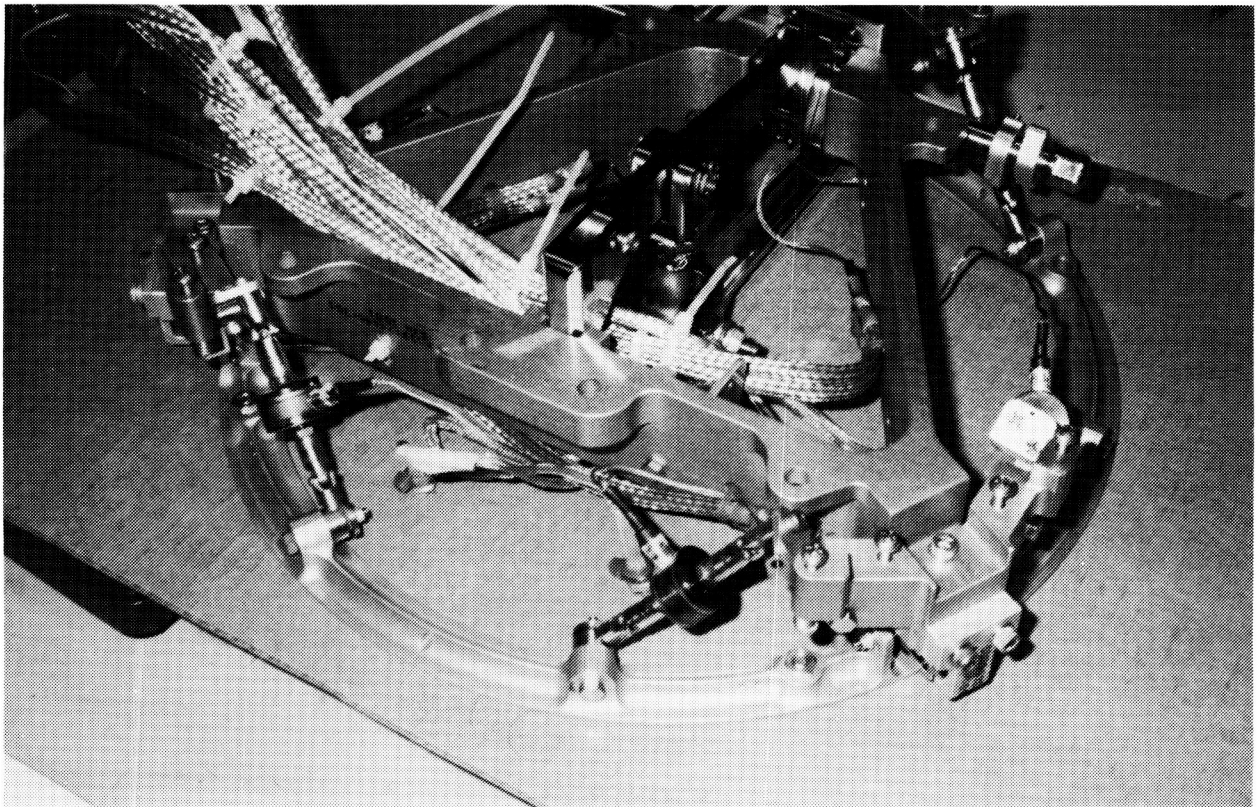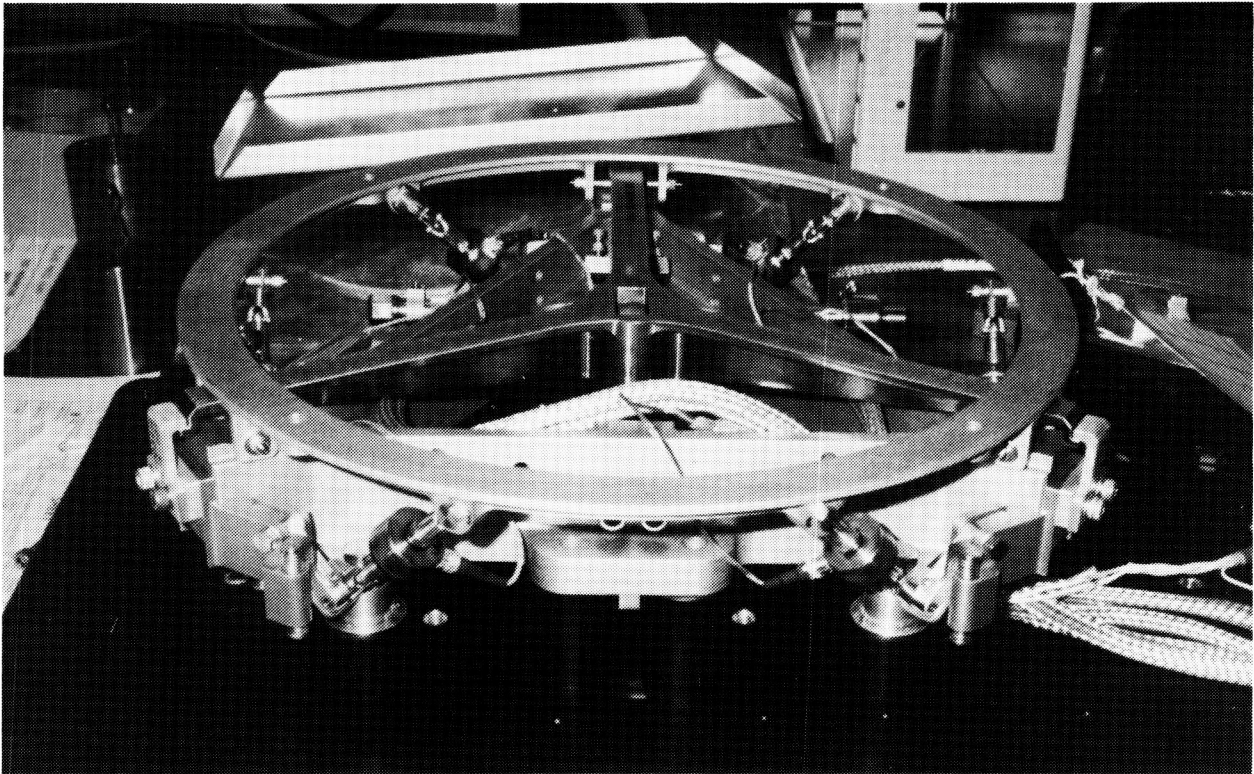
Figure 5. The Load Measurement System with Lock-Out Mechanism

389

Notes - Load Plate Force Derivation

The general equations to calculate the forces acting on the Load Plate can be determined given the following Load Ring geometric properties:

L	= length of load cell strut between pivot points.
β	= angle of load cell relative to x-y plane.
α	= angle of load cell relative to x-axis.
r	= radius of load cell upper pivot points.
PU, PL	= upper and lower universal joint x-y pivot points.
i	= number of struts (6).

First, the angle of each load cell strut projected into the x-y plane is calculated relative to the x-axis.

$$\alpha_i := \text{angle}\left(PUx_i - PLx_i, PUy_i - PLy_i\right) \tag{1}$$

Once the x-axis orientation of each strut is known including the Load Ring geometric properties, the force, **F**, from each load cell is broken down into component **x-y-z** forces and then summed to get the composite forces. The moments acting about the axis of interest on the Load Plate are calculated and then summed to get the composite moments. Any initial force or moment offset is also removed from the result. The equations are given below.

$$Fx_i = F_i \cdot \cos(\beta) \cdot \cos\left(\alpha_i\right)$$
$$Fy_i = F_i \cdot \cos(\beta) \cdot \sin\left(\alpha_i\right)$$
$$Fz_i = F_i \cdot \sin(\beta)$$

$$Mx_i = Fz_i \cdot \left(PUy_i - Yoff\right) + Fy_i \cdot Zoff$$
$$My_i = (-Fz)_i \cdot \left(PUx_i - Xoff\right) - Fx_i \cdot Zoff$$
$$Mz_i = Fy_i \cdot \left(PUx_i - Xoff\right) - Fx_i \cdot \left(PUy_i - Yoff\right) \tag{2}$$

$$FX = \sum_{(i=1..6)} Fx_i - FXoff$$

$$MX = \sum_{(i=1..6)} Mx_i - MXoff$$

$$FY = \sum_{(i=1..6)} Fy_i - FYoff$$

$$MY = \sum_{(i=1..6)} My_i - MYof$$

$$FZ = \sum_{(i=1..6)} Fz_i - FZoff$$

$$MZ = \sum_{(i=1..6)} Mz_i - MZoff \tag{3}$$

To determine the forces, **F**, on each of the load cells, the equations (2) and (3) are combined to form six simultaneous equations (4).

$$FX = \sum_{(i=1..6)} F_i \cdot \cos(\beta) \cdot \cos(\alpha_i) - FXoff$$

$$FY = \sum_{(i=1..6)} F_i \cdot \cos(\beta) \cdot \sin(\alpha_i) - FYoff$$

$$FZ = \sum_{(i=1..6)} F_i \cdot \sin(\beta) - FZoff$$

$$MX = \sum_{(i=1..6)} \left[F_i \cdot \sin(\beta) \cdot (PUy_i - Yoff) + F_i \cdot \cos(\beta) \cdot \sin(\alpha_i) \cdot Zoff \right] - MXoff$$

$$MY = \sum_{(i=1..6)} \left[-F_i \cdot \sin(\beta) \cdot (PUx_i - Xoff) - F_i \cdot \cos(\beta) \cdot \cos(\alpha_i) \cdot Zoff \right] - MYof$$

$$MZ = \sum_{(i=1..6)} \begin{bmatrix} F_i \cdot \cos(\beta) \cdot \sin(\alpha_i) \cdot (PUx_i - Xoff) \dots \\ + (-F)_i \cdot \cos(\beta) \cdot \cos(\alpha_i) \cdot (PUy_i - Yoff) \end{bmatrix} - MZoff$$

(4)

The six equations in (4) are then placed in the following matrix format.

$$\begin{bmatrix} FX \\ FY \\ FZ \\ MX \\ MY \\ MZ \end{bmatrix} = T \cdot F - \begin{bmatrix} FXoff \\ FYoff \\ FZoff \\ MXoff \\ MYoff \\ MZoff \end{bmatrix}$$

(5)

Where the constant matrix **T** in (5) is defined as

$$T_{1,i} := \cos(\beta) \cdot \cos(\alpha_i)$$

$$T_{2,i} := \cos(\beta) \cdot \sin(\alpha_i)$$

$$T_{3,i} := \sin(\beta)$$

$$T_{4,i} := \left[\sin(\beta) \cdot (PUy_i - Yoff) + \cos(\beta) \cdot \sin(\alpha_i) \cdot Zoff \right]$$

$$T_{5,i} := \left[-\sin(\beta) \cdot (PUx_i - Xoff) - \cos(\beta) \cdot \cos(\alpha_i) \cdot Zoff \right]$$

$$T_{6,i} := \left[\cos(\beta) \cdot \sin(\alpha_i) \cdot (PUx_i - Xoff) - \cos(\beta) \cdot \cos(\alpha_i) \cdot (PUy_i - Yoff) \right] \tag{6}$$

/995/20872

4058/7
/0p-

Micromechanisms for Optimism Seismometer

Nicolas Paulin*, Pierre Dumas* and Marc Pochard*

Abstract

Within the framework of the Mars 94 mission, it was decided to design and build a new vertical axis seismometer in order to continuously record the seismic events occurring on the Mars planet. The mission requirements lead to very stringent constraints on power, volume, mass and shock resistance at the landing. The seismometer must be able of automatic leveling and automatic fitting to the local gravity. This paper deals with the mechanisms designed for this seismometer. Due to the short allotted time for its development and low cost, the baseline was to apply the rules of spatial tribology and, when it was possible, to customize existing components for space applications.

Introduction

Seismology is a powerful method to determine the inner structure of a planet, including its crust, mantle and core. As the internal structure of Mars is rather poorly known, it was decided in the framework of the Mars 94 mission to design and build a new vertical axis seismometer in order to record the first observation of marsquake and to get information about the internal structure of the planet. The work was supported by the CNES and the prime contractor was "Institut National des Sciences de l'Univers." SODERN was in charge of the seismometer sensor head.

The main functions of the seismic sensor head are:
• Continuous recording of the seismic events
• Automatic fitting to the local gravity of the landing spot by mass centering
• Automatic leveling in a half cone angle of 40 degrees

The main constraints were:
• Size: <1 dm^3
• Mass: ≤350 g
• Low power consumption
• Shock resistance: 200 g 10 ms
• Able to be sterilized

Seismometer description

The seismometer sensor head (Figure 1) is shared in two parts: the packaging and a seismic sensor. The packaging must protect the seismic sensor from shock during landing and a caging mechanism was designed to do this.

The seismic sensor is a leaf spring sensor. It uses an inertial mass of 50 g suspended like a pendulum by a leaf spring at one end and pivoting with respect to the mainframe at the other end.

---

* SODERN, Brevannes, France

The displacement of the seismic mass is recorded by two transducers. The first transducer is a low-power differential capacitive transducer, and in order to keep the mass in mid position between the two electrodes, a feedback is produced by a coil moving through a magnetic field. The second transducer is a velocity transducer based on the coil magnet principle.

In order to fit the local gravity of the landing spot, or to adjust the system after thermoelastic distortion, a movable mass fitted on the boom can be recentered by a micromotor. The sensitivity of the seismometer is expected to be 10^{-8} ms^{-2} in the period range from 0.2 s to 30 s. The seismic sensor is enclosed under vacuum to obtain the best sensitivity. As the small station could land on soil with a tilt of 40 degrees, a leveling mechanism is needed. When vertical is reached by the seismic sensor, it is clamped in position.

Mechanisms requirements, description and tests :

Motor
For development time and money savings, it was decided to use the same motor for several mechanisms. The main requirements for the motor were:
• Torque: up to 50 mN•m
• Mass: less than 10 g
• Size: less than 5 cm^3
• Able to work in vacuum environment
• Able to be sterilized
• Low cost
• Temperature range   -30 °C to +50 °C   in operating mode
                              -50 °C to +80 °C   in non operating mode

The PORTESCAP micro-motor was chosen because of its very low mass (5 g with a 1/1700 gear box) and its very small size. The most difficult problem was for this motor to be able to work in high vacuum, within a large range of temperature, and with very low outgassing. The main difficulties lie with the lubrication of the collector, of the bearing, and of the gear box:
• For the collector, it was decided to avoid any fluid lubricant and to use gold as a solid lubricant.
• For the bearing, the first criterion was to use an oil with a very low outgassing. Two families of oil were selected: a perfluoropolyether (Fomblin Z25 and Krytox) and a hydrocarbon (Pennzane SHF X2000) [1]. Figure 2 gives an idea of the elastohydrodynamic film thickness versus temperature. It appears that Krytox 143AD does not work at low temperature and that Fomblin Z25 has the curve with the lowest slope. The drawback of the PFPE oil (Fomblin Z25) is that it reacts with clean freshly worn steel surfaces. In our case, the operating time is very short, of the order of about ten minutes for the total lifetime, so it appears that Fomblin Z25 could be used and was the best candidate.
• For the gear box, the same basic oil was used, but to be sure that the lubricant will stay in contact, we used the Braycote 601 grease, which is a mixture of Fomblin Z25 oil and polytetrafluoroethylene (PTFE) particules.

A remaining problem was the outgassing of the motor, which was too high even with the new lubricants. To reduce the outgassing, it was decided to bake all the parts at 80 °C under primary vacuum before assembling and to cable with wires insulated with PTFE instead of PVC. Figure 3 gives the torque of the motor at different temperatures.

Caging mechanisms
To withstand shock and vibration during transportation, launching and landing, the seismic sensor needs a caging mechanism. This mechanism is a one shot mechanism.

After leveling on Mars, the seismic sensor must be caged and eventually uncaged for re-leveling if the station moves (e.g., by wind). For mass and space savings, it was decided to use the same motor for the two caging mechanisms. As the motor has a low torque (50 mN•m), great care was taken to reduce parasitic torque due to friction. An elastic linking was done between the motor shaft and the crank arm to avoid flexure on the shaft. A rotative potentiometer was used, and this potentiometer is mounted on a ball bearing to reduce friction torque. Friction compatible couples of materials were selected and solid lubrication based on molybdenum disulphide was used.

Leveling mechanism
Its principle is based on gravity forces. The trade off leads to a double-axis gimbal equipped with unlubricated ball bearings. The ball bearings are preloaded through Belleville spring washers. To reduce the friction on the ball, the bearings have a loose crimped ribbon retainer. The ball bearings were designed in order to avoid false brinelling between the ball and the track under the 200 g shock. Great care was taken to reduce any parasitic torque due to the electrical connections, which are made of very thin flexible printed circuits, the thickness of the tracks is around 7 μm. Figure 4 gives the result of the leveling before and after mechanical tests done on Earth and extrapolated to Mars gravity.

Seismometer sensor
It is designed with a pivot, a seismic mass and a leaf spring. To obtain a high sensitivity, it is necessary to reduce the noise of the seismometer. Even if the seismometer has no mechanical imperfection, different sources of intrinsic noise must be considered.

One of these noise sources is the Brownian motion of the mass. This noise with an inertial mass M, an angular frequency w_0 and a mechanical quality factor Q corresponds to an acceleration power density [2] of:

$$PSD = \frac{4 k T w_0}{M Q^2}$$

T: absolute temperature
k: Boltzmann's constant

To reach the required sensitivity, a quality factor of 100 is required. This was obtained by taking great care with the clamping at both ends of the leaf spring and to select a pivot with a very low torque and a low structural damping.

The pivot is of the crossed spring type in order to determine the rotation axis with precision. The low torque is obtained by using very thin leaves (25 μm). The low damping is achieved by clamping the leaves with brazing instead of another mechanical fastening, by screws for example. To avoid mechanical damping due to the electrical connections between the seismic mass and the fixed mainframe, it was decided to use the leaves of the pivot as electrical connections. This imposed brazing the leaves on a ceramic. To withstand the shock at 200 g, the trade-off leads to a pivot flexible enough to be able to down on stops under the constraints.

Recentering mechanism
This mechanism compensates the difference between the theoretical gravity of Mars and the gravity at the landing spot, by moving the location of the center of gravity of the seismic mass. This mechanism used the same motor as the caging mechanism. The motor assembly moves along an Archimedes' screw. The lubrication is a solid lubrication based on compatible materials (polyimide reinforced with graphite on copper alloy). During the outgassing of the seismometer in vacuum at 80 °C, the polyimide part bent, and it was necessary to loosen up a bit this part with the Archimedes' screw.

Velocity sensor
It works on the coil magnet principle. It was designed with a generator constant of 140 $ms^{-1}v^{-1}$, which gives a resolution of 1 nms^{-1} at the resonance frequency. To achieve this generator constant in a small volume, it is necessary to have very efficient magnets. The trade off leads to using samarium cobalt magnets. The coil is made of a 20-μm-diameter wire. The coil is wound without a shell to save space. Particular care was taken to shield efficiently the velocity sensor for two reasons: the seismometer is located in the vicinity of a very sensitive magnetometer, and the temperature-compensated spring material is ferromagnetic.

Capacitive displacement transducer
It has a very low power consumption. The resolution is about 1 nm. For signal cleanliness, the electronics are hybrided on the transducer.

Electromagnetic actuator
It is built on the same principle as the velocity transducer. This actuator holds a double coil. The first one is used as a feedback actuator for the capacitive displacement transducer and the second one allows testing the seismometer on Earth by balancing the difference of gravity between Mars and Earth with an offset DC current.

Seismometer development and performances

Within two years, this seismometer head was developed and four models manufactured: an engineering model with a leaf spring designed for Earth gravity, two flight models with leaf springs for Mars gravity, and a spare model. The engineering model has operated since January, 1994, and two days after its starting it recorded in Paris the Los Angeles (Northridge) Earthquake. Despite its small size, OPTIMISM's performance is similar with other good seismometers, and Figure 5 compares its performances with an STS seismometer [3].

Conclusion

A new vertical axis seismometer was designed to record the marsquake in order to get information about the internal structure. This seismometer will continuously record the seismic events, it will be capable of automatic leveling in a half cone tilt of 40 degrees, and will adjust automatically to the local gravity of the landing spot by mass centering.
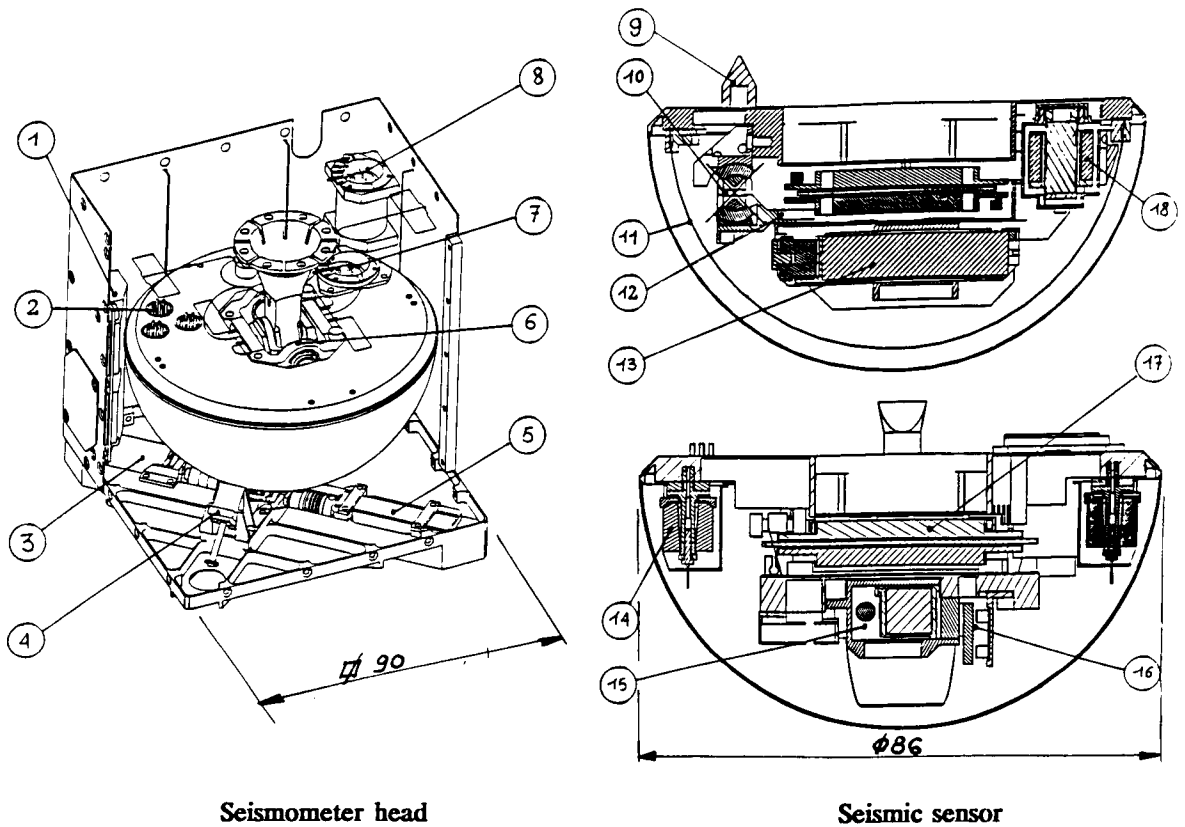
This seismometer has a very low volume, low mass, and low power consumption.

Computer-aided design was a powerful tool during this development because of the small size and complexity of the parts.

This seismometer needs a number of mechanisms. Because of the short development duration, the design of the mechanisms was based on applying the rules of spatial tribology and, when it was possible, in customizing existing components for space applications.

References

[1]   Caractérisation triboligique de lubrifiants pour applications sous vide
       Laboratoire de mécanique des contacts. R et T CNES (1992)

[2]   Usher, et al. The design of miniature wideband seismometers.
       Geophys. J 55, 605 613 (1978)

[3]   E. Wielandt, G. Streckeisen. The leaf spring seismometer: design and
       performance. Bulletin of the Seismological Society of America, Vol.72 N.6, pp
       2349-2367 (Dec 1982)

Seismometer head

Seismic sensor

1. Front end electronics
2. Sealed hermetic connector
3. Rotative potentiometer
4. Caging mechanism
5. Motor
6. Double gimbal
7. Mobile tiltmeter
8. Fixed tiltmeter
9. Pip

10. Pivot
11. Leaf spring
12. Boom
13. Motor
14. Getter
15. Recentering mechanism
16. Linear potentiometer
17. Capacitive displacement transducer with hybrided electronic
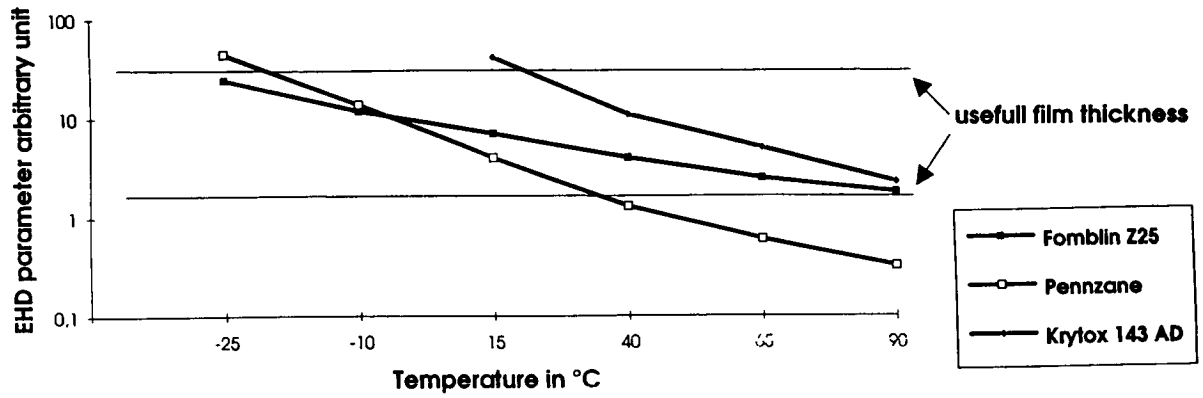18. Velocity transducer and feed back actuator

Figure 1 - Optimism seismometer

Figure 2 - Behavior of some "space" oils

distance in 0.1 mm
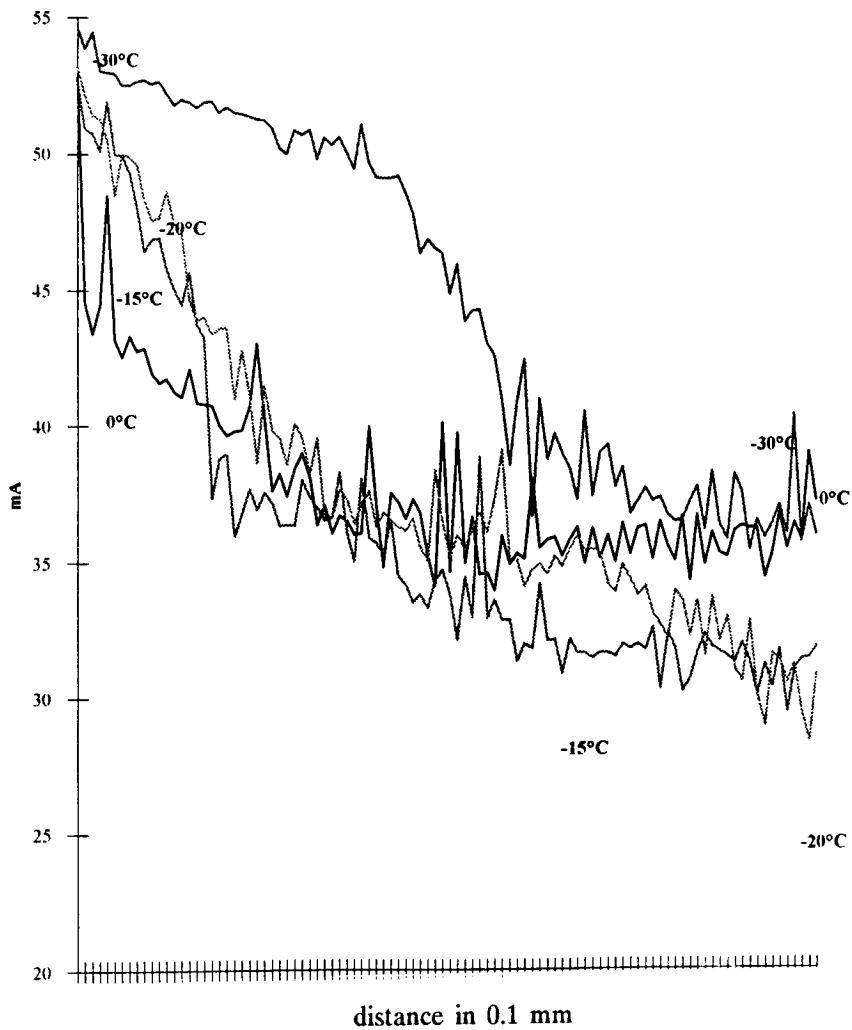
Figure 3 - Motor torque at different temperatures
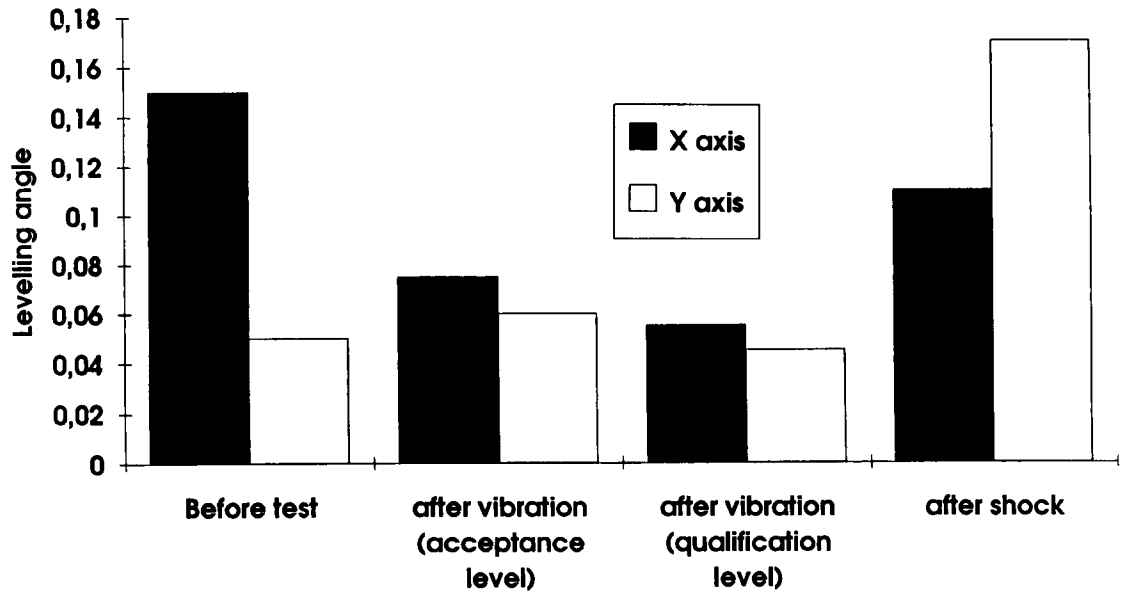
Figure 4 - Leveling accuracy
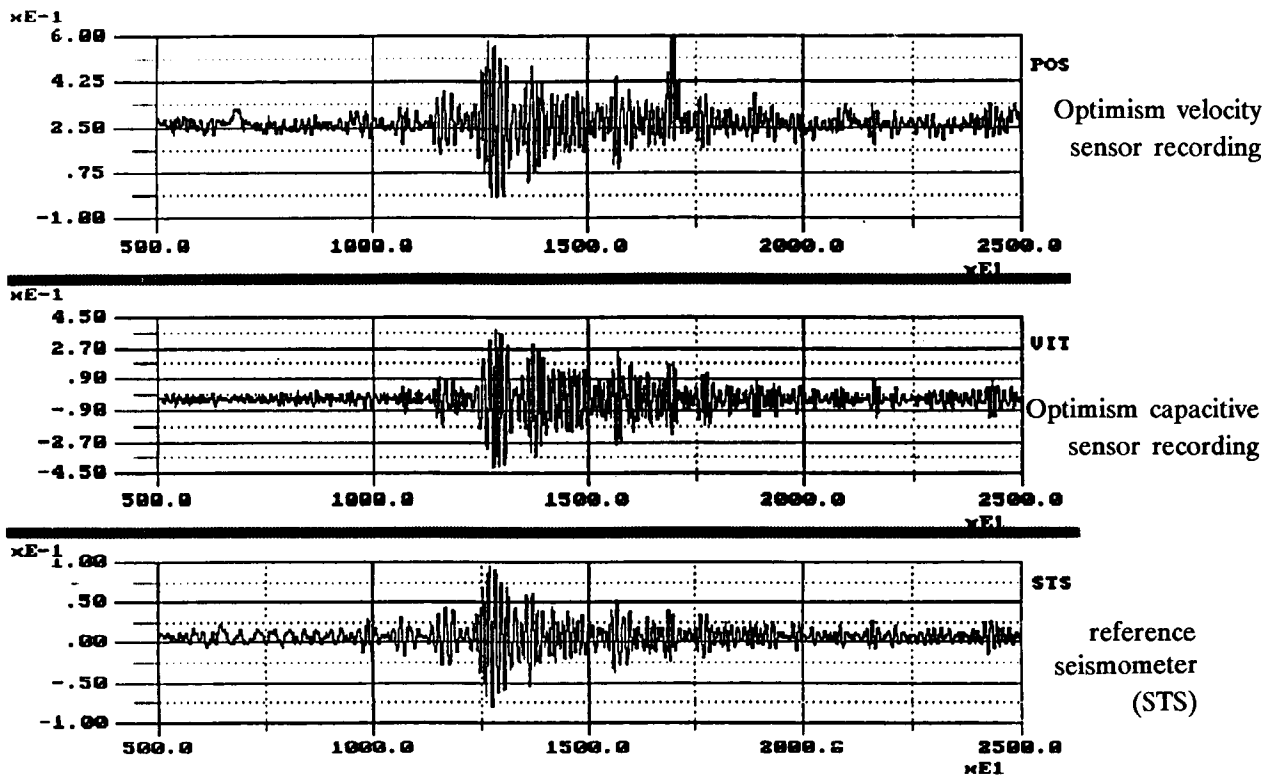
Figure 5 - 1994 Los Angeles (Northridge) earthquake recorded in Paris by Optimism

1. AGENCY USE ONLY (Leave Blank)	2. REPORT DATE May/95	3. REPORT TYPE AND DATES COVERED Conference Publication	
4. TITLE AND SUBTITLE 29th Aerospace Mechanisms Symposium			5. FUNDING NUMBERS
6. AUTHOR(S) William C. Schneider, Ph.D., Compiler			
7. PERFORMING ORGANIZATION NAME(S) AND ADDRESS(ES) Lyndon B. Johnson Space Center Houston, Texas 77058			8. PERFORMING ORGANIZATION REPORT NUMBERS S-794
9. SPONSORING/MONITORING AGENCY NAME(S) AND ADDRESS(ES) National Aeronautics and Space Administration Washington, D.C. 20546-0001			10. SPONSORING/MONITORING AGENCY REPORT NUMBER CP-3293

11. SUPPLEMENTARY NOTES

Proceedings of a symposium cosponsored by Lyndon B. Johnson Space Center and Lockheed Missiles and Space Company, Inc., Sunnyvale, CA 94088, and held at South Shore Harbour Conference Facility, League City, Texas, May 17-19, 1995. Responsible person is William C. Schneider, Ph.D., Engineering Directorate, telephone number 713-483-0313.

12a. DISTRIBUTION/AVAILABILITY STATEMENT Unclassified/Unlimited Available from the NASA Center for AeroSpace Information (CASI) 800 Elkridge Landing Road Linthicum Heights, MD 21090-2934 (301) 621-0390 Subject Category: 15	12b. DISTRIBUTION CODE

13. ABSTRACT *(Maximum 200 words)*

The proceedings of the 29th Aerospace Mechanisms Symposium, which was hosted by NASA Johnson Space Center and held at the South Shore Harbour Conference Facility on May 17-19, 1995, are reported. Technological areas covered include actuators, aerospace mechanism applications for ground support equipment, lubricants, pointing mechanisms joints, bearings, release devices, booms, robotic mechanisms, and other mechanisms for spacecraft.

14. SUBJECT TERMS spacecraft components, array deployment; robotics; end effectors; actuators; dampers; reaction compensation; pointing mechanisms; antenna deployment; booms	15. NUMBER OF PAGES 414
	16. PRICE CODE

17. SECURITY CLASSIFICATION OF REPORT Unclassified	18. SECURITY CLASSIFICATION OF THIS PAGE Unclassified	19. SECURITY CLASSIFICATION OF ABSTRACT Unclassified	20. LIMITATION OF ABSTRACT Unlimited